Electrical and Thermal Performance Evaluations for Repurposed Electric Vehicle Batteries in Second Life Electricity Grid Energy Storage

by

Christopher White

Submitted in partial fulfilment of the requirements
for the degree of Doctor of Philosophy

at

Dalhousie University
Halifax, Nova Scotia
April 2025

Dalhousie University is located in Mi'kma'ki, the ancestral and unceded territory of the Mi'kmaq. We are all Treaty people.

© Copyright by Christopher White, 2025

I dedicate this work to the forces that guided me to the finish line.

TABLE OF CONTENTS

List of Tables xi

List of Figures xii

Abstract xxiii

List of Abbreviations and Symbols xxiv

Acknowledgements xxx

Chapter 1 Introduction 1

Chapter 2 Review of Lithium-Ion Battery Technology 6

2.1. Cell Design 6

2.1.1. Components 6

2.1.2. Intercalation Reactions 7

2.1.3. Positive Electrode Materials 9

2.1.4. Negative Electrode Materials 13

2.1.5. Cell Assembly 15

2.2. Reversible Voltage 17

2.2.1. Thermodynamics 18

2.2.2. Mean Field Theory 20

2.2.3. Ordered Lithium Distributions 23

2.2.4. Solid State Redox Reactions 28

2.2.5. Alloyed Electrode Materials 36

2.2.6. Blended Electrode Materials 41

2.2.7. Full Cell Voltage 43

2.3. Operational Overpotentials 45

2.3.1. Ohmic Resistance 47

2.3.2. Charge Transfer 47

2.3.3. Electrolyte Concentration Gradients 48

2.3.4. Solid State Diffusion 49

2.3.5. Impedance Evaluation 50
2.4. Energy Storage 52
2.4.1. Energy Evaluation 53
2.4.2. Energy Utilization 54
2.4.3. Irreversible Energy 57
2.5. Degradation 59
2.5.1. Degradation Mechanisms 60
2.5.2. Influences on Degradation 64
2.5.3. Degradation Evaluation 65
2.6. Temperature 69
2.6.1. Thermodynamics 70
2.6.2. Heat Capacity 72
2.6.3. Heat Generation 74
2.6.4. Heat Dissipation 78
2.6.5. Heat Diffusion 83
2.6.6. Thermal Runaway 85
2.6.7. Temperature Evaluation 87
2.7. Chapter Summary 88
Chapter 3 Review of Second-Life Battery Technology 89
3.1. Electric Vehicle Batteries 89
3.1.1. Design Parameters 90
3.1.2. Battery Management Systems 93
3.1.3. Thermal Management Systems 95
3.1.4. End of Vehicular Life 99
3.2. Electricity Grid Operation 103
3.2.1. Electricity Supply and Demand 103
3.2.2. Electricity Grid Frequency 106

3.2.3. Electricity Markets 111
3.3. Stationary Energy Storage Applications 117
3.3.1. Grid Capacity 118
3.3.2. Grid Energy Management 119
3.3.3. Grid Ancillary Services 124
3.3.4. Consumer Services 126
3.3.5. Stacked Services 127
3.4. Prospects and Challenges for Second-life Batteries 128
3.4.1. Technical Considerations 128
3.4.2. Economic Considerations 139
3.4.3. Environmental and Social Considerations 143
3.4.4. Regulatory and Policy Considerations 144
3.4.5. Industry Development 147
3.5. Gaps in Second-life Battery Research 148
3.5.1. Pack-level Performance Studies 148
3.5.2. Comparative Performance Studies 149
3.5.3. Performance Test Methods 151
3.5.4. Thermal Models 154
3.5.5. Proposed Research Questions 156
3.6. Chapter Summary 157
Chapter 4 Methods for Experimental Evaluation of Second-Life Battery Performance 158
4.1. Acquired EV Battery Packs 158
4.1.1. Pack Specifications 159
4.1.2. Pack Preparations 163
4.2. Test Setup 167
4.2.1. Laboratory Equipment 167
4.2.2. Test Apparatus 169

4.3. Baseline Capacity Test 170
4.4. Symmetrical Constant Power Test 172
4.4.1. Test Protocol 172
4.4.2. Test Sequence 174
4.4.3. Test Parameters 176
4.5. Performance Evaluation 178
4.5.1. Electrical Performance Metrics 179
4.5.2. Thermal Performance Metrics 185
4.6. Chapter Summary 188
Chapter 5 Comparative Analysis of Electrical and Thermal Performance for Five Second-Life Battery packs 190
5.1. Baseline Capacity 190
5.2. Voltage Profiles 192
5.2.1. Cell Characteristics 192
5.2.2. Response to Different Power Rates 194
5.2.3. Impact of Thermal Management 197
5.2.4. Consistency 198
5.3. Electrical Performance Results 201
5.3.1. Energy Density 203
5.3.2. Energy Utilization Ratio 205
5.3.3. Unutilized Energy Components 208
5.3.4. Energy Efficiency 209
5.3.5. Dependence on Internal Resistance 212
5.3.6. Heat generation 215
5.4. Thermal Performance Results 217
5.4.1. Temperature Profiles 219
5.4.2. Temperature Rise 222
5.4.3. Cooldown Requirements 226

5.4.4. Temperature Distribution 231
5.4.5. Dependence on Heat Generation 239
5.5. Repeatability of Results 242
5.6. Impact of Degradation on Performance Metrics 246
5.6.1. Impact on Voltage Profile 247
5.6.2. Impact on Discharge Energy 250
5.6.3. Impact on Energy Efficiency 252
5.6.4. Impact on Heat Generation 254
5.6.5. Impact on Temperature Rise 256
5.7. Ranking Battery Performance 257
5.7.1. Volume Score 258
5.7.2. Energy Score 260
5.7.3. Thermal Score 264
5.7.4. Overall Performance Rankings 269
5.8. Chapter Summary 273
Chapter 6 Performance Extrapolation Model for Second-Life Battery Packs 275
6.1. Empirical Relationships to Describe Battery Performance 275
6.1.1. Discharge Energy 275
6.1.2. Energy Efficiency 281
6.1.3. Heat Generation 284
6.1.4. Temperature Rise 287
6.2. Performance Extrapolation Methods 291
6.2.1. Extrapolative Empirical Equations for Battery Performance 291
6.2.2. Extrapolation from Two Experimental Datasets 295
6.2.3. Extrapolation from a Single Experimental Dataset 296
6.3. Accuracy of Performance Extrapolation Model 303
6.3.1. Estimation of Model Parameters 304

6.3.2. Extrapolation of Performance Metrics 307
6.4. Condensed Performance Characterization Test Methods 313
6.4.1. Test Protocols 313
6.4.2. Test Parameters 317
6.4.3. Test Evaluation 321
6.5. Impact of Degradation on Performance Extrapolation Model 324
6.5.1. Impact on Model Parameters 324
6.5.2. Impact on Pulse Method 329
6.5.3. Impact on Test Parameters 330
6.6. Limitations and Recommendations 333
6.6.1. Limitations of Experimental Data 333
6.6.2. Limitations of Single-Dataset Solution 335
6.6.3. Extension to Other Cycle Types 335
6.6.4. Specification of Module Volume 338
6.6.5. Recommended Use Cases 343
6.7. Chapter Summary 344
Chapter 7 Spatial Extrapolation Model For Second-Life Battery Pack Temperatures 347
7.1. Motivation and Concept 347
7.2. Thermal Model 349
7.2.1. Battery Characteristics 350
7.2.2. Simplified Thermal Network 353
7.2.3. System Equations 355
7.2.4. Numerical Solutions 357
7.2.5. Heat Generation Approximation 359
7.2.6. Functionality 362
7.3. Heat Dissipation Parameters 364
7.3.1. Pack Geometry 365

7.3.2. Natural Convection 367
7.3.3. Radiation 370
7.3.4. Practical Expression 372
7.3.5. Finalized Model 375
7.4. Parameter Optimization 377
7.4.1. Empirical Training Data 378
7.4.2. Curve Fitting 380
7.4.3. Heat Generation Constraints 381
7.4.4. Parameter Estimates and Constraints 386
7.5. Results 393
7.5.1. Model Accuracy 394
7.5.2. Inherent Error Decay 397
7.5.3. Heat Validation 399
7.5.4. Parameter Validation 401
7.5.5. Sensitivity Analysis 404
7.5.6. Model Versatility 410
7.5.7. Practical Case Study 413
7.6. Future SETS Research 415
7.6.1. Heat Generation Modelling 416
7.6.2. Diverse Training Data 419
7.6.3. Customized Parameter Optimization 420
7.6.4. Different SETS Models 420
7.6.5. Recommended Approach 421

7.7. Chapter Summary 423
Chapter 8 Conclusions and Recommendations 425
8.1. Methods for Evaluating Second-life Battery Performance 425
8.2. Electrical Performance of Second-life Batteries 427
8.3. Thermal Performance of Second-life Battery Packs 429
8.4. Recommendations for Industry 431
8.5. Recommendations for Research 432
References 434
Appendix A Analytical Solution for SETS Model System Equations 466
Appendix B Recursive Solution for SETS Model System Equations 468
Appendix C Uncertainty Analysis 470
Appendix D Copyright License Agreement 474

LIST OF TABLES

Table 2.1 Comparison of key characteristics for common positive electrode materials. 12

Table 2.2 Summary of the main degradation mechanisms for various lithium-ion battery electrode materials. Significant degradation rates are represented by 'X' while problematic degradation rates are represented by shading. 60

Table 2.3 Approximate specific heat capacities for various lithium-ion cell components. Based on reviewed data from [183]. 73

Table 4.1 Specifications of acquired EV battery packs. 161

Table 4.2 Baseline capacity test parameters applied to EV battery packs. 171

Table 4.3 Summary of SCP test protocol. 174

Table 4.4 Summary of SCP test sequence. 175

Table 4.5 Selected SCP test parameters applied to five EV battery packs. 177

Table 4.6 Primary performance metrics used to evaluate SCP test results. 178

Table 5.1 Results of baseline capacity tests. 191

Table 5.2 Measured electrical performance results from the SCP tests. 201

Table 5.3 Calculated electrical performance results from the SCP tests. 202

Table 5.4 Measured thermal performance results from the SCP tests. 218

Table 5.5 Calculated thermal performance results from the SCP tests. 219

Table 6.1 Summary of novel mathematical contributions 345

Table 7.1 Properties of air evaluated at a 300 K average boundary layer temperature. 368

Table 7.2 Summary of equations used in the SETS model. 376

Table 7.3 Estimated values and ranges for physical and SETS model parameters. 392

Table 7.4 Heat capacity calculations for each cell and constant-power rate. 401

Table 7.5 Comparison of optimized physical parameters to initial estimates and constraints. 402

Table 7.6 Comparison of optimized convection coefficients to initial estimates. 413

LIST OF FIGURES

Figure 1.1 Projected growth in annual battery demand for transportation and electricity sectors. Based on data from [3] and [4]. 2

Figure 2.1 Simplified illustration showing the basic components of a lithium-ion battery during discharge (left) and charge (right). Images of electrode material structures were created in VESTA software [23] using lattice structure data from the Materials Project [24]. 7

Figure 2.2 Simplified cross-sectional illustration of a single intercalation electrode particle immersed in electrolyte with Li^+ intercalation reactions occurring at the surface and intercalated Li^+ diffusing inward such that additional surface reactions can take place (for visual clarity, electrons are not shown)..... 9

Figure 2.3 Lithiated crystal structures for LCO (layered), LMO (spinel), and LFP (olivine) positive electrode materials. Images were created in VESTA software [23] using lattice structure data from the Materials Project [24]. 10

Figure 2.4 Two types of Li^+ intercalation sites in three common positive electrode materials. Images were created in VESTA software [23] using lattice structure data from the Materials Project [24]. 11

Figure 2.5 Layers of lithiated graphite (LiC_6) viewed from two angles. Images were created in VESTA software [23] using lattice structure data from the Materials Project [24]..... 14

Figure 2.6 Illustration of cell components assembled into a 'cell stack'. 15

Figure 2.7 The three main lithium-ion cell formats: cylindrical, pouch, and prismatic. 16

Figure 2.8 Simplified breakdown of the main factors that determine the operational voltage of a lithium-ion battery. 17

Figure 2.9 Experimental voltage data for a $LiMo_6Se_8$ electrode fitted with the model given in Equation 2.10. Based on data and figures from [81] and [83]. 22

Figure 2.10 Illustrative example showing how entropy and Li^+ interactions impact the voltage profile based on Equation 2.10. 23

Figure 2.11 Illustrative example of an ordered state occurring in a Li^+ intercalation layer at a fractional x value ($x = 1/3$ is shown) and the corresponding drop in the voltage profile. This scenario could result from repulsive Li^+ interactions or one third of the host sites having a lower site energy than the others. 24

Figure 2.12 Simplified illustration of the lattice expansion and staging phenomenon observed during intercalation of a graphite electrode. 26

Figure 2.13 Simplified illustration of the 'shrinking core' model for a first-order phase transition during intercalation into a single graphite particle. 27

Figure 2.14 Illustration showing how staging and phase transitions impact the voltage profile of a graphite electrode during the intercalation process. Based on data and figures from [85], [93]. 28

Figure 2.15 Simplified illustration of solid state redox reaction during the intercalation of lithium into graphite..... 30

Figure 2.16 Simplified illustration of solid state redox reaction during the intercalation of lithium into LCO..... 32

Figure 2.17 Simplified illustration of solid state redox reactions during the intercalation of lithium into LCO (left), LMO (middle) and LFP (right)..... 33

Figure 2.18 Comparison of discharge voltage profiles plotted against lithium content (left) and specific capacity (right) for LCO, LMO and LFP positive electrodes. Based on data and figures from [107]. 35

Figure 2.19 Simplified illustration of solid-state redox reactions occurring during the intercalation of lithium into NMC111. The reacting transition metal cation in each step is highlighted in blue. 38

Figure 2.20 Comparison of voltage profiles for LCO, LNO, NMC111, and NCA during first charge. Based on data and figures from [39]. 39

Figure 2.21 Comparison of discharge voltage profiles for various compositions of cobalt-substituted LNO (left) and NMC (right). Based on data and figures from [31], [124]..... 40

Figure 2.22 Comparison of discharge voltage profiles for NMC-LMO blended electrodes. Based on data and figures from [128]..... 42

Figure 2.23 Comparison of discharge and charge voltage profiles for graphite-silicon blended electrodes. Based on data and figures from [66], [129]..... 43

Figure 2.24 Illustrative example showing how the voltage of a full lithium-ion cell is influenced by its positive electrode and negative electrode depending on their relative capacities. Based on data and figures from [85], [93], [124]..... 45

Figure 2.25 Example of an equivalent circuit used to model the overpotentials that arise when current is flowing through a battery..... 46

Figure 2.26 Example of the concentration gradients and overpotentials that can result from limited Li^+ diffusion through the electrolyte and electrode particles. Generated using AutoLion software [145]. 51

Figure 2.27 Illustrative example of how the energy storage utilization of a battery is impacted by small (left) vs large (right) overpotentials, which could be caused by small vs large current, high vs low temperature, or thin vs thick electrode coatings. 55

Figure 2.28 Illustrative example of how degradation affects the internal resistance (left) and coulombic capacity (right) of a lithium-ion battery. 67

Figure 2.29 Examples of differential voltage (top) and incremental capacity (bottom) analysis methods used to evaluate battery degradation. Based on data and figures from [181]. 68

Figure 2.30 Simplified breakdown of the main factors that determine the operational temperature of a lithium-ion battery. 69

Figure 2.31 Examples of reversible heating coefficients for graphite (left) and NCA (right) electrodes with comparisons to voltage profiles as a function of Li^+ content. Based on data and figures from [186]. 75

Figure 2.32 Examples of the net heat generation rate in a NCA/graphite cell during discharge and charge at two different rates. Based on data and figures from [186]. 76

Figure 3.1 Growth in global sales (top) and stock (bottom) of passenger car EVs since 2010. Based on data from [3]. 90

Figure 3.2 Example of a lithium-ion battery from a 2018 Chevrolet Bolt electric car, including single pouch cell (top left); single 10S3P module (top right); open pack comprising eight 10S3P modules and two 8S3P modules (bottom left); and closed pack with housing cover secured in place (bottom right). 91

Figure 3.3 Basic schematic of the main functions of a battery management system. 93

Figure 3.4 Summary of thermal management technologies being researched for EV battery applications. 96

Figure 3.5 Expected quantities of retired EV batteries by size and SOH in the United Kingdom. Based on data from [5]. 101

Figure 3.6 Illustration of EV battery life cycle without repurposing (left) and with repurposing (right). Partially based on figure from [227]. 103

Figure 3.7 Illustrative example of base load, intermediate load, and peak load over a two-day period in winter (left) and autumn (right). Load profiles are based on Nova Scotia hourly net load data from [229]. 104

Figure 3.8 Example of load following and frequency regulation as components of total electricity demand. Based on data and figure from [242]. 107

Figure 3.9 Illustrative example of an electricity grid disruption causing a sudden frequency drop and the time scales of the main system response mechanisms used to restore the frequency. Based on figure from [236]. .. 109

Figure 3.10 Illustrative example of how clearing prices are determined in Alberta's capacity market. Partially based on figure from [246]. 113

Figure 3.11 Illustrative example of how clearing prices are determined in California's day-ahead energy market. Partially based on figure from [247]. 114

Figure 3.12 Illustrative example of how clearing prices are determined in California's real-time energy market. Partially based on figure from [247]. 115

Figure 3.13 Graphical summary of stationary battery energy storage applications. 118

Figure 3.14 Example of battery response to volatile prices in the German real-time energy market. Based on data and figure from [214]. 120

Figure 3.15 Illustrative example of stationary energy storage providing load levelling service over a two-day period. 121

Figure 3.16 Illustrative example of how high solar energy generation impacts the daily net load profile that must be met by other power plants. Based on data and figure from [257]. 124

Figure 3.17 Graphical summary of the EV battery repurposing process. 129

Figure 3.18 Possible repurposing pathways for EV batteries. Partially based on figure from [272]. 130

Figure 3.19 Examples of pack-level (left) and module-level (right) repurposing of Nissan Leaf EV batteries in second-life energy storage applications. 133

Figure 3.20 Simplified examples of two different power conversion architectures for second-life battery systems. Partially based on figures from [291]. 137

Figure 3.21 One rendition of the PNNL test protocol for evaluating the performance of energy storage systems in peak shaving service. Based on data from [339]. 152

Figure 4.1 Five acquired EV battery packs shown in closed cover (left) and open cover (right) configurations. 160

Figure 4.2 Construction of 2019 Tesla Model 3 SR+ battery module. 162

Figure 4.3 Example of test preparations applied to Bolt-18 battery pack. 164

Figure 4.4 Example of test preparations applied to Model3-19 battery pack..... 164

Figure 4.5 Thermal monitoring of five EV battery packs including retrofitted thermocouple placements (left) and applicable liquid flows (right). 166

Figure 4.6 Customized active-liquid thermal management system..... 168

Figure 4.7 Test apparatus used for experimental testing of EV battery packs. 169

Figure 4.8 Example of a baseline capacity test cycle. 170

Figure 4.9 Example of an SCP test cycle. 173

Figure 4.10 Superimposed voltage profiles measured during the coulomb counting verification test (left) and a sample SCP test sequence (right). 176

Figure 4.11 Example of graphical evaluation of energy utilization and energy efficiency at different power rates..... 182

Figure 5.1 Average cell voltage profiles of five EV battery packs measured during a 4 h CC discharge following a CCCV charge. 192

Figure 5.2 Superimposed average cell voltage profiles of five EV battery packs measured during the third cycle of 4 h, 2 h, and 1 h SCP tests..... 195

Figure 5.3 Impact of liquid cooling on superimposed average cell voltage profiles at end of discharge and end of charge. 198

Figure 5.4 Minimum, average, and maximum cell voltage profiles of five EV battery packs measured during the third cycle of a 1 h SCP test. 200

Figure 5.5 Calculated energy densities and specific energies based on 4 h, 2 h, and 1 h SCP tests..... 203

Figure 5.6 Calculated (left) and normalized (right) energy utilization ratios based on 4 h, 2 h, and 1 h SCP tests..... 205

Figure 5.7 Calculated (left) and normalized (right) energy utilization ratios showing significant dependence on temperature at end of charge..... 207

Figure 5.8 Unutilized energy components for 2 h and 1 h tests compared to the 4 h test. 209

Figure 5.9 Calculated (left) and normalized (right) cycle energy efficiencies based on 4 h, 2 h, and 1 h SCP tests..... 210

Figure 5.10 Calculated (left) and normalized (right) cycle energy efficiencies showing no significant dependence on the average cycle temperature..... 211

Figure 5.11 Comparison of calculated (left) and normalized (right) energy efficiency and BOL module energy density showing impacts of cell internal resistance and voltage profile shape on electrical performance.... 213

Figure 5.12 Calculated cycle volumetric heat generation (left) and average volumetric heat generation rate (right) based on 4 h, 2 h, and 1 h SCP tests..... 216

Figure 5.13 Influence of cycle energy efficiency (left) and module energy density (right) on calculated cycle volumetric heat generation. 217

Figure 5.14 Highest pack temperatures and TMS temperature measured during the third cycle of 4 h, 2 h, and 1 h SCP tests. 221

Figure 5.15 Maximum temperature rise above ambient measured during discharge (left) and charge (right) of each SCP test. 223

Figure 5.16 Maximum temperature rise of the full SCP cycle plotted against power-to-energy ratio (left) and cycle average temperature rise (right). ... 225

Figure 5.17 Step durations measured during 4 h, 2 h, and 1 h SCP tests. 227

Figure 5.18 Calculated achievable cycling frequencies plotted against power-to-energy ratio (left) and maximum temperature rise (right). 228

Figure 5.19 Measured cycle cooldown duration (left) and associated calculations for average cooling time constant (right). 230

Figure 5.20 Highest, middle, and lowest pack temperatures and TMS temperatures measured during the third cycle of 1 h SCP tests..... 232

Figure 5.21 Calculated average pack temperature differentials (left) and comparison of average temperature rise for the coolest and of hottest cells/modules measured foreach battery pack (right)..... 236

Figure 5.22 Dependence of maximum temperature rise on cycle volumetric heat generation (left) and average volumetric heat generation rate (right)..... 239

Figure 5.23 Dependence of average temperature rise on cycle volumetric heat generation (left) and average volumetric heat generation rate (right)..... 241

Figure 5.24 Dependence of pack temperature differential on cycle volumetric heat generation (left) and average volumetric heat generation rate (right)..... 242

Figure 5.25 Comparison of energy utilization ratio (left) and cycle energy efficiency (right) results measured during the second and third cycle of each test. 243

Figure 5.26 Comparison of maximum (left) and average (right) temperature rise results measured during the second and third cycle of each test..... 244

Figure 5.27 Comparison of cycle cooldown duration (left) and cooling time constant (right) results measured during the second and third cycle of each test. 245

Figure 5.28 Superimposed average cell voltage profiles for 4 h, 2 h, and 1 h SCP cycles conducted at different SOH levels. 248

Figure 5.29 Measured (left) and estimated BOL (right) module energy densities taken at different SOH levels. 250

Figure 5.30 Calculated (left) and normalized (right) energy utilization ratios taken at different SOH levels. 252

Figure 5.31 Calculated (left) and normalized (right) cycle energy efficiencies taken at different SOH levels. 253

Figure 5.32 Calculated cycle volumetric heat generation (left) and average volumetric heat generation rate (right) taken at different SOH levels. 255

Figure 5.33 Measured maximum (left) and average (right) temperature rise taken at different SOH levels. 257

Figure 5.34 Battery rankings according to volume score. 259

Figure 5.35 Battery rankings according to two unique energy scores and overall energy performance score. 263

Figure 5.36 Battery rankings according to four unique thermal scores and overall thermal performance score. 268

Figure 5.37 Overall performance ranking of EV battery samples for 4 h (left) and 1 h (right) rates according to weighted combinations of volume, energy, and thermal performance scores 270

Figure 5.38 Graphical summary of the proposed performance ranking system. 272

Figure 6.1 Unadjusted Peukert equation (left) and adjusted Peukert equation (right) fitted to measured data as a function of discharge duration 277

Figure 6.2 Measured 4 h and 1 h data (left) used to calculate Peukert numbers (right) 279

Figure 6.3 Empirical energy efficiency equation fitted to measured data as a function of power-to-energy ratio (left) and discharge duration (right). 282

Figure 6.4 Measured 4 h and 1 h data (left) used to calculate energy efficiency exponents (right). 283

Figure 6.5 Empirical heat generation equation fitted to measured data as a function of power-to-energy ratio (left) and discharge duration (right). 285

Figure 6.6 Peukert numbers and energy efficiency exponents (left) used to calculate heat generation exponents (right). 287

Figure 6.7 Empirical temperature rise equations fitted to experimental data for maximum (left) and average (right) temperature rise as a function of average volumetric heat generation rate. 289

Figure 6.8 Comparison of measured average temperature rise data and fitted model as a function of maximum temperature rise (left) and average volumetric heat generation rate (right). 291

Figure 6.9 Ratio of discharge voltage to charge voltage at common SOC values for 4 h, 2 h, and 1 h power rates. 298

Figure 6.10 Results of an SCPP test showing SCP voltage profiles mathematically reconstructed from the SCPP voltage profile (left) and a comparison of the reconstructed SCP voltage profiles to measured SCP voltage profiles (right). 299

Figure 6.11 Comparison of performance extrapolation model parameters determined from the 4 h and 1 h datasets, the two-dataset estimation technique, and the single-dataset estimation technique. 305

Figure 6.12 Measured electrical performance test results compared to values extrapolated from 2 h test results using the single-dataset solution. 308

Figure 6.13 Measured thermal performance test results compared to values extrapolated from 2 h test results using the single-dataset solution. 309

Figure 6.14 Errors produced by two-dataset and single-dataset solutions in extrapolation of electrical performance test results. 311

Figure 6.15 Errors produced by two-dataset and single-dataset solutions in extrapolation of thermal performance test results. 312

Figure 6.16 Proposed condensed test methods for performance characterization of second-life battery packs utilizing the two-dataset (top) and single-dataset (bottom) extrapolation techniques. 315

Figure 6.17 Energy utilization ratios from 4 h (left) and 2 h (right) SCP tests as a function of module rated energy density. 319

Figure 6.18 Visualization of the proposed condensed test procedure and performance extrapolation model utilizing the single-dataset extrapolation technique. Purple represents battery specifications, red represents test inputs, green represents measured test results, yellow represents user-specified model inputs, pale blue represents intermediate model calculations, and bright blue represents desired outcomes. 322

Figure 6.19 Adjusted Peukert equation fitted to results measured at different SOH levels (left) and associated Peukert numbers (right). 325

Figure 6.20 Empirical energy efficiency equation fitted to results measured at different SOH levels (left) and associated energy efficiency exponents (right)..... 326

Figure 6.21 Empirical heat generation equation fitted to results measured at different SOH levels (left) and associated heat generation exponents (right)..... 327

Figure 6.22 Empirical temperature rise equation fitted to experimental results measured at different SOH levels for maximum (left) and average (right) temperature rise as a function of average volumetric heat generation rate. 328

Figure 6.23 Voltage profiles (top) and voltage ratios (bottom) compared for the same battery pack at 95 % SOH (left) and 87 % SOH (right). 330

Figure 6.24 Energy utilization ratios from 4 h (left) and 2 h (right) SCP tests at different SOH levels..... 331

Figure 6.25 Proposed SOH-dependent technique for estimating 4 h (left) and 2 h (right) energy utilization ratios..... 332

Figure 6.26 Peukert number (left) and energy utilization ratio (right) as a function of pack rated specific energy..... 340

Figure 6.27 Empirical temperature rise equations fitted to experimental data for maximum (left) and average (right) temperature rise as a function of pack average specific heat generation rate. 341

Figure 7.1 The built-in thermistors of a 2019 Tesla Model 3 SR+ battery pack. 350

Figure 7.2 Illustration of heat transfer in an operational Tesla Model 3 SR+ battery pack. Red arrows represent heat conduction pathways. Blue arrows represent convection and radiation pathways. Not drawn to scale. 352

Figure 7.3 Illustration of the proposed simplified thermal model. Red arrows represent heat conduction pathways. Blue arrows represent convection and radiation pathways. Yellow masses generate heat, while grey masses do not. Not drawn to scale. 354

Figure 7.4 Visualization of the proposed SETS model. 363

Figure 7.5 Dimensions of the Tesla Model 3 SR+ battery modules and the number of cells adjacent to the front and side surfaces. Not drawn to scale. 366

Figure 7.6 Approximation of the radiation equation over a typical operational battery temperature range using linearization and scaling. 371

Figure 7.7 Expected values of convective and radiative components of the heat dissipation coefficients over a typical operational battery temperature range. 372

Figure 7.8 Practical expression of the heat dissipation coefficients with inconsistent accuracy. 374

Figure 7.9 Practical expression of the heat dissipation coefficients with enhanced accuracy 375

Figure 7.10 Visualization of the finalized SETS model with temperature-dependent heat dissipation coefficients. 377

Figure 7.11 Experimental datasets used for empirical determination of SETS model parameters, including 4 h (top), 2 h (middle), and 1 h (bottom) constant power tests conducted on a 2019 Tesla Model 3 SR+ battery pack. 379

Figure 7.12 Visualization of parameter optimization scheme applied to the SETS model. 380

Figure 7.13 Example of time-series data (left) converted to a summation of total cycle heat generation for the third cycle of a 2 h constant-power test conducted on a 2019 Tesla Model 3 SR+ battery pack (cell X data shown). 383

Figure 7.14 Calculated heat generation for cell X and cell Z during the third cycle of each test 383

Figure 7.15 Model used to estimate thermal conductivity between cell Z and cell X. 390

Figure 7.16 Updated parameter optimization scheme including physical constraints. 393

Figure 7.17 Optimized parameters applied to the SETS model with an empirical dataset featuring three tests at three different constant-power rates. 395

Figure 7.18 Effectiveness of modelling heat diffusion lag in T_z using a $T_{z'}$ 'pseudo-temperature'. 396

Figure 7.19 Illustrative example of inherent error decay in the SETS model. 397

Figure 7.20 Adiabatic temperature change datapoints used to determine cell heat capacity. 400

Figure 7.21 Sensitivity analysis results for all seven physical parameters. 405

Figure 7.22 Changes in $h^*_{conv,z}$ compensated by changes in $k_{z'z}$ and $k_{z'x}$ 406

Figure 7.23 Correlation between λ_z and $\tau_{z'z}$ (left) and between $m_{z'}/m_{cell}$ and $k_{z'z}$ (right). All datapoints give acceptable accuracy for T_z and T_x in the SETS model. 408

Figure 7.24 Correlation between $k_{z'z}$ and $m_{cell}c_p$. All datapoints give acceptable accuracy for T_z and T_x in the SETS model 408

Figure 7.25 Three viable sets of parameter values illustrating the effect of λ_z and $\tau_{z'z}$ on the modelled $T_{z'}$ profile. 409

Figure 7.26 SETS model results with re-optimized values of heat dissipation parameters $\tau_{z\infty}$ and $\tau_{x\infty}$ based on a new empirical dataset with the battery housing cover removed. 412

Figure 7.27 Example of how a SETS model can predict a more accurate battery pack temperature differential during second-life operation based on real-time BMS temperature data and pre-determined SETS model parameters. 414

Figure 7.28 Voltage and heat generation for four different cells in the Tesla Model 3 SR+ battery pack during a single cycle at three different power rates 416

Figure 7.29 Graphical summary of advanced SETS model concept proposed for future research. 418

ABSTRACT

The yearly production of lithium-ion batteries for electric vehicles (EVs) is expected to increase sevenfold by 2035 to enable decarbonization of the transportation sector. When an EV battery is removed from EV service, it can usually be repurposed to serve a 'second life' in electricity grid energy storage before it is finally recycled to recover key materials. Second-life batteries have been the subject of much research and development in recent years, but there are still many challenges that need to be overcome in this new industry. For example, since there are many different EV battery designs with unique performance characteristics, second-life battery researchers and developers must have the means to characterize the electrical and thermal performance of any EV battery in a consistent and comparable way. The adoption of appropriate performance evaluation methods would allow researchers and developers to assess and compare the various strengths and weaknesses of different EV batteries for the purposes of modelling, designing, and operating second-life battery systems.

This thesis presents novel research focused on evaluating the second-life performance of used EV batteries. The objective is to develop suitable electrical and thermal performance evaluation methods, and to use these methods to compare the second-life performance of different EV battery designs. To achieve this objective, five unique EV batteries are acquired and tested at the pack level using a series of constant-power tests. The test results are used to compare the five battery packs according to 21 performance metrics, revealing significant performance differences among different EV battery designs. Despite these differences, the test results are shown to vary predictably with the applied power rate based on a set of novel empirical equations, leading to a newly proposed method for standardized second-life battery performance characterization. A specialized thermal model is also developed to facilitate real-time monitoring of temperature distributions in second-life battery packs. Altogether, this research contributes powerful new tools and practical insights for the second-life battery industry.

LIST OF ABBREVIATIONS AND SYMBOLS

Abbreviations

AC	Alternating current
AGC	Automatic generation control
AL	Active liquid
BMS	Battery management system
BOL	Beginning of life
CAN	Controller area network
CC	Constant current
CCCV	Constant current constant voltage
CP	Constant power
CPCV	Constant power constant voltage
CV	Constant voltage
DC	Direct current
DV	Differential voltage
e^-	Electron(s)
EIS	Electrochemical impedance spectroscopy
EOL	End of life
EOVL	End of vehicular life
EPR	Extended producer responsibility
EV	Electric vehicle
IC	Incremental capacity
ISO	Independent system operator
Li^+	Lithium ion(s)
LAM	Loss of active material
LCO	Lithium cobalt oxide
LFP	Lithium iron phosphate
LLI	Loss of lithium inventory
LMO	Lithium manganese oxide
LNO	Lithium nickel oxide
LR	Long range
LTO	Lithium titanate

NCA	Lithium nickel cobalt aluminum oxide
NMC	Lithium nickel manganese cobalt oxide
NMCA	Lithium nickel manganese cobalt aluminum oxide
PA	Passive air
PNNL	Pacific Northwest National Laboratory
RTO	Regional transmission organization
RUL	Remaining useful life
SCP	Symmetrical constant power
SCPP	Symmetrical constant power pulse
SEI	Solid electrolyte interphase
SETS	Spatially extrapolation temperature sensor
SOC	State of charge
SOH	State of health
SR	Standard range
TMS	Thermal management system

Symbols

A	Area, m^2 or cm^2
b_η	Empirical energy efficiency exponent (dimensionless)
b_q	Empirical heat generation exponent (dimensionless)
$b_{T_{\max}}$	Empirical maximum temperature rise exponent (dimensionless)
$b_{T_{\text{avg}}}$	Empirical average temperature rise exponent (dimensionless)
Bi	Biot number (dimensionless)
c_p	Specific heat capacity at constant pressure, J/kg·K
C_p	Heat capacity at constant pressure, J/K
D	Diffusion coefficient, cm^2/s
e	Elementary charge, 1.602×10^{-19} C
E	Battery electrical energy, Wh
E_a	Activation energy of a chemical reaction, J
$\bar{E}_m$	Battery specific energy, Wh/kg
$\bar{E}_v$	Battery energy density, Wh/L

Err	Error in numerical model, °C ,
f_{cyc}	Achievable daily cycling frequency in energy arbitrage, cycles/day
F	Faraday constant, 96,485 C/mol
g	Acceleration due to gravity, 9.81 m/s^2
G	Gibbs free energy, J
Gr	Grashof number (dimensionless)
h	Heat dissipation coefficient, W/m^2·K
H	Enthalpy, J
i	Variable time increment or chemical species (dimensionless)
I	Current, A
I_∞	Theoretical maximum exchange current of an electrochemical reaction, A
j	Exact time increment or chemical species (dimensionless)
k	Thermal conductivity, W/m·K
$k_\parallel$	Directional thermal conductivity parallel to electrode layers, W/m·K
$k_\perp$	Directional thermal conductivity perpendicular to electrode layers, W/m·K
k_B	Boltzmann constant, 1.381×10^{-23} J/K
L	Length or distance, m or cm
m	Mass, kg
n	Amount of a chemical species, mol
n_{Li}	Number of intercalated lithium ions
n_{int}	Number of interacting lithium ions in nearby intercalation sites
N	Number of intercalation sites
Nu	Nusselt number (dimensionless)
p	Pressure, Pa
P	Electrical power, W or kW
Pr	Prandtl number (dimensionless)
q	Heat, J or kJ
$\dot{q}$	Rate of heat flow, W
$\bar{q}_v$	Total volumetric heat generated during a battery test cycle, Wh/L
$\dot{\bar{q}}_v$	Average volumetric heat generation rate during a battery test cycle, W/L
Q	Coulombic capacity, C or Ah
r	Performance score weighting ratio (dimensionless)

R	Battery internal resistance, Ω
Ra	Rayleigh number (dimensionless)
Re	Reynolds number (dimensionless)
S	Entropy , J/K
t	Time or duration, s or h
t_{rate}	Nominal prescribed discharge duration for a battery test, h
T	Temperature, °C or K
T_{BL}	Temperature of the boundary layer between a surface and a fluid stream, K
T_{ctrl}	Temperature control setpoint, °C
T_{s}	Temperature of a surface, °C or K
T_{∞}	Temperature of the ambient environment or a reference fluid, °C or K
ΔT	Temperature change or temperature difference, °C
u_{∞}	Fluid flow speed, m/s
U	Internal energy, J
U_{site}	Site energy of an intercalation host lattice, J
U_{int}	Interaction energy of an intercalation host lattice, J
v	Volume, L or m^3
V	Voltage, V
V_{gap}	Gap between discharge and charge on voltage vs state of charge chart, V
w	Work, J or Wh
$\dot{w}$	Rate of work, W
x	Ratio of filled intercalation sites (dimensionless)
y	Direction of heat transfer, m
Z_{dl}	Double-layer impedance, Ω
Z_{w}	Warburg impedance, Ω
α_{Θ}	Correction factor for modelled adiabatic temperature rate (dimensionless)
α_{σ}	Correction factor for adjusted Peukert equation (dimensionless)
β	Expansion coefficient of a fluid, K^{-1}
γ	Peukert adjustment factor (dimensionless)
$\varepsilon_{\mathrm{rad}}$	Radiative emissivity of a surface (dimensionless)
ζ	Energy utilization ratio, %
ζ^*	Normalized energy utilization ratio, %

η	Cycle energy efficiency, %
η^*	Normalized cycle energy efficiency, %
η_Q	Cycle coulombic efficiency, %
θ	Battery performance score (dimensionless)
Θ	Adiabatic temperature rate, °C/s or °C/h
λ	Cell mass ratio (dimensionless)
μ	Chemical potential, J/mol
ν	Kinematic viscosity of a fluid, m^2/s
ρ	Mass density, kg/m^3
σ	Peukert number (dimensionless)
σ_{SB}	Stefan-Boltzmann constant, 5.67×10^{-8} $W/m^2 \cdot K$
τ	Time constant for heat transfer, s or h
φ	Overpotential, V
ψ	Concentration of lithium ions, mol/L
ω	Unutilized energy component (dimensionless)
Ω	Multiplicity of an intercalation host lattice (dimensionless)

Common Subscripts and Superscripts

ad	Reference to a theoretical adiabatic condition
avg	Reference to an average value
best	Reference to the best value expected among commercial batteries
cell	Reference to a single cell within a battery pack
chg	Reference to battery charge
cond	Reference to thermal conduction
conv	Reference to thermal convection
cool	Reference to battery standby cooldown period
ct	Reference to electrochemical charge transfer
CT	Reference to truncation of battery charge
cyc	Reference to complete battery cycle of discharge, charge, and cooldowns
diff	Reference to a differential between battery temperature nodes
dis	Reference to battery discharge

DT	Reference to truncation of battery discharge
endChg	Reference to the instant at which battery charge ends
endDis	Reference to the instant at which battery discharge ends
front	Reference to a vertical front surface of a battery
gen	Reference to heat generated
high	Reference to the highest-temperature cell within a battery pack
in	Reference to an input or inflow
irr	Reference to an irreversible component
limit	Reference to a limiting acceptable value expected for commercial batteries
low	Reference to the lowest-temperature cell within a battery pack
max	Reference to a maximum value
meas	Reference to a measured value
min	Reference to a minimum value
mod	Reference to battery modules within a battery pack
NE	Reference to a battery negative electrode
out	Reference to an output or outflow
pack	Reference to a full battery pack
PE	Reference to a battery positive electrode
pulse	Reference to a power pulse applied to a battery
rad	Reference to thermal radiation
ref	Reference to a value obtained from an experimental reference test
rev	Reference to a theoretical reversible condition
side	Reference to a vertical side surface of a battery
spec	Reference to a manufacturer specification
startChg	Reference to the instant at which battery charge begins
startDis	Reference to the instant at which battery discharge begins
top	Reference to a horizontal top surface of a battery
VD	Reference to depression of battery discharge voltage
x	Reference to a battery cell designated as cell X
z	Reference to the inactive component of a battery cell designated as cell Z
z'	Reference to the active component of a battery cell designated as cell Z

ACKNOWLEDGEMENTS

I am very privileged to have spent the first twelve years of my research career working with Dr. Lukas Swan: from undergraduate research, to a master's program, to entrepreneurial research, and finally to a PhD program. He is a tremendous researcher, engineer, teacher, supervisor, and mentor, and I owe much of who I am today to his generosity and guidance. I would like to thank him for his endless support and encouragement, for always making time for his students, and for granting me the freedom to do research in my own unique way. It is through all these gestures of his that this thesis has been able to grow into something I can feel proud of.

I would like to thank Drs. Dominic Groulx, Timothy Little, and Roydon Fraser for serving on my examining committee, and for taking a genuine interest in helping me succeed. I would like to thank the entire faculty and staff at the Department of Mechanical Engineering for all the support and opportunities I have benefited from during my PhD. Kate Hide and Donna Laffin in particular have come through for me countless times. I would also like to thank the fine folks at Oak Ridge National Laboratory and UC San Diego for hosting me as a research collaborator and spurring ideas that would eventually grow into thesis chapters. I should also thank Dr. Jeff Dahn for giving me my first experience in lithium-ion battery research back when I was 19 years old and surely unable to imagine my future self writing a 500-page dissertation about lithium-ion batteries.

To all of the awesome and brilliant graduate students who have come through the Renewable Energy Storage Lab during my time there, thank you for always contributing to a fun and supportive work environment where real friendships can form. I would like to acknowledge Ben Thompson in particular for laying the groundwork for my research project during his master's program, as well as the many engineering co-op students who contributed to my project through hands-on lab work over the years.

Lastly, I would like to thank my family and friends for their continuous love and support, and especially for keeping me grounded and sane as I battled through the final two years of this PhD while juggling many extracurricular responsibilities. I very much look forward to spending more time with you all now that I can finally lay down this load.

Chapter 1 INTRODUCTION

Lithium-ion batteries are a key technology for the global transition toward renewable energy. These high-performance energy storage devices make it possible to manufacture electric vehicles (EVs) that can meet the mobility demands of the modern world, thereby enabling the ongoing electrification of the transportation sector and reduced reliance on fossil fuels. At the same time, lithium-ion batteries have also become the technology of choice for constructing new stationary energy storage systems that provide cost-saving services for electricity grid operators as well as electricity consumers. These stationary batteries are especially critical for ensuring electricity grid reliability as traditional fossil fuel power plants are displaced by variable-output wind turbines and photovoltaic solar panels. This in turn allows for EVs to be charged with more renewably sourced electricity, further reducing the EV carbon footprint. Lithium-ion batteries are therefore enabling global decarbonization on two connected fronts: transportation and electricity supply.

The urgency of the climate crisis has compelled many governments to set ambitious targets for the rapid adoption of both EVs and renewable energy. In Canada, the European Union, the United Kingdom, and many other regions around the world, all new vehicle sales will be required to be zero-emission vehicles by 2035 [1]. Based on currently stated energy policies, the International Energy Agency projects that wind and solar resources will provide 35 % of global electricity supply by 2035 and 60 % by 2050 [2]. As illustrated in Figure 1.1, both these trends call for major upscaling in lithium-ion battery production, with EV batteries accounting for about 90 % of the combined annual demand [3]. Due to the anticipated increase in EV battery production in particular, there are growing concerns surrounding the environmental consequences of increased mining, processing, manufacturing, and inevitable battery disposal. This sustainability problem has spurred significant research and investment focused on improving the circularity of the EV battery supply chain, with the goal of maximizing the reuse, repurposing, and recycling of EV batteries.

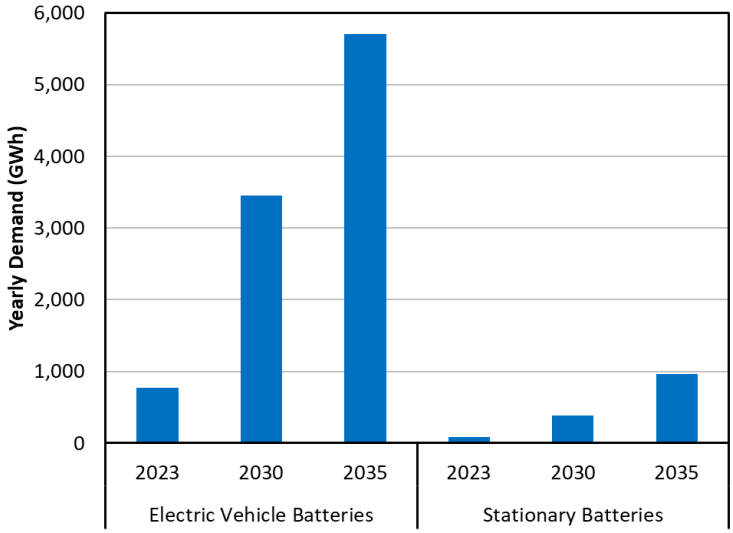


Figure 1.1 Projected growth in annual battery demand for transportation and electricity sectors. Based on data from [3] and [4].

All batteries degrade over time until they no longer have any practical use, at which point they should be recycled to recover key materials that can be used in the production of new batteries. However, the latest EV battery designs are expected to outlast the vehicles they are installed in, and older EV battery designs will typically be removed from the vehicle once battery performance no longer meets the demanding requirements of EV service [5]. In either case, used EV batteries will still be capable of meeting the less demanding requirements of stationary applications. Instead of wasting the remaining economic value in many millions of used EV batteries by immediately recycling them, these batteries can be repurposed for a 'second life' to help meet the rising demand for stationary energy storage. Used EV batteries are generally expected to operate for an additional ten years or more in second-life service [6], though this depends on the usage history of a given EV battery as well as its intended second-life application [7].

Compared to newly built batteries, second-life batteries can offer lower prices and reduced environmental impact for stationary energy storage systems. A new industry has therefore emerged over the past decade to capitalize on this opportunity. Many EV manufacturers and startup companies are already deploying second-life battery systems [8-11], and governments around the world are starting to develop new regulations [12] and funding programs [13], [14] to facilitate industry growth. Despite this recent progress, the

second-life battery industry still faces many technical challenges that are being researched extensively, such as: evaluating the remaining value in each used EV battery [9]; reducing the costs and complexity associated with the repurposing process [10]; and accounting for performance limitations compared to new stationary batteries [17].

One notable challenge for the second-life battery industry is EV battery diversity [18]. With dozens of different EV manufacturers deploying a wide range of unique EV battery designs, there is significant uncertainty regarding the electrical, thermal, and degradation performance that should be expected for different EV batteries in second-life service. Electrical performance determines how much economic value a stationary battery can theoretically generate on a given day; thermal performance determines how much daily value can be practically achieved without exceeding specified battery temperature limits; and degradation performance determines how much cumulative value can be realized over time before the battery must be decommissioned and recycled. The lack of standard performance metrics for second-life batteries makes it difficult to compare the many unique options in the used EV battery market and make informed decisions when modelling and designing second-life battery systems.

A great number of studies have focused on measuring, modelling, and predicting second-life battery degradation, and many researchers advocate for the development of new standard methods and metrics for these evaluations [19]. However, there has been no attempt to directly compare the electrical and thermal performance characteristics of different EV battery designs. Such an evaluation would require suitable test methods to reflect second-life battery operation, accompanied by a set of electrical and thermal performance metrics that can be applied equitably to all EV batteries regardless of their design and age. This thesis will therefore present a novel second-life battery research project that develops and applies these test methods and metrics.

Another important consideration for second-life battery companies is whether to repurpose a given EV battery pack with minimal modifications to the original design, or to disassemble the original battery pack and repurpose the smaller battery modules housed within. Pack-level repurposing can significantly reduce the upfront repurposing costs,

while module-level repurposing allows for more customizations that can improve long-term system performance in second-life service [20]. Both methods are employed in the nascent second-life battery industry, but very few second-life battery studies have focused on testing or modelling pack-level performance. This is a significant research gap, since large EV battery packs will likely exhibit thermal behaviours that differ considerably from relatively small battery modules. The research project presented in this thesis therefore focuses primarily on the repurposing of used EV battery packs rather than modules.

The main objectives of the research project are as follows:

1. To develop reliable experimental and analytical methods for characterizing the electrical and thermal performance of repurposed EV battery packs in a way that facilitates direct comparison of different EV battery designs
2. To apply the developed methods to a diverse set of EV battery packs and analyze the differences and similarities observed across different EV battery designs
3. To draw practical conclusions about the performance capabilities of repurposed EV battery packs and make recommendations to the second-life battery industry
4. To build new numerical modelling tools that facilitate the characterization and operation of second-life battery packs

To preface the research project, the next two chapters of this thesis review a variety of relevant scientific theories, technical concepts, state-of-the-art research outcomes, and other background information related to the field of second-life batteries:

- Chapter 2 provides a detailed review of lithium-ion battery technology, which is necessary for understanding the different lithium-ion cell designs used by EV battery manufacturers as well as their nuanced electrical and thermal performance characteristics.
- Chapter 3 provides a more focused review on second-life battery technology, expanding on the basic concepts introduced in this chapter before proposing a set of specific research questions to be investigated.

The subsequent four chapters then present the main phases of research project, which contribute a variety novel experimental, analytical, and numerical methods and results to answer the proposed research questions stated at the end of Chapter 3:

- Chapter 4 describes test methods and performance metrics for conducting comparative second-life battery performance studies, as well as a first-of-its-kind collection of five unique EV battery packs acquired for experimental testing.
- Chapter 5 applies a variety of graphical techniques to analyze the electrical and thermal performance results acquired using the experimental methods described in Chapter 4, ultimately producing valuable new insights and guidelines regarding second-life battery performance as well as a performance ranking system for second-life battery packs.
- Chapter 6 demonstrates a numerical model that describes how the measured experimental results vary with the applied power rate, forming the basis of a newly proposed second-life battery performance test method that achieves complete electrical and thermal performance characterization with minimal testing time.
- Chapter 7 demonstrates a thermal modelling technique that can be used to predict temperature distributions in EV battery packs and thereby overcome one of the shortcomings of pack-level repurposing methods.

Finally, Chapter 8 closes with conclusions and recommendations drawn from the research project. Recognizing that many EV battery designs exist beyond those tested and that EV battery designs will continue to evolve in the future, emphasis is placed on the evaluation methods and the overarching lessons learned about the electrical and thermal performance of second-life battery packs.

Chapter 2 REVIEW OF LITHIUM-ION BATTERY TECHNOLOGY

Chapter 2 will provide theoretical background on lithium-ion batteries with a focus on their design parameters, electrochemical functions, energy storage capabilities, and thermal characteristics. The reviewed concepts will be necessary for the design of second-life battery performance tests in Chapter 4, the analysis of second-life battery voltage, temperature, and energy measurements in Chapter 5 and Chapter 6, and the development of a novel battery thermal model in Chapter 7.

2.1. Cell Design

A lithium-ion battery cell is designed with the same basic principles underpinning all rechargeable battery technologies. Specialized materials store energy in their chemical bonds and release that energy in the form of electricity as they undergo electrochemical reactions, which can be reversed to recharge the battery. The nature of the materials and the reactions makes one battery technology unique from another. This section will review the key design features of lithium-ion batteries.

2.1.1. Components

Figure 2.1 illustrates the basic components of a lithium-ion battery. The design features a positive electrode and a negative electrode positioned on either side of a separator material, all of which feature porous structures that are filled with electrolyte. The separator allows lithium ions (Li^+, shown as green circles) to flow directly between the electrodes but forces electrons (e^-, shown as blue circles) to flow through an external electric circuit. For lithium-ion batteries, the electrolyte typically consists of a lithium salt in an organic solvent, which allows Li^+ to conduct through the separator and electrode pores. The two electrodes are adhered to metallic current collectors which conduct e^- to and from the external circuit.

Common materials for each lithium-ion battery component in Figure 2.1 are provided in [21]. The electrolyte is most commonly composed of a mixture of organic solvents including ethylene carbonate, ethyl methyl carbonate, and dimethyl carbonate with lithium hexafluorophosphate ($LiPF_6$) as the lithium salt, along with various additives to achieve desired performance enhancements such as longer cycle life and lower

impedance [22]. The separator is typically a microporous film of polyethylene or polypropylene that is electrically insulating but ionically conductive. The negative electrode is most commonly composed of a microporous coating of graphite on a copper current collector with a binding compound, while the positive electrode is most commonly composed of a microporous coating of a transition metal oxide/phosphate on an aluminum current collector. Conductive carbon is typically added into the electrode coating as well to improve electronic conductivity. The active materials are adhered to the current collectors using polyvinylidene fluoride as a binding compound. There are a number of common variants for positive and negative electrode materials, which will be discussed in more detail in Sections 2.1.3 and 2.1.4, respectively.

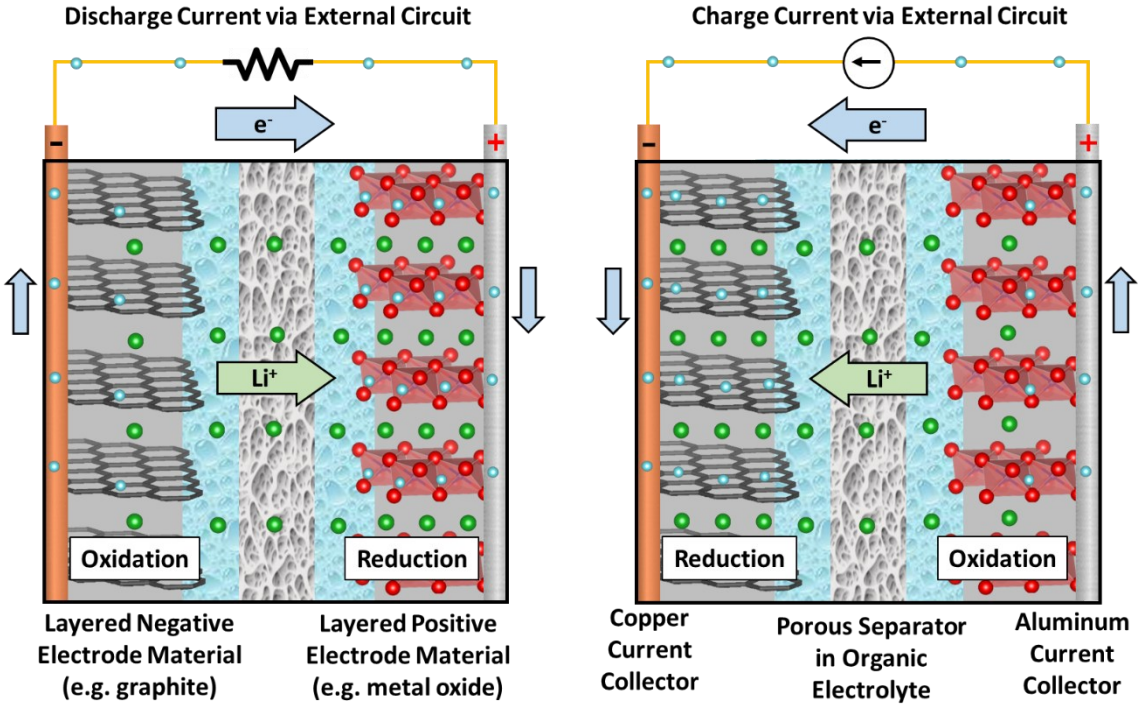


Figure 2.1 Simplified illustration showing the basic components of a lithium-ion battery during discharge (left) and charge (right). Images of electrode material structures were created in VESTA software [23] using lattice structure data from the Materials Project [24].

2.1.2. Intercalation Reactions

The fundamental process within any rechargeable battery is a pair of reversible oxidation and reduction reactions taking place at the two electrodes, whereby electrons and ions are released at one electrode and accepted at the other electrode. For a lithium-ion battery, the

redox reactions take place through a process known as intercalation, whereby Li^+ are physically inserted into a host structure within the electrode material, as illustrated in Figure 2.1. The reverse process is called deintercalation, whereby Li^+ are physically removed from the host structure. Other elements such as sodium can also undergo intercalation, but Li^+ have some of the best intercalation properties, such as low ionic radius and low atomic weight [25].

The reversible electrochemical reactions of a lithium-ion battery are given in general form below, where M_{PE} represents a generalized positive electrode material and M_{NE} represents a generalized negative electrode material. When the reactions run from left to right (i.e. discharge), the negative electrode releases an equal number of Li^+ and e^-, while the positive electrode receives an equal number of Li^+ and e^-. The reverse occurs when the reaction runs from right to left (i.e. charge). From the perspective of the full cell, the exchange of Li^+ and e^- is balanced.

(charged) $M_{PE} + Li^+ + e^- \leftrightarrow LiM_{PE}$ (discharged) Positive electrode

(charged) $LiM_{NE} \leftrightarrow M_{NE} + Li^+ + e^-$ (discharged) Negative electrode

(charged) $M_{PE} + LiM_{NE} \leftrightarrow LiM_{PE} + M_{NE}$ (discharged) Full cell

Intercalation is fundamentally different from the electrochemical reactions that occur in other battery technologies. For example, in a lead-acid battery the active electrode materials (lead and lead dioxide) react with the electrolyte (sulfuric acid) to form entirely different chemical compounds (lead sulphate and water) [21]. With intercalation, the electrode materials largely maintain their chemical structure, and simply 'accommodate' the Li^+ in open spaces that are held in place by weak van der Waals forces [26]. While the electrochemical reaction itself always takes place at the interface between electrode and electrolyte, intercalation allows the reduction product (i.e. intercalated Li^+) to diffuse deep into the bulk of an electrode particle such that reactions can continue to take place at the same surface sites until the particle is filled with Li^+. This is illustrated in Figure 2.2. With other battery technologies such as lead-acid, the reaction can only take place once at a given surface site until the reaction is reversed. The thermodynamics and kinetics of Li^+ intercalation will be discussed in greater detail in Section 2.2.

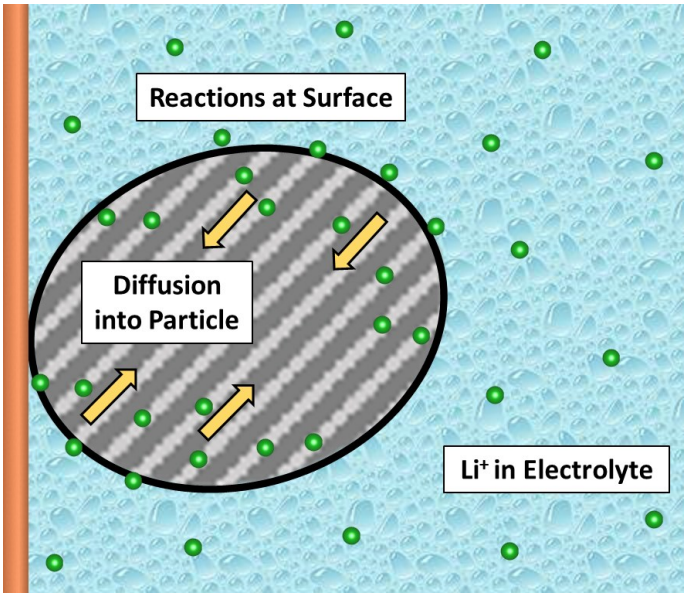


Figure 2.2 Simplified cross-sectional illustration of a single intercalation electrode particle immersed in electrolyte with Li^+ intercalation reactions occurring at the surface and intercalated Li^+ diffusing inward such that additional surface reactions can take place (for visual clarity, electrons are not shown).

Only specialized materials are capable of serving as intercalation hosts for battery applications, generally featuring a molecular structure with empty layers or tunnels through which Li^+ can intercalate. A variety of such materials have been developed since the 1970s, with unique design requirements for positive and negative electrodes. The most relevant electrode materials for modern lithium-ion batteries are discussed in the next subsections.

2.1.3. Positive Electrode Materials

At the positive electrode, early research focused on transition metal dichalcogenides such as titanium sulfide (TiS_2) and molybdenum sulfide (MoS_2) [26], but development shifted to transition metal oxides in the 1980s due to their higher energy storage capacity. The first commercial lithium-ion batteries in 1991 used lithium cobalt oxide ($LiCoO_2$ or LCO for short) for the positive electrode [27], and LCO batteries are still commonly used today. However, LCO batteries do not perform well under high currents and elevated temperatures, and are therefore only suitable for small-scale, low-power applications such as portable electronics. Researchers needed to develop alternative positive electrode materials for more demanding applications such as power tools, EVs and electricity grid energy storage.

During the 1990s, lithium manganese oxide ($LiMn_2O_4$ or LMO for short) and lithium iron phosphate ($LiFePO_4$ or LFP for short) were developed and commercialized as high-power alternatives to LCO. These three materials each have unique intercalation characteristics due to their different crystal structures. The three structures are shown in Figure 2.3, with Li^+ in green, oxygen atoms in red, cobalt atoms in blue, manganese atoms in purple, iron atoms in brown, and phosphorous atoms in grey. The host structures are shown as polyhedrons to clearly distinguish the Li^+ intercalation pathways.

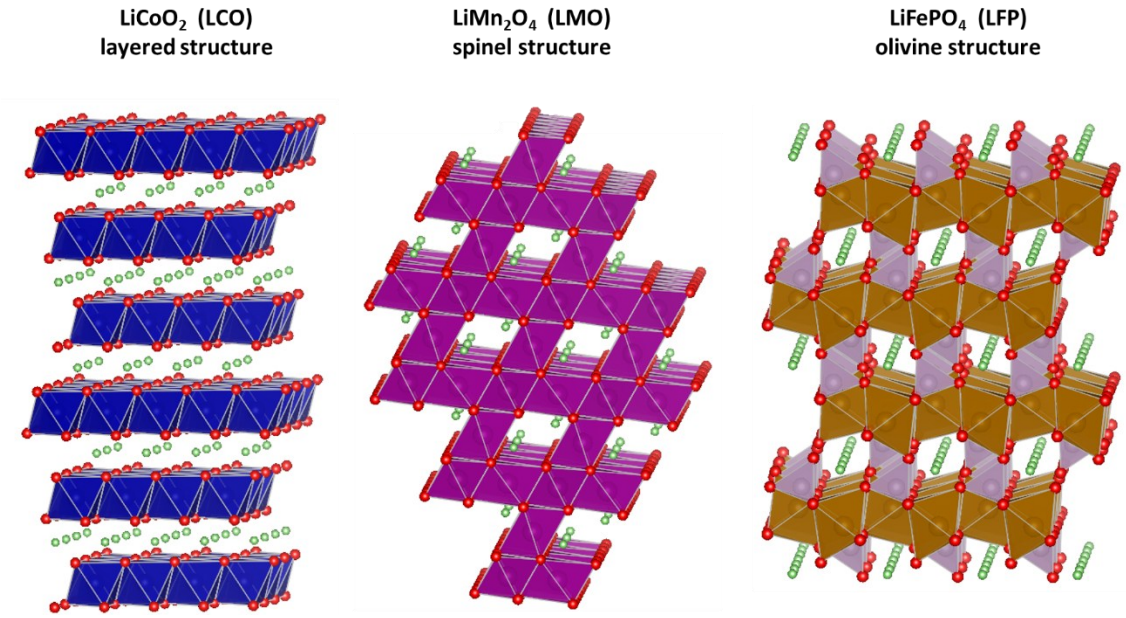


Figure 2.3 Lithiated crystal structures for LCO (layered), LMO (spinel), and LFP (olivine) positive electrode materials. Images were created in VESTA software [23] using lattice structure data from the Materials Project [24].

LCO has a layered structure, where Li^+ can intercalate between planes of CoO_2 molecules. This structure allows the intercalated Li^+ to move in two dimensions. LMO has a spinel structure, where Li^+ can intercalate through tunnels formed between the Mn_2O_4 molecules. Though not visible in Figure 2.3, the LMO tunnels extend in three dimensions, giving high mobility for intercalated Li^+ [28]. LFP has an olivine structure, where Li^+ can intercalate through tunnels formed between the $FePO_4$ molecules. The LFP tunnels only allow the intercalated Li^+ to move in one dimension, which limits Li^+ mobility compared to LMO and LCO. To perform in high-power applications such as EVs, LFP materials often employ

smaller particle sizes to facilitate Li^+ mobility as well as carbon-coated particles to improve electrical conductivity [29].

Within these three electrode structure types, the Li^+ intercalation sites are always located between a set of oxygen atoms. These intercalation sites can take an octahedral shape between six oxygen atoms or a tetrahedral shape between four oxygen atoms. The two site types are illustrated in Figure 2.4, with Li^+ in green and oxygen atoms in red. While all three materials in Figure 2.3 feature both octahedral and tetrahedral intercalation sites, the octahedral sites are utilized in layered LCO and olivine LFP while the tetrahedral sites are utilized in spinel LMO.

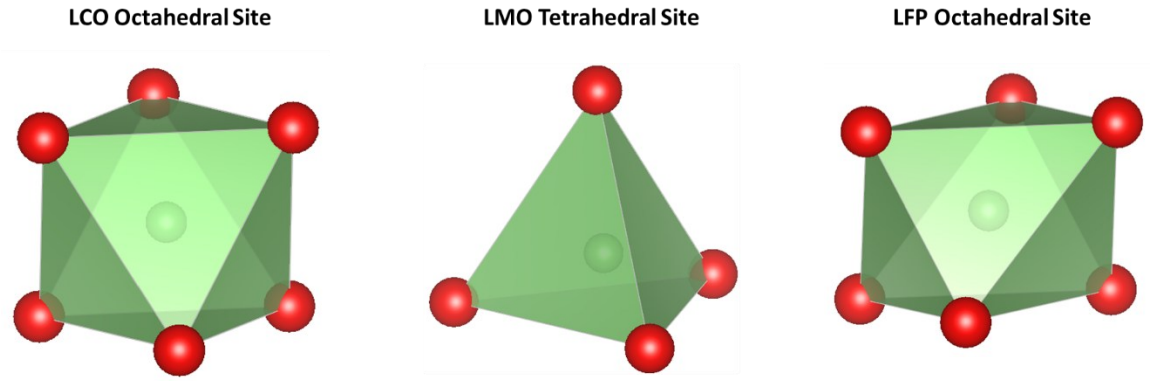


Figure 2.4 Two types of Li^+ intercalation sites in three common positive electrode materials. Images were created in VESTA software [23] using lattice structure data from the Materials Project [24].

Lithium nickel oxide ($LiNiO_2$ or LNO for short) was also proposed as a positive electrode material in the 1980s, featuring the same layered structure as LCO. While LNO was shown to provide more energy storage capacity than LCO, LMO, and LFP, it proved to have no practical value due to its poor cycling stability [30]. However, research in the 1990s demonstrated how the cycling stability of LNO could be improved at the expense of capacity by substituting some of the nickel with other metals such as cobalt [31], manganese [32], and aluminum [33], thus combining the strengths of multiple metals in a single alloyed electrode material. By 2001, researchers had demonstrated the viability of $LiNi_{1-y-z}Co_yMn_zO_2$ (NMC for short) [34-36] and $LiNi_{1-y-z}Co_yAl_zO_2$ (NCA for short) [37], [38], both of which would be refined and commercialized in the early 2000s.

Today, a large share of EV batteries feature a positive electrode composed of either NMC with Ni > 30 % or NCA with Ni ≥ 80 % [39]. The first commercial NMC batteries used a 1:1:1 ratio of Ni, Mn, and Co (termed NMC111), but continued research has progressively increased the nickel content to improve energy density and EV driving range, leading to a wide range of NMC variants such as NMC532, NMC622, and NMC811 [30]. Higher nickel content generally results in poorer safety and cycling stability [40], but a variety of techniques are being explored to improve these properties for EV applications, such as doping, particle coatings, and electrolyte additives [41], [42]. The latest advancements have sought to push this trend to Ni > 85 % by combining the benefits of NMC and NCA in new NMCA electrode variants such as $LiNi_{0.89}Co_{0.05}Mn_{0.05}Al_{0.01}O_2$ [43].

Battery materials must achieve an appropriate balance of energy capacity, power capability, safety (i.e. fire risk), cycle life, cost, and environmental impact to meet the requirements of the intended energy storage application. While numerous cell design parameters also influence battery characteristics (discussed in Section 2.1.5), Table 2.1 draws on a number of publications [29], [44-47] to give qualitative comparisons of the five most common positive electrode materials used in commercial lithium-ion batteries.

Table 2.1 Comparison of key characteristics for common positive electrode materials.

Category	LCO (layered)	LMO (spinel)	LFP (olivine)	NMC [a] (layered)	NCA [b] (layered)
Energy	Medium	Poor	Poor	Good	Best
Power	Poor	Best	Good	Medium	Medium
Cycle life	Poor	Poor	Best	Good	Medium
Safety	Poor	Good	Best	Medium	Poor
Cost	Poor	Best	Good	Medium	Poor
Environment	Poor	Good	Best	Medium	Medium

[a] NMC considered to have 33 % ≤ Ni ≤ 60 %.
[b] NCA considered to have 80 % ≤ Ni ≤ 85 %.

The differences in cost in Table 2.1 are based on raw material prices, which evolve over time. Cobalt is known to be the most expensive material, while manganese and iron are relatively inexpensive [29]. Note that the lifetime cost effectiveness of a given battery design requires a detailed economic analysis of production and operation, which is outside the scope of this thesis. The differences in environmental impact in Table 2.1 are based on

raw material toxicity. It is generally accepted that iron-based materials are the least toxic [48], while for transition metal oxides the toxicity increases from manganese < nickel < cobalt [49]. It should be noted that evaluating the total lifetime environmental impacts of a given lithium-ion battery design requires a comprehensive life cycle assessment accounting for various impact categories, electricity generation sources, operational use cases, second life, and recycling processes, as well as the energy density, energy efficiency, and degradation of the battery [50-52]. Such in-depth environmental evaluations are outside the scope of this thesis. The underlying factors of the energy, power, cycle life, and safety categories in Table 2.1 will be discussed in more detail later in this chapter.

Table 2.1 shows that while no single positive electrode material scores high in all categories, the weaknesses of some materials correspond to the strengths of others. Researchers have therefore developed 'blended' positive electrode materials which combine multiple distinct intercalation compounds to achieve synergistic benefits. Most studies in this area have experimented with the blending of LCO, NMC, or NCA (high energy) with LMO or LFP (high-power, low-cost, good safety, low environmental impact) to achieve a more balanced electrode material [53-57]. A range of NMC-LMO blends have been deployed in commercial EVs such as the Chevrolet Volt, Nissan Leaf, and BMW i3 [58].

2.1.4. Negative Electrode Materials

Lithium metal was originally preferred as the negative electrode due to its high energy storage capacity. A lithium metal electrode does not undergo intercalation but instead increases and decreases in mass as Li^+ are reduced and oxidized at its surface, making it more lithium-dense than any intercalation electrode can be. However, unresolvable issues with cycling stability and safety made lithium metal impractical for commercial cells [27], and the approach was largely abandoned by 1990 [59]. Carbon-based intercalation compounds such as graphite and petroleum coke had already been studied extensively by that time, and were known to be the best alternatives to lithium metal. The first commercial lithium-ion batteries in 1991 employed petroleum coke as the negative electrode material [60], but the next few years brought important electrolyte enhancements

that enabled the use of graphite, which has greater energy storage capacity. The graphite negative electrode became the industry standard starting in 1994 and remains so three decades later [60].

The layered structure of lithiated graphite (LiC_6) is illustrated in Figure 2.5, with Li^+ in green and carbon atoms in brown. Graphite is essentially a stack of parallel graphene sheets, and Figure 2.5 shows how the Li^+ intercalate in the spaces between these sheets. The bonds of the C_6 molecules are also shown in Figure 2.5 to demonstrate the hexagonal pattern formed in each graphene sheet.

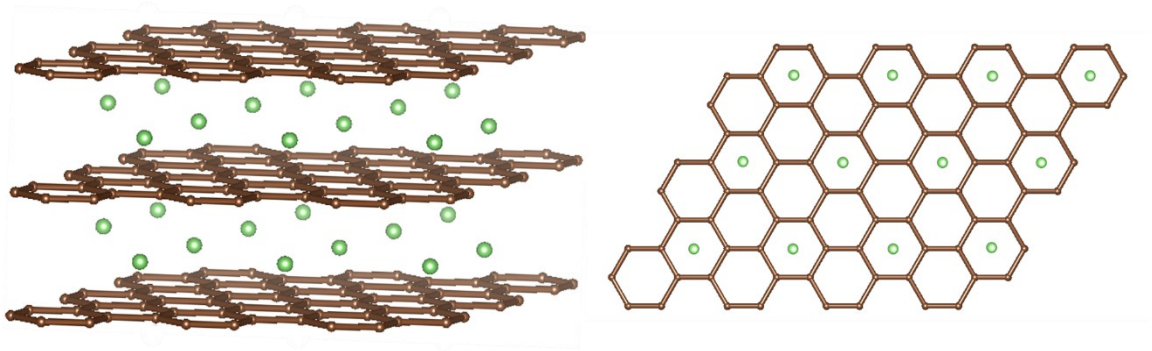


Figure 2.5 Layers of lithiated graphite (LiC_6) viewed from two angles. Images were created in VESTA software [23] using lattice structure data from the Materials Project [24].

Hard carbon and lithium titanate ($Li_4Ti_5O_{12}$, or LTO for short) are also used as negative electrode materials, though far less commonly than graphite. Hard carbon (i.e. charcoal) consists of disordered graphene sheets in contrast to the parallel graphene sheets of graphite [61], while LTO has a spinel structure similar to LMO. Hard carbon and LTO have lower chemical potentials and more rigid structures than lithiated graphite, which contributes to lower energy storage capacity but better long-term stability and safety [62], [63].

Silicon has also been investigated as a negative electrode material for lithium-ion batteries. Unlike the materials discussed above, silicon is not an intercalation material, but rather alloys with Li^+ to give a large specific capacity nearly 10 times that of graphite [64]. Unfortunately, silicon electrodes have poor cycling stability due to extreme volume change ($> 300\,\%$) during cycling, and are therefore unsuitable for commercial lithium-ion batteries [65]. However, blending graphite with small amounts of silicon has been shown

to give a practical electrode material with higher energy capacity and power capability than a pure graphite electrode [66]. Lithium-ion batteries featuring a graphite-silicon blended negative electrode have been deployed in some modern EVs such as the Tesla Model 3 [67].

2.1.5. Cell Assembly

Commercial lithium-ion batteries are composed of a 'cell stack' featuring a layered sequence of electrode, separator, electrode, separator, where each electrode layer consists of a metallic current collector with active material coated on both sides [68]. This cell stack concept is illustrated in Figure 2.6. Active material coatings are typically less than 100 µm thick on a given side of the current collector, while the separator and current collectors are significantly thinner (on the order of 10 µm each) [69], giving a total cell stack thickness of less than 0.5 mm.

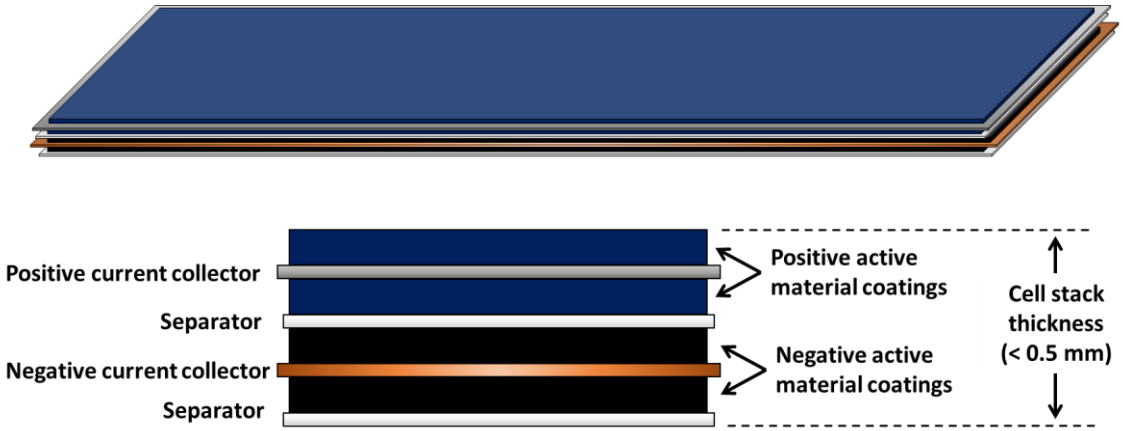


Figure 2.6 Illustration of cell components assembled into a cell stack.

For EV applications, the cell stack can be packaged into a cylindrical, pouch, or prismatic cell format [68], which are each illustrated in Figure 2.7. In the cylindrical format, a single cell stack is constructed with a long length such that it can be wound into a 'jellyroll' and placed inside a cylindrical container. As the cell stack is rolled up, the separator layer at the bottom of the cell stack in Figure 2.6 will be in contact with the positive active material coating at the top of the cell stack. The outermost surface of the current collector (facing the inside of the container) is left uncoated to avoid wasted active material [68]. Cylindrical cells are typically the smallest of the three formats and offer advantages for mechanical strength but disadvantages for packing density [70], as well as heat dissipation

disadvantages for larger diameters [71]. In the pouch format, the cell stack is cut to size such that it can be placed inside a flexible metallic pouch foil without rolling or folding. Multiple cell stack units can be stacked on top of one another inside a single pouch. Pouch cells have advantages for weight and heat dissipation but disadvantages for mechanical durability due to the flexible pouch material [70], [71]. The prismatic format is essentially a thicker, hardshell version of the pouch format, using either winding or stacking to fit the cell stack into the container. Prismatic cells have advantages for packing density [70] and disadvantages for heat dissipation due to their relatively high volume-to-surface-area ratio [68]. For all three cell formats, the positive and negative current collectors respectively connect to the positive and negative terminals which protrude to the outside of the container to connect with the external circuit. The terminals are indicated by '+' and '−' signs in Figure 2.7.

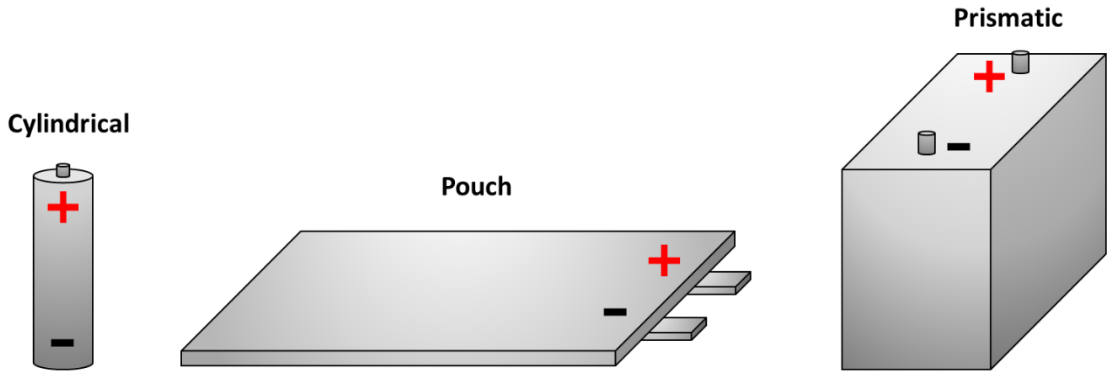


Figure 2.7 The three main lithium-ion cell formats: cylindrical, pouch, and prismatic.

Aside from the chemical makeup of the electrode materials, the cell stack includes a number of key design parameters which have significant implications for battery performance, such as the porosity and thickness of the electrode coatings and separator as well as the particle size of the electrode material [72]. In general, smaller particles, larger pores, and thinner electrode coatings improve Li^+ mobility such that higher power can be achieved, but also decrease the amount of active material relative to inactive material, which decreases the energy capacity per unit weight and volume [73-75]. Conversely, larger particles, smaller pores, and thicker electrode coatings serve to increase the energy capacity per unit weight and volume, but inhibit Li^+ mobility at higher power rates. There is also a trade-off between energy storage capacity and electronic conductivity based on

the amounts of conductive carbon in the electrode coatings and the thickness of the current collectors [76].

2.2. Reversible Voltage

The voltage of a lithium-ion battery is a sum total of a vast array of complex processes occurring within the battery at an atomic level. While the voltage can be easily measured between the terminals of the positive and negative electrodes, interpreting the measured value and its rate of change requires a deeper understanding of the intercalation process and the factors which influence it, which are summarized in Figure 2.8. A comprehensive interpretation of cell voltage must examine the molecular physics and chemistry at the root of these factors, which is beyond the scope of this thesis. However, some of the basic principles are useful for understanding the unique voltage characteristics exhibited by different EV battery designs. This section will review some of the key principles in thermodynamics and electrochemistry which determine the voltage of a lithium-ion battery in reversible equilibrium conditions (i.e. no current flow). Section 2.3 will review the various sources of irreversibility that arise under practical operating conditions.

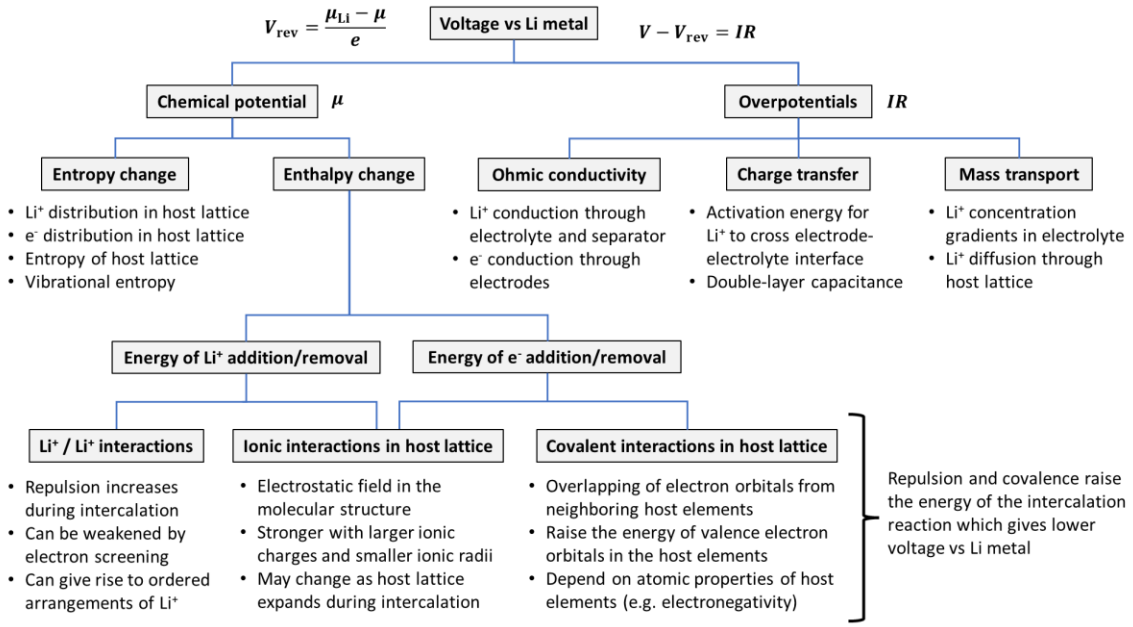


Figure 2.8 Simplified breakdown of the main factors that determine the operational voltage of a lithium-ion battery.

2.2.1. Thermodynamics

The first step in understanding battery voltage is through the fundamental equations that govern all thermodynamic processes. Equation 2.1 describes an incremental change in the Gibbs free energy $\mathrm{d}G$ of a multi-component chemical system as a function of the entropy S, an incremental change in temperature $\mathrm{d}T$, the volume v, an incremental change in pressure $\mathrm{d}p$, the chemical potential μ_i of each chemical species i, and an incremental change in the number $\mathrm{d}n_i$ of each chemical species.

$$\mathrm{d}G = -S\mathrm{d}T + v\mathrm{d}p + \sum_i \mu_i \mathrm{d}n_i \tag{2.1}$$

The chemical potential of a given molecular species can therefore be described as the change that occurs in the Gibbs free energy of the entire system as a result of a change in the amount of that species when the temperature, pressure, and the amounts of all other species are held constant. This is stated in Equation 2.2.

$$\mu_i = \left.\frac{\partial G}{\partial n_i}\right|_{T,p,j\neq i} \tag{2.2}$$

Thus, at a fixed temperature and pressure, the $\mathrm{d}G$ that results from the transfer of an incremental amount $\mathrm{d}n$ of Li^+ and e^- can be determined as per Equation 2.3 below. Note that μ_{PE} and μ_{NE} are defined as the chemical potential of the lithium atom (i.e. $Li^+ + e^-$) in the positive electrode and negative electrode, respectively [77].

$$\begin{aligned}\mathrm{d}G &= \sum_i \mu_i \mathrm{d}n_i \\ &= \mu_{\mathrm{LiM_{PE}}}\mathrm{d}n + \mu_{\mathrm{M_{PE}}}(-\mathrm{d}n) + \mu_{\mathrm{M_{NE}}}\mathrm{d}n + \mu_{\mathrm{LiM_{PE}}}(-\mathrm{d}n) \\ &= \left(\mu_{\mathrm{LiM_{PE}}} - \mu_{\mathrm{M_{PE}}}\right)\mathrm{d}n - \left(\mu_{\mathrm{LiM_{NE}}} - \mu_{\mathrm{M_{PE}}}\right)\mathrm{d}n \\ &= (\mu_{\mathrm{PE}} - \mu_{\mathrm{NE}})\mathrm{d}n\end{aligned} \tag{2.3}$$

The second law of thermodynamics requires that $\mathrm{d}G < 0$ for a spontaneous process. Therefore, a spontaneous transfer of Li^+ (i.e. discharge) will occur when $\mu_{\mathrm{PE}} < \mu_{\mathrm{NE}}$. Essentially, the reaction naturally flows from high chemical potential energy to low chemical potential energy.

When an incremental amount $\mathrm{d}n$ of Li^+ and e^- are spontaneously discharged from the negative electrode to the positive electrode, $\mathrm{d}G$ can also be described as the reversible electrical work that is done by transferring a charge $e\mathrm{d}n$ over a reversible voltage V_{rev}, where e is the elementary charge (approximately 1.602×10^{-19} C). This relationship is stated in Equation 2.4. Note that V_{rev} is the theoretical voltage obtained when an infinitesimally small current is applied, such that no energy losses occur.

$$\mathrm{d}G = -V_{\mathrm{rev}} e \mathrm{d}n \tag{2.4}$$

Thus, the reversible voltage of a lithium-ion cell can be described by Equation 2.5.

$$V_{\mathrm{rev}} = \frac{\mu_{\mathrm{Li_{NE}}} - \mu_{\mathrm{Li_{PE}}}}{e} \tag{2.5}$$

Equation 2.5 implies that V_{rev} can be predicted through an accurate characterization of μ for each electrode. For lithium-ion batteries, μ is typically given as a value relative to the chemical potential of a lithium metal electrode, $\mu_{\mathrm{Li}} = 0$. Lithium metal has a strong tendency to oxidize, so a wide range of electrode materials will meet $\mu < \mu_{\mathrm{Li}}$ and thus spontaneously intercalate Li^+ from a lithium metal electrode.

To characterize μ for a given electrode material, another fundamental thermodynamic relationship must be applied. Equation 2.6 gives the Gibbs free energy as a function of enthalpy H, internal energy U, temperature T, entropy S, pressure p, and volume v. Note that $H = U + pv$.

$$\begin{aligned} G &= H - TS \\ &= U - TS + pv \end{aligned} \tag{2.6}$$

The reversible voltage V_{rev} can therefore be determined by taking the derivative of G with respect to the amount n_{Li} of intercalated Li^+ as per Equation 2.2 and Equation 2.5. For an electrode with a fixed number N of intercalation sites and a ratio $x = n_{\mathrm{Li}}/N$ of sites filled with Li^+, Equation 2.7 gives a general description of the cell voltage as a function of x for a given temperature and pressure. The voltage is thus a function of how the internal energy, entropy, and mechanical work of the system change as a function of Li^+ content.

$$
\begin{aligned}
V_{\text{rev}} &= -\frac{1}{e}\frac{\partial G}{\partial n_{\text{Li}}}\bigg|_{T,p} \\
&= -\frac{1}{eN}\frac{\partial G}{\partial x}\bigg|_{T,p} \\
&= -\frac{1}{eN}\left(\frac{\partial U}{\partial x}\bigg|_{T,p} - T\frac{\partial S}{\partial x}\bigg|_{T,p} + p\frac{\partial v}{\partial x}\bigg|_{T,p}\right)
\end{aligned} \tag{2.7}
$$

2.2.2. Mean Field Theory

To quantify the values on the right side of Equation 2.7, a model is required to characterize the energy, entropy, and work of Li^+ intercalation. The lattice gas model is commonly applied such that the Li^+ are treated as gas particles moving within a fixed lattice of intercalation sites [78]. The movement of the Li^+ will depend on a number of competing factors such as the electrostatic forces between charged particles and the randomizing tendency of entropy. Since the pioneering days of lithium-ion battery modelling, mean field theory has been applied to simplify this complex dynamic [79]. The theory assumes that intercalated Li^+ remain randomly distributed at all values of x regardless of the electrostatic interactions between Li^+.

Based on mean field theory, the 'enthalpy change' branch in Figure 2.8 can be simplified by assigning a single 'site energy' value U_{site} to describe the total effect of ionic and covalent interactions in the host lattice on each intercalation reaction ($U_{\text{site}} < 0$ relative to μ_{Li}) and a single 'lithium interaction energy' value $n_{\text{int}}U_{\text{int}}$ to describe the electrostatic repulsion experienced by each intercalated Li^+ due to a number n_{int} of nearby Li^+ [79]. This allows the internal energy of the intercalation system to be described as a function of x (ratio of filled intercalation sites) as stated in Equation 2.8.

$$
U = U_{\text{site}}x + \frac{1}{2}n_{\text{int}}U_{\text{int}}x^2 \tag{2.8}
$$

Note that while the positive charges of Li^+ should give a repulsive interaction ($U_{\text{int}} > 0$), for some electrode materials it is possible for the Li^+ to experience a net attractive interaction ($U_{\text{int}} < 0$) due to the screening effect of e^- in the host lattice and the strain field that arises from the gradual expansion of the host lattice during intercalation [80].

The 'entropy change' branch in Figure 2.8 can be simplified by focusing on the Li^+ multiplicity Ω, which is the number of different ways to place n_{Li} indistinguishable Li^+ on N intercalation sites [79]. This is given in Equation 2.9, where k_B is the Boltzmann constant (approximately 1.381×10^{-23} J/K) and the final step is given by Stirling's approximation. Note that Equation 2.9 will give zero entropy when $x = 0$ and $x = 1$ since there is only one possible arrangement of Li^+ in both these cases (i.e. no sites filled and all sites filled, respectively). There is maximum entropy at $x = 0.5$.

$$\begin{aligned} S &= k_B \ln \Omega \\ &= k_B \ln\left[\frac{N!}{n_{Li}!\,(N-n_{Li})!}\right] \\ &\approx -k_B N(x \ln x + (1-x)\ln[1-x]) \end{aligned} \tag{2.9}$$

It should be noted that Equation 2.9 only describes the ionic configurational entropy of an intercalation system, referring to the distribution of Li^+ in the host lattice. In reality however, there are other dynamic components to the total entropy of the system, including the entropy of the host lattice itself as a function of x [81], the electronic configurational entropy as a function of x (referring to the distribution of electrons in the host lattice) [82], and the temperature dependence of vibrational entropy in non-isothermal conditions. For the illustrative purposes of this section, Equation 2.9 is sufficient to describe the entropy of intercalation.

Neglecting the mechanical work associated with small changes in volume v with respect to x, Equations 2.7 through 2.9 can be combined to describe V_{rev}. The final solution is given in Equation 2.10, showing that the voltage will vary with x throughout the intercalation process.

$$V_{rev} = -\frac{1}{e}\left(U_{site} + n_{int}U_{int}x + k_B T \ln\left[\frac{x}{1-x}\right]\right) \tag{2.10}$$

Figure 2.9 fits Equation 2.10 to experimental data measured by Dahn et al. for a cell with a $LiMo_6Se_8$ electrode vs lithium metal during constant-current cycling at a 70 h rate in a constant 28 °C environment [81], [83]. This shows that Equation 2.10 fits the experimental data quite well using the parameter values stated in Figure 2.9.

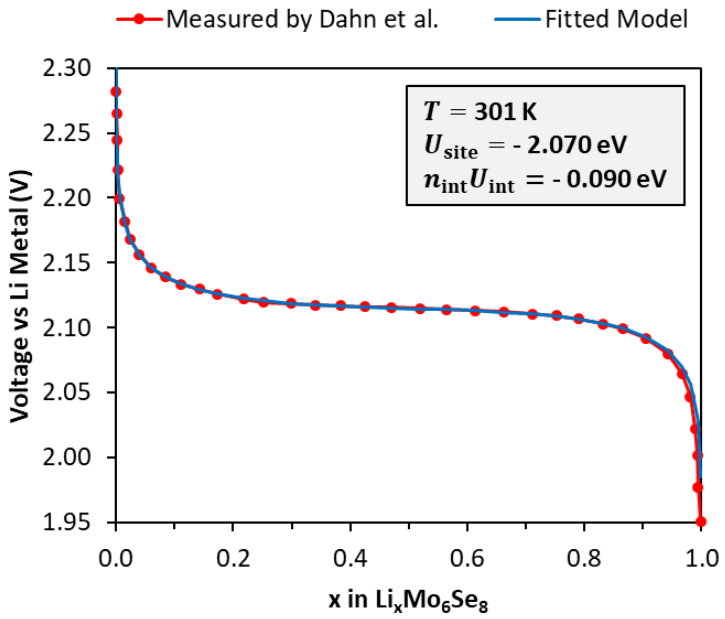


Figure 2.9 Experimental voltage data for a $LiMo_6Se_8$ electrode fitted with the model given in Equation 2.10. Based on data and figures from [81] and [83].

To examine Equation 2.10 further, Figure 2.10 illustrates how U_{site}, $n_{\text{int}}U_{\text{int}}$, and S each contribute to the overall voltage profile. If there were no entropy ($T = 0$ K) and no Li^+ interactions ($U_{\text{int}} = 0$ eV), the cell voltage would remain constant throughout the intercalation process based on the value of U_{site}. At a realistic temperature of 301 K, the entropy raises the voltage at $x < 0.5$ and lowers the voltage at $x > 0.5$, with sharp voltage spikes at $x \to 0$ and $x \to 1$. As x increases from 0, there is a rapid increase in S and thus a rapid decrease in G, which gives a high voltage. But as S tapers off to its maximum value at $x = 0.5$, the net effect on the voltage decreases to zero. As x increases further, S decreases at a growing rate, causing an increasingly negative effect on the voltage. Overall, the entropy causes the constant voltage profile to become tilted downwards with increasing lithium content. When there is an attractive Li^+ interaction ($U_{\text{int}} < 0$), it becomes increasingly easy to intercalate more Li^+, so the voltage tilt is dampened. Conversely, when there is a repulsive Li^+ interaction ($U_{\text{int}} > 0$), it becomes increasingly difficult to intercalate more Li^+, (but still thermodynamically favourable overall due to U_{site}), so the voltage tilt is amplified.

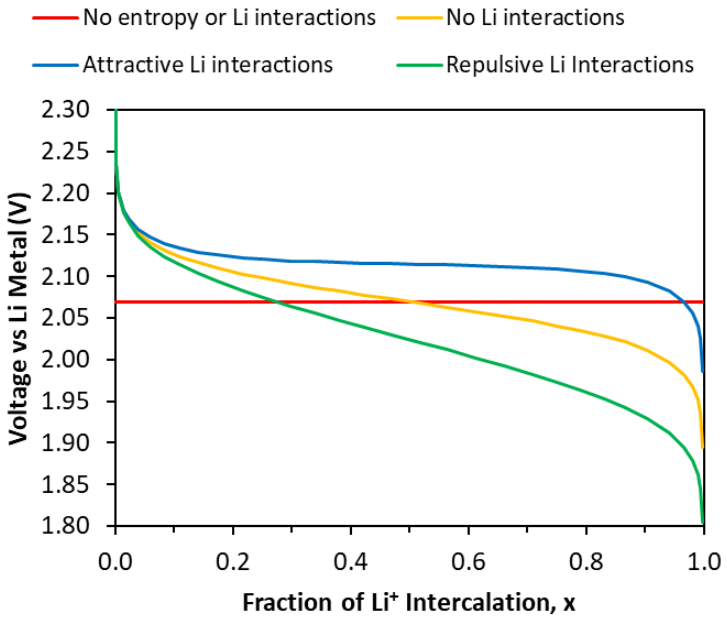


Figure 2.10 Illustrative example showing how entropy and Li^+ interactions impact the voltage profile based on Equation 2.10.

2.2.3. Ordered Lithium Distributions

The curve fit in Figure 2.9 proved highly accurate despite the simplifications of mean field theory. This is due to the fact that Li^+ interactions are relatively weak in a $LiMo_6Se_8$ electrode because of the superconducting properties of Mo_6Se_8 [80], [84]. However, the laws of thermodynamics require that the intercalated Li^+ always arrange themselves into the lowest free energy state. When the Li^+ interactions are strong enough to compete with the entropy, the lowest free energy state will not always be a random distribution as mean field theory assumes.

For example, some electrode materials exhibit a phenomenon known as 'ordering', which can occur when strong repulsive interactions cause the Li^+ to arrange themselves in an ordered pattern within each intercalation layer at favourable values of x such that the distance between them is maximized and the total interaction energy is thus minimized [79]. An illustrative example of this is shown in Figure 2.11. At $x = 1/3$, the lowest free energy state is achieved when the intercalated Li^+ arrange themselves on the green sites (note that ordering can occur at other fractional values of x as well). Once an ordered pattern has been completely formed in the electrode, subsequent Li^+ intercalations will not

fit into the ordered pattern and will therefore experience a greater repulsive interaction energy and thus a smaller $\mathrm{d}G$. This results in a relatively sharp decrease in V_{rev} at that value of x, as illustrated in Figure 2.11. Note that if the temperature is increased such that entropy outcompetes the repulsive Li^+ interactions, a random Li^+ distribution will become thermodynamically favourable and repulsive ordering will not occur.

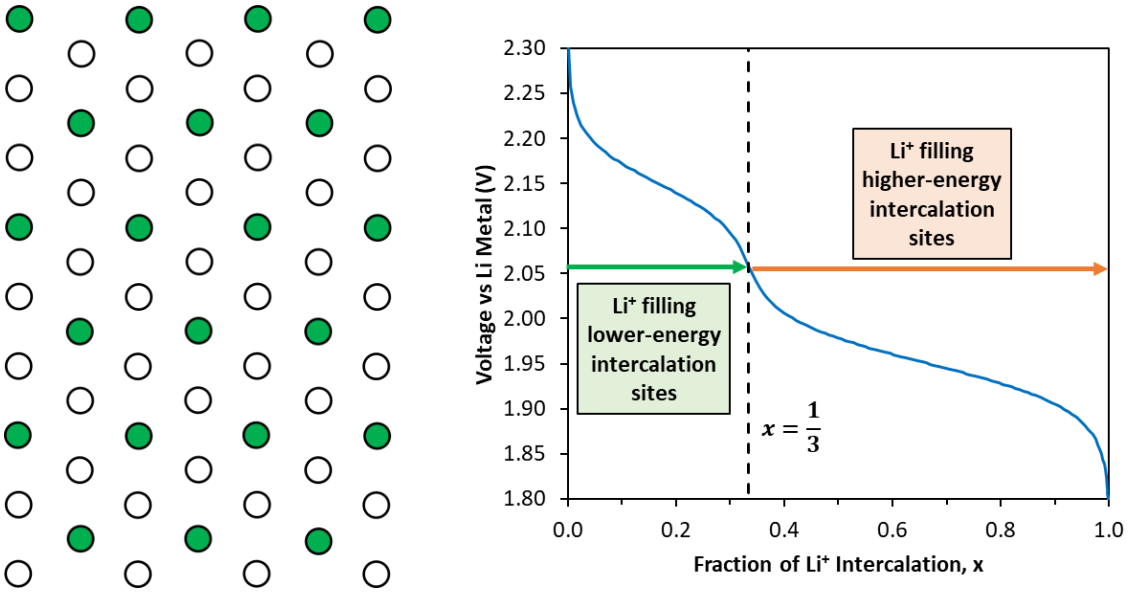


Figure 2.11 Illustrative example of an ordered state occurring in a Li^+ intercalation layer at a fractional x value ($x = 1/3$ is shown) and the corresponding drop in the voltage profile. This scenario could result from repulsive Li^+ interactions or one third of the host sites having a lower site energy than the others.

A similar effect can result when an electrode features different types of intercalation sites with different values of U_{site}. In this case, Li^+ will tend to intercalate into the sites with the most negative U_{site} (relative to μ_{Li}) until all those sites are filled, after which point subsequent Li^+ intercalations will experience a smaller $\mathrm{d}G$, which causes a relatively sharp decrease in V_{rev}. The voltage profile in Figure 2.11 was calculated using two instances of Equation 2.10 to represent an electrode with two types of intercalation sites (such as octahedral and tetrahedral sites) where the number of one site type is double the number of the other type ($N_2 = 2N_1$) as was demonstrated in [79]. One instance uses U_{site1} and x_1 to produce V_{rev,x_1} while the second uses U_{site2} and x_2 to produce V_{rev,x_2}, where $x = x_1 + x_2$ and $U_{\mathrm{site1}} < U_{\mathrm{site2}}$ (for simplification, $U_{\mathrm{int}} = 0$). Since the entire electrode experiences a uniform voltage under equilibrium conditions, the equations can be easily solved for x_1

and x_2 by setting $V_{\mathrm{rev},x_1} = V_{\mathrm{rev},x_2}$. Solving for repulsive ordering requires more complex computational techniques [77], but Figure 2.11 serves as an illustrative example of the voltage drops associated with both these phenomena. Note that the size, shape, and number of these voltage drops will vary depending on the properties of a given electrode material.

Some layered electrode materials exhibit Li^+ interactions that are attractive within each layer (intralayer) but repulsive between different layers (interlayer). This gives rise to a different phenomenon known as 'staging', where one or more empty layers exist between intercalated layers, depending on the value of x. One important example of staging is the graphite electrode, which is the most commonly used negative electrode material in commercial lithium-ion batteries [60]. This example is illustrated in Figure 2.12, which shows six unique stages that have been observed in graphite at different points during Li^+ intercalation [85]. The stages are labelled 1 through 4, with the number referring to the number of graphite layers between Li^+ layers and the 'L' referring to 'liquid-like', which means that the number of Li^+ in a given layer is small enough that the Li^+ remain disordered within individual layers.

Figure 2.12 illustrates that in stage 1L the Li^+ are so diffuse that the repulsive interlayer interactions have little impact, and the Li^+ are therefore distributed throughout all the layers to maximize the entropy. As the number of Li^+ increases, the repulsive interlayer interactions also increase such that the Li^+ start to arrange themselves in every fourth intercalation layer to minimize the interaction energy. As more Li^+ are added, it eventually becomes thermodynamically favourable for the Li^+ to arrange themselves on every third intercalation layer, and then every second intercalation layer. The number of Li^+ in every second layer then increases until the 'liquid-like' stage 2L becomes a more ordered stage 2, which is fully formed around $x = 0.5$. Then between $x = 0.5$ and $x = 1$, stage 2 transitions to stage 1 until every layer is completely filled with Li^+. Note that the Li^+ do not need to exit one layer and enter a different layer during staging transitions, as suggested by the simplified diagram in Figure 2.12. Theoretical models such as the widely cited Daumas-Herold model offer explanations for how the complex structure of real graphite allows the staging transitions to occur [86], [87].

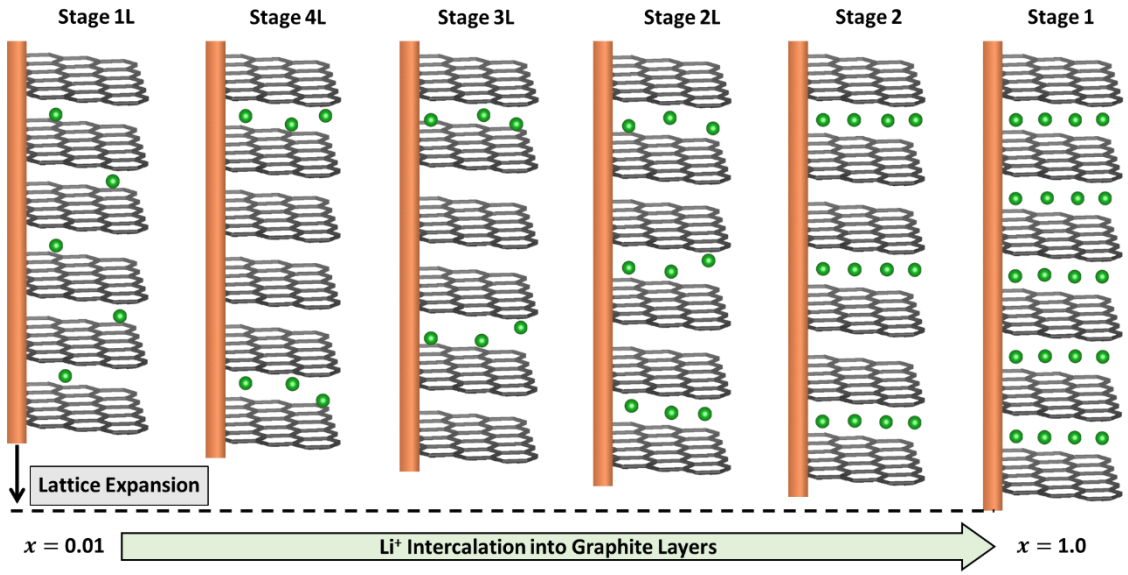


Figure 2.12 Simplified illustration of the lattice expansion and staging phenomenon observed during intercalation of a graphite electrode.

Figure 2.12 also shows qualitatively how the host lattice expands as the layers are pushed apart by the intercalating Li^+, which occurs to some degree in most layered intercalation electrode materials [88]. This is another component of the intercalation energy not accounted for in Equation 2.10, though the lattice gas model can be modified to account for this elastic energy. This was done for a titanium sulfide intercalation electrode in [89], which showed that the elastic strain increases the energy required for intercalation and therefore depresses the voltage profile, particularly at low x. The amount of lattice expansion has been reported at 10 to 13 % for Li^+ intercalation into graphite [90], which is reversed on deintercalation. The strain field created by the expanding lattice is thought to be what gives rise to attractive Li^+ intralayer interactions, which in turn makes staging possible [91]. However, this cyclic stress is also a source of long-term electrode degradation, which will be discussed in Section 2.5.

The example of graphite also highlights another important intercalation phenomenon: phase transitions. In many electrode materials, different molecular structures (i.e. phases) can form at various points in the intercalation process (such as the staging structures in Figure 2.12). In a first-order phase transition, two distinct phases coexist over a range of x, with one phase growing while the other shrinks. This is known as the 'shrinking core' model [92], which applies to other chemical reactions as well. Figure 2.13 illustrates an

example of a first-order phase transition from stage 2L to stage 2 in a single spherical graphite particle immersed in electrolyte. At the beginning of the transition, the entire particle is in stage 2L with every 2nd layer partially filled with Li^+ in a random distribution. As x increases, the newly intercalated Li^+ continue to fill these layers to minimize the interlayer repulsive interactions. This could proceed in such a way that all the 2L layers throughout the particle fill at the same rate and a single phase is maintained, but instead, the 2L layers near the surface of the particle fill first, even at infinitesimal current. This occurs because the attractive intralayer interactions make it more thermodynamically favourable for an incoming Li^+ to intercalate into a layer with more Li^+ already present. As a result, the particle separates into two distinct phases with the surface in stage 2 and the inner bulk of the particle still in stage 2L. As x continues to increase, the excess Li^+ will diffuse deeper into the particle such that the phase boundary gradually moves into the core until the entire particle is in stage 2.

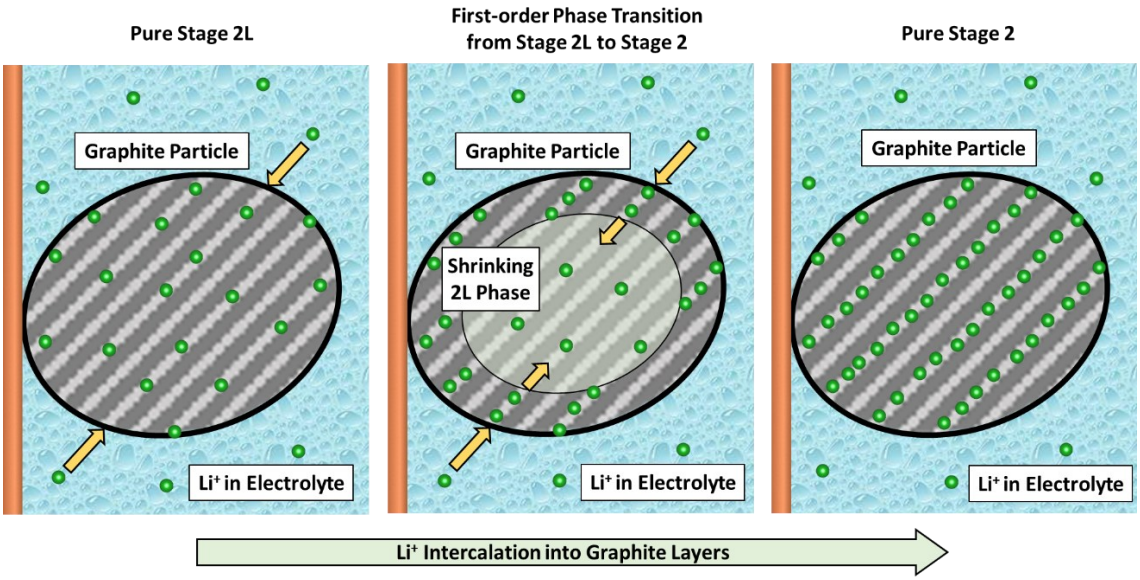


Figure 2.13 Simplified illustration of the 'shrinking core' model for a first-order phase transition during intercalation into a single graphite particle.

First-order phase transitions have significant impacts on the voltage profile of a lithium-ion cell. As the phase boundary advances into the particle, the intercalation energy of each incoming Li^+ remains constant, which results in a voltage plateau during the phase transition. This is analogous to the 0 °C temperature plateau during the phase transition between liquid water and ice. To illustrate this effect, Figure 2.14 shows the voltage profile

measured during the intercalation of a graphite electrode, with the various stages from Figure 2.12 indicated. The voltage drops rapidly in stage 1L due to the logarithmic increase in configurational entropy (as modelled in Figure 2.10), followed by a voltage plateau during the first-order phase transition from stage 1L to stage 4L. The transition from stage 4L to stage 3L does not give a voltage plateau because this is not a first-order transition, but rather a continuous phase transition without coexistence of distinct 4L and 3L phases [85]. This is followed by three subsequent first-order phase transitions from stage 3 to stage 2L, from stage 2L to stage 2, and from stage 2 to stage 1, each with its own voltage plateau. When x continues to increase after a given first-order phase transition reaches completion, excess Li^+ at the particle surface can no longer diffuse towards the core and must therefore begin to form a new phase that has greater repulsive interactions. This gives rise to the relatively sharp voltage drops between the plateaus in Figure 2.14.

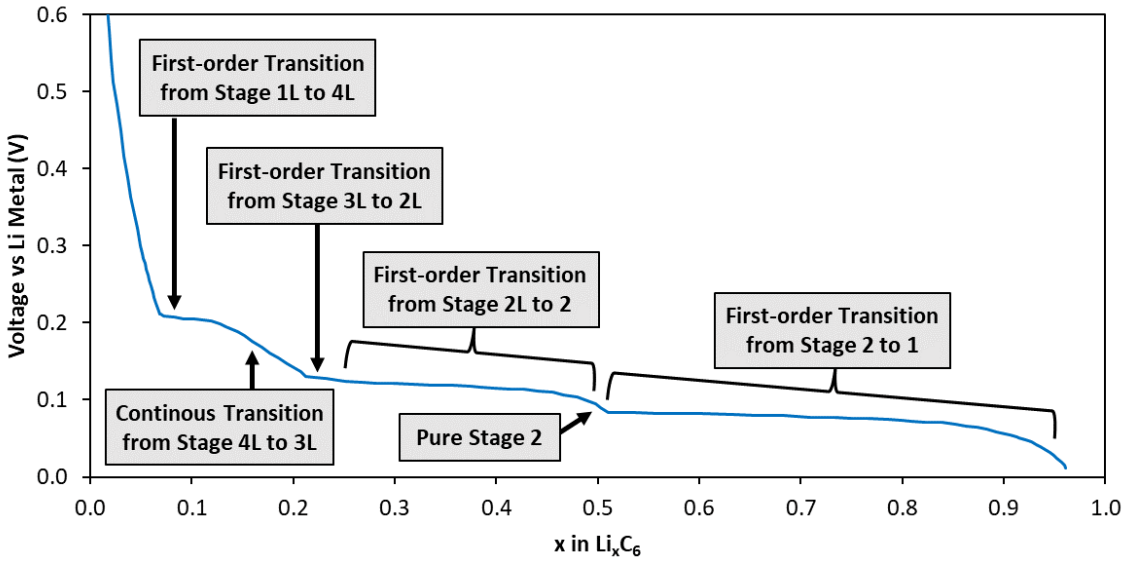


Figure 2.14 Illustration showing how staging and phase transitions impact the voltage profile of a graphite electrode during the intercalation process. Based on data and figures from [85], [93].

2.2.4. Solid State Redox Reactions

Mean field theory employs U_{site} as a single value representing the change in energy associated with transferring Li^+ and e^- from Li metal into the host lattice of a given intercalation electrode, excluding the effect of Li^+ interactions. The value of U_{site} is determined by two main factors: the electric field present at the Li^+ intercalation sites

resulting from the electrostatic charges of the elements comprising the electrode material; and the energy level of the valence orbitals that receive the incoming e^- when they enter the electrode material from the external circuit, which has a strong dependence on the nature of the ionic and covalent molecular bonding within the electrode material [94]. The effect of the e^- transfer is the focus of this section, as it is essential for understanding the different cell voltage characteristics exhibited by different EV batteries. During intercalation, a reduction reaction takes place when e^- enter the valence orbitals of the elements comprising the electrode material. During deintercalation, an oxidation reaction takes place in the electrode material when e^- are removed from the same valence orbitals. These solid state redox reactions have a significant influence on U_{site} and therefore on V_{rev}. While the nature of these reactions is highly complex, this section will provide a basic overview.

Continuing with the example of graphite used in Section 2.2.3, Figure 2.15 provides a simplified illustration of what happens at a molecular level during Li^+ intercalation into a graphite electrode. Each carbon is covalently bonded to three other carbons in what are known as σ bonds (represented by the straight grey lines in Figure 2.15), whereby valence electrons are shared between neighboring carbons in overlapping hybridized sp^2 orbitals [95]. Since carbon atoms have four valence electrons, this leaves one spare valence electron per carbon. All these spare valence electrons are located in p orbitals which overlap or 'conjugate' to form what is known as a π bond (represented by the grey inner circle in Figure 2.15) where the π electrons are delocalized and free to move throughout the graphite, giving high electrical conductivity [95].

When graphite is paired with Li metal in an electrochemical cell, the Li metal will spontaneously oxidize to give Li^+ and e^-. The Li^+ transfer through the electrolyte to intercalate between the graphite layers, while the e^- transfer through an external circuit and enter into the carbon π bonds [95], which further increases the electrical conductivity of the graphite electrode [96]. The incoming e^- enter into the carbon π bonds at a relatively high energy level and thus experience a relatively small drop in energy relative to the Li/Li^+ redox reaction [97]. This gives graphite a relatively low voltage vs Li metal (about 0.2 V on average), which contributes to its suitability as a negative electrode material.

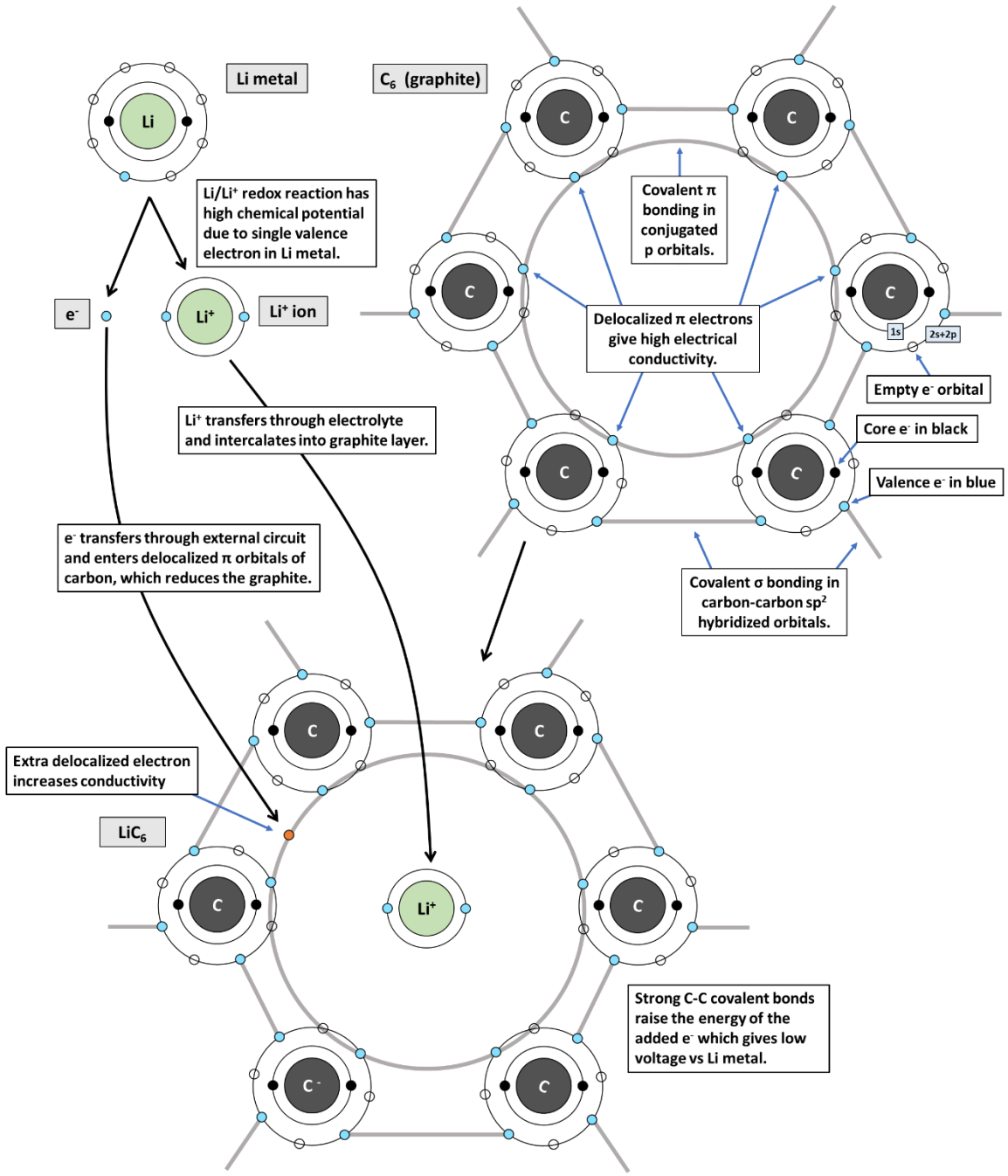


Figure 2.15 Simplified illustration of solid state redox reaction during the intercalation of lithium into graphite.

A similar process occurs during solid state redox reactions in positive electrode materials like LCO, LMO, and LFP, but since these materials feature multiple elements, there are additional considerations compared to graphite. Each of these positive electrode materials features a transition metal (denoted as 'M' in this section) cation located in octahedral sites

between six O^{2-} anions [88], but the arrangement of MO_6 octahedra is different for layered, spinel, and olivine material structures (see Figure 2.3). During the intercalation of Li^+ into these materials, the incoming e^- are added into the valence d orbitals of the transition metal cations [88].

Figure 2.16 provides a simplified illustration of the relatively straightforward case of LCO. The top of the figure represents the deintercalated state with Li metal and CoO_2 (shown as a two-dimensional MO_6 octahedron), where a balanced charge requires $Co^{4+}(O^{2-})_2$. During the spontaneous intercalation reaction, the Li metal oxidizes to give Li^+ and e^-. The Li^+ transfers though the electrolyte to intercalate into an empty octahedral site between layers of MO_6 octahedrons, while the e^- transfers through an external circuit before entering into an empty cobalt d orbital. The added e^- causes a reduction from Co^{4+} to Co^{3+}, giving a lithiated electrode ($LiCoO_2$ at the bottom of Figure 2.16) with a new charge balance of $Li^+Co^{3+}(O^{2-})_2$. It should be noted that there is some degree of covalence between transition metal cations and oxygen anions, so representing CoO_2 as $Co^{4+}(O^{2-})_2$ is not strictly accurate. This covalence means that the O^{2-} can also participate in the e^- transfer, especially near the delithiated state [98], [99].

The voltage of positive electrode materials like LCO, LMO, and LFP is strongly dependent on the energy level of the transition metal d orbitals which receive the incoming e^-. This energy level depends on a variety of competing factors. For example, the greater number of protons (27) in cobalt will attract its valence e^- more strongly compared to the smaller number of protons (25) in manganese. This gives cobalt a smaller ionic radius than manganese, which allows for a greater drop in energy (relative to Li metal) when an e^- enters into a cobalt d orbital compared to a manganese d orbital [100]. This atomic property trend will tend to give a cobalt-based electrode a higher cell voltage than an equivalent manganese-based electrode. The oxidation state of the transition metal is also an important factor, as a more positively charged transition metal cation will attract e^- more strongly and thereby give a larger drop in energy relative to Li metal. For example, a Co^{3+}/Co^{4+} redox couple will tend to give a higher cell voltage than a Co^{2+}/Co^{3+} redox couple [101].

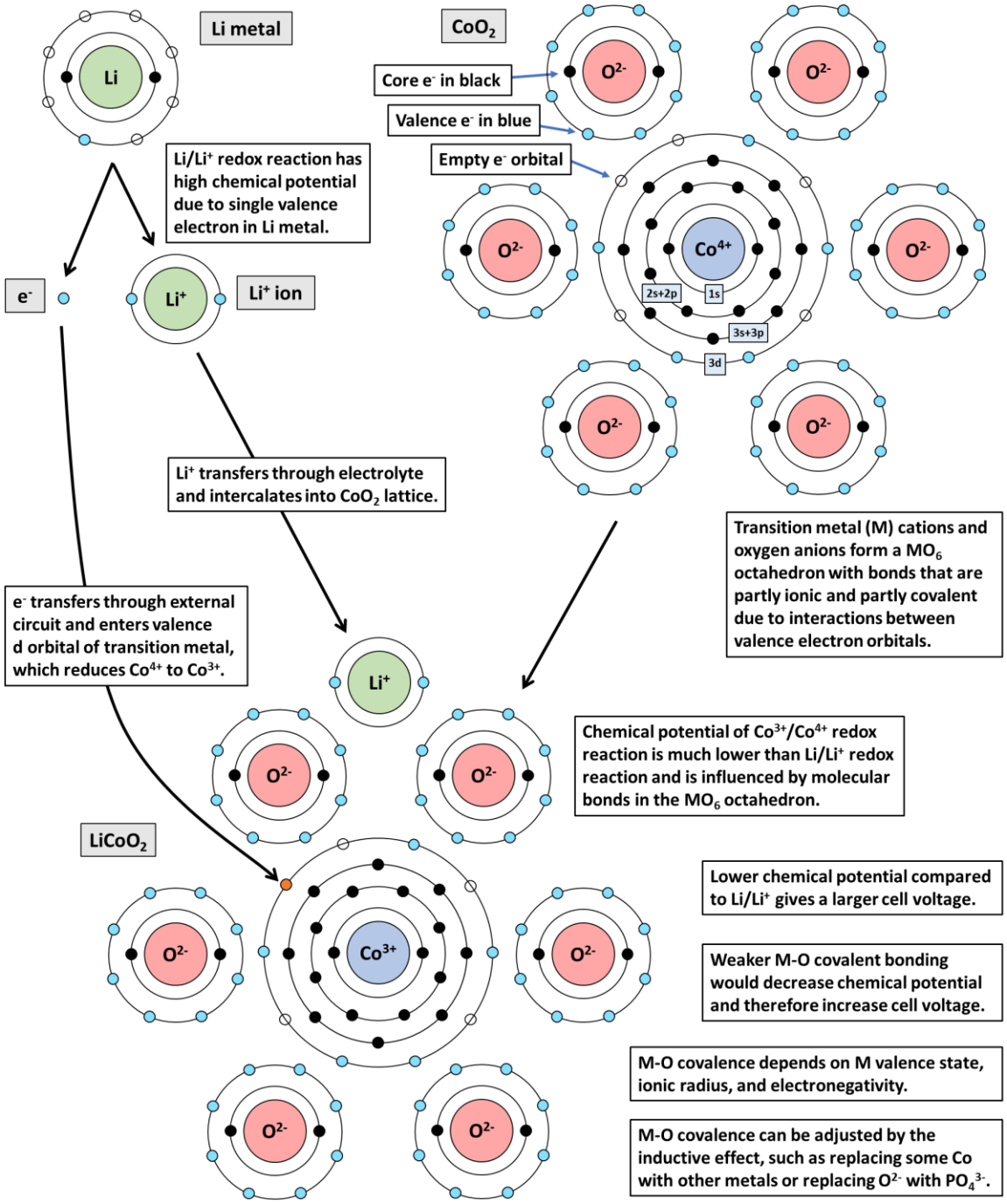


Figure 2.16 Simplified illustration of solid state redox reaction during the intercalation of lithium into LCO.

Figure 2.17 provides a simplified illustration to compare the solid state redox reactions in LCO, LMO, and LFP positive electrodes during intercalation. In LCO, all of the cobalt cations are reduced from Co^{4+} to Co^{3+}. In LMO, only half of the manganese cations are reduced from Mn^{4+} to Mn^{3+} since additional intercalation has been shown to cause a

significant lattice distortion and a sharp 1 V drop in voltage [102]. In LFP, all of the iron cations are reduced from Fe^{3+} to Fe^{2+}. The redox reactions shown are reversed during deintercalation. Note that LFP uses the PO_4^{3-} polyanion instead of the O^{2-} anion used in LCO and LMO. The charge balance thus requires that the solid sate redox couple in LFP is Fe^{2+}/Fe^{3+} instead of Fe^{3+}/Fe^{4+}, which will tend to give a lower voltage.

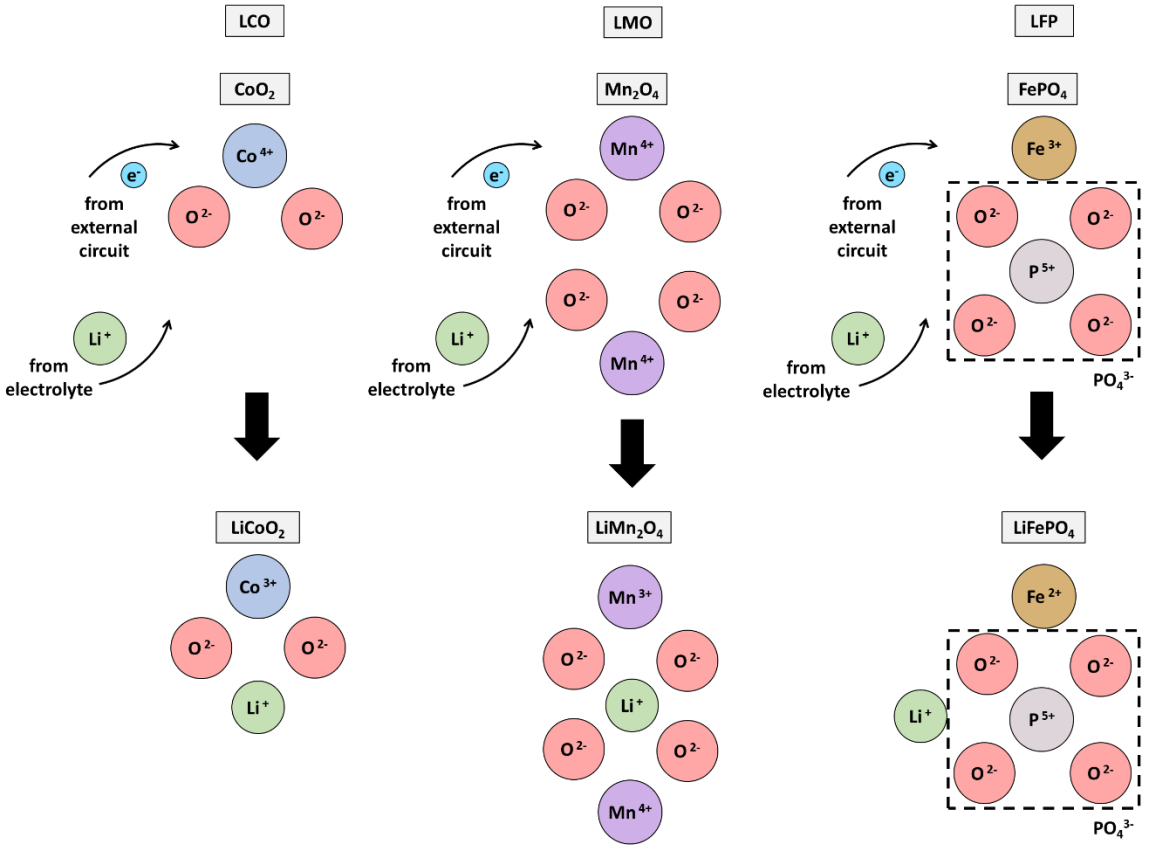


Figure 2.17 Simplified illustration of solid state redox reactions during the intercalation of lithium into LCO (left), LMO (middle) and LFP (right).

The energy level of the transition metal d orbitals also depends on the nature of the bonding in the MO_6 octahedrons. While the MO_6 bonds are partly ionic due to the attractive electrostatic forces between oppositely charged transition metal cations and oxygen anions, the bonds are also partly covalent due to interactions between the valence orbitals of the transition metal cation and surrounding oxygen anions [100]. The covalent bonding raises the energy level of the transition metal d orbitals that receive the incoming e^-, which gives a lower cell voltage compared to a purely ionic equivalent [100]. The degree of covalent bonding in the MO_6 octahedron therefore has a significant impact on the cell

voltage. Replacing the O^{2-} anions with polyanions such as PO_4^{3-} can alter the covalent bonding in the MO_6 octahedron through a phenomenon known as the 'inductive effect', whereby the strong covalent bonding within the polyanion effectively weakens the covalent bonding in the MO_6 octahedron such that an incoming e^- arrives at a lower energy level [103]. The use of a polyanion can therefore have the effect of 'inducing' an increase in the cell voltage. For example, the Fe^{2+}/Fe^3 redox couple in $LiFe_2O_3$ gives a relatively low cell voltage of < 2.5 V vs Li metal, while the Fe^{2+}/Fe^3 redox couple in $LiFePO_4$ (i.e. LFP) gives a higher cell voltage around 3.4 V vs Li metal thanks to the strong P-O covalent bonds in the PO_4^{3-} polyanion [104].

Figure 2.18 compares the 3.4 V voltage profile of LFP with the higher voltage profiles of LCO and LMO, which both feature a M^{3+}/M^{4+} redox couple. As discussed earlier in this section, the atomic properties (e.g. ionic radius) of manganese tend to give a lower cell voltage compared to cobalt. However, Figure 2.18 shows that LCO and LMO have similar overall voltage magnitudes centered near 4 V (noting that LCO voltage is higher at $x < 0.5$ such that it cannot be operated in this range due to stability and safety issues at high voltage). This is because the layered structure of LCO and the spinel structure of LMO affect the molecular bonding differently. When the Co^{3+}/Co^{4+} redox couple is active in an LMO-type spinel structure, the voltage profile is centered near 5 V [105], and when the Mn^{3+}/Mn^{4+} redox couple is active in a LCO-type layered structure, the voltage profile is centered near 3 V [106]. A spinel electrode material tends to give a higher voltage compared to a layered electrode material because the tetrahedral Li^+ intercalation sites in a spinel structure experience weaker repulsive forces compared to the octahedral Li^+ intercalation sites in a layered structure [88]. This effect also gives spinel electrodes a relatively shallow voltage slope compared to the steeper voltage slopes of layered electrodes, along with the fact that spinel structures do not expand as much as layered structures during intercalation [88]. The different positive electrode material structures and Li^+ intercalation site geometries were shown previously in Figure 2.3 and Figure 2.4, respectively.

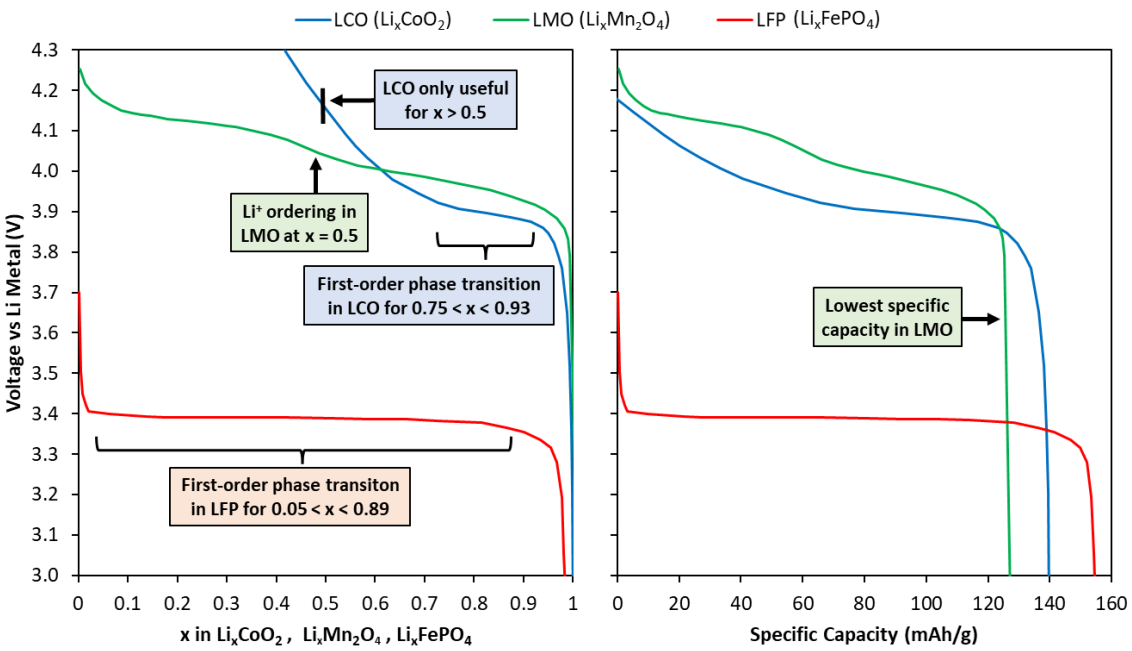


Figure 2.18 Comparison of discharge voltage profiles plotted against lithium content (left) and specific capacity (right) for LCO, LMO and LFP positive electrodes. Based on data and figures from [107].

The three voltage profiles in Figure 2.18 also demonstrate some of the special intercalation phenomena described in Section 2.2.3. The intercalation process for LFP is essentially one continuous first-order phase transition near 3.4 V (evidenced by the relatively flat LFP voltage profile), where a $LiFePO_4$ phase propagates from the surface of the electrode particles into a 'shrinking core' $FePO_4$ phase [92]. Studies have demonstrated the existence of intermediate phases at low and high values of Li^+ composition x, such that the first-order phase transition approximately spans $0.05 < x < 0.89$ [108]. A first-order phase transition has also been shown to occur in LCO at $0.75 < x < 0.93$ [109], exhibited by the LCO voltage plateau near 3.9 V in Figure 2.18. Unlike the phase transitions described for graphite and LFP, the LCO phase transition is not defined by the ordered arrangement of Li^+, but rather by a transition from metallic properties at $x < 0.75$ to semiconductor properties at $x > 0.93$ [110]. For LMO, the intercalated Li^+ form an ordered arrangement in the electrode host lattice at a composition of $x = 0.5$ [77], exhibited by the relatively sharp drop around the midway point of the voltage profile in Figure 2.18.

The right chart in Figure 2.18 uses specific capacity (mAh/g) as the x-axis, showing how the LMO spinel structure cannot store as many Li^+ per unit mass of electrode material compared to layered LCO and olivine LFP. The layered structure of LCO has a much higher theoretical capacity than shown in Figure 2.18 (273 mAh/g), but only about 50 % of this can be utilized in the practical voltage range used in commercial cells [111].

While the LCO, LMO, and LFP voltage profiles shown in Figure 2.18 agree well with experimental data from numerous publications, it is important to note that the reversible voltage profile V_{rev} for a given electrode material stoichiometry is not set in stone. During material synthesis, a number of adjustable parameters such as temperature and heating rate can influence the molecular interactions present in the final material and therefore influence V_{rev}. For example, lower synthesis reaction temperatures have been used to produce smaller particle sizes (< 20 nm) in LCO to improve high-power performance, resulting in an increased slope of the LCO voltage profile and elimination of the 3.9 V voltage plateau [112].

It is also important to note that V_{rev} for a given electrode material is not necessarily identical for both intercalation and deintercalation. A number of factors give V_{rev} some degree of hysteresis between the intercalation profile and the deintercalation profile. For example, mechanical stresses associated with lattice volume changes impact V_{rev} in different ways depending on the direction of the reaction [113]. First-order phase transitions are also known to give rise to hysteresis due to stresses at the phase boundary [80].

2.2.5. Alloyed Electrode Materials

Section 2.2.4 focused on three common positive electrode materials (layered LCO, spinel LMO, and olivine LFP) which each feature a single type of transition metal and give practical specific capacities in the range of 120 to 160 mAh/g [114]. The layered LNO electrode can give over 200 mAh/g [115] but has little practical value due to a variety of stability issues. As mentioned in Section 2.1.3, the stability issues of LNO can be mitigated by substituting some of the nickel for other metals such as cobalt, manganese, and aluminium, leading to alloyed positive electrode materials such as NMC and NCA [47]. The presence of multiple transition metals in the same electrode material can have

significant impacts on the voltage profile, with different transition metal cations undergoing solid state redox reactions in different voltage ranges. For example, when some of the manganese in LMO is substituted with nickel to give spinel $LiMn_{2-y}Ni_yO_4$, nickel redox reactions take place at 4.7 V during intercalation until all the nickel has been reduced, after which point manganese redox reactions take place at 4 V, giving a sharp voltage drop in between [116].

Figure 2.19 provides a simplified illustration of the solid state redox reactions during the intercalation of lithium into an NMC electrode, based on early theoretical work in [117] and [118]. At the start of intercalation, the first third of the e^- will be accepted into cobalt orbitals to reduce Co^{4+} to Co^{3+}. This is because the $Co^{3+/4+}$ orbitals are at a lower energy level (relative to Li metal) than the $Ni^{3+/4+}$ and $Mn^{3+/4+}$ orbitals in NMC. After the $Co^{3+/4+}$ orbitals are filled, the final two thirds of the e^- are accepted into nickel orbitals to reduce Ni^{4+} to Ni^{3+} and then to Ni^{2+}. The $Ni^{3+/4+}$ and $Ni^{2+/3+}$ orbitals are at similar energy levels and both are at lower energy then $Mn^{3+/4+}$ [117]. Manganese is therefore electrochemically inactive in NMC and remains as Mn^{4+} during intercalation, serving only to stabilize the material for extended cycle life. Note that experimental studies have shown that cobalt effectively remains as Co^{3+} during intercalation in NMC [88]. This is because the incoming e^- tend to enter into the orbitals of the oxygen anions neighboring the Co^{3+} [119]. The case of NCA is similar, with the redox reactions carried primarily by $Ni^{3+/4+}$ with some $Co^{3+/4+}$ activity at higher voltage [39], while aluminum remains inactive as Al^{3+} and serves only to stabilize the material for improved cycling [120], [121].

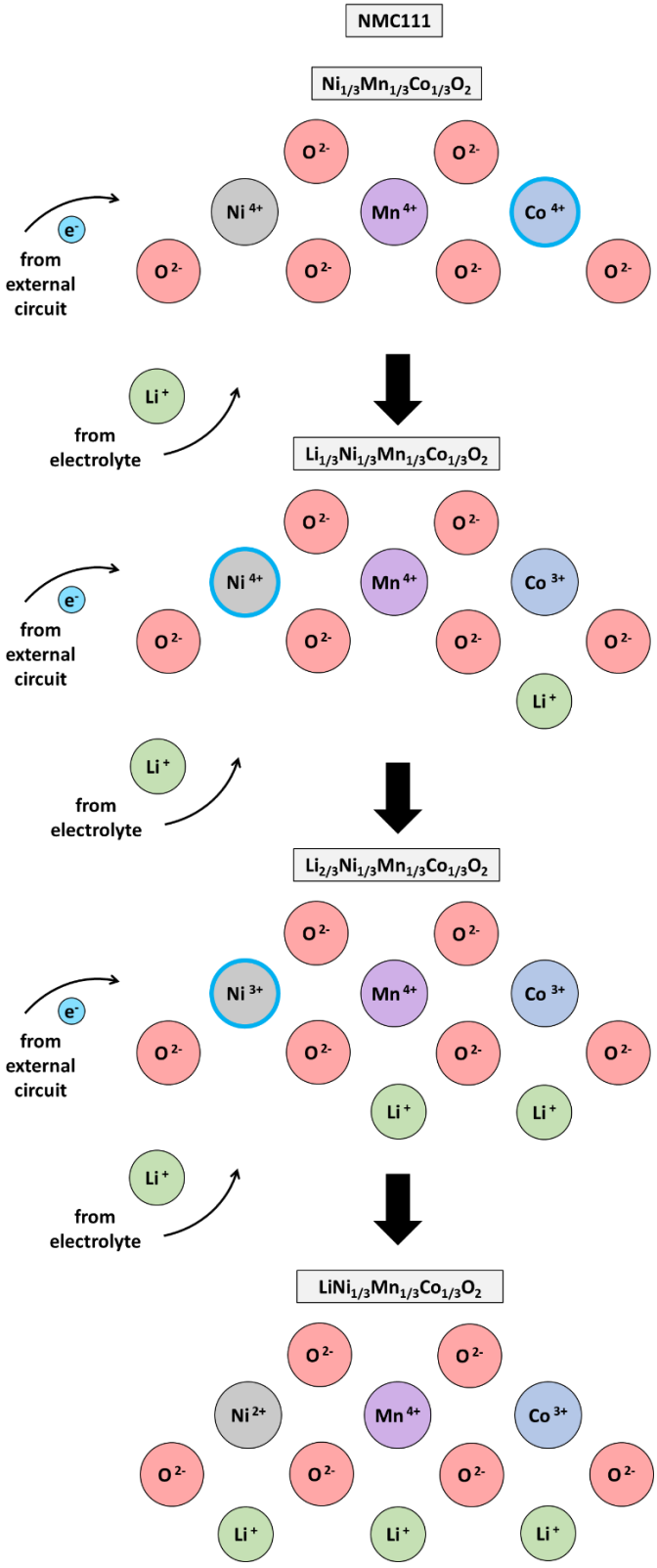


Figure 2.19 Simplified illustration of solid-state redox reactions occurring during the intercalation of lithium into NMC111. The reacting transition metal cation in each step is highlighted in blue.

Figure 2.20 shows the resulting voltage profiles for NMC111 and NCA in comparison to pure LNO and pure LCO (during the first charge after material synthesis). The LCO voltage profile is significantly higher than LNO due to the lower energy level of the $Co^{3+/4+}$ orbitals compared to the $Ni^{3+/4+}$ orbitals [39], [118]. Both NMC111 and NCA lie in between the higher voltage of LCO and the lower voltage of LNO, but the higher cobalt content of NMC111 gives a slightly higher voltage. As expected from the diagram in Figure 2.19, NMC111 and NCA more closely resemble the higher LCO voltage at low values of x where the $Co^{3+/4+}$redox couple is most active, and more closely resemble the lower LNO voltage at higher values of x where the $Ni^{3+/4+}$ and $Ni^{2+/3+}$ redox couples are most active.

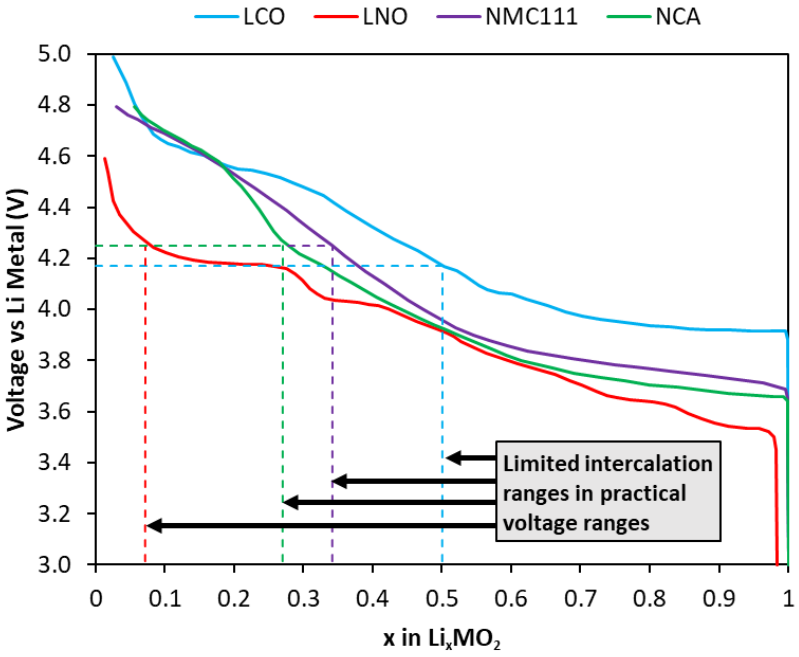


Figure 2.20 Comparison of voltage profiles for LCO, LNO, NMC111, and NCA during first charge. Based on data and figures from [39].

The dashed lines in Figure 2.20 represent practical upper voltage limits that would be employed in commercial applications to ensure safety and cyclability (noting the more restrictive limit on LCO as described in Section 2.2.4). This shows that higher nickel content allows for more usable capacity in a practical voltage range (recall that NCA is $LiNi_{0.8}Co_{0.15}Al_{0.05}O_2$).While the practical capacity of LNO decreases with greater amounts of substituted cobalt, manganese, and aluminum, these substitutions significantly improve the physical, electrical, and chemical properties of LNO such that NMC and NCA

electrodes can provide increased capacity compared to LMO and LFP while still maintaining competitive cycle life and safety characteristics [31], [121], [122].

The shape of the voltage profile in NMC and NCA depends strongly on the relative content of nickel vs substituted metals. Figure 2.21 demonstrates how LNO (left) and NMC (right) voltage profiles are impacted by different amounts of metal substitution. The left chart shows varying amounts of cobalt substituted into LNO. The pure LNO voltage profile features three distinct voltage plateaus, each representing a first-order phase transition in the LNO lattice [123]. These plateaus progressively disappear as more cobalt is substituted into the LNO, since the presence of cobalt in the LNO structure suppresses the phase transition [41]. The right chart in Figure 2.21 shows four NMC variants including NMC111 (33 % Ni), NMC622 (60 % Ni), NMC811 (80 % Ni) and $LiNi_{0.85}Mn_{0.075}Co_{0.75}O_2$ (85 % Ni). This shows how NMC variants with higher nickel content bear a closer resemblance to the pure LNO voltage profile in the left chart. Notably, lower nickel content gives a smoother voltage profile with a steep slope at high voltage, while higher nickel content gives a more tapered slope near the upper voltage limit.

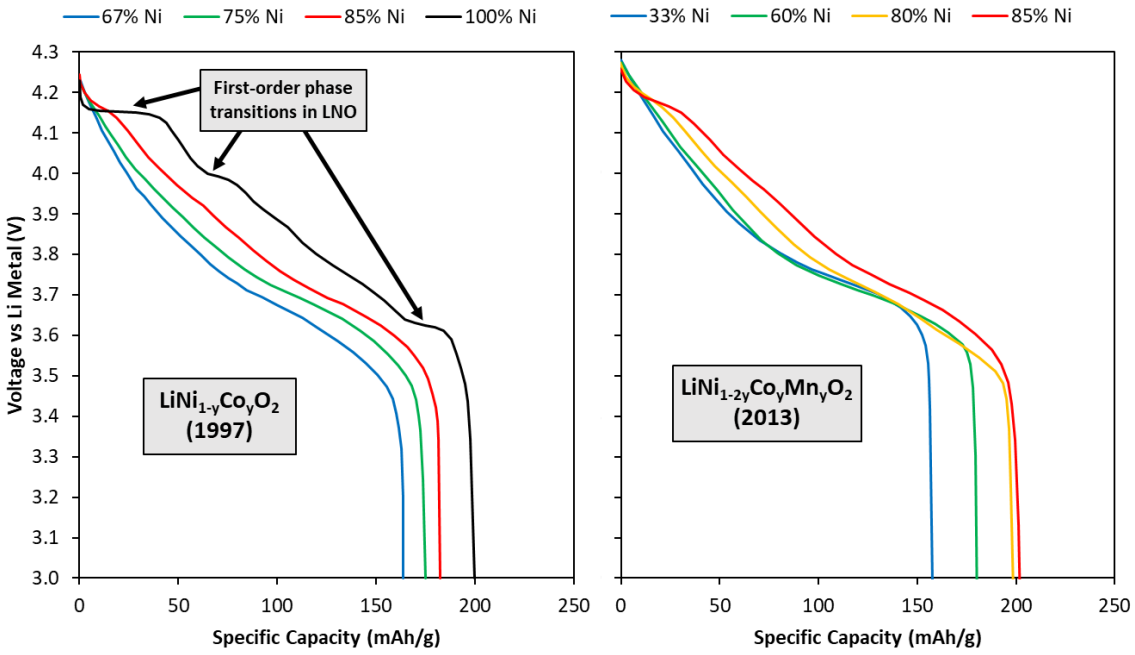


Figure 2.21 Comparison of discharge voltage profiles for various compositions of cobalt-substituted LNO (left) and NMC (right). Based on data and figures from [31], [124].

The LNO phase transition near 4.2 V in Figure 2.21 has been shown to result from a sharp change in lattice volume [125]. The LNO lattice volume decreases relatively slowly throughout most of the deintercalation process, with metal-oxide layers shrinking as e^- are removed from the nickel cations, and lithium layers expanding as the decreasing lithium content results in stronger repulsive forces between oxygen anions on either side of each lithium layer. But as the electrode approaches 4.2 V during deintercalation, the metal-oxide layers shrink due to the relatively small ionic radius of Ni^{4+} compared to Ni^{3+} and Ni^{2+}, while the intercalation layers shrink due to the decreased repulsion between oxygen layers as e^- are removed from oxygen anions [99]. The lattice contraction forms a new crystal phase, which propagates through the LNO particles as the Li^+ content continues to decrease, giving the 4.2 V plateau. The tapered slope in this upper voltage region for nickel-rich NMC in Figure 2.21 is a reflection of this lattice volume change. Due to the presence of cobalt and manganese in NMC however, a single phase is maintained during this volume change as opposed to the two coexisting phases in LNO [115]. As a result, NMC variants with Ni > 60 % feature a tapered voltage slope during this transition instead of the voltage plateau exhibited by LNO. The same tapered slope can be seen in the voltage profile for NCA (80 % Ni) shown in Figure 2.20, which also corresponds to a lattice volume change [43]. This voltage characteristic is important to consider for charge termination in second-life batteries with nickel-rich positive electrodes, as will be demonstrated in Chapter 5. In contrast, there is insignificant volume change in this voltage range for NMC111 and NMC622 due to their lower nickel content, which is better for long-term cycling stability [126].

2.2.6. Blended Electrode Materials

Section 2.1.3 discussed the advantages of blending multiple positive electrode materials to combine their unique strengths in a single electrode. Since NMC-LMO blended electrodes can be found in a number of different EVs in use today [58], it is important to understand how this blending impacts the voltage profile. Figure 2.22 presents four voltage profiles including pure NMC111, pure LMO, a 70/30 NMC-LMO blend, and a 30/70 NMC-LMO blend. This comparison shows that higher LMO content gives a higher voltage and a lower capacity, as would be expected based on the previously discussed characteristics of LMO

and NMC. The differences in the shapes of the voltage profiles are less intuitive, but have a simple explanation. Studies on the intercalation dynamics of layered-spinel blended electrodes have found that spinel LMO primarily participates in the intercalation reaction above 3.85 V vs Li metal where the LMO redox couple is most active, while the layered material participates across the full voltage range [127]. This is evidenced in Figure 2.22 by the notable voltage drop occurring around 3.8 to 3.9 V for the two blended electrodes, signalling that most of the LMO intercalation sites have been used up and the reaction is being carried by NMC at lower voltages. Similar results have been demonstrated for NCA-LMO blended electrodes [57]. Also note that the volage drop due to Li^+ ordering near the midway point of the pure LMO voltage profile disappears when LMO is blended with NMC.

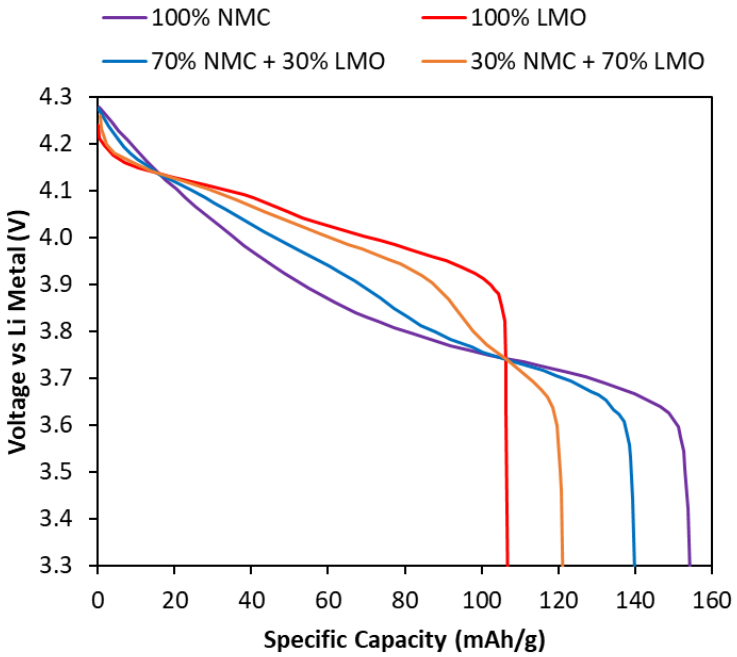


Figure 2.22 Comparison of discharge voltage profiles for NMC-LMO blended electrodes. Based on data and figures from [128].

Section 2.1.4 introduced graphite-silicon blended negative electrodes as a means of increasing the energy capacity and power capability compared to pure graphite. Since this technology is now being deployed in commercial EVs such as the Tesla Model 3 [67], it is worth reviewing how silicon blending impacts the voltage profile of a graphite electrode. Figure 2.23 compares the discharge and charge voltage profiles for three electrodes: pure

graphite (Gr), graphite blended with 7 % (by mass) silicon (Si), and graphite blended with 15 % (by mass) silicon. Apart from the expected increase in specific capacity, Figure 2.23 illustrates how even a small amount of silicon has a dramatic effect on the graphite voltage profile. Specifically, silicon raises the voltage to higher values vs Li metal, alters the shape of the voltage profile, and introduces a large hysteresis between the intercalation and deintercalation voltage profiles. Studies of the internal dynamics of graphite-silicon blended electrodes have determined that silicon dominates the intercalation reaction when the electrode voltage is > 0.2 V vs Li metal, while graphite dominates at lower voltages [66], [129]. The large voltage hysteresis is attributed to the mechanical work associated with the silicon undergoing significant volume change (> 300 %) during intercalation and deintercalation [66]. As a result, both the magnitude and shape of the voltage profile is notably different depending on the direction of the reaction, especially at higher voltages where silicon dominates the reaction.

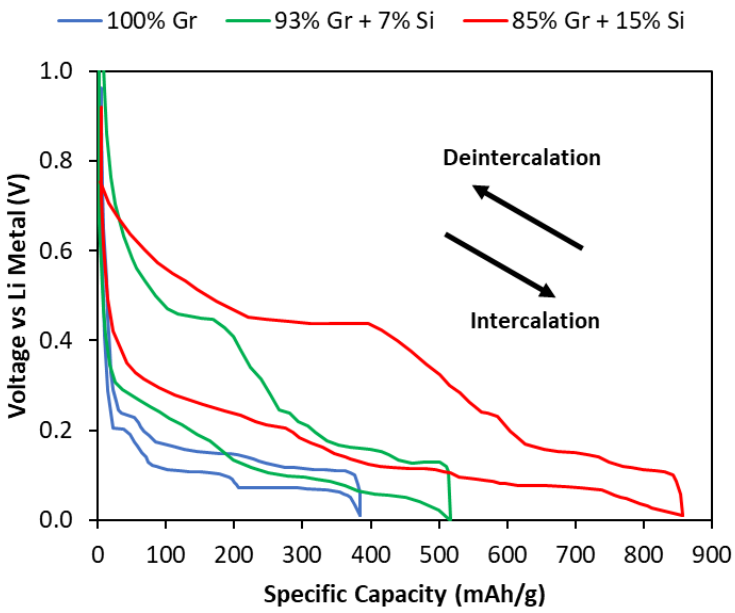


Figure 2.23 Comparison of discharge and charge voltage profiles for graphite-silicon blended electrodes. Based on data and figures from [66], [129].

2.2.7. Full Cell Voltage

In research applications, lithium metal is typically used as the negative electrode as it provides a convenient reference point with its high capacity and fixed chemical potential $\mu_{\mathrm{Li}} = 0$. This is the case in all voltage profiles shown previously in this chapter. However,

as mentioned in Section 2.1.4, lithium metal is not used in commercial lithium-ion batteries due to unresolved issues with cycling stability and safety. The voltage of a full lithium-ion cell will therefore depend on the combined characteristics of two intercalation electrodes, each with a voltage profile dependent on x.

Based on the effects of entropy and Li^+ interactions discussed in Section 2.2.2, it is theoretically possible to construct a functional lithium-ion battery with two identical intercalation electrodes. Although U_{site} will effectively be zero, if one electrode is fully intercalated ($x = 1$) and the other is fully deintercalated ($x = 0$), then entropy and repulsive Li^+ interactions will drive a spontaneous, reversible reaction that reaches equilibrium when $x = 0.5$ at both electrodes. However, the cell voltage will be relatively low with $U_{\text{site}} = 0$, and only 50 % of the Li^+ capacity will be accessible during discharge. Therefore, to construct a lithium-ion battery with high energy capacity, the cell should feature a positive electrode material with a large value of U_{site} and a negative electrode material with a small value of U_{site}.

Figure 2.24 gives an illustrative example of a full cell consisting of an NMC111 positive electrode and a graphite negative electrode. The V_{rev} profile of each electrode vs Li metal is shown, and the cell voltage is calculated as the difference between the two electrodes at common 'state of charge' (SOC) values. As the cell is charged towards 100 % SOC in Figure 2.24, Li^+ deintercalate from the NMC (causing its voltage to increase) and intercalate into the graphite (causing its voltage to decrease), so the difference between them increases. Conversely, when the cell is discharged towards 0 % SOC, Li^+ intercalate in the reverse direction such that the NMC voltage decreases, the graphite voltage increases, and the difference between them decreases. The full cell V_{rev} profile features a combination of the smooth, sloping profile of NMC111 and the sudden changes associated with graphite staging. Any lithium-ion cell with a pure graphite negative electrode should thus be expected to exhibit signs of graphite staging in its voltage profile.

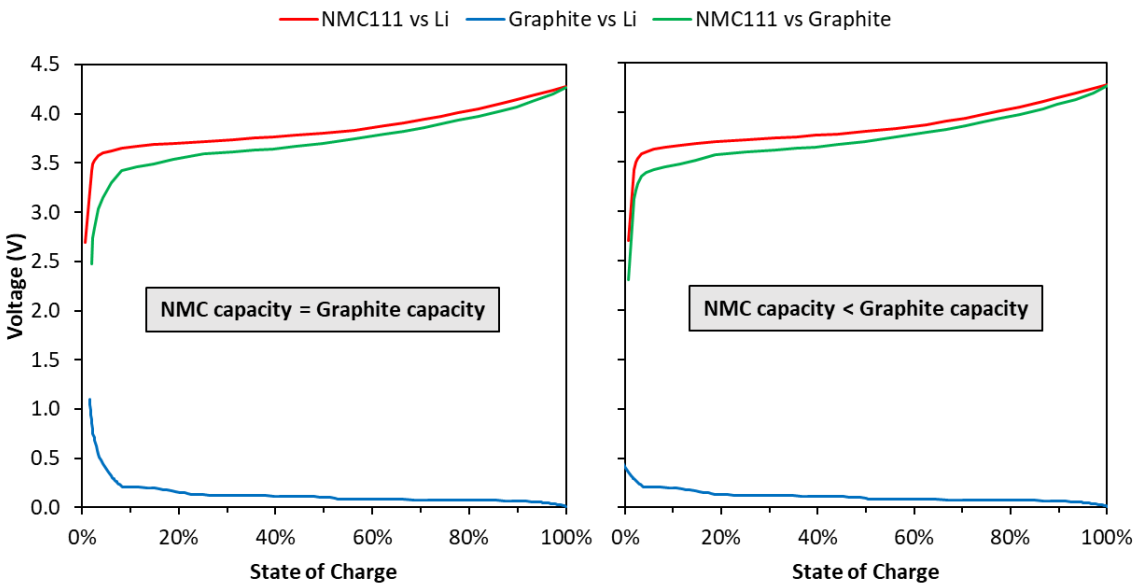


Figure 2.24 Illustrative example showing how the voltage of a full lithium-ion cell is influenced by its positive electrode and negative electrode depending on their relative capacities. Based on data and figures from [85], [93], [124].

The full cell V_{rev} profile also depends on the relative capacities of the positive and negative active materials, which may vary based on cell manufacturing as well as cell degradation. The right chart in Figure 2.24 shows a hypothetical case where the NMC becomes fully lithiated on discharge well before the graphite becomes fully delithiated, which could occur due to loss of active material at the NMC electrode. In this case, the discharge is limited by the NMC capacity, and the resulting shape of the full cell V_{rev} profile at low SOC is different from the left chart where the graphite plays more of a limiting role. Based on this observation, the shape of the full cell V_{rev} profile should change over the course of battery life if the two electrodes degrade at different rates, as was demonstrated in [130].

2.3. Operational Overpotentials

Section 2.2 described the reversible voltage V_{rev} of a lithium-ion cell under equilibrium conditions, which can serve as a useful indicator of battery SOC [131], [132] and provide important insights into the electrochemical processes occurring within the cell. However, the reversible voltage is only realized at infinitesimal current and therefore does not represent the operational voltage in practical engineering applications. When current I is flowing, there is inevitably some irreversibility as with any real thermodynamic process. For batteries, the irreversibility manifests in an overpotential IR that causes the measured

voltage V to deviate from the reversible voltage V_{rev}, where R is the internal resistance of the battery ($R > 0$). This is stated in Equation 2.11.

$$V = V_{\text{rev}} + IR \tag{2.11}$$

When the cell is discharging ($I < 0$), IR will be a negative number, resulting in a work output IV that is smaller than the reversible work output IV_{rev}. When the cell is charging ($I > 0$), IR will be a positive number, resulting in a work input that is larger than the reversible work input. Some of the useful energy must therefore be lost as heat when the battery is discharging or charging, equal to I^2R. The thermal implications of this internal heat generation will be discussed in Section 2.6.

The internal resistance R is a complex combination of physical, chemical, and electrical sources of irreversibility which vary with temperature, current, SOC, and battery age. To simplify the qualitative visualization and quantitative characterization of R, equivalent circuit models are commonly employed [133], such as the example given in Figure 2.25. Each element is discussed in detail below. Note that additional elements can be added beyond those shown in Figure 2.25 to improve the accuracy of the model. For instance, two sets of each element can be used to better model the unique characteristics of the positive and negative electrodes [134].

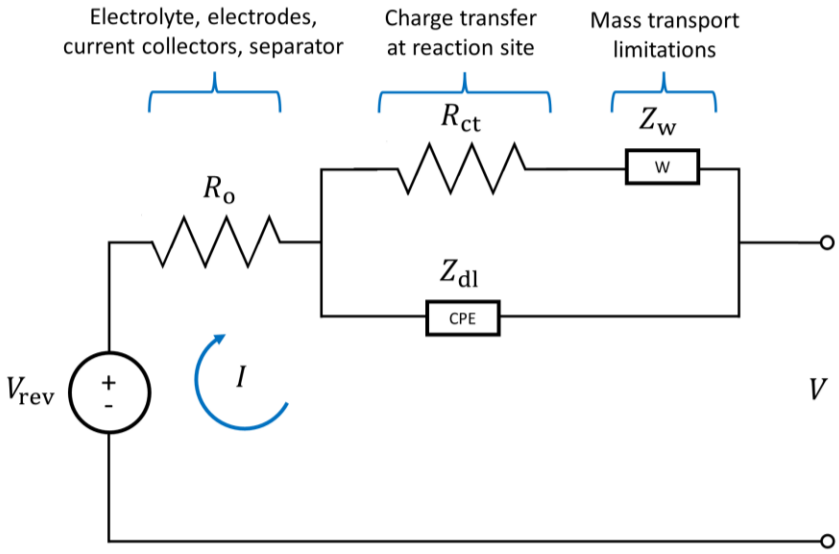


Figure 2.25 Example of an equivalent circuit used to model the overpotentials that arise when current is flowing through a battery.

2.3.1. Ohmic Resistance

The ohmic resistance R_{o} is a simplified sum of the electronic resistance in the electrodes and current collectors, as well as the ionic resistance in the electrolyte and separator. These resistances follow Ohm's law, but may vary significantly under different operational conditions. For example, it was shown in [135] that the ionic conductivity of a common 1 mol/L lithium salt is about 50 % greater at 40 °C (~15 mS/cm) compared to 20 °C (~10 mS/cm). Electrolyte conductivity also depends on properties such as the dielectric constant and viscosity of the organic solvent as well as the concentration of the lithium salt [136], so electrolytes must be tailored accordingly to reduce R_{o}.

2.3.2. Charge Transfer

The electrochemical reaction itself takes place at the interface between the electrolyte and the surface of an electrode particle. The charge at the electrode surface attracts ions of the opposite charge in the electrolyte, which accumulate at the interface to form an 'electrochemical double layer' consisting of opposite charges separated by a layer of solvent molecules [137]. When the intercalation reaction takes place, energy must be consumed for Li^+ to transfer across this double layer. In Figure 2.25, the charge-transfer resistance R_{ct} is used to model the irreversibility of this process. In order for a current I to flow, a charge-transfer overpotential φ_{ct} must exist across the double layer to drive the reaction. For a symmetrical redox system, Equation 2.12 describes the charge-transfer current I_{ct} as a function of φ_{ct} and T as per the Butler-Volmer equation [138], where E_{a} is the activation energy and $I_{\infty} > 0$ represents the theoretical maximum exchange current when $T \to \infty$ for a given concentration of reactants and products [139].

$$I_{\mathrm{ct}} = -I_{\infty}\,\mathrm{e}^{-\left(\frac{E_{\mathrm{a}}+\frac{1}{2}\varphi_{\mathrm{ct}}e}{k_{\mathrm{B}}T}\right)} + I_{\infty}\mathrm{e}^{-\left(\frac{E_{\mathrm{a}}-\frac{1}{2}\varphi_{\mathrm{ct}}e}{k_{\mathrm{B}}T}\right)} \tag{2.12}$$

The first and second terms on the right side of Equation 2.12 respectively represent the discharge and charge reactions, which coexist in equilibrium but become favoured in one direction as the magnitude of φ_{ct} increases. Note that for discharge, $I_{\mathrm{ct}} < 0$ and $\varphi_{\mathrm{ct}} < 0$. When discharging in practical operational conditions, the first term dominates and Equation 2.12 can be rearranged for φ_{ct} to give Equation 2.13, where $I_{\infty} > |I_{\mathrm{ct}}|$. This

shows that $|\varphi_{\mathrm{ct}}|$ should decrease linearly with higher temperature (at a given current) and increase logarithmically with greater current (at a given temperature). Since I_{∞} depends on Li^+ concentration, φ_{ct} will also vary with SOC.

$$\varphi_{\mathrm{ct}} = I_{\mathrm{ct}} R_{\mathrm{ct}} = -\frac{2}{e}\left(E_{\mathrm{a}} + k_{\mathrm{B}} T \ln\left[\frac{I_{\infty}}{-I_{\mathrm{ct}}}\right]\right) \tag{2.13}$$

The charge separation across the electrochemical double layer exhibits a non-ideal capacitance, and this is often modelled as a double-layer impedance Z_{dl} using a constant phase element in parallel with R_{ct} [140] as shown in Figure 2.25 (labelled 'CPE'). When there is a sudden increase or decrease in I, the change will initially be carried by a non-faradaic current through Z_{dl} as the distribution of ions at the interface changes in response [137]. As the interface approaches a new steady state, the non-faradaic current through Z_{dl} decreases to zero while I_{ct} (the faradaic current through R_{ct}) increases such that I is maintained. The overall effect of Z_{dl} is that $\varphi_{\mathrm{ct}} = I_{\mathrm{ct}} R_{\mathrm{ct}}$ will give a transient response to a change in I and gradually approach a new steady-state value. This transient behaviour will therefore be reflected in the cell voltage V in Figure 2.25.

2.3.3. Electrolyte Concentration Gradients

For current to flow, Li^+ must move between the electrodes at a rate that can sustain the current. This mass flow occurs both in the electrolyte and within the intercalation layers of the electrode particles, and in both cases the flow is restricted by the diffusion properties of the medium. In the electrolyte, a Li^+ concentration gradient $\nabla\psi$ forms based on the ratio of the current density to the diffusion coefficient D (in cm^2/s), as per Fick's law of diffusion [21]. This is shown in Equation 2.14, where A_{ψ} is the cross-sectional area of the Li^+ flow path between the electrodes (in cm^2), ψ_{PE} and ψ_{NE} are respectively the electrolyte concentrations at the positive and negative electrodes (in mol/L), F is the Faraday constant (approximately 96,485 C/mol), and L_{ψ} is the distance between the electrodes (in cm).

$$\begin{aligned} \nabla\psi &= -\frac{I}{2A_{\psi}FD} \\ &\approx \frac{\psi_{\mathrm{NE}} - \psi_{\mathrm{PE}}}{1000 L_{\psi}} \end{aligned} \tag{2.14}$$

When the cell is discharging ($I < 0$), Li^+ tend to accumulate at the negative electrode as they deintercalate, while Li^+ tend to deplete at the positive electrode as they intercalate, such that $\psi_{\mathrm{NE}} > \psi_{\mathrm{PE}}$. This effect is exacerbated at larger currents and smaller diffusion coefficients. The concentration gradient in the electrolyte results in a concentration overpotential φ_ψ, as defined in Equation 2.15 [141].

$$\varphi_\psi = -\frac{2k_B T}{e} \ln\left[\frac{\psi_{\mathrm{NE}}}{\psi_{\mathrm{PE}}}\right] \tag{2.15}$$

The '2' is included in Equation 2.15 because the effect of the concentration gradient on φ_ψ is two-fold. For one, V_{rev} depends on the concentration of Li^+ at the electrode-electrolyte interface, and is therefore lowered during discharge when $\psi_{\mathrm{NE}} > \psi_{\mathrm{PE}}$, which decreases the work output. At the same time, the concentration gradient creates an electric field which the Li^+ must work against in order to migrate from the negative electrode to the positive electrode, which further decreases the work output. Note that Figure 2.25 does not depict φ_ψ explicitly as this overpotential can be grouped in with other elements.

Electrolyte concentration gradients will also impact the electrolyte conductivity [135] as well as the exchange current I_∞ [138]. Equivalent circuit models should therefore account for concentration gradients in calculations of R_{o} and R_{ct}. The diffusion coefficient itself can also vary significantly with electrolyte concentration and temperature. One study showed that the diffusion coefficient of a common electrolyte is about 67 % greater at 40 °C (~5×10^{-6} cm^2/s) compared to 20 °C (~3×10^{-6} cm^2/s) [135]. Their battery model indicated that the temperature dependence of the diffusion coefficient has a significant mitigating effect on the overpotential when the battery self-heats during high-power operation.

2.3.4. Solid State Diffusion

Diffusion of Li^+ within the intercalation layers of individual electrode particles is significantly slower (~10^{-10} cm^2/s) than the diffusion of Li^+ in the electrolyte outside the particle (~10^{-6} cm^2/s) [141]. At larger currents, this can create significant Li^+ gradients within an electrode particle, which results in a diffusion overpotential. For example, during

a fast discharge, Li^+ will intercalate into the surface of a positive electrode particle, but because the diffusion rate is significantly slower than the current, the Li^+ content at the particle surface x_s will increase faster than the average Li^+ content x. Because the cell voltage is determined at electrode-electrolyte interface, the discharge will terminate when $x_s = 1$ even if $x \ll, 1$ such that a significant portion of the total intercalation capacity is unutilized. The difference between the voltage at x_s and the voltage at x is essentially a diffusion overpotential. A mathematical model was presented in [141] to demonstrate this behaviour. In a more advanced equivalent circuit model, the large time constant of solid-state diffusion is often modelled using a Warburg element with impedance Z_w [133], as shown in Figure 2.25 (labelled 'W').

2.3.5. Impedance Evaluation

Experimental methods are available for quantifying the circuit elements in Figure 2.25 for a given lithium-ion cell. Electrochemical impedance spectroscopy (EIS) is a technique that involves injecting an alternating current (AC) into the cell, measuring the AC voltage response and phase angle, and plotting the real and imaginary components of the AC impedance on a Nyquist plot [137]. By applying a wide AC frequency range, different elements in the equivalent circuit model can be isolated and quantified at different frequencies. For example, a number of studies have characterized R_o and R_{ct} for different lithium-ion battery designs under various conditions, showing that both values increase at lower temperature and SOC [138], [142-144].

Sophisticated software can be used to accurately model the operational overpotentials of a specified lithium-ion battery. Figure 2.26 was generated using AutoLion software [145] to demonstrate how cell design can influence the overpotentials associated with electrolyte concentration gradients and solid-state diffusion. The blue and red lines respectively represent cell designs with a thin electrode coating vs a thick electrode coating, while the solid and dashed lines respectively represent a low-current discharge vs a high-current discharge. The left chart shows the resulting cell voltage while the right chart shows the electrolyte concentration through the cell at the end of discharge.

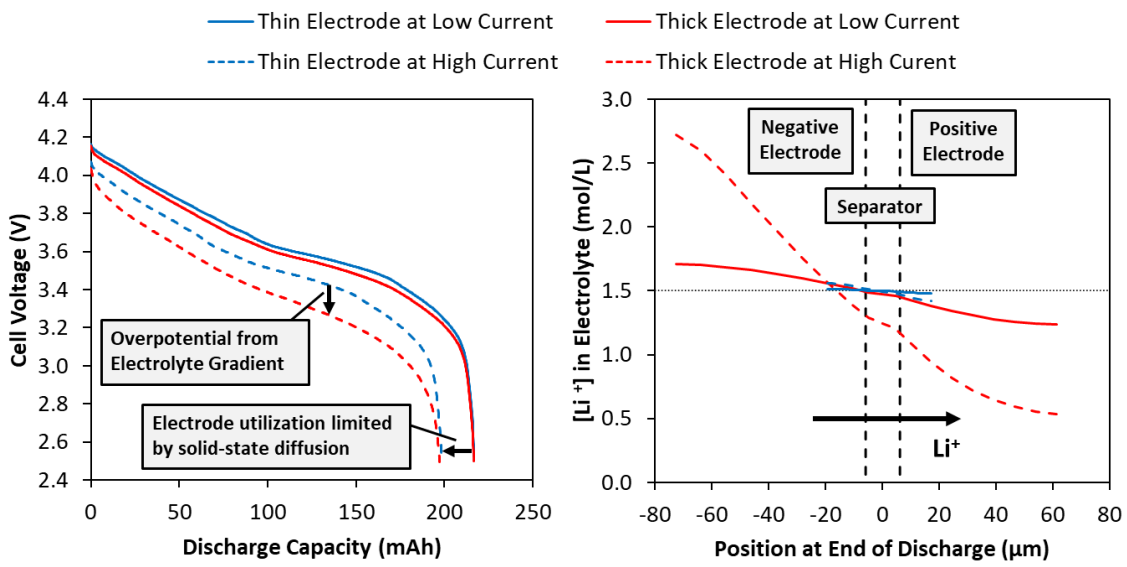


Figure 2.26 Example of the concentration gradients and overpotentials that can result from limited Li^+ diffusion through the electrolyte and electrode particles. Generated using AutoLion software [145].

During the high-current discharge in Figure 2.26, the voltage of the thin cell grows increasingly depressed compared to the low-current discharge such that significant capacity is lost. Since the right chart in Figure 2.26 shows that there is no concentration gradient forming in the thin cell, this indicates that solid-state diffusion is limiting the cell at higher current. The same would be true for the thick cell, but its high-current discharge voltage is shifted vertically downward compared to the thin cell. This indicates that the significant concentration gradient of the thick cell causes a concentration overpotential that depresses the voltage profile without losing additional discharge capacity. These observations demonstrate why lithium-ion batteries with thicker electrodes designs tend to underperform at high currents compared to thinner electrode designs.

It has now been demonstrated that a number of complex factors can cause the operational voltage of a lithium-ion battery to differ from its reversible voltage, and that these factors are dependent on lithium-ion cell design parameters as well as current and temperature. These operational overpotentials will therefore impact the energy, power, and thermal performance of different EV battery designs, especially at high currents where mass transport limitations can have a significant effect.

2.4. Energy Storage

The energy storage capacity of a battery is a measure of its ability to deliver useful electrical work to a load and is therefore one of the most important evaluations of battery performance. The coulombic capacity (in Ah) describes the amount of Li^+ available for intercalation, but this measure is more relevant for electrochemical research. For engineering applications, electrical energy (in Wh) is the more practical measure, combining both the coulombic capacity and voltage profile of the battery. Sections 2.2 and 2.3 demonstrated how the chemistry, cell design, and operational conditions of a lithium-ion battery can impact its voltage profile. This section will elaborate on these impacts in the context of the energy storage capabilities of a lithium-ion battery.

Note that in this section, a complete battery cycle is considered to consist of a discharge and a charge between the same two SOC end points. Under this condition, the coulombic efficiency η_Q of a single cycle can be assumed to be 100 %. This is defined in Equation 2.16, where $I_{\text{dis}} < 0$ and $I_{\text{chg}} > 0$ are respectively the electric current during discharge and charge while Q_{dis} and Q_{chg} are respectively the total electric charge accumulated during discharge and charge.

$$\begin{aligned}\eta_Q &= \frac{Q_{\text{dis}}}{Q_{\text{chg}}} \times 100\ \% \\ &= \frac{-\int I_{\text{dis}} \mathrm{d}t}{\int I_{\text{chg}} \mathrm{d}t} \times 100\ \% \\ &\approx 100\ \%\end{aligned} \tag{2.16}$$

Under practical operating conditions, $\eta_Q > 99.5$ % as long as the discharge and charge are carried out over a fixed SOC window [146]. This is because only a small fraction of the current gets diverted to parasitic reactions in a lithium-ion cell (discussed in Section 2.5), whereas battery technologies with an aqueous electrolyte (e.g. lead-acid batteries) can have $\eta_Q < 90$ % due to electrolysis side-reactions [147]. For lithium-ion battery technology, $Q_{\text{dis}} \approx Q_{\text{chg}} \approx Q$, and η_Q is therefore not typically used to evaluate energy storage capability.

2.4.1. Energy Evaluation

There are a number of common metrics for evaluating the energy storage capability of a battery, and they all involve the electrical energy delivered during discharge. The discharge energy capacity E_{dis} (in Wh) is calculated as the product of the discharge current I_{dis} and voltage V_{dis} integrated over the discharge time t (in hours). This is shown in Equation 2.17, where $I_{\text{dis}} < 0$.

$$E_{\text{dis}} = -\int I_{\text{dis}} V_{\text{dis}} \mathrm{d}t \tag{2.17}$$

The discharge energy capacity is often scaled so that batteries of different sizes can be compared. Two common metrics are energy density $\bar{E}_v$ (in Wh/L) and specific energy $\bar{E}_m$ (in Wh/kg), which respectively scale the energy capacity of a battery by its physical volume v and mass m as shown in Equations 2.18 and 2.19.

$$\bar{E}_v = \frac{E_{\text{dis}}}{v} \tag{2.18}$$

$$\bar{E}_m = \frac{E_{\text{dis}}}{m} \tag{2.19}$$

The energy capacities per unit volume and mass are important for evaluating the economics of battery energy storage, since they respectively determine how large and heavy a battery-powered system must be. This is especially significant for mobile applications such as EVs and portable electronics, where lithium-ion batteries have become the dominant energy storage technology due to their relatively high $\bar{E}_v$ and $\bar{E}_m$.

For a rechargeable battery such as lithium-ion, a charge energy E_{chg} must be applied before E_{dis} can be delivered. The charge energy is defined in Equation 2.20, where $I_{\text{chg}} > 0$.

$$E_{\text{chg}} = \int I_{\text{chg}} V_{\text{chg}} \mathrm{d}t \tag{2.20}$$

Due to unavoidable sources of irreversibility (discussed in Section 2.3), E_{chg} will always be greater than E_{dis}. It is therefore necessary to consider E_{dis} in relation to E_{chg} when

evaluating the energy storage capability of a battery. This is described by the cycle energy efficiency η as shown in Equation 2.21, where $0\ \% < \eta < 100\ \%$.

$$\eta = \frac{E_{\text{dis}}}{E_{\text{chg}}} \times 100\ \% = \frac{-\int I_{\text{dis}} V_{\text{dis}} \mathrm{d}t}{\int I_{\text{chg}} V_{\text{chg}} \mathrm{d}t} \times 100\ \% \tag{2.21}$$

Energy efficiency is another common metric used to evaluate the economics of energy storage. A lower η means a higher cost to operate the battery at a given electricity price, since more charging energy is required per unit discharge energy. Equation 2.21 also shows that the voltage profile will impact the energy efficiency. Generally, lithium-ion batteries have a high η compared to other battery chemistries and energy storage technologies [148], which is another reason for the widespread adoption of lithium-ion technology.

The energy storage metrics discussed above are impacted by the chemical and physical design of a lithium-ion battery, as well as the conditions under which the battery operates. These impacts are realized in both the real-time utilization and long-term degradation of battery energy capacity, which will be discussed in Section 2.4.2 and 2.5, respectively.

2.4.2. Energy Utilization

As demonstrated in Section 2.3, larger currents, lower temperatures, and thicker electrode coatings will increase the overpotentials during battery operation. Figure 2.27 uses two voltage vs SOC charts to illustrate how larger overpotentials result in lower utilization of battery energy capacity, using a sample of real experimental data obtained as part of this research project. Charts similar to Figure 2.27 will be evaluated in Chapter 5, so it is worthwhile to discuss a general case here.

The dashed blue line in Figure 2.27 represents the estimated reversible voltage, while the solid blue line represents the measured operational voltage. The discharge voltage V_{dis} decreases from high SOC to low SOC when a discharge current I_{dis} is applied, while the charge voltage V_{chg} increases from low SOC to high SOC when a charge current I_{chg} is applied. To protect the battery from extreme voltages, discharge and charge are

respectively terminated at lower and upper voltage limits. In experimental research, it is common to apply lower and upper voltage limits of 2.5 V and 4.2 V for most lithium-ion batteries [21], as is the case in Figure 2.27. One notable exception is LFP chemistry, which features a lower operational voltage range than other lithium-ion chemistries (shown previously in Figure 2.18). Note that battery voltage limits used in commercial applications are often narrower than those used in experimental research, since narrower voltage limits can help slow the battery degradation process and extend system life. Battery degradation will be discussed in Section 2.5.

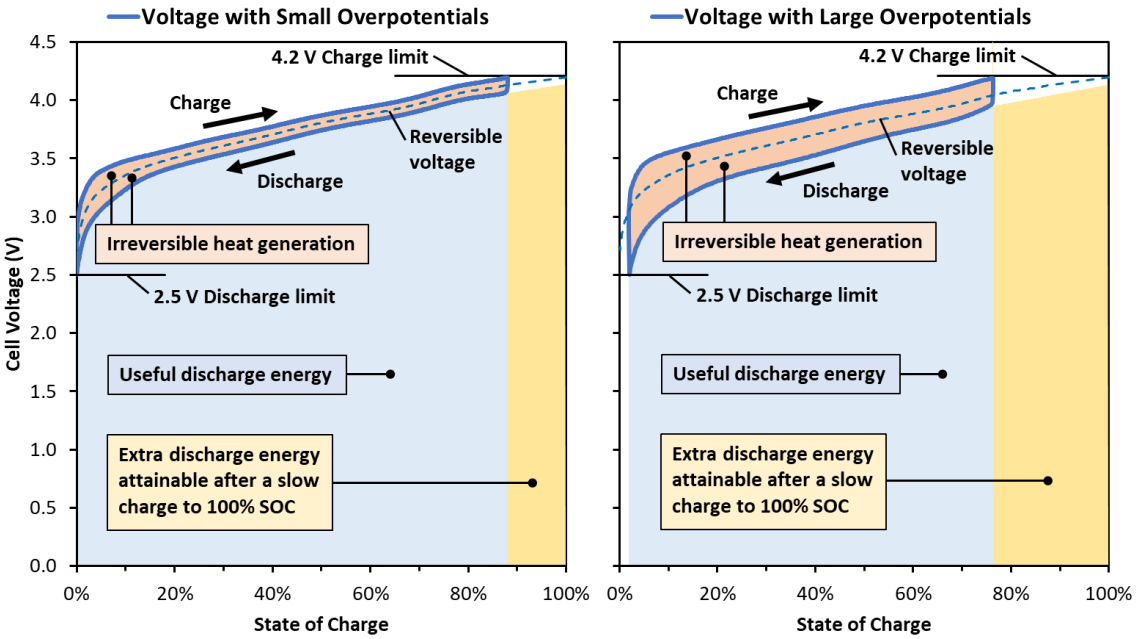


Figure 2.27 Illustrative example of how the energy storage utilization of a battery is impacted by small (left) vs large (right) overpotentials, which could be caused by small vs large current, high vs low temperature, or thin vs thick electrode coatings.

For the x-axis in Figure 2.27, SOC provides a normalized gauge for the intercalation process, which is convenient for comparing batteries of different sizes. The mathematical definition for an incremental change in SOC is stated in Equation 2.22, where $Q_{\text{rev}} > 0$ is the total electric charge available in the cell when V_{rev} is maintained within the given upper and lower voltage limits. In the example in Figure 2.27, SOC $= 0$ % when $V_{\text{rev}} = 2.5$ V, and SOC $= 100$ % when $V_{\text{rev}} = 4.2$ V.

$$\begin{aligned} \mathrm{dSOC} &= \frac{\mathrm{d}Q}{Q_{\mathrm{rev}}} \times 100\ \% \\ &= \frac{I\mathrm{d}t}{Q_{\mathrm{rev}}} \times 100\ \% \end{aligned} \tag{2.22}$$

New definitions for E_{dis} and E_{chg} can be derived by applying Equation 2.22 to Equations 2.17 and 2.20. This is done in Equations 2.23 and 2.24, respectively, where $\mathrm{dSOC} > 0$ is used as a convention (i.e. integrating from left to right in Figure 2.27 for both discharge and charge).

$$E_{\mathrm{dis}} = \frac{Q_{\mathrm{rev}}}{100\ \%} \int V_{\mathrm{dis}} \mathrm{dSOC} \tag{2.23}$$

$$E_{\mathrm{chg}} = \frac{Q_{\mathrm{rev}}}{100\ \%} \int V_{\mathrm{chg}} \mathrm{dSOC} \tag{2.24}$$

Equations 2.23 and 2.24 demonstrate how the area under the curve on a voltage vs SOC plot is directly proportional to energy (the area would be equivalent to energy for a voltage vs coulombic capacity chart). In Figure 2.27, the blue area under the V_{dis} curve is thus proportional to E_{dis}, while the combined blue and red area under the V_{chg} curve is proportional to E_{chg}. Note that this assumes Q_{rev} is a constant, which is valid for a single discharge and charge. However, Q_{rev} will decrease as the battery degrades over the course of many cycles, as will be discussed in Section 2.5.

In Figure 2.27, the blue area representing E_{dis} is observably smaller for the case with large overpotentials. This is due to three reasons:

1. The charge reaches the 4.2 V upper limit at a lower SOC, meaning that there are fewer Li^+ in the negative electrode when discharge begins. This is termed ‘charge truncation’ in this thesis.
2. The cell voltage is lower throughout the discharge, which reduces the work output of each Li^+ that intercalates from the negative electrode to the positive electrode. This is termed ‘voltage depression’ in this thesis.
3. The discharge reaches the 2.5 V lower limit at a higher SOC, meaning that there are more Li^+ left unutilized in the negative electrode when the discharge ends. This is termed ‘discharge truncation’ in this thesis.

The yellow areas in Figure 2.27 represent the unutilized energy due to the discharge beginning at SOC < 100 %. This energy can be recovered by applying a constant-voltage (CV) charge once the 4.2 V upper limit is reached, such that the charge current decreases exponentially toward zero over the course of several hours and SOC approaches 100 %. However, it is not always feasible to apply a CV charge in practical engineering applications. In such cases, Figure 2.27 shows how the energy utilization can be significantly impacted by charging overpotentials, as the yellow area is observably larger for the case with large overpotentials.

Since E_{dis} depends on the size of the overpotentials, another metric can be used to characterize energy storage utilization for different currents, temperatures, and cell designs. In this thesis, this metric will be referred to as the 'energy utilization ratio' with symbol ζ, which normalizes the discharge energy E_{dis} by the theoretical maximum work output w_{rev} that could be utilized with $V_{\mathrm{dis}} = V_{\mathrm{rev}}$. This is given in Equation 2.25, where $0\ \% < \zeta < 100\ \%$. Note that Q_{rev} cancels out in the numerator and denominator, making ζ a suitable metric for comparing batteries of different sizes as long as V_{rev} can be measured or estimated.

$$\begin{aligned}\zeta &= \frac{E_{\mathrm{dis}}}{w_{\mathrm{rev}}} \times 100\ \% \\ &= \frac{\int V_{\mathrm{dis}} \mathrm{dSOC}}{\int V_{\mathrm{rev}} \mathrm{dSOC}} \times 100\ \%\end{aligned} \tag{2.25}$$

In some applications, batteries are evaluated not just for the amount of stored energy they can deliver, but also how quickly they can deliver it. This refers to the power capability of the battery, which is directly related to how the energy utilization is affected by high currents. If the energy utilization ratio ζ decreases significantly at higher currents, then the battery would be considered to have poor power capability.

2.4.3. Irreversible Energy

The red areas in Figure 2.27 represent the total energy that is irreversibly converted to heat during discharge ($V_{\mathrm{dis}} < V_{\mathrm{rev}}$) and charge ($V_{\mathrm{chg}} > V_{\mathrm{rev}}$). The total irreversible heat

generation during discharge $q_{\mathrm{irr}}^{\mathrm{dis}}$ and charge $q_{\mathrm{irr}}^{\mathrm{chg}}$ can thus be expressed by Equations 2.26 and 2.27, respectively.

$$q_{\mathrm{irr}}^{\mathrm{dis}} = \frac{Q_{\mathrm{rev}}}{100\ \%} \int (V_{\mathrm{rev}} - V_{\mathrm{dis}})\mathrm{dSOC} \tag{2.26}$$

$$q_{\mathrm{irr}}^{\mathrm{chg}} = \frac{Q_{\mathrm{rev}}}{100\ \%} \int (V_{\mathrm{chg}} - V_{\mathrm{rev}})\mathrm{dSOC} \tag{2.27}$$

Summing Equations 2.26 and 2.27 gives the total heat generation for a complete cycle of discharge and charge. By defining a new parameter V_{gap} as per Equation 2.28, the total irreversible heat generation of the cycle can be simplified as shown in Equation 2.29. This demonstrates that the area in the gap between the V_{dis} and V_{chg} curves on a voltage vs SOC chart is directly proportional to the total cycle heat generation, even if V_{rev} is unknown.

$$V_{\mathrm{gap}}\big|_{\mathrm{SOC}} = V_{\mathrm{chg}}\big|_{\mathrm{SOC}} - V_{\mathrm{dis}}|_{\mathrm{SOC}} \tag{2.28}$$

$$\begin{aligned} q_{\mathrm{irr}}^{\mathrm{dis}} + q_{\mathrm{irr}}^{\mathrm{chg}} &= \frac{Q_{\mathrm{rev}}}{100\ \%} \oint (V_{\mathrm{chg}} - V_{\mathrm{dis}})\mathrm{dSOC} \\ &= \frac{Q_{\mathrm{rev}}}{100\ \%} \oint V_{\mathrm{gap}}\mathrm{dSOC} \end{aligned} \tag{2.29}$$

Comparing Equations 2.23 and 2.24 with Equation 2.29 reveals another important relationship for battery operation, which is stated in Equation 2.30. This essentially says that battery charging must make up for the irreversible energy losses that occur during both discharge and charge.

$$E_{\mathrm{chg}} - E_{\mathrm{dis}} = q_{\mathrm{irr}}^{\mathrm{dis}} + q_{\mathrm{irr}}^{\mathrm{chg}} \tag{2.30}$$

In Figure 2.27, the red area representing $q_{\mathrm{irr}}^{\mathrm{dis}} + q_{\mathrm{irr}}^{\mathrm{chg}}$ is observably larger in the case with large overpotentials. Based on Equations 2.21 and 2.30, the smaller blue area and larger red area imply that the energy efficiency η is lower when the overpotentials are larger, as would be expected. It is also helpful to redefine η by combining Equations 2.21, 2.22, and 2.28 to produce Equations 2.31 and 2.32.

$$\eta = \frac{\int V_{\mathrm{dis}} \mathrm{dSOC}}{\int V_{\mathrm{chg}} \mathrm{dSOC}} \times 100\ \% \tag{2.31}$$

$$1 - \eta = \frac{\oint V_{\mathrm{gap}} \mathrm{dSOC}}{\int V_{\mathrm{chg}} \mathrm{dSOC}} \times 100\ \% \tag{2.32}$$

This shows that the energy efficiency depends on the ratio of V_{dis} to V_{chg}, and that a visual observation of the vertical gap between the discharge voltage and charge voltage on a voltage vs SOC chart can be used as a qualitative indicator of energy inefficiency $1 - \eta$. In Figure 2.27, the fact that V_{gap} is observably larger throughout the cycle for the case with large overpotentials is sufficient to conclude that the energy efficiency is lower.

It has now been demonstrated how operational overpotentials can impact battery energy storage performance, and several suitable metrics have been presented for characterizing and comparing energy utilization performance for different lithium-ion batteries. A simple voltage vs SOC chart has also been shown to be a useful tool for visually assessing energy utilization performance. These metrics and tools will be instrumental in characterizing and comparing the energy storage performance of different second-life batteries in Chapter 4 and Chapter 5.

2.5. Degradation

The energy storage capability of a lithium-ion battery gradually declines over the course of its life due to a variety of internal degradation mechanisms. When the battery is first constructed, it is considered to be at beginning of life (BOL), and when it eventually degrades to a point where it can no longer provide practical value, it is considered to have reached end of life (EOL). The operational pathway from BOL to EOL is termed the 'cycle life' of the battery, which gives the approximate number of cycles required to reach EOL under a given set of operating conditions. Cycle life is therefore an important metric for assessing the economics of battery energy storage, since it determines how long a battery will be able to meet system requirements before needing replacement. Cycle life depends on how a battery is designed and operated, but in general, lithium-ion batteries have a relatively long cycle life (> 4000 cycles) compared to other battery technologies like lead-acid (< 1000 cycles) [149].

2.5.1. Degradation Mechanisms

The degradation mechanisms of a lithium-ion battery can be grouped into two main categories: capacity fade and power fade [150]. Capacity fade is an irreversible decrease in the coulombic capacity Q_{rev} of the cell, which can occur through the consumption of Li^+ in side-reactions (termed 'loss of lithium inventory' or LLI) or through the isolation or blockage of intercalation sites in the electrodes (termed 'loss of active material' or LAM) [151]. Power fade is the result of an irreversible increase in the cell internal resistance R and the corresponding overpotentials, which reduces energy utilization through voltage depression, discharge truncation, and charge truncation (see Section 2.4.2).

Lithium-ion batteries can undergo a wide variety of degradation mechanisms during their operational life, and different electrode materials are more susceptible to different degradation mechanisms. Table 2.2 summarizes the main degradation mechanisms and their prevalence for different electrode materials, with 'X' representing significant degradation rates and shading representing problematic degradation rates that inhibit commercialization in EV battery applications. While the vast majority of lithium-ion batteries employ graphite at the negative electrode, the choice of positive electrode material will clearly have a significant impact on the mechanism and rate of degradation in the battery. Each degradation mechanism is discussed in more detail below.

Table 2.2 Summary of the main degradation mechanisms for various lithium-ion battery electrode materials. Significant degradation rates are represented by 'X' while problematic degradation rates are represented by shading.

Mechanism	Graphite	LCO	LNO	NMC [a]	NCA [b]	LMO	LFP
Lithium plating	X						
SEI growth	X		X		X		
Electrolyte decomposition	X	X	X	X	X	X	
Particle cracking	X	X	X	X	X	X	X
Oxygen loss		X	X	X	X		
Transition metal dissolution		X	X	X	X	X	X
Cation mixing [c]			X	X	X		

[a] NMC considered to have 33 % ≤ Ni ≤ 60 %.
[b] NCA considered to have 80 % ≤ Ni ≤ 85 %.
[c] Cation mixing occurs during material synthesis rather than battery operation, but it is included here for a more complete comparison of the main issues affecting different electrode materials.

Lithium Plating

When the charging overpotential is large at high SOC, the low potential of a graphite electrode can be pushed below 0 V vs lithium metal, which makes it thermodynamically favourable for Li^+ to reduce to lithium metal and deposit or 'plate' onto the graphite surface instead of intercalating into the graphite layers [152]. The plated lithium can still re-oxidize to Li^+ and resume intercalation when it is thermodynamically favourable, but a portion may lose electrical contact with the electrode or react with the electrolyte, at which point the process is irreversible and results in LLI [153].

Solid Electrolyte Interphase Growth

Another way LLI occurs is through side-reactions between the electrode and electrolyte, which form a layer of reaction products that separates the electrode from the electrolyte. This layer is called the solid electrolyte interphase (SEI), and Li^+ are irreversibly consumed in its formation. During discharge and charge, Li^+ must pass through the SEI as they intercalate and deintercalate, which adds to the cell internal resistance as well [143]. After the first few cycles from BOL, the SEI is fully formed such that the electrode surface is largely protected from further reaction with the electrolyte [154]. However, the SEI continues to grow at a slow rate throughout battery life, particularly at the graphite electrode, resulting in LLI and internal resistance growth at the negative electrode [155]. Nickel-rich positive electrode materials can also experience SEI growth at high SOC due to the presence of unstable Ni^{4+} ions which readily react with the electrolyte [49], which is especially problematic for LNO [156]. These reactions do not consume Li^+ (i.e. no LLI) but do result in the conversion of surface active material into structures which are inactive (i.e. LAM) and resistive to Li^+ diffusion [156].

Electrolyte Decomposition

The organic solvents in the electrolyte are not stable in the upper voltage range of a typical lithium-ion cell, and readily undergo reduction at the low potential of a graphite electrode as well as oxidation at the high potential of most positive electrode materials when the cell is at high SOC [107], [155]. In addition to contributing to SEI growth as described above, these electrode-electrolyte reactions produce gases which can block the electrode surface (effectively LAM) and inhibit ionic transport through the electrodes and separators

(increased internal resistance) [157]. The long-term buildup of these gases also increases the pressure in the cell, imposing greater mechanical stresses [158]. Electrolyte decomposition is not an issue for LFP electrodes due to their relatively low voltage [159].

Particle Cracking

All electrode materials will suffer from particle cracking to varying degrees as a result of cyclic mechanical stresses over the course of extended cycling. These cracks can result in LAM when electrode particles become isolated from the electronic pathways in the electrode [160], as well as LLI if there are intercalated Li^+ trapped in the isolated electrode particles [151]. The newly exposed particle surface will also react with the electrolyte to form new SEI at the cost of LLI [161]. The mechanical stresses can arise due to the cyclic expansion and contraction of the electrode volume during intercalation and deintercalation [162], or due to the crystal lattice distortions associated with phase transitions [163] (both discussed in Section 2.2.3). The numerous phase transitions of LNO are particularly problematic, but these can be mitigated by substituting some of the nickel with other metals, as is the case in NMC and NCA [49], [120]. Nickel-rich positive electrode materials are more susceptible to particle cracking due to their greater similarity to LNO, which brings more pronounced phase changes and volume changes at high SOC [45], [49].

Oxygen Loss

All the positive electrode materials listed in Table 2.2 feature oxygen as part of their molecular structure. Under the right conditions, some of the oxygen can undergo a reduction reaction and break free of the molecular structure as oxygen gas. Oxygen loss is particularly problematic for LCO since the $Co^{3+/4+}$ redox energy level overlaps with the oxygen redox energy level, such that the intercalation reaction can reduce the oxygen at high SOC. In comparison, this overlap is relatively small for LNO and nonexistent for LMO and LFP [107]. However, oxygen loss can still be significant in nickel-based materials like LNO, NMC, and NCA at high SOC where unstable Ni^{4+} cations make it thermodynamically favourable for the layered structure to irreversibly transform into a rock salt phase featuring more stable Ni^{2+} cations, which necessitates the release of O^{2-} anions to balance the charge [42], [161]. Apart from the gas evolution issues described above, oxygen loss is associated with LAM and internal resistance growth due to the rock salt

phase being unable to intercalate Li^+ [47]. Oxygen loss also has important safety implications, as will be discussed in Section 2.6.6.

Transition Metal Dissolution

The transition metal cations at the surface of positive electrode particles are also known to gradually dissolve in the electrolyte due to reactions with acidic products in the electrolyte [163]. This can cause some LAM at the positive electrode, but the more severe consequence is that the transition metal cations will then migrate through the separator and deposit on the negative electrode, which results in additional SEI formation at the cost of LLI and internal resistance growth [164]. Transition metal dissolution is particularly problematic for LMO, as Mn^{3+} ions have a high tendency to disproportionate into Mn^{2+} and Mn^{4+}, with the Mn^{2+} dissolving in the electrolyte and depositing on the graphite electrode, especially at higher temperatures [74]. This is the reason for the poor cycle life of LMO, limiting its role in EV applications to blended positive electrodes only [45].

Cation Mixing

During the synthesis of layered positive electrode materials, some of the transition metal cations can migrate into the octahedral sites of the Li^+ intercalation layer, resulting in decreased capacity as well as impeded solid-state diffusion [124]. This phenomenon is known as ‘cation mixing’, and while it is technically not a degradation mechanism (it is primarily a material synthesis issue), it is an undesirable chemical process which impacts battery performance, and is therefore included in this section. LNO is particularly susceptible to cation mixing, as the unstable Ni^{3+} tend to convert to Ni^{2+} and swap places with Li^+ in the intercalation layer due to their similar ionic radii [165]. This same process occurs in NMC [166] and NCA [167] due to their nickel content, but the cobalt content helps to stabilize the structure and mitigate cation mixing compared to pure LNO [165]. In the case of NMC, greater manganese content corresponds to greater Ni^{2+} content (see Figure 2.19) which tends to increase the amount of cation mixing [166]. Cation mixing is not reported as a significant issue for the more stable structures of spinel LMO and olivine LFP.

Calendar Degradation

Degradation will occur even if a battery is idle for long periods, since parasitic reactions such as electrolyte decomposition, SEI growth, and transition metal dissolution can proceed inside a lithium-ion cell without an external current [168]. This is referred to as calendar degradation. The parasitic reaction rates tend to follow the square root of time, but increase with cell voltage and temperature [150]. One study evaluated calendar degradation in NCA, NMC, and LFP cells over a 10-month period, and measured significantly greater capacity fade and power fade in cells stored at 40 to 50 °C and 80 to 100 % SOC compared to cells stored at 25 °C and < 50 % SOC [169]. Therefore, it is generally recommended that lithium-ion batteries be stored at or below 50 % SOC and in temperate or cooled environments.

2.5.2. Influences on Degradation

The rates at which the various degradation mechanisms occur in lithium-ion batteries also depends strongly on physical design parameters and operational conditions. For instance, lithium plating is more likely to occur when charging takes place at high currents, low temperatures, and high SOC, since these factors increase the overpotentials at the negative electrode [170]. Thicker electrode coatings and larger cell sizes also promote lithium plating, as there is increased likelihood of local variations in temperature and SOC, such that plating may occur in localized areas within the graphite electrode where the overpotentials are highest [152]. Higher temperatures and voltages will generally accelerate the lithium-consuming parasitic reactions between electrode and electrolyte [171], and can even lower the oxidation potential of the electrolyte such that it is easier for SEI growth to occur at the positive electrode [155]. While higher upper voltage limits can increase the energy utilization of layered positive electrode materials, this also promotes electrolyte decomposition and gas evolution at the positive electrode [42]. Stress-induced electrode cracking is exacerbated at extreme levels of intercalation (mitigated by tighter voltage limits) as well as high currents [172]. Transition metal dissolution increases at higher temperatures and currents [173].

Since some degradation mechanisms (e.g. lithium plating) are exacerbated at lower temperatures while other degradation mechanisms (e.g. SEI growth, transition metal

dissolution) are exacerbated at higher temperatures, an intermediate temperature range is generally preferred for prolonging the life of lithium-ion batteries. As discussed in Section 2.3, lower temperatures also tend to increase battery impedance, which is detrimental to battery energy and power performance. Higher temperatures also increase the safety risks associated with lithium-ion batteries, which will be discussed further in Section 2.6.6. A recommended temperature range of 25 to 40 °C [174] is commonly cited in the literature for balancing battery performance and cycle life, though other recommended ranges are reported as well, such as 20 to 45 °C [175], 15 to 40 °C [176], or 15 to 35 °C [177].

Similarly, since some degradation mechanisms (e.g. lithium plating, electrolyte decomposition, oxygen loss) are exacerbated at high SOC levels while others degradation mechanisms (e.g. particle cracking) are exacerbated at both high and low SOC levels, it is also common for battery operators to apply strategic limits on SOC or cell voltage as a means of prolonging the life of lithium-ion batteries. For example, one study reported that NCA cells degrade at a lower rate when cycled between 3.4 V and 4.0 V compared to identical cells cycled between 3.0 V and 4.3 V [172]. Though tightening the voltage limits will of course reduce the usable capacity of the battery on a given day, the battery will last longer in a commercial application before needing replacement.

2.5.3. Degradation Evaluation

Given the complex path-dependence of lithium-ion battery degradation, it is difficult to accurately quantify the extent of degradation at a given point in battery life. A 2021 review [178] reported the two most common definitions of 'state of heath' (SOH) used in the literature, which are given in Equations 2.33 and 2.34.

$$\mathrm{SOH}_Q = \frac{Q_{\mathrm{dis}}}{Q_{\mathrm{dis}}^{\mathrm{BOL}}} \times 100\ \% \tag{2.33}$$

$$\mathrm{SOH}_R = \frac{R_{\mathrm{EOL}} - R}{R_{\mathrm{EOL}} - R_{\mathrm{BOL}}} \times 100\ \% \tag{2.34}$$

The capacity-based SOH_Q definition compares the present value of coulombic capacity Q_{dis} to the BOL value, which would be the more appropriate metric in applications where

the importance of energy capacity outweighs the importance of power capability (e.g. EVs). A simple discharge test can determine the present value of Q_{dis} for a given battery. The resistance-based SOH_R definition compares the present value of internal resistance R to the BOL and EOL values, which would be the more appropriate metric for applications where power capability is most important (e.g. electricity grid ancillary services). The definition of R in Equation 2.34 may refer to one or more components of battery internal resistance (described in Section 2.3), which may be assessed by various methods such as current pulse tests [169]. Regardless of how SOH is defined, it provides a metric for estimating the position of a given battery in its cycle life between BOL and EOL. Advanced modelling techniques can also be used to estimate the remaining useful life of a given battery before it reaches EOL [179].

As an alternative to SOH_Q and SOH_R, an energy-based SOH_E definition was proposed in [180] as shown in Equation 2.35. Since the discharge energy depends on both Q_{rev} and R (see Section 2.4.2), this definition combines the effects of capacity fade and power fade into a single value to give a practical assessment of the ability of a battery to deliver useful energy throughout its life compared to BOL.

$$\mathrm{SOH}_E = \frac{E_{\mathrm{dis}}}{E_{\mathrm{dis}}^{\mathrm{BOL}}} \times 100\ \% \tag{2.35}$$

To clarify the relationships between SOC, SOH, Q_{rev}, and R, Figure 2.28 gives an illustrative example comparing a lithium-ion cell at 100 % SOH (i.e. BOL) and 80 % SOH, where Q_{rev} =100 Ah at BOL. The left chart plots both cell voltages against SOC, while the right chart plots both cell voltages against the actual coulombic capacity (in Ah). The right chart shows that the 80 % SOH cell has a shortened reversible voltage profile, indicating capacity fade due to decreased Q_{rev}. In the left chart, both cells have a similar reversible voltage profile when plotted against SOC, which demonstrates how SOC is a normalization of the present value of Q_{rev}. The left chart also shows that the 80 % SOH cell has a larger voltage gap at a given SOC, indicating power fade due to increased R.

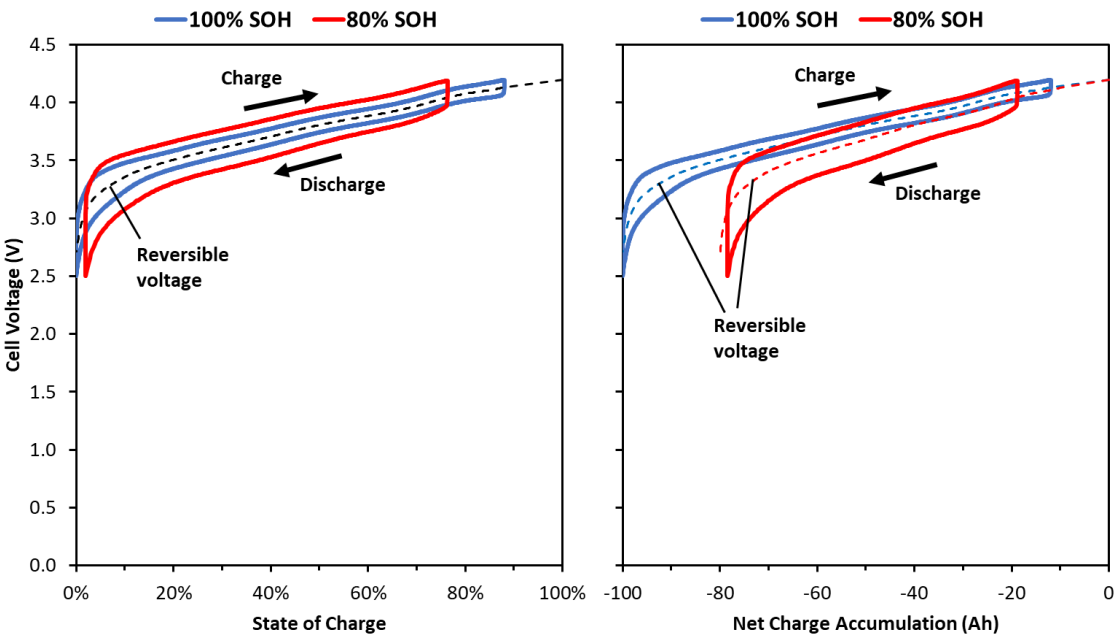


Figure 2.28 Illustrative example of how degradation affects the internal resistance (left) and coulombic capacity (right) of a lithium-ion battery.

Degradation is highly complex and remains an important area of research in the field of lithium-ion batteries. Beyond the basic SOH equations in Equations 2.33 through 2.35, there are a number of more advanced experimental and analytical methods which can be employed to evaluate long-term degradation mechanisms in different cell designs. For instance, Section 2.3.5 described how the EIS test method can be used to evaluate cell impedance over a range of AC frequencies. By conducting EIS tests over the course of battery life, valuable insights can be gained regarding long-term impedance growth [150].

Differential voltage (DV) analysis and incremental capacity (IC) analysis are two other common methods for evaluating battery degradation. Both these techniques require voltage data measured during a low-rate deep cycle test. In DV analysis, the derivative of voltage with respect to capacity $\frac{\mathrm{d}V}{\mathrm{d}Q}$ is plotted vs capacity Q, while in IC analysis, $\frac{\mathrm{d}Q}{\mathrm{d}V}$ is plotted vs V [151]. Both these graphical techniques allow for an assessment of how the slope of the voltage profile changes as a given battery degrades over time. Examples of DV and IC profiles are respectively shown in the top and bottom charts of Figure 2.29. The solid blue lines show the DV and IC profiles for a fresh NMC-LMO/graphite cell, while the dashed red lines show the profiles after 1000 deep cycles, at which point $\mathrm{SOH}_Q = 87$ %. The

various peaks and valleys of the DV and IC profiles can be linked to the known electrochemical signatures of specific positive and negative electrode materials, such as those described in Section 2.2 (e.g. phase transitions, ordering, graphite staging). The way in which the peaks and valleys change in magnitude and position can help researchers identify the degradation mechanisms that are occurring within a given battery without having to disassemble and inspect the cell. Figure 2.29 shows that some DV and IC peaks tend to shrink as the cell degrades, indicating that the voltage profile is becoming smoother due to structural changes in the degrading electrode materials [181].

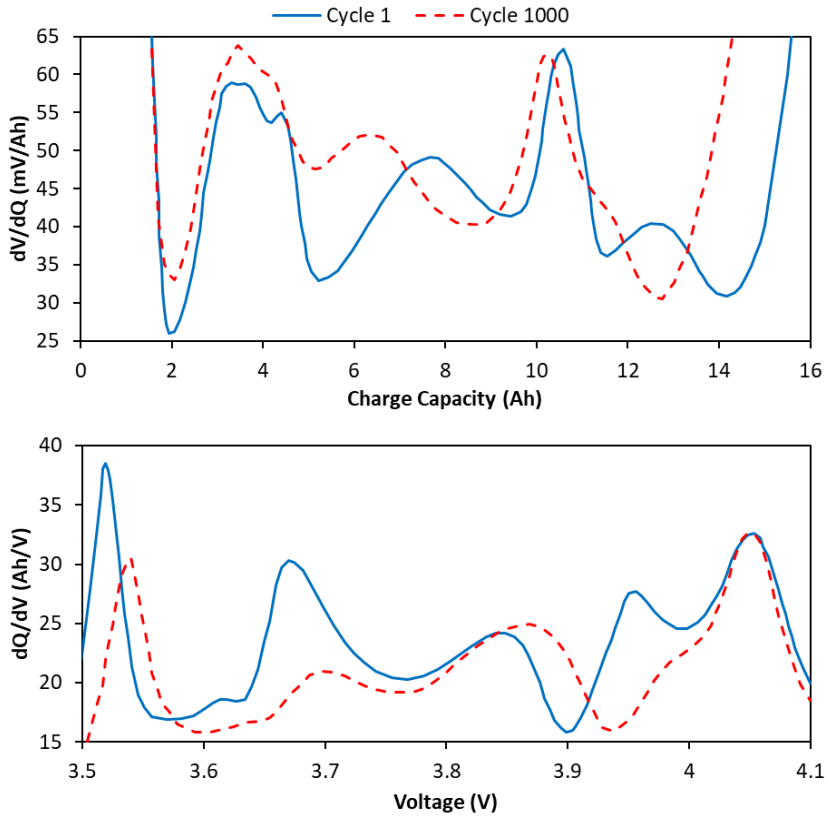


Figure 2.29 Examples of differential voltage (top) and incremental capacity (bottom) analysis methods used to evaluate battery degradation. Based on data and figures from [181].

Advanced evaluations of battery degradation through EIS, DV, and IC analyses are beyond the scope of this thesis, but several key takeaways will be applicable in the evaluation of second-life battery performance. For one, repurposed EV batteries will already have undergone a degree of degradation from their first life in EV service, so it is necessary to evaluate SOH when comparing EV batteries with different usage histories. Furthermore,

since the long-term economic value of second-life batteries will be partially determined by their degradation rates, the factors that influence degradation rates must also be considered in the evaluation of second-life batter performance. It has now been established that various degradation mechanisms will generally be accelerated at higher operational temperatures (with the exception of lithium plating), larger current rates, and wider SOC windows. Cell voltage profiles can also be expected to undergo small changes as batteries degrade. These various influencing factors will be revisited in Chapter 5.

2.6. Temperature

Chapter 2 has made numerous references to the impacts that temperature can have on the voltage, energy, power, and degradation of a lithium-ion battery. The safety of commercial lithium-ion batteries is also critically dependent on temperature. This section will elaborate on the main factors that determine the operational temperature of a lithium-ion battery, which are summarized in Figure 2.30. The net effect of internal heat generation and external heat dissipation determines how much heat accumulates in the battery, while the heat capacity determines how much the battery temperature increases for a given amount of accumulated heat. Since different lithium-ion batteries will exhibit different thermal responses to a given set of operational conditions, temperature evaluation metrics will also be introduced to supplement the energy storage evaluations described in Section 2.4.

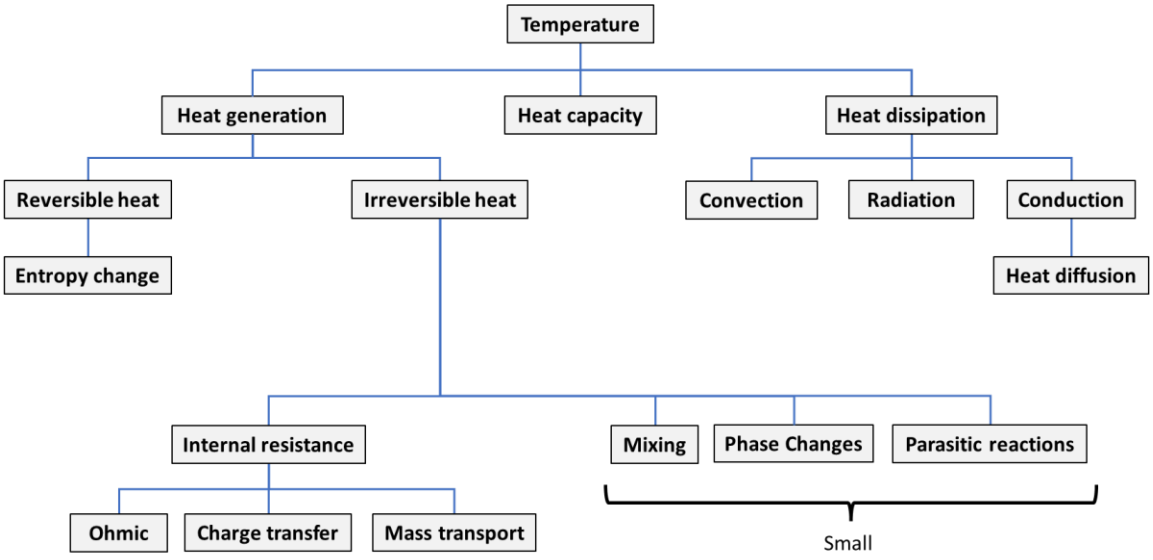


Figure 2.30 Simplified breakdown of the main factors that determine the operational temperature of a lithium-ion battery.

2.6.1. Thermodynamics

Similar to the explanations of battery voltage in Section 2.2, the first step in understanding battery temperature is through the laws of thermodynamics. Though Section 2.5 explained how gas evolution can gradually increase the pressure in a lithium-ion cell over extended cycling, on a shorter time scale the battery can be treated as a constant pressure system. For such a system, the incremental change in the total system enthalpy $\mathrm{d}H$ over an incremental time $\mathrm{d}t$ depends on the rate of heat input $\dot{q}_{\mathrm{in}}$ from the surroundings and the rate of work output $\dot{w}_{\mathrm{out}}$ performed on the surroundings. For a lithium-ion battery, $\dot{w}_{\mathrm{out}}$ depends on the current I and the voltage V. This relationship is given by Equation 2.36, where $I < 0$ during discharge ($\dot{w}_{\mathrm{out}} > 0$) and $I > 0$ during charge ($\dot{w}_{\mathrm{out}} < 0$).

$$\frac{\mathrm{d}H}{\mathrm{d}t} = \dot{q}_{\mathrm{in}} - \dot{w}_{\mathrm{out}} = \dot{q}_{\mathrm{in}} + IV \tag{2.36}$$

Within the battery, $\mathrm{d}H$ is a sum total of all the incremental enthalpy changes in each chemical species i, which depends on their partial molar enthalpies $\bar{H}_i$ and their amounts n_i, both of which change during intercalation. This is stated in Equation 2.37, which requires application of the product rule.

$$\frac{\mathrm{d}H}{\mathrm{d}t} = \sum_i \frac{\mathrm{d}}{\mathrm{d}t}(\bar{H}_i n_i) = \sum_i \left(\frac{\mathrm{d}\bar{H}_i}{\mathrm{d}t} n_i\right) + \sum_i \left(\bar{H}_i \frac{\mathrm{d}n_i}{\mathrm{d}t}\right) \tag{2.37}$$

The first of the two terms on the right of Equation 2.37 describes the aggregate heat capacity of the cell based on the constant-pressure heat capacity of each individual species $\bar{C}_{p,i}$. Assuming uniform temperature distribution within the cell, these can be lumped into a single constant heat capacity for the cell C_p, as shown in Equation 2.38. Heat capacity will be discussed in more detail in Section 2.6.2.

$$\sum_i \left(\frac{\mathrm{d}\bar{H}_i}{\mathrm{d}t} n_i\right) = \sum_i \left(\frac{\partial \bar{H}_i}{\partial T} \frac{\mathrm{d}T}{\mathrm{d}t} n_i\right) = \frac{\mathrm{d}T}{\mathrm{d}t} \sum_i (\bar{C}_{p,i} n_i) \approx C_p \frac{\mathrm{d}T}{\mathrm{d}t} \tag{2.38}$$

The final term on the right of Equation 2.37 describes the aggregate enthalpy of reaction, which can be divided into a Gibbs free energy component and an entropy component by

applying the fundamental thermodynamic relationship $H = G + TS$, as shown in Equation 2.39

$$\sum_i \bar{H}_i \frac{\mathrm{d}n_i}{\mathrm{d}t} = \sum_i \bar{G}_i \frac{\mathrm{d}n_i}{\mathrm{d}t} + T \sum_i \bar{S}_i \frac{\mathrm{d}n_i}{\mathrm{d}t} \tag{2.39}$$

The first of the two terms on the right of Equation 2.39 describes the reversible work output during intercalation. This can be given in terms of I and the reversible voltage V_{rev} by applying Equation 2.3 and Equation 2.4 from Section 2.2.1. This is done in Equation 2.40, recalling that $\mathrm{d}n$ refers to the amount of Li^+ and e^- spontaneously transferred to the positive electrode during discharge and that $I < 0$ on discharge. Note that the partial molar Gibbs free energy $\bar{G}_i$ is equivalent to the chemical potential μ_i.

$$\sum_i \left(\bar{G}_i \frac{\mathrm{d}n_i}{\mathrm{d}t} \right) = \frac{1}{\mathrm{d}t} \sum_i (\bar{G}_i \mathrm{d}n_i) = \frac{\mathrm{d}G}{\mathrm{d}t} = -V_{\mathrm{rev}} e \frac{\mathrm{d}n}{\mathrm{d}t} = I V_{\mathrm{rev}} \tag{2.40}$$

The final term on the right of Equation 2.39 describes the reversible heat consumption rate during intercalation. Equation 2.41 restates this in terms of I, V_{rev} and T by applying Equation 2.40 and the fundamental thermodynamic relationship $S = -\frac{\partial G}{\partial T}\Big|_p$.

$$T \sum_i \left(\bar{S}_i \frac{\mathrm{d}n_i}{\mathrm{d}t} \right) = -T \sum_i \left(\frac{\partial \bar{G}_i}{\partial T} \frac{\mathrm{d}n_i}{\mathrm{d}t} \right) = -T \frac{\partial}{\partial T} \left(\frac{1}{\mathrm{d}t} \sum_i (\bar{G}_i \mathrm{d}n_i) \right) = -IT \frac{\partial V_{\mathrm{rev}}}{\partial T} \tag{2.41}$$

Equations 2.36 through 2.41 can be combined and rearranged to give the energy balance for a lithium-ion battery. This is shown in Equation 2.42, which is commonly cited in the literature [182]. Note that $\dot{q}_{\mathrm{out}} = -\dot{q}_{\mathrm{in}}$ has been applied since heat transfer with the surroundings typically flows out of the battery. Section 2.6.4 will elaborate on the nature of $\dot{q}_{\mathrm{out}}$.

$$C_p \frac{\mathrm{d}T}{\mathrm{d}t} = I(V - V_{\mathrm{rev}}) + IT \frac{\partial V_{\mathrm{rev}}}{\partial T} - \dot{q}_{\mathrm{out}} \tag{2.42}$$

2.6.2. Heat Capacity

The term on the left of Equation 2.42 describes how the thermal energy of the battery changes with time. The thermal energy associated with a given temperature change $\mathrm{d}T$ depends on the heat capacity C_p of the battery, which in turn depends on its mass m and specific heat capacity c_p. Since a lithium-ion battery has many unique components, the heat capacity is a composite value which can be calculated based on the mass m_i and specific heat capacity $c_{p,i}$ of each component i, as shown in Equation 2.43.

$$C_p = mc_p = \sum_i m_i c_{p,i} \tag{2.43}$$

A 2022 review by Steinhardt et al. [183] compiled dozens of studies that reported experimental values of $c_{p,i}$ for various lithium-ion battery components as well as c_p values for different lithium-ion cell designs. While a range of $c_{p,i}$ values were reported for the different cell components, median values are summarized in Table 2.3. Notably, the electrode coatings and negative current collector (aluminum) are in similar ranges, the positive current collector (copper) is relatively low, and the separator and electrolyte are relatively high. This means that the cell c_p will be higher when the electrode coatings have higher porosity (greater electrolyte content for given cell size) and/or thickness (lower copper content for given cell size). For example, the authors noticed a positive correlation between specific coulombic capacity (Ah/kg) and specific heat capacity in cylindrical LCO cells due to the lower mass fraction of the copper current collector in high-energy cell designs with thick electrode coatings. Note that since lithium has a high specific heat capacity of 3582 J/kg·K, the value of $c_{p,i}$ for a given electrode material will tend to increase with Li^+ content, but the net effect of SOC on the full cell is limited to a few percent [183].

Table 2.3 also lists $c_{p,i}$ values for the most common cell housing materials for the three major cell formats (discussed in Section 2.1.5). Steel is used for cylindrical cell housings and some prismatic cell housings, and has a relatively low $c_{p,i}$ compared to the other cell components. Aluminum alloys are also used for prismatic cell housings, and have a $c_{p,i}$ similar to the aluminum current collector and electrode coatings. A specialized pouch foil is used for pouch cell housings, and its combination of aluminum and plastic components

gives a relatively high $c_{p,i}$. Steinhardt et al. noticed that the c_p values reported for full cells tended to be higher for pouch cells and lower for cylindrical cells, and attributed this to the differences in cell housing $c_{p,i}$ values [183].

Table 2.3 Approximate specific heat capacities for various lithium-ion cell components. Based on reviewed data from [183].

Cell Component	Specific Heat Capacity (J/kg·K)
Negative current collector (copper)	387
Negative electrode coating (graphite)	718
Separator	1600
Electrolyte	1635
Positive electrode coating (various)	750
Positive current collector (aluminum)	897
Steel cell housing (cylindrical and some prismatic)	440
Aluminum alloy cell housing (some prismatic)	893
Pouch foil cell housing (pouch)	1191

For full cells, the vast majority of experimental c_p values compiled by [183] fell in the range of 850 to 1150 J/kg·K, with NCA tending towards the lower half of this range, LFP tending towards the upper half, and NMC and LCO tending towards the middle half (LMO studies were not reported). The slightly lower values for NCA could be related to NCA only being studied in cylindrical format while the other chemistries were studied in all three formats. The slightly higher values of LFP are likely related to the phosphorous content and greater oxygen content ($FePO_4$ vs MO_2), since these two elements have relatively high specific heat capacities compared to iron, nickel, manganese, and cobalt.

Acknowledging the nuances described above, lithium-ion batteries can generally be expected to give $c_p = 1000$ J/kg·K ± 15 % at the cell level. Some of the studies reviewed by Steinhardt et al. also reported that the measured c_p values had a slight dependence on temperature and SOC, but this would amount to a c_p variance of only about 2 to 7 % for a given battery in typical operational conditions. The only reviewed study that had explored the influence of SOH on c_p concluded that c_p does change significantly over cell lifetime [184]. Note that the variance in c_p between different cell designs does not account for the other components that may be built into a larger battery pack like those used in EVs. The design of EV battery packs will be reviewed in Chapter 3.

2.6.3. Heat Generation

The first two terms on the right of Equation 2.42 give the net heat generation rate of a lithium-ion battery. The $I(V - V_{\text{rev}})$ term is the difference between the actual work and the ideal reversible work, which is equivalent to the irreversible heat generation rate I^2R that arises due to the operational overpotentials associated with battery internal resistance R (discussed in Section 2.3). When the cell is discharging, $I < 0$ and $V - V_{\text{rev}} < 0$, and when the cell is charging, $I > 0$ and $V - V_{\text{rev}} > 0$, so this term is always a positive value during battery operation.

The $IT\frac{\partial V_{\text{rev}}}{\partial T}$ term in Equation 2.42 is the reversible heat generation rate arising from entropy change in the intercalation system, where $\frac{\partial V_{\text{rev}}}{\partial T}$ is referred to as the 'entropic heat coefficient'. The general thermodynamic equation for V_{rev} (see Equation 2.7) can be differentiated to give $\frac{\partial V_{\text{rev}}}{\partial T} = \frac{\partial S}{\partial x}$, showing that the entropic heat coefficient is the rate of entropy change in the intercalation system at a given Li^+ content x. A thermodynamic system reversibly consumes heat when its entropy increases, and reversibly releases heat when its entropy decreases. Therefore, $\frac{\partial V_{\text{rev}}}{\partial T} > 0$ corresponds to endothermic intercalation and exothermic deintercalation, while $\frac{\partial V_{\text{rev}}}{\partial T} < 0$ corresponds to exothermic intercalation and endothermic deintercalation. Entropy changes are primarily driven by the configurational entropy of Li^+ in the electrode host lattice (discussed in Section 2.2.2) as well as structural changes in the host lattice such as phase transitions and volume change [185]. Since the net entropy change is zero for a complete discharge-charge cycle, the total reversible heat generation also sums to zero over a complete cycle.

Researchers have employed a number of techniques to determine $\frac{\partial V_{\text{rev}}}{\partial T}$ vs SOC for lithium-ion batteries, but the most common method involves placing a cell in a thermal chamber, measuring the value of V_{rev} over a range of temperatures, and then repeating these measurements at different SOC value [182]. An example of the results of such an experiment are given in Figure 2.31 for graphite and NCA electrodes.

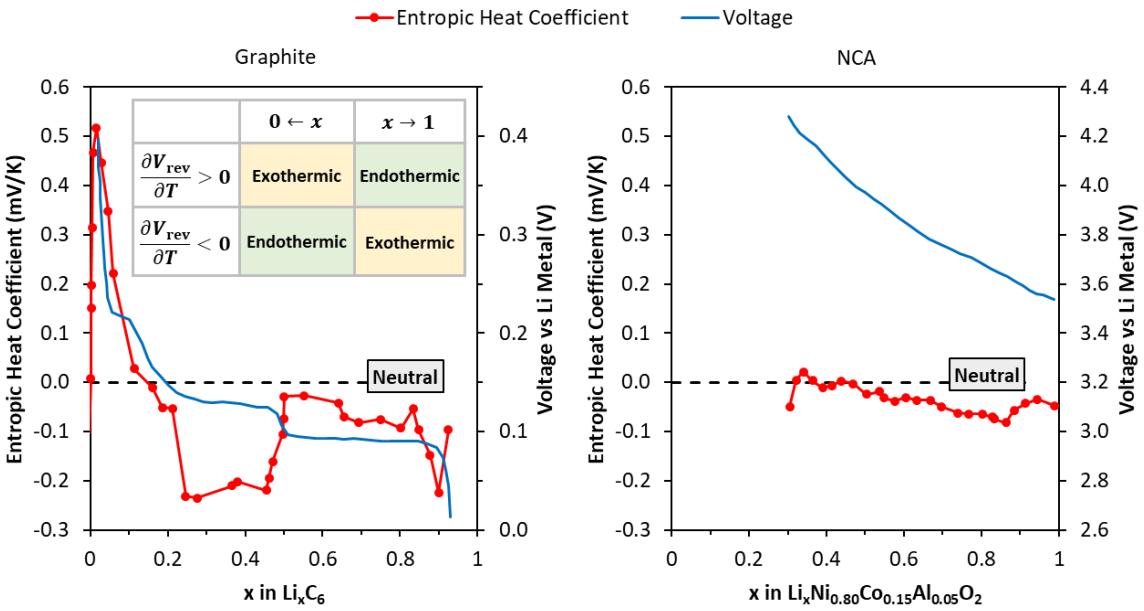


Figure 2.31 Examples of reversible heating coefficients for graphite (left) and NCA (right) electrodes with comparisons to voltage profiles as a function of Li^+ content. Based on data and figures from [186].

Comparing $\frac{\partial V_{\text{rev}}}{\partial T}$ to V_{rev} for the two electrode materials in Figure 2.31 helps illustrate the nature of entropic heating. In the case of graphite, the entropic heat coefficient exhibits discontinuities which correspond precisely to the various first-order phase transitions associated with graphite staging, which are indicated by the voltage plateaus in Figure 2.31. At the beginning of intercalation, the entropy change is positive due to the increase in configurational entropy as x increases from zero, resulting in endothermic heat consumption [186]. After the voltage decreases below 0.2 V vs Li metal, the entropy change is negative due to the ordered Li^+ distributions that form during graphite staging (discussed in Section 2.2.3), resulting in exothermic heat release. Figure 2.31 shows that the first order phase transition from stage 2L to stage 2 (approximately $0.25 < x < 0.5$) is particularly exothermic during graphite intercalation, likely due to the departure from the 'liquid-like' state of stage 2L. In the case of NCA, deintercalation must be terminated around $x = 0.3$ to maintain a practical voltage range, so the configurational entropy is already high when intercalation begins and thus does not change as rapidly as the case of graphite. Figure 2.31 shows that NCA intercalation is fairly neutral for $x < 0.5$, but becomes more exothermic for $x > 0.5$. The presence of cobalt and aluminum in NCA suppresses the phase transitions observed in pure LNO (see Section 2.2.5), resulting in a

smooth voltage profile and a correspondingly smooth entropic heat coefficient profile at a relatively low magnitude compared to graphite. For both electrodes, the reversible heat flows in the opposite direction during deintercalation.

The net heat generation rate can be experimentally determined through techniques such as calorimetry, where a battery is cycled in an isothermal test chamber and the resulting heat flows are measured [182]. Continuing with the same example of NCA and graphite electrodes, Figure 2.32 shows the net heat generation rate during discharge and charge of a full NCA/graphite cell at a 5 h rate and a 1 h rate. Note that the x-axis is reversed in the left chart such that both discharge and charge proceed from left to right.

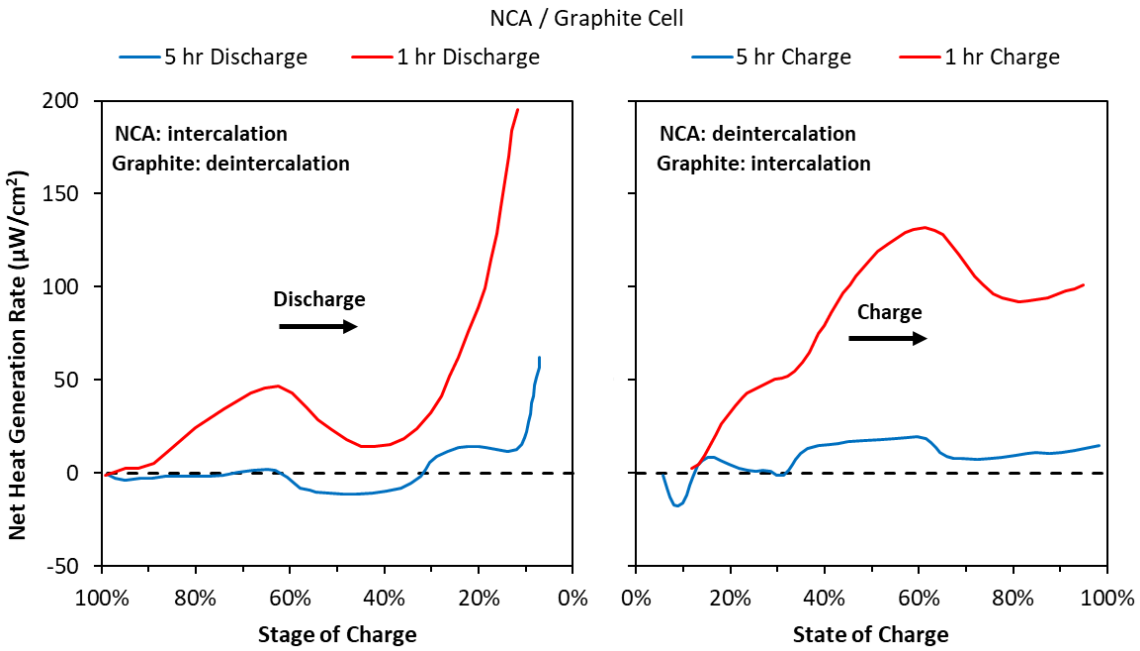


Figure 2.32 Examples of the net heat generation rate in a NCA/graphite cell during discharge and charge at two different rates. Based on data and figures from [186].

Recall that for a full cell, discharge corresponds to NCA intercalation and graphite deintercalation, while charge corresponds to NCA deintercalation and graphite intercalation. Based on Figure 2.31, the reversible heat should be dominated by graphite, with NCA giving a relatively small exothermic contribution during discharge and a relatively small endothermic contribution during charge. The contribution from irreversible heat is always exothermic. Researchers have measured the internal resistance of

NCA/graphite cells and considered the corresponding irreversible heating rate to be fairly constant throughout most of discharge and charge but with a sharp increase towards 0 % SOC, likely due to decreased electrical conductivity in fully lithiated NCA as well as impeded Li^+ transport as the NCA electrode approaches the fully lithiated state during discharge [186].

At the 5 h rates in Figure 2.32, the magnitude of the irreversible heating is relatively small compared to the reversible heating [186], so the profile of the net heat generation rate for the full cell is dominated by the dynamic entropic heating effects of graphite at these smaller currents. For the 5 h discharge, the net heat generation rate is slightly negative for 100 % > SOC > 65 % due to the weaker endothermic effect of graphite transitioning from stage 1 to stage 2, then more negative for 65 % > SOC > 30 % due to the stronger endothermic effect of graphite transitioning from stage 2 to stage 2L, and then increasingly positive for 30 % > SOC > 5 % due to the exothermic effect of graphite approaching the fully delithiated state combined with an appreciable amount of irreversible heating as NCA approaches the fully lithiated state [186]. For the 5 h charge, the net heat generation rate is negative for 5 % > SOC > 15 % due to the endothermic effect of graphite departing the fully delithiated state, then slightly positive for 15 % > SOC > 30 % due to the relatively neutral entropy change of graphite combined with appreciable irreversible heating, then more positive for 30 % > SOC > 65 % due to the stronger exothermic effect of graphite transitioning from stage 2L to stage 2, then less positive for 65 % > SOC > 100 % due to the weaker exothermic effect of graphite transitioning from stage 2 to stage 1.

For the 1 h rates in Figure 2.32, the higher current increases the magnitude of both $I(V - V_{\mathrm{rev}})$ and $IT\frac{\partial V_{\mathrm{rev}}}{\partial T}$, but the irreversible heating is more strongly impacted since the magnitude of $V - V_{\mathrm{rev}}$ also increases with higher current (see Section 2.3). As a result, the net heat generation rate remains positive throughout the 1 h discharge and 1 h charge, but the shapes of the profiles are still clearly impacted by graphite staging, particularly in the mid-SOC range where the stage 2+2L phase transition takes place. Towards the end of the 1 h discharge, the exothermic effects of graphite approaching the fully delithiated state add to the significant irreversible heat generation arising from the growing internal resistance as NCA approaches the fully lithiated state. Towards the end of the 1 h charge, the

exothermic effects of graphite staging have decreased from mid-SOC and the irreversible heat generation is not as high as the end of discharge because NCA does not approach the fully delithiated state in a practical voltage range. The result is that the cell experiences an accelerated heating rate towards the end of discharge and a dampened heating rate towards the end of charge. This is an important consideration for assessing and managing the thermal response of second-life batteries, as asymmetric thermal loads will give different temperature profiles for discharge vs charge. This will be revisited in Chapter 5.

It should be noted that the heat generation terms in Equation 2.42 are a significant simplification of a complex thermal system. A more comprehensive energy balance by Bernardi et al. [187] includes additional terms to account for the irreversible heat generation associated with side reactions, material phase changes, and the mixing of concentration gradients in the battery. However, these are generally considered to be small compared to $I(V - V_{\mathrm{rev}})$ and $IT\frac{\partial V_{\mathrm{rev}}}{\partial T}$ [182]. While the irreversible heat is typically greater than the reversible heat (especially at higher current rates), the reversible heat clearly has a significant impact on the cell and must be accounted for in the thermal analysis of lithium-ion batteries. One study determined that the reversible heat can contribute more than 50 % of total heat generation for current rates slower than 5 h [188]. Note that significant heat is also produced by electrode-electrolyte reactions that occur above safe temperatures and lead to a thermal runaway condition. This will be discussed in Section 2.6.6.

2.6.4. Heat Dissipation

The final term on the right of Equation 2.42 represents the dissipative heat transfer that flows from the battery to its surroundings when the battery temperature increases during operation. The heat dissipation rate $\dot{q}_{\mathrm{out}}$ includes conduction $\dot{q}_{\mathrm{cond}}$, convection $\dot{q}_{\mathrm{conv}}$, and radiation $\dot{q}_{\mathrm{rad}}$, as given by Equation 2.44. Each component is discussed below.

$$\dot{q}_{\mathrm{out}} = \dot{q}_{\mathrm{cond}} + \dot{q}_{\mathrm{conv}} + \dot{q}_{\mathrm{rad}} \tag{2.44}$$

Conduction

Conductive heat dissipation will occur when a mass (e.g. electrical wires, mounting rack, cooling plate) is in direct contact with the battery. The rate of conduction from the battery depends on the thermal conductivity of the thermal conductor k_{cond}, the cross-sectional area A_{cond} of the thermal conductor perpendicular to the direction y of heat transfer, and the temperature gradient of the thermal conductor $\frac{\mathrm{d}T_{\mathrm{cond}}}{\mathrm{d}y}$ extending from the battery in direction y, as given by Equation 2.45.

$$\dot{q}_{\mathrm{cond}} = -k_{\mathrm{cond}} A_{\mathrm{cond}} \frac{\mathrm{d}T_{\mathrm{cond}}}{\mathrm{d}y} \tag{2.45}$$

If the temperature of the thermal conductor is assumed to be equal to the ambient environment T_∞ at a length L_{cond} from the battery surface temperature T_{s} with a linear temperature gradient in between, then Equation 2.45 can be approximated by Equation 2.46.

$$\dot{q}_{\mathrm{cond}} \approx \frac{k_{\mathrm{cond}} A_{\mathrm{cond}}}{L_{\mathrm{cond}}} (T_{\mathrm{s}} - T_\infty) \tag{2.46}$$

Convection

Convective heat dissipation will occur when a fluid is in direct contact with the battery, which could refer to the ambient air surrounding the battery or a liquid coolant passing through channels within the battery. The rate of convection from the battery depends on the convection coefficient h_{conv}, the exposed battery surface area A_{conv}, and the difference between the battery surface temperature T_{s} and the ambient temperature T_∞, as given by Equation 2.47. The value of h_{conv} is determined by the physical properties, temperature, and movement of the fluid, as well as the battery surface geometry [189].

$$\dot{q}_{\mathrm{conv}} = h_{\mathrm{conv}} A_{\mathrm{conv}} (T_{\mathrm{s}} - T_\infty) \tag{2.47}$$

Convection is essentially heat conduction that takes place within the fluid boundary layer between the battery surface temperature T_{s} and the free stream temperature T_∞ of the fluid. The fluid temperature within the boundary layer T_{BL} features a temperature gradient $\frac{\mathrm{d}T_{\mathrm{BL}}}{\mathrm{d}y}$

in direction y perpendicular to the battery surface. The rate of convection from the battery depends on the thermal conductivity of the fluid k_{fluid}, the exposed battery surface area A_{conv}, and the value of $\frac{\mathrm{d}T_{\text{BL}}}{\mathrm{d}y}$ at the battery surface ($y = 0$), as given by Equation 2.48.

$$\dot{q}_{\text{conv}} = -k_{\text{fluid}} A_{\text{conv}} \left.\frac{\mathrm{d}T_{\text{BL}}}{\mathrm{d}y}\right|_{y=0} \tag{2.48}$$

The temperature gradient of the boundary layer depends on the surface geometry as well as the nature of the fluid flow. The Nusselt number Nu is a dimensionless parameter used to describe the dimensionless temperature gradient at the surface, as given by Equation 2.49.

$$Nu = \left.\frac{\mathrm{d}\left(\frac{T_{\text{BL}} - T_{\infty}}{T_{\infty} - T_{\text{s}}}\right)}{\mathrm{d}\left(\frac{y}{L_{\text{conv}}}\right)}\right|_{y=0} \tag{2.49}$$

Note that L_{conv} refers to the 'characteristic length' of the exposed surface, which has a number of definitions specific to given surface geometries. For example, L_{conv} can refer to the height of a vertical surface or the area-to-perimeter ratio of a horizontal flat plate [189].

Equations 2.47 through 2.49 allow h_{conv} to be defined in terms of the Nusselt number, fluid thermal conductivity, and surface geometry, as shown in Equation 2.50.

$$h_{\text{conv}} = Nu \frac{k_{\text{fluid}}}{L_{\text{conv}}} \tag{2.50}$$

The Nusselt number has been characterized empirically for a variety of forced convection and natural convection scenarios [189]. These empirical definitions can be used to calculate h_{conv} for a given fluid flow condition based on Equation 2.50. For forced convection, the Nusselt number is commonly given in terms of the Reynolds number Re and Prandtl number Pr. These two dimensionless numbers are respectively defined in Equations 2.51 and 2.52, where u_{∞} is the fluid flow speed (in m/s) and ν_{fluid}, ρ_{fluid}, and $c_{p,\text{fluid}}$ are respectively the kinematic viscosity (in m^2/s), mass density (in kg/m^3), and specific heat capacity of the fluid.

$$Re = \frac{u_\infty L_{\text{conv}}}{\nu_{\text{fluid}}} \tag{2.51}$$

$$Pr = \frac{\nu_{\text{fluid}} \rho_{\text{fluid}} c_{p,\text{fluid}}}{k_{\text{fluid}}} \tag{2.52}$$

For natural convection, the Nusselt number is commonly given in terms of the Rayleigh number Ra, which is the product of the Grashof number Gr and Prandtl number. This dimensionless number is defined in Equation 2.53, where g is acceleration due to gravity (approximately 9.81 m/s^2) and β_{fluid} is the expansion coefficient of the fluid (in 1/K).

$$\begin{aligned} Ra &= GrPr \\ &= \frac{g\beta_{\text{fluid}}(T_s - T_\infty)L_{\text{conv}}^3}{\nu_{\text{fluid}}^2} Pr \\ &= \frac{g\beta_{\text{fluid}}\rho_{\text{fluid}} c_{p,\text{fluid}}(T_s - T_\infty)L_{\text{conv}}^3}{\nu_{\text{fluid}} k_{\text{fluid}}} \end{aligned} \tag{2.53}$$

It is important to note that the Reynold's number does not directly depend on temperature (though fluid properties typically have some temperature dependence), while the Rayleigh number depends directly on $T_s - T_\infty$. This means that over a typical battery temperature range of 25 to 50 °C, h_{conv} will be a relatively constant value for forced convection but will vary with surface temperature for natural convection. The exact temperature dependence will depend on how the Nusselt number is defined for a given natural convection condition. One relevant example is given in Equation 2.54, which applies for the upper surface of a flat, horizontal plate that is at a higher temperature than its surroundings with $10^7 < Ra < 10^{11}$ [189]. In this example, Equation 2.54 shows that h_{conv} will increase nonlinearly as $T_s - T_\infty$ increases.

$$Nu = 0.15(Ra)^{1/3} \tag{2.54}$$

Radiation

Radiative heat dissipation will always occur, even in a vacuum [190]. The radiation rate is determined by the Stefan-Boltzmann constant σ_{SB} (approximately 5.67 × 10^{-8} W/m^2·K), the emissivity ε_{rad} of the battery surface, the exposed battery surface area A_{rad}, and the

difference between the fourth powers of the battery surface temperature T_s and the ambient temperature T_∞ (absolute temperatures), as given by Equation 2.55.

$$\dot{q}_{rad} = \sigma_{SB}\varepsilon_{rad}A_{rad}[(T_s + 273\ \text{K})^4 - (T_\infty + 273\ \text{K})^4] \tag{2.55}$$

For a typical battery temperature range of 25 to 50 °C, Equation 2.55 can be approximated through Taylor expansion to give Equation 2.56, as was done by Hatchard et al. [191].

$$\dot{q}_{rad} \approx 4\sigma_{SB}\varepsilon_{rad}A_{rad}(T_\infty + 273\ \text{K})^3(T_s - T_\infty) \tag{2.56}$$

Total Heat Dissipation

With the equations and approximations described above, it is possible to express $\dot{q}_{conv}$, $\dot{q}_{rad}$, and $\dot{q}_{cond}$ as linear functions of $T_s - T_\infty$, which follows Newton's law of cooling. This allows for the application of a single heat dissipation coefficient h which defines the proportionality between $\dot{q}_{out}$ and $T_s - T_\infty$ for a given battery, as shown in Equation 2.57 and Equation 2.58. Note however that in the case of natural convection, h_{conv} will cause h to vary with $T_s - T_\infty$.

$$\dot{q}_{out} = h(T_s - T_\infty) \tag{2.57}$$

$$h \approx h_{conv}A_{conv} + 4\sigma_{SB}\varepsilon_{rad}A_{rad}{T_\infty}^3 + \frac{k_{cond}A_{cond}}{L_{cond}} \tag{2.58}$$

Substituting Equation 2.57 into Equation 2.42 with $C_p = mc_p$ gives a general energy balance for a battery as shown in Equation 2.59. Note that this assumes a uniform temperature distribution within the battery ($T = T_s$). This assumption will be scrutinized in Section 2.6.5.

$$mc_p\frac{\mathrm{d}T}{\mathrm{d}t} = I(V - V_{rev}) + IT\frac{\partial V_{rev}}{\partial T} - h(T - T_\infty) \tag{2.59}$$

When an operational battery goes into standby mode ($I = 0$), the irreversible and reversible heat generation rates will go to zero. If a constant h can be assumed, this reduces Equation 2.59 to a simple Newton cooling problem which can easily be solved for the

battery temperature T as a function of time t. This is done in Equations 2.60 and 2.61, where $\tau = mc_p/h$ is the cooling time constant of the battery.

$$\frac{\mathrm{d}T}{\mathrm{d}t} = -\frac{h}{mc_p}(T - T_\infty) = -\frac{T - T_\infty}{\tau} \tag{2.60}$$

$$T = T_\infty + (T_{t=0} - T_\infty)\mathrm{e}^{-\frac{t}{\tau}} \tag{2.61}$$

The result in Equation 2.61 shows that a battery in standby mode will cool asymptotically toward the ambient temperature at a rate determined by the cooling time constant τ, which is a function of the physical properties of the battery and its surroundings. These same properties therefore determine the ability of a battery to dissipate heat while it is operating as well. The value of c_p is fixed in a relatively narrow range near 1000 J/kg·K (discussed in Section 2.6.2), and the mass m is typically constrained by system design requirements. The value of h therefore controls battery thermal management for a given T_∞.

As implied by Equation 2.58, increasing the value of h for a battery can be achieved by increasing its exposed surface area (high A_{conv} and A_{rad}), increasing its surface emissivity (high $\varepsilon_{\mathrm{rad}}$), applying forced convection with a suitable fluid (high h_{conv}), increasing the thermal conductivity of the battery housing (high k_{cond}), or actively cooling a thermal conductor that makes good contact with the battery (high A_{cond} and low L_{cond}). All of these techniques can be applied in practice using air blowers, cooling fins, liquid cooling plates, etc. [182]. Hatchard et al. demonstrated that radiation can contribute more than half of the total surface heat dissipation for a single cylindrical cell completely exposed to its environment, and that surface emissivity can be improved significantly simply by applying an appropriate paint or label compared to a bare steel housing [191].

2.6.5. Heat Diffusion

Another important consideration for battery thermal management is heat conduction within the battery itself. Since a lithium-ion battery is composed of layers of different materials (see Figure 2.6), the composite thermal conductivity of a cell is different along the length of the cell stack (parallel to the layers) vs through the thickness of the cell stack (perpendicular to the layers). The review by Steinhardt et al. [183] concluded that the

parallel thermal conductivity $k_{\parallel}$ tends to be relatively high since the copper and aluminum current collectors (about 399 W/m·K and 238 W/m·K, respectively) can effectively conduct heat along the length of the cell stack, but the perpendicular thermal conductivity $k_{\perp}$ tends to be relatively low since heat must transfer through the less thermally conductive plastic separator layers (about 0.3 W/m·K) and electrode coatings (about 0.5 to 1.5 W/m·K) as well as the thermal contact resistance between the various layers in the cell stack. For full cells, the review found that $k_{\parallel}$ values are typically in the range of 20 to 40 W/m·K while $k_{\perp}$values are typically in the range of 0.2 to 1.4 W/m·K.

For an object being cooled by surface convection, the Biot number Bi is used to assess the effectiveness of heat diffusion within the object. This is defined in Equation 2.62, where the characteristic length L_{Bi} is taken as the volume-to-surface-area ratio of the object and k_{int} is the internal thermal conductivity of the object. Temperature gradients within the object should not be significant for $Bi < 0.1$ [189].

$$Bi = \frac{h_{\text{conv}} L_{Bi}}{k_{\text{int}}} < 0.1 \tag{2.62}$$

A general case can be demonstrated with Equation 2.62 to illustrate the risk of internal temperature gradients for a lithium-ion battery. Though h_{conv} can vary significantly based on surface geometry and ambient conditions, values in the range of 2 to 25 W/m^2·K are typical for natural convection in ambient air [189], so h_{conv} =10 W/m^2·K can be applied for illustrative purposes. Based on the range of $k_{\perp}$ values reported by Steinhardt et al. [183], $k_{\text{int}} = 1$ W/m·K can be applied for illustrative purposes. With these values, satisfying $Bi < 0.1$ requires $L_{Bi} < 10$ mm. To put this in perspective, Waldmann et al. [68] reported the volume-to-surface-area ratio to be about 3 mm for a pouch cell with 7 mm thickness, 4.5 mm for a cylindrical cell with 21 mm diameter, and 8 mm for a prismatic cell of unspecified dimensions. This shows that single lithium-ion cells are indeed at risk of temperature gradients due to limited heat diffusion through the cell stack, especially if radiative heat dissipation is significant or if h_{conv} is increased through forced convection to improve the heat dissipation rate. Since the volume-to-surface area ratio will tend to increase when multiple cells are packaged into larger units, the potential for temperature

gradients is even greater for large EV battery packs if heat dissipation only occurs at the outer surface.

Temperature gradients can give rise to a number of issues for a commercial lithium-ion battery. For one, battery temperature is typically monitored by a sensor adhered to the outer surface, which may not adequately capture the maximum temperature in the core of the cell. Battery control systems should therefore employ a conservative upper temperature limit to account for the likelihood that the maximum battery temperature is higher than what is being measured. Furthermore, Sections 2.2 and 2.4 discussed how the temperature of a battery influences its internal resistance and degradation rate. If different cells in a pack are consistently operating at different temperatures due to limited heat diffusion through the pack, those cells will exhibit different performance characteristics which may diverge over time as the cells degrade at different rates, potentially causing the pack to be limited by its weakest cell. It is generally recommended that the temperature differential between the warmest and coolest cells in a battery pack be maintained below 5 °C to prevent cell SOH levels from diverging over time [174], [175].

Battery temperature gradients can be mitigated by an active thermal management system, which consumes energy to actively extract heat from the interior of the battery pack. This requires the pack to be built with hollow channels that can carry a fluid such as air or liquid coolant through the interior of the pack [182]. However, this comes at the cost of decreased pack energy density. Different thermal management system designs for EV battery packs will be reviewed in Chapter 3.

2.6.6. Thermal Runaway

One of the biggest safety concerns with lithium-ion batteries is that their components begin to react and decompose exothermically when the battery is at elevated temperatures, which can lead to a dangerous self-heating chain reaction known as thermal runaway. The self-heating process typically begins when the cell temperature reaches about 85 to 90 °C, where exothermic decomposition of the SEI on the graphite negative electrode becomes significant [192], [193]. If the cell cannot dissipate the resulting heat generation, the temperature will continue to increase, leading to more aggressive SEI decomposition and

the breakdown of the separator material, which can short-circuit the cell and generate greater amounts of heat [194]. The self-heating process becomes dangerous when the temperature reaches the threshold at which the positive electrode begins to decompose at a significant rate. At this 'onset temperature', it becomes thermodynamically favourable for the positive electrode to convert into more stable phases, which is accompanied by the release of oxygen from the electrode material [44]. The reaction can be highly exothermic, and the released oxygen also promotes combustion of the organic electrolyte components which can auto-ignite at temperatures near 450 °C [195]. All the cell components eventually break down or melt as the temperature rises to 800 °C or more [194], resulting in catastrophic failure in the form of smoke, fire or explosion.

While it is SEI decomposition at the negative electrode that initiates the process of thermal runaway, it is the highly exothermic decomposition reactions at the positive electrode which drive the catastrophic failure [196]. The onset temperature of the positive electrode material is therefore an important consideration for lithium-ion battery safety, along with the rates and total amounts of heat generation and oxygen release [47]. These safety metrics are strongly dependent on SOC [197], but it is generally accepted that LFP and LMO have the best safety properties among lithium-ion variants while LNO, LCO, and NCA have the poorest [44], [192]. Nickel-rich materials like LNO, NCA, and NMC811 decompose more readily due the presence of unstable Ni^{4+} ions at high SOC, while NMC with $33\ \% \leq Ni \leq 50\ \%$ provides a significant improvement [47], [124], [197]. In the case of LFP and LMO, thermal runaway is primarily driven by decomposition of the graphite negative electrode [198]. LFP has the additional safety benefit of strong P-O covalent bonds, which prevent the release of oxygen during decomposition [49].

The elevated temperatures that trigger thermal runaway may arise in a variety of ways. Continuous high-power cycling can generate enough heat to reach these temperatures if the heat cannot be effectively dissipated [182]. Temperature is typically monitored in commercial batteries so these elevated temperatures can be avoided, but large battery systems may feature localized hotspots due to poor thermal conductivity or nonuniform current distribution (as discussed in Section 2.6.5). Battery thermal management strategies therefore strive to maintain measured battery temperatures in a safe range; typically below

60 °C where SEI decomposition can first be detected [194]. Thermal runaway incidents are usually triggered by unintentional overcharging or by a short circuit within an individual cell, which may be caused by external damage or by metallic dendrites penetrating the separator after extensive degradation by lithium plating [198]. Once an individual cell is in thermal runaway, the process can propagate via heat transfer or physical rupture to neighboring cells in a battery pack.

In order to decrease the likelihood of thermal runaway, commercial lithium-ion batteries include safety features designed to limit or interrupt the current when the voltage, temperature or pressure exceeds a set threshold. Some examples include pressure-sensitive current interrupt devices, temperature-sensitive resistors, and specialized separators which shut down Li^+ transfer at a set temperature [198]. When multiple cells are connected in series, a battery management system is necessary to monitor and balance individual cell voltages to ensure that no cells become overcharged [182]. Individual cell temperatures can also be monitored and reported to the battery control system. The various functions of battery management systems will be reviewed in Chapter 3.

2.6.7. Temperature Evaluation

Given the importance of temperature for lithium-ion battery performance and safety, appropriate metrics must be used to evaluate the temperature of operational batteries. To ensure safety, the maximum battery temperature should be monitored and maintained below a conservative upper limit. Since battery degradation will be influenced by long-term temperature levels, the overall pack temperature should also be monitored and averaged over appropriate time scales. To evaluate temperature gradients, temperature sensors should capture the extremes of temperature distribution across the battery. These considerations suggest that the following three temperature metrics should be evaluated when operating lithium-ion batteries:

- $T_{\text{high}}^{\text{max}}$ is the maximum instantaneous temperature over a given period at the location exhibiting the highest temperatures of the entire battery. This can be used to evaluate thermal safety risk and trigger alarms or mitigative measures.
- $T_{\text{high}}^{\text{avg}}$ is the average temperature over a given period at the location exhibiting the highest temperatures of the entire battery. This can be used to evaluate thermal impacts on the degradation rate of the hottest cells.

- $\Delta T_{\text{low}}^{\text{high}}$ is the average temperature differential over a given period between the two locations exhibiting the highest and lowest temperatures of the entire battery. This can be used to evaluate the impacts of temperature gradients on battery performance.

These temperature metrics imply that at least two temperature sensors should be applied to a battery to capture the hottest and coolest locations distributed across the battery during operation. While these three metrics are important for optimizing battery operation in commercial applications, they also can also serve as research metrics for comparing the thermal performance of different batteries and battery cooling systems. This will be revisited in Chapter 4.

2.7. Chapter Summary

Chapter 2 has provided a detailed review of the design, function, and evaluation of lithium-ion batteries. Many of the reviewed concepts are essential for the design and analysis of lithium-ion battery experiments, including the fundamentals of Li^+ intercalation and cell design, the array of complex processes that underpin simple voltage and temperature measurements, the inevitable irreversibility that impacts energy storage capabilities, the implications of heat transfer, and the differences between various electrode materials. These concepts will be referred to throughout the remainder of this thesis.

One key takeaway is that the range of viable positive electrode materials and adjustable cell design parameters allows for significant diversity among lithium-ion battery designs. Chapter 2 has demonstrated that this design diversity can lead to very different voltage profiles, internal resistances, degradation rates, and thermal characteristics, and described the scientific reasons for these differences. This same diversity is prevalent among commercial EV batteries, making it necessary to investigate how different EV battery designs perform in second-life energy storage applications. This thesis conducts such an investigation through experimental research. Chapter 3 will first provide a more focused review of second-life battery technology.

Chapter 3 REVIEW OF SECOND-LIFE BATTERY TECHNOLOGY

Chapter 2 covered the basics of lithium-ion battery technology. Due to a strong combination of energy density, energy efficiency, power capability, and cycle life, lithium-ion has become the battery technology of choice for the rapidly growing EV industry. Chapter 3 will now expand on lithium-ion battery technology in the context of second-life battery applications by reviewing EV battery packs, electricity grids, stationary energy storage applications, and the various opportunities and challenges associated with repurposing EV batteries. Key research gaps in the field of second-life batteries will also be identified to set up the novel research that will be presented in the remaining chapters of this thesis.

3.1. Electric Vehicle Batteries

According to the International Energy Agency [3], the global passenger car EV stock reached 28 million in 2023 (not counting another 12 million plug-in hybrid electric cars with relatively small batteries). The global sales of new passenger car EVs exceeded 9 million in 2023, which represents an increase of 30 % above 2022 sales and a 12 % share of all passenger car sales in 2023. Of these 9 million new EV sales, 57 % were in China, 23 % were in Europe, and 12 % were in the United States (92 % combined). The rapid growth in global EV sales and stock since 2010 are respectively depicted in the top and bottom charts of Figure 3.1. As introduced in Chapter 1, the ongoing and anticipated growth in the EV industry has given rise to much research and development in the field of second-life batteries. To understand the unique challenges faced by the second-life battery industry, the various aspects of EV battery design must first be examined. This section will review key design features of EV battery packs as well as the potential pathways these batteries can take after being removed from EV service.

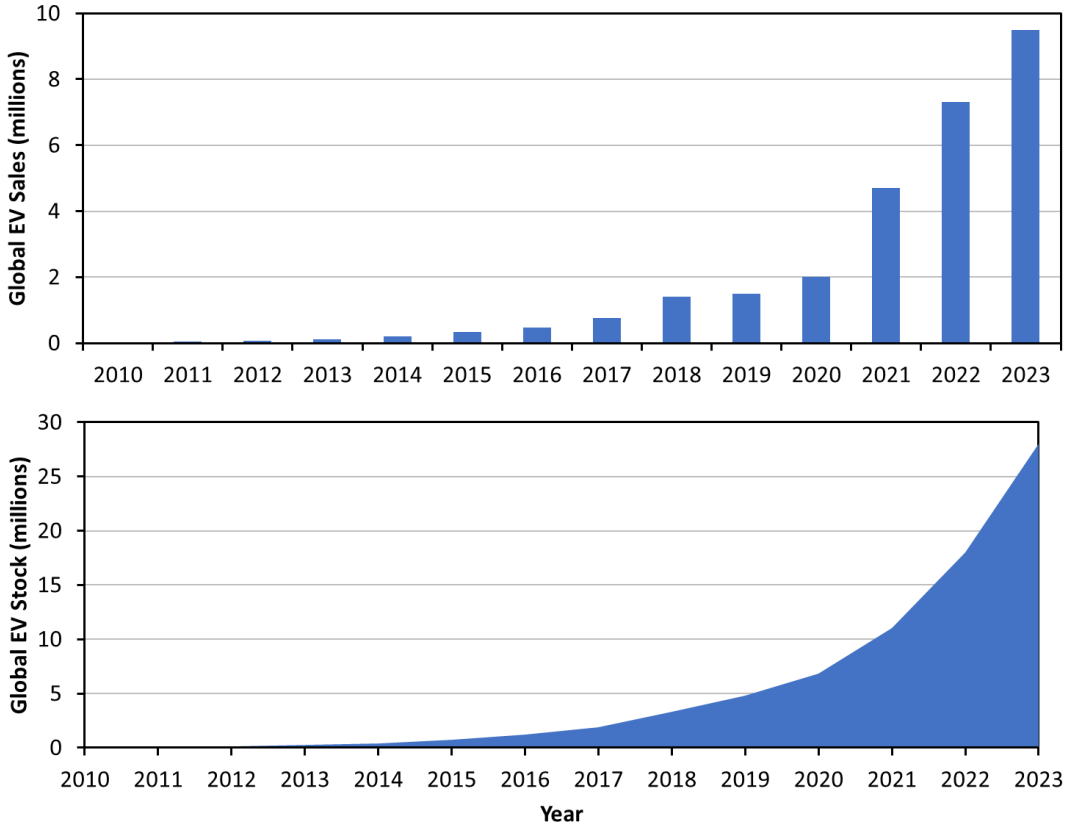


Figure 3.1 Growth in global sales (top) and stock (bottom) of passenger car EVs since 2010. Based on data from [3].

3.1.1. Design Parameters

Two major EV manufacturers currently dominate the global market: China-based BYD and US-based Tesla together accounted for 35 % of all passenger car EV sales in 2023 [3]. Numerous unique EV models are also being produced by major vehicle brands across the United States, Europe, and Asia, including Chevrolet, Ford, BMW, Mercedez-Benz, Renault, Volkswagen, Volvo, Honda, Hyundai, Nissan, Toyota, and many others.

Different EV models tend to feature unique battery designs, which can vary significantly in terms of cell design, module design, and pack design. A given EV battery pack generally comprises multiple battery modules connected in a series string, each of which comprises multiple cells connected in series and/or parallel strings. These three battery design levels are illustrated in Figure 3.2 for the example of a 2018 Chevrolet Bolt electric car. This particular battery pack features two different module sizes. Eight of the ten modules feature a ‘10S3P’ configuration (i.e. ten series-connected cell groups and three parallel-connected

cells within each cell group) while the other two modules feature an 8S3P configuration. The ten modules are connected in series to give an overall 96S3P configuration for the pack. Note that the bottom left image in Figure 3.2 shows the 'housing cover' removed from the 'housing base' to reveal the modules inside. The housing cover is sealed to the housing base in EV service, as pictured in the bottom right of Figure 3.2. While most existing EV battery designs feature cells, modules, and pack housings, there is an emerging trend towards eliminating the module level to increase pack energy density [199] and/or eliminating the pack housing in favour of integrating cells or modules directly into the vehicle chassis as structural components [200].

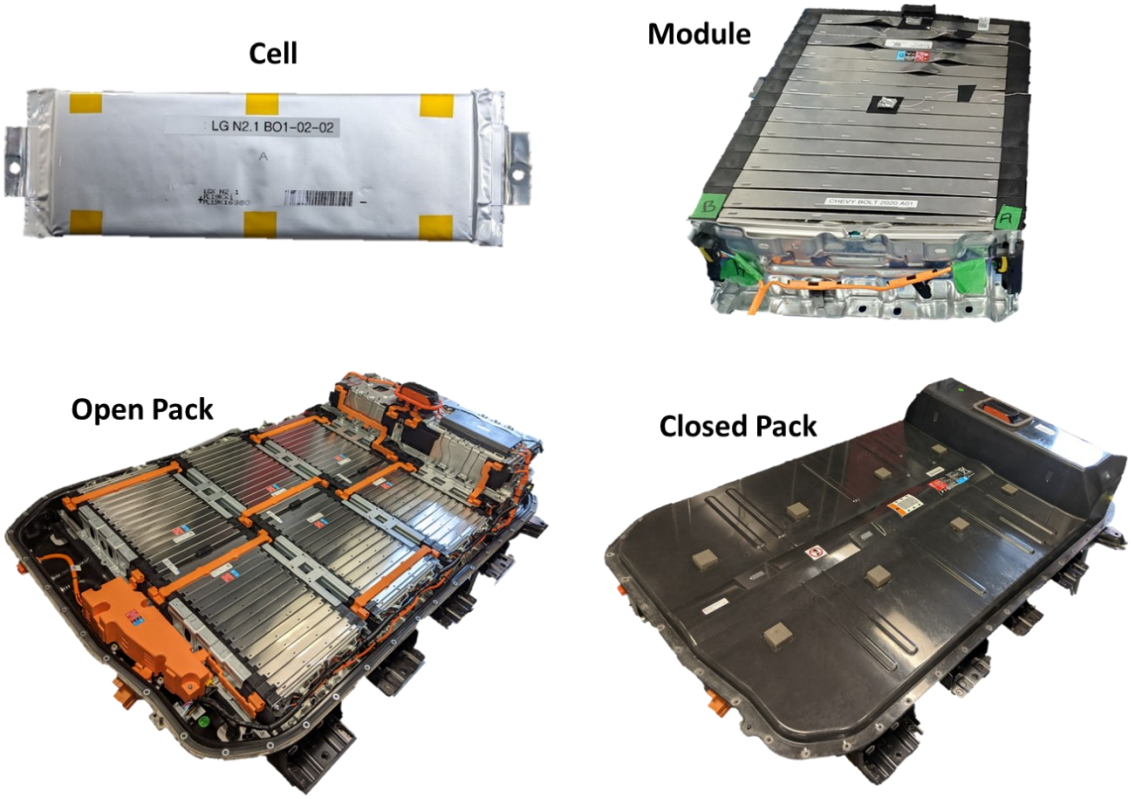


Figure 3.2 Example of a lithium-ion battery from a 2018 Chevrolet Bolt electric car, including single pouch cell (top left); single 10S3P module (top right); open pack comprising eight 10S3P modules and two 8S3P modules (bottom left); and closed pack with housing cover secured in place (bottom right).

At the cell level, manufacturers can vary the design parameters of any of the cell components described in Section 2.1. These may include positive and negative active materials, dopants, binders, and conductive additives; electrode coating thickness,

porosity, and particle size; electrolyte solvents, salt concentrations, and additives; separator material, thickness, and porosity; current collector thickness; cell format (cylindrical, pouch, prismatic); and cell size. Different safety features can also be included in the cell design as described in Section 2.6.6. It was reported in 2022 that 65 to 70 % of EVs use NMC (some blended with LMO), 15 to 20 % use NCA (the preferred choice of Tesla), and 10 to 20 % use LFP (the dominant choice in China where urban driving allows for lower driving range and thus lower battery energy density), while > 99 % use graphite at the negative electrode [29].

Battery modules are generally constructed in a rectangular format, but there are many module-level design parameters which manufacturer can vary. These may include the number of cells connected in series and/or parallel strings; module housing materials; module dimensions; and the inclusion of other inactive materials which provide mechanical and/or thermal protection for the cells. For example, specialized foams are sometimes featured in EV battery module designs to dampen mechanical vibrations, to absorb impact forces, and to thermally insulate neighbouring cells from each other to inhibit propagation in the event of thermal runaway [201]. Commercial examples of different module design features will be shown in Chapter 4.

All EV battery packs must of course be designed to fit within their intended vehicle. For private passenger vehicles, the pack is generally situated at the base of the vehicle, beneath the floor of the passenger cabin. A short and wide rectangular format is therefore commonly employed at the pack level, but some packs may feature irregular shapes that allow the pack to utilize more space within the vehicle. For example, the taller section of the EV battery pack shown in Figure 3.2 would sit beneath the rear passenger seats in the vehicle. Aside from size and shape, there are a number of pack-level design parameters which manufacturers can vary. These may include the quantity and layout of battery modules; the overall pack voltage (typically 400 V or 800 V nominal); the electrical circuitry (interconnects, contactors, fuses, etc.); the pack housing material; the method of fastening the housing cover to the housing base; the battery management system (BMS); and the thermal management system (TMS). Some EV battery packs also feature a mid-pack connector which allows for the high pack voltage to be manually halved for the sake

of safety while technicians are handling the battery pack. Sections 3.1.2 and 3.1.2 will respectively elaborate on BMS and TMS technologies.

The numerous EV battery design parameters produce a wide range of EV battery energy ratings, typically ranging from 20 to 100 kWh in nominal energy capacity. Note that energy density and specific energy will decrease from cell to module to pack for a given EV battery design due to the additional inactive components at module and pack levels.

3.1.2. Battery Management Systems

As discussed in Section 2.6.6, the voltages of individual lithium-ion cells in a series string must be monitored and controlled to ensure that no cells become overcharged or enter into thermal runaway. This 'cell balancing' operation is performed by a BMS. A BMS may carry out a variety of important functions for a battery system, as described in [202]. This section will summarize the main functions of a BMS in a typical EV battery pack, which are illustrated in Figure 3.3.

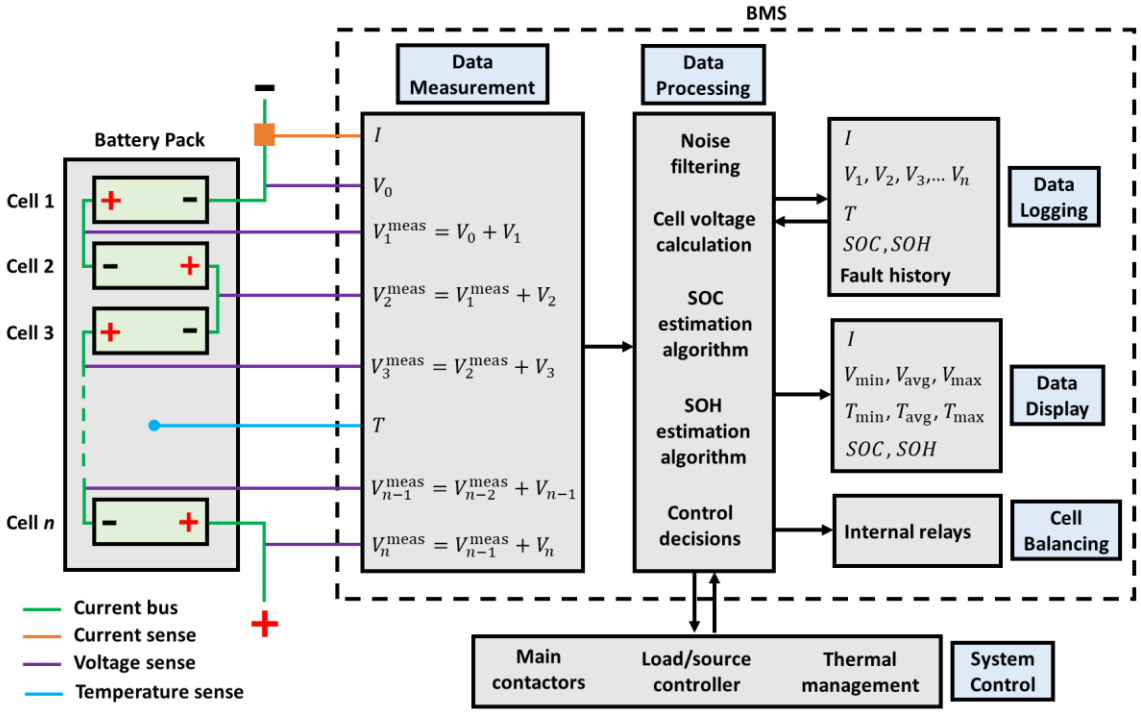


Figure 3.3 Basic schematic of the main functions of a battery management system.

The BMS monitors cell voltages using voltage sensors placed between each cell or cell group in the series string. The measured voltages (shown as V_i^{meas} in Figure 3.3) are

referenced to a common voltage point (shown as V_0 in Figure 3.3) placed at the negative end of the string, allowing the BMS to calculate individual cell voltages (shown as V_i in Figure 3.3) using basic arithmetic. Typically, the BMS also measures the battery current through a current transducer, as well as temperatures at various locations in the pack using thermistors. The measured data is processed, logged in internal recorders, and displayed on a user interface, often including statistics such as minimums, averages, and maximums.

Cell balancing is a key BMS function which prevents overcharge of individual cells while the battery is charging. There are passive and active cell balancing techniques, but passive balancing is most common due to its simplicity and affordability. To conduct passive balancing, the BMS features switches which can be closed to place a resistor across any individual cell. When a cell reaches a specified upper voltage limit during charge, the BMS closes the appropriate switch, causing a portion of the applied current to dissipate through the resistor as waste heat. This prevents the voltage of the cell in question from increasing further while the other cells continue to charge. The cell balancing process continues on subsequent cells until the whole battery reaches a specified charge termination threshold. Active balancing employs more advanced and expensive techniques to redirect current from a high-voltage cell to a low-voltage cell during charge or discharge. Passive balancing can only be performed during charge, and it results in some charge energy being curtailed as waste heat.

In addition to current, voltage, and temperature, modern BMS designs often feature specialized algorithms that can process present and historical measurements to estimate the SOC and SOH of the battery pack and/or individual cells [203]. For SOC estimation, algorithms often include a combination of 'coulomb counting' (i.e. integration of battery current over time) and a means of using voltage and temperature measurements to correct the coulomb counting error that inevitably accumulates over time due to imperfect current measurements and battery degradation. Correction techniques typically use a battery model (such as the equivalent circuit model shown in Section 2.3) as the basis for Kalman filters, particle filters, fuzzy logic, or artificial neural networks, which vary in terms of complexity, reliability, and computational requirements [202], [204], [205]. For SOH estimation, algorithms often rely on historical measurements and complex predictive models to assess

capacity fade and internal resistance growth. The same types of correction techniques that are applied to SOC estimation algorithms can also be applied to SOH algorithms.

The BMS also uses the processed data to detect faults and make decisions regarding battery control. For example, if the BMS detects that the battery is approaching a specified SOC limit, the BMS will communicate with the load/source controller to reduce the power envelope for discharge or charge. If the BMS detects that battery temperatures are outside the preferred range, the BMS will engage the TMS or adjust the power envelope. If the BMS detects that one or more cells have become disconnected or reached unsafe temperatures, the BMS will record a fault and open the main contactors to disconnect the battery from power flow. Communication between the BMS and external devices is typically done using a digital communication protocol such as controller area network (CAN bus) or Modbus.

Note that a BMS may be designed with a centralized or distributed architecture. A centralized BMS is a single unit which monitors and manages the entire battery pack, while a distributed BMS features a master unit that reads, analyzes, and controls multiple slave units assigned to individual battery modules within the pack. Distributed systems offer the advantage of modularity, but require multiple BMS units and communication circuits and therefore tend to be more expensive than centralized systems [202].

3.1.3. Thermal Management Systems

As described in Section 2.5.2, lithium-ion batteries have an optimal operational temperature range of approximately 25 to 40 °C, with lower temperatures leading to lithium plating and reduced energy and power performance, and higher temperatures accelerating numerous degradation mechanisms and elevating safety risks. Since EV battery packs feature many interconnected cells in a densely packed arrangement, there is also a potential for significant temperature gradients to arise. As explained in Section 2.6.5, the temperature differential across a battery pack should be held below 5 °C to prevent cell SOH levels from diverging over time. The TMS of an EV battery pack is therefore essential to maintain both battery temperatures and temperature gradients within preferred ranges set by the manufacturer. Most studies on novel TMS designs for EV batteries use both the

maximum temperature and the temperature differential as metrics to evaluate and optimize TMS performance [206].

Just as there is significant variability in battery design, there is also significant variability in TMS design. Many different studies have investigated or reviewed various EV battery TMS technologies in recent years [206-213]. These TMS technologies are summarized graphically in Figure 3.4, where red bordering is used to designate the technologies that are presently deployed in commercial EV batteries. The various TMS technologies can generally be classified as either passive or active, which are respectively designated by blue and green shading in Figure 3.4. Passive TMS designs require no energy input during operation, while active TMS designs consume electrical energy to drive heat transfer. The main heat transfer mediums discussed in the literature are air, liquid, phase change materials, the thermoelectric effect, as well as various hybrids of these unique technologies.

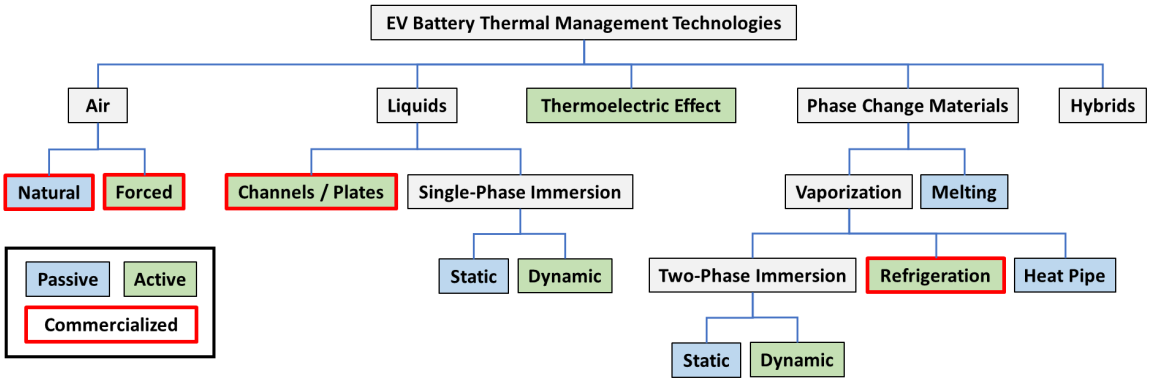


Figure 3.4 Summary of thermal management technologies being researched for EV battery applications.

Passive-air TMS designs generally rely on natural convection (essentially the absence of a designated TMS), though some designs allow for air to flow through channels in the battery pack while the vehicle is in motion [212]. Active-air TMS designs include electric fans or blowers to force air through the battery (independent of vehicle speed), with a wide variety of air channel designs and flow patterns proposed in the literature. Both passive-air and active-air TMS designs have been deployed in commercial EV batteries. For example, the Nissan Leaf battery uses a passive-air TMS, while the Renault Zoe battery uses an active-air TMS [209].

For EV battery packs with greater thermal management loads, the relatively low thermal conductivity, heat capacity, and convection coefficients of air-based TMS designs can be improved upon with liquid-based TMS designs at the expense of system complexity and cost [208]. Many commercial EV batteries feature an active-liquid TMS using a glycol/water mixture as the liquid coolant. Since water-based coolants are electrically conductive, the coolant must not make direct contact with the cells or else an electrical short circuit could lead to a fire. Instead, an electric pump forces the liquid coolant through thermally conductive channels that exchange heat directly with cell or module surfaces. Many different liquid channel designs have been proposed in the literature, but commercial designs generally feature either 'side cooling' (i.e. channels passing between adjacent cells within a module) or 'bottom cooling' (i.e. channels within a large plate sitting directly above or below the module) [208]. Different liquid flow patterns have also been explored, such as multiple parallel channels with a common header vs a single serpentine channel [207]. Chapter 4 will show the active-liquid TMS designs of a Tesla Model 3 battery and a Chevrolet Bolt battery, which respectively feature parallel side cooling and serpentine bottom cooling.

Active-liquid TMS designs featuring liquid channels are sometimes referred to as 'indirect liquid' TMS designs. In contrast, 'direct liquid' TMS designs allow for the liquid to make direct contact with the cells or modules without the use of liquid channels. This TMS technology is also called 'immersion cooling'. The liquid used for immersion cooling is typically a dielectric fluid such as a silicone oil or specialized hydrocarbon so that electricity cannot be conducted through the liquid and short-circuit the battery. Immersion TMS designs can be passive or active depending on whether a pump is used to force the dielectric fluid through the battery for enhanced heat transfer. This TMS technology has not yet been widely commercialized in EV applications, but it has been introduced into high-end electric sports cars such as the McLaren Speedtail [208]. Wider commercial adoption is expected in the future.

Immersion TMS designs can be subdivided into 'single-phase' and 'two-phase' immersion. Single-phase immersion strictly uses a liquid to exchange sensible heat with the battery, while two-phase immersion uses a dielectric fluid with a boiling point below the specified

upper temperature limit of the battery [208]. Figure 3.4 therefore classifies two-phase immersion with other phase change TMS technologies that can absorb latent heat to further mitigate battery temperature rise. Like two-phase immersion, refrigeration and heat pipe technologies also capitalize on the latent heat of vaporization, though in these cases the working fluid does not make direct contact with the battery. In contrast, solid-liquid phase change materials capitalize on the latent heat of melting, typically by encapsulating the cells in a specialized paraffin wax [206]. The BMW i3 is one commercial example of a refrigeration TMS in EV battery applications [214], but other phase change TMS technologies presently remain in the research stage due to performance limitations, cost, or technical immaturity [176]. For example, the poor thermal conductivity of suitable solid-liquid phase change materials makes it challenging to reject the heat that has been absorbed from the battery, so ongoing research seeks to embed thermally conductive materials such as metals or graphite within the phase change materials [213].

Research has also explored the possibility of actively exchanging heat with EV batteries using the thermoelectric effect. Though it has been generally concluded that the thermoelectric effect cannot efficiently meet TMS requirements for EV batteries [215], there is potential to combine thermoelectric technology with other TMS technologies for hybridized performance benefits. Combining various TMS technologies into hybrid TMS designs is the subject of much research [216], though no such systems have yet been commercialized in EV battery applications.

While all proposed TMS technologies can be used to prevent an EV battery from self-heating beyond a set upper temperature limit during operation, not all TMS technologies can be used to raise the temperature of an EV battery above a set lower temperature limit. To avoid the large overpotentials associated with low-temperature (e.g. < 0 °C) battery operation [207], an EV battery should be pre-heated before the vehicle is driven in cold environments. Battery pre-heating cannot be directly achieved by passive TMS technologies, so it is necessary to operate the battery in a specialized self-heating mode using resistive heaters applied directly to the battery instead of pre-heating the air or liquid in an active TMS [215]. It has also been proposed to apply an AC current to EV batteries while plugged in as a means of pre-heating in cold environments [207].

Apart from the physical system design, TMS control strategies are also a popular area of research. For example, one study demonstrated a novel control algorithm which reduced the energy consumption of an active-liquid TMS by adjusting the liquid flow rate based on real-time cooling demand in EV applications [217].

3.1.4. End of Vehicular Life

Every EV battery will eventually reach the end of its useful life in the vehicle. This can occur in one of two ways: either the vehicle itself reaches the end of its life (due to collision or long-term wear); or the battery degrades to the point that it no longer meets the minimum requirements for EV applications [218]. In either case, this point in the battery life cycle is called the 'end of vehicular life' (EOVL). When the battery is fully degraded to the point of having no practical use other than the recycling of its constituent components, the battery is considered to have reached EOL.

The specific threshold that triggers EOVL is an interesting subject discussed widely in the literature. Many early EVs (approximately year 2010 to 2015) featured relatively small battery capacities ranging from 20 to 25 kWh (e.g. first generation Nissan Leaf and BMW i3), corresponding to driving ranges of only about 100 to 150 km. Due to this low driving range, it was commonly expected that EOVL would be reached due to reduced driving range when these relatively small batteries degraded to approximately 80 % SOH [5], at which point the battery could be replaced and the vehicle continue in service. Newer EVs usually feature battery capacities ranging from 40 to 80 kWh (e.g. Chevrolet Bolt and Tesla Model 3), with some exceeding 100 kWh (e.g. BMW i7), corresponding to driving ranges of 250 to 700 km. This means that lower SOH levels can still provide functional EV driving ranges (for resale if not for the original driver). Another important point is that larger EV batteries will tend to degrade at slower rates in EV service (per year and per km travelled) compared to smaller EV batteries [5]. For example, if a 30 kWh battery and a 60 kWh battery are subjected to the same EV drive cycle and power magnitude (neglecting differences in cell, module, and pack design as well as vehicle mass), the 30 kWh battery will experience double the depth of discharge, double the energy throughput, double the power density, and therefore significantly higher temperatures, all of which tend to accelerate the various battery degradation mechanisms discussed in Section 2.5. The

combination of higher battery capacity, lower battery degradation rates, and technology maturation in newer EVs increases the likelihood that the vehicle will trigger EOVL before the battery does. A 2020 analysis of global EV battery data concluded that the average EV battery installed in a 2020 private passenger vehicle will be able to last 15 years or more before SOH declines to 80 % [219].

To better quantify EOVL expectations in the coming years, Casals et al. [5] conducted a 2022 statistical analysis for the United Kingdom market based on publicly available EV battery degradation data. The authors assumed that publicly available age and mileage data for retired diesel vehicles (which generally last longer than gasoline vehicles) give reasonable expectations for the retirement age and mileage of EVs independent of battery degradation (distributions of 2 to 20 years and up to 500,000 km). Some of the key results of the study are summarized in Figure 3.5. The left chart shows that retired EV batteries at present day are a mix of small (e.g. 24 kWh), medium (e.g. 40 kWh), and large (e.g. 70 kWh) batteries, with smaller batteries most often retired below 75 % SOH (indicating retirement due to unacceptable driving range) and larger batteries most often retired above 85 % SOH (indicating early vehicle retirement, perhaps due to collision). However, Figure 3.5 also shows that the overall quantities of retired EV batteries are currently very small compared to what is expected in the coming years. The right chart shows that small batteries will soon make up an insignificant portion of retired EV batteries, while quantities of retired medium and large EV batteries will increase dramatically and frequently reach EOVL at SOH levels of 85 % or higher (indicating batteries outlasting the vehicles). The study concluded that by 2035, 55 % of all retired EV batteries in the United Kingdom will have reached EOVL above 85 % SOH, with 89 % of all retired EV batteries above 75 % SOH. Only 1 % were projected to reach EOVL below 60 % SOH. The authors also noted that the United Kingdom only represents about 5 % of the global EV market, so the 500,000 scale in the right chart of Figure 3.5 could be scaled up to 10 million to get a sense of global scale.

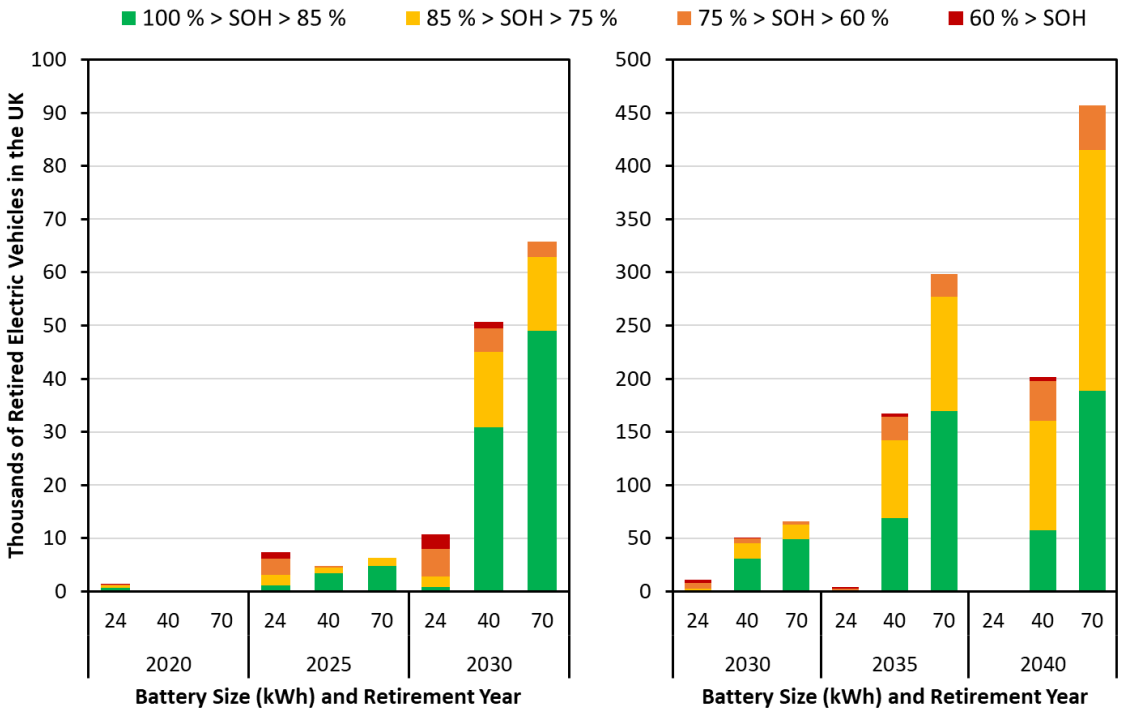


Figure 3.5 Expected quantities of retired EV batteries by size and SOH in the United Kingdom. Based on data from [5].

It is worth mentioning here that battery SOH levels at EOVL may be influenced by emerging technologies that allow EVs to be used as stationary energy storage while parked and plugged in, such as 'vehicle-to-grid' applications [220]. This would cause the EV battery to degrade faster over time, since the battery would be cycling even when the vehicle is parked for long periods. These technologies are still in development, so they are not factored into the results shown in Figure 3.5.

With many millions of retired EV batteries entering waste management streams, effective recycling processes are essential for sustainability. Battery recycling can also provide a domestic supply of essential base materials that might otherwise need to be imported from foreign mining industries [221]. When EV batteries enter the recycling stream, they must first be discharged, disassembled, and sorted before being treated with one of the two established lithium-ion battery recycling technologies: pyrometallurgy and hydrometallurgy. Pyrometallurgical methods use a high-temperature furnace to smelt full cells or modules such that valuable metals can be separated out and recovered [221]. This

approach is relatively efficient in terms of time, equipment, and labour requirements, but it requires large amounts of energy and releases significant environmental pollutants [222]. Hydrometallurgical methods use an acid or other leaching fluid to dissolve and extract key metals from the battery components. This is the preferred approach for newer recycling facilities since it consumes less energy, generates less pollution, and produces purer end products [223]. However, hydrometallurgy requires additional pre-processing steps to disassemble the cells and separate the various cell components, which results in additional time and labour [224]. Alternative recycling technologies are being researched extensively, but are not yet commercialized. One example is 'direct recycling', which physically separates electrode materials from the cell so they can be restored to commercial-grade quality without breaking them down into base elements [225].

The EV battery recycling industry still faces substantial challenges. For one, the diversity in EV battery designs makes it difficult to automate the various recycling processes. It is commonly stated in the literature that EV battery manufacturers should 'design for recycling' to make recycling easier and more economical [222]. It is also widely acknowledged that material recovery rates still need to be significantly improved as the battery recycling industry scales up to meet the rapidly growing demand [224].

Another important consideration arises when referring back to Figure 3.5. If the vast majority of EV batteries will be reaching EOVL at 75 % SOH or higher in the coming years, then significant economic value will be wasted if these batteries are sent directly to recycling after EOVL. To make better use of the manufacturing value embedded in retired EV batteries, these batteries should be reused as much as possible before they are sent to a recycling facility. While some used EV batteries may be suitable for reuse in another EV with lower driving demands [226], many will be better suited for repurposing into 'second-life' stationary energy storage applications where lithium-ion batteries are already being deployed. This additional utilization step within the EV battery life cycle is illustrated in Figure 3.6.

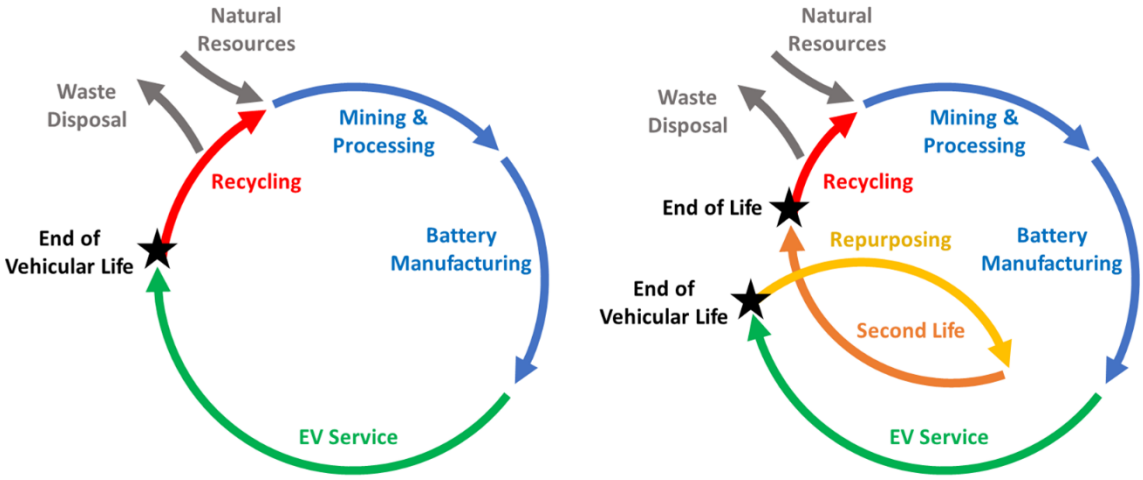


Figure 3.6 Illustration of EV battery life cycle without repurposing (left) and with repurposing (right). Partially based on figure from [227].

Stationary energy storage applications are typically less demanding than EV applications since they are not subject to vibration, outdoor climatic conditions, and sporadic drive cycles [226], [228]. This makes stationary applications a viable option for used EV batteries at EOVL. Section 3.3 will review various stationary energy storage applications that are suitable for repurposed EV batteries.

3.2. Electricity Grid Operation

Before reviewing stationary energy storage applications for second-life batteries, it is first necessary to understand how modern electricity grids are operated. Electricity grid operation is a highly complex field, so this section will provide a basic overview.

3.2.1. Electricity Supply and Demand

Electricity grid operators must generate a reliable and versatile electricity supply in order to meet highly variable electricity demands. On weekly to yearly time scales, electricity demand varies with environmental conditions (e.g. summer vs winter) and social influences (e.g. weekday vs weekend). For example, in cooler climates, the yearly peak in electricity demand would likely occur on the winter day with the greatest heating load, while in warmer climates, the yearly peak would likely occur on the summer day with the greatest cooling load. On a daily time scale, electricity demand tends to vary with the common patterns of daily human activity: increasing in the morning, peaking in the afternoon, decreasing in the evening, and reaching a minimum overnight. An illustrative example of

these patterns is shown by the two-day electricity demand profiles in Figure 3.7, with load profiles for winter and autumn respectively shown in the left and right charts. On smaller time scales of seconds to minutes, electricity demand is continually fluctuating due to the aggregation of lights, appliances, machinery, etc. being used intermittently across the grid. This means that real-time electricity demand profiles are not as smooth as the ones shown in Figure 3.7. Since electricity demand is constantly changing, electricity supply must be carefully controlled to match demand in real time. If this balance is not maintained, system failures such as blackouts may occur.

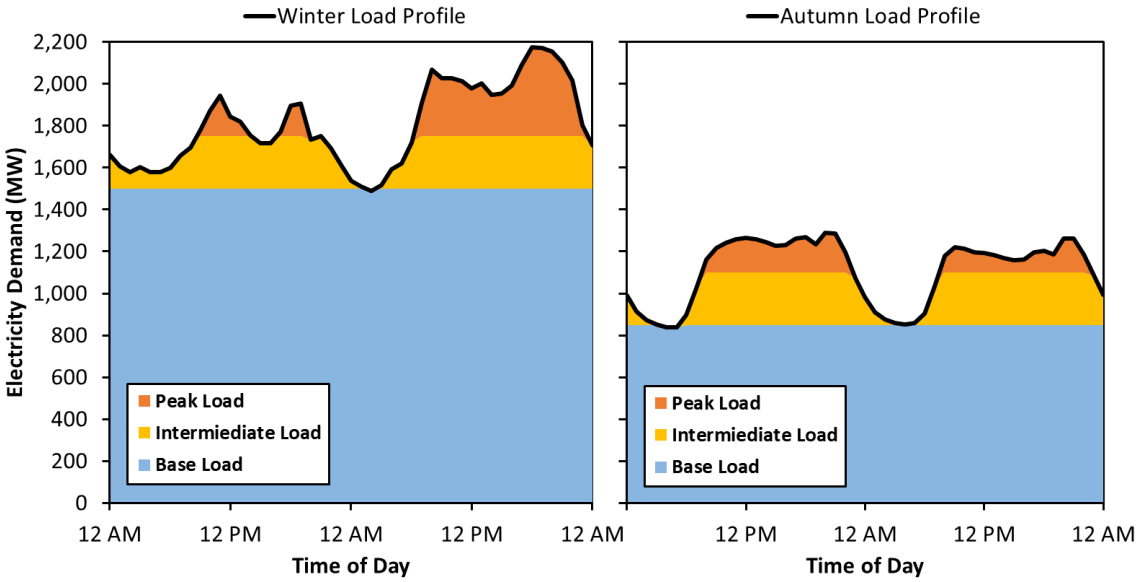


Figure 3.7 Illustrative example of base load, intermediate load, and peak load over a two-day period in winter (left) and autumn (right). Load profiles are based on Nova Scotia hourly net load data from [229].

As shown in Figure 3.7, the daily demand profile is typically divided into three segments: base load, intermediate load, and peak load. Base load reflects the minimum demand, which can be met by a relatively constant supply that runs uninterrupted day and night, whereas peak load must be met by a controllable supply that can come online and ramp up quickly in the morning, follow the variations during the peak period, and ramp down quickly to an eventual shutdown in the evening [230]. Intermediate load is a transition region, requiring a more versatile supply than base load but not so much as peak load. The example in Figure 3.7 shows that base load in winter (high heating requirements) can exceed peak load in autumn (low heating and cooling requirements).

Electricity supply can be provided by a mix of different sources which vary from region to region. Large steam-based power plants (e.g. coal, nuclear, oil, geothermal) typically have relatively low operating costs but do not perform well in fast-ramping operation, so these generators are typically used to meet base loads [231]. Combined-cycle gas turbines include a heat recovery steam cycle, but they can ramp faster than steam-based power plants and can therefore meet both base loads and intermediate loads [232]. Open-cycle gas turbines do not include a steam cycle and can therefore ramp very quickly, but the lower cycle efficiency and high fuel prices result in relatively high operating costs [233], making these generators most suitable for meeting intermediate and peak loads [232]. Dammed hydroelectric power plants typically have low operating costs and can ramp very quickly, so hydroelectricity can meet any type of load depending on the size of the generator [232]. In microgrid applications, diesel generators have conventionally been used to meet the entire load profile [234].

As explained in Chapter 1, electricity grids are becoming increasingly reliant on wind and solar energy in place of conventional power plants. In most parts of the world, onshore wind farms and photovoltaic solar farms now offer the lowest levelized cost of energy of any electricity generation technology [2]. However, the power output of wind turbines and solar panels are respectively dependent on variable wind speeds and variable sunshine. Wind and solar are therefore often referred to as ‘variable renewable energy’ sources to distinguish them from conventional electricity generators that can be controlled by adjusting fuel consumption rates or hydroelectric discharge rates. Without energy storage, the inherent variability of wind and solar farms makes them unsuitable for tightly-controlled peak load applications, and also unsuitable for pairing with slow-response power plants in base load applications [235]. However, variable renewable energy sources can be paired with fast-response conventional generators such as hydroelectric power plants and gas turbines, primarily in intermediate load applications [235]. A functional alternative is ‘pre-curtailment’, which involves intentionally operating wind farms or solar farms below their available power output level so they can provide a more steady and controllable electricity supply [236], but this of course wastes significant renewable energy unless it can be stored.

3.2.2. Electricity Grid Frequency

Electricity grids are operated at a nominal electrical frequency (60 Hz in the Americas and 50 Hz in most other countries). Conventional power plants generate electricity with a turbine (driven by water, steam, or combustion exhaust) coupled or geared to a generator which rotates at a nominal mechanical frequency to give the electricity grid its nominal electrical frequency (the ratio between the two frequencies being dependent on the number of magnetic pole pairs in the generator) [237]. Conventional power plants are considered 'synchronous' since the generators are synchronized to this common electrical frequency on a given electricity grid, even if individual power plants are separated by significant geographical distance. Variable renewable energy sources are not synchronized to the grid in this way. Photovoltaic solar panels generate direct current (DC) electricity, so power electronics are required to convert the generated DC electricity to match the AC frequency of the electricity grid. Wind farms are generally composed of variable-speed wind turbines, which require power electronics to convert the variable AC frequency to match the AC frequency of the grid [238]. Wind turbines and solar panels are therefore often referred to as 'asynchronous', 'nonsynchronous', or 'inverter-based' resources to distinguish them from synchronous generators.

Electrical equipment is designed for the nominal frequency of a given electricity grid, so the frequency is typically held within a normal operating band of ± 0.2 Hz to ensure efficient operation of electrical equipment across the grid [233]. If electricity supply and demand remain in perfect balance, then the generators will remain at the nominal frequency. In practice, this balance is never perfectly maintained due to the continual electricity demand fluctuations that result from human activity. When electricity demand exceeds supply, the increased torque on the generator decreases the rotational speed (thereby lowering the electrical frequency) until the power plant output is raised to match the demand [239]. Conversely, when electricity supply exceeds demand, frequency increases until the power plant output is lowered to match the demand. Maintaining an optimal frequency range is therefore an effective means of maintaining the balance of electricity supply and demand. Electricity system operators use 'automatic generation control' (AGC) to accomplish this. As the measured frequency continually deviates from the nominal value under normal operating conditions, the AGC algorithm sends control

signals to continually adjust the power output of designated power plants every few seconds so that the frequency converges back towards the nominal value [240]. This operation is called 'frequency regulation'. Note that AGC is actually determined by the 'area control error', which accounts for both deviations from the nominal system frequency and deviations from scheduled power flows between defined jurisdictional areas within the system [241]. On longer time scales of minutes to hours, the system operator will make larger adjustments to the total electricity supply by ramping certain power plants (typically intermediate or peak load power plants) up or down to match the evolving trends of electricity demand throughout the day [242]. This operation is called 'load following', and the rate at which it occurs is often called 'ramping'. Figure 3.8 illustrates how the real-time electricity demand can be separated into load following and frequency regulation components based on the time scale of variability (3 h time period shown).

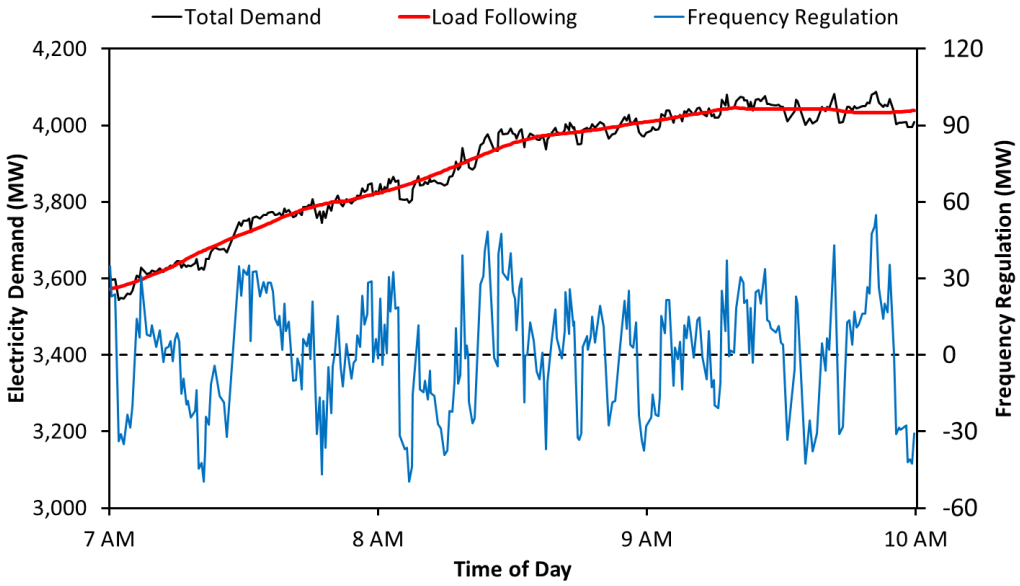


Figure 3.8 Example of load following and frequency regulation as components of total electricity demand. Based on data and figure from [242].

Unexpected events on the electricity grid can cause abrupt and significant deviations in frequency. A common example is an unplanned generator outage, creating a sudden deficiency in electricity supply which causes the frequency to drop. Such significant deviations from the nominal frequency can cause damage to electrical equipment and cascading failures that can lead to a blackout [241]. Electricity grid operators must therefore ensure that the system can respond swiftly to unexpected disruptions in the

supply-demand balance. In the case of an unplanned generator outage, electricity grid operators will implement ‘under-frequency load shedding’ if the frequency falls below a set threshold (e.g. 0.5 Hz below nominal), effectively cutting off power supply to certain loads as a means of restoring the supply-demand balance so the rest of the grid remains operational [239]. However, other mechanisms can help to slow and arrest the frequency decline so that load shedding does not become necessary.

The first measure to avoid load shedding is the ‘inertial response’ of conventional power plants. Large turbines and generators store significant rotational kinetic energy, and when a system disturbance causes the generator to slow down, some of that stored energy is discharged into the electricity grid. This inertial response is instantaneous, autonomous, and lasts for a few seconds [241]. The discharge of kinetic energy through the generator provides additional electricity supply to partially offset the supply-demand imbalance, which slows the rate of frequency decline following the disturbance [236]. Conventional power plants also feature a governor mechanism which provides ‘primary frequency response’ by rapidly converting a change in frequency to a counteracting change in power output [239]. For example, steam power plants feature a valve which throttles the steam flow into the turbine. As long as the steam is partially throttled, the power plant has some reserve capacity that can be used to provide primary frequency response. Historically, mechanical governors were used to directly convert a change in generator speed to a counteracting change in valve position. Electronic governors are more common today, relying on sensors and control signals to provide primary frequency response [239].

While the inertial response is instantaneous, primary frequency response engages within a few seconds and typically lasts for no more than a minute or so [241]. These two responses are often sufficient to slow and arrest the frequency decline. A ‘secondary frequency response’ is then required to bring the frequency back up to its optimal range. This secondary response is provided by the same AGC mechanism that carries out frequency regulation, engaging in less than a minute and typically running for no more than a few minutes [241]. If the generator outage has not yet been corrected during the secondary response, a ‘tertiary frequency response’ is manually initiated to maintain the necessary power supply and restore the optimal frequency range. The tertiary response is provided

by ‘spinning reserves’, which are power plants that are synchronized to the electricity grid but do not operate at full power output unless called upon during a contingency event [236]. This reserve capacity is left ‘spinning’ so that the power plant can respond to a contingency in less than a minute and ramp up to full power within 10 minutes. Spinning reserves typically operate for less than an hour. If the contingency is not corrected within this time frame, ‘non-spinning reserves’ must be provided by offline power plants that can be brought online in 10 to 30 minutes and operate for several hours [236]. If the contingency lasts for many hours, additional offline power plants may need to be brought online to provide ‘replacement reserves’. Figure 3.9 shows an illustrative example of how the different system mechanisms respond on different time scales to an electricity grid disruption causing a sudden drop in frequency.

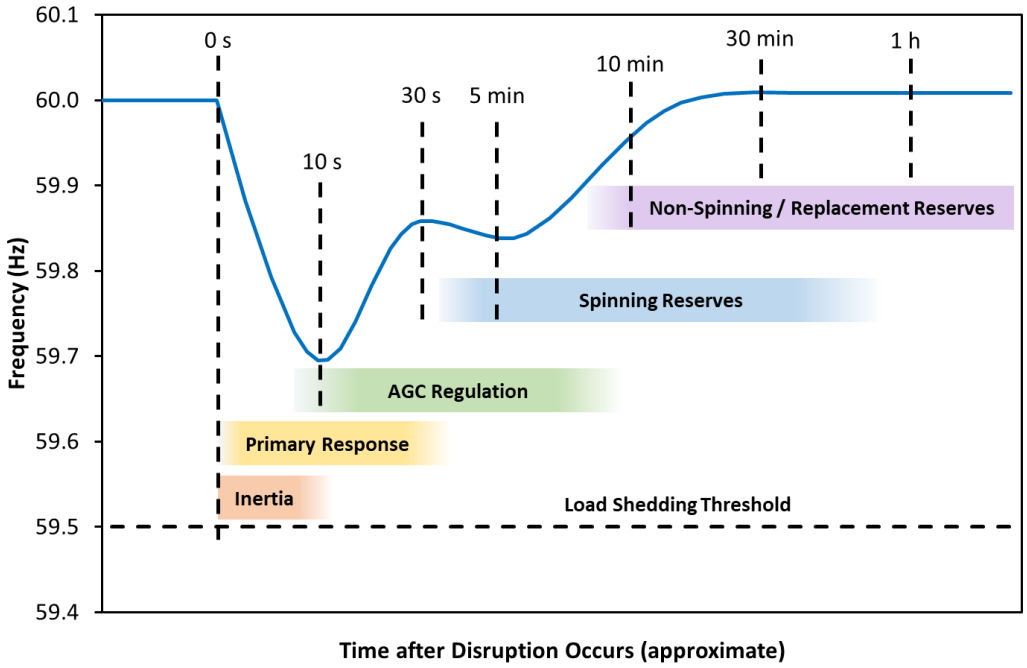


Figure 3.9 Illustrative example of an electricity grid disruption causing a sudden frequency drop and the time scales of the main system response mechanisms used to restore the frequency. Based on figure from [236].

All conventional power plants provide inertial response and primary frequency response, and all are technically capable of providing frequency regulation and the various reserves. However, base load power plants tend to prefer operations with slower ramp rates and longer durations (e.g. non-spinning reserves and replacement reserves) [236]. For

frequency regulation in particular, the rapid ramping up and down of any turbine-generator system exacerbates mechanical wear and tear and lowers system efficiency [233].

Since wind turbines and solar panels are asynchronous, they do not inherently convert stored kinetic energy into additional electricity supply when the grid frequency drops. Wind turbines and solar panels also do not feature governors like those featured in conventional power plants, which means they do not feature a built-in primary frequency response mechanism. This suggests that significant levels of wind and solar power generation will leave electricity grids with a reduced ability to respond to sudden frequency disruptions during the critical first few seconds, leading to a greater number of load shedding events and blackouts. However, 'fast frequency response' technology can overcome this issue. This inverter-based solution uses sensors and control algorithms to rapidly sense a sudden drop in frequency and draw additional power from the wind turbines or solar panels, effectively mimicking the inertial response and primary frequency response of conventional generators [239].

Both wind turbines and solar panels can provide fast frequency response if they are pre-curtailed so that there is operational 'headroom' for a sudden power increase on command. This pre-curtailment also allows wind farms and solar farms to provide frequency regulation, spinning reserves, non-spinning reserves, and replacement reserves, but the latter two services are less suitable since it can be challenging to guarantee several hours of reserves from a variable renewable energy source [236]. Unlike solar panels, wind turbines can also provide fast frequency response from the kinetic energy stored in the spinning rotor. While synchronous generators inherently provide an inertial response, wind turbines rely on sensors and controls to quickly detect a drop in grid frequency and then increase the torque in the system such that the rotor speed rapidly decreases, thereby discharging the stored kinetic energy through the generator and into the grid [243]. This produces a short burst of extra power supply to counteract a sudden supply deficiency on the grid, bridging the gap until other power reserves can engage [239].

In Quebec and Texas, wind turbines have been providing fast frequency response capabilities to the electricity grid for more than a decade [239]. These two jurisdictions

feature the smallest of the four main North American electrical interconnections, which makes them more susceptible to frequency deviations. A combination of smaller grid size and high levels of wind energy production makes fast frequency response capabilities especially important. Researchers are still investigating how the stability of electricity grid frequency will be impacted as more and more synchronous generators get replaced by inverter-based wind and solar farms in the future [239].

Electricity grid frequency can also be managed on the demand side. For example, synchronous loads such as large industrial motors also provide inertia and primary frequency response to the electricity grid [241]. Interruptible loads such as industrial cooling facilities can also provide fast frequency response by disconnecting from the grid for short periods to help avoid large-scale load shedding measures. Such measures have allowed Texas to increase its dependence on wind farms beyond what would otherwise be feasible without jeopardizing grid reliability [239].

3.2.3. Electricity Markets

In North America, generated electricity is delivered to consumers through a mix of regulated and deregulated electricity systems. Regulated systems are 'vertically integrated', with a single utility responsible for electricity generation, transmission, distribution, and sale for a given geographical region [231]. Vertically integrated utilities are either publicly owned (such as Hydro Quebec) or privately owned and publicly regulated (such as Nova Scota Power Inc.). Beginning in the 1990s, some vertically integrated utilities have been restructured to allow for electricity prices to be determined by market-driven competition instead of regulation. In these deregulated systems, electricity generation companies compete to sell electricity into a wholesale market, while electricity delivery companies compete to purchase electricity from the wholesale market and sell electricity to consumers in the retail market [231]. A non-profit independent system operator (ISO) or regional transmission organization (RTO) is responsible for overseeing the deregulated market in a given geographical region.

In Canada, the provinces of Ontario and Alberta have their own ISOs to oversee deregulated electricity markets, while all other provinces and territories are vertically

integrated. The system in Nova Scotia may change in the future, as a government-appointed task force officially recommended in 2024 that a competitive electricity market be established under the oversight of a new provincial ISO [244]. In the United States, most of the western and southeastern regions remain fully regulated with numerous vertically integrated utilities, while much of the midwestern and northeastern regions now use deregulated markets [236]. The states of California, Texas, and New York have their own ISOs, while four multi-state ISOs and RTOs oversee the other deregulated markets. Each individual ISO and RTO establishes its own electricity market rules, but the markets are generally divided into capacity markets, energy markets, and ancillary services markets [245]. The many rules governing each market can be quite complex and are outside the scope of this thesis, but basic overviews of the main market types are provided below to help frame the stationary energy storage applications that will be discussed in Section 3.3.

Capacity Markets

Capacity markets are focused on 'resource adequacy', which simply means that a given electricity system must procure sufficient generation capacity to meet anticipated electricity demand peaks in the years ahead. Figure 3.10 illustrates the basic function of the capacity market in Alberta, which covers a one-year period three years in advance [246]. The ISO estimates the minimum capacity that must be procured for that year, as well as the prices that can be paid to power generators for additional capacity beyond the estimated minimum. This produces the ISO price curve shown in Figure 3.10. Companies then participate in an auction in which they offer to commit power generation capacity for the one-year period at prices reflecting the operating costs of their power plants. The ISO then ranks the supply offers from lowest to highest price to give the cumulative supply curve shown in Figure 3.10. The point at which the two curves intersect gives the appropriate amount of capacity to secure as well as the clearing price for that capacity. All supply offers at or below the clearing price will be paid the clearing price in exchange for making the offered generating capacity available for the one-year period. Supply offers above the clearing price are not awarded. Note that while the ISOs and RTOs in Alberta, Ontario, and the northeastern United States all use capacity markets, the ISOs and RTOs in California, Texas, and the midwestern United States use other mechanisms to ensure resource adequacy [236].

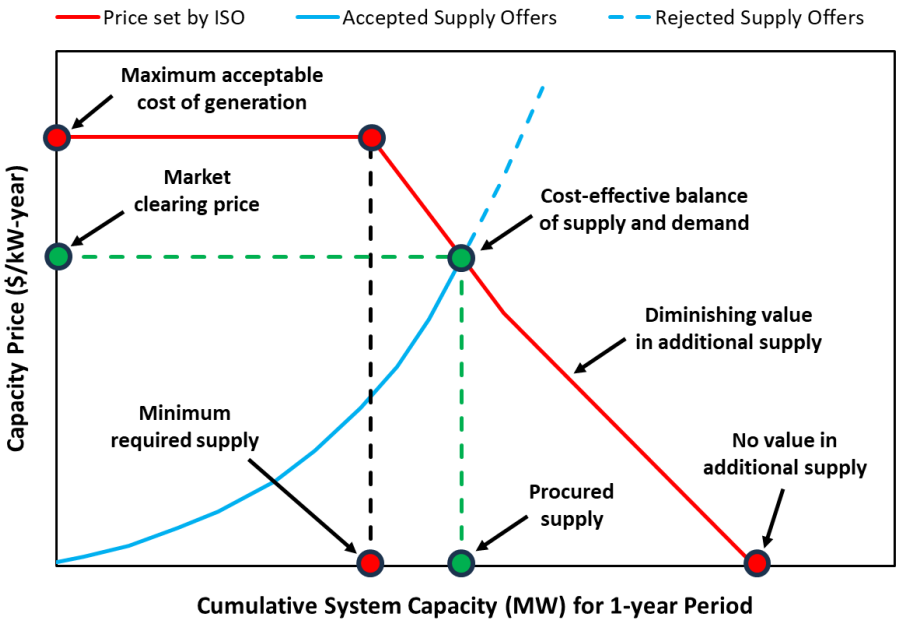


Figure 3.10 Illustrative example of how clearing prices are determined in Alberta's capacity market. Partially based on figure from [246].

Energy Markets

Energy markets ensure that electricity supply actually meets electricity demand throughout each day. To meet demand at the lowest cost, ISOs and RTOs typically operate both a day-ahead market and a real-time market. Whereas capacity markets are typically run annually and cover large blocks of months or years, day-ahead markets are typically run every morning and cover 24 hourly blocks to plan ahead for the following day. Real-time markets are run at even smaller time intervals to dispatch physical electricity to the grid.

Figure 3.11 illustrates the basic function of the California day-ahead energy market for a given 1-hour block. Electricity retailers and end users submit bids detailing the amount of electricity they will commit to purchasing for each 1-hour block as a function of price, and electricity generators submit offers detailing how much electricity they will commit to generating for each 1-hour block as a function of price [247]. The ISO then ranks the demand bids from highest to lowest price and ranks the supply offers from lowest to highest price, producing the supply and demand curves shown in Figure 3.11. Some bids and offers are 'self-scheduling', meaning that they agree to buy or generate a certain amount of power regardless of price (e.g. a large base load power plant that must operate above a minimum load at all times), so the ISO ranks these bids and offers first [247]. Similar to the capacity

market, the day-ahead generation procurement and market clearing price are set where the two curves intersect. All demand bids at or above the clearing price are awarded and pay the clearing price into the wholesale market. All supply offers at or below the clearing price are paid the clearing price and are expected to generate the offered power during the given 1-hour block on the following day. Besides the market clearing price, transmission congestion and losses across the electricity system must also be taken into account in energy pricing [248]. The true energy price (often called the 'locational marginal price') therefore varies by geographical location. The final amounts paid out are influenced by a number of other pricing factors which are outside the scope of this thesis.

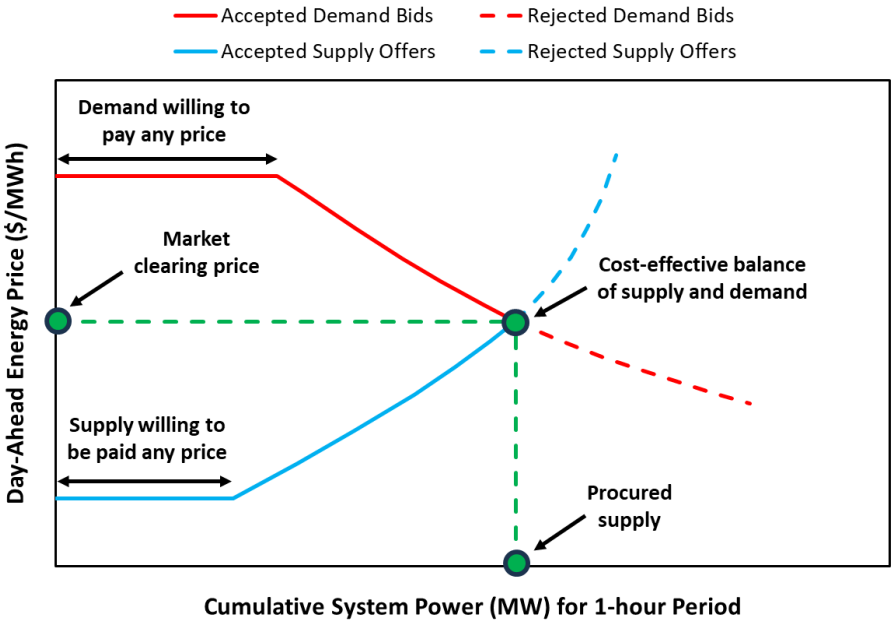


Figure 3.11 Illustrative example of how clearing prices are determined in California's day-ahead energy market. Partially based on figure from [247].

The day-ahead market procures the vast majority of supply needed to meet demand during each hour of the following day, but additional demand bids and supply offers may be submitted into the real-time market for each 1-hour block up until about 1 hour (e.g. 75 minutes in California) before the given 1-hour block commences. Since the actual real-time supply and demand may not completely match the submitted offers and bids, the real-time market also provides the ISO or RTO with the opportunity to assess real-time supply and demand on smaller time scales and adjust the generation procurement as necessary. In California, the real-time market determines these generation adjustments and

corresponding prices at 15-minute intervals within each 1-hour block, and also at 5-minute intervals within each 15-minute block. The 5-minute blocks are where the ISO actually dispatches physical electricity to the grid from the various generators [247].

Figure 3.12 illustrates the basic function of the California real-time energy market for a given 5-minute block [249]. Similar to the day-ahead market, companies submit electricity generation offers into the real-time market for the given 1-hour block, and the ISO ranks these offers from lowest to highest price to produce the supply curve shown in Figure 3.12. This supply curve is fixed for all 15-minute and 5-mintue intervals within the given 1-hour block. But whereas the day-ahead market produces a demand curve based on bids submitted by electricity retailers and end users, the real-time market instead relies on the ISO's load forecasting algorithms to produce a single demand value that must be met by supply for the given 15-minute or 5-minute block [247]. The clearing price is set wherever the supply curve meets the forecasted demand.

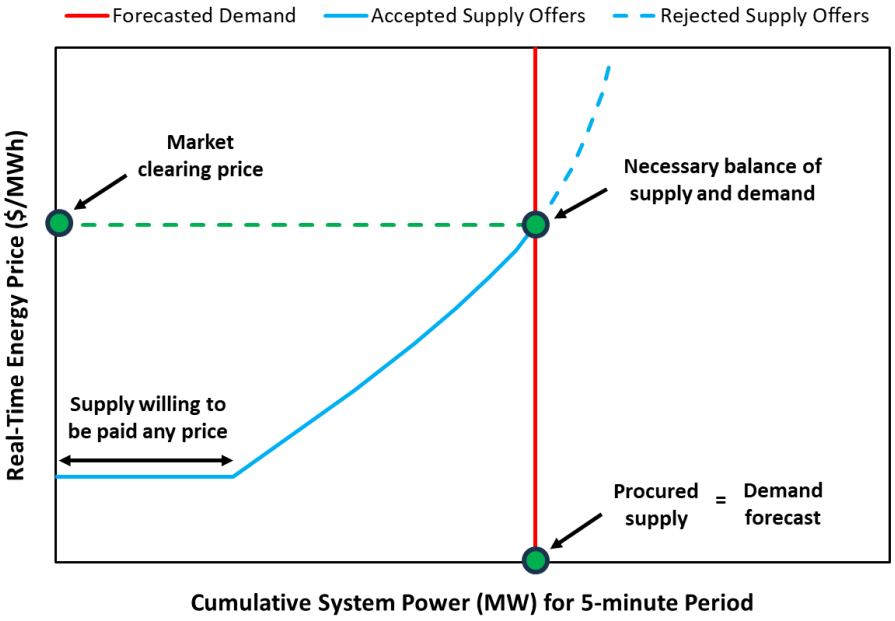


Figure 3.12 Illustrative example of how clearing prices are determined in California's real-time energy market. Partially based on figure from [247].

Importantly, the real-time energy price applies to the *difference* between the real-time dispatch and the day-ahead commitment for each electricity generator. If the generator dispatches more energy than its day-ahead commitment for a given time interval, the

generating company is paid the real-time price on the difference. Conversely, if the generator dispatches less energy than its day-ahead commitment for a given time interval, the generating company must pay the real-time price on the difference. These real-time payments are supplemental to the day-ahead payments. For example, a company might get paid $30/MWh in the day-ahead market for committing 100 MW of generation for a given 1-hour block, but then dispatch 120 MW during the actual hour and get paid $40/MWh on the additional 20 MWh generated. For that particular hour, the company would be paid $3,000 for the day-ahead commitment and $800 for the additional real-time generation for a total of $3,800.

Real-time energy prices tend to be much more volatile than day-ahead energy prices since the real-time market is forced to match forecasted demand regardless of price [250]. Electricity systems with high levels of variable renewable energy generation also tend to have more volatile energy prices, since real-time supply is more likely to fall short of supply commitments (e.g. if the wind speed drops or a cloud blocks the sun) and thereby drive up real-time clearing prices [251]. However, since wind and solar farms have low operating costs, increased renewable energy also tends to reduce the overall level of the energy price by displacing more expensive generators from the market.

Ancillary Services Markets

Ancillary services help maintain grid reliability in real time by maintaining power, frequency, and voltage to counter the continual fluctuations of the supply-demand balance as well as unexpected disruptions on the grid. Specific ancillary services include the mechanisms discussed previously in Section 3.2.2 (load following, frequency regulation, frequency response, and the various reserves), as well as other mechanisms to maintain the optimal voltage range of the grid (typically called ‘voltage support’) and to bring generators back online after a blackout (typically called ‘black start’). Similar to energy markets, frequency regulation and reserves are typically procured through day-ahead and real-time markets, but with different market rules tailored to the specific ancillary service in question. For example, frequency regulation markets allow companies to offer a portion of their supply or demand capacity (typically on an hourly basis) to ramp up and/or down every few seconds as the ISO or RTO requires to maintain the optimal frequency range [248]. Voltage

support and black start ancillary services are typically procured on a fixed 'cost-of-service' rate instead of through designated markets [245], and Texas is the only North American jurisdiction with a designated frequency response market [239]. Though load following is typically categorized as an ancillary service, it is executed through the operations of the real-time energy market [240]. Ancillary service markets are typically co-optimized with day-ahead and real-time energy markets to ensure that all the requirements of the electricity grid are met at the lowest possible overall cost [247].

3.3. Stationary Energy Storage Applications

Energy storage can serve in a variety of stationary applications that benefit electricity grid operators as well as electricity consumers. Lithium-ion batteries are especially well suited for these applications since they can retain stored energy for long periods, deliver full power very quickly, discharge for up to several hours, and last for many years. Steadily declining costs in recent years have led to rapidly growing adoption of lithium-ion battery systems to serve in stationary applications, ranging from small-scale residential systems to large-scale utility applications. As stated in Section 3.1.4, the significant future supply of retired EV batteries can be repurposed to serve a second life in these same stationary applications instead of building new stationary batteries.

This section will review the various stationary applications for which repurposed EV batteries could be considered as a potential energy storage technology solution. These stationary applications are summarized graphically in Figure 3.13, with the four main categories being grid capacity, grid energy management, grid ancillary service, and consumer services. The battery discharge periods associated with each service can range from seconds to minutes to hours, so Figure 3.13 indicates the typical discharge period of each application by colour. Note that while there is considerable overlap among some of these applications, Figure 3.13 separates the applications based on how the direct benefits of energy storage are realized. For example, 'peak shaving' and 'demand charge reduction' are very similar, but peak shaving directly benefits the electricity grid operator while demand charge reduction directly benefits the consumer. Ultimately, all stationary energy storage applications provide the same basic function: to store electricity when demand is relatively low and dispatch it later when demand is relatively high.

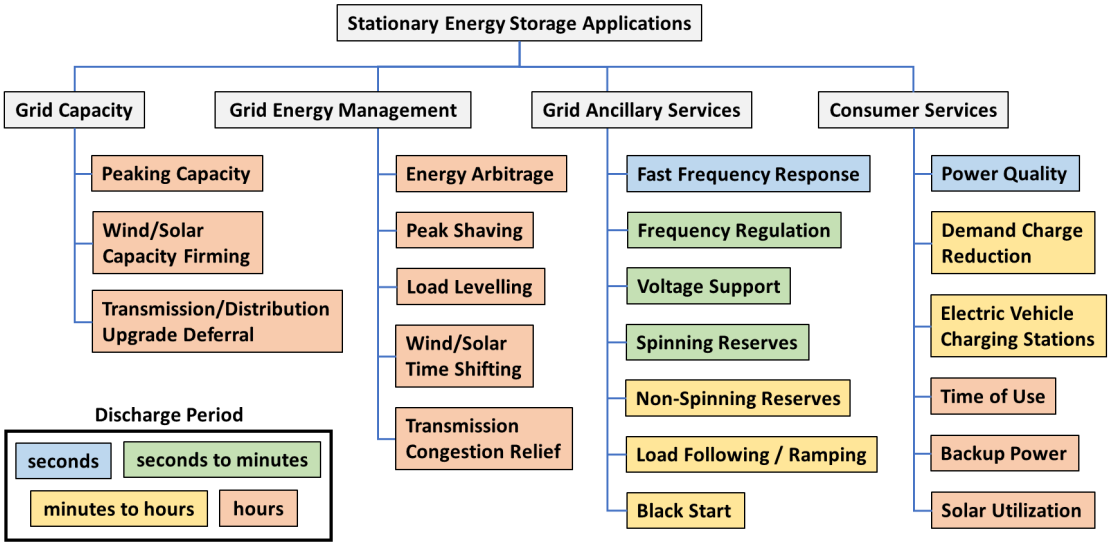


Figure 3.13 Graphical summary of stationary battery energy storage applications.

3.3.1. Grid Capacity

Section 3.2.1 explained how electricity demand profiles reach daily and seasonal peaks due to patterns in human activity and environmental conditions, and how more expensive electricity generation sources (i.e. gas turbines) often need to be used to meet peak load. Section 3.2.3 further explained how electricity grid operators must plan ahead to ensure that the system will be able to meet future peak loads. Each of these considerations is related to grid capacity.

Battery energy storage can help to alleviate some of the costs associated with grid capacity while also facilitating grid decarbonization. For example, if the peak load for a given electricity system is expected to rise in the future, it may mean that a new gas turbine power plant will need to be built in order to provide 'peaking capacity', and if the existing transmission or distribution systems cannot accommodate the increased power flow, it may mean that expensive transmission or distribution upgrades must be carried out. These are significant investments to accommodate a peak load that may only span a few hours of the year. Instead, a utility-scale battery system can be constructed to discharge the required additional electricity supply into the grid during the most significant peak load periods, thereby providing peaking capacity and potentially displacing a natural gas power plant. If the battery is sited downstream of a congested transmission or distribution line, the battery can also defer or negate transmission/distribution upgrades [245]. These considerations are

especially relevant given the growing demand for EV charging as the transportation sector becomes increasingly electrified [252].

Conventional power plants can run at full power output whenever necessary by simply maximizing the rate of fuel consumption or hydroelectric discharge. In contrast, wind farms and solar farms cannot guarantee that maximum power output will be available when the grid operator requires it. This means that variable renewable energy sources cannot provide as much 'firm capacity' as an equivalently sized conventional power plant, and are therefore disadvantaged when grid operators are securing resource adequacy [253]. Battery energy storage can provide 'capacity firming' for wind farms and solar farms by storing excess wind or solar energy when demand is low and discharging that energy into the grid during times of peak load so that the wind farm or solar farm can fulfill their capacity commitments even if the real-time wind or solar generation is low. This makes it easier for low-cost wind and solar resources to displace conventional power plants without compromising resource adequacy.

3.3.2. Grid Energy Management

As explained in Section 3.2.1, more expensive electricity sources are often needed to meet peak demand periods near the middle of each day, while low-cost wind and solar resources are not always available when they are most needed. Stationary energy storage can therefore be used for grid energy management so that supply can meet demand throughout each day at a reduced overall cost. In deregulated electricity markets, stationary batteries can lower the day-ahead and real-time market clearing prices by storing low-cost electricity and offering it into the markets as supply. Vertically integrated utilities can also use stationary batteries to minimize their daily costs of generation and transmission so that lower electricity prices can be offered to their customers.

The term 'energy arbitrage' can be used to describe any process that purchases energy when it is valued relatively low and sells it when it is valued relatively high. In the context of stationary energy storage, 'energy arbitrage' refers specifically to the buying (i.e. charging) and selling (i.e. discharging) of electricity in deregulated energy markets [245]. If a battery can consistently buy electricity from the grid (through demand bids)

when energy prices are relatively low and sell electricity into the grid (through supply offers) when energy prices are relatively high (accounting for energy efficiency losses), the battery owner will earn a net positive profit. But since batteries have a finite energy storage capacity, advanced price forecasting and optimization algorithms are required to successfully perform energy arbitrage [251]. While earning a private profit, energy arbitrage also lowers the energy market clearing prices when the battery supply offers displace more expensive generators, ultimately lowering the retail electricity prices for consumers. As described in Section 3.2.3, energy markets include day-ahead and real-time markets, the latter of which features more volatile prices over the course of each day. Due to this price volatility, real-time markets tend to be more lucrative for energy arbitrage than day-ahead markets [250]. Figure 3.14 shows an experimental example from [214] where a battery cycles aggressively in response to volatile prices in the German real-time energy market.

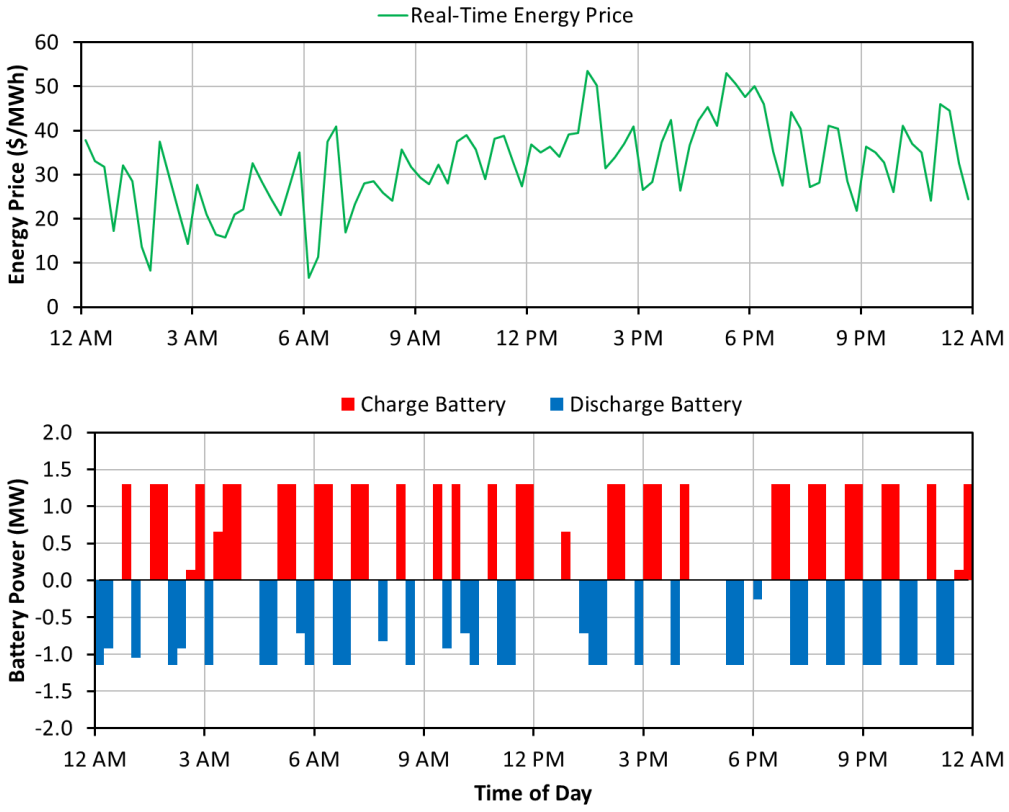


Figure 3.14 Example of battery response to volatile prices in the German real-time energy market. Based on data and figure from [214].

In vertically integrated electricity systems, energy arbitrage takes the form of 'load levelling' and 'peak shaving'. As with energy arbitrage, load levelling and peak shaving involve charging a battery with low-cost electricity and discharging the stored energy at times when electricity generation is relatively expensive. In the absence of an electricity market, load levelling and peak shaving are driven by the utility's responsibility to minimize the overall cost of electricity generation, rather than a company's pursuit of advantageous electricity price fluctuations.

An example of load levelling is illustrated in Figure 3.15, which revisits the two-day winter load profile from Figure 3.7. As explained in Section 3.2.1, base load, intermediate load, and peak load power plants are typically required to track the uneven load profile, with peak load being the most expensive. Figure 3.15 shows how a stationary battery can be used to 'level' the load profile by redistributing the peak load to off-peak periods. This is done by charging the battery with low-cost base load electricity overnight (thereby raising the base load) and discharging this stored energy into the grid during peak periods (thereby lowering the peak load that must be met by power plants). In this illustrative example, the levelled load profile can be met by base load and intermediate load power plants without the peak load power plants that are required for the original load profile (see Figure 3.7).

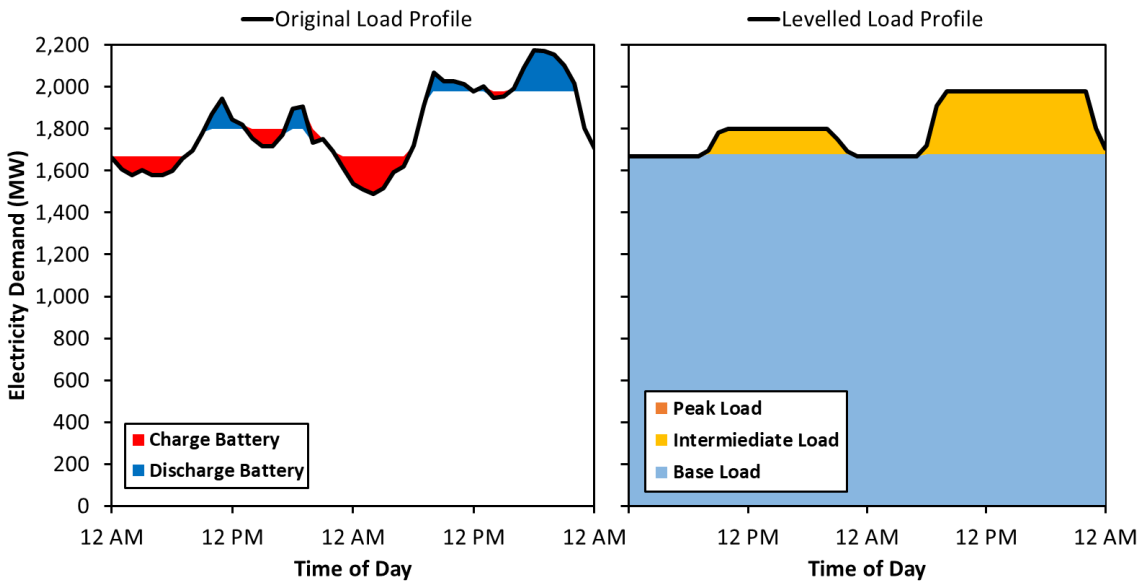


Figure 3.15 Illustrative example of stationary energy storage providing load levelling service over a two-day period. Original load profile based on Nova Scotia hourly net load data from [229].

Load levelling provides several benefits that reduce the overall cost of electricity delivery. For one, raising the base load allows base load power plants to operate at higher power levels during off-peak periods, which improves their capacity factor and allows for increased reliance on low-cost base load generation. The overall smoothing of the load profile also eases the ramping requirements for power plants, which improves their efficiency and reduces mechanical wear and tear [254]. Furthermore, the lowering of the peak load can reduce or eliminate the requirement for expensive peak load generation.

The lowering of the peak load is commonly called 'peak shaving', and it is often considered as a distinct stationary energy storage application due to its significant implications for the displacement of peak load generation. Note that in some jurisdictions with an abundance of low-cost hydroelectricity (e.g. Quebec), expensive gas turbines are already unnecessary for meeting peak load. However, peak shaving still has other economic benefits regardless of the generation resource. For example, since transmission and distribution losses are proportional to the square of current, peak shaving results in higher system efficiency [255]. As described in Section 3.3.1, peak shaving can also defer or negate the construction of new power plants and transmission/distribution upgrades. Unlike load levelling, peak shaving is not necessarily concerned with raising the base load or smoothing the overall load profile.

In deregulated electricity markets, load levelling and peak shaving are not directly procured by ISOs and RTOs in designated markets, but are instead the financially-driven outcomes of energy arbitrage as more battery systems enter into the energy markets. For example, a battery performing energy arbitrage based on day-ahead energy prices would undergo charge and discharge periods similar to those shown in the left chart of Figure 3.15, since day-ahead energy prices tend to be relatively low when demand is relatively low and vice versa. This contrasts with the more dynamic battery cycling profile shown in Figure 3.14 for the case of real-time energy prices.

Energy arbitrage can also take the form of 'time shifting' variable renewable energy sources. As discussed in Section 3.2.1, wind farms and solar farms are now the most inexpensive electricity sources available, but the variable supply does not always align with

the load profile. This presents another opportunity for stationary energy storage to benefit grid energy management in both deregulated electricity markets and vertically integrated electricity systems. Batteries can be used to store low-cost wind or solar generation during periods of excess supply and deliver this energy to the grid during periods of high demand [256]. This time shifting operation avoids curtailment of excess wind and solar generation and increases the amount of renewable energy being utilized on the grid [253], thereby enabling greater displacement of conventional power generation with wind and solar resources (noting the important implications for ancillary services as discussed in Section 3.2.2). For example, performing peak shaving with stored wind or solar energy can directly displace gas turbine power plants with low-cost renewable energy [254], [257]. While it is technically possible for combinations of wind farms, solar farms, and battery systems to cover base loads, this is not yet economically viable due to the significant energy storage capacity required to ensure reliability [258]. Still, partial displacement of conventional base load generation can be achieved through time shifting.

High levels of variable renewable energy in an electricity system can also increase the value in energy arbitrage, load levelling, and peak shaving services compared to a conventional electricity system. For instance, energy prices tend to become more volatile as more variable renewable energy sources enter deregulated markets [251], enhancing the financial opportunities for energy arbitrage. Energy prices can even reach negative values when there is a significant excess of renewable energy supply [254], making battery charging a revenue source during these periods instead of an expense. Load levelling and peak shaving can become especially important in jurisdictions with significant solar power generation (e.g. California). This is illustrated in Figure 3.16, which shows the total electricity load over a 24-hour period compared to the net load after accounting for solar generation. The net load profile (commonly called the ‘duck curve’ due to its shape) clearly exhibits more distinct peaks and ramp rates, which conventional power plants struggle to follow. Batteries can provide critical load levelling and peak shaving service in such cases by charging with excess solar energy during the afternoon and discharging during the evening peak load [257]. This improves the performance of conventional power plants, lowers the peak load, and allows for further solar installations without concern of worsening the duck curve.

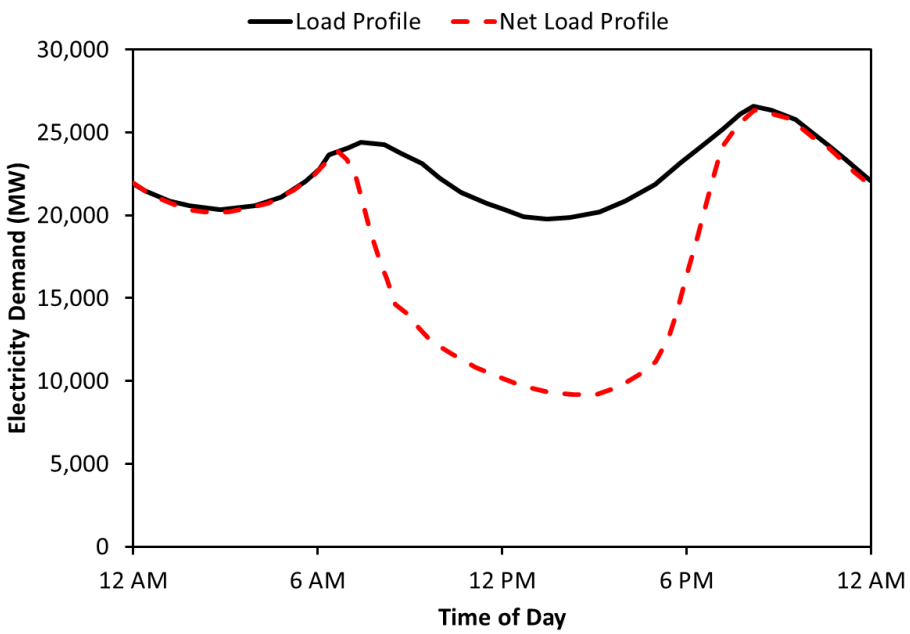


Figure 3.16 Illustrative example of how high solar energy generation impacts the daily net load profile that must be met by other power plants. Based on data and figure from [257].

Another way in which stationary energy storage can benefit grid energy management is through 'transmission congestion relief'. As explained in Section, 3.2.3, deregulated energy markets use the 'locational marginal price' to account for transmission congestion in the energy price. Siting batteries downstream of congested transmission lines can therefore reduce the day-ahead and real-time energy prices in the congested area. The same concept applies to vertically integrated electricity systems, where transmission congestion can limit the power supply from low-cost generators and force the utility to draw on more expensive generators. Battery systems can store the low-cost electricity during off-peak times and then deliver this electricity to end users when upstream transmission lines are congested [245]. There is some overlap between the concepts of transmission congestion relief and transmission upgrade deferral, but the latter is a benefit for grid capacity.

3.3.3. Grid Ancillary Services

Sections 3.2.2 and 3.2.3 described the various ancillary services that electricity grid operators use to ensure the stability and reliability of the grid. Stationary battery systems are capable of providing these ancillary services. Since batteries can ramp quickly and charge or discharge for several hours, batteries can provide load following and ramping

services as well as reserve services by participating in energy markets and reserve markets, or by being dispatched accordingly by vertically integrated utilities [253]. Batteries can also be co-located with wind farms or solar farms to provide ramping compensation to smooth the generated power output when wind speed or cloud cover is in flux [259], or installed at power plants to provide black start services in the event of a blackout [260]. As an inverter-based resource, batteries are also capable of injecting and absorbing reactive power to provide volage support services [261].

Fast frequency response typically requires a power response within 0.5 to 2.0 s of a frequency excursion [262]. Since batteries can ramp up to full power very quickly, fast frequency response capabilities are actually limited by the inverter rather than the battery [263]. Studies have shown that response times of 80 ms can be achieved for batteries connected to the grid through an inverter [263], making stationary battery systems well suited for fast frequency response.

Batteries are particularly well suited for frequency regulation, since this ancillary service requires continuous cycles of ramping up and down for seconds or minutes at a time (as shown previously in Figure 3.8). This type of operation tends to incur costs for power plants, such as reduced efficiency, mechanical wear and tear, as well opportunity costs in the energy market [242]. The opportunity costs arise because power plants must retain operational headroom in order to 'regulate up', which results in lost revenue in the energy market if energy prices are high (e.g. during peak load periods). Conversely, power plants must operate above a minimum load in order to 'regulate down', which can be uneconomical if energy prices are low (e.g. overnight). Batteries designated for frequency regulation service can simply fluctuate about mid-SOC and incur lower costs than conventional power plants.

The rapid response capabilities of batteries also enables more accurate tracking of volatile AGC signals compared to conventional power plants, thereby providing a more tightly regulated grid frequency. Recognizing that certain power sources offer superior frequency regulation performance, the Federal Energy Regulatory Commission (the government agency that regulates the various ISOs and RTOs in the United States outside of Texas)

issued Order 755 in 2011, which sets 'pay for performance' rules so that superior frequency regulation providers get paid at a higher price [264]. This enhances the economic opportunity for stationary battery systems to provide frequency regulation services. PJM Interconnect (the ISO for the mid-Atlantic United States) filters its frequency regulation signal into a 'Regulation A' signal and a 'Regulation D' signal, the latter of which is more volatile and is designated specifically for fast-response technologies like batteries [265].

As explained in 3.2.2, ancillary services become increasingly critical as electricity systems become more reliant on variable renewable energy sources. Stationary batteries can therefore facilitate grid decarbonization not only through capacity firming and time shifting of wind and solar resources, but by providing enhanced ancillary services for grid stability as well.

3.3.4. Consumer Services

Battery energy storage systems serving grid capacity, energy, and ancillary services will generally be co-located with power plants or sited elsewhere along transmission or distribution systems. These grid-scale batteries ultimate benefit electricity consumers by enabling utilities and retailers to offer more affordable and sustainable electricity to their customers. However, batteries can also used for 'behind-the-meter' energy storage to provide direct benefits to consumes. These batteries are installed at commercial, industrial, or residential sites so that the stored electricity can be delivered on-site when needed.

Commercial and industrial facilities may use batteries to provide power quality services to improve the efficiency of electrical loads and thereby reduce costs [266]. Similar to grid-scale voltage support services, consumer-scale power quality services require the battery to inject or absorb reactive power through the inverter on short time scales to reduce voltage and frequency fluctuations behind the meter. More commonly, commercial and industrial facilities use batteries for 'demand charge reduction': since a significant component of commercial and industrial power bills are charged based on the monthly or annual demand peaks of the facility, batteries can be used to provide a behind-the-meter version of 'peak shaving' to reduce the peak demand and the associated charges [245]. Commercial EV charging stations can also use stationary battery energy storage systems

to provide fast charging services without drawing these significant demand spikes (typically 50 to 350 kW per vehicle) directly from the electricity grid [267].

Some electricity providers offer 'time-of-use' electricity rates to their customers to encourage load leveling at the consumer scale. By charging customers lower rates during off-peak periods, customers are incentivized to shift their consumption to off-peak periods [266]. This shift in consumption is facilitated by behind-the-meter battery systems, which can charge from the grid during off-peak periods and deliver electricity to the consumer during on-peak periods. Since a growing number of homes and businesses are using roof-top solar panels for behind-the-meter electricity generation, batteries can also help to maximize utilization or 'self-consumption' of the generated solar energy by providing solar time shifting at the consumer scale so that excess generation does not need to be curtailed or sold back to the utility at a low price [245]. Backup power is also an important behind-the-meter battery application for commercial, industrial, and residential end users, providing hours of energy availability during unexpected power interruptions [245].

Note that behind-the-meter battery systems can technically be used to provide any of the aforementioned grid-scale energy storage services as well, but regulatory barriers inhibit behind-the-meter batteries from participating in certain grid-scale applications and markets [245].

3.3.5. Stacked Services

Stationary battery systems are not always capable of yielding a net economic benefit when serving a single energy storage service, but the economics can be improved by 'value stacking' so that a single battery system can perform multiple energy storage services and thereby access multiple revenue streams [253]. For example, a stationary battery can participate in energy markets and ancillary service markets at the same time. Some existing regulatory barriers limit the potential of value stacking [245], but regulations are trending towards opening up more opportunities for stationary energy storage. In 2018 for example, the Federal Energy Regulatory Commission issued Order 841 to guide ISOs and RTOs towards the removal of barriers for stationary energy storage systems to participate in all capacity, energy, and ancillary service markets [268].

One commercial example of stacked services is the Hornsdale Power Reserve in South Australia, which is a utility-scale lithium-ion battery rated for 100 MW of power and 129 MWh of energy (the largest in the world at the time of its construction in 2017). This stationary battery system was commissioned in response to a state-wide blackout in 2016 that was attributed to reduced electricity grid inertia during a time of high wind energy generation [269]. Of its 100 MW capacity, 30 MW are used to compete in Australia's deregulated energy market (i.e. energy arbitrage) while the other 70 MW are used for various ancillary services including fast frequency response, frequency regulation, and spinning reserves [270]. In 2019, this battery reportedly reduced Australia's total cost of providing these ancillary services by 40 % and successfully responded to several significant contingency events on the grid [271]. This single year of ancillary service cost savings reportedly amounted to $116 million (Australian dollars), exceeding the $90 million capital cost of the battery.

3.4. Prospects and Challenges for Second-life Batteries

Section 3.1.4 concluded that most EV batteries will reach EOVL with high enough SOH levels that they should be repurposed for a second life in stationary energy storage applications before they are recycled. Section 3.3 established that there are many stationary energy storage applications with suitability for lithium-ion batteries. This section will review the prospects for repurposed EV batteries to serve in second-life energy storage applications, as well as the various challenges which researchers, developers, and regulators must address to ensure the success of the second-life battery industry.

3.4.1. Technical Considerations

Technical considerations for second-life batteries can be broadly categorized into considerations regarding the various steps in the repurposing process and considerations regarding the operational performance of second-life battery systems. Since the primary competition for second-life batteries will be purpose-built stationary batteries, it is especially important to consider repurposing processes and operational performance in relation to the manufacturing and operation of stationary batteries. These relative technical considerations directly influence the economic and environmental aspects of second-life batteries, which will be respectively discussed in Sections 3.4.2 and 3.4.3.

Figure 3.17. depicts the main steps in the EV battery repurposing process, which include:

- Removing the battery from the vehicle
- Inspecting the battery for damage
- Transporting the battery to a specialized facility
- Evaluating the SOH of the battery to confirm its viability for second life
- Modifying the battery for its intended second-life application (potentially including partial or complete disassembly of the original battery pack)
- Testing and certifying the repurposed battery
- Integrating the repurposed battery into a stationary energy storage system
- Operating, monitoring, and maintaining the second-life battery system until the battery reaches EOL and must be recycled

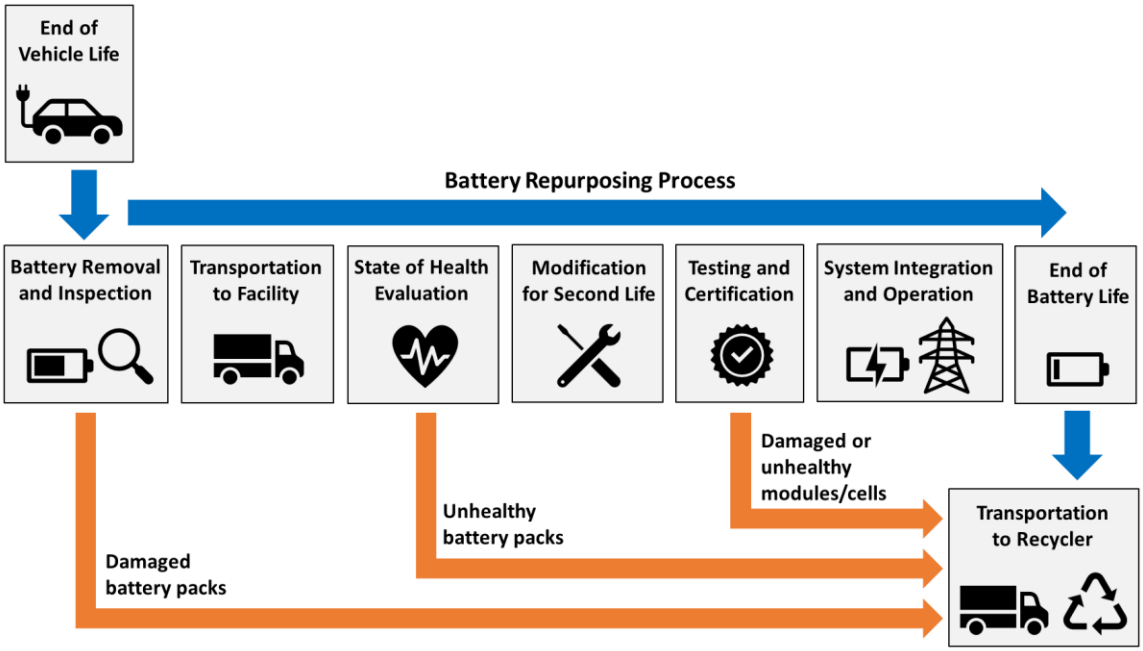


Figure 3.17 Graphical summary of the EV battery repurposing process.

Note that there are different pathways that used EV batteries may follow before being repurposed in second-life applications, as illustrated in Figure 3.18. If an EV battery is being replaced under warranty, it will most likely be removed from the vehicle by dealerships and service centres that are owned or contracted by the original manufacturer [272]. The manufacturer will then determine whether the battery should be repaired or remanufactured for continued EV service, sold to a battery repurposing company, or sent

to a battery recycler. In some cases, the original manufacturer will contract an independent battery remanufacturing facility (such as Cox Automotive in the United Sates [273]) to make this determination. If the battery is suitable for repurposing, the original manufacturer may elect to retain battery ownership for their own second-life battery projects instead of selling the battery to an independent battery repurposing company [228]. If the battery is initially removed from the vehicle after the warranty period (typically 8 to 10 years), then it may be an automotive recycler or repair garage that removes the battery and then sells it to a repurposing company, battery recycler, or a private buyer [272]. These different pathways mean that a battery repurposing company could acquire an EOVL battery that has already been identified and evaluated for SOH (e.g. from the original manufacturer or a remanufacturer), or acquire an EOVL battery with very little accompanying information (e.g. from an automotive recycler, repair shop, or private buyers). The second-life battery supply chain is nascent and still evolving.

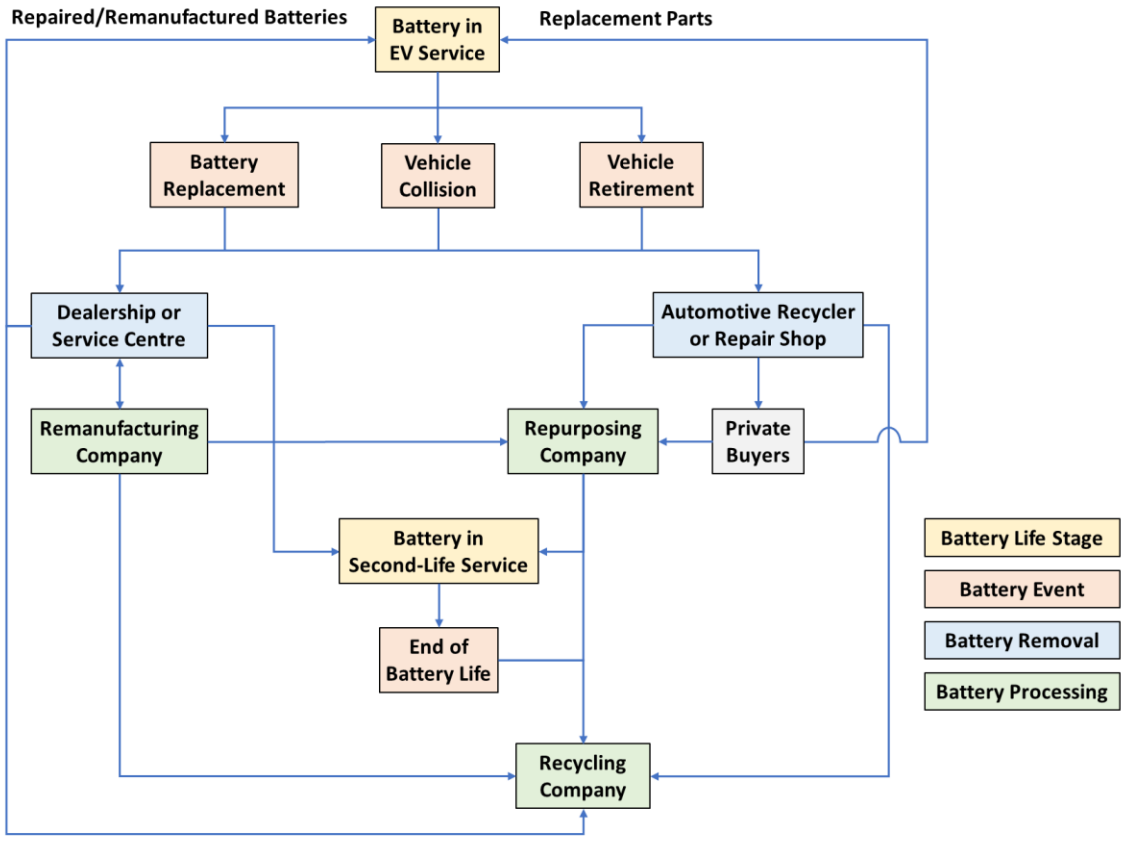


Figure 3.18 Possible repurposing pathways for EV batteries. Partially based on figure from [272].

Removing, Inspecting, and Transporting EV Batteries

Removing an EV battery from the vehicle is not a straightforward task and should be carried out by qualified technicians [16]. Apart from the complexity of the procedure, the high voltage of EV batteries calls for appropriate training and safety equipment during handling. Transportation of the removed battery is also non-trivial, since used lithium-ion batteries are classified as dangerous goods and sometimes also as hazardous waste, and are therefore subject to transportation regulations that require the batteries to be handled by trained personnel and shipped in approved containers on approved vehicles [272]. It is also considered best practice that the batteries be discharged below 30 % SOC before being shipped. This figure comes from United Nations classification UN3480 for air shipment of lithium-ion batteries [274], though air shipment of used lithium-ion batteries is not permitted at all [226], [275]. If an immediate visual inspection reveals damage to the battery after removal from the vehicle, then it should be transported directly to a recycling facility [276]. Otherwise, the battery can proceed along the repurposing pipeline.

Identifying and Screening EV Batteries

Somewhere along the supply chain, used EV batteries must be identified and screened before they are repurposed. To ensure that a given EV battery can be repurposed safely and effectively, battery repurposing facilities must have as much identifying information about the battery as possible, such as make and model, manufacturing year, rated voltage and energy capacity, cell chemistry, module design, TMS design, and pack disassembly steps. If the battery has been acquired directly from the original manufacturer, this information should be readily accessible. However, detailed identification may be challenging if the battery has been acquired from an automotive recycler or intermediate handler. Ensuring that necessary identifying information is available throughout the battery life cycle would facilitate both repurposing and recycling [277]. The relatively new concept of a ‘battery passport’ will be discussed further in Section 3.4.4.

Screening is the process of evaluating the SOH of the battery to determine its remaining value as an energy storage device. If the SOH is very high (e.g. > 95 %), then it may be most valuable in continued EV service. If the SOH is low (e.g. < 60 %) then it may be best to recycle the battery right away. Intermediate SOH levels are suitable for repurposing, and

the specific SOH level of a given battery may help determine which stationary energy storage applications the battery is best suited for. Appropriate battery test equipment and expertise is of course required to determine the SOH of a given EV battery.

As explained in Section 2.5, SOH does not have a universal definition due to the complexities of lithium-ion battery degradation, which means there is no universal method for screening second-life batteries. The complexities of degradation also make it challenging to assess the long-term value of second-life batteries based on SOH alone. One consideration is that different lithium-ion cell designs can exhibit very different degradation characteristics (see Section 2.5), so two different EV batteries could degrade at very different rates in second-life service despite yielding the same SOH at EOVL. Even if two EV batteries are of identical design and SOH at EOVL, they might still degrade at different rates in second-life service if their usage histories are significantly different (e.g. city driving vs highway driving). To address these challenges, 'remaining useful life' (RUL) is often used as an additional battery metric alongside SOH. However, RUL assessment typically requires historical data for the battery in question, which may not be available to companies who acquire used EV batteries [19].

Modifying EV Batteries for Second-life Service

Once a used EV battery has been deemed suitable for second-life service, it can be repurposed at either the pack level or the module level, as shown in Figure 3.19. Module level repurposing entails completely disassembling the original battery pack, removing the modules from the pack, and repackaging the modules into a new enclosure designed for the intended second-life application. Pack-level repurposing foregoes most or all of these steps so that the EV battery pack can be repurposed in its original battery housing. Cell-level repurposing is generally considered impractical due to the additional effort required to disassemble each module and repackage the cells [19].



Figure 3.19 Examples of pack-level (left) and module-level (right) repurposing of Nissan Leaf EV batteries in second-life energy storage applications.

There are advantages and disadvantages associated with both module-level and pack-level repurposing. Module-level repurposing provides more opportunity to customize the system for second-life service, as well as the opportunity to screen and sort individual modules to improve SOH homogeneity in the second-life system. However, the additional disassembly and repackaging steps associated with module-level repurposing can amount to significant time and labour costs, as the complexity and diversity of EV battery designs makes it difficult to automate these processes [19]. The time and labour requirements for complete pack disassembly depend on how difficult it is to remove the pack housing cover (typically bolted and sealed), disconnect the electrical circuitry and sensors (potentially hundreds of connections, with some at high voltage), disconnect and flush the TMS (where applicable), and remove the modules (typically fastened in place within the pack), all of which can vary substantially for different pack designs. Repackaging also comes with equipment costs, including a new BMS [278]. Repurposing the entire pack without modification would be the most economical approach, but there must be a reasonable level of SOH homogeneity among the cells since the useful energy capacity of the pack will be limited by the weakest cell group [279]. Partial pack disassembly can allow for weak cell groups to be removed

from the pack, but this may render the original BMS inoperable unless it can be reprogrammed.

The BMS is itself an important technical consideration for second-life batteries. Even if the pack is not physically modified in any way, the original BMS is configured for EV service and may not be optimized for second-life service. For example, different cell balancing settings may be appropriate for repurposed EV batteries at lower SOH levels [19]. It will not always be possible to reprogram or even access the original BMS installed by the manufacturer, as some manufacturers employ proprietary BMS communication protocols [280]. Retrofitting an aftermarket BMS may be necessary in such cases, which would offset some of the advantages of pack-level repurposing. As an alternative, it has been proposed that original manufacturers could sell a BMS gateway tool to second-life battery developers, which would enable sufficient access to the original BMS while preserving necessary security levels for the manufacturer [281].

Testing and Certifying Second-life Batteries

A variety of established safety standards are used to certify lithium-ion batteries both in EV and stationary applications [282], but very few standards give specific consideration to second-life batteries. Until very recently, the only notable safety standard for second-life batteries has been UL 1974, which was published in 2018 by Underwriters Laboratories [283]. The standard, titled *Standard for Evaluation for Repurposing Batteries*, outlines a procedure for testing, grading, and sorting used EV batteries during repurposing, thereby offering certification for the second-life battery manufacturing process rather than the actual batteries. The cells are required to have been previously certified by the original manufacturer, otherwise the repurposing company must apply existing battery safety standards to ensure the cells are compliant. UL 1974 also recommends that repurposing companies adopt existing lithium-ion battery safety test methods (e.g. overcharge, thermal abuse, short circuit) and consider adjusting second-life battery operating limits based on how the test results compare to new batteries, but this is not officially standardized.

For the repurposing process, UL 1974 recommends a series of test protocols for evaluating the open-circuit voltage, high-voltage isolation, discharge capacity, internal resistance,

BMS functionality, cycling performance, and self-discharge rate of acquired EV batteries so that underperforming batteries can be rejected. However, it is left up to the repurposing company to select appropriate pass/fail criteria for these tests, and the complexities of battery SOH are not directly considered. The main requirement of UL 1974 is that the repurposing company develop a grading system with which to rank battery test results, and that second-life energy storage systems be assembled using same-grade batteries to promote system homogeneity. Notably, UL 1974 does not allow for different EV battery designs to be assembled into the same second-life energy storage system.

In 2023, Canadian startup Moment Energy became the first North American company to achieve UL 1974 certification [284]. The only earlier UL 1974 certification was in 2019 by Japanese company 4R Energy, which is joint-owned by Nissan [285]. Representatives from Moment Energy have indicated that they have achieved UL 1974 certification for both pack-level and module-level repurposing. Note that commercial second-life battery systems must also achieve other certifications not specific to second-life batteries, such as UL 1973, titled *Standard for Batteries for Use in Stationary and Motive Auxiliary Power Applications*, and UL 9540, titled *Standard for Energy Storage Systems and Equipment* [18].

More recently, the International Electrotechnical Commission has also published standards focused on second-life batteries. These include IEC 63330, titled *Repurposing of Secondary Batteries*, and IEC 63338, titled *General Guidance on Reuse and Repurposing of Secondary Cells and Batteries*, both of which were published in 2024. These brand new standards have not yet been purchased for detailed review in this thesis, but other researchers have reported on some of the contents [282]. One noteworthy takeaway is that both IEC 63330 and IEC 63338 require repurposing companies to work directly with original manufacturers. This seems geared towards reducing uncertainty and risk in the second-life battery supply chain.

Despite recent progress in developing standard test procedures for second-life batteries, researchers have highlighted the need for further advancement in this area [286]. For example, standard battery test procedures often require many hours to complete, which is

economically inhibitive for mass production of second-life batteries [19]. Rapid test procedures for second-life batteries are being researched extensively, but have not yet been adopted into certification standards. Rapid estimation methods for SOH and RUL are especially common in the literature, since repurposing would benefit significantly from fast and accurate quantification of these two metrics. The most basic SOH evaluations involve capacity tests and/or pulse tests, which are currently included in UL 1974. Some of the more advanced methods include the equivalent circuit modelling, EIS, DV, and IC methods described previously in Sections 2.3 and 2.5, while data-driven methods such as machine learning can be used to reduce test time when the usage history of the battery is available [15]. For RUL estimation, data-driven methods are most common [287]. A detailed explanation of different SOH and RUL estimation methods is outside the scope of this thesis, but their advancement and standardization are of great importance for the second-life battery industry. One startup company claims they can perform a battery health assessment in less than 10 minutes [288].

Integrating Second-life Energy Storage Systems

The integration of second-life batteries into a complete energy storage system has its own unique technical considerations, primarily regarding power conversion and thermal management. For power conversion, relatively small-scale second-life battery systems (e.g. 50 kWh of repackaged modules in a behind-the-meter application) can be treated similarly to new stationary batteries, often requiring a single DC/AC power converter for the whole system. For larger systems (e.g. many units of repurposed packs), second-life batteries may require special power conversion considerations. This is especially true when different battery units (e.g. unique pack designs) within the second-life energy storage system feature different voltage ratings, capacities, SOH levels, power limits, etc., since the power conversion system must be flexible to this heterogeneity [289]. In such cases, it is necessary to install a power converter on each unique battery unit so that all battery units can connect to a common bus [290]. A number of different power converter architectures can be used to accomplish this, such as the two examples illustrated in Figure 3.20. A detailed review of power conversion technology is outside the scope of this thesis, but these two simplified examples illustrate the kinds of considerations that second-life battery developers must address when integrating the energy storage system.

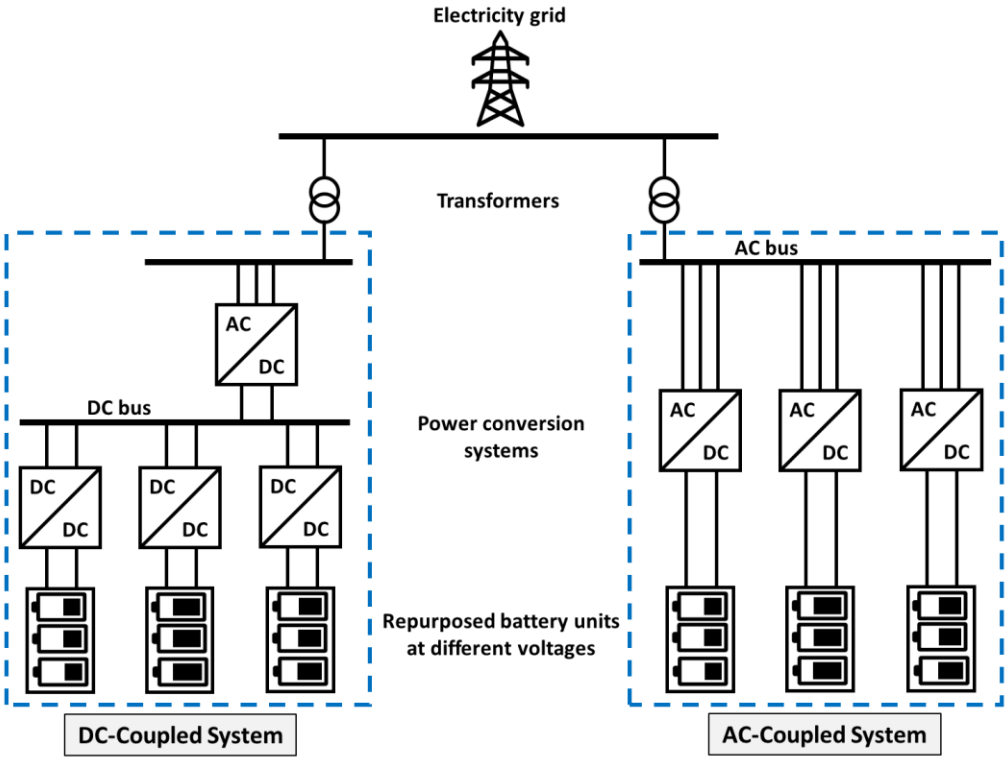


Figure 3.20 Simplified examples of two different power conversion architectures for second-life battery systems. Partially based on figures from [291].

The example of a DC-coupled system in Figure 3.20 includes a DC/DC converter for each unique battery unit, which connects the different units to a common DC bus. The common DC voltage is then converted to AC through a centralized DC/AC converter, which finally connects to the electricity grid through a transformer. In contrast, the example of an AC-coupled system includes a DC/AC converter for each unique battery unit, connecting all units to a common AC bus that connects to the transformer. Other variants of these architectures exist as well, each with advantages and disadvantages in terms of cost, modularity, flexibility, complexity, physical space, and efficiency [291]. For example, DC/DC converters tend to have wider voltage ranges than DC/AC converters (beneficial for accommodating different battery units), but DC-coupled systems require more hardware which adds cost and space requirements [292]. Note that a new stationary battery system could also employ both architectures shown in Figure 3.20, but each individual converter would be of identical voltage and power rating, which would not necessarily be the case for a second-life battery system.

Thermal management is also an important consideration for system integration, both for module-level and pack-level repurposing. For example, if an EV battery pack is designed with an active-liquid TMS, the second-life battery developer must decide if they will construct a liquid circulation system to utilize the liquid-cooling capabilities of the pack or modules in second-life service at the expense of increased system complexity and cost. One potential issue is the possibility of liquid leaks from retrofitted liquid circulation systems, which introduces a risk of electrical short circuits. Active-air TMS retrofits would be another alternative to operating second-life batteries with passive cooling. Since second-life batteries are already somewhat degraded and may have unknown usage histories, there is also a heightened safety risk compared to new batteries. Second-life battery project developers may therefore opt to integrate additional safety measures into the energy storage system for risk mitigation, such as fire suppression systems [18].

Operating Second-life Energy Storage Systems

As with any stationary battery system, second-life energy storage systems require appropriate hardware and software to enable remote monitoring, data logging, and control of the system [290]. An energy management system is used to automatically control the power flow in a way that optimizes battery operation for the given stationary energy storage application, sometimes using artificial intelligence methods [17]. For second-life batteries, the wide variety of EV battery designs presents a challenge for operational control of second-life battery systems, as the optimal control strategy for one EV battery design may not be transferrable to systems using other EV battery designs [278].

New stationary battery systems are often composed of LFP batteries due to their long cycle life [293], but second-life battery control systems may have to account for pronounced degradation in the system as a whole as well as SOH differences among individual modules and cells. For example, batteries at lower SOH may need to be constrained within narrower SOC windows in order to prolong cycle life [294], or be constrained within narrower power envelopes to account for increased internal resistance compared to new batteries [17]. Such limitations will influence the economic viability of second-life batteries in more demanding stationary energy storage applications, at least in comparison to new stationary batteries. One way to overcome these limitations is to oversize the second-life battery system

(i.e. add more repurposed batteries) so that individual batteries can undergo relatively light cycling over an extended life without limiting the energy and power capabilities of the system as a whole [280]. Depending on how frequently and aggressively second-life batteries are cycled before and after repurposing, they can generally be expected to last up to 10 years or longer in second-life service [6], [7].

3.4.2. Economic Considerations

Numerous studies and reviews have explored the economic performance of second-life batteries in different stationary energy storage applications [214], [218], [295-299], and their findings indicate that second-life batteries have the potential to generate economic benefits in any of the stationary energy storage applications described in Section 3.3. The economic viability of second-life battery systems is therefore mainly dependent on their competitiveness with newly manufactured stationary batteries and battery recycling streams [280].

Cost of Second-life Batteries

As described in Section 3.4.1, the EV battery repurposing process includes a series of steps that incur financial costs: regulated handling and transportation; equipment and skilled labour for screening, modification, and certification tests; and in some cases, specialized equipment for integrating the second-life energy storage system. For second-life batteries to compete economically with newly manufactured stationary batteries, the sum of these repurposing costs must be offset by the market price advantage of used EV batteries compared to a new stationary batteries.

Opinions vary considerably in the literature regarding what price ranges should be expected and/or targeted for EOVL batteries [300], and estimates do not remain relevant for long given the rate at which industry practices and market forces are evolving. But given that the price of new lithium-ion batteries continues to decrease thanks to innovations and economies of scale as the battery industry grows [301], minimizing costs is essential for the success of the second-life battery industry. The literature suggests that most of the costs of a second-life battery come from the purchase price of the used EV battery, the skilled labour required for the repurposing process, and the additional components required to

modify the battery for second-life service [228], [301]. As stated in Section 3.4.1, pack-level repurposing can significantly reduce the labour and modification costs, assuming the pack is sufficiently healthy and the original BMS is accessible. Regarding the battery price, collaborative business models between repurposing companies and EV manufacturers could be more economical than simply having the manufacturer sell the battery to the repurposing company at the market price [228]. It has also been suggested that some handlers of used EV batteries may offer them to repurposing companies for free in exchange for taking on the responsibility of battery disposal at EOL [228].

Confidence in Second-life Batteries

Depending on the second-life business model, achieving price equivalence with new stationary batteries may not be sufficient. For example, if a battery repurposing company intends to sell second-life battery products to customers, those customers will typically require a product warranty to guarantee battery performance over a set period of time. The repurposing company must in turn acquire insurance on the warranty to cover product replacement costs in case the second-life battery system underperforms. These steps are relatively straightforward for companies selling new stationary battery systems, since the company will be confident that the vast majority of their products will outlast the warranty period. Warranty and insurance can be more challenging for repurposed batteries, since there is more uncertainty regarding the rate at which battery performance will degrade in a given second-life application after having already degraded considerably during EV service [19]. Warranty aside, some customers may feel deterred from purchasing a used battery system due to concerns around predictability and safety, and therefore opt for new stationary batteries even if price is comparable [19]. These points suggest that second-life battery companies should take steps to instill confidence in their products (such as UL 1974 certification) and strive to offer those products at lower prices than new stationary batteries.

In a different business model, the repurposing company could own and operate one or more second-life battery systems on the electricity grid and sell electricity and/or ancillary services to an ISO, RTO, or vertically integrated utility. This would alleviate the burdens of product warranty and customer management, but it introduces new considerations around complying with utility regulations and attracting investments to finance the

construction of a utility-scale energy storage system. Electricity system operators and financial investors will also need assurances that proposed second-life battery systems are safe and reliable [19].

Abundance of Second-life Batteries

As explained in Section 3.4.1, the potential performance limitations of second-life batteries compared to new stationary batteries also have economic implications, possibly requiring systems to be oversized so that individual batteries undergo relatively light cycling. Oversizing second-life battery systems would help ensure that their performance remains competitive with new stationary batteries, but this approach would rely on costs being significantly lower for repurposed batteries compared to new batteries. Widespread oversizing would also require a sufficient supply of EOVL batteries.

In the long term, it appears that the oversizing of second-life batteries will not be constrained by the supply chain. Due to the rapid growth of EV battery production, the yearly energy storage capacity of the global EOVL battery feedstock is eventually expected to far exceed the yearly global demand for stationary energy storage, likely reaching a crossover point sometime between the years 2030 and 2035 [5], [228], [280]. This means there will be an ample supply of used EV batteries that can be repurposed into oversized second-life battery systems. Furthermore, the excess supply of used EV batteries could lead to lower market prices for acquiring these batteries, which would make oversizing more economically viable.

The excess EOVL battery supply could also reduce the necessity of oversizing second-life battery systems. With this excess supply, second-life batteries could theoretically saturate the stationary energy storage market using only the batteries that reach EOVL at relatively high SOH levels (recall Figure 3.5), leaving the remainder to be sent directly to recyclers to help offset the demand for raw battery materials. These relatively healthy second-life battery systems could operate with relatively wide SOC ranges and power envelopes over a long second life, which would enhance their long-term economic potential. Relatively healthy EOVL batteries are also more likely to qualify for pack-level repurposing, which reduces the repurposing cost and further improves economic viability.

Possibility of Material Scarcity

Future growth in EV battery production will significantly increase demand for the required raw materials, and there is some concern that the material supply chain will struggle to keep pace with this growth [302]. If material supply shortages do arise, then scarcity will drive up the prices of battery materials. Higher material prices would in turn increase the cost of new stationary batteries, which would represent an economic advantage for companies seeking to sell repurposed EV batteries into the stationary energy storage market [19]. On the other hand, higher material prices would also increase the economic value of battery recycling, which would represent an economic disadvantage for companies seeking to buy used EV batteries to repurpose [303]. This latter point highlights the potential for competition between battery repurposing companies and battery recyclers, since a repurposed battery could be withheld from recycling for a decade or more [6].

While the general concept of circularity dictates that EV batteries should be repurposed before they are recycled so as to extract maximum economic value from the manufactured product, some researchers speculate that the rising demand for new EV batteries may create market forces that push used EV batteries towards immediate recycling to offset the demand for raw materials [303]. However, the rising demand for stationary energy storage means that second-life batteries can also help offset demand for raw materials [19]. This interesting dynamic is further complicated by the ongoing development of other battery technologies such as flow batteries, which can be manufactured from low-cost materials and could therefore become advantaged in the stationary energy storage market if lithium-ion battery material prices rise in the future [301].

Economic Outlook

The inevitability of an excess EOVL battery supply suggests that a significant share of global stationary energy storage demand could be met by oversized systems of fairly healthy EV battery packs repurposed for second-life service, potentially as soon as the early 2030s. In stark contrast, it is also possible that rising EV battery material demands will eventually force the EOVL battery supply to bypass repurposing in favour of immediate recycling, while flow batteries or other inexpensive battery technologies gradually displace lithium-ion technology from the stationary energy storage market. A range of possible

futures exist between these two extremes, so it remains critical to advance research and development in battery repurposing while the economics of EOVL batteries evolve. Government polies and regulations will also factor into the outcome, as demonstrated by new regulations in the European Union that recognize the importance of battery repurposing [12]. Regulatory and policy considerations will be reviewed in Section 3.4.4.

3.4.3. Environmental and Social Considerations

If second-life batteries can reduce the cost of stationary energy storage systems, then there is an obvious environmental benefit in expediting the decarbonization of the electricity sector. However, there are other important environmental and social benefits associated with second-life batteries that go beyond their relative market price vs new stationary batteries. While the production of lithium-ion battery packs for both EV and stationary applications is essential for decarbonization, it is not free of negative environmental and social impacts. The required mining, refining, and manufacturing processes generate significant greenhouse gas emissions [304], and the mining of key raw materials like lithium, nickel, cobalt, and copper can also inflict other environmental harms, such as water resource depletion and contamination [305]. Many of these mining operations also come at the expense of vulnerable communities in developing nations. For example, most of the world's cobalt supply comes from mining operations in the Democratic Republic of Congo, which are notorious for their exploitative artisanal mines and use of child labour [306]. Furthermore, most of the world's battery-grade lithium supply is mined in the Atacama Desert region of Chile and Argentina, where international mining companies are known to take advantage of local Indigenous communities while endangering precious water resources on their ancestral lands [307]. The rapid growth of lithium-ion battery production in the coming years has the potential to aggravate such environmental and social impacts.

While international efforts towards more responsible mineral sourcing practices will be essential for minimizing the environmental and social harms of battery production [308], it is also important to take appropriate measures to mitigate the projected rise in demand for raw battery materials so that mining operations do not need to ramp up any more than what is necessary to sustain the clean energy transition. Such measures include investing in public transportation systems so that fewer EV batteries are required to maintain citizen

mobility in a decarbonized world [309], reusing and repurposing EV batteries to respectively offset the impacts of producing new EV batteries and new stationary batteries [50], [310], and recycling spent batteries to offset demand for raw materials by minimizing waste disposal [221]. Battery repurposing on its own is far from a complete solution, but it is an important component of a multi-faceted solution.

Life cycle analysis studies have also shown that repurposing an EV battery provides the battery with an extended opportunity to offset its own production emissions by reducing electricity grid emissions during second-life service (e.g. peak shaving or renewable energy time shifting) [227], [311]. This is essentially a 'return' on the emissions required to initially construct the battery, which is not realized if the battery is recycled immediately after EOVL. This return is made more important by the fact that pyrometallurgical and hydrometallurgical battery recycling processes are energy intensive [221], which raises the gross emissions of the battery life cycle even further. And since battery repurposing delays the recycling process for a decade or more, repurposing also allows time for recycling processes to achieve greater energy efficiency and material recovery rates [6], [276].

Repurposing an EV battery therefore offers four distinct environmental/social benefits:

1. Using second-life service to offset the existing emissions released when the battery was originally produced
2. Avoiding the production impacts of a new stationary battery
3. Enabling variable renewable energy sources to be paired with more affordable energy storage to help decarbonize electricity grid capacity
4. Potentially reducing the emissions and waste disposal associated with the inevitable recycling of the battery if recycling processes improve during second life

These benefits provide justification for governments to encourage and facilitate the growth of the second-life battery industry. This will be explored further in Section 3.4.4.

3.4.4. Regulatory and Policy Considerations

In addition to the safety standards mentioned in Section, 3.4.1, there are many ways in which governments can help to overcome some of the challenges faced by the second-life battery industry. Regulations and policies focused on second-life batteries are generally lacking due to the nascency of the industry, but there has been progress in recent years. In

2023, the European Union brought into effect a new regulation (commonly referred to as the EU Battery Regulation) concerning batteries and waste batteries [12]. This is one of the leading regulations for battery waste management, featuring recycling targets, prohibitions against landfill disposal, and a significant focus on facilitating battery repurposing as a preferred option over immediate recycling after EOVL.

Extended Producer Responsibility

One significant issue is the question of who is responsible for an EV battery after EOVL. The original manufacturer is responsible for the battery while it is under warranty, but EOVL will generally occur after the warranty period [312]. Given that many millions of EV batteries will reach EOVL in the coming years, it is important for regulators to clearly establish who will be responsible for handling these batteries after EOVL. One solution is 'extended producer responsibility' (EPR) for EV batteries, which makes the original manufacturer responsible for the costs of handling the battery regardless of when EOVL occurs [313]. This could have advantages and disadvantages for the second-life battery industry. On the one hand, EPR would ensure that all EV batteries enter a consistent and reliable pipeline after EOVL, facilitating battery acquisition and identification for battery repurposing companies. On the other hand, if the original manufacturers will be held liable for their batteries even after the batteries are acquired by repurposing companies, then the original manufacturers might prefer to handle repurposing internally or simply direct EOVL batteries to recycling instead of second-life service [19].

The new EU Battery Regulation specifies that EPR will generally apply to original manufacturers. However, when batteries are repurposed and commercialized as second-life battery systems, EPR will apply to the repurposing company [12]. The EU Battery Regulation also allows for original manufacturers and repurposing companies to partner in a cost-sharing mechanism for handling batteries at EOL. China also introduced an EPR plan for EV batteries in 2016 [218], but EV battery EPR has not yet been widely adopted in North America, where waste management is largely under the jurisdiction of individual states, provinces, and territories. However, a national EPR framework for EV batteries is currently being developed in the United States [314], and Canadian policy researchers have recommended a similar approach [312].

Battery Passport

Another significant challenge is in the identification and screening of used EV batteries. Section 3.4.1 explained that safe and effective battery repurposing requires access to as much information as possible regarding the design specifications, performance characteristics, health, and usage history of batteries acquired after EOVL. To ensure that this information is accessible throughout the battery life cycle, the concept of a 'battery passport' was proposed in a 2019 report by the Global Battery Alliance [304], which is a public-private collaboration platform established in 2017 to help foster a sustainable global battery value chain. The idea is to maintain a digital, cloud-based record of all pertinent information related to a given battery throughout its life, accessible by a scannable code attached to the battery. The Global Battery Alliance has since conducted two battery passport pilot programs in 2023 and 2024 to demonstrate feasibility and gain industry feedback for future developments [304]. Following the lead of the Global Battery Alliance, the 2023 EU Battery Regulation requires that all manufactured EV batteries feature a battery passport beginning on February 18, 2027, and that repurposing companies and other battery users must be granted access to the SOH and RUL data stored in the original BMS [12]. Similar regulations have not yet been developed in North America, but policy researchers have recommended that the EU Battery Regulation be used as a model [312].

Repurposing Mandates

There do not appear to be any existing government policies or regulations that address the market competition that second-life batteries face from new stationary batteries and battery recyclers. The EU Battery Regulation states that batteries found suitable for repurposing should be repurposed, but this is not specifically mandated. Some researchers have recommended policies that mandate a certain share of the stationary battery market for repurposed batteries, as well as policies that mandate a maximum SOH threshold for recycling undamaged EOVL batteries [303]. Other researchers have advised against mandating repurposing over recycling, instead recommending that market forces be permitted to play out [272]. Others have recommended that guidelines be established instead of mandates [312].

Incentives and Collaborations

Beyond direct regulation, there are other economic and technical opportunities for governments to support the nascent second-life battery industry. For example, as an alternative to repurposing mandates, some researchers have recommended that governments use grants and subsidies to incentivize market conditions for second-life batteries based on their importance for battery circularity [17], [312]. It is also commonly pointed out in the literature that many EV battery packs are not designed for ease of disassembly, which is inhibitive both for repurposing and recycling [228]. Instead of directly regulating EV battery pack designs and potentially stifling innovation, some researchers have recommended international collaboration between governments, manufacturers, and researchers with the goal of tracking and encouraging circular design practices in EV battery manufacturing [304], [312].

3.4.5. Industry Development

Despite the various challenges and uncertainties associated with repurposing EV batteries, the second-life battery industry has already undergone substantial development over the past decade. There are many early examples of small-scale and large-scale battery repurposing projects dating back to 2010, primarily led by various EV manufacturers in joint ventures with industrial partners [218], [279], [300], [315], [316]. These early projects have served in a range of stationary energy storage applications, including peak shaving, renewable energy time shifting, back-up power, EV fast charging, power quality, and grid ancillary services. For example, a Nissan-led joint venture in Japan commissioned the world's first large-scale second-life battery system in 2014 by repurposing 16 Nissan Leaf EV batteries at the pack level to assemble a 400 kWh system capable of supporting a nearby 10 MW solar farm [317]. In 2015, a Daimler-led joint venture commissioned a much larger 13 MWh second-life battery system to participate in the German wholesale energy market, repurposing 1000 Smart ForTwo EV batteries at the module level [318].

The first independent second-life battery startup companies were founded in the 2010s, and many such companies now exist all over the world, including Connected Energy [319], BeePlanet Factory [320], Allye Energy [321], ECO STOR [322], Zenobē [323], and Reefilla [324] in Europe; BTU Storage Solutions [325], RePurpose Energy [326],

Smartville [327], and Higher Wire [328] in the United States; Moment Energy [329] in Canada; and Relectrify [330] in Australia. Some larger energy companies that have long operated in the battery business now offer second-life battery products to their customers as well, such as BELECTRIC [331], Enel X [332], and TERREPOWER [333]. In 2024, the United Sates Department of Energy awarded Moment Energy a $20 million grant to support the construction of a large-scale second-life battery manufacturing facility in Texas, which will have UL 1974 certification and produce 1 GWh of energy storage capacity annually [14]. The growing investments in the second-life battery industry indicate that battery repurposing will play a significant role in the clean energy transition.

3.5. Gaps in Second-life Battery Research

Due to the economic potential of the second-life battery industry, battery repurposing is an increasingly popular field of research. Some of the most frequently explored topics in the literature were discussed in Section 3.4, including SOH and RUL estimation methods, power conversion systems, control strategies, economic models, life cycle analyses, and regulatory hurdles. This section will review other focus areas that have not yet been adequately explored, and propose specific research questions that need to be addressed.

3.5.1. Pack-level Performance Studies

Despite the known economic benefits of pack-level repurposing, the vast majority of experimental second-life battery studies focus on cells or modules from EV batteries [181], [294], [334-336]. From a performance standpoint, packs, modules, and cells should exhibit fairly consistent electrical characteristics for a given EV battery design, but their thermal characteristics could differ significantly given the likelihood of temperature gradients in large lithium-ion battery packs (see Section 2.6.5). This means that the thermal performance of second-life battery packs is not adequately represented in the literature. Some of the most relevant research is focused on the thermal management of battery packs in EV service without direct consideration of second-life service [217]. One recent pack-level study tested the capacity and power capability of a used LFP battery from a Chinese EV, but there were no results reported for temperature or energy efficiency [337]. Another pack-level study demonstrated methods for operating a repurposed Nissan Leaf EV battery pack by communicating directly with the original BMS [338], but again, no

operational temperature data was reported. Clearly, more comprehensive pack-level performance studies are needed.

An interesting example of a pack-level performance study was published by BMW researchers in 2017, which reported on a 166 kWh second-life battery pilot project which the company built in Germany [214]. The system includes seven BMW i3 EV battery packs integrated into a functional stationary energy storage system with a refrigerant-based active TMS. The system was tested under a duty cycle derived from historical real-time energy market price fluctuations, which required the battery to undergo multiple high-power deep cycles over a 24 h period (see Figure 3.14 for a sample of the results). The study examined how the thermal performance varied under this demanding duty cycle both with and without the TMS activated, providing a comparison of active-refrigerant and passive-air thermal management. It was found that refrigerant cooling held the battery temperature rise to 3 °C above the 22 °C setpoint, allowing the battery to cycle continuously. In contrast, passive cooling resulted in the battery temperature rising steadily until it reached the 39 °C upper limit, forcing the battery to reduce power and eventually shut down.

The BMW study highlights an important opportunity for further second-life battery research. Given the wide range of EV battery pack designs and associated TMS designs, the thermal and economic consequences of disabling the original TMS in favour of passive cooling in second-life service should be examined for multiple EV battery pack designs. This will help second-life battery project developers understand potential economic trade-offs between TMS costs and system power capability.

3.5.2. Comparative Performance Studies

Despite the great diversity among EV battery designs, there do not appear to be any experimental studies in the literature focused on comparing multiple EV battery designs tested in a common second-life test regime, particularly at the pack level. There are examples of studies comparing the long-term degradation rates of different EV battery cells, and this is certainly important for assessing the cycle life of second-life battery systems. However, there is likely significant variance in the short-term electrical and thermal performance of different EV battery designs as well, which will impact the value

that different second-life battery systems can generate on a given day. Second-life project developers would therefore benefit from knowing which EV battery designs are best suited for a given stationary energy storage application. Just as UL 1974 requires a grading system to rank used EV batteries of the same design according to SOH, other grading systems could be developed to rank different EV battery designs according to various performance metrics evaluated through common experimental test protocols. Comparative performance studies could be used to develop these metrics and ranking systems.

Another justification for comparative performance studies arises from the concept of 'value stacking'. Section 3.3.5 explained how value stacking can enhance the economics of stationary energy storage, with a single battery system performing multiple energy storage services to access multiple revenue streams. Value stacking could make it economically advantageous to combine multiple EV battery designs in a single second-life battery system, since some battery designs may be better suited for high-energy applications like peak shaving and energy arbitrage, while other battery designs may be better suited for high-power ancillary services. This hypothetical 'mixed battery array' system [292] could not be certified under the current edition of UL 1974, and is therefore not currently an attractive option for a company looking to sell packaged second-life battery systems to customers. However, a mixed battery array could be feasible for a company looking to construct, own, and operate a second-life battery system and sell stacked energy storage services to the electricity system operator. The energy management system would be especially critical for a mixed battery array, since the control strategy would have to account for the unique performance characteristics of each battery design in the array [278]. The control strategy would therefore need to be informed by comparable performance metrics assigned to each battery design. Comparative EV battery performance studies would be highly valuable for the development of mixed battery array technology.

While there will likely be performance differences across different EV battery designs, there may also be common performance patterns that could prove useful in identifying and mapping key parameters that influence second-life battery performance. Comparative performance studies of diverse EV battery designs might reveal such patterns and open up opportunities to build new tools for second-life battery researchers and developers.

3.5.3. Performance Test Methods

A comparative study of second-life battery performance would require suitable test methods that can produce comparable performance results for a diverse range of EV battery designs. Though many studies have experimentally evaluated the performance of second-life batteries, there is little consistency among the test methods used. As a starting point, UL 1974 prescribes a capacity test (to assess the useful discharge capacity at a base current rate) and a current pulse test (to assess power capability), and some laboratory studies have employed similar methods for evaluating second-life batteries [294], [337]. The pulse test is mostly useful for evaluating the internal resistance of a given battery (i.e. the change in voltage divided by the change in current) to track its growth as the battery degrades over time, which has value for screening EOVL batteries. However, unless the battery will undergo short, infrequent, high-power pulses in second-life service (e.g. fast frequency response), the pulse test carries little practical meaning. For energy management applications like energy arbitrage and peak shaving, what matters is how the internal resistance (which varies with SOC) impacts the energy capacity and energy efficiency of an operational battery as a function of the applied power (see Figure 2.27). A simple pulse test, while conveniently rapid, cannot provide this practical information. Internal resistance also influences the waste heat generation of a battery and therefore impacts its operational temperature, but a pulse test cannot capture the thermal performance of a battery that cycles continually. Pulse testing is therefore of limited value if these various aspects of battery performance are to be experimentally characterized.

Instead of a single capacity test and a pulse test, much more information about battery performance can be gained by cycling batteries at a range of power levels. Pacific Northwest National Laboratory (PNNL) recommended this type of approach in 2016 with the publication of a test protocol for evaluating the performance of energy storage systems in peak shaving applications [339]. The test protocol is intended to emulate a peak shaving scenario where the energy storage system first charges at relatively low power to a maximum SOC level during off-peak periods and then discharges at higher power to a minimum SOC during peak load periods. Three test cycles are carried out in sequence, with the discharge duration decreasing from 6 h to 4 h to 2 h (i.e. increasing power magnitude) over the three cycles. A single charge duration is selected between 4 h and

12 h, and each charge and discharge is followed by a rest period selected between 1 h and 5 h. An example of what this test protocol could look like in terms of battery power vs test time is illustrated in Figure 3.21, where discharge is considered to be negative power. The authors from PNNL recommended energy capacity and energy efficiency as performance metrics for this test protocol.

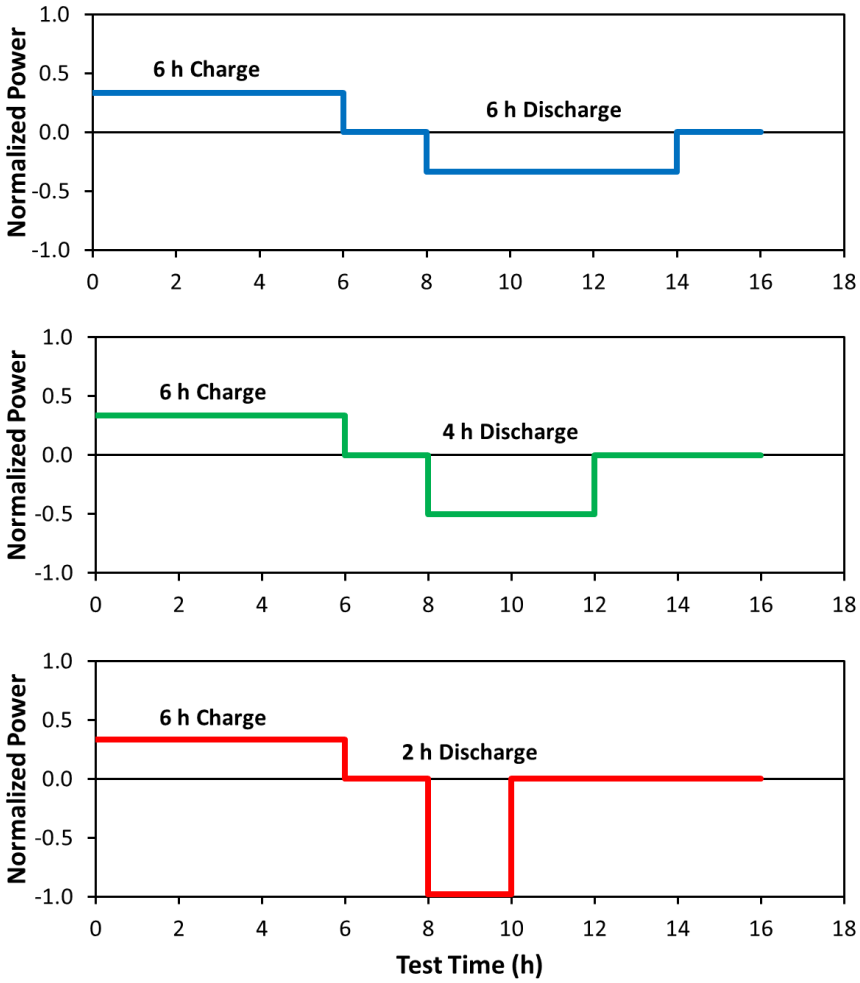


Figure 3.21 One rendition of the PNNL test protocol for evaluating the performance of energy storage systems in peak shaving service. Based on data from [339].

It is important to note that the PNNL peak shaving test protocol prescribes durations rather than C rates. A 'C rate' is determined by dividing the applied current by the rated coulombic capacity of the given battery. For example, discharging a 100 Ah battery at 50 A, 100 A, and 200 A would respectively be called a C/2 rate, a 1C rate, and a 2C rate. This is a useful technique for comparing the current rates applied to batteries of different

sizes. However, since the discharge capacity of batteries tends to decrease at higher discharge rates (see Figure 2.27) these three rates do not necessarily produce 2.0 h, 1.0 h, and 0.5 h discharge durations. Prescribing a 2 h discharge rate means that the appropriate current or power is selected so that the battery discharges its stored capacity in 2.0 h. The difference between these two methods is especially important for second-life batteries, as evidenced in a 2021 study comparing the performance of new (97 % SOH) and aged (66 % SOH) Nissan Leaf EV battery modules. All modules were tested using C rates of C/2, 1C, and 1.5C based on the rated coulombic capacity of the modules (66 Ah), despite the present capacity of the aged modules (44 Ah) being significantly lower than the new modules (64 Ah). Even if the modules delivered all of their present capacity at each C rate, the aged modules would have effectively been tested with discharge durations of 1.33 h, 0.67 h, and 0.44 h, compared to 1.94 h, 0.97 h, and 0.65 h for the new modules. The authors of the study reported very poor performance for the aged modules, but did not acknowledge that the aged modules were put at an inherent disadvantage by the inflated discharge rates. When evaluating the performance of different second-life batteries at different SOH levels, discharge durations are much more equitable than C rates. The PNNL test protocol is therefore suitable for second-life batteries. Note that the PNNL test protocol also prescribes constant power (CP) for charge and discharge instead of constant current (CC). While CC testing is common in cell-level battery research, stationary energy storage services are provided in terms of power rather than current, making CP more appropriate for second-life battery testing. The PNNL test protocol does not specify a CV component of the CP charge.

The PNNL test protocol is suitable for evaluating peak shaving performance. However, since the maximum power is a 2 h rate and only one cycle is carried out per day, this test protocol may not be suitable for evaluating more demanding stationary energy storage applications. For example, Sections 3.2.3 and 3.3.2 explained how real-time energy markets can exhibit volatile price fluctuations, which would potentially incentivize a battery to cycle multiple times per day at high power to maximize arbitrage profits. This provides a justification for modifying the PNNL test protocol with higher charge and discharge rates and shorter rest periods to reflect real-time energy arbitrage conditions. A more demanding test protocol such as this would likely be more effective for identifying

performance differences between different EV battery designs. In the BMW study described in Section 3.5.1 and Figure 3.14, the researchers concluded that energy arbitrage service has high technical requirements for batteries and thus serves as a suitable test regime for evaluating stationary battery energy storage performance [214].

Some battery test protocols have been developed based on real electricity market signals for energy arbitrage [214], [340] and frequency regulation [181], but since different electricity markets can be quite unique, it can be challenging to justify a test protocol based on one specific market, especially if the goal is to encourage other researchers and developers to use the same test protocol. Real-world battery operations also tend to be somewhat stochastic in nature, which makes analysis of test results needlessly complicated for the purposes of laboratory research. In contrast, the PNNL test protocol employs simple CP deep cycles, which are easy to program and analyze and are therefore also conducive to adoption in research and industry. A modified version of the PNNL test protocol would therefore be suitable for comparably characterizing the performance of different second-life batteries. This will be revisited in Chapter 4. While PNNL recommends energy capacity and energy efficiency as performance metrics, additional electrical and thermal performance metrics could also be developed. Appropriate TMS hardware and software should also be integrated with the test protocol so that different EV batteries can be tested with their original TMS using consistent temperature control schemes.

3.5.4. Thermal Models

In addition to experimental performance characterization, thermal modelling is a powerful tool that can be leveraged to benefit second-life battery research and development. Battery temperatures can be modelled if the heat generation rates, heat transfer rates, and thermal properties are known or can be estimated. Battery thermal models generally employ theoretical or empirical approaches to describing the various thermal properties and processes of the battery. Theoretical models require detailed specifications of the battery design in order to calculate the variable rates of heat generation and heat transfer based on electrochemical and thermal processes. Required specifications may include electrode thickness and porosity, electrolyte conductivity and diffusivity, and particle radius [341], [342], [343]. While these specifications will be known by the battery manufacturer, most

second-life battery developers will not have access to this proprietary information, making theoretical thermal models unsuitable for most second-life applications.

Empirical thermal models estimate unknown battery parameters by fitting the simulated results to experimental test data. For example, one study described an electro-thermal model for which the lithium-ion diffusivity and chemical reaction rate were estimated by fitting the model to experimental current pulse tests [344]. However, their model still required specifications for other battery parameters which would be unknown in most second-life applications. Anther study used polynomial expressions to estimate the rates of heat generation and heat transfer for a single lithium-ion pouch cell by fitting the model to battery surface temperature measurements obtained from empirical tests [345]. Since their model assumed lumped capacitance for a single pouch cell, it is not directly applicable to large EV batteries where nonuniform temperature distributions must be accounted for. Most studies on battery modules and packs employ advanced models to account for temperature distributions throughout the battery. Three-dimensional heat conduction problems can be solved numerically by applying finite element analysis with computational software tools [346-348], which require initial conditions as well as boundary conditions for convection and/or radiation at the outer surfaces of the battery. Many such models have been described in the literature, with simulations potentially requiring many hours depending on the size of the battery, the number of nodes used in the model, and the degree of simplification applied [349]. The relatively greater size and complexity of EV batteries are generally associated with greater computational requirements.

Thermal network models are commonly employed to reduce computational requirements compared to finite element analysis. Ramotar et al. designed a thermal resistance network to empirically characterize the thermal behaviour of a liquid-cooled Chevrolet Volt hybrid EV battery pack [350]. Their model achieved reasonable results, but required characterization of over 40 individual parameters. Shi et al. developed a simpler thermal network model for a hybrid EV battery pack, consisting of three battery temperature nodes representing the minimum, average, and maximum temperatures in the pack [351]. Their model required just six constant parameters to describe the pack thermal mass and heat transfer coefficients, which were fitted to experimental data obtained from battery tests

within a controlled environmental chamber. The simplified model achieved reasonable accuracy in modelling battery temperatures under a shallow-cycle current pulse duty cycle. However, it is worth noting that the model did not account for reversible heat generation, which can have a significant impact on battery temperature during larger SOC changes (see Section 2.6.3). Furthermore, the model assumes constant convection coefficients for both forced convection and natural convection, despite the well-established temperature dependence of natural convection coefficients (see Section 2.6.4). This may explain why the average root-mean-square error of the model was reported as 1.1 °C for forced convection and 1.6 °C for natural convection.

Thermal network models appear to be the most practical thermal modelling tool for second-life batteries. However, researchers have not yet explored whether thermal network models have unique applications for second-life batteries that would not normally apply to new stationary batteries and batteries in EV service. Pack-level repurposing could be one such application, where modifications to the original battery pack are minimized to reduce repurposing costs. In cases where the original temperature monitoring system of a given EV battery pack design does not meet the needs of the repurposing company, thermal network models could be a practical and cost-effective alternative to opening the pack and modifying or replacing the original temperature monitoring system.

3.5.5. Proposed Research Questions

Given the economic potential of pack-level repurposing, the lack of comparative, pack-level performance studies presents an opportunity to fill an important research gap for second-life batteries. Battery degradation is already a very popular and complex research topic, which points to a more specific opportunity to characterize and compare the electrical and thermal performance of different EV battery packs in second-life applications. Energy arbitrage appears to be a suitable representative application with which to evaluate battery performance, and the PNNL peak shaving protocol provides a good template from which to build an energy arbitrage test protocol. Since thermal performance is especially important for second-life batteries repurposed at the pack level, thermal network models present another potential opportunity to help minimize costly pack modifications.

Based on the identified research gaps and opportunities, the following questions are proposed for second-life battery research:

1. What experimental methods and performance metrics can be used to characterize and compare different EV battery pack designs in second-life applications?
2. How do the significant differences among EV battery pack designs impact their relative performance characteristics in second-life applications?
3. How do modern EV battery packs perform when an active TMS is deactivated in second-life service?
4. Are there any useful performance correlations that apply to all EV battery packs despite their unique design features?
5. What tools can be used to guide the selection of suitable EV battery pack designs and control strategies for a given second-life energy storage project?
6. How might second-life battery performance characterizations be standardized?
7. How can thermal network models be used to facilitate pack-level repurposing?

Through comparative experimental testing and numerical modelling of EV battery pack performance, these research questions could lead to the development of new tools and practical insights that can benefit other researchers and developers in the field of second-life batteries.

3.6. Chapter Summary

Chapter 3 has provided a detailed review of various concepts related to second-life batteries, including the design of EV batteries and their status at EOVL, the functioning of electricity grids and associated electricity markets, and the many unique stationary energy storage services that repurposed EV batteries can perform for electricity system operators and consumers alike. The main challenges and opportunities of the second-life battery industry have also been reviewed in full, including various technical, economic, environmental, and regulatory factors that will continue to evolve in the coming years.

Based on the state-of-the-art in second-life battery research and development, several important research gaps have been identified with respect to pack-level repurposing of EV batteries. To help fill these research gaps, a set of seven specific research questions have been proposed. The remaining chapters of this thesis will describe novel second-life battery research contributions that directly address each of these questions.

Chapter 4 METHODS FOR EXPERIMENTAL EVALUATION OF SECOND-LIFE BATTERY PERFORMANCE

Chapter 3 identified a need for experimental studies focused on characterizing the electrical and thermal performance of different EVs battery pack designs in a consistent test regime representative of electricity grid energy storage services. Chapter 4 will now present experimental methods used to fill this research gap, including a set of five acquired EV battery packs, various test equipment and apparatus designs, specialized test protocols, and a set of electrical and thermal performance metrics for evaluating test results. The results of the described experiments will be presented and analyzed in Chapter 5.

Portions of this chapter have been published in the following two journal articles:

> C. White, L. G. Swan, Pack-level performance of electric vehicle batteries in second-life electricity grid energy services, Journal of Energy Storage 57 (2023) 106265. [352]
>
> C. White, B. Thompson, L.G. Swan, Comparative performance study of electric vehicle batteries repurposed for electricity grid energy arbitrage, Applied Energy 288 (2021), 116637. [353]

Chris White is the principal researcher and author for both articles, which were completed over the course of this research project. The work is reprinted here under the terms of the license agreement with Elsevier, which is provided in Appendix D. Some aspects of the work have been expanded upon for publication in this thesis. Note that the contributions of Thompson and Swan include preliminary development of the battery test protocols described in this chapter.

4.1. Acquired EV Battery Packs

Chapter 2 demonstrated how the numerous positive electrode materials and cell design parameters have given rise to a wide range of shapes, sizes, voltage profiles, internal resistances, and thermal characteristics among EV batteries. Section 3.1.3 further elaborated on the different thermal management strategies that EV battery manufacturers use to control battery temperatures during operation. To assess EV battery pack performance in second-life applications, test batteries must be representative of the diversity among EV battery designs. This section will describe five unique EV battery

packs that were acquired for experimental testing. Acquisition sources include insurance company auctions, private online resellers, and professional contacts in the EV industry. Note that the scope of this research project is limited to EV batteries from private passenger vehicles (as opposed to buses, transport trucks, etc.).

4.1.1. Pack Specifications

The five acquired EV battery packs are pictured in Figure 4.1, with the left column showing each pack with its housing cover secured in place, and the right column showing each pack with the housing cover removed to reveal the module layout inside. The acquired battery packs come from a 2019 Tesla Model 3 Standard Range Plus (SR+), a 2018 Chevrolet Bolt, a 2015 BMW i3, a 2012 Nissan Leaf (first generation), and a 2012 Lishen EV-LFP.

The annotated photos in Figure 4.1 highlight the different shapes, sizes, housing materials, and module layouts among the five battery packs. Three of the packs feature a uniform module arrangement, with a consistent module height across the pack, while the Bolt and Leaf packs feature nonuniform module arrangements. The Bolt pack features eight uniform modules and two stacked modules at the rear, and the Leaf pack features three distinct module groupings. Note that while the Lishen pack features a uniform module height, it includes three different module lengths with either five, six, or seven series cell groups. Chapter 5 will discuss how the different module arrangements affect thermal performance.

While four of the five acquired battery packs include all their original modules, the acquired BMW i3 battery is missing two of its eight original modules, which were separated prior to acquisition of the pack. The i3 pack is therefore tested with six of eight modules, arranged in the original pack housing as pictured in Figure 4.1 This is only a potential limitation for thermal performance evaluation, as a partial pack may exhibit lower temperatures than a full pack. Preliminary tests were therefore conducted on the i3 pack, which showed that heat generation in the i3 modules is low enough that the temperatures measured on a given module are only affected by the presence of the immediately-adjacent module. This confirmed that six modules can sufficiently represent the thermal performance of the centre module of a BMW i3 battery pack.

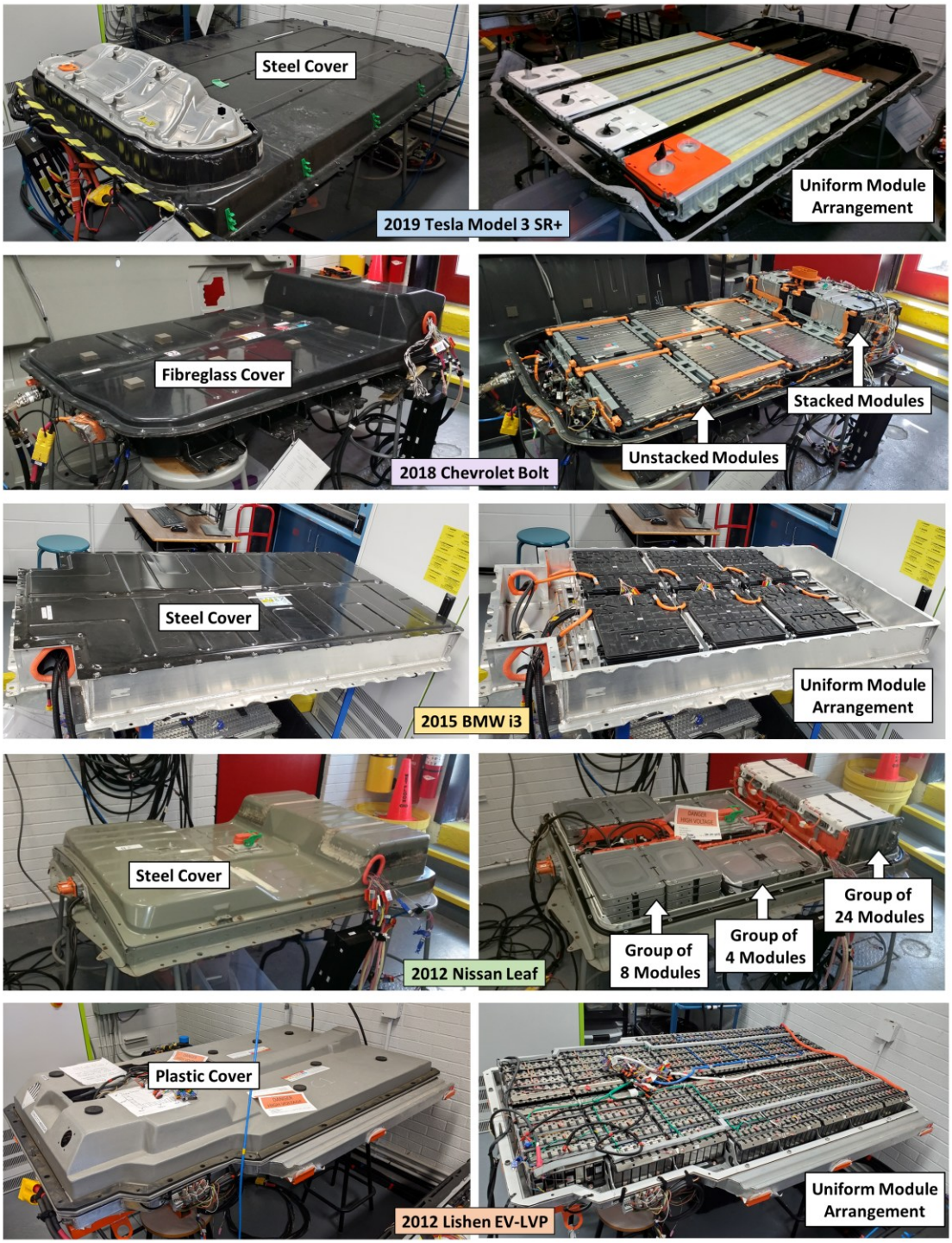


Figure 4.1 Five acquired EV battery packs shown in closed cover (left) and open cover (right) configurations.

Specifications for the five EV battery packs are summarized in Table 4.1. The top row shows the naming convention adopted for the five packs based on EV model and build year. The specifications highlight the significant diversity among the acquired battery

packs. Together, the five packs represent five EV manufacturers, four manufacturing years between 2012 and 2019, five cell suppliers, six positive electrode materials, two negative electrode materials, three cell formats, three cell housing materials, five cell groupings, five module quantities between 4 and 48, and three TMS types. The five packs also cover a wide range of rated coulombic capacities (60 to 170 Ah) and energy capacities (22 to 60 kWh). For most packs, the positive and negative electrode materials are either stated in manufacturer spec sheets. For Bolt-18 and Model 3-19, positive and negative electrode materials were determined experimentally by 'inductively coupled plasma' scans conducted on disassembled cells acquired from other Bolt and Model 3 packs with comparable manufacturing years.

Table 4.1 Specifications of acquired EV battery packs.

Specification	Model3-19	Bolt-18	i3-15 [a]	Leaf-12	Lishen-12
EV manufacturer	Tesla	Chevrolet	BMW	Nissan	Lishen
EV model	Model 3 SR+	Bolt	i3	Leaf Gen 1	EV-LFP
EV build year	2019	2018	2015	2012	2012
Cell supplier	Panasonic	LG Chem	Samsung	AESC	Lishen
Positive electrode material	NCA	NMC622	NMC111 + LMO	LMO + LNO	LFP
Negative electrode material	Graphite + silicon	Graphite	Graphite	Graphite	Graphite
Cell format	Cylindrical	Pouch	Prismatic	Pouch	Prismatic
Cell housing	Steel	Pouch foil	Aluminum	Pouch foil	Aluminum
Cell grouping	96S 31P	96S 3P	96S	96S 2P	104S 7P
Module quantity	4	10	8	48	16
TMS type	Active liquid	Active liquid	Active refrigerant	Passive air	Passive air
Rated coulombic capacity (Ah)	144	170	60	65	115
Rated energy capacity (kWh)	50	60	22	24	38

[a] The BMW i3 pack specifications refer to a pack with all eight original modules.

Due to the differences in cell design, the five battery packs also feature very different cell quantities: i3-15 and Lishen-12 respectively feature 96 and 728 prismatic cells; Leaf-12

and Bolt-18 respectively feature 192 and 288 pouch cells; and Model3-19 features 2976 cylindrical cells. In the case of Model3-19, the relatively large number of relatively small cells implies that more cell housing material is used per module compared to packs with larger cells, which may impact mass density and energy density. These considerations will be revisited in the performance analysis in Chapter 5.

All five packs feature rectangular modules consisting of multiple connected cells, but the unique module construction of Model3-19 is worth highlighting. Each of the four Model3-19 modules includes seven parallel liquid channels that pass between cylindrical cells as pictured in Figure 4.2, where the red circles are drawn at individual cell locations for illustrative purposes. The liquid channels make direct contact with one side of each cell as a means of heat rejection. None of the other four packs feature modules with internal liquid channels. Figure 4.2 also shows the light-green foam that fills all empty space within the Model3-19 modules and separates each individual cylindrical cell from its neighbors. As mentioned in Section 3.1.1, some EV battery designs feature specialized foam materials to protect the cells from vibrations, impacts, and thermal events. The properties of the foam used by Tesla are unspecified, so there is a potential for unique influences on thermal behaviour compared to the other battery packs.

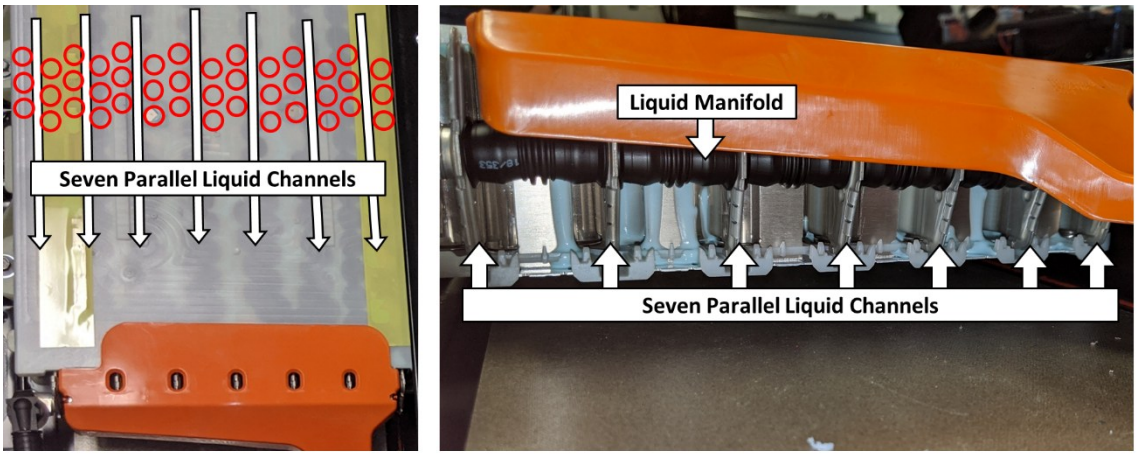


Figure 4.2 Construction of 2019 Tesla Model 3 SR+ battery module.

Due to the limited availability of used EV battery packs for research, it is difficult to study a significant sample size for each battery design as would be typical for cell-level studies. Sample size is not a concern for this comparative research project since the manufacturing

variance of a single EV battery design is relatively small compared to the significant differences among the five unique EV battery designs acquired for testing. Battery SOH can have a significant impact on performance, which will be considered in Chapter 5.

4.1.2. Pack Preparations

After initial acquisition, each EV battery pack is visually inspected for signs of damage to confirm its external integrity. Where applicable, the mid-pack disconnect is detached to mitigate the > 300 V electrical risk before attempting to remove the pack housing cover. In most cases, cover removal requires only the removal of a number of bolts or screws. In the case of the Model 3 battery, additional steps are required to cut through the adhesive that Tesla uses to create a seal between the housing cover and housing base. Once a pack is opened, individual modules and other internal components are visually inspected to confirm the internal integrity of the pack before beginning test preparations.

Several retrofitting measures are carried out to prepare the packs for testing. First, the original BMS is disconnected and replaced with a laboratory BMS to facilitate CAN bus communication of cell voltage measurements to the laboratory test control software (the test apparatus is described in more detail in Section 4.2). For most of the acquired packs, this retrofitting measure requires severing of the original BMS connectors from the cell voltage sense wires and crimping new connectors adapted for the laboratory BMS. Figure 4.3 shows an example of this for Bolt-18. For the unique case of Model3-19, mini-grabber clips are applied to connect the laboratory BMS to the original cell voltage sense wires, as shown in Figure 4.4.

Each pack is also retrofitted with a power connector to cycle the battery, as well as a pack voltage sense to monitor the voltage of the pack as a whole. Examples of these retrofitting measures are shown in Figure 4.3 and Figure 4.4. Note that some of the original internal pack circuitry is bypassed so that power flow is exclusively governed by the laboratory test control software. Any pack that does not already feature an easily accessible mid-pack disconnect is retrofitted with one so that the high-voltage risk can be mitigated while working on the pack. A research-grade multimeter is used to verify the pack voltage as well as each individual cell voltage prior to testing.

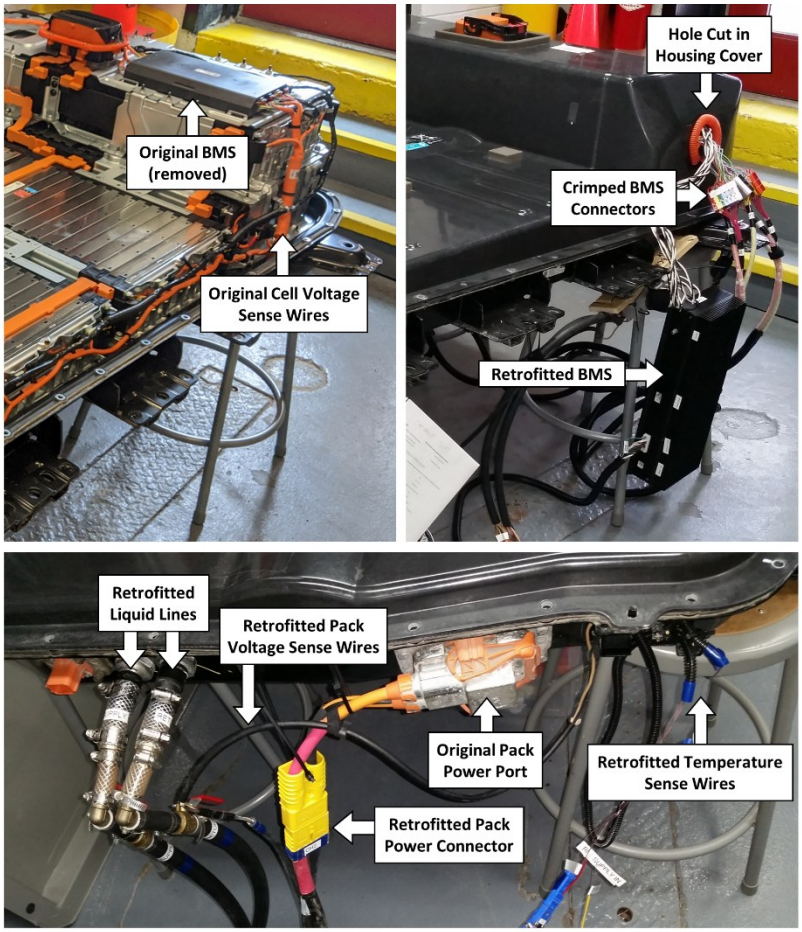


Figure 4.3 Example of test preparations applied to Bolt-18 battery pack.

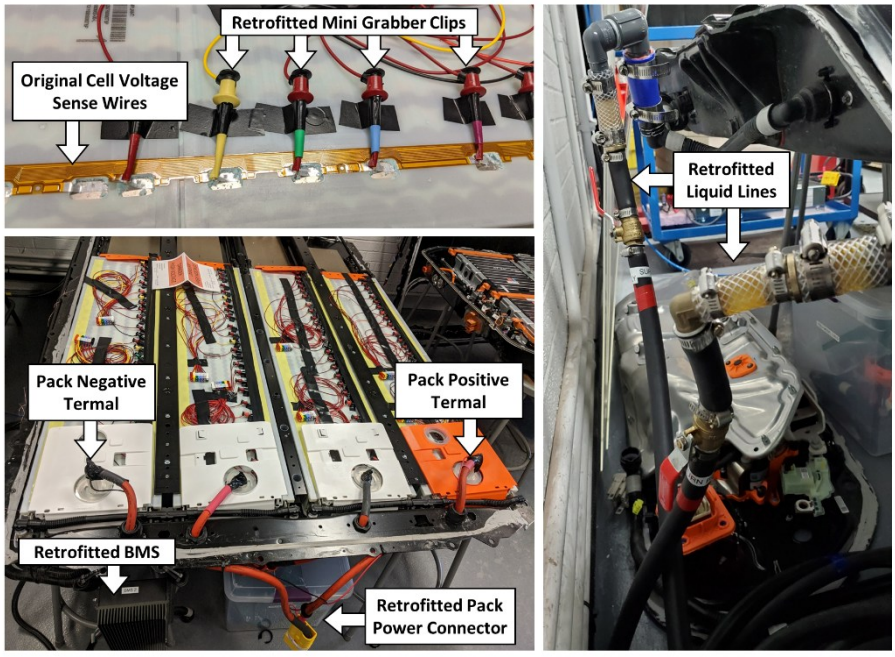


Figure 4.4 Example of test preparations applied to Model3-19 battery pack.

Any EV battery pack may be tested with a passive air (PA) TMS (i.e. natural convection). However, the Model 3, Bolt, and i3 battery packs feature active TMS designs for EV service. The i3 battery features eight parallel refrigerant channels that absorb latent heat from the bottom of the modules, meaning that a second-life system would require an external chiller to run the refrigeration cycle. Construction of such a system was considered but ultimately deemed impractical for this research project, so i3-15 is evaluated as a passive-cooled battery only. A discussed in Section 3.5.1, a study by BMW [214] has already shown that refrigerant cooling provides a significant performance enhancement over passive cooling for BMW i3 battery packs in energy arbitrage service. The Model 3 and Bolt batteries both feature an active liquid (AL) TMS in EV service, which is easier to replicate both in the laboratory and in commercial second-life projects. Model3-19 and Bolt-18 are therefore primarily tested as liquid-cooled batteries using a customized AL-TMS (described in Section 4.2), but PA tests are also conducted on these two packs to compare results with and without the AL-TMS. To prepare Model3-19 and Bolt-18 for AL tests, custom liquid lines are retrofitted to the original liquid ports on both of these packs, as pictured in Figure 4.3 and Figure 4.4.

The final retrofitting measure is to adhere research-grade temperature sensors at strategic locations within each pack. It was suggested in Section 2.6.7 that at least two temperature sensors should be applied to a given battery pack to capture high and low temperatures distributed across the pack. Three or more T-type thermocouples are therefore placed on each pack to capture temperature distributions. Two additional thermocouples are used during the AL tests to monitor the temperature of liquid entering and exiting the liquid-cooled packs. Temperature sensor locations for each pack are pictured in the left column of Figure 4.5.

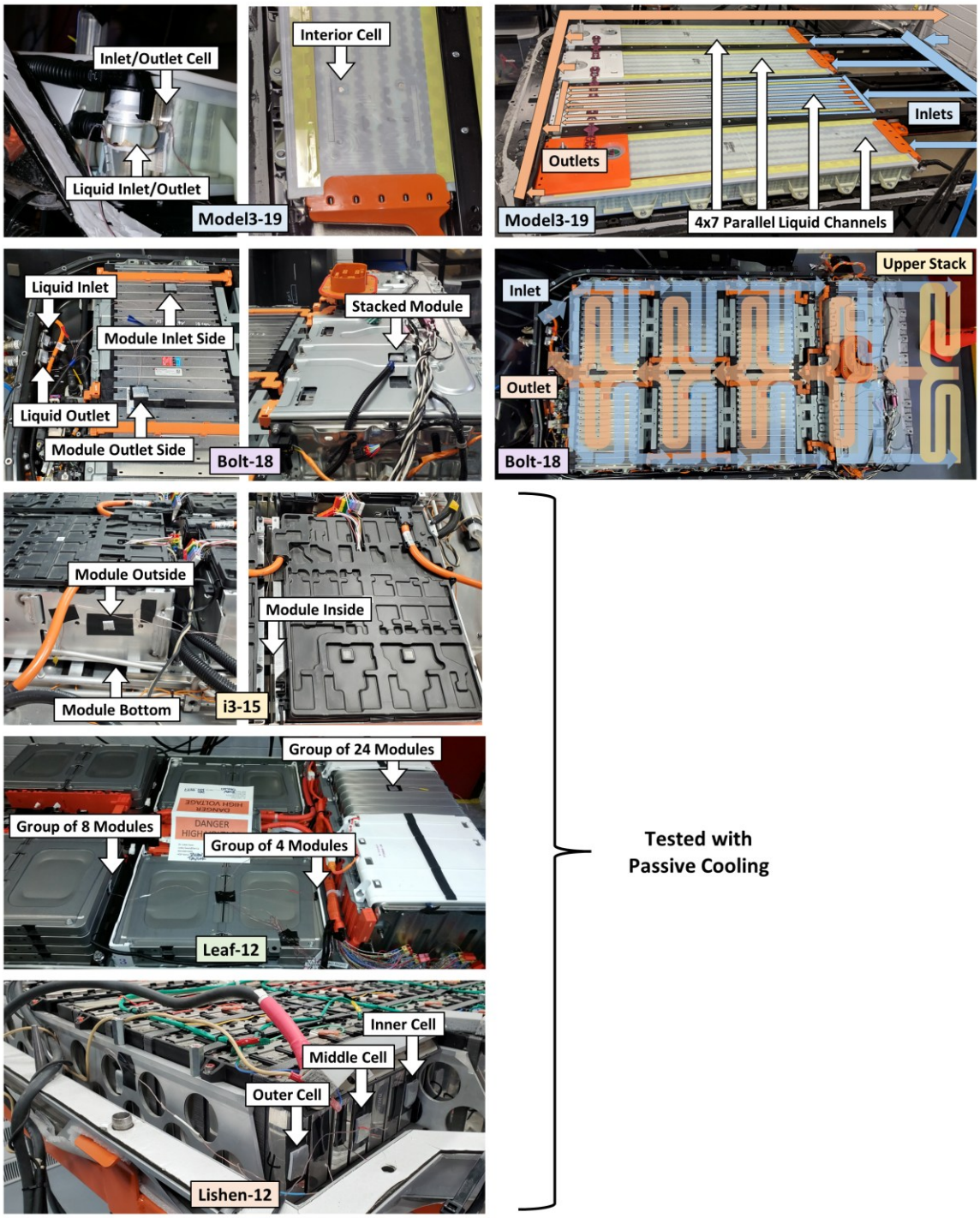


Figure 4.5 Thermal monitoring of five EV battery packs including retrofitted thermocouple placements (left) and applicable liquid flows (right).

The right column of Figure 4.5 shows the liquid channel layout in the Model 3 and Bolt battery packs. As explained in Section 4.1.1, the Model 3 battery features 28 parallel liquid channels (seven in each module) that pass between cylindrical cells along the length of the

modules. Thermocouples are therefore attached to Model3-19 at the liquid inlet and outlet of an outer module, the exposed cylindrical cell surface immediately adjacent to the inlet and outlet, and the partially exposed cell surface at the top of the module interior, as shown in Figure 4.5. The Bolt battery uses a different TMS layout, featuring an aluminum cooling plate that exchanges heat between the bottom of the modules and a serpentine liquid channel. Figure 4.5 shows how the liquid channel carries liquid down both sides of the battery before returning up the middle, such that each module sits on both the supply side and the return side. Thermocouples are therefore attached to Bolt-18 at the main liquid inlet and outlet, the top surface of a module near the inlet and outlet, and the top surface of the stacked module, which lies in the middle of the liquid flow path.

The i3, Leaf, and Lishen batteries are tested as passive-cooled batteries, so thermocouples are placed on module surfaces only. For i3-15, thermocouples are attached to a module at its outer surface (facing the pack housing), inner surface (adjacent to another module) and bottom surface. For Leaf-12, thermocouples are attached to side edges of each of the three different module groupings. For Lishen-12, cell wall surfaces are only accessible along the outer edge of the pack, so thermocouples are attached to a module at its outermost cell (facing the pack housing), middle cell, and innermost cell (adjacent to another module).

All hands-on work with the EV battery packs is conducted with appropriate personal protective equipment, including high-voltage gloves, safety glasses, face shields, arc flash suits, and steel-toe boots. Laboratory personnel receive appropriate training before undertaking any hands-on work on EV battery packs.

4.2. Test Setup

Experimental testing of EV battery packs requires sophisticated laboratory equipment and a well-designed test apparatus. This section describes the complete test setup for this research project, including the power-cycler, BMS, TMS, and various sensors, as well as the layout of the test apparatus.

4.2.1. Laboratory Equipment

The experimental tests are conducted using a two-channel Gustav-Klein power-cycler rated to 800 V DC, ± 400 A DC, and ± 100 kW DC, with test control software provided by

Greenlight Innovation. The two test channels allow for testing two battery packs simultaneously at ± 200 A DC each, or testing a single pack at ± 400 A DC using paralleled channels. During testing, the power cycler measures pack voltages and pack currents with built-in voltage sensors and current transducers (all accurate to within ± 0.1 % of full scale). One 180-channel Orion BMS is used on each of the two test channels for cell voltage measurements and passive cell balancing. Temperatures are measured using calibrated 24-gauge T-type thermocouples (accurate to within ± 1 °C) adhered directly to cell or module surfaces as well as the AL-TMS. An additional thermocouple is hung in free air near the middle of the test area to monitor the ambient air temperature, which is maintained near 20 °C. An uncertainty analysis is provided in Appendix C to assess how the various measurements introduce uncertainty into the test results. Despite unavoidable measurement uncertainty, Section 5.5 will demonstrate that the test results are highly repeatable.

A customized AL-TMS was constructed in-house so that Model3-19 and Bolt-18 could be tested as liquid-cooled packs. The constructed AL-TMS is pictured in Figure 4.6, consisting of a 50/50 by volume glycol/water mixture, a 10 L liquid reservoir with a 1400 W heating element, a radiator/fan assembly, two parallel pumps which circulate the liquid in a closed loop, and a thermostatic temperature controller which operates the heating element and fan to control the temperature of the liquid reservoir.

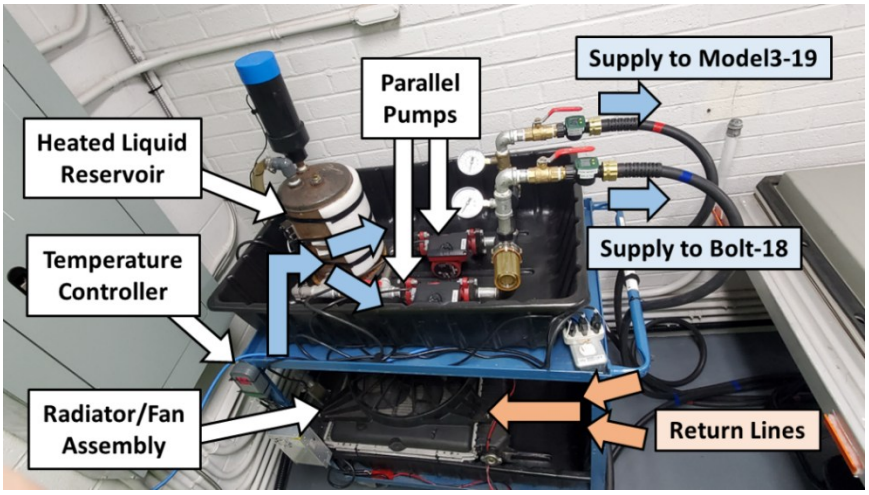


Figure 4.6 Customized active-liquid thermal management system.

Each pump in the AL-TMS has its own separate liquid line supplying either Bolt-18 or Model-19 during simultaneous tests to ensure that heat exchange within each pack is

limited by the pack liquid channels and not by the AL-TMS. The accumulated heat in the liquid returning from the packs is rejected through the radiator/fan assembly before the liquid re-enters the reservoir. A 27 kPa-g supply pressure was selected based on specifications in the Chevrolet Bolt service manual [354], which produced a 5 L/min flow rate. The thermostatic temperature controller is set to maintain the reservoir temperature within ± 0.5 °C of the assigned 31 °C setpoint. The selection of this setpoint is explained in Section 4.4.3.

4.2.2. Test Apparatus

Figure 4.7 illustrates the complete experimental test apparatus used for this research project. The test control software operates the two power-cycler channels to cycle the battery packs as desired. For Model3-19 and Bolt-18, the custom AL-TMS circulates liquid through the packs throughout testing. Measurements of pack current, pack voltage, pack temperature, and TMS temperature are sampled by a data acquisition system and reported to the test control software. Individual cell voltage measurements for each pack are sampled by a BMS and reported to the control software via CAN bus communication.

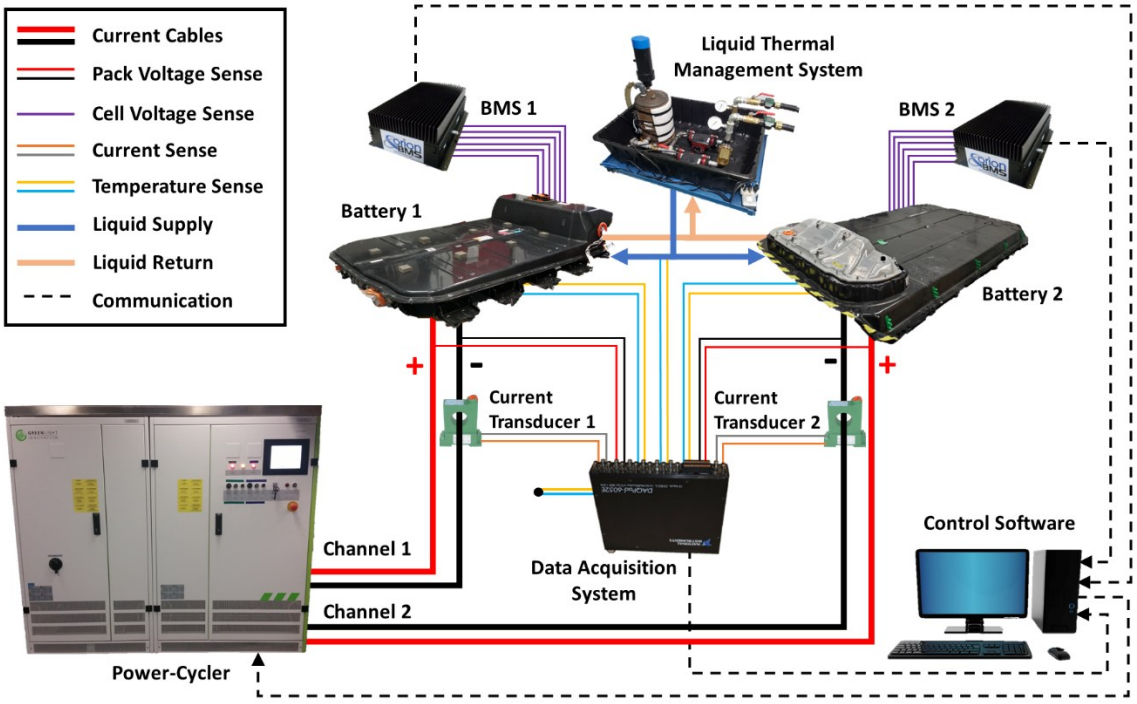


Figure 4.7 Test apparatus used for experimental testing of EV battery packs.

4.3. Baseline Capacity Test

Before beginning second-life performance tests on a given battery pack, a baseline capacity test is carried out to assess the present energy capacity and SOH of the pack. This test consists of a constant-current-constant-voltage (CCCV) charge to bring the pack to 100 % SOC, followed by a CC discharge to bring the pack to 0 % SOC. Three consecutive cycles are executed to verify that results are consistent. The measured energy output of the third discharge is taken as the present energy capacity of the pack.

Figure 4.8 shows an example of a baseline capacity test cycle (extracted from the Leaf-12 test results). The CC charge raises the battery voltage until the average cell voltage reaches a set upper voltage limit. The CV charge then holds the voltage at this upper limit until a prescribed 1 h period has elapsed, during which time the charge current decreases to an insignificant magnitude, indicating a complete charge to 100 % SOC. The CC discharge then lowers the battery voltage until any cell in the pack reaches a set lower voltage limit. This point is defined as 0 % SOC in this research project, recognizing that a small amount of additional capacity could be discharged if the test were conducted at a lower discharge rate or a higher temperature.

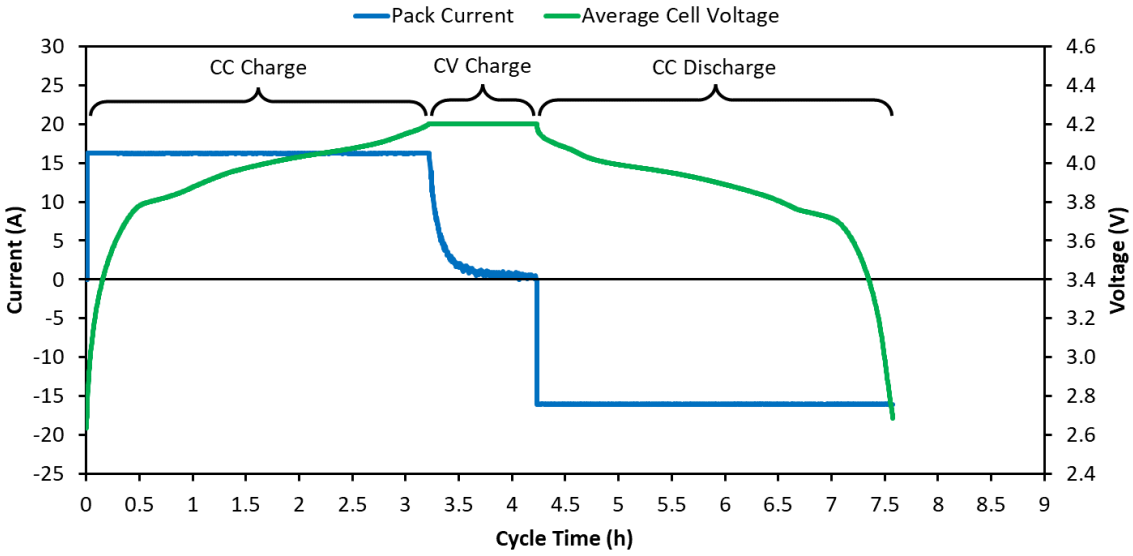


Figure 4.8 Example of a baseline capacity test cycle.

Section 2.4.2 explained that battery discharge capacity depends on the applied discharge rate, since greater currents give greater overpotentials and thus lower energy utilization. A

4 h discharge rate is used for the baseline capacity tests since this is common industry practice for assessing energy capacity at a relatively low but practical current rate. The results of the baseline capacity tests can therefore be directly compared to the manufacturer rated energy capacities listed in Table 4.1, which provides the necessary information to calculate an energy-based SOH value as described in Section 2.5. The applied calculation is stated in Equation 4.1, where $E_{\mathrm{dis}}^{\mathrm{CCCV}}$ is the measured discharge energy from the baseline capacity test and $E_{\mathrm{dis}}^{\mathrm{spec}}$ is the rated discharge energy specified by the manufacturer (see Table 4.1). A more comprehensive characterization of the various aspects of battery degradation (described in Section 2.5) is beyond the scope of this research project.

$$\mathrm{SOH} = \frac{E_{\mathrm{dis}}^{\mathrm{CCCV}}}{E_{\mathrm{dis}}^{\mathrm{spec}}} \times 100\ \% \tag{4.1}$$

Table 4.2 summarizes the currents and cell voltage limits applied to each battery pack during baseline capacity testing. Current setpoints are determined for each pack by dividing the rated coulombic capacities from Table 4.1 by 4 h. It was stated in Section 2.4.2 that upper and lower cell voltage limits of 4.20 V and 2.50 V are commonly applied in lithium-ion battery research. These values are adopted unless otherwise specified by the manufacturer (Lishen-12 being the one exception due to its LFP chemistry). The resulting energy capacity measurements and SOH calculations will be presented in Chapter 5. For Model3-19 and Bolt-18, the baseline capacity tests is conducted using the AL-TMS since this is the intended mode of operation for these packs.

Table 4.2 Baseline capacity test parameters applied to EV battery packs.

Test Parameter	Model3-19	Bolt-18	i3-15	Leaf-12	Lishen-12
4 h CC setpoint (A)	36.0	40.0	15.0	16.2	28.8
Upper cell voltage limit (V)	4.20	4.20	4.20	4.20	3.55
Lower cell voltage limit (V)	2.50	2.50	2.50	2.50	2.50
CV step duration (h)	1.0	1.0	1.0	1.0	1.0

4.4. Symmetrical Constant Power Test

Section 3.3 described a number of energy storage services that second-life batteries may provide for electricity grids, and Section 3.5.3 concluded that energy arbitrage service would be a suitable representative service for battery testing since batteries in energy arbitrage may be required to perform deep cycles of discharge and charge at a wide range of power rates. A 'symmetrical constant-power' (SCP) test is therefore designed as a means of evaluating EV battery performance in second-life electricity grid energy storage. This section provides a comprehensive description of the designed SCP test method.

4.4.1. Test Protocol

The designed SCP test consists of a test protocol which captures the deep-cycling operation that second-life batteries may undergo in energy arbitrage service. The applied test protocol builds upon the PNNL peak shaving test protocol described in Section 3.5.3, with several modifications. Similar to the PNNL test protocol, the applied test protocol consists of a sequence of CP discharge and charge periods separated by rest periods. Unlike the PNNL test protocol, the applied test protocol applies the same CP magnitude to both discharge and charge (hence the 'symmetrical' distinction). This modification is made because the PNNL test protocol is designed to emulate the low-rate overnight charging and medium-rate daytime discharging associated with peak shaving services, while batteries in energy arbitrage may be required to operate at low, medium, or high rates for both discharge and charge, depending on electricity market price signals and the operational control strategy. The latter is the more demanding type of operation and is therefore the preferred option for this research project. The applied test protocol also controls the rest durations based on the measured battery temperatures rather than the fixed time limits prescribed by PNNL. To account for the fact that the temperature and SOC window tend to evolve through the first one or two cycles of a given test, the applied test protocol executes three consecutive cycles. The test results are evaluated using the measurements from the third cycle only.

Figure 4.9 shows an example of an SCP test cycle (extracted from the Leaf-12 test results). The CP discharge lowers the battery voltage until any single cell reaches a set lower voltage limit, at which point the discharge terminates and the battery enters a cooldown period with

no power flow. The cooldown period continues until all measured battery temperatures are below a 'temperature control setpoint' with value T_{ctrl}. Once this condition is met, the CP charge (same magnitude as the CP discharge) raises the battery voltage until the average cell voltage reaches a set upper voltage limit, at which point the charge terminates and the battery enters another cooldown period governed by the same temperature control setpoint. Importantly, the lack of a CV charge means that the battery SOC will be less than 100 % when the charge terminates.

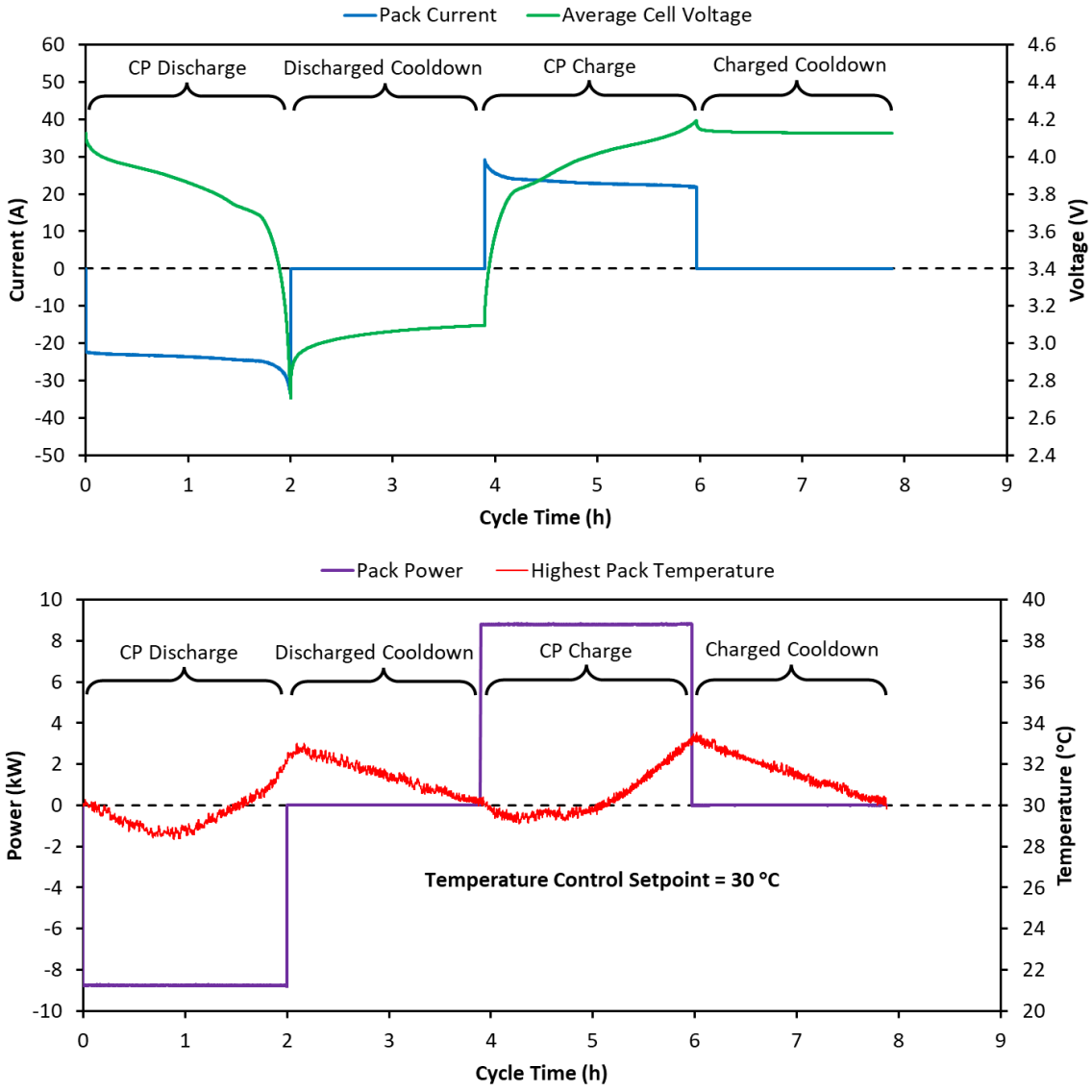


Figure 4.9 Example of an SCP test cycle.

The temperature control setpoint is a simple means of incorporating temperature control into the applied test protocol. In addition to rejecting heat from the battery through a TMS, commercial battery projects also control the battery power as necessary to maintain battery temperatures within desired limits. The applied test protocol uses a temperature control setpoint to this effect, ensuring that battery temperatures are always at or below T_{ctrl} at the beginning of each discharge and charge. Without this feature, battery temperatures could compound through consecutive cycles and reach unsafe levels, forcing interruption of the test before completion. The cooldown periods enforced by the temperature control setpoint allow for high-power tests to be conducted without concern of compounding temperatures. This also ensures thermally consistent initial conditions for the third cycle of each test, which facilitates comparison of test results for the five battery packs.

The SCP test protocol is summarized in Table 4.3. Note that the applied test protocol is similar to the baseline capacity test described in Section 4.3, with the main differences being the usage of CP instead of CC, the inclusion of rest periods, and the lack of a CV charge. These three features are also built into the PNNL peak shaving test protocol since they better reflect commercial energy storage operations. The baseline capacity test is not concerned with commercial operations.

Table 4.3 Summary of SCP test protocol.

Step	Description
Discharge	CP discharge until any cell voltage reaches the lower voltage limit.
Discharged cooldown	Rest in the discharged state until all measured battery temperatures are below the temperature control setpoint.
Charge	CP charge until the average cell voltage reaches the upper voltage limit.
Charged cooldown	Rest in the charged state until all measured battery temperatures are below the temperature control setpoint.
Loop	Repeat all previous steps until three cycles have been completed.

4.4.2. Test Sequence

As described in Section 3.5.3, prescribed discharge durations are more appropriate than C rates for second-life battery testing. For a given battery pack and TMS, the SCP test protocol described in Section 4.4.1 is therefore repeated in a sequence of three consecutive

tests at 4 h, 2 h, and 1 h power rates, which respectively represent low, medium, and high power rates in energy arbitrage. Before beginning the three tests, a CCCV charge is applied to reference the battery at 100 % SOC. Section 2.5.1 mentioned that lithium-ion batteries should be stored at or below 50 % SOC to avoid accelerated calendar degradation at higher SOC, so a partial discharge is applied to bring the battery close to 50 % SOC after the three tests have completed. The complete SCP test sequence is summarized in Table 4.4.

Table 4.4 Summary of SCP test sequence.

Stage	Description
Full charge	4 h CCCV charge to bring battery to 100 % SOC before tests begin.
4 h test	Three cycles of 4 h CP discharge, cooldown, 4 h CP charge, cooldown.
2 h test	Three cycles of 2 h CP discharge, cooldown, 2 h CP charge, cooldown.
1 h test	Three cycles of 1 h CP discharge, cooldown, 1 h CP charge, cooldown.
Partial discharge	4 h CP discharge of approximately 50 % coulombic capacity to bring battery to approximately 50 % SOC after tests are completed.

Referencing the battery at 100 % SOC at the beginning of the test sequence eliminates any existing SOC uncertainty so that SOC can be accurately tracked throughout the remainder of the test sequence using the coulomb counting method (introduced in Section 3.1.2). This allows voltage vs SOC plots to be constructed from the SCP test results, as shown in Figure 4.10.

The coulomb counting method is simple to implement, but can accumulate errors over long timespans depending on the accuracy of the current measurements, especially at low currents where measurement tends to be less accurate. A coulomb counting verification test is therefore conducted to confirm SOC tracking accuracy over ten consecutive 4 h SCP cycles since the 4 h SCP test uses the lowest currents. The left chart of Figure 4.10 shows that the measured cell voltage profile does not drift left or right in the SOC window over the ten consecutive 4 h cycles (the individual cycles are layered on top of one another in the chart and are thus indistinguishable). Current measurements at 2 h and 1 h rates are more accurate since these rates approach the optimal range of the current transducers, so the 4 h verification test confirms that SOC can be accurately tracked over the nine consecutive cycles of the SCP test sequence. The right chart of Figure 4.10 shows an

example of average cell voltage profiles from consecutive 4 h, 2 h, and 1 h SCP tests (extracted from the Model3-19 test results), superimposed in the SOC window based on coulomb counting. This novel graphical technique will be used to evaluate battery performance in Chapter 5. Test evaluation methods will be discussed further in Section 4.5.

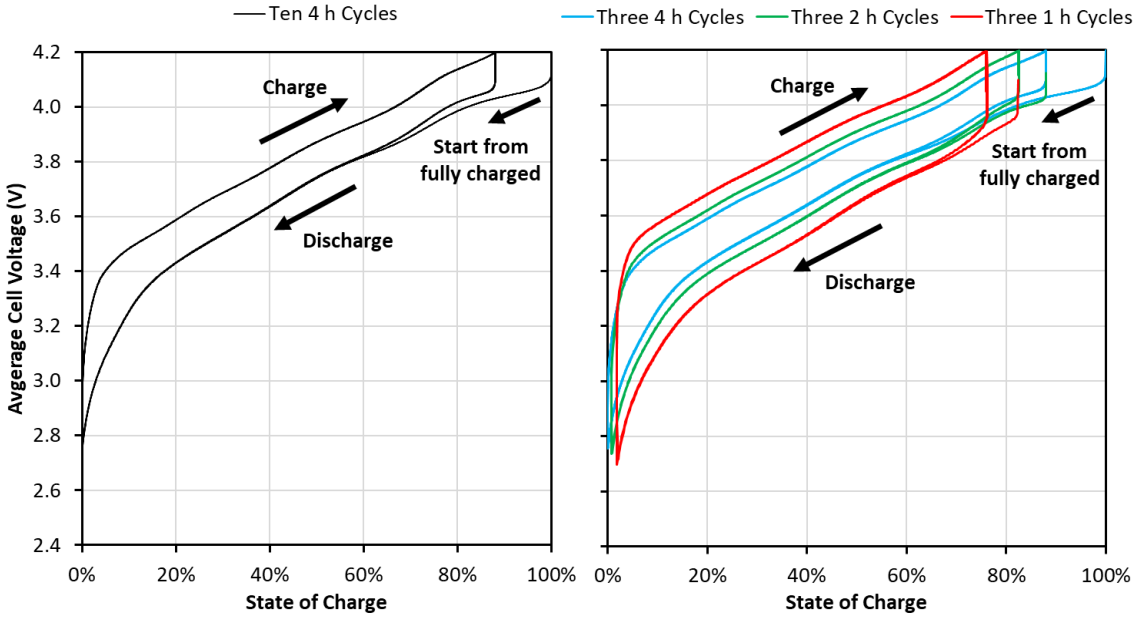


Figure 4.10 Superimposed voltage profiles measured during the coulomb counting verification test (left) and a sample SCP test sequence (right).

4.4.3. Test Parameters

The SCP test is governed by a set of test parameters which control each step in the test protocol. Table 4.5 lists the complete set of test parameters applied to the SCP tests, including CP setpoints, cell voltage limits, temperature safety limits, TMS setpoints, and temperature control setpoints. Some test parameters must be defined for each individual battery pack, power rate, or TMS, while others are applied universally.

The CP setpoints listed in Table 4.5 are determined empirically for each battery by iterating the CP setpoint until the desired discharge duration (i.e. 4 h, 2 h, or 1 h) is achieved within about 2 %. For Model3-19 and Bolt-18 and, the CP setpoint is determined with the AL configuration and then applied to both the AL and PA tests for consistency. The cell voltage limits listed in Table 4.5 are the same as those assigned for the baseline capacity test in Section 4.3. A 55.0 °C high-temperature safety limit is also applied so that tests are

interrupted well in advance of a battery approaching the threshold for thermal runaway, as discussed in Section 2.6.6.

Table 4.5 Selected SCP test parameters applied to five EV battery packs.

Test Parameter	Model3-19	Bolt-18	i3-15	Leaf-12	Lishen-12
4 h CP setpoint (kW)	9.5	14.0	4.3	4.5	8.6
2 h CP setpoint (kW)	17.3	26.3	8.4	8.7	16.9
1 h CP setpoint (kW)	30.8	47.0	16.1	16.2	32.8
Upper cell voltage limit (V)	4.20	4.20	4.20	4.20	3.55
Lower cell voltage limit (V)	2.50	2.50	2.50	2.50	2.50
High-temperature safety limit (°C)	55.0	55.0	55.0	55.0	55.0
PA-TMS setpoint (°C)	20.0	20.0	20.0	20.0	20.0
AL-TMS setpoint (°C)	30.0	30.0	N/A	N/A	N/A
Temperature control setpoint for PA tests (°C)	30.0	30.0	30.0	30.0	30.0
Temperature control setpoint for AL tests (°C)	35.0	35.0	N/A	N/A	N/A

The PA-TMS setpoint is the ambient air temperature of the test laboratory, which is maintained near a nominal 20 °C during testing. Since liquid-cooled batteries will experience smaller temperature changes than passive-cooled batteries, 30 °C is used for the AL-TMS setpoint such that battery temperatures remain at or above 30 °C throughout the AL tests. This is an appropriate temperature setpoint since it balances accelerated degradation rates at higher temperatures with impeded power capability at lower temperatures, as discussed in Section 2.5.2. The 30 °C AL-TMS setpoint also ensures a minimum 10 °C temperature differential between the liquid entering the radiator/fan assembly and the 20 °C ambient air, which enables sufficient heat rejection without requiring a more complex compressor-based system. The thermostatic temperature controller of the customized AL-TMS is set to 31 °C to achieve a resting battery temperature of 30 °C, accounting for heat losses in the liquid lines.

The selected T_{ctrl} value has significant implications for the test results, since a lower T_{ctrl} will result in lower battery temperatures and longer cooldown periods, and vice versa. An

appropriate T_{ctrl} selection must therefore be made to balance safety with practicality. For the PA tests, $T_{\mathrm{ctrl}} = 30.0$ °C is applied, which provides a 25 °C safety differential as well as a 10 °C cooling differential to mitigate the asymptotic behaviour of natural convection. For the AL tests, $T_{\mathrm{ctrl}} = 35.0$ °C is applied, which provides a 20 °C safety differential and a 5 °C cooling differential. The AL temperature differentials are smaller compared to PA, but this is acceptable given the significantly greater convection coefficient of AL compared to PA.

4.5. Performance Evaluation

Second-life batteries in energy arbitrage must optimize discharging revenues over charging costs. The SCP tests should therefore be evaluated in terms of appropriate performance metrics that impact this economic relationship during second-life service. Table 4.6 lists three electrical performance metrics and four thermal performance metrics selected for test evaluation, along with the symbol assigned to each metric. The table also summarizes the battery design aspect that each metric evaluates, as well as the corresponding value each design aspect provides for energy arbitrage.

Table 4.6 Primary performance metrics used to evaluate SCP test results.

Performance Metric	Symbol	Design Aspect	Value for Energy Arbitrage
Module energy density (Wh/L)	$\bar{E}_v$	High energy storage capacity	Generate more revenue per discharge for a given space
Energy utilization ratio (%)	ζ	Fast charging and discharging	Quickly capitalize on opportune electricity prices
Cycle energy efficiency (%)	η	Low energy losses	Lower charging costs and heat rejection requirements
Maximum pack temperature rise (°C)	$\Delta T_{\mathrm{high}}^{\mathrm{max}}$	Low safety risk	Avoid costly disruptions and/or damage
Average pack temperature rise (°C)	$\Delta T_{\mathrm{high}}^{\mathrm{avg}}$	Long operational lifetime	Sustain revenues over a longer period
Average pack temperature differential (°C)	$\Delta T_{\mathrm{diff}}^{\mathrm{avg}}$	Thermal consistency	Avoid long-term divergence in cell performance
Cycle cooldown duration (h)	t_{cool}	Reliable availability	Avoid missing opportunities to generate revenue

To compare the experimental results at different power rates, the applied CP setpoint is a suitable independent variable for graphical analysis. However, since battery packs with more energy storage capacity are tested with larger CP setpoints, the applied power must be scaled to facilitate comparison of different packs. The selected scaling method is to divide each CP setpoint (in kW) by the measured discharge energy E_{dis} (in kWh) for that test, resulting in a 'power-to-energy ratio' with units of h^{-1}. For a CP discharge, this is equivalent to taking the inverse of the measured discharge duration t_{dis}.

4.5.1. Electrical Performance Metrics

Section 2.4 introduced the concepts of energy density, energy utilization ratio, and energy efficiency, which are now adopted as electrical performance metrics for this research project. The energy density $\bar{E}_v$ was defined as the ratio of battery discharge energy capacity E_{dis} to the battery volume v (Equation 2.18). The specific energy $\bar{E}_m$ was also defined as the ratio of E_{dis} to battery mass m (Equation 2.19), but this metric is typically less important for stationary applications and is therefore only considered as a point of interest in relation to the $\bar{E}_v$ results. For this research project, $\bar{E}_v$ and $\bar{E}_m$ are respectively determined based on the total module volume v_{mod} and mass m_{mod} within a given battery pack, as shown in Equations 4.2 and 4.3.

$$\bar{E}_v = \frac{E_{\mathrm{dis}}}{v_{\mathrm{mod}}} \tag{4.2}$$

$$\bar{E}_m = \frac{E_{\mathrm{dis}}}{m_{\mathrm{mod}}} \tag{4.3}$$

The modules provide a more meaningful comparison of $\bar{E}_v$ and $\bar{E}_m$ than pack-level values due to the inconsistency among the different packs in terms of the shape of their housings well as their balance of plant including BMS, contactors, and circuitry. For each pack, v_{mod} and m_{mod} are determined by measuring an individual module in the laboratory and scaling the results by the number of modules in the pack. This requires either temporary removal of an individual module from the tested pack or acquisition of a separate individual module from the same EV battery pack design.

In addition to the calculated $\bar{E}_v$ and $\bar{E}_m$, Equations 4.4 and 4.5 are used to estimate the BOL energy density $\bar{E}_v^{\mathrm{BOL}}$ and BOL specific energy $\bar{E}_m^{\mathrm{BOL}}$ to facilitate comparison of battery packs at different SOH. This metrics estimate the $\bar{E}_v$ and $\bar{E}_m$ each pack would exhibit at a common 100 % SOH. The measured v_{mod} and m_{mod} are also used with Equation 4.6 to calculate module mass density ρ_{mod} as an additional metric for comparing different module designs.

$$\bar{E}_v^{\mathrm{BOL}} = \frac{\bar{E}_v}{\mathrm{SOH}} \tag{4.4}$$

$$\bar{E}_m^{\mathrm{BOL}} = \frac{\bar{E}_m}{\mathrm{SOH}} \tag{4.5}$$

$$\rho_{\mathrm{mod}} = \frac{m_{\mathrm{mod}}}{v_{\mathrm{mod}}} \tag{4.6}$$

The energy utilization ratio ζ was defined in Equation 2.25 as the ratio of E_{dis} to the theoretical maximum work output w_{rev} . Since w_{rev} is an unobtainable theoretical limit, it will be approximated by the results of the baseline capacity test $E_{\mathrm{dis}}^{\mathrm{CCCV}}$ as shown in Equation 4.7. While slower CC rates would provide a more accurate approximation for w_{rev}, the 4 h CC rate applied in the baseline capacity tests is adequate for the comparative purposes of this research project. In industry, a second-life battery may be purchased based on its rated discharge energy and SOH, but ζ quantifies the percentage of this energy that can actually be delivered when the battery is cycled at a given power rate.

$$\zeta = \frac{E_{\mathrm{dis}}}{E_{\mathrm{dis}}^{\mathrm{CCCV}}} \times 100\ \% \tag{4.7}$$

It will also prove useful to normalize the ζ results to the 4 h value as shown in Equation 4.8, as this isolates the result from the impacts of the CV charge. This gives the ‘normalized energy utilization ratio’ ζ^*.

$$\zeta^* = \frac{\zeta}{\zeta^{4\text{h}}} \times 100\ \% = \frac{E_{\text{dis}}}{E_{\text{dis}}^{4\text{h}}} \times 100\ \% \tag{4.8}$$

The cycle energy efficiency η was defined in Equation 2.21 as the ratio of E_{dis} to the charge energy E_{chg}. This is restated in Equation 4.9 for emphasis. Since both E_{dis} and E_{chg} are measured during the SCP tests, η can be calculated for a given test cycle. Note that the measured E_{dis} and E_{chg} do not account for any energy consumed by the AL-TMS, as this research project is focused specifically on battery performance.

$$\eta = \frac{E_{\text{dis}}}{E_{\text{chg}}} \times 100\ \% \tag{4.9}$$

As was done with ζ, the the η results can also be normalized to the 4 h value as shown in Equation 4.10 to show how η changes with increased power rate. This gives the 'normalized cycle energy efficiency' η^*.

$$\eta^* = \frac{\eta}{\eta^{4\text{h}}} \times 100\ \% \tag{4.10}$$

Voltage vs SOC charts were introduced in Section 2.4 as a technique for graphical evaluation of ζ and η. This technique is modified for evaluating the SCP tests using the superimposed voltage profile method presented in Section 4.4.2. An example of this is illustrated in Figure 4.11, which shows superimposed average cell voltage profiles measured during 4 h and 1 h SCP tests (extracted from the Model3-19 test results). The red, blue, and green areas show the three distinct ways in which energy utilization is impacted by the power rate, while the voltage gaps between the discharge and charge profiles near mid-SOC show how energy efficiency is impacted by power rate (concepts discussed in Section 2.4). This novel evaluation method will be applied in Chapter 5 to explore how the unique voltage characteristics of the five EV battery packs impact their electrical performance at different power rates.

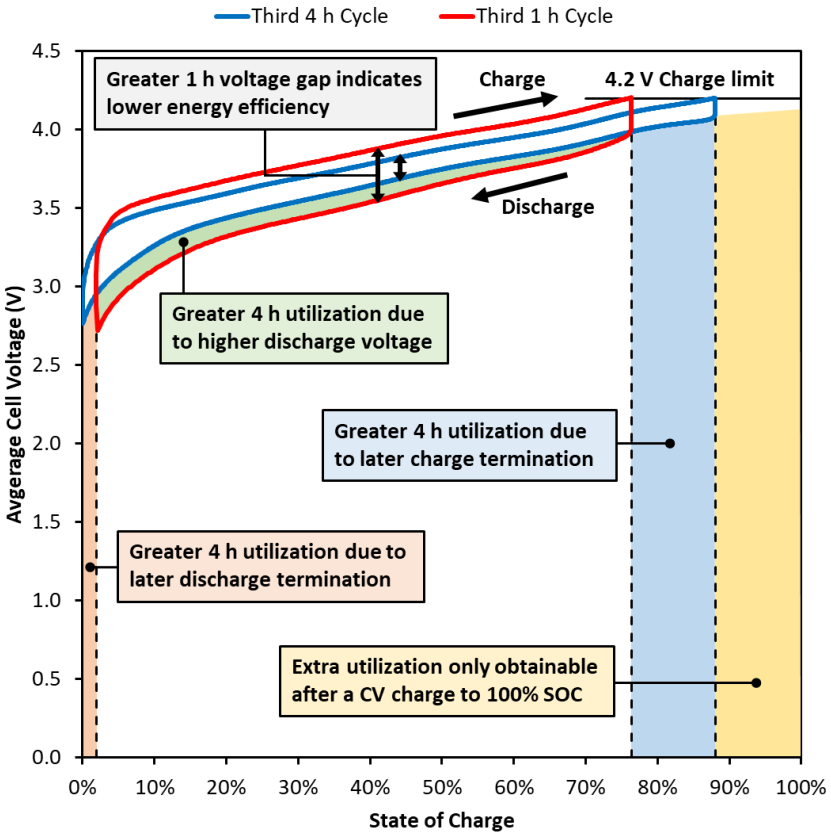


Figure 4.11 Example of graphical evaluation of energy utilization and energy efficiency at different power rates.

The red, blue, and green areas in Figure 4.11 can also be quantified to compare the sources of lost energy utilization for different batteries. The mathematical definitions of these three areas are respectively stated in Equations 4.11, 4.12, and 4.13, where 'xh' refers to either a 2 h or a 1 h rate being evaluated relative to a 4 h rate. The red area is defined as the 'discharge truncation energy' E_{DT}; the blue area is defined as the 'charge truncation energy' E_{CT}; and the green area is defined as the 'voltage depression energy' E_{VD}. Each of these quantities is expressed as an integral of the V vs SOC curves in Figure 4.11, scaled by the total coulombic capacity Q of the battery under test. The sum of E_{DT}, E_{CT}, and E_{VD} is equal to the difference between the discharge energy E_{dis} and the 4 h discharge energy $E_{\mathrm{dis}}^{4\mathrm{h}}$, as stated in Equation 4.14.

$$E_{\mathrm{DT}} = Q \int_{\mathrm{SOC}_{\mathrm{min}}^{4\mathrm{h}}}^{\mathrm{SOC}_{\mathrm{min}}^{\mathrm{xh}}} V_{\mathrm{dis}}^{4\mathrm{h}} \mathrm{dSOC} \tag{4.11}$$

$$E_{\mathrm{CT}} = Q \int_{\mathrm{SOC}_{\mathrm{max}}^{\mathrm{xh}}}^{\mathrm{SOC}_{\mathrm{max}}^{4\mathrm{h}}} V_{\mathrm{dis}}^{4\mathrm{h}} \mathrm{dSOC} \tag{4.12}$$

$$E_{\mathrm{VD}} = Q \int_{\mathrm{SOC}_{\mathrm{min}}^{\mathrm{xh}}}^{\mathrm{SOC}_{\mathrm{max}}^{\mathrm{xh}}} \left(V_{\mathrm{dis}}^{4\mathrm{h}} - V_{\mathrm{dis}}^{\mathrm{xh}}\right) \mathrm{dSOC} \tag{4.13}$$

$$E_{\mathrm{dis}}^{4\mathrm{h}} - E_{\mathrm{dis}} = E_{\mathrm{DT}} + E_{\mathrm{CT}} + E_{\mathrm{VD}} \tag{4.14}$$

When working with experimental data collected at a fixed data sampling time interval Δt, Equations 4.15 through 4.17 provide practical calculations for E_{DT}, E_{CT}, and E_{VD}. Note that these equations assume a negative discharge current $I_{\mathrm{dis}} < 0$. The calculations require identification of the 4 h discharge time interval i corresponding to the minimum and maximum SOC values reached at each power rate.

$$E_{\mathrm{DT}} = -\sum_{i=i_{\mathrm{minSOC}}^{4\mathrm{h}}}^{i_{\mathrm{minSOC}}^{\mathrm{xh}}} I_{\mathrm{dis},i}^{4\mathrm{h}} V_{\mathrm{dis},i}^{4\mathrm{h}} \Delta t \tag{4.15}$$

$$E_{\mathrm{CT}} = -\sum_{i=i_{\mathrm{maxSOC}}^{\mathrm{xh}}}^{i_{\mathrm{maxSOC}}^{4\mathrm{h}}} I_{\mathrm{dis},i}^{4\mathrm{h}} V_{\mathrm{dis},i}^{4\mathrm{h}} \Delta t \tag{4.16}$$

$$E_{\mathrm{VD}} = E_{\mathrm{dis}}^{4\mathrm{h}} - E_{\mathrm{dis}} - E_{\mathrm{DT}} - E_{\mathrm{CT}} \tag{4.17}$$

To compare the E_{DT}, E_{CT}, and E_{VD} results for different battery packs, the values should be evaluated relative to the 4 h discharge energy $E_{\mathrm{dis}}^{4\mathrm{h}}$ of each pack as shown in Equations 4.18 through 4.20. This produces a 'discharge truncation ratio' ω_{DT}, 'charge truncation ratio' ω_{CT}, and 'voltage depression ratio' ω_{VD}. Collectively, these three metrics will be referred to as the 'unutilized energy components' for a higher power rate relative to a 4 h rate.

$$\omega_{\mathrm{DT}} = \frac{E_{\mathrm{DT}}}{E_{\mathrm{dis}}^{4\mathrm{h}}} \tag{4.18}$$

$$\omega_{\mathrm{CT}} = \frac{E_{\mathrm{CT}}}{E_{\mathrm{dis}}^{4\mathrm{h}}} \tag{4.19}$$

$$\omega_{\mathrm{VD}} = \frac{E_{\mathrm{VD}}}{E_{\mathrm{dis}}^{4\mathrm{h}}} \tag{4.20}$$

Two final electrical performance metrics will prove useful for bridging electrical and thermal performance. As described in Section 2.4.3, the difference between E_{chg} and E_{dis} gives the total irreversible heat generated during the cycle. Battery temperatures will depend on the amount of heat generated per unit volume, the specific heat capacity, the mass density, and the rate of heat dissipation. In order to quantify and compare the heat generation of the five EV battery packs, the 'cycle volumetric heat generation' $\bar{q}_v$ is defined according to Equation 4.21. Note that $\bar{q}_v$ can be defined in terms of the measured E_{chg}, E_{dis}, and v_{mod}, or in terms of the calculated η and $\bar{E}_v$.

$$\begin{aligned} \bar{q}_v &= \frac{E_{\mathrm{chg}} - E_{\mathrm{dis}}}{v_{\mathrm{mod}}} \\ &= \frac{E_{\mathrm{dis}}\left(\frac{1}{\eta} - 1\right)}{v_{\mathrm{mod}}} \\ &= \bar{E}_v\left(\frac{1}{\eta} - 1\right) \end{aligned} \tag{4.21}$$

By scaling $\bar{q}_v$ by the combined durations of discharge t_{dis} and charge t_{chg}, the 'average volumetric heat generation rate' $\dot{\bar{q}}_v$ of the cycle is defined by Equation 4.22. Since $\eta = \frac{t_{\mathrm{dis}}}{t_{\mathrm{chg}}}$ and $E_{\mathrm{dis}} = P t_{\mathrm{dis}}$ apply for an SCP cycle with power setpoint P, $\dot{\bar{q}}_v$ can be defined in terms of $\bar{E}_v$, t_{dis}, and η or in terms of P, v_{mod}, and η.

$$\dot{\bar{q}}_v = \frac{\bar{q}_v}{t_{\text{dis}} + t_{\text{chg}}} = \frac{\bar{E}_v}{t_{\text{dis}}}\left(\frac{1-\eta}{1+\eta}\right) = \frac{P}{v_{\text{mod}}}\left(\frac{1-\eta}{1+\eta}\right) \tag{4.22}$$

Though $\bar{q}_v$ and $\dot{\bar{q}}_v$ are determined from electrical measurements, they have a direct impact on thermal performance. These two metrics therefore serve to bridge the electrical and thermal aspects of battery performance, which will be explored in Chapter 5.

4.5.2. Thermal Performance Metrics

Section 2.6 introduced the various aspects of battery thermal performance and deduced that $T_{\text{high}}^{\text{max}}$, $T_{\text{high}}^{\text{avg}}$, and $\Delta T_{\text{low}}^{\text{high}}$ should be used as metrics to respectively evaluate thermal safety risks, thermal impacts on degradation rates, and pack temperature gradients. These are now adopted as thermal performance metrics for this research project, with appropriate modifications. Recall that $T_{\text{high}}^{\text{max}}$ and $T_{\text{high}}^{\text{avg}}$ are respectively the maximum and average temperatures over a given period at the measured pack location exhibiting the highest temperatures, while $\Delta T_{\text{low}}^{\text{high}}$ is the average temperature differential over a given period between the two measured pack locations exhibiting the highest and lowest temperatures.

To account for the different PA-TMS and AL-TMS setpoints, $T_{\text{high}}^{\text{max}}$ and $T_{\text{high}}^{\text{avg}}$ are evaluated relative to the average measured temperature T_{∞}^{avg} of the TMS fluid (i.e. ambient air for PA tests or liquid supply for AL tests), as shown in Equations 4.23 and 4.24. This creates two new thermal performance metrics: the 'maximum pack temperature rise' $\Delta T_{\text{high}}^{\text{max}}$ and the 'average pack temperature rise' $\Delta T_{\text{high}}^{\text{avg}}$. Note that since the fluid temperature T_{∞} can vary slightly during a given test, Equation 4.23 uses $T_{\infty}^{\text{stepavg}}$ to signify that the average is assessed over either the CP discharge step or the CP charge step depending on which step gives the greater $\Delta T_{\text{high}}^{\text{max}}$. All other temperature averages are assessed over the entire third cycle of the given SCP test (including, discharge, charge, and both cooldown periods), while $T_{\text{high}}^{\text{max}}$ is the instantaneous maximum of the entire third cycle.

$$\Delta T_{\text{high}}^{\text{max}} = T_{\text{high}}^{\text{max}} - T_{\infty}^{\text{stepavg}} \tag{4.23}$$

$$\Delta T_{\text{high}}^{\text{avg}} = T_{\text{high}}^{\text{avg}} - T_{\infty}^{\text{avg}} \tag{4.24}$$

For this research project, the pack temperature differential $\Delta T_{\text{diff}}^{\text{avg}}$ is defined by Equation 4.25, where $T_{\text{low}}^{\text{avg}}$ is the average temperature (assessed over the complete third cycle of the test) at the measured pack location exhibiting the lowest temperatures. This metric is used to assess the average temperature gradient across a given battery pack for a given test. The 'average low temperature rise' $\Delta T_{\text{low}}^{\text{avg}}$ is also evaluated according to Equation 4.26 so that $\Delta T_{\text{low}}^{\text{avg}}$ and $\Delta T_{\text{high}}^{\text{avg}}$ can be compared across different packs and TMS types.

$$\Delta T_{\text{diff}}^{\text{avg}} = T_{\text{high}}^{\text{avg}} - T_{\text{low}}^{\text{avg}} \tag{4.25}$$

$$\Delta T_{\text{low}}^{\text{avg}} = T_{\text{low}}^{\text{avg}} - T_{\infty}^{\text{avg}} \tag{4.26}$$

The SCP test protocol includes mandatory cooldown periods following charge and discharge. Commercial second-life batteries in energy arbitrage may be required to undergo similar cooldown periods before they can safely dispatch power after reaching high temperatures, potentially resulting in missed energy arbitrage opportunities. The cycle cooldown duration t_{cool} quantifies the total amount of time required for the prescribed cooldown periods following discharge $t_{\text{cool}}^{\text{dis}}$ and charge $t_{\text{cool}}^{\text{chg}}$ according to the SCP test protocol, as stated in Equation 4.27. This provides a fourth thermal performance metric to evaluate the impact of battery cooling rates on economic availability. All durations use units of h.

$$t_{\text{cool}} = t_{\text{cool}}^{\text{dis}} + t_{\text{cool}}^{\text{chg}} \tag{4.27}$$

The total cycle duration t_{cyc} can also be calculated by combining t_{cool} with the measured durations of discharge t_{dis} and charge t_{chg}, as shown in Equation 4.28. The calculation scales the measured t_{dis} and t_{chg} based on the nominal discharge duration t_{rate} prescribed for each SCP test (i.e. 4 h, 2 h, or 1 h) such that $t_{\text{dis}} = 4.00$ h for each 4 h test, $t_{\text{dis}} = 2.00$

h for each 2 h test, and $t_{\mathrm{dis}} = 1.00$ h for each 1 h test. This minor correction ensures that t_{cyc} is comparable for all SCP tests despite some measured t_{dis} values being slightly above or below the target value. It is assumed that the implied change in power rate would not be significant enough to impact the measured battery temperatures and corresponding cooldown durations.

$$t_{\mathrm{cyc}} = t_{\mathrm{cool}} + \left(t_{\mathrm{dis}} + t_{\mathrm{chg}}\right)\frac{t_{\mathrm{rate}}}{t_{\mathrm{dis}}} \tag{4.28}$$

To assess the practical implications of t_{cyc}, Equation 4.29 defines the 'achievable cycling frequency' f_{cyc} (in cycles/day). This novel metric compares a 24 h period to the total time required for a battery to complete an SCP test cycle at a given power rate, including the required cooldown periods. The resulting value of f_{cyc} provides an estimate for the maximum number of complete cycles that a battery can achieve in a 24 h period if the cooldown periods are enforced. In practice, battery cycling frequency and depth of discharge depend strongly on electricity market price signals, but f_{cyc} provides a theoretical upper limit that a given EV battery pack design could achieve in deep-discharge operation.

$$f_{\mathrm{cyc}} = \frac{24}{t_{\mathrm{cyc}}} \tag{4.29}$$

Section 2.6.4 described the three main modes of battery heat dissipation (i.e. conduction, convection, and radiation) and derived a simplified expression for cooldown temperature as a function of time, according to 'Newton cooling' (Equation 2.61). This expression is adapted to the SCP test in Equation 4.30, showing how T_{high} will decrease from its maximum value $T_{\mathrm{high}}^{\mathrm{max}}$ at the end of discharge or charge towards the TMS temperature $T_{\infty}^{\mathrm{avg}}$ based on a cooling time constant τ.

$$T_{\mathrm{high}} = T_{\infty}^{\mathrm{avg}} + (T_{\mathrm{high}}^{\mathrm{max}} - T_{\infty}^{\mathrm{avg}})\mathrm{e}^{-\frac{t}{\tau}} \tag{4.30}$$

The two cooldown durations $t_{\mathrm{cool}}^{\mathrm{dis}}$ and $t_{\mathrm{cool}}^{\mathrm{chg}}$ of the SCP cycle are each determined by the temperature control setpoint, which terminates each cooldown period when $T_{\mathrm{high}} < T_{\mathrm{ctrl}}$.

A τ value can therefore be calculated for each cooldown period by rearranging Equation 4.30. Rather than calculate and average two τ values for each test, a single τ value can be calculated using t_{cool} and the 'cycle cooldown temperature drop' ΔT_{cool} defined in Equation 4.31. This expression sums the two temperature drops that occur during the two cooldown periods.

$$\Delta T_{\text{cool}} = T_{\text{high}}^{\text{max}}\big|_{\text{dis}} - T_{\text{ctrl}} + T_{\text{high}}^{\text{max}}\big|_{\text{chg}} - T_{\text{ctrl}} \tag{4.31}$$

Equation 4.32 defines the average cooling time constant of the SCP cycle based on t_{cool} and ΔT_{cool}. For a given battery pack, τ should be dependent on the physical properties of the battery and surrounding environment, and should therefore be independent of power rate. This means that consistent τ results should be expected for different tests applied to a given battery pack. Note that Equation 4.32 only produces a value if $\Delta T_{\text{cool}} > 0$ (i.e. if a cooldown period takes place).

$$\tau = \frac{t_{\text{cool}}}{2 \ln\left[\dfrac{\frac{1}{2}\Delta T_{\text{cool}} + T_{\text{ctrl}} - T_{\infty}^{\text{avg}}}{T_{\text{ctrl}} - T_{\infty}^{\text{avg}}}\right]} \tag{4.32}$$

It should be emphasized that Equation 4.32 is a simplified analysis of battery pack heat dissipation. It does not account for heat diffusion within the battery pack, nor does it account for the temperature dependence of the natural convection coefficient (discussed in Section 2.6). However, the calculated τ value can still be used as a simple metric to evaluate the cooldown rates of different EV battery pack designs for the comparative purposes of Chapter 5. A more detailed analysis of heat diffusion and heat dissipation in EV battery packs will be presented in Chapter 7.

4.6. Chapter Summary

Chapter 4 has presented an experimental approach for testing the electrical and thermal performance of repurposed EV battery packs in second-life service. Five acquired EV battery packs have been described, featuring a diverse range of electrochemical and

physical design parameters. To evaluate the performance of these five battery packs in a common test regime, a suitable test protocol has been proposed consisting of symmetrical CP cycling at three different power rates. Importantly, the three tests are based on discharge duration rather than C rate since discharge duration provides a more equitable performance comparison for second-life batteries at different SOH levels. A custom AL-TMS has also been described to enable comparison of liquid-cooled and passive-cooled performance. A set of electrical and thermal performance metrics has been proposed as a means of interpreting the measured experimental data through a practical engineering lens.

While some of the described methods are adopted from existing theory and literature, most are either modified in novel ways to suit the research objectives or newly created to advance experimental practice. The proposed test protocols are based on existing test methodologies, but feature a number of modifications which facilitate comparative analysis of second-life batteries. The method of superimposing measured voltage profiles for different power rates on a voltage vs SOC plot is a novel technique which provides valuable qualitative insights into electrical performance. These qualitative insights can also be quantified using the unutilized energy components ω_{DT}, ω_{CT}, and ω_{VD}, which are novel metrics used to assess the different ways in which battery energy utilization declines at higher power rates. The cycle volumetric heat generation $\bar{q}_v$ and average volumetric heat generation rate $\dot{\bar{q}}_v$ are also novel metrics used to quantify the waste heat generated during an SCP cycle based on electrical measurements, which has direct implications for thermal performance. The achievable cycling frequency f_{cyc} is another novel metric used to evaluate the practical implications of battery cooldown requirements during SCP cycling.

Though the designed SCP test is a straightforward experiment consisting of discharge and charge between fixed voltage limits, the variety of test batteries, applied power rates, temperature sensor locations, and TMS types yields an abundance of experimental data with numerous opportunities for comparative analysis. Chapter 5 will use this experimental data to generate practical insights and analytical tools for the benefit of the second-life battery industry.

Chapter 5 COMPARATIVE ANALYSIS OF ELECTRICAL AND THERMAL PERFORMANCE FOR FIVE SECOND-LIFE BATTERY PACKS

Chapter 4 described a set of experimental methods for evaluating the electrical and thermal performance of second-life battery packs. Chapter 5 will now present the experimental results obtained from the described tests and conduct detailed analyses to compare the performance of the five tested EV battery packs. Since second-life batteries will be acquired at various SOH levels and degrade further throughout second-life service, Section 5.6 gives consideration to how the established performance metrics are impacted by degradation. Section 5.7 will then demonstrate a novel technique for converting the performance metrics into a dimensionless form which facilitates the ranking of different EV battery pack designs by expected performance in second-life applications.

Portions of this chapter have been published in the following two journal articles:

> C. White, L. G. Swan, Pack-level performance of electric vehicle batteries in second-life electricity grid energy services, Journal of Energy Storage 57 (2023) 106265. [352]
>
> C. White, B. Thompson, L.G. Swan, Comparative performance study of electric vehicle batteries repurposed for electricity grid energy arbitrage, Applied Energy 288 (2021), 116637. [353]

Chris White is the principal researcher and author for both articles, which were completed over the course of this research project. The work is reprinted here under the terms of the license agreement with Elsevier, which is provided in Appendix D. Some aspects of the work have been expanded upon for publication in this thesis.

5.1. Baseline Capacity

The results of the baseline capacity tests described in Section 4.3 are listed in Table 5.1, including the measured 4 h discharge energy capacity $E_{\text{dis}}^{\text{CCCV}}$ following a CCCV charge and the calculated SOH based on Equation 4.1. For Model3-19 and Bolt-18, the results are for the liquid-cooled case since this is the intended mode of operation for these packs. The manufacturer rated energy capacity $E_{\text{dis}}^{\text{spec}}$ for each pack is also restated from Table 4.1 for reference. The 22 kWh manufacturer rating for the BMW i3 battery is scaled by 75 % in

Table 5.1 since i3-15 is tested with six of its eight original modules, as explained in Section 4.1.1.

Table 5.1 Results of baseline capacity tests.

	Model3-19	Bolt-18	i3-15	Leaf-12	Lishen-12
Result	**AL**	**AL**	**PA**	**PA**	**PA**
Rated energy capacity (kWh)	50	60	16.5	24	38
Baseline discharge energy output (kWh)	43.4	59.2	17.4	18.3	34.5
Calculated SOH (%)	86.8	98.7	105.5	76.3	90.8

The results in Table 5.1 show that Leaf-12 has undergone substantial degradation prior to testing, but still retains 76.3 % of its original energy capacity and can therefore function normally within typical voltage and current bounds. Lishen-12 has retained 90.8 % of its original energy capacity despite sharing the same build year as Leaf-12, indicating either lighter usage or lower degradation rate. Model3-19, Bolt-18, and i3-15 were relatively new and only lightly used at the time of acquisition, but Model3-19 has lower SOH due to previous experimental testing. Note that the 105.5 % SOH result for i3-15 indicates underrating by the manufacturer. It will therefore be assumed that i3-15 has an SOH of 100%. Overall, the calculated SOH values in Table 5.1 indicate that all battery samples are fully functional and represent lightly-worn to moderately-worn EV batteries.

Since the EV industry is still in its early years, heavily-worn EV battery packs were not common when these packs were acquired between 2015 and 2020. The calculated SOH results for Bolt-18 and i3-15 in particular are not representative of the aging levels that are expected for future second-life batteries. However, it will be demonstrated in Section 5.6 that most of the established performance metrics are fairly insensitive to moderate changes in SOH. Furthermore, Sections 5.3 and 5.4 will demonstrate that the five EV battery packs vary widely in terms of performance, which means that a small degree of SOH sensitivity does not have significant consequences for comparative analyses. The acquired packs are therefore sufficient for demonstrating the relative performance of different EV battery pack designs in second-life applications.

5.2. Voltage Profiles

Sections 2.2 and 2.3 described the electrochemical concepts that give rise to a wide range of lithium-ion cell voltage characteristics, both for theoretical reversible conditions and practical operating conditions. This section will apply these concepts to explain the measured voltage characteristics of the five tested EV battery packs.

5.2.1. Cell Characteristics

The average cell voltage profiles measured during the 4 h CC discharge of the baseline capacity test provide a means of comparing the voltage characteristics of the five EV battery designs over the complete SOC range. These discharge voltage profiles are plotted in Figure 5.1 All batteries begin the discharge at 100 % SOC following the CCCV charge and reach 0 % SOC at the end of discharge. As explained in Section 4.3, 0 % SOC is defined as the point when any cell in the pack first reaches 2.5 V during a 4 h discharge. The average cell voltage profiles do not reach 2.5 V in Figure 5.1 since discharge is terminated based on the minimum cell voltage.

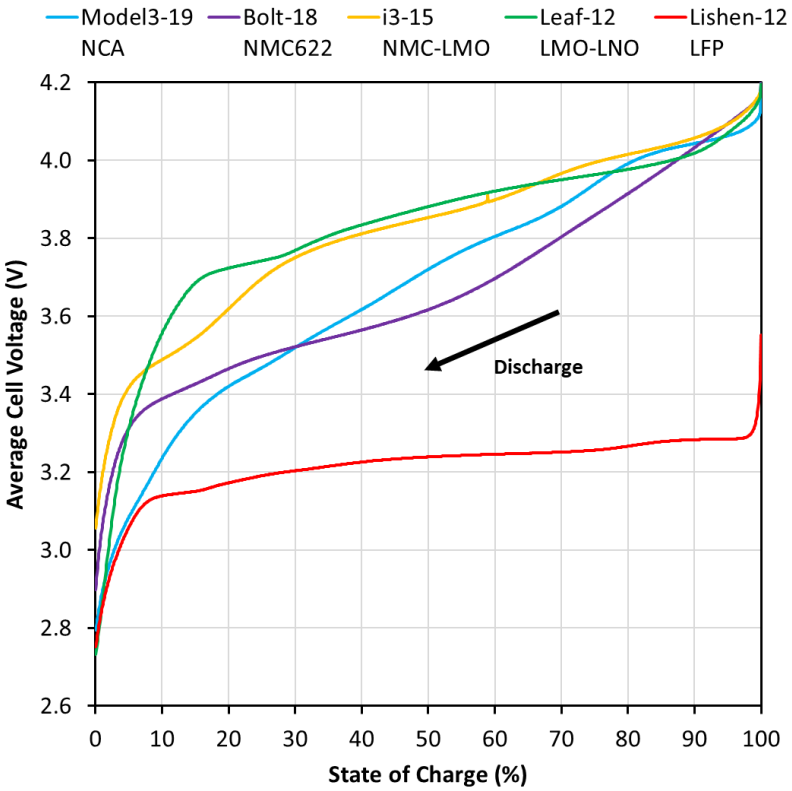


Figure 5.1 Average cell voltage profiles of five EV battery packs measured during a 4 h CC discharge following a CCCV charge.

Though the cell chemistry of the EV battery packs is nominally specified by each manufacturer, the specifications can be examined in greater detail by comparing the five voltage profiles in Figure 5.1 to the cell voltage concepts described in Section 2.2. The Lishen-12 profile in Figure 5.1 exhibits a lower magnitude and flatter profile compared to the other batteries, as is expected for LFP chemistry. While an LFP electrode is expected to give a completely flat voltage profile over most of the SOC range due to the extensive first-order phase transition (see Figure 2.18), the Lishen-12 profile in Figure 5.1 features several small voltage drops. These voltage drops are due to the graphite staging phenomena described in Section 2.2.3. All five batteries in Figure 5.1 feature a graphite negative electrode, as evidenced by the sharp voltage drop towards 0 % SOC as the graphite is emptied of Li^+. The subtler voltage characteristics of graphite staging over the full SOC range are most evident in the Lishen-12 profile, which would otherwise be completely flat. Note that the Model3-19 profile exhibits a relatively shallow voltage drop towards 0 % SOC. Section 2.2.6 described how blending with silicon can cause the graphite voltage profile to become more tapered near the delithiated state (see Figure 2.23), and the Tesla Model 3 battery is known to feature a graphite-silicon blended negative electrode.

Section 2.2.5 explained that NMC variants between NMC111 and NMC622 give a smooth voltage profile with a relatively steep slope above 50 % SOC (see Figure 2.21). The measured voltage profile for Bolt-18 (NMC622) in Figure 5.1 aligns with these expectations. In contrast, the voltage profile for Model3-19 (NCA) features the relatively bumpy profile associated with nickel-rich positive electrodes such as NCA, including the tapered slope near 100 % SOC due to lattice volume changes (explained in Section 2.2.5).

The cell manufacturer for Leaf-12 specifies the chemistry as LMO with a small amount of blended LNO. The Leaf-12 voltage profile in Figure 5.1 supports this, exhibiting the relatively high magnitude and shallow slope associated with pure LMO (see Figure 2.18), but lacking evidence of Li^+ ordering near 50 % SOC due to blending and/or degradation at 76 % SOH. The chemistry of i3-15 is reported as a blend of NMC111 and LMO. Interestingly, the i3-15 voltage profile in Figure 5.1 more closely resembles Leaf-12 (LMO dominant) than Bolt-18 (pure NMC622). The unique “double knee” feature of the i3-15 profile below 30 % SOC would be expected for a blended positive electrode material with

roughly 70 % LMO and 30 % NMC (see Figure 2.22), since LMO primarily participates in the intercalation reaction above 3.85 V vs Li meatal. It is therefore possible that i3-15 features more LMO than NMC.

Overall, Figure 5.1 shows that all five EV battery packs exhibit unique voltage characteristics, owing to the significant diversity in electrode chemistries employed across the industry. The electrochemical theories reviewed in Section 2.2 have proven useful for understanding the unique voltage characteristics of different EV batteries.

5.2.2. Response to Different Power Rates

Section 4.5.1 presented a novel technique for using measured voltage profiles to assess how energy utilization and energy efficiency are impacted by power rate (see Figure 4.11). This technique is applied to the SCP test results in Figure 5.2, where the average cell voltage profiles (both discharge and charge) measured during the third cycle of the 4 h, 2 h, and 1 h tests are superimposed in the SOC window based on coulomb counting. A visual assessment of Figure 5.2 provides a wealth of qualitative insights into how the five EV battery packs respond to different power rates.

The first insight that can be drawn from Figure 5.2 is that some batteries experience greater overpotentials than others as the power rate increases. This is especially evident when comparing the vertical gap between the 2 h and 1 h voltage profiles of Bolt-18 and i3-15, indicating a greater impact from internal resistance in Bolt-18. As illustrated previously in Figure 2.27, the impacts of increased overpotentials on battery electrical performance are fourfold:

1. It raises the voltage throughout charge, which increases the charge energy for a given depth of charge and thereby reduces the energy efficiency
2. It triggers the upper voltage limit at a lower SOC, which truncates the charge and thereby reduces the amount of energy stored in the battery prior to discharge
3. It depresses the voltage throughout discharge, which decreases the discharge energy for a given depth of discharge
4. It triggers the lower voltage limit at a higher SOC, which truncates the discharge and thereby reduces the amount of discharge energy that can be accessed

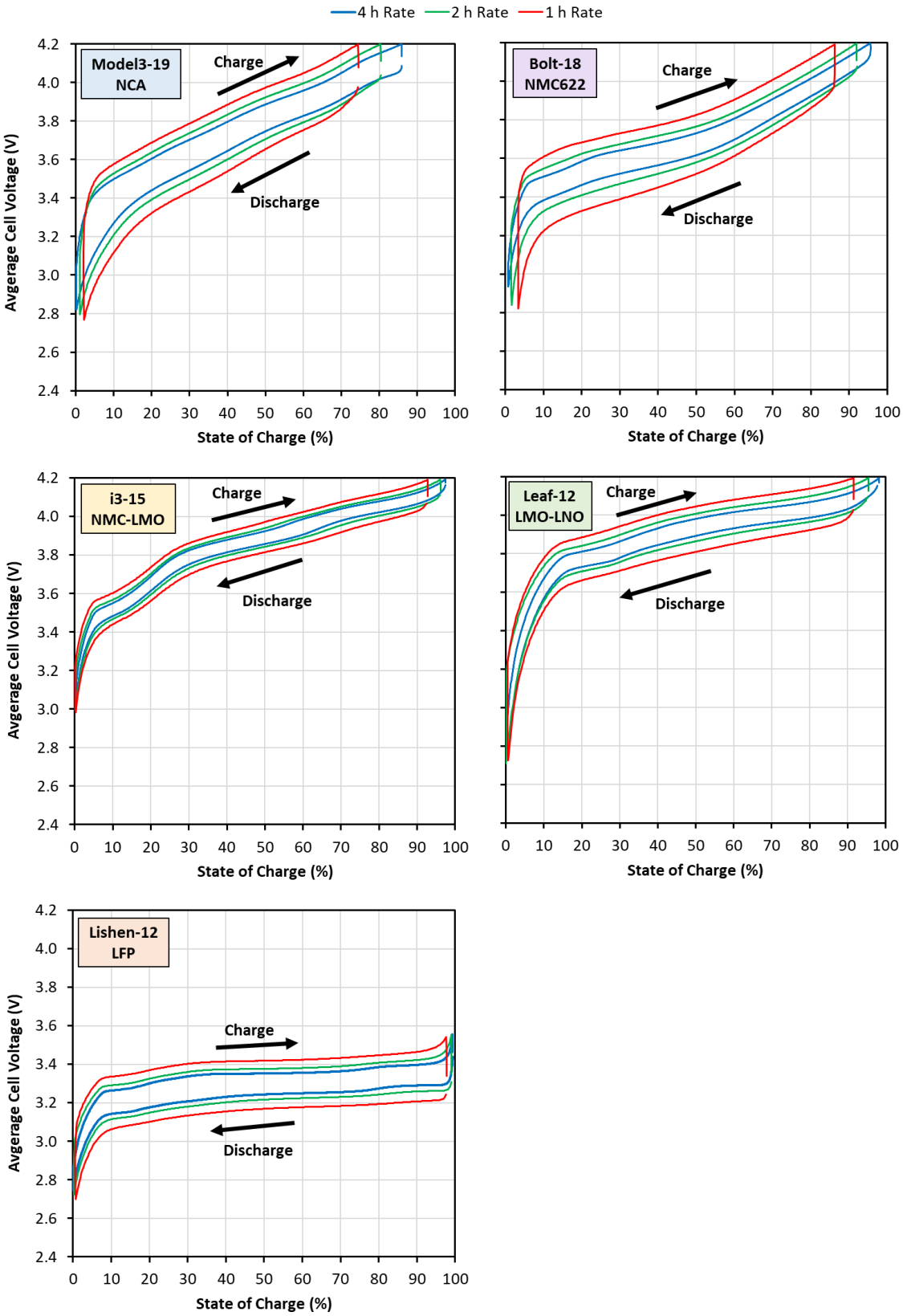


Figure 5.2 Superimposed average cell voltage profiles of five EV battery packs measured during the third cycle of 4 h, 2 h, and 1 h SCP tests.

A second insight provided by Figure 5.2 is that overpotentials are not the only factor contributing to the truncation of charge and discharge. This is especially evident when comparing Model3-19 and Lishen-12, which differ significantly in terms of charge termination points and voltage profile shapes. These two batteries exhibit similar overpotentials between the 2 h and 1 h voltage profiles, yet Lishen-12 charges to 98 % SOC at a 1 h rate while Model3-19 only charges to 74 %. The 4 h charge profile of Lishen-12 rises at a relatively low slope until it reaches > 95 % SOC (due to the first-order phase transition in LFP), at which point the voltage rises sharply to the upper limit, so greater overpotentials at higher power rates will be of little consequence below 95 % SOC. In contrast, the 4 h charge profile of Model3-19 rises at a relatively steep slope until it reaches > 75 % SOC, at which point the voltage slope tapers off for a gradual approach to the upper limit (due to the lattice volume change in nickel-rich NCA), so greater overpotentials at higher power rates can trigger the upper voltage limit at a significantly lower SOC. This comparison shows how the crystal structures of different positive electrode materials can give advantages or disadvantages for charging capacity in electricity grid services.

A third insight from Figure 5.2 is that energy utilization is more dependent on charge termination than on discharge termination. All batteries in Figure 5.2 exhibit greater rightward shifts in charge termination than leftward shifts in discharge termination as the power rate increases from 4 h to 1 h. This is because all batteries exhibit a relatively steep slope at the end of discharge, so overpotentials cause smaller horizontal SOC shifts at the end of discharge compared to the end of charge. Furthermore, charge termination takes place at higher voltage than discharge termination, so more energy is left unutilized for a given horizontal SOC shift at the end of charge compared to the end of discharge. Of course, the energy capacity that is lost to early charge termination can be regained by applying a CV charge once the upper voltage limit is reached, but this requires substantially more charge time, which may not be feasible in some electricity grid services.

A fourth insight from Figure 5.2 is that the impact of power rate on discharge energy is dependent on the upper and lower voltage limits used during cycling. Since the shape of each voltage profile changes with SOC, the overpotentials associated with a given power

rate will cause a different horizontal SOC shift as the upper and lower voltage limits are lowered or raised. This means that the electrical performance results of the SCP tests will be somewhat sensitive to the selection of voltage limits.

The insights offered by Figure 5.2 could easily be missed if a battery performance test were evaluated based solely on the measured energy results without considering the voltage profiles. The design of second-life battery systems should consider all the available EV battery types and examine how the electrical performance of each battery is affected by its overpotentials, the shape of its voltage profile, the applied power rates, and the chosen upper and lower voltage limits. The technique applied in Figure 5.2 is recommended as a tool for assessing different EV battery designs for second-life battery modelling and commercial developments.

5.2.3. Impact of Thermal Management

An examination of the discharge termination points in Figure 5.2 reveals that the three passive-cooled batteries (i3-15, Leaf-12, and Lishen-12) reach roughly the same minimum SOC at all three power rates, while the two liquid-cooled batteries (Bolt-18 and Model3-19) reach a lower minimum SOC at a 4 h rate compared to 2 h and 1 h rates. To demonstrate the impact of TMS on battery voltage profiles, Figure 5.3 compares the voltage profiles of Model3-19 and Bolt-18 measured during the AL tests (the same as those shown in Figure 5.2) and PA tests. This shows that the passive-cooled Model3-19 and Bolt-18 reach roughly the same minimum SOC at all three power rates, just like the three passive-cooled packs in Figure 5.2. It can therefore be surmised that the increased temperature rise of passive-cooled batteries at higher power rates leads to a lower internal resistance which counteracts the increased overpotentials that would otherwise result from higher currents. Enhanced heat rejection with an AL-TMS apparently prevents this attenuation of internal resistance, resulting in early discharge termination for the liquid-cooled Model3-19 and Bolt-18.

The other notable difference between the AL and PA voltage profiles can be seen at the end of charge, where the higher temperatures of the passive-cooled packs clearly mitigate the charge overpotentials compared to the liquid-cooled packs. This allows the

passive-cooled packs to operate within a wider SOC window, particularly during the 1 h test where overpotentials are greatest. This effect is especially evident for Model3-19, which implies that the AL-TMS provides significant temperature mitigation for Model3-19. Thermal performance will be evaluated in Section 5.4.

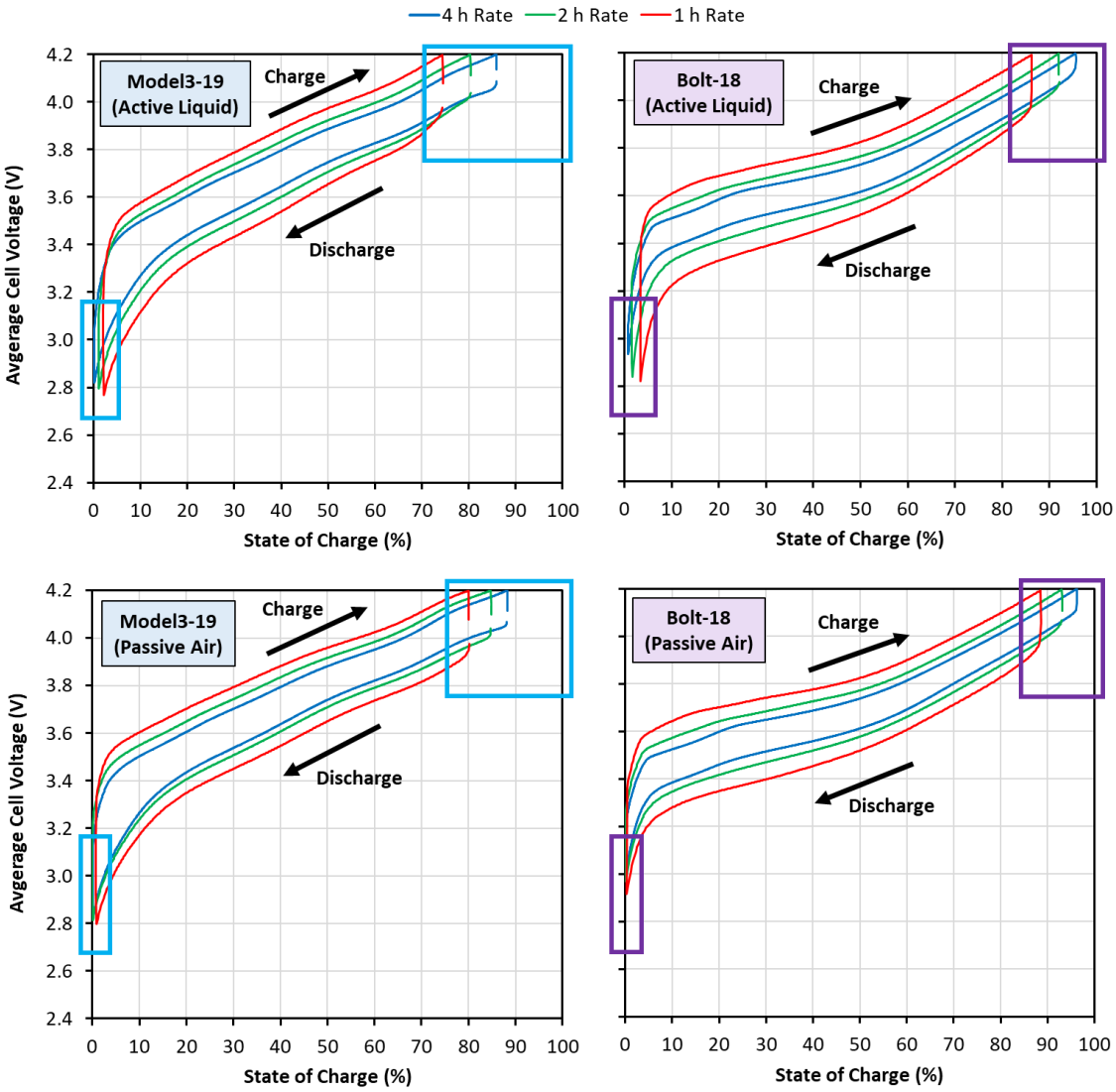


Figure 5.3 Impact of liquid cooling on superimposed average cell voltage profiles at end of discharge and end of charge.

5.2.4. Consistency

Most EV battery packs consist of hundreds or thousands of connected cells which can diverge in SOC and SOH through prolonged use. Any inconsistency among the cells within a given pack can cause some cells to reach the upper or lower voltage limits before other

cells during cycling, and thereby reduce the usable energy capacity of the pack compared to a single healthy cell. Figure 5.2 demonstrated how charge termination in particular can have a significant impact on a battery's usable energy capacity, so it is worth investigating whether cell consistency exacerbates this effect in the five tested EV battery packs.

Figure 5.4 shows the minimum, average, and maximum cell voltage profiles of the five EV battery packs during a 1 h cycle. Only the 1 h test is shown since cell-to-cell voltage variance is more prominent at higher power rates. For all five batteries, cell inconsistencies become obvious towards the end of discharge but remain relatively insignificant throughout charge. This is largely due to the fact that the cells are balanced in the charged state rather than the discharged state, which means that the cells with lowest capacity (due to variance in manufacturing or degradation rates) will reach 0 % SOC before the other cells. Another contributing factor can be identified by observing in Figure 5.2 that charging falls increasingly short of 100 % SOC as the power rate increases, while discharging approaches 0 % SOC regardless of the power rate. Cell internal resistance is highest when the electrodes approach the limits of intercalation at 0 % SOC and 100 % SOC, so it can be surmised that internal resistance increases as the cells approach the lower voltage limit but remains relatively low as the cells approach the upper voltage limit. The CP test method could also be a contributing factor, since this causes the current magnitude to be highest at the end of discharge (low voltage) and lowest at the end of charge (high voltage).

Bolt-18 and i3-15 are both near 100 % SOH, so the cell consistency shown in Figure 5.4 for these two packs does not necessarily represent what might be seen in real second-life applications where more degraded EV batteries are in use. Leaf-12 is at 76 % SOH and therefore provides a more practical example where greater cell inconsistency might be expected. Compared to the heathier packs, Leaf-12 does show more cell inconsistency towards the upper voltage limit. In the case of Lishen-12, the LFP voltage profile reaches near 100 % SOC even at a 1 h rate, meaning that cell internal resistance increases towards the end of charge, and cell inconsistency becomes more prominent. Due to the sharp rise in LFP voltage near the end of charge, some cells can reach significantly higher voltages than others if the cells are unbalanced. It proved necessary to treat Lishen-12 with a long (approximately 8 h) CV charge so the BMS could balance the cells and mitigate this effect.

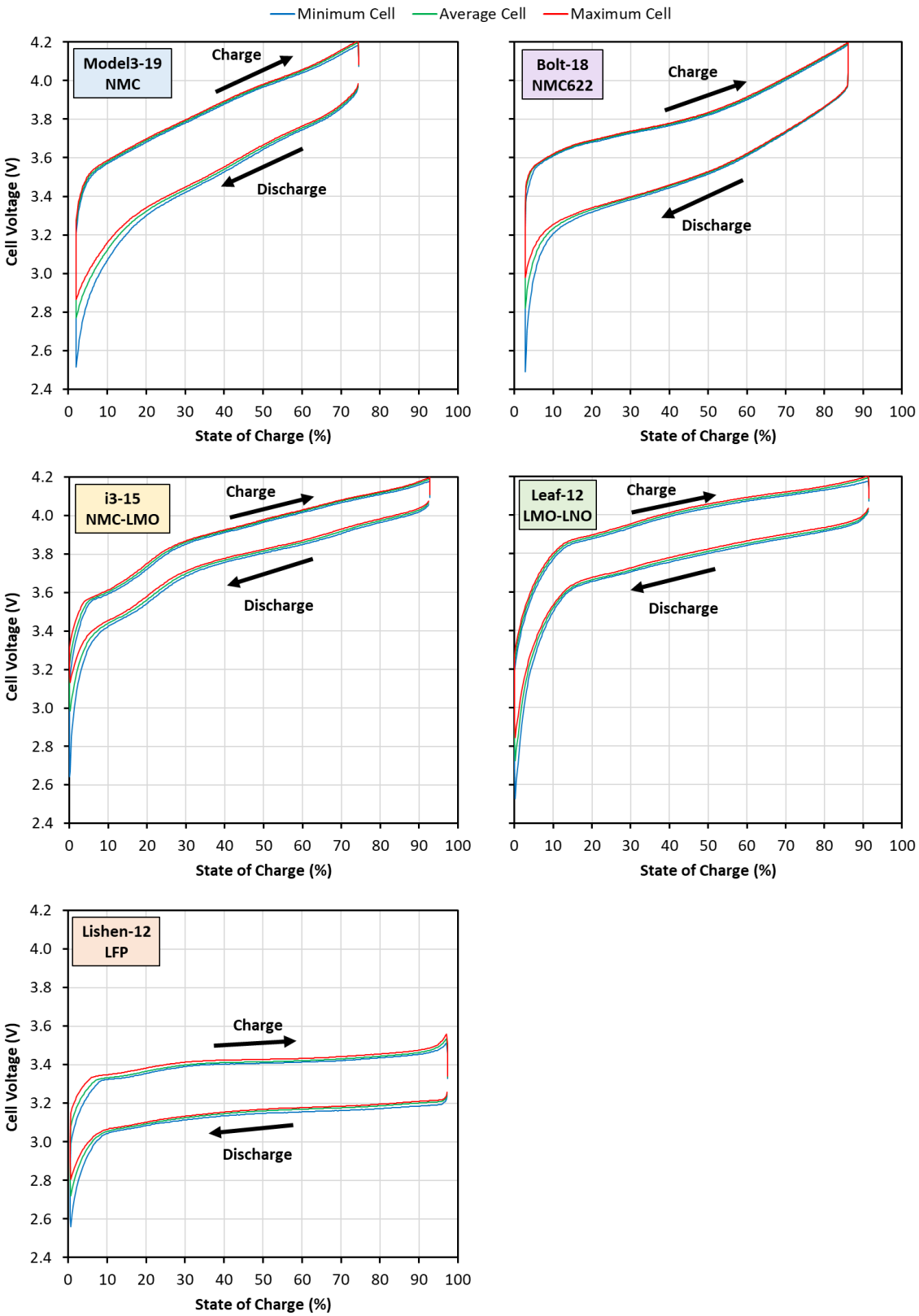


Figure 5.4 Minimum, average, and maximum cell voltage profiles of five EV battery packs measured during the third cycle of a 1 h SCP test.

Overall, Figure 5.4 confirms that the results of this study are not significantly influenced by cell consistency. Though cell voltages do diverge at the end of discharge, all cells reach the final voltage 'knee' by time the minimum cell reaches the 2.5 V lower voltage limit, meaning that little additional capacity can be discharged from any cell. Minimum and maximum cell voltages should be considered in all second-life battery research, especially in older battery packs.

5.3. Electrical Performance Results

Section 4.5.1 described a set of electrical performance metrics that can be used to evaluate EV battery packs for second-life applications. This section will present the results of the SCP tests with a focus on these electrical performance metrics. For reference, Table 5.2 and Table 5.3 respectively summarize all measured and calculated results pertaining to electrical performance, including the total mass and volume of all modules in each battery pack.

Table 5.2 Measured electrical performance results from the SCP tests.

Measured Result		Model3-19 AL	Model3-19 PA	Bolt-18 AL	Bolt-18 PA	i3-15 PA	Leaf-12 PA	Lishen-12 PA
m_{mod} (kg) Mass of all modules		236		288		200	181	353
v_{mod} (L) Volume of all modules		111		170		127	123	224
E_{dis} (kWh) Discharge energy output	4 h 2 h 1 h	37.1 33.8 30.1	38.1 36.2 33.2	55.8 52.3 46.7	54.1 51.6 47.9	16.9 16.5 15.8	18.1 17.5 16.5	34.4 33.9 32.7
E_{chg} (kWh) Charge energy input	4 h 2 h 1 h	38.7 36.0 33.1	39.9 38.6 36.4	57.5 55.2 51.2	56.0 54.6 52.5	17.2 17.0 16.5	18.6 18.2 17.5	35.6 35.7 35.6

Table 5.3 Calculated electrical performance results from the SCP tests.

Calculated Result		Model3-19		Bolt-18		i3-15	Leaf-12	Lishen-12
		AL	PA	AL	PA	PA	PA	PA
ρ (kg/L) Module mass density		2.14		1.69		1.58	1.48	1.58
$\bar{E}_m$ (Wh/kg) Module specific energy	4 h 2 h 1 h	157 143 127	161 153 141	194 182 162	188 179 166	85 83 79	100 96 91	97 96 93
$\bar{E}_m^{\mathrm{BOL}}$ (Wh/L) Module specific energy at BOL	4 h 2 h 1 h	181 165 147	186 177 162	196 184 164	196 187 174	85 83 79	131 126 119	107 106 102
$\bar{E}_v$ (Wh/L) Module energy density	4 h 2 h 1 h	335 305 272	344 327 300	327 307 274	318 303 281	133 130 124	147 142 134	154 151 146
$\bar{E}_v^{\mathrm{BOL}}$ (Wh/L) Module energy density at BOL	4 h 2 h 1 h	386 352 313	397 377 346	332 311 278	332 317 294	133 130 124	193 186 176	169 167 161
ζ (%) Energy utilization ratio	4 h 2 h 1 h	85.4 77.8 69.3	87.7 83.3 76.5	93.7 87.9 87.5	94.2 89.8 83.4	97.0 94.9 90.4	98.7 95.5 89.9	99.7 98.2 94.9
ω_{DT} (%) Discharge truncation ratio	2 h 1 h	0.8 0.9	0.0 0.5	0.3 2.0	0.0 0.6	0.1 0.1	0.0 0.3	0.2 0.7
ω_{CT} (%) Charge truncation ratio	2 h 1 h	7.0 14.6	4.3 10.1	3.8 9.9	3.7 8.1	1.6 5.5	2.6 6.7	0.4 1.6
ω_{VD} (%) Voltage depression ratio	2 h 1 h	1.1 3.3	0.7 2.2	1.1 3.2	0.9 2.8	0.5 1.3	0.6 1.8	0.9 2.5
η (%) Cycle energy efficiency	4 h 2 h 1 h	95.7 93.8 90.8	94.4 93.7 91.2	97.0 94.7 91.2	96.6 94.5 91.3	98.3 97.2 95.5	97.2 96.0 93.8	96.5 94.8 92.0
$\bar{q}_v$ (Wh/kg) Cycle volumetric heat generation	4 h 2 h 1 h	15.2 20.2 27.5	16.6 22.2 29.2	10.3 17.0 26.4	11.2 17.7 26.9	2.3 3.8 5.9	4.2 6.0 8.8	5.5 8.3 12.8
$\dot{\bar{q}}_v$ (W/kg) Average volumetric heat generation rate	4 h 2 h 1 h	1.9 5.0 13.4	2.0 5.1 12.9	1.3 4.2 12.7	1.4 4.4 12.6	0.29 0.94 3.0	0.51 1.4 4.2	0.67 2.0 6.1

5.3.1. Energy Density

The revenue-generating capacity of different second-life batteries can be compared by scaling the measured discharge energy capacity E_{dis} by volume or mass. The calculated results for module energy density $\bar{E}_v$ are plotted in Figure 5.5, where the x-axis shows the corresponding results of module specific energy $\bar{E}_m$ for each test. This graphical technique allows for simultaneous comparison of energy density, specific energy, and mass density, where mass density ρ_{mod} is reflected by the slope of each trend line. The BOL values are estimated by scaling the 4 h results for $\bar{E}_v$ and $\bar{E}_m$ by the SOH results from Table 5.1 in accordance with Equations 4.4 and 4.5 (note that 100 % SOH is applied for i3-15 instead of the calculated 105.5 %). Only the 4 h values of $\bar{E}_v^{\text{BOL}}$ and $\bar{E}_m^{\text{BOL}}$ are shown in Figure 5.5 for visual clarity. Note that data marker shapes are used to denote 4 h, 2 h and 1 h results.

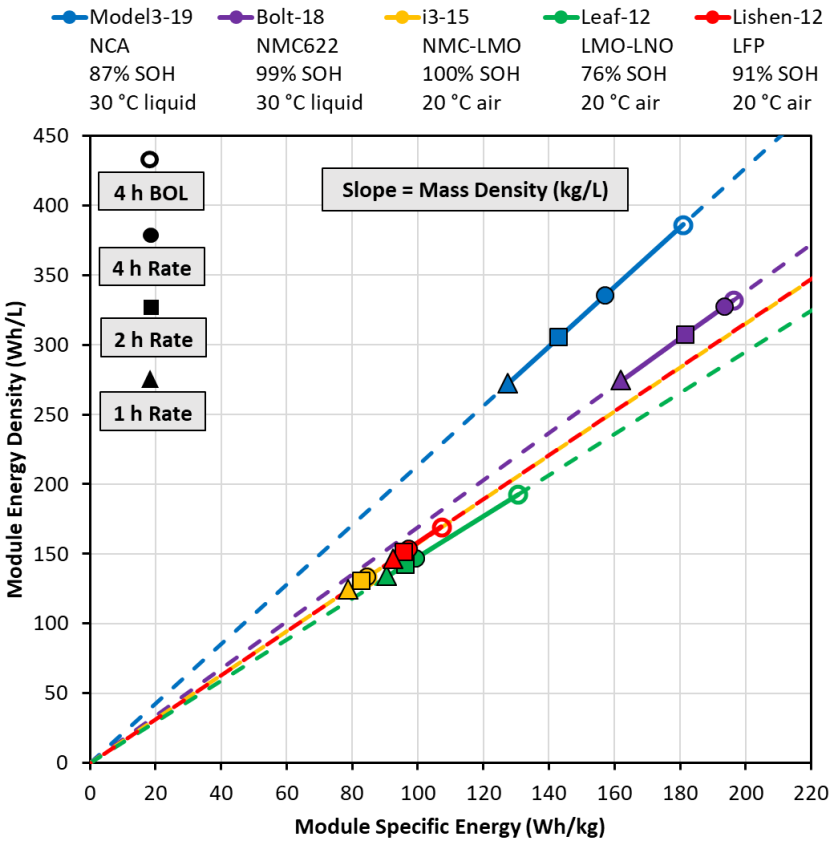


Figure 5.5 Calculated energy densities and specific energies based on 4 h, 2 h, and 1 h SCP tests.

Figure 5.5 shows that the $\bar{E}_v$ and $\bar{E}_m$ results for Leaf-12, Lishen-12 and i3-15 are within relatively narrow ranges of 124 to 154 Wh/L and 79 to 100 Wh/kg, though Leaf-12 has the

highest BOL values among these three batteries. Since Lishen-12 uses LFP chemistry with lower operating voltage compared to the other batteries, Lishen-12 would be expected to give relatively low $\bar{E}_v$ and $\bar{E}_m$. The lowest values are given by i3-15, which may be due to cell design as well as module design. Note that both Nissan and BMW have been using higher-capacity batteries in their more recent Leaf and i3 vehicle models.

The $\bar{E}_v$ and $\bar{E}_m$ results for Model3-19 and Bolt-18 are both within ranges of 272 to 335 Wh/L and 127 to 194 Wh/kg, which are more than double the corresponding i3-15 values. Note that while Model3-19 gives measured energy densities comparable to Bolt-18, Figure 5.5 shows that at BOL, Model-19 would have given substantially higher energy densities near 400 Wh/L. Despite its superior energy density, Model3-19 gives lower specific energies than Bolt-18, even at BOL. The slope lines in Figure 5.5 demonstrate that this is because Model3-19 has significantly higher ρ_{mod} (2.14 kg/L) than the other four batteries, which all fall in a relatively narrow range of 1.48 to 1.69 kg/L. The high mass density of the Model3-19 modules could be attributable to a relatively dense cell housing material (steel) and high cell quantity (744 per module), as well as an energy-dense NCA cell design and a tightly-packed module design. Note that only the liquid-cooled results for Model-19 and Bolt-18 are shown in Figure 5.5. The corresponding passive-cooled results for these packs are slightly higher due to thermal advantage, but lie on the same ρ_{mod} lines as the liquid-cooled datapoints.

The Tesla Model 3 and Chevrolet Bolt are relatively new EV models designed to achieve greater driving range, and Figure 5.5 shows that battery energy density is significantly improved in these newer EV designs. However, the wider ranges of Model3-19 and Bolt-18 in Figure 5.5 compared to the other batteries suggest that Model3-19 and Bolt-18 are more negatively impacted by higher power rates. This reflects a common cell design trade-off between energy density and internal resistance, which will be discussed further in Section 5.3.5. Despite this drawback, Model3-19 and Bolt-18 would be able to deliver significantly more energy than the other three EV batteries for a given second-life system size and/or weight, even at higher power rates. This is an important consideration for second-life energy storage projects confined to a limited space (e.g. urban shipping container).

5.3.2. Energy Utilization Ratio

Power rates impact the fraction of total battery energy capacity that can be utilized for generating revenue. The calculated results for energy utilization ratio ζ are plotted against the power-to-energy ratio (i.e. the inverse of discharge duration t_{dis}) in Figure 5.6, where the right chart normalizes the ζ results to the 4 h values of each dataset according to Equation 4.8 to give the normalized energy utilization ratio ζ^*.

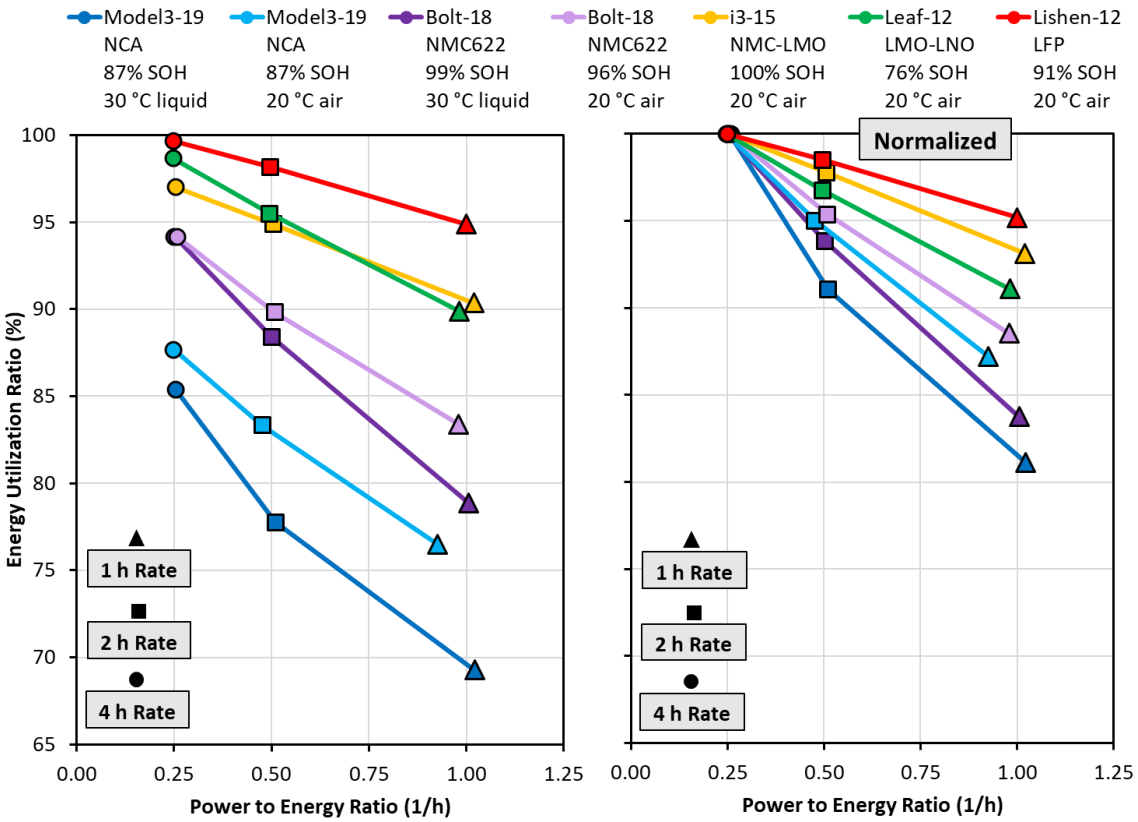


Figure 5.6 Calculated (left) and normalized (right) energy utilization ratios based on 4 h, 2 h, and 1 h SCP tests.

Lishen-12 gives the best ζ results in Figure 5.6, ranging from nearly 100 % at a 4 h rate to 95 % at a 1 h rate. Leaf-12 and i3-15 both deliver $\zeta > 97$ % at a 4 h rate and $\zeta \approx 90$ % at a 1 h rate, though ζ decreases more rapidly at high power rates for Leaf-12. The results are notably lower for Bolt-18, with $\zeta \approx 94$ % at a 4 h rate and 79 % $< \zeta <$ 84 % at a 1 h rate depending on TMS. The results are even lower for Model3-19, with 85 % $< \zeta <$ 88 % at a 4 h rate and 69 % $< \zeta <$ 76 % at a 1 h rate depending on TMS. Both Model3-19 and Bolt-18 give lower ζ when operated with an AL-TMS compared to a PA-TMS.

The results in Figure 5.6 agree well with Section 5.2.2, which demonstrated how energy utilization is impacted by the combined effects of overpotentials and voltage profile shape. For example, though Model3-19, Bolt-18, and Lishen-12 all exhibited relatively large overpotentials at higher power rates in Figure 5.2, Lishen-12 gives the best ζ results due to its mostly flat LFP voltage profile, while Model3-19 gives the poorest ζ results due to the tapered shape of its nickel-rich NCA voltage profile towards high SOC. Leaf-12 and i3-15 exhibited relatively small overpotentials in Figure 5.2, and they exhibit similar ζ results in Figure 5.6 due to the voltage profile similarities arising from their similar blends of LMO and nickel-based oxides (LNO for Leaf-12 and NMC111 for i3-15).

The normalized ζ^* results in the right chart of Figure 5.6 require that the 4 h result for each pack is set at 100 %. This technique neglects the additional energy capacity obtainable through a CV charge and treats the 4 h SCP energy capacity as the reference point, which provides additional insights for electrical performance evaluation. The chart shows that Lishen-12 still gives the best ζ^* results while i3-15 now gives slightly better results than Leaf-12. The ζ^* results for Model3-19 are now much closer to the Bolt-18 results, but Model3-19 still gives the poorest results for a given TMS. Overall, the ζ^* results range from 91 to 99 % at a 2 h rate and from 81 to 95 % at a 1 h rate.

As discussed in Sections 2.3 and 2.4, temperature can have a significant impact on the operational overpotentials that dictate discharge termination and charge termination. Since the voltage profiles in Figure 5.2 indicated that energy utilization is especially dependent on charge termination, Figure 5.7 replots the ζ results against the value of T_{high} measured at the end of charge $T_{\text{high}}^{\text{endChg}}$ for each SCP test, with ζ^* values in the right chart. This shows that both Model3-19 and Bolt-18 experience higher $T_{\text{high}}^{\text{endChg}}$ values when operated with a PA-TMS compared to an AL-TMS, with an especially significant difference for Model3-19. The black dashed lines in Figure 5.7 highlight the correlation between higher $T_{\text{high}}^{\text{endChg}}$ and higher ζ results for these two battery packs. This helps explain the impact of TMS on the Model3-19 and Bolt-18 voltage profiles observed in Section 5.2.3. Temperature results will be discussed in greater detail in Section 5.4

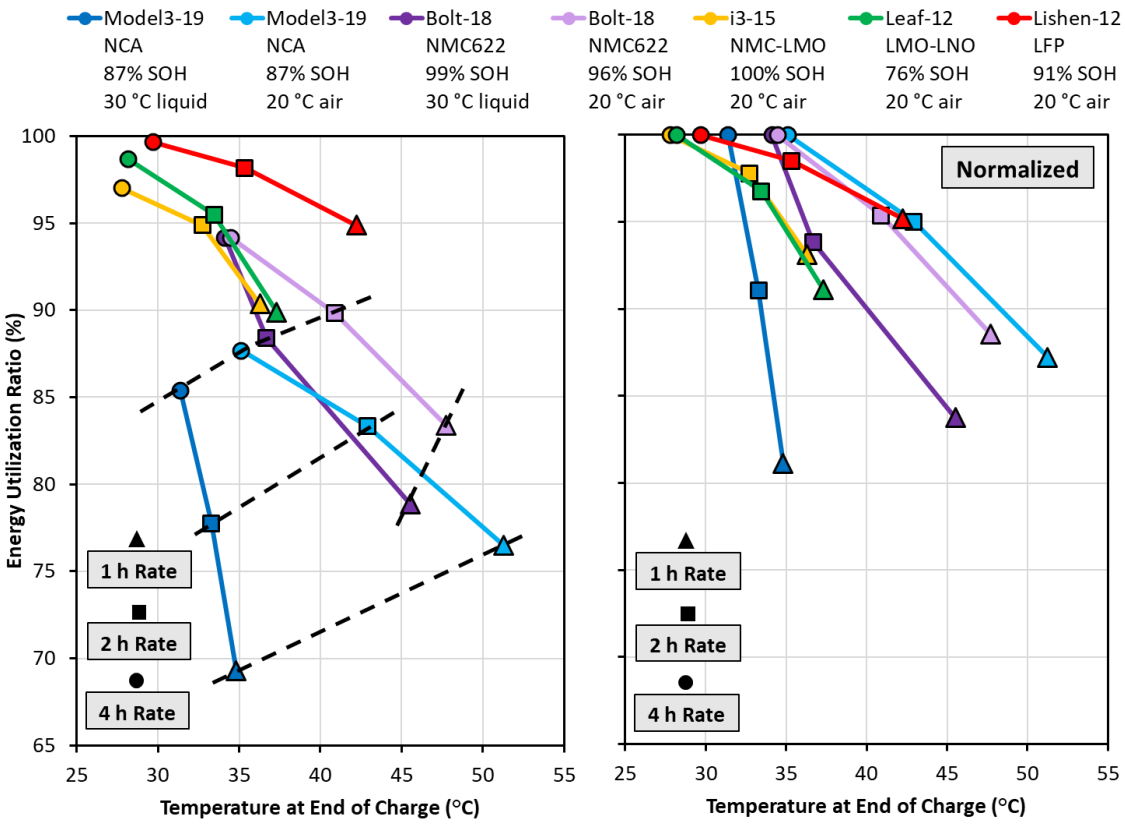


Figure 5.7 Calculated (left) and normalized (right) energy utilization ratios showing significant dependence on temperature at end of charge.

It should also be noted in Figure 5.7 that Lishen-12 experiences higher temperatures than i3-15 and Leaf-12, which may contribute to its higher ζ results. However, the influences of chemistry and cell design used in different packs likely dominate the effects of temperature. For example, the passive-cooled Model3-19 and Bolt-18 exhibit significantly larger ζ drops at higher power rates compared to the other three packs despite experiencing greater temperatures. This suggests that the Model3-19 and Bolt-18 cell designs are more severely impacted by internal resistance compared to the other three packs, leading to greater heat generation (which gives higher temperature) and greater overpotentials (which gives lower ζ). Furthermore, the passive-cooled Model3-19 experiences higher temperatures than the passive-cooled Bolt-18, but still gives lower ζ results.

The significant differences among the five EV battery packs in Figure 5.6 and Figure 5.7 have important practical implications for the economics of second-life energy storage. For example, a second-life Model 3 battery (or a similar nickel-rich EV battery) purchased on

a capacity basis may provide less than 70 % of the expected returns when cycled at a 1 h rate with an AL-TMS, while a second-life Lishen battery (or a similar LFP EV battery) may provide more than 95 % of the expected returns when cycled at a 1 h rate. When possible, low-power charging can be applied to achieve greater energy utilization for high-power discharge.

It is important to recall from Section 2.5 that battery internal resistance typically increases as the battery ages, which means that the ζ results may be influenced by battery SOH. The detrimental effect of higher power rates on the Model3-19 voltage profile further suggests that ζ may be sensitive to SOH for Model3-19, since both high power rates and cell degradation give rise to greater overpotentials. The impacts of degradation on the ζ results will be considered in Section 5.6.

5.3.3. Unutilized Energy Components

Section 4.5.1 introduced the concept of unutilized energy components, which provide a means of quantifying the three sources of unutilized energy when the power rate is increased above a 4 h rate. The results for discharge truncation ratio ω_{DT}, charge truncation ratio ω_{CT}, and voltage depression ratio ω_{VD} are plotted in Figure 5.8. This shows that charge truncation accounts for a large majority of the unutilized energy for most battery packs at both a 2 h rate and a 1 h rate, as was qualitatively concluded in Section 5.2.2. The only exception is Lishen-12, where ω_{CT} is relatively small due to the flat LFP voltage profile. As a result, voltage depression accounts for the majority of the unutilized energy for Lishen-12. Discharge truncation only makes up a small component of the unutilized energy in all cases, but ω_{DT} is largest for the two liquid-cooled packs due to the impacts of temperature mitigation on internal resistance.

It is interesting to note in Figure 5.8 that if charge truncation was eliminated, the total unutilized energy compared to $E_{\mathrm{dis}}^{4\mathrm{h}}$ would be no more than 5.1 % for all liquid-cooled packs and no more than 3.3 % for all passive-cooled packs. This emphasizes the impact of applying a long CV charge to 100 % SOC. If a CV charge is always applied, then the ζ metric is of little practical consequence. In commercial energy arbitrage applications, battery power is applied in response to market price signals, so CV charging cannot always

be relied upon. For this research project, SCP cycles are used to reflect cases where CV charging cannot be applied to demonstrate the significant performance differences that arise among different EV battery pack designs operating under this condition.

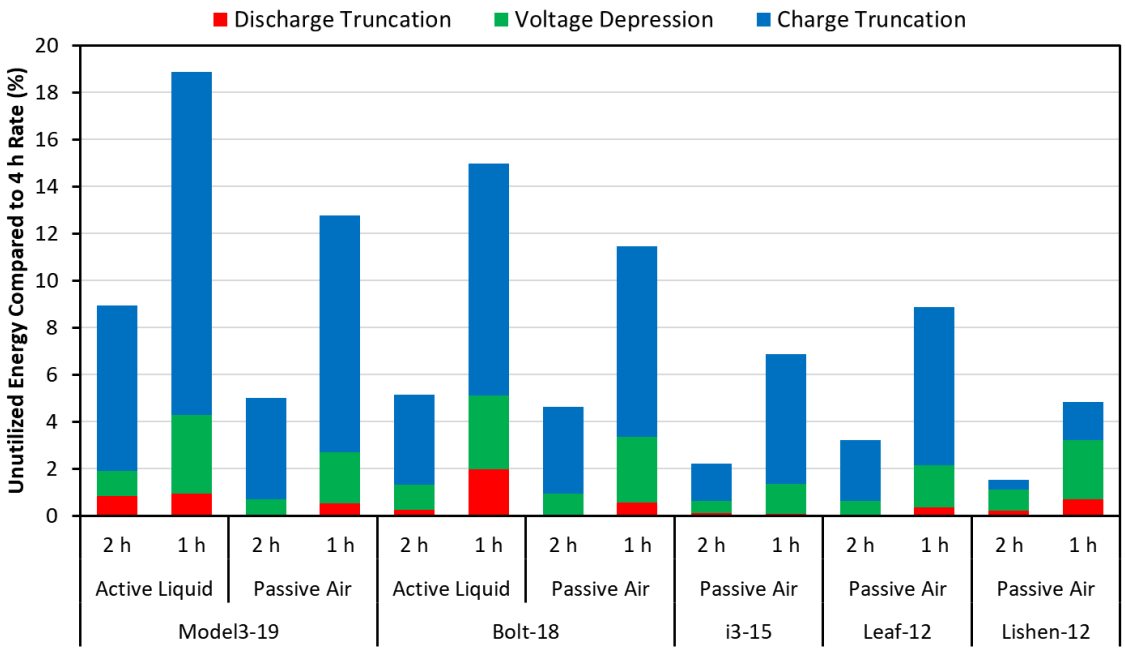


Figure 5.8 Unutilized energy components for 2 h and 1 h tests compared to the 4 h test.

An analysis of the unutilized energy components can also be used to inform strategic thermal management techniques. For example, the significant increase in ω_{CT} for the liquid-cooled Model3-19 compared to the passive-cooled Model3-19 indicates that the lower temperature at the end of charge causes a significant drop in ζ for the liquid-cooled case. This information could be used to design a TMS controller that allows the battery temperature to briefly rise (within safe limits) towards the end of charge as a means of mitigating ω_{CT} and storing more energy in the battery without decreasing the charge power. Figure 5.8 suggests that such a technique would be of little benefit for an LFP battery.

5.3.4. Energy Efficiency

For many stationary energy storage applications, the net value that a second-life battery can offer will depend on the amount of charge energy required per unit discharge energy, which refers to battery energy efficiency. The calculated results for cycle energy efficiency η are plotted against power-to-energy ratio in Figure 5.9, where the right chart normalizes

the η results to the 4 h values for each dataset according to Equation 4.10 to give the normalized energy efficiency η^*.

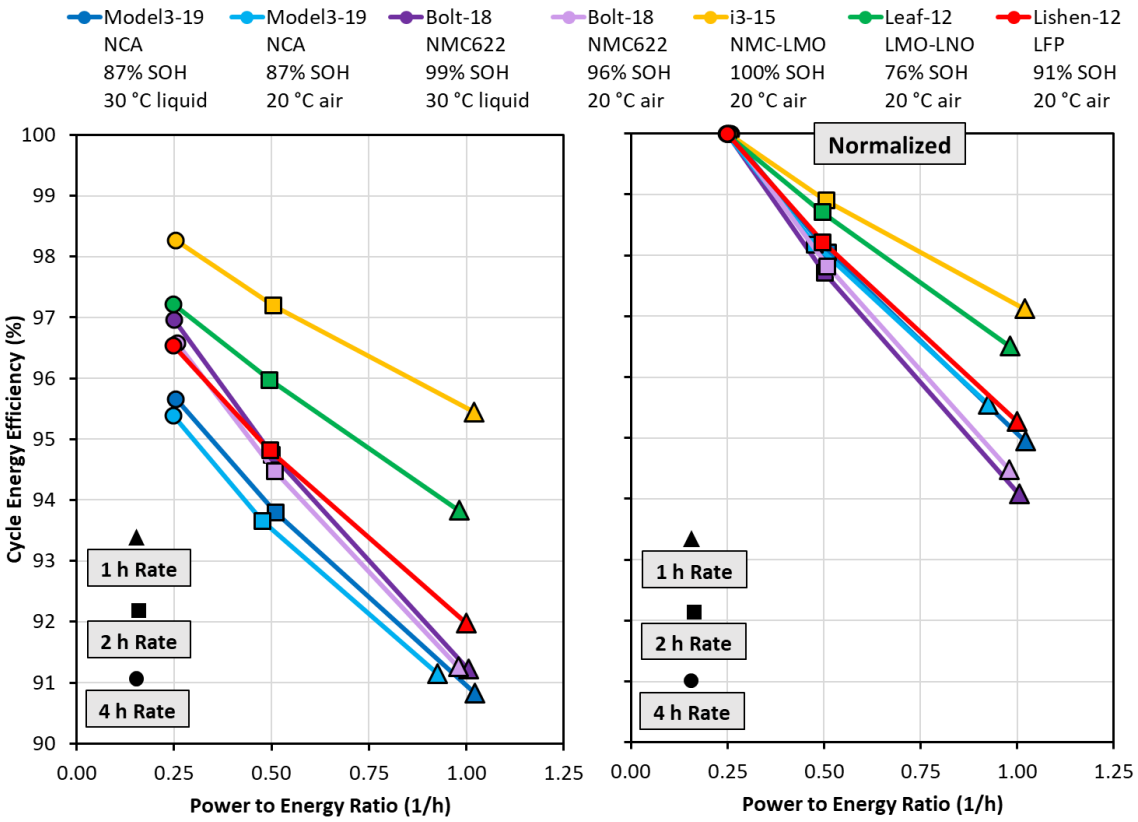


Figure 5.9 Calculated (left) and normalized (right) cycle energy efficiencies based on 4 h, 2 h, and 1 h SCP tests.

Figure 5.9 shows that i3-15 gives the best η results at all power rates, ranging from 98.3 % at a 4 h rate to 95.5 % at a 1 h rate. Model3-19 exhibits the lowest η results at all power rates, ranging from 95.4 % at a 4 h rate to 90.8 % at a 1 h rate. Bolt-18 and Lishen-12 both give relatively low η, while Leaf-12 gives mid-range η. The normalized η^* values in the right chart of Figure 5.9 emphasize how i3-15 is the best at handling higher power rates in terms of η, while Bolt-18 exhibits the sharpest drop in η at higher power rates. The reasons for this were previously discussed in Section 5.2.2, where the voltage gap between the discharge and charge profiles in Figure 5.2 becomes relatively large as the power rate increases for Bolt-18 but remains relatively small for i3-15. This suggests that current is more restricted in the Bolt-18 cell design, causing large overpotentials at high currents. The AL and PA results for Model3-19 and Bolt-18 show that the TMS has little impact on η.

Since η is dependent on the operational overpotentials throughout discharge and charge, η will be influenced by the battery temperature throughout the cycle, with higher temperatures corresponding to lower η. To explore this influence, Figure 5.10 plots the η results against the corresponding results of $T_{\text{high}}^{\text{avg}}$ for each test, with η^* values in the right chart. This shows that at each power rate, higher temperatures tend to be associated with lower η results. This demonstrates how η influences temperature (due to generation of waste heat) more than temperature influences η. The black dashed lines in the left chart of Figure 5.10 show that the AL and PA η results are fairly consistent for Model3-19 and Bolt-18 despite differences in temperature. This contrasts with the strong temperature dependence of the ζ results shown in Section 5.3.2.

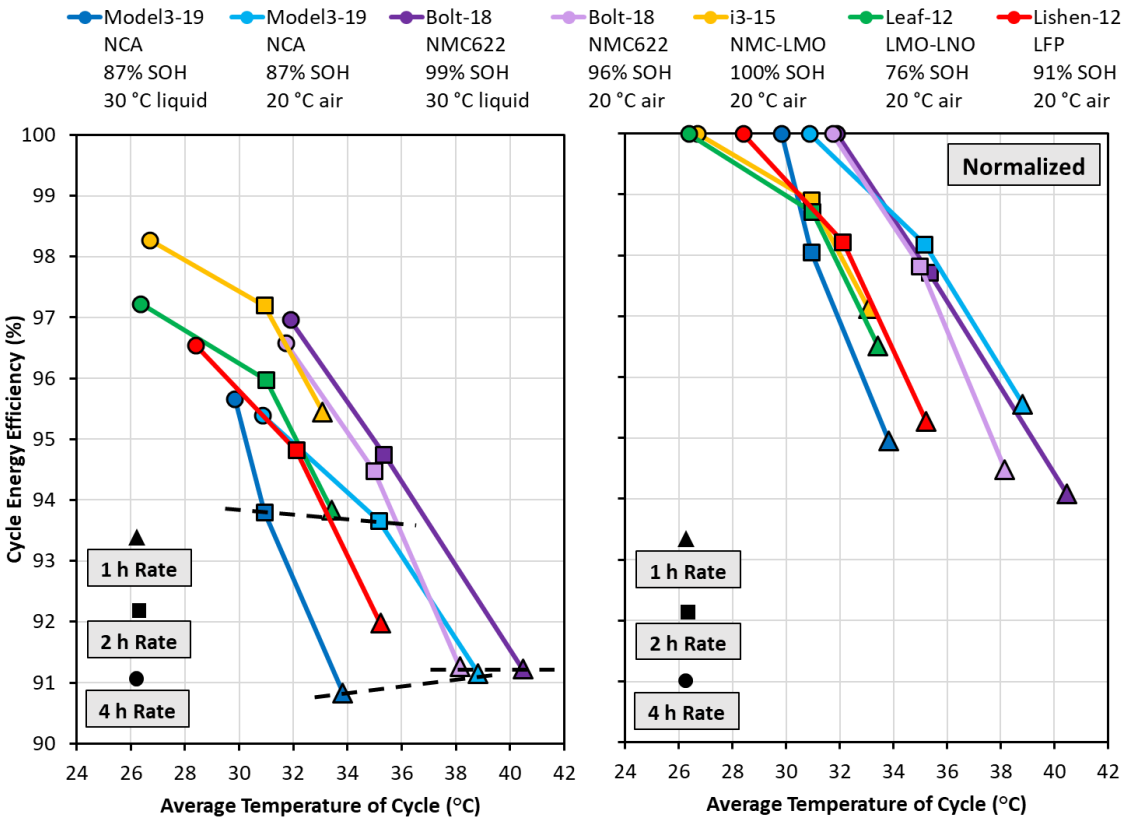


Figure 5.10 Calculated (left) and normalized (right) cycle energy efficiencies showing no significant dependence on the average cycle temperature.

Overall, Figure 5.9 and Figure 5.10 demonstrate that η is relatively high at a 4 h rate (> 95 %) for all five tested EV battery packs but decreases substantially at higher power rates (< 92 % at a 1 h rate) for batteries with high energy density (Model3-19 and Bolt-18)

or LFP chemistry (Lishen-12). In a given energy arbitrage application, net profitability would be relatively high for i3-15 and relatively low for Model3-19, Bolt-18, and Lishen-12, with Leaf-12 in between. At a 1 h rate, the relative energy losses of a full cycle would be more than double for Model3-19 (9.2 %) compared to i3-15 (4.5 %). These energy losses also have important implications for thermal performance, which will be discussed in Section 5.4.5.

Battery degradation typically causes internal resistance to increase, which reduces energy efficiency as the battery ages, but the effect of degradation on energy efficiency is generally less significant than its effect on energy capacity [181]. Figure 5.9 shows that the 76 % SOH Leaf-12 gives significantly higher η than the 100 % SOH Bolt-18, so the variance between the different pack designs is clearly more significant than the influence of SOH. The impacts of degradation on the η results will be considered in Section 5.6.

5.3.5. Dependence on Internal Resistance

Section 5.3 has thus far presented the experimental results for energy density $\bar{E}_v$, energy utilization ratio ζ, and cycle energy efficiency η. While these three electrical performance metrics have unique practical implications, they are all linked to battery internal resistance and are therefore connected. As discussed in Section 2.1.5, $\bar{E}_v$ generally requires thicker electrode coatings, lower porosity, larger particle sizes, smaller amounts of conductive carbon, and thinner current collectors, all of which increase internal resistance. Higher internal resistance then causes larger overpotentials during discharge and charge (especially at higher power rates), and these overpotentials are a key determining factor in both ζ and η. The connections between $\bar{E}_v$, ζ, and η will now be investigated to draw additional insights into the electrical performance of the five tested EV battery packs and second-life batteries in general.

The left chart of Figure 5.11 plots the η results against the $\bar{E}_v^{\mathrm{BOL}}$, revealing a clear correlation between these two metrics. Among the seven datasets, η tends to decease as $\bar{E}_v^{\mathrm{BOL}}$ increases at a given power rate, which agrees with the cell design trade-off between energy density and internal resistance. The datapoints for i3-15, Leaf-12, Bolt-18, and Model3-19 all fall neatly into line at each power rate, as highlighted by the black dashed

lines in the left chart of Figure 5.11 (linear lines of best fit calculated for all datapoints but Lishen-12 at each power rate). Lishen-12 sits well below these lines, but this can be attributed to the relatively low operating voltage of LFP chemistry, which reduces both energy density and energy efficiency compared to other commercial lithium-ion chemistries. This effectively shifts the Lishen-12 datapoints towards the lower left of the chart, away from the trend lines. Adjusting the $\bar{E}_v^{\mathrm{BOL}}$ and η results for Lishen-12 according to this voltage difference causes the Lishen-12 datapoints to better align with the trends lines, reinforcing the universality of the correlation between $\bar{E}_v^{\mathrm{BOL}}$ and η. The left chart of Figure 5.11 also shows that the packs with the highest $\bar{E}_v^{\mathrm{BOL}}$ exhibit the largest vertical and horizontal data ranges, which illustrates how the higher internal resistance of energy-dense cell designs results in significant attenuation of both energy capacity and energy efficiency at higher power rates.

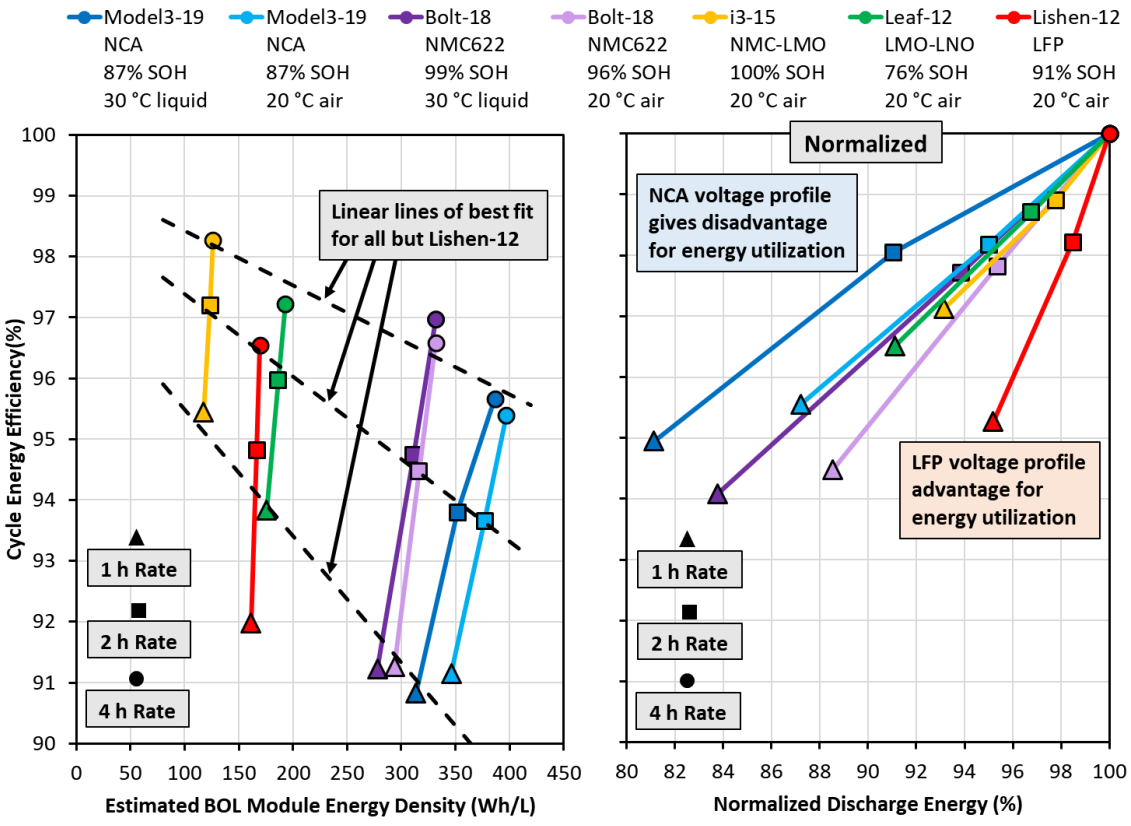


Figure 5.11 Comparison of calculated (left) and normalized (right) energy efficiency and BOL module energy density showing impacts of cell internal resistance and voltage profile shape on electrical performance.

The right chart of Figure 5.11 plots η^* against ζ^* to create a normalized equivalent of the left chart (note that ζ^* is equivalent to normalizing $\bar{E}_v^{\mathrm{BOL}}$ to the 4 h value). The slopes of the normalized curves yield additional insights about battery electrical performance. First, all seven datasets are fairly linear, which supports the notion that energy utilization and energy efficiency are connected by internal resistance. Second, since η is primarily determined by internal resistance, while ζ is determined by a combination of internal resistance and the voltage profile shape (discussed in Section 5.2.2), a η^* vs ζ^* plot can be used to isolate the impact that voltage profile shape has on energy utilization. The fact that Lishen-12 exhibits a relatively steep slope indicates an advantageous LFP voltage profile shape that mitigates the impact of overpotentials on energy utilization. This is why Lishen-12 has the best ζ results despite having relatively poor η results. In contrast, the liquid-cooled Model3-19 exhibits a relatively low slope, indicating a disadvantageous NCA voltage profile shape that exacerbates the impact of overpotentials on energy utilization. Note that the slopes of Model3-19 and Bolt-18 are improved when operating with a PA-TMS due to the reduced internal resistance at higher temperatures. However, referring back Figure 5.7 shows that the $T_{\mathrm{high}}^{\mathrm{endChg}}$ of the liquid-cooled Model3-19 and Bolt-18 are closer to the temperatures of i3-15, Leaf-12, and Lishen-12, which indicates that Bolt-18, i3-15, and Leaf-12 all experience similar effects of voltage profile shape, while the nickel-rich positive electrode of Model3-19 gives a notable disadvantage for a comparable $T_{\mathrm{high}}^{\mathrm{endChg}}$.

The novel graphical techniques applied in Figure 5.11 demonstrate that different EV battery packs follow similar rules of cell design that determine their electrical performance at different power rates. Since this trend is observed for packs featuring different cell formats and chemistries, electrode thickness is likely the primary factor. Though the voltage profile of a specific battery chemistry can be an important factor, batteries with high energy density can generally be expected to lose substantial profitability at higher power rates due to a reduction in energy utilization and an increase in required charge energy, while batteries with low energy density can generally be expected to better maintain their profitability at higher power rates. Since EV battery designs are becoming increasingly energy-dense (Model3-19 and Bolt-18 are the newest of the five tested packs),

it appears that EV batteries are becoming increasingly disadvantaged for electrical performance in high-power electricity grid services. However, batteries with high energy density may still be significantly more profitable than those with low energy density if space is a constraint in a given energy storage application, even at higher power rates. Newer EV battery designs also tend to be liquid-cooled, which provides thermal advantages in high-power operation. The profitability of second-life batteries will of course depend on their capital cost and operating costs as well as the nature of the given electricity market, which are considerations outside the scope of this thesis.

In practice, second-life battery developers could use graphical correlations like the one demonstrated in the left chart of Figure 5.11 as a guide for qualitatively judging the relative energy efficiencies (and corresponding cooling requirements) of available second-life batteries based on their specified 4 h energy capacity, SOH, and module volume. Since energy efficiency is not typically specified in battery resale, this technique could provide insight into energy efficiency performance that would otherwise only be attainable after purchasing and testing a battery. Battery packs could also be characterized with a 'voltage shape factor' using the slope of the normalized curves in the right chart of Figure 5.11 to quantify how a given lithium-ion chemistry will impact energy utilization in second-life service, though the temperature dependence of these slopes must be accounted for.

5.3.6. Heat generation

Section 4.5.1 introduced the novel concepts of cycle volumetric heat generation $\bar{q}_v$ and average volumetric heat generation rate $\dot{\bar{q}}_v$, which are calculated for a given SCP cycle using the measured $\bar{E}_v$, η, and t_{dis}. The calculated $\bar{q}_v$ and $\dot{\bar{q}}_v$ results are respectively plotted against the power-to-energy ratio in the left and right charts of Figure 5.12. This shows that Model3-19 generates the most heat per unit volume for a given power rate, followed closely by Bolt-18. Volumetric heat generation is significantly lower for the other three packs, with i3-15 giving the lowest values. The left chart of Figure 5.12 shows that $\bar{q}_v$ increases somewhat logarithmically at higher power rates for all battery packs, while the right chart shows that $\dot{\bar{q}}_v$ increases in a more exponential fashion at higher power rates. Both $\bar{q}_v$ and $\dot{\bar{q}}_v$ increase at higher power rates due to the lower energy efficiency, but $\bar{q}_v$ increases at a diminishing rate since the energy capacity of each pack decreases at higher power rates.

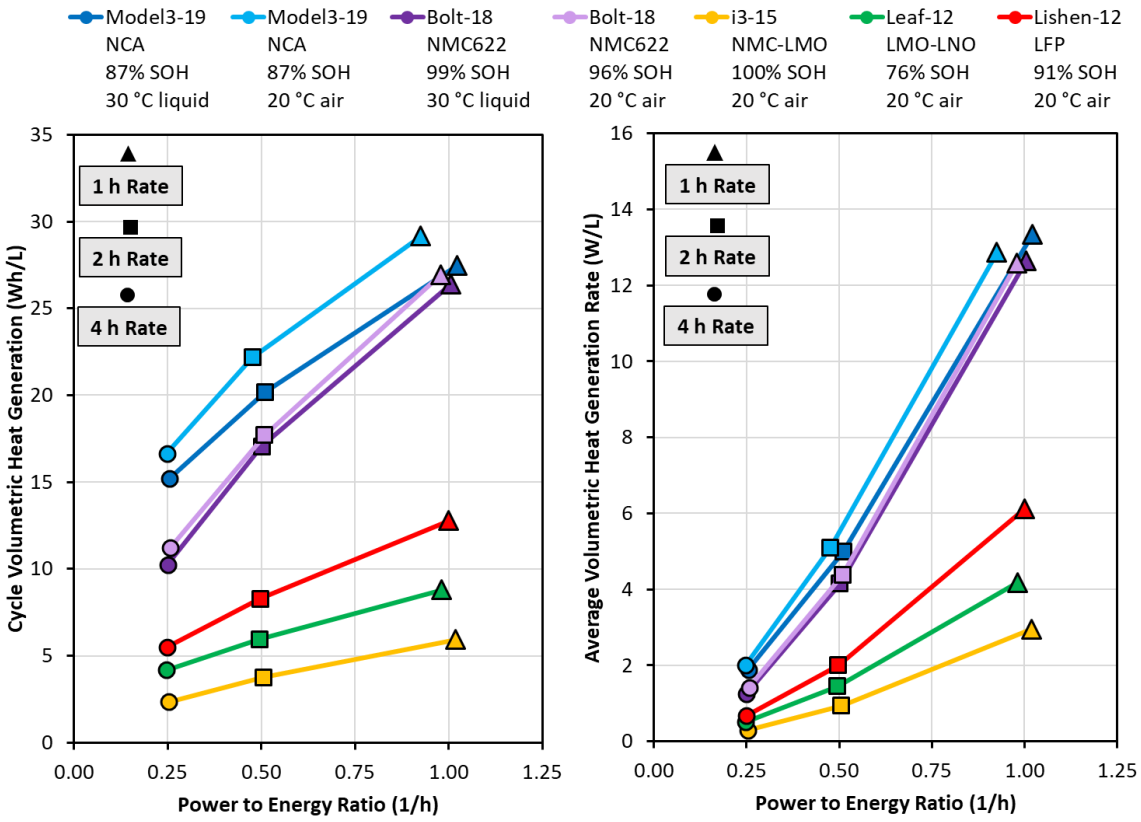


Figure 5.12 Calculated cycle volumetric heat generation (left) and average volumetric heat generation rate (right) based on 4 h, 2 h, and 1 h SCP tests.

To explore the unique contributions of energy efficiency and energy density towards heat generation, $\bar{q}_v$ is plotted against η and $\bar{E}_v$ in the left and right charts of Figure 5.13, respectively. The left chart shows that for a given η, Model3-19 and Bolt-18 generate comparable amounts of heat, while Lishen-12, Leaf-12, and i3-12 also generate comparable amounts of heat. The significant gap between these two sets of battery packs at a given η is due to their significant differences in energy density, as illustrated in the right chart of Figure 5.13. Battery packs that discharge significantly more energy per unit volume will generate significantly more heat per unit volume even if η is held constant. As discussed in Section 5.3.5, energy-dense packs also tend to have lower η, which compounds the volumetric heat generation. This means that energy-dense battery packs have a two-fold disadvantage when it comes to heat generation, which is exacerbated at higher power rates. The right chart of Figure 5.13 also shows that $\bar{q}_v$ always increases at higher power rates in spite of $\bar{E}_v$ decreasing at higher power rates, illustrating that both $\bar{E}_v$ and η play significant roles in determining $\bar{q}_v$.

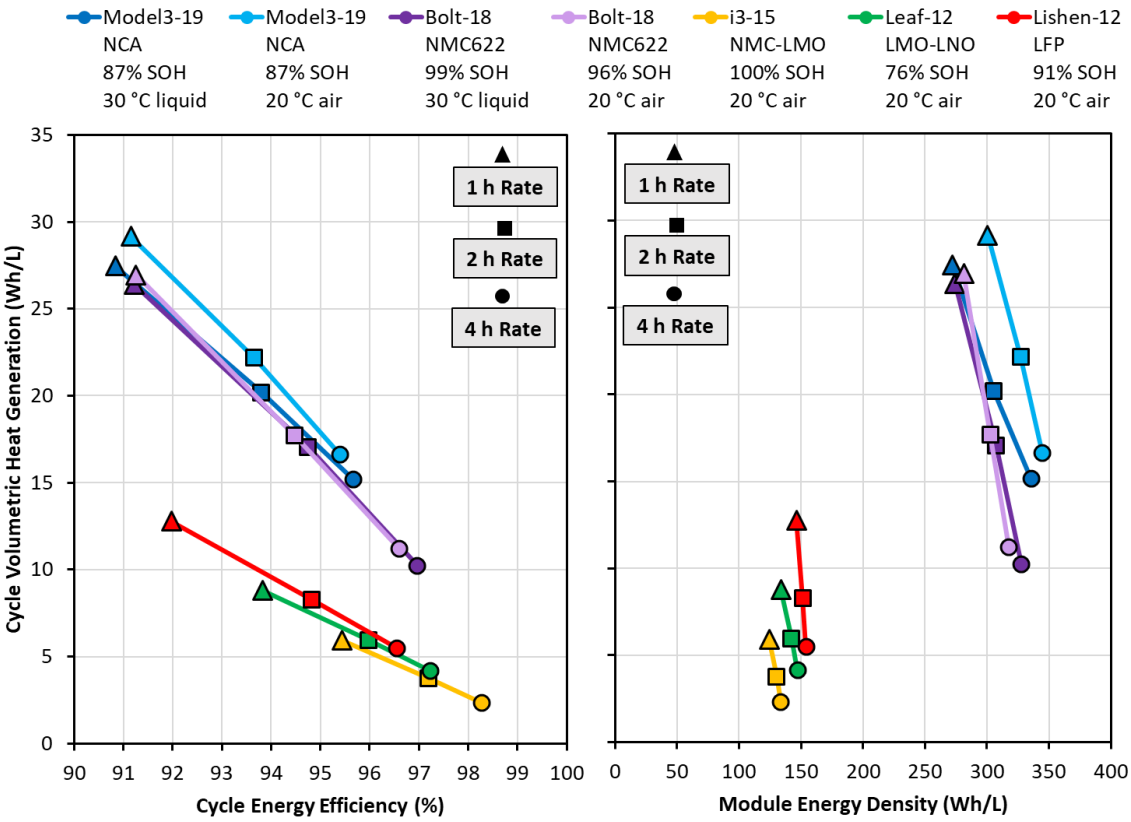


Figure 5.13 Influence of cycle energy efficiency (left) and module energy density (right) on calculated cycle volumetric heat generation.

The significant variance in $\bar{q}_v$ and $\dot{\bar{q}}_v$ among the five EV battery packs has important implications for thermal performance. The fact that Model3-19 and Bolt-18 are designed for liquid cooling in EV service can be clearly understood according to the relatively high $\bar{q}_v$ and $\dot{\bar{q}}_v$ values they produce. This contrasts with i3-15, which is designed for refrigerant-based cooling in EV service despite its relatively low heat generation. Some second-life project developers may elect to forego the intended active TMS of an acquired EV battery in the interest of simplicity and cost. The completed experiments can be used to evaluate how such a decision impacts the thermal performance of Model3-19, Bolt-18, and i3-15. Section 5.4 will focus on battery thermal performance.

5.4. Thermal Performance Results

Section 4.5.2 described a set of thermal performance metrics for evaluating second-life battery packs in energy arbitrage. This section will present the results of the SCP tests with a focus on thermal performance metrics. For reference, Table 5.4 and Table 5.5

respectively summarize all measured and calculated results pertaining to thermal performance.

Table 5.4 Measured thermal performance results from the SCP tests.

Measured Result		Model3-19		Bolt-18		i3-15	Leaf-12	Lishen-12
		AL	PA	AL	PA	PA	PA	PA
$T_{\text{high}}^{\text{max}}$ (°C) Maximum pack high temperature	4 h 2 h 1 h	31.4 33.5 37.4	35.1 42.9 51.3	34.1 39.1 49.5	34.5 40.9 49.5	27.8 32.4 36.3	28.2 33.5 37.6	29.7 35.3 42.2
$T_{\text{high}}^{\text{avg}}$ (°C) Average pack high temperature	4 h 2 h 1 h	29.8 30.9 33.8	30.9 35.2 38.8	31.9 35.4 40.5	31.7 35.0 38.2	26.7 30.9 33.1	26.4 31.0 33.4	28.4 32.1 35.2
$T_{\text{low}}^{\text{avg}}$ (°C) Average pack low temperature	4 h 2 h 1 h	29.4 29.9 31.4	25.6 27.9 29.6	31.3 34.7 38.5	28.1 30.6 32.9	25.9 29.4 31.3	22.6 25.0 26.0	27.1 30.2 32.8
T_{∞}^{avg} (°C) Cycle average TMS temperature	4 h 2 h 1 h	29.6 29.8 30.3	19.1 19.2 19.0	29.8 30.0 30.5	19.2 19.5 18.9	19.3 19.0 19.4	18.8 18.8 18.1	19.6 20.0 19.8
$T_{\infty}^{\text{stepavg}}$ (°C) Step average TMS temperature	4 h 2 h 1 h	29.5 29.9 30.2	19.2 19.0 18.5	29.7 29.9 30.5	18.5 19.4 18.3	19.3 18.7 19.1	18.5 18.7 18.0	19.4 19.9 19.7
t_{dis} (h) Discharge duration	4 h 2 h 1 h	3.93 1.96 0.98	4.03 2.10 1.08	4.00 1.99 0.99	3.88 1.97 1.02	3.99 2.03 1.03	4.05 2.02 1.02	4.02 2.01 1.00
$t_{\text{cool}}^{\text{dis}}$ (h) Discharged cooldown duration	4 h 2 h 1 h	0.00 0.00 0.11	1.12 3.10 4.58	0.01 0.48 1.03	3.48 7.16 9.88	0.00 1.39 3.76	0.01 2.12 3.96	0.01 2.04 4.20
t_{chg} (h) Charge duration	4 h 2 h 1 h	4.07 2.08 1.08	4.20 2.23 1.19	4.11 2.11 1.09	4.01 2.08 1.12	3.99 2.03 1.03	4.12 2.09 1.08	4.15 2.12 1.09
$t_{\text{cool}}^{\text{chg}}$ (h) Charged cooldown duration	4 h 2 h 1 h	0.00 0.00 0.00	1.60 3.19 4.55	0.00 0.15 0.88	3.44 7.24 10.1	0.00 1.56 3.29	1.01 1.97 3.85	0.01 2.13 4.11

Table 5.5 Calculated thermal performance results from the SCP tests.

Calculated Result		Model3-19		Bolt-18		i3-15	Leaf-12	Lishen-12
		AL	PA	AL	PA	PA	PA	PA
$\Delta T_{\text{high}}^{\text{max}}$ (°C) Maximum pack temperature rise	4 h	1.9	15.9	4.4	16.0	8.5	9.7	10.3
	2 h	3.6	23.9	9.2	21.5	13.7	14.8	15.4
	1 h	7.2	32.8	19.0	31.2	17.2	19.6	22.5
$\Delta T_{\text{high}}^{\text{avg}}$ (°C) Average pack temperature rise	4 h	0.2	11.8	2.1	12.5	7.4	7.6	8.8
	2 h	1.1	16.0	5.4	15.5	11.9	12.2	12.1
	1 h	3.5	19.8	10.0	19.3	13.7	15.3	15.4
$\Delta T_{\text{low}}^{\text{avg}}$ (°C) Average low temperature rise	4 h	-0.2	6.5	1.5	9.0	6.6	3.8	7.5
	2 h	0.1	8.7	4.7	11.0	10.4	6.2	10.2
	1 h	1.1	10.6	8.0	14.0	11.9	7.9	13.0
$\Delta T_{\text{diff}}^{\text{avg}}$ (°C) Average pack temperature differential	4 h	0.4	5.3	0.6	3.6	0.8	3.8	1.3
	2 h	1.0	7.3	0.7	4.4	1.5	6.0	1.9
	1 h	2.4	9.2	2.0	5.3	1.8	7.4	2.4
t_{cool} (h) Cycle cooldown duration	4 h	0.00	2.72	0.00	6.92	0.00	0.00	0.00
	2 h	0.00	6.29	0.15	14.4	1.56	1.97	4.17
	1 h	0.11	9.13	0.88	20.0	3.29	3.85	8.31
t_{cyc} (h) Total cycle duration	4 h	8.15	10.9	8.12	15.0	8.05	8.09	8.15
	2 h	4.13	10.4	4.74	18.5	7.00	8.17	8.27
	1 h	2.21	11.2	4.00	22.1	9.09	9.87	10.40
f_{cyc} (cycles/day) Achievable cycling frequency	4 h	2.9	2.2	3.0	1.6	3.0	3.0	2.9
	2 h	5.8	2.3	5.1	1.3	3.4	2.9	2.9
	1 h	10.9	2.1	6.0	1.1	2.6	2.4	2.3
ΔT_{cool} (°C) Cycle cooldown temperature drop	4 h	N/A	7.9	N/A	8.5	N/A	N/A	N/A
	2 h	N/A	23.6	5.8	21.3	5.1	6.4	9.9
	1 h	2.4	40.7	25.0	37.2	13.2	14.9	24.3
τ (h) Average cooling time constant	4 h	N/A	4.36	N/A	10.4	N/A	N/A	N/A
	2 h	N/A	4.26	0.69	10.3	7.06	8.12	5.19
	1 h	0.23	4.35	0.72	10.1	7.27	8.02	5.30

5.4.1. Temperature Profiles

Before calculating the temperature maximums, averages, and differentials associated with each SCP test, the measured temperature profiles should first be assessed graphically. Figure 5.14 plots the time-series measurements of highest pack temperature T_{high} and TMS temperature T_{∞} obtained from the third cycle of each test. The x-axes use time relative to

the end of discharge or charge, which facilitates comparison of temperature rise and cooldown for tests conducted at different power rates. The temperature control setpoints (35 °C for liquid AL and 30 °C for PA) are depicted by horizontal dashed lines in each chart. If the test control software detects the condition $T_{\text{high}} \geq T_{\text{ctrl}}$ at the end of discharge or charge, the battery enters a cooldown period until the condition $T_{\text{high}} < T_{\text{ctrl}}$ is met. The nominal 30 °C liquid supply temperature used for AL tests and nominal 20 °C ambient air temperature used for PA tests are also depicted by horizontal dashed lines in each chart, which facilitates comparison of the measured T_{∞} to the nominal TMS setpoints.

Since all five battery packs feature a graphite-based negative electrode, every chart in Figure 5.14 exhibits the reversible heating characteristics associated with entropy changes in the graphite intercalation system. As discussed in Section 2.6.3, these entropy changes are typically endothermic near mid-SOC during discharge and near low-SOC during charge, and are thus exothermic near mid-SOC during charge and near low-SOC during discharge. With the exception of the liquid-cooled Model3-19, the T_{high} measurements for each 4 h test show clear evidence of these endothermic and exothermic effects, including relatively sharp decreases near the middle of discharge and at the beginning of charge, as well as relatively sharp increases at the end of discharge and near the middle of charge.

The entropic effects visible in the 4 h data become less distinct at higher power rates as irreversible heating becomes dominant. Yet the reverse is true for the liquid-cooled Model3-19 data, where the entropic effects are seemingly absent at the 4 h rate but become increasingly distinct as the power rate increases. This unique behaviour is due to the parallel liquid channels that run between the cylindrical cell housings within the Model3-19 modules (described in Section 4.1), which is evidently a highly effective design for exchanging heat with the cells. The AL-TMS is therefore able to counteract the endothermic and exothermic effects at the 4 h rate and hold T_{high} at the 30 °C TMS setpoint throughout the cycle. At the 1 h rate, the increased irreversible heating has raised T_{high} above the 30 °C TMS setpoint, but the AL-TMS is able to capitalize on the endothermic stages of discharge and charge and pull T_{high} back towards 30 °C until the discharge or charge becomes exothermic, at which point T_{high} increases again.

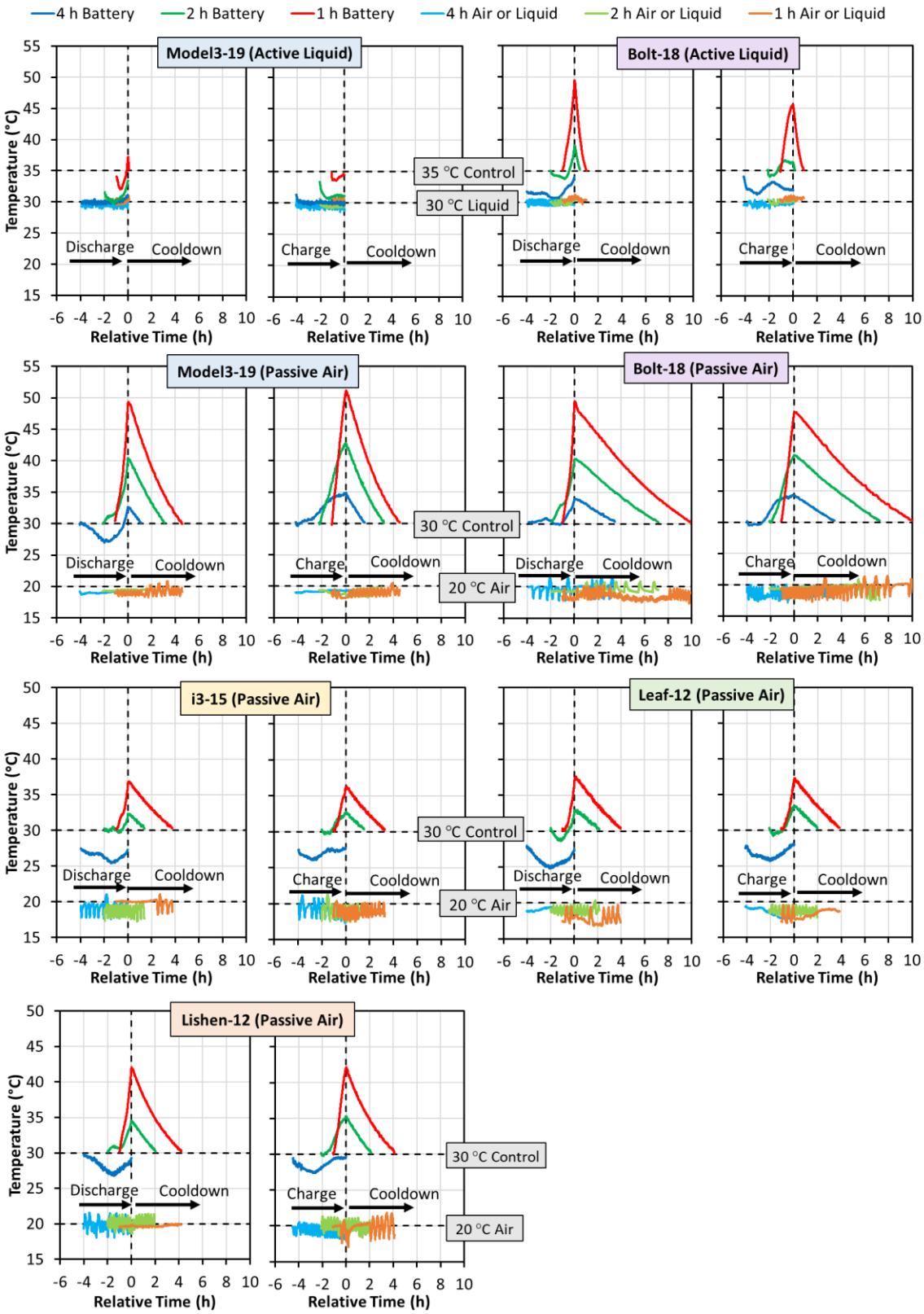


Figure 5.14 Highest pack temperatures and TMS temperature measured during the third cycle of 4 h, 2 h, and 1 h SCP tests.

Figure 5.14 also shows that i3-15, Leaf-12, and Lishen-12 all exhibit similar temperature changes, while the passive-cooled Model3-19 and Bolt-18 exhibit significantly greater temperature changes. This contrast agrees with the heat generation results discussed in Section 5.3.6, and explains why the Model 3 and Bolt packs are designed for liquid-cooled operation. Among the five PA test sets, higher temperature maximums correspond to longer cooldowns, though Bolt-18 requires notably longer cooldowns than Model-19 despite comparable temperature maximums. Cooldown rates will analyzed further in Section 5.4.3.

Figure 5.14 also shows significant differences between the AL and PA test results for Model3-19 and Bolt-18. The impact of the AL-TMS is especially evident for Model3-19, which exhibits the smallest temperature changes of the seven test sets when operated with an AL-TMS despite exhibiting the largest temperature changes when operated with a PA-TMS. Even though Model3-19 and Bolt-18 were supplied with the same liquid temperature, pressure, and flow rate, the liquid-cooled Bolt-18 exhibits much larger temperature changes than the liquid-cooled Model3-19. Unlike the parallel liquid channels featured in Model3-19, Bolt-18 features a serpentine liquid channel that only makes contact with the bottom of the modules (both systems described in Section 4.1.2). Figure 5.14 indicates that the Bolt-18 liquid channel design is less effective at rejecting heat compared to Model3-19, but the AL-TMS still has a significant benefit for Bolt-18 cooldown periods compared to the PA-TMS.

5.4.2. Temperature Rise

The temperature measurements presented in Section 5.4.1 are used to calculate the maximum temperature rise $\Delta T_{\text{high}}^{\text{max}}$ and average temperature rise $\Delta T_{\text{high}}^{\text{avg}}$ for the third cycle of each SCP test, as described in Section 4.5.2. Before assessing the cycle as a whole, the maximum temperature rise for the discharge and charge steps of each test are plotted against the power-to-energy ratio in the left and right charts of Figure 5.15, respectively. For all PA tests, the temperature rise increases at a diminishing rate as the power increases, while the AL tests show a fairly linear correlation between discharge temperature rise and power rate. This difference may be related to the fact that natural convection coefficients increase at larger temperature differentials, while forced convection coefficients are

independent of temperature differential (explained in Section 2.6.4). Due to the entropic effects described in Section 5.4.1, the maximum charge temperature for the 4 h and 2 h AL tests does not occur at the end of charge, causing the AL charge temperature rise trends to appear nonlinear in Figure 5.15.

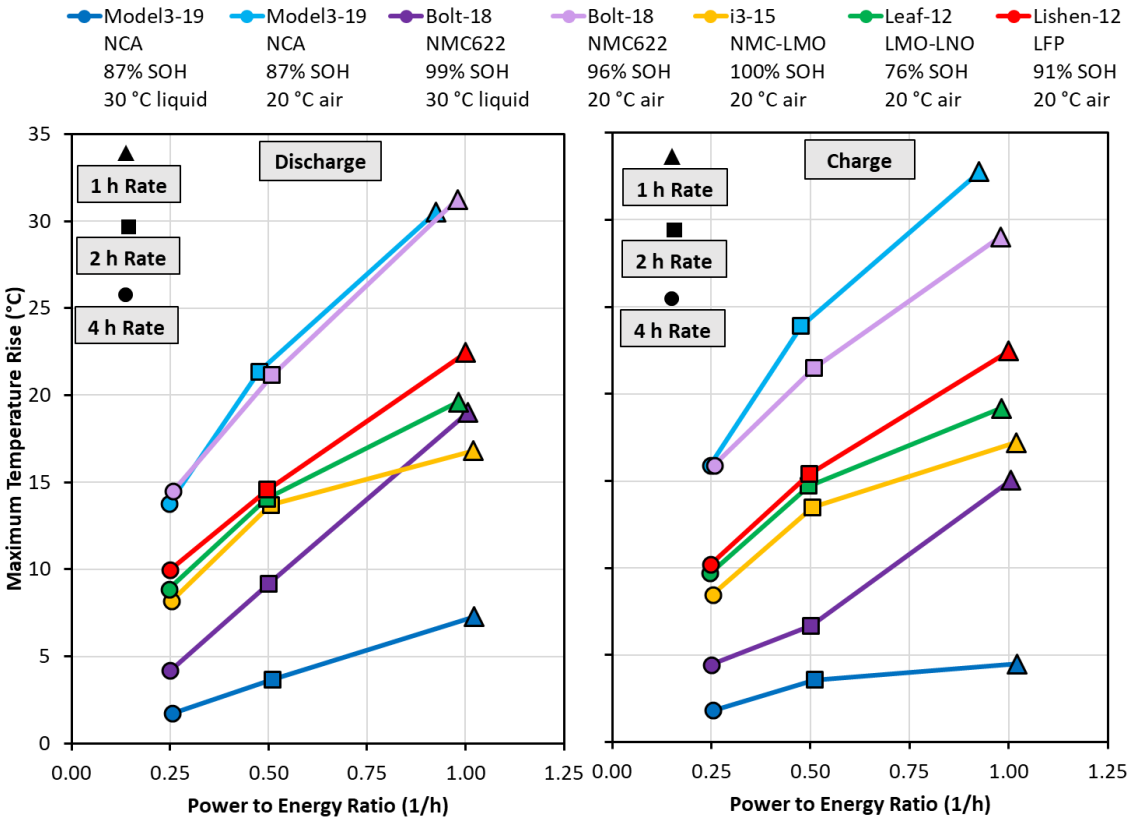


Figure 5.15 Maximum temperature rise above ambient measured during discharge (left) and charge (right) of each SCP test.

Figure 5.15 also shows that i3-15, Leaf-12, and Lishen-12 exhibit consistency between their respective charge and discharge maximum temperature rises. Model3-19 and Bolt-18 do not exhibit this consistency for either TMS type. For the AL tests, both Model3-19 and Bolt-18 exhibit smaller temperature rises during charge compared to discharge. This is because reversible and irreversible heating are both relatively high at the end of discharge, but relatively low at the end of charge. The high heat rejection rate of an AL-TMS can therefore dampen the temperature rise at the end of charge more effectively than the end of discharge. The passive-cooled Bolt-18 also exhibits lower temperature rise during the 1 h charge compared to the 1 h discharge, likely because the 30 °C temperature rise

provides a large cooling differential for the PA-TMS to dampen temperature rise at the end of charge. This implies that i3-15, Leaf-12, and Lishen-12 also dampen the charge temperature rise, but the effect is more obvious in Bolt-18 due to its 50 % larger passive cooling differential.

The opposite effect is observed for the passive-cooled Model3-19, which exhibits greater temperature rises during charge compared to discharge for all three power rates. This is likely an indicator of heat diffusion limitations in the Model3-19 modules when operated with a PA-TMS. If it is assumed that more total net heat is generated during charge compared to discharge (the thermal model presented in Chapter 7 provides strong evidence supporting this notion), then all battery packs would exhibit greater temperature rise during charge if it were not for the relatively low heat generation rate at the end of charge. While the other four packs are able to passively dissipate heat at a sufficient rate to dampen temperature rise at the end of charge, the hottest measured cell of the Model3-19 pack cannot achieve this. It will be shown in Section 5.4.4 that the cooler cells at the corners of the Model3-19 modules exhibit the same behaviour as the other four packs, with lower temperature rise during charge compared to discharge. This suggests that heat diffusion from the interior of the passive-cooled Model3-19 module is limited, particularly at faster power rates. This is likely related to the unique module design of Model3-19, which features internal liquid channels and a foam material with unspecified properties (see Figure 4.2). Both these design features could potentially inhibit passive heat transfer compared to the module designs of the other four battery packs.

Figure 5.16 plots the calculated $\Delta T_{\text{high}}^{\text{max}}$ results for the entire third cycle of each test, with the power-to-energy ratio as the x-axis in the left chart and the calculated $\Delta T_{\text{high}}^{\text{avg}}$ results as the x-axis in the right chart. The left chart shows that i3-15, Leaf-12, and Lishen-12 reach similar values of $\Delta T_{\text{high}}^{\text{max}}$ at 4 h and 2 h rates, but diverge more at a 1 h rate where Lishen-12 reaches $\Delta T_{\text{high}}^{\text{max}} = 22$ °C and i3-15 reaches $\Delta T_{\text{high}}^{\text{max}} = 17$ °C. Model3-19 and Bolt-18 each exceed $\Delta T_{\infty}^{\text{max}} = 30$ °C when operated with a PA-TMS at a 1 h rate, while the AL-TMS reduces this to 19 °C for Bolt-18 and to 7 °C for Model3-19. Despite the AL-TMS, Bolt-18 reaches a greater 1 h $\Delta T_{\text{high}}^{\text{max}}$ than i3-15, and nearly exceeds Leaf-12 as well. The

passive-cooled Model3-19 and Bolt-18 both reach higher $\Delta T_{\text{high}}^{\text{max}}$ at a 4 h rate than the other three packs reach at a 2 h rate.

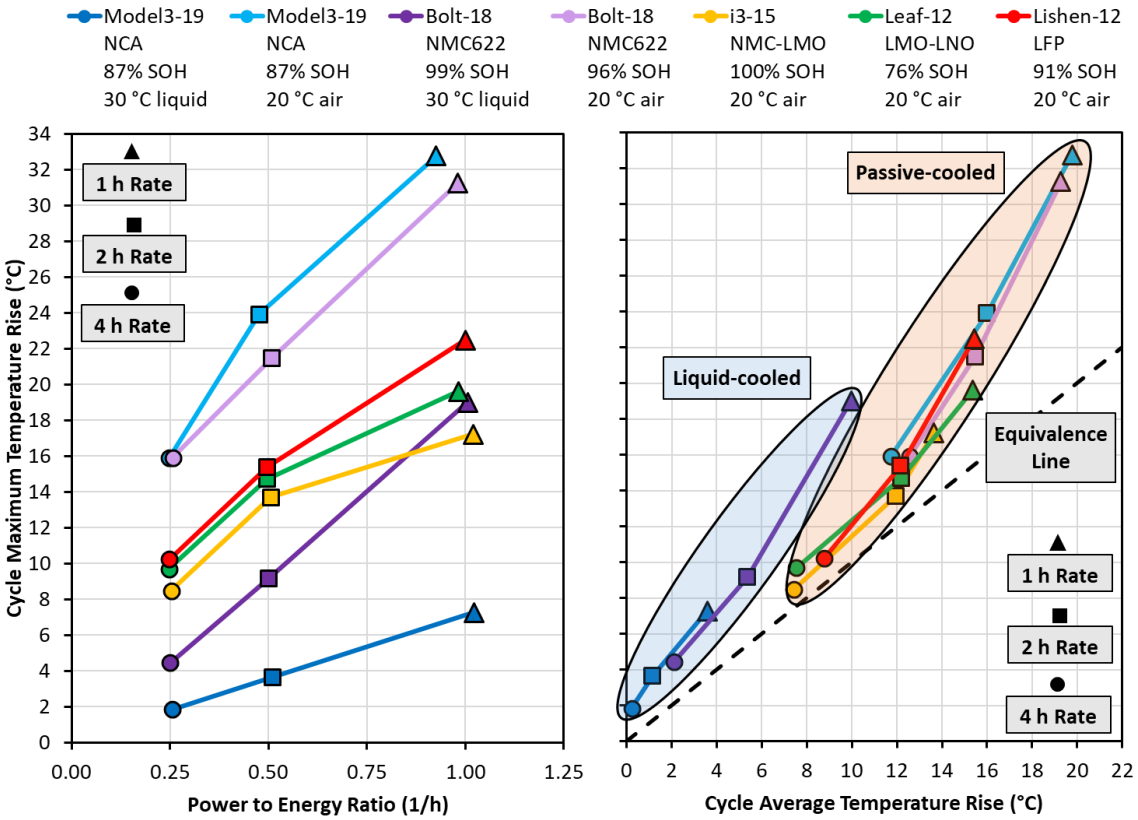


Figure 5.16 Maximum temperature rise of the full SCP cycle plotted against power-to-energy ratio (left) and cycle average temperature rise (right).

The right chart of Figure 5.16 illustrates how $\Delta T_{\text{high}}^{\text{max}}$ exceeds $\Delta T_{\text{high}}^{\text{avg}}$ for each test, with the black dashed 'equivalence line' representing the theoretical limit where $\Delta T_{\text{high}}^{\text{max}} = \Delta T_{\text{high}}^{\text{avg}}$ (i.e. no temperature change). All datapoints lie above this equivalence line, with increasing divergence at higher power rates. This divergence reflects the sharper temperature changes observed at higher power rates in Figure 5.14. At a 1 h rate, $\Delta T_{\text{high}}^{\text{max}}$ exceeds $\Delta T_{\text{high}}^{\text{avg}}$ by as much as 13 °C for passive-cooled Model 3-19. Overall, the 1 h $\Delta T_{\infty}^{\text{avg}}$ values range from 3 °C (liquid-cooled Model3-19) to 20 °C (passive-cooled Model3-19), while i3-15, Leaf-12, and Lishen-12 are near 14 to 15 °C.

The right chart of Figure 5.16 also features two coloured ellipses to highlight the common trends among the two AL tests and among the five PA tests. For both groupings, a given

$\Delta T_{\text{high}}^{\text{avg}}$ corresponds to fairly consistent values of $\Delta T_{\text{high}}^{\text{max}}$ regardless of power rate, with the AL tests shifted towards the origin due to enhanced heat rejection. For the five PA tests, Model3-19 and Bolt-18 are shifted towards higher temperatures such that their 4 h and 2 h $\Delta T_{\text{high}}^{\text{avg}}$ values align with the 2 h and 1 h $\Delta T_{\text{high}}^{\text{avg}}$ values of the other three packs, respectively near 12 °C and 15 °C. The two AL tests are also fairly aligned, though Model3-19 covers a much smaller range than Bolt-18. Although the AL-TMS clearly mitigates temperature rise in Bolt-18 at a 4 h rate, at higher power rates the heat generation becomes overwhelming for the cooling plate design such that Bolt-18 starts to behave like the passive-cooled packs. The liquid-cooled Model3-19 could likely be cycled at very high power rates before exhibiting this behaviour, further demonstrating the superiority of the Model3-19 liquid channel design. The two distinct groupings show that there is no universal relationship between $\Delta T_{\text{high}}^{\text{max}}$ and $\Delta T_{\text{high}}^{\text{avg}}$ that is independent of TMS. However, the two TMS-based trends suggest that it may be possible to infer $\Delta T_{\text{high}}^{\text{max}}$ from $\Delta T_{\text{high}}^{\text{avg}}$ (or vice versa) for a given TMS with reasonable accuracy. Relationships such as this will be explored further in Chapter 6.

In practice, project developers should design second-life energy storage systems with operational temperature ranges that balance power and energy capacity with battery degradation and safety. When lower temperatures are preferred, passive-cooled batteries could be limited to a 4 h rate (especially energy-dense packs), while a liquid-cooled Chevrolet Bolt battery could be limited to a 2 h rate. A liquid-cooled Tesla Model 3 battery could operate at a 1 h rate continuously without concern over temperature rise.

5.4.3. Cooldown Requirements

The temperature profiles presented in Section 5.4.1 showed that different EV battery packs require different cooldown durations following discharge and charge. To compare these cooldown requirements, Figure 5.17 plots the measured step durations for discharge t_{dis}, discharged cooldown $t_{\text{cool}}^{\text{dis}}$, charge t_{chg}, and charged cooldown $t_{\text{cool}}^{\text{chg}}$, such that the stacked columns sum to the total cycle time t_{cyc} required for each SCP test. Note that t_{dis} and t_{chg} are adjusted as per Equation 4.27 so that the stacked columns reflect the t_{cyc} calculation.

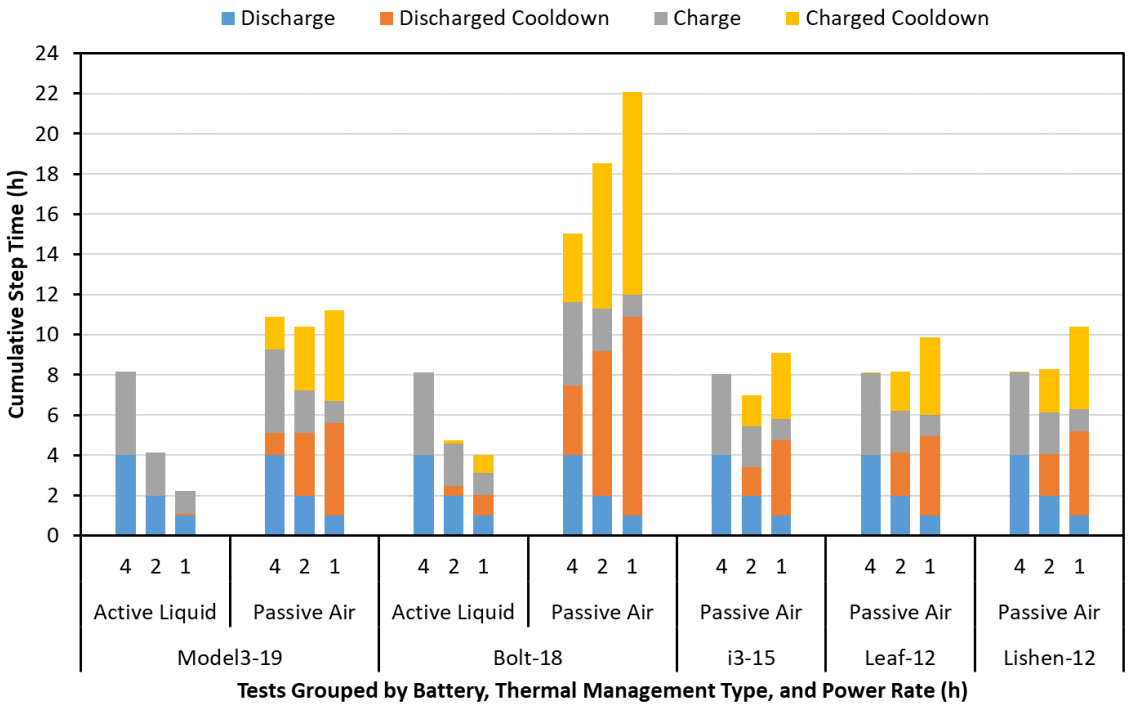


Figure 5.17 Step durations measured during 4 h, 2 h, and 1 h SCP tests.

Figure 5.17 highlights the prolonged cycle durations that result from high-power cycling of passive-cooled EV battery packs. While t_{cyc} decreases at higher power rates for the two liquid-cooled packs, the passive-cooled packs yield a longer t_{cyc} for the 1 h test compared to the 4 h test due to the extensive cooldown periods required by the temperature control setpoint. This is especially pronounced for the passive-cooled Bolt-18, which requires $t_{\mathrm{cool}} = 20$ h for the 1 h SCP cycle. The AL-TMS provides a significant improvement for Bolt-18, reducing the cooldown requirements to $t_{\mathrm{cool}} = 1.9$ h for the 1 h SCP test. The liquid-cooled Model3-19 requires just 6 minutes of cooldown following the 1 h discharge since its temperature does not rise significantly above the 35 °C control setpoint.

Section 4.5.2 introduced the achievable cycling frequency f_{cyc} as a novel thermal performance metric for assessing the practical implications of battery cooldown requirements. The calculated f_{cyc} results are presented in Figure 5.18, with the power-to-energy ratio used as the x-axis in the left chart and $\Delta T_{\mathrm{high}}^{\mathrm{max}}$ used as the x-axis in the right chart. The left chart features three black dashed lines representing the ideal f_{cyc} at each power rate. A battery pack with no cooldown periods and 100 % energy efficiency

can achieve 3 cycles/day at a 4 h rate, 6 cycles/day at a 2 h rate, and 12 cycles/day at a 1 h rate. This shows that the passive-cooled Model3-19 and Bolt-18 can only achieve about 2 cycles/day at a 4 h rate, while all other packs approach the ideal 3 cycles/day. At a 1 h rate, no passive-cooled pack can achieve 3 cycles/day, and the passive-cooled Bolt-18 can only achieve 1cycle/day. The AL-TMS allows Bolt-18 to achieve 6 cycles/day at a 1 h rate, while the liquid-cooled Model3-19 can achieve nearly 11 cycles/day. Even though the liquid-cooled Model3-19 barely requires any cooldown periods, its 1 h energy efficiency of 91 % means that a 1 h discharge requires a 1.1 h charge for an SCP cycle, making the ideal 12 cycles/day unachievable.

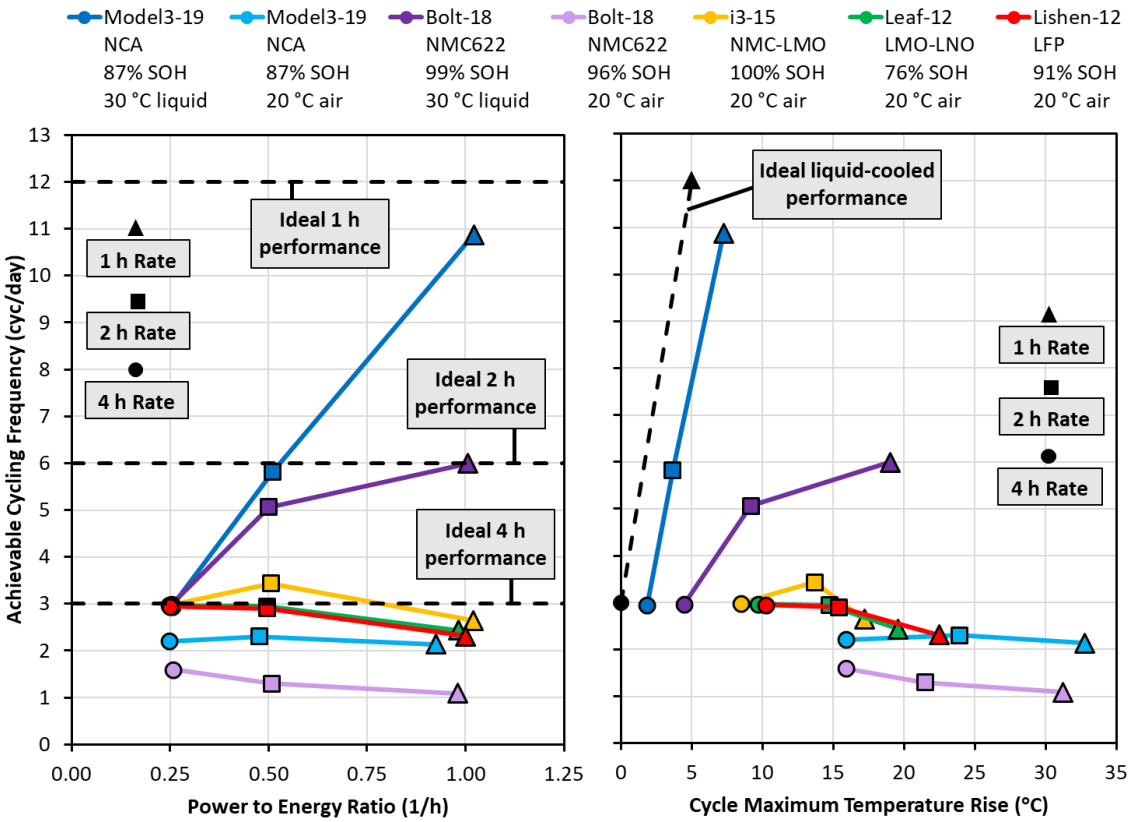


Figure 5.18 Calculated achievable cycling frequencies plotted against power-to-energy ratio (left) and maximum temperature rise (right).

The right chart of Figure 5.18 is a useful graphical technique for assessing different aspects of thermal performance simultaneously. The chart features a black dashed line representing the required liquid-cooled performance to achieve ideal cycling frequencies with zero cooldown periods. The ideal 12 cycles/day can be achieved at a 1 h rate if $\Delta T_{\text{high}}^{\max}$ remains

below a nominal 5 °C (i.e. 35 °C control setpoint vs 30 °C liquid setpoint). This shows how close to ideal the liquid-cooled Model3-19 is to the ideal case, while the liquid-cooled Bolt-18 falls well short of the ideal case in terms of both f_{cyc} and $\Delta T_{\mathrm{high}}^{\mathrm{max}}$. However, the liquid-cooled Bolt-18 is still a dramatic improvement over the passive-cooled Bolt-18 in terms of both f_{cyc} and $\Delta T_{\mathrm{high}}^{\mathrm{max}}$.

Whether a second-life battery might actually undergo 11 cycles/day in electricity grid services will depend on the dynamics of a given electricity market, but Figure 5.18 clearly demonstrates the effectiveness of the Model3-19 active-liquid system at minimizing temperatures and maximizing battery availability for revenue-generating opportunities. In contrast, project developers should expect that passive-cooled second-life battery packs will typically be limited to 2 or 3 cycles/day if moderate temperatures are to be maintained, especially for more energy-dense packs. These results would of course change for asymmetrical CP testing where a lower rate is applied during charge, which could be more directly applicable to certain second-life use cases such as peak shaving. Future research could expand on this study by exploring asymmetrical CP test protocols in place of SCP.

Higher temperatures will result in longer cooldown periods for a given battery pack, but different packs may exhibit different cooldown rates for a given temperature. To assess the cooldown rate of each pack, the left and right charts of Figure 5.19 respectively plot the total cycle cooldown duration t_{cool} and the average cooling time constant τ against the total cycle cooldown temperature drop ΔT_{cool} (all defined in Section 4.5.2). The left charts show that t_{cool} increases at a diminishing rate as ΔT_{cool} increases, which is to be expected since temperatures drop faster when the cooling differential is larger. The right chart shows that the τ calculations are quite consistent for all tests conducted on each battery pack (noting that some 4 h tests required no cooldown periods and therefore did not produce a τ value). This means that a τ calculation (see Equation 4.32) for a single test on a given battery pack can be used to accurately predict the cooldown duration from any initial battery temperature to any desired temperature control setpoint if the temperature of the cooling fluid is known. The τ value effectively represents the time it would take to dissipate 63 % (i.e. $1 - \mathrm{e}^{-1}$) of a given $\Delta T_{\mathrm{high}}^{\mathrm{max}}$.

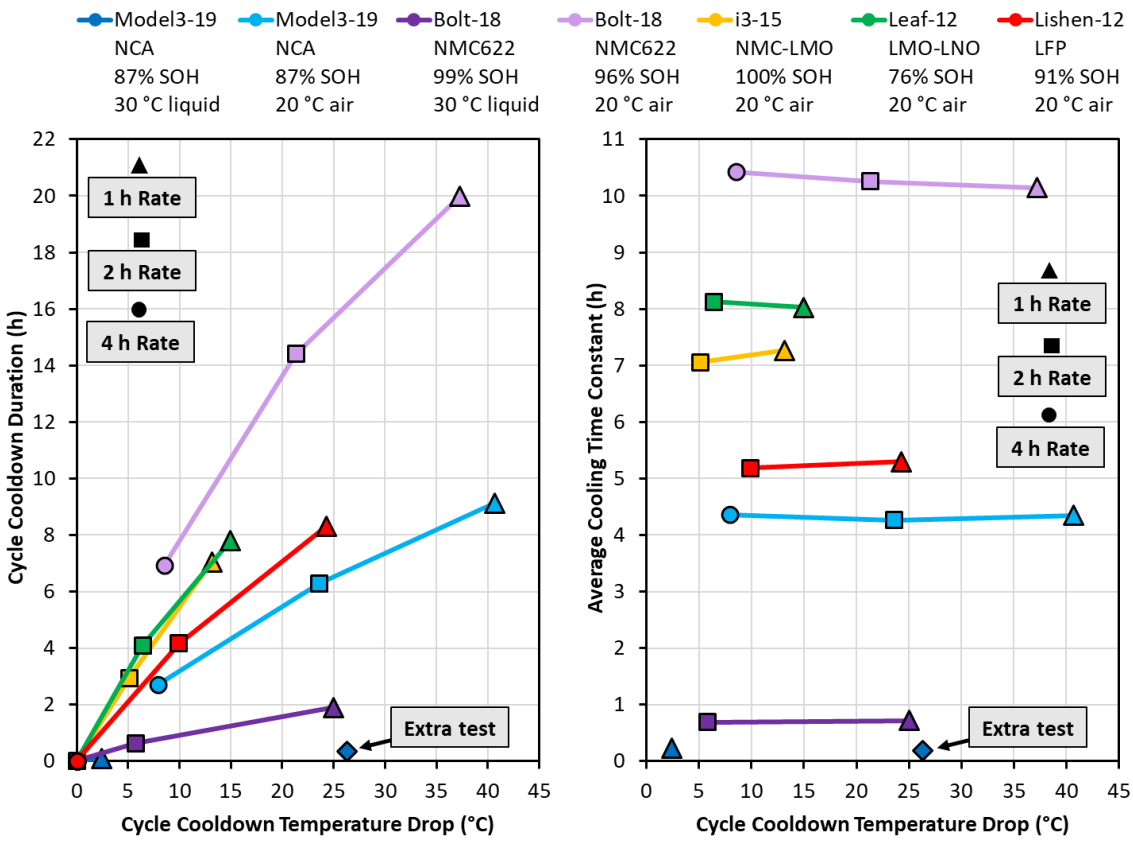


Figure 5.19 Measured cycle cooldown duration (left) and associated calculations for average cooling time constant (right).

Figure 5.19 shows that the passive-cooled Bolt-18 has the lowest cooling rate, with a τ exceeding 10 h. Leaf-12 and i3-15 both give τ values around 7 to 8 h, while Lishen-12 and the passive-cooled Model3-19 give τ around 4 to 5 h. Though Figure 5.17 demonstrated that the passive-cooled Model3-19 requires longer cooldown periods than i3-15, Leaf-12, and Lishen-12, Figure 5.19 reveals that this is only because the passive-cooled Model3-19 experienced greater $\Delta T_{\text{high}}^{\text{max}}$. Of the five passive-cooled packs, Model3-19 has the highest cooling rate with a τ just above 4 h.

The battery pack photos shown previously in Figure 4.1 may provide some insight into the τ results in Figure 5.19. The photos show that Model3-19 and Lishen-12 feature relatively wide and short aspect ratios, which provides more surface area for natural convection. In contrast, Bolt-18 features a stacked module which likely inhibits passive cooling. Based on these observations, it is likely that the physical size and shape of the different packs is a determining factor in their passive cooling rates. It should also be noted that some packs

feature different housing cover materials (plastic for Lishen-12, fibreglass for Bolt-18, and steel for Model3-19, i3-15, and Leaf-12), which may influence convection coefficients. The influence of the stacked module on the Bolt-18 passive cooling rate in will be discussed further in Section 5.4.4.

Since the AL tests for Model3-19 only produced one τ value based on a brief 6-minute cooldown period with $\Delta T_{\text{cool}} = 2.4$ °C, an extra test was conducted on Model3-19 to improve confidence in the AL cooldown characterization. A 1 h CP discharge was carried out with the AL-TMS pumps switched off, allowing T_{high} to reach 48.2 °C by the end of discharge. At the instant the discharge ended, the AL-TMS pumps were switched back on. The AL-TMS required about 11 minutes for T_{high} to drop 13.2 °C to the 35.0 °C control setpoint. The measured cooldown duration and temperature drop were doubled to give $t_{\text{cool}} = 0.38$ h and $\Delta T_{\text{cool}} = 26.4$ °C, which enables direct comparison with the other datapoints in the left chart of Figure 5.19. These measurements produce $\tau = 0.18$ h, which is close to the $\tau = 0.23$ h result produced by the 6-minute cooldown during the 1 h SCP test. These low τ values further demonstrate the superiority of the Model3-19 liquid channel design over the Bolt-18 cooling plate design, which produced $\tau = 0.7$ h. The liquid-cooled Bolt-18 is still a dramatic improvement over the $\tau > 10$ h results produced for the passive-cooled Bolt-18, despite the 5 °C liquid cooling differential being half of the 10 °C passive cooling differential.

5.4.4. Temperature Distribution

As described in Section 4.1.2, at least three thermocouples are placed on each battery pack during testing to capture operational temperature distribution across each pack. Figure 5.20 shows the battery temperature profiles measured by three thermocouples during the 1 h SCP tests since temperature distributions are most prominent at high power rates. The three battery temperatures in each chart represent the highest and lowest temperatures measured for each pack as well as one ‘middle’ temperature in between. The same chart design from Figure 5.14 is applied in Figure 5.20, but with a legend added to each chart pair to specify which thermocouple locations (as pictured in Figure 4.5) correspond to the highest, middle, and lowest temperature measurements.

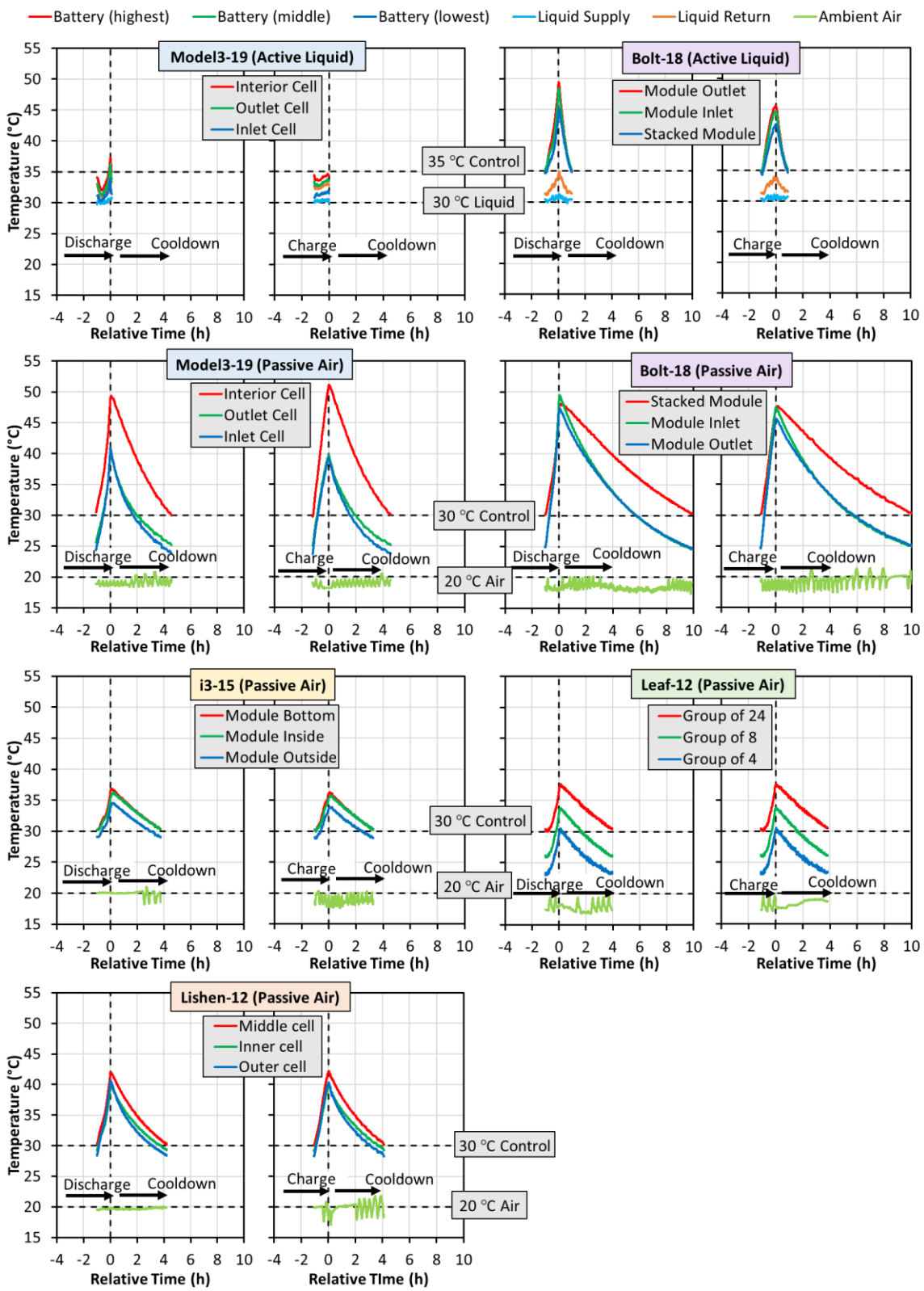


Figure 5.20 Highest, middle, and lowest pack temperatures and TMS temperatures measured during the third cycle of 1 h SCP tests.

For the liquid-cooled Model3-19, Figure 5.20 shows that the cell nearest the liquid inlet corresponds to T_{low}, which remains close to the liquid supply temperature throughout the cycle except at the end of the 1 h discharge when heat generation is highest. The cell nearest the liquid outlet is about 2 °C warmer than the inlet cell and remains close to the liquid return temperature throughout the cycle, demonstrating good heat transfer between the cylindrical cell housing and the liquid channel. The cell in the interior of the module corresponds to T_{high} but is less than 1 °C warmer than the outlet cell throughout the cycle, suggesting fairly even temperature distribution within the Model3-19 module when operating with an AL-TMS.

The passive-cooled Model3-19 features the same assignment of T_{low} and T_{high} as the liquid-cooled Model3-19. However, Figure 5.20 shows a dramatic change in the Model3-19 temperature distribution when the AL-TMS is disabled, resulting in the largest pack temperature differential observed for the seven test sets. The inlet and outlet cells (located at two outer corners of the pack) have more exposed surface area for natural convection compared to the interior cell, and the significant temperature gradient between corner and interior suggests that heat diffusion is limited in the module interior when operated with a PA-TMS. The corner cells also exhibit a higher temperature maximum during discharge compared to charge, while the interior cell exhibits a higher maximum during charge. As mentioned in Section 5.4.2, this indicates that the corner cells can dissipate heat more effectively than the interior cell, allowing the corner cell temperature rise to be dampened when heat generation is relatively low at the end of charge. This observation further supports the notion that heat diffusion is limited within the Model3-19 modules, possibly due to the intumescent foam surrounding each individual cylindrical cell. Since there are no exposed cell services near the centre of the pack on which to place temperature sensors, it is possible that even larger undetectable temperature gradients exist between the edge of the pack and its centre.

For the liquid-cooled Bolt-18, Figure 5.20 shows that the outlet side of the front module corresponds to T_{high}, which remains fairly close to the temperature of the inlet side of the module throughout the cycle. This suggests that the Bolt-18 liquid channel design (see Figure 4.5) does not cause significant horizontal temperature gradients across a given

module. However, Figure 5.20 also shows that Bolt-18 module temperatures rise significantly above the liquid return temperature during the 1 h test. This may indicate the presence of significant vertical temperature gradients within the module, and/or relatively poor heat transfer between the aluminum cooling plate and the modules sitting on top of it. The stacked module corresponds to T_{low}, which is up to 4 °C cooler than the two temperatures measured at the front module near the liquid inlet/outlet. This suggests that the Bolt-18 liquid channel design is most effective near the midpoint of the serpentine flow path where the supply and return lines are of equal temperature.

As with Model3-19, the Bolt-18 temperature distribution changes significantly when the AL-TMS is disabled. For the vast majority of the PA test shown in Figure 5.20, the Bolt-18 stacked module corresponds to T_{high} while the outlet side of the front module corresponds to T_{low} (the opposite of the AL test). However, at the end of the 1 h discharge the inlet side of the front module briefly exceeds the stacked module, meaning that T_{high} does not always correspond to the same temperature sensor for the passive-cooled Bolt-18. Figure 5.20 reveals that the outlet side of the front module undergoes the greatest temperature change between the beginning and end of discharge and charge, but the significantly slower passive heat dissipation rate of the stacked module causes it to experience higher temperatures throughout most of the cycle. Figure 5.20 also reveals that the stacked module is the reason why the passive-cooled Bolt-18 requires such long cooldown periods, as the outlet-side module undergoes a similar temperature drop in about 60 % of the time (6 h vs 10 h). This shows how the non-uniform module arrangement of Bolt-18 (see Figure 4.1) introduces a significant disadvantage for passive cooling. Though the stacked module has more exposed surface area around its edges compared to the other modules of Bolt-18, this advantage appears to be outweighed by the presence of another module beneath the stacked module. This suggests that heat diffuses upward from the lower modules into the stacked modules when Bolt-18 is operated with a PA-TMS. With an AL-TMS, the cooling plate located between the lower modules and stacked modules prevents this from occurring.

For i3-15, Figure 5.20 shows that the bottom surface of the module corresponds to T_{high}, which remains close to the temperature of the inward-facing module wall throughout the cycle. The outward-facing module wall corresponds to T_{low}, which is up to 4 °C cooler

than T_{high}. While this shows the temperature gradient between the middle of the six-module arrangement and its outer edge, it should be noted that each i3-15 module is about 36 cm long and 30 cm wide, containing 12 prismatic cells. Since temperature sensors could only be placed on the sides and bottom of the aluminum module housings, it is possible that larger undetectable temperature gradients exist within the individual modules.

Leaf-12 exhibits the second-largest pack temperature differential of the seven test sets shown in Figure 5.20, demonstrating a thermal disadvantage for the non-uniform module arrangement of Leaf-12 (see Figure 4.1). The group of 24 modules at the rear of the pack corresponds to T_{high}, which is up to 4 °C warmer than the temperature of the group of 8 modules at the front of the pack. The group of 4 modules in the middle of the pack corresponds to T_{low}, which is up to 7 °C cooler than T_{high}. This significant difference is due to the shorter heat diffusion pathways through smaller groupings of Leaf-12 modules, resulting in less heat accumulation and lower temperatures compared to larger groupings.

For Lishen-12, Figure 5.20 shows that while the outermost cell of the module (at the edge of the pack) corresponds to T_{low}, the innermost cell (adjacent to another module) exhibits very similar temperatures throughout the cycle, noting a slightly slower cooling rate due to the smaller amount of surface area exposed for natural convection. The middle cell of the module corresponds to T_{high} and is consistently about 2 °C warmer than the inner and outer cells. This suggests that temperature gradients do not compound across multiple adjacent Lishen-12 modules, and that the most significant temperature gradients exist within individual modules. Note that each Lishen-12 module extends from the middle of the pack to the side of the pack (see Figure 4.1). Since temperature sensors could only be placed on exposed cell surfaces at the side of the pack, it is possible that larger undetectable temperature gradients exist between the middle of the pack and its outer edges.

The temperature distribution results for all three power rates are presented in Figure 5.21. The left chart plots the calculated average pack temperature differential $\Delta T_{\text{diff}}^{\text{avg}}$ against the power-to-energy ratio, showing that significant temperature gradients can arise in some EV battery packs, even at a 4 h rate. The passive-cooled Model3-19 gives the largest $\Delta T_{\text{diff}}^{\text{avg}}$ at all power rates, ranging from about 5.3 °C at a 4 h rate to 9.2 °C at a 1 h rate. Recall that

$\Delta T_{\text{diff}}^{\text{avg}}$ represents an average pack differential over the full cycle, since long-term averages are more relevant for assessing degradation divergence within the pack. The instantaneous pack differential reaches as high as 12 °C for Model3-19 at the end of the 1 h charge. Leaf-12 and Bolt-18 also gives relatively large $\Delta T_{\text{diff}}^{\text{avg}}$ at all power rates, respectively reaching values of 7.4 °C and 5.2 °C at a 1 h rate. Lishen-12, i3-15, and the two liquid-cooled packs all exhibit a relatively low $\Delta T_{\text{diff}}^{\text{avg}} < 2.5$ °C at all power rates, which is well below the generally accepted 5 °C upper limit for optimal thermal consistency [175].

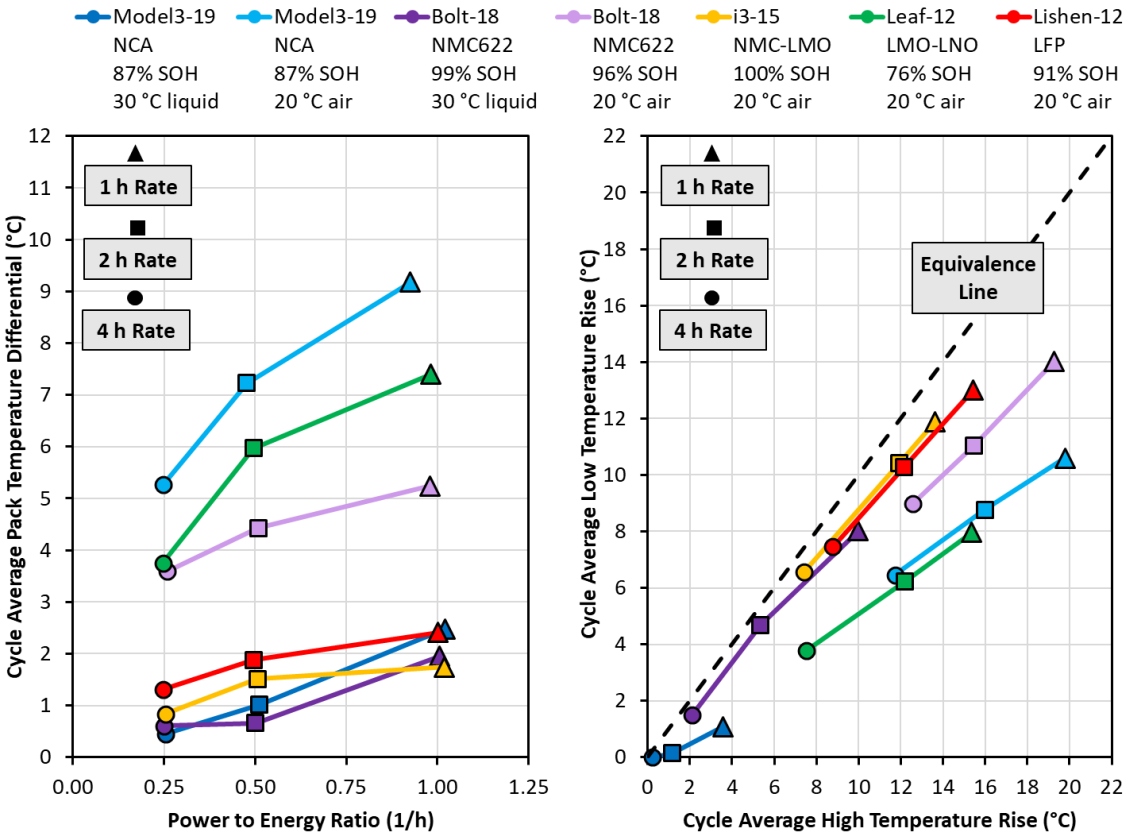


Figure 5.21 Calculated average pack temperature differentials (left) and comparison of average temperature rise for the coolest and of hottest cells/modules measured foreach battery pack (right).

For a more detailed analysis of the $\Delta T_{\text{diff}}^{\text{avg}}$ results, the right chart of Figure 5.21 plots the average low temperature rise $\Delta T_{\text{low}}^{\text{avg}}$ vs the average high temperature rise $\Delta T_{\text{high}}^{\text{avg}}$. The black dashed 'equivalence line' represents the theoretical limit where $\Delta T_{\text{low}}^{\text{avg}} = T_{\text{high}}^{\text{avg}}$ (i.e. no temperature gradient), such that the vertical distance between the datapoints and the

equivalence line is equal to $\Delta T_{\text{diff}}^{\text{avg}}$. Each dataset exhibits a fairly linear relationship between $\Delta T_{\text{low}}^{\text{avg}}$ and $\Delta T_{\text{high}}^{\text{avg}}$, with increasing divergence from the equivalence line at higher power rates. Lishen-12 and i3-15 are nearly colinear, as are Leaf-12 and the passive-cooled Model3-19, meaning that a given value of $\Delta T_{\text{high}}^{\text{avg}}$ produces a similar value of $\Delta T_{\text{low}}^{\text{avg}}$ and $\Delta T_{\text{diff}}^{\text{avg}}$ for both these pairs regardless of power rate. The chart also shows how the AL-TMS shifts the Model3-19 and Bolt-18 results closer to the origin and the equivalence line, with significant mitigation of $\Delta T_{\text{high}}^{\text{avg}}$, $\Delta T_{\text{low}}^{\text{avg}}$, and $\Delta T_{\text{diff}}^{\text{avg}}$.

Since i3-15, Leaf-12, and Lishen-12 experience similar $\Delta T_{\text{high}}^{\text{avg}}$ at all power rates, they can be directly compared in the right chart of Figure 5.21. This shows that the larger $\Delta T_{\text{diff}}^{\text{avg}}$ values of Leaf-12 are primarily due to its coolest measured module group. The temperatures of the larger module group within Leaf-12 are consistent with i3-15 and Lishen-12, while the smaller module group is anomalously cool due to the shorter heat diffusion pathways and smaller volume-to-surface-area ratio.

A similar comparison can be made between the passive-cooled Model3-19 and Bolt-18, which also experience similar $\Delta T_{\text{high}}^{\text{avg}}$ at all power rates. This shows that the larger $\Delta T_{\text{diff}}^{\text{avg}}$ values of the passive-cooled Model3-19 are primarily due to its coolest measured cell. The temperature profiles in Figure 5.20 show the corner cells of the passive-cooled Model3-19 exhibit a relatively fast cooldown rate, resulting in significantly cooler temperatures compared to the interior cells throughout the cycle. The fast cooldown rate of the corner cells may be due to their significant exposed surface area for natural convection, as well as their direct contact with the end of the liquid channel, which may help conduct heat away from the cell to the liquid manifold outside the module (essentially acting like a cooling fin for the corner cells).

Whereas Leaf-12 features a physical separation between its hottest and coolest modules, Model3-19 features a direct heat diffusion pathway from the interior cells to the corner cells. The fact that the interior cells remain significantly hotter than the corner cells despite the enhanced heat dissipation at the corner cells suggests that heat diffusion is limited within the passive-cooled Model3-19. As discussed in Section 2.6.5, cell thermal

conductivity is about an order of magnitude lower through the cell stack layers ($k_{\perp}$) compared to the parallel direction ($k_{\parallel}$) due to the electrode coatings and separators having low thermal conductivity compared to the metal current collectors. The heat diffusion pathway between the interior and corners of the Model3-19 modules depends on the lower $k_{\perp}$ value, but all five battery packs should be limited by $k_{\perp}$ in one direction. Since batteries with higher energy density tend to have thicker electrode coatings, higher energy density should be associated with lower $k_{\perp}$, which would be a disadvantage for Model3-19. However, Bolt-18 has a comparable energy density and does not seem to exhibit a large temperature gradient across a given module (the $\Delta T_{\text{diff}}^{\text{avg}}$ of Bolt-18 is primarily due to the slow cooldown rate of the stacked module). One unique feature of the Model3-19 modules is the presence of the liquid channels that pass between the cylindrical cells within the four modules of the pack. These liquid channels are highly effective at rejecting heat from the cells when operated with an AL-TMS, but with a PA-TMS the air-filled liquid channels may introduce a thermal resistance across the width of the modules, forcing heat to diffuse along the longer length of the modules. The spaces between the cylindrical cells of the Model3-19 modules are also filled with a material of unspecified thermal properties, which may change the overall thermal conductivity compared to the modules of the other four packs. The anisotropic thermal conductivity of the Model3-19 modules will be considered in greater detail in Chapter 7.

Figure 5.21 confirms that significant temperature differentials in excess of 5 °C can arise within second-life battery packs, particularly for passive-cooled packs with nonuniform module arrangements (e.g. Leaf-12) and packs operated without their intended AL-TMS (e.g. passive-cooled Model3-19 and Bolt-18), with exacerbated effects at higher power rates. Project developers should be aware of these potential limitations and consider limiting such packs to 4 h power rates to avoid significant thermal inconsistency. In contrast, some passive-cooled packs with more uniform module arrangements (e.g. i3-15 and Lishen-12) and liquid-cooled packs (e.g. Model3-19 and Bolt-18) can maintain unproblematic temperature differentials below 2.5 °C. However, it should be recognized that accessibility can be a limitation when it comes to measuring pack temperature differentials. It is relatively easy to apply temperature sensors to the coolest cells/modules

near the outer edges of the pack, but for some packs it can be difficult to apply temperature sensors to the hottest cells/modules in the pack interior. The results in Figure 5.21 should therefore be viewed conservatively. Second-life battery researchers and developers should take care to apply multiple temperature sensors at strategic locations to ensure that the system is monitoring the highest measurable temperatures and temperature differentials.

5.4.5. Dependence on Heat Generation

Battery temperatures depend on the relative rates of heat generation and heat dissipation, as well as specific heat capacity. Since different lithium-ion batteries generally have similar specific heat capacities (discussed in Section 2.6.2), the measured temperatures from the SCP tests should exhibit a dependence on heat generation for a given TMS. To explore this relationship, the $\Delta T_{\text{high}}^{\max}$ results are plotted against the calculated cycle volumetric heat generation $\bar{q}_v$ and the average volumetric heat generation rate $\dot{\bar{q}}_v$ in the left and right charts of Figure 5.22.

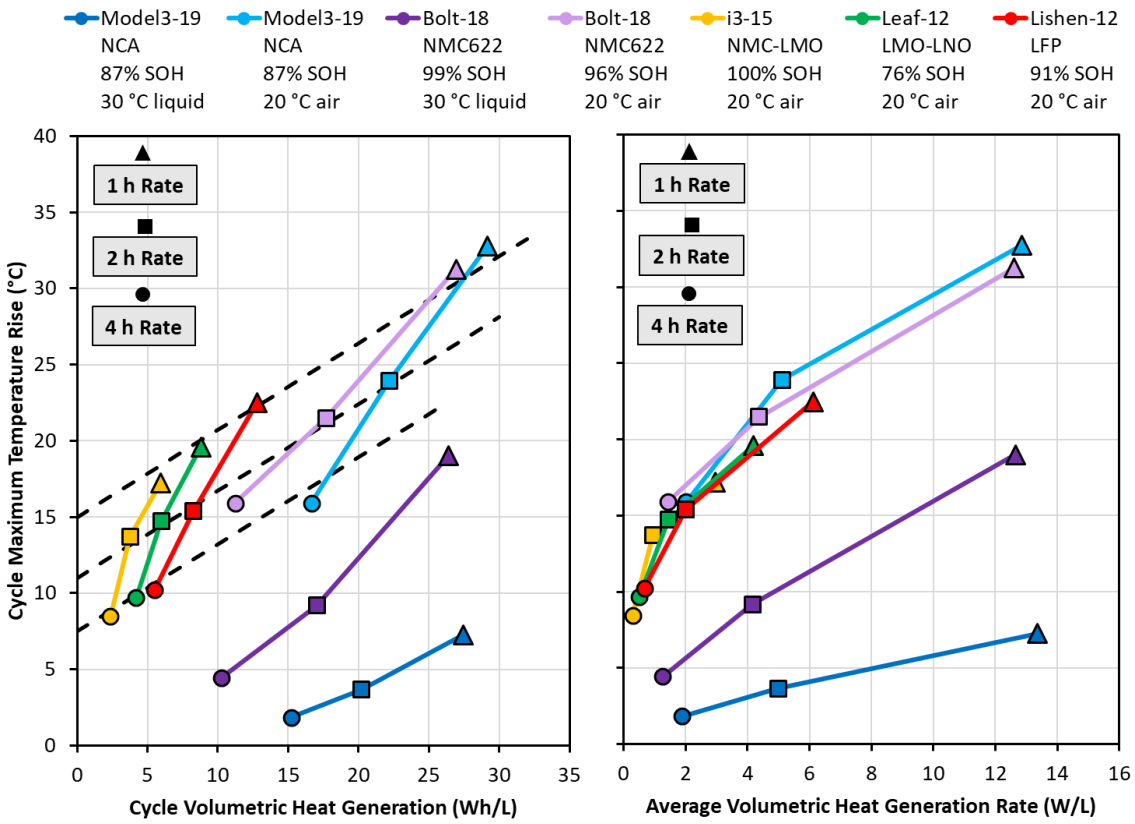


Figure 5.22 Dependence of maximum temperature rise on cycle volumetric heat generation (left) and average volumetric heat generation rate (right).

The two graphical techniques in Figure 5.22 reveal clear similarities between the five passive-cooled packs. The left chart features three black dashed lines of equal slope to highlight the fairly linear relationship between $\Delta T_{\text{high}}^{\text{max}}$ and $\bar{q}_v$ among the 4 h, 2 h, and 1 h PA test results. When $\bar{q}_v$ is scaled by the combined discharge and charge durations of each test to produce $\dot{\bar{q}}_v$ in the right chart of Figure 5.22, the passive-cooled datapoints exhibit a clear and consistent dependence on $\dot{\bar{q}}_v$. This is a significant level of consistency given the diversity in design among the five battery packs. Notably, the wide range of passive cooling time constants presented in Section 5.4.3 (between $\tau \approx 4$ h for Model3-19 and $\tau \approx 10$ h for Bolt-18) does not appear to significantly impact the $\Delta T_{\text{high}}^{\text{max}}$ results for a given $\dot{\bar{q}}_v$. This is likely due to a combination of the asymptotic nature of passive cooling, the relatively slow passive cooling rates of all five battery packs, and the comparable size, shape, and material composition of different EV battery packs. In contrast, the much higher cooling rate of the liquid-cooled Model3-19 ($\tau \approx 0.2$ h) provides a significant suppression of its $\Delta T_{\text{high}}^{\text{max}}$ vs $\dot{\bar{q}}_v$ curve. The liquid-cooled Bolt-18 falls approximately halfway between the liquid-cooled Model3-19 and the passive-cooled trend.

Note that the passive-cooled Model3-19 sits slightly above the trend in the right chart of Figure 5.22. This is because the passive-cooled Model3-19 exhibits anomalously high temperatures at the end of charge compared to the other passive-cooled packs, as discussed in Section 5.4.2. When Figure 5.22 is reconstructed for discharge temperature rise alone, the passive-cooled datapoints become even more closely aligned. Despite the apparent heat diffusion limitation of the passive-cooled Model3-19 modules (discussed previously in Section 5.4.2), its $\Delta T_{\text{high}}^{\text{max}}$ results remain fairly consistent with the other packs when plotted against $\dot{\bar{q}}_v$.

The same graphical analysis is applied to the $\Delta T_{\text{high}}^{\text{avg}}$ results in Figure 5.23, where the y-axis range is retained for comparison of scale with the $\Delta T_{\text{high}}^{\text{max}}$ results in Figure 5.22. This shows that $\Delta T_{\text{high}}^{\text{avg}}$ also exhibits a clear dependence on and $\bar{q}_v$ and $\dot{\bar{q}}_v$. Since Section 5.4.2 identified a clear correlation between $\Delta T_{\text{high}}^{\text{max}}$ and $\Delta T_{\text{high}}^{\text{avg}}$ among passive-cooled packs and among liquid-cooled packs, it makes sense that Figure 5.23 resembles Figure 5.22 on a smaller scale.

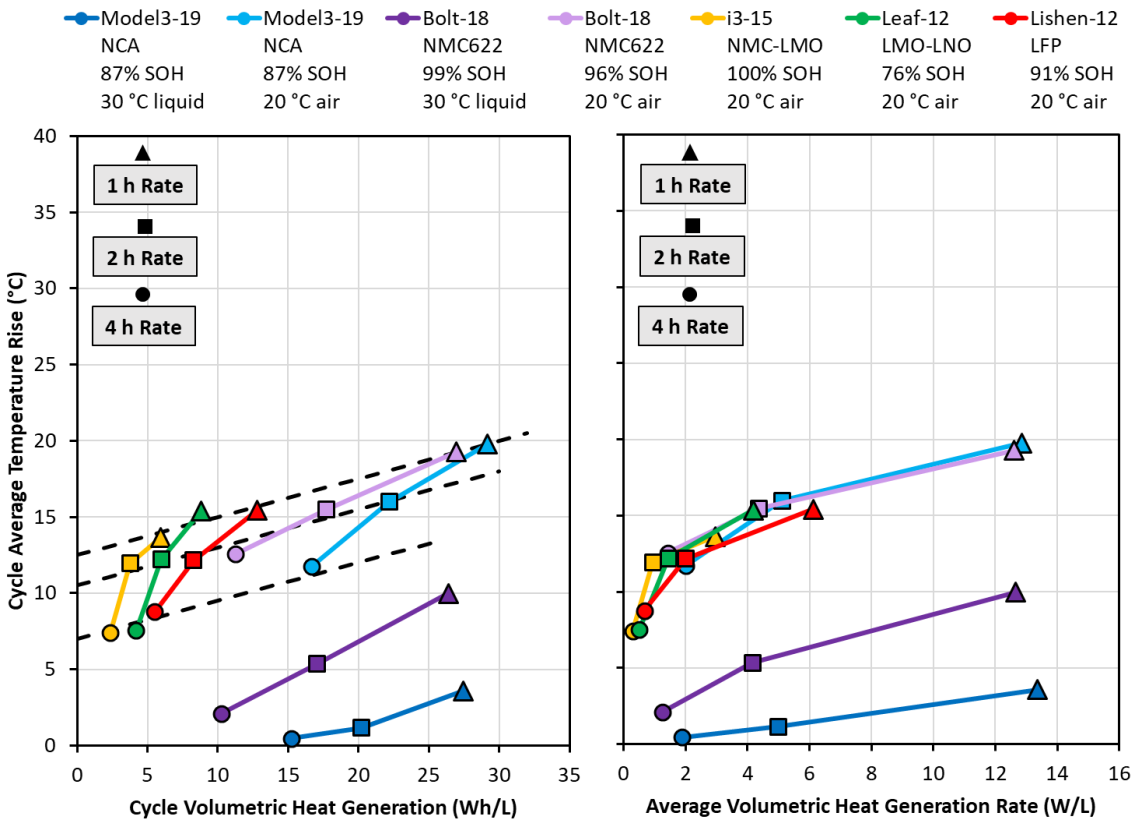


Figure 5.23 Dependence of average temperature rise on cycle volumetric heat generation (left) and average volumetric heat generation rate (right).

The same graphical analysis is applied to the $\Delta T_{\text{diff}}^{\text{avg}}$ results in Figure 5.24. This shows that there is no consistent dependence on heat generation among the five passive-cooled packs when it comes to temperature gradients. This is because $\Delta T_{\text{diff}}^{\text{avg}}$ depends strongly on the design of cells and modules within the pack, which varies considerably among the five battery packs. In contrast, $\Delta T_{\text{high}}^{\text{max}}$ and $\Delta T_{\text{high}}^{\text{avg}}$ depend more on the physical size and shape of the pack exterior as well as the battery material composition, which are relatively consistent among the five battery packs (i.e. short, wide rectangular prisms made of aluminum, copper, lithium, graphite, organic electrolytes, plastic separators, transition metal oxides, etc.).

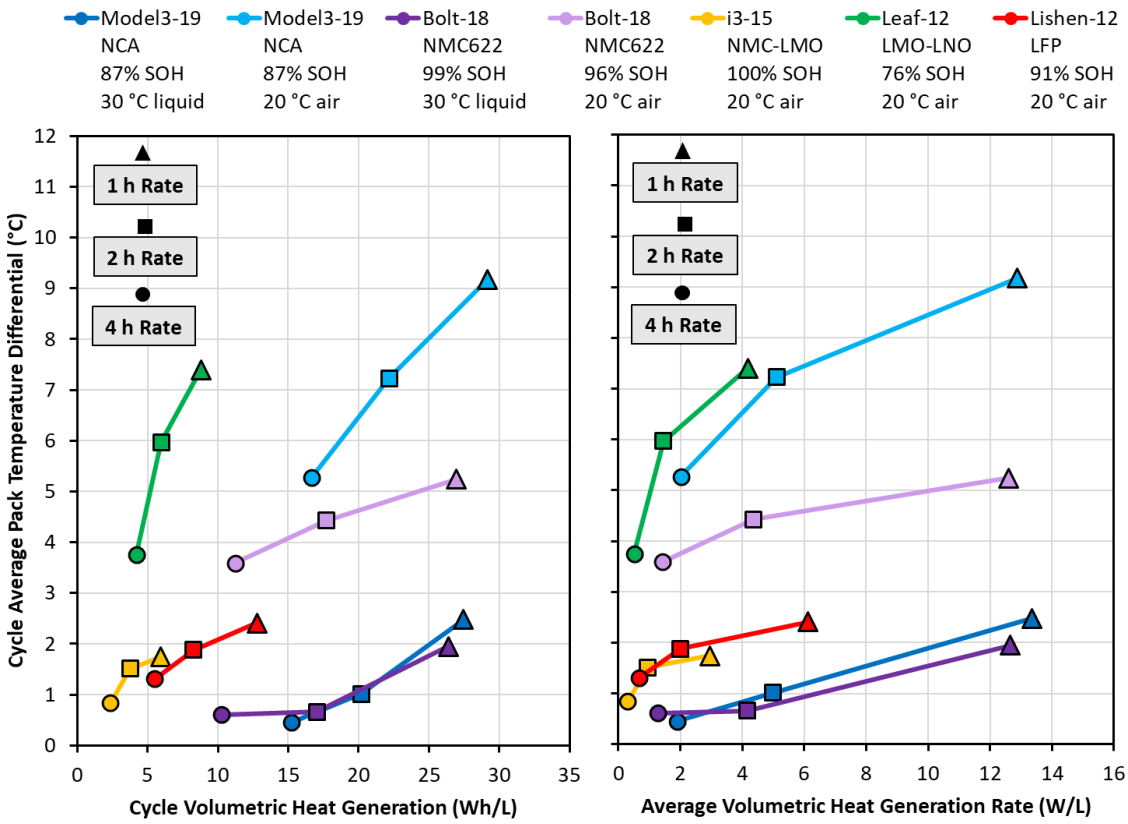


Figure 5.24 Dependence of pack temperature differential on cycle volumetric heat generation (left) and average volumetric heat generation rate (right).

The consistent trends shown in Figure 5.22 and Figure 5.23 suggest that it is possible to predict $\Delta T_{\text{high}}^{\text{max}}$ and $\Delta T_{\text{high}}^{\text{avg}}$ for a passive-cooled EV battery pack without actually measuring temperature, as long as $\dot{\bar{q}}_v$ can be calculated from a known energy efficiency η and energy density $\bar{E}_v$ for a given discharge duration t_{dis} (see Equation 4.22). Chapter 6 will explore the potential for predicting a range of SCP test results based on minimal empirical data.

5.5. Repeatability of Results

Sections 5.3 and 5.4 compared electrical and thermal performance results across five battery packs, two TMS types, and three power rates for a total of 21 SCP tests, but only one datapoint per test was shown for each performance metric. To instill confidence in the reliability of measured results and comparative analyses, multiple datasets should be acquired for each combination of battery, TMS, and power rate to ensure that all measured results are repeatable under fixed test parameters. The complete set of 21 tests could only be run once due to the limited testing window for some packs within this research project,

but each test features three consecutive SCP cycles which produce a set of results for the electrical and thermal performance metrics. Only the results of the third cycle were presented in Sections 5.3 and 5.4. While the results of the first cycle are not reliable due to the influence of the initial battery temperature and SOC, the test conditions should be fairly consistent for both the second and third cycle. If the results of the second and third cycle are in close alignment, it can be concluded that the results are repeatable. This would also indicate that two cycles may be sufficient for the SCP test protocol instead of three.

Figure 5.25 compares the results for the main electrical performance metrics measured during the second and third cycle of each test, where larger data markers denote the third cycle (previously presented in Section 5.3) and smaller data markers denote the second cycle. The left chart shows the energy utilization ratio ζ while the right chart shows the cycle energy efficiency η. The comparison demonstrates that both ζ and η are highly repeatable. The difference between the two cycles is about 0.1 % on average for both ζ and η, with a maximum difference of 0.4 % for ζ and 0.3 % for η.

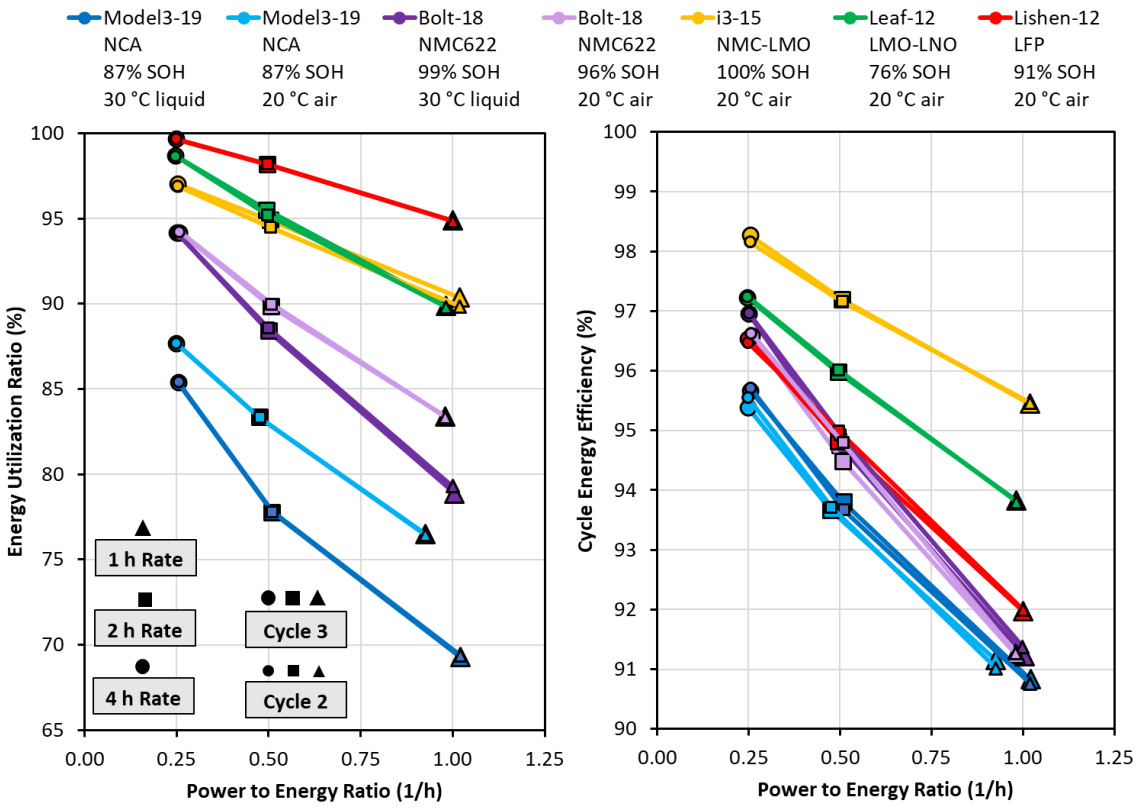


Figure 5.25 Comparison of energy utilization ratio (left) and cycle energy efficiency (right) results measured during the second and third cycle of each test.

Figure 5.26 compares the temperature rise results measured during the second and third cycle of each test. The left and right charts respectively show the maximum $\Delta T_{\text{high}}^{\text{max}}$ and average $\Delta T_{\text{high}}^{\text{avg}}$ temperature rise, demonstrating a high degree of repeatability in both cases. The difference between the two cycles is about 0.2 °C on average for both $\Delta T_{\text{high}}^{\text{max}}$ and $\Delta T_{\text{high}}^{\text{avg}}$, with a maximum difference of 0.7 °C for $\Delta T_{\text{high}}^{\text{max}}$ and 0.5 °C for $\Delta T_{\text{high}}^{\text{avg}}$. An investigation revealed that the cases with larger differences also feature notable differences between the average ambient temperatures T_{∞}^{avg} of the two cycles. This indicates that $\Delta T_{\text{high}}^{\text{max}}$ and $\Delta T_{\text{high}}^{\text{avg}}$ are somewhat sensitive to ambient temperature, which is likely a result of a highly simplified calculation method being applied to a complex thermal system influenced by heat diffusion. Chapter 7 will present a more detailed thermal analysis of an EV battery pack. For the purposes of comparing temperature rise in different battery packs, the impact of ambient temperature fluctuations is not significant. Even so, the sensitivity emphasizes the importance of testing batteries under consistent ambient conditions.

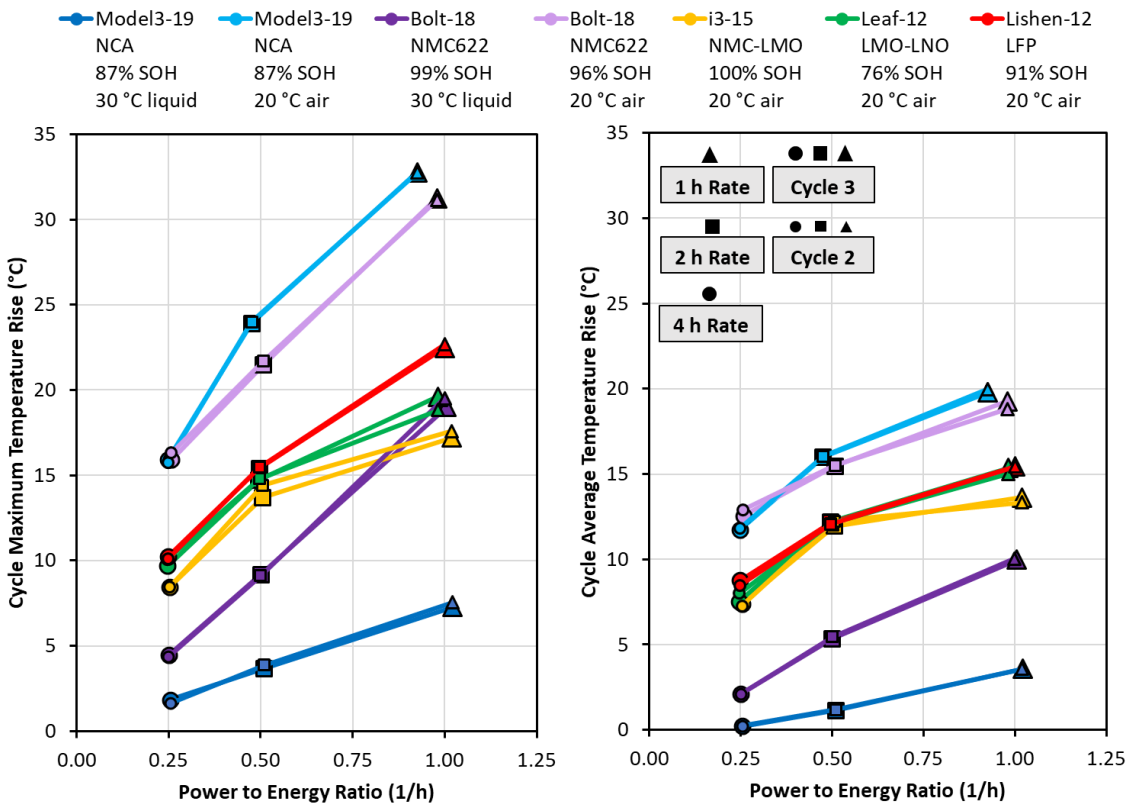


Figure 5.26 Comparison of maximum (left) and average (right) temperature rise results measured during the second and third cycle of each test.

Figure 5.27 compares the cooldown performance results measured during the second and third cycle of each test. The left and right charts respectively show the cycle cooldown duration t_{cool} and the average cooling time constant τ, demonstrating a high degree of repeatability in both cases. The difference between the two cycles is about 0.1 h on average for both t_{cool} and τ, with a maximum difference of 0.3 h for t_{cool} and 0.4 h for τ. Since t_{cool} is dependent on the temperatures reached during discharge and charge, the cycle cooldown temperature drop ΔT_{cool} is used as the x-axis to directly compare cooldown characteristics between the two cycles. This shows that cases with larger t_{cool} differences also feature larger ΔT_{cool} differences. Plotting t_{cool} against ΔT_{cool} makes these cases fall neatly into line, demonstrating consistent cooldown characteristics.

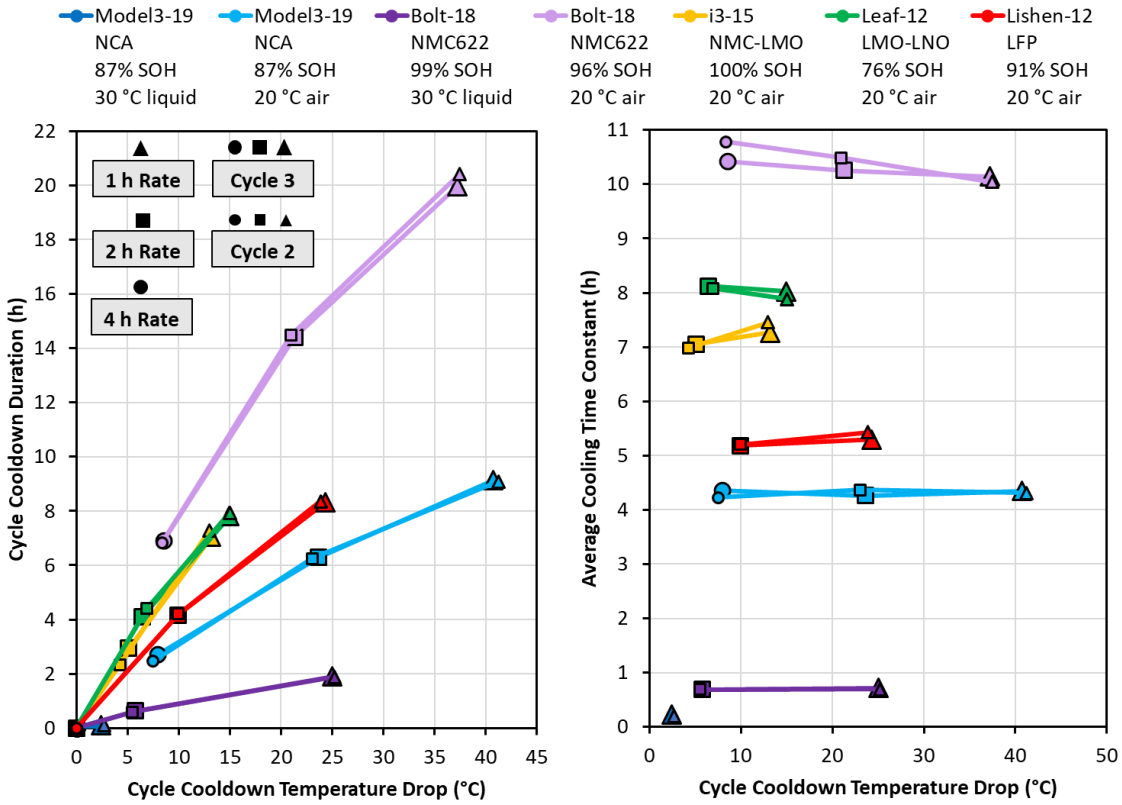


Figure 5.27 Comparison of cycle cooldown duration (left) and cooling time constant (right) results measured during the second and third cycle of each test.

Overall, the main electrical and thermal performance results have been shown to be highly repeatable. This means that the comparative analyses in Sections 5.3 and 5.4 can be considered reliable for the present SOH of each battery pack. Section 5.6 will consider how battery degradation may influence the results and analyses.

5.6. Impact of Degradation on Performance Metrics

Since second-life batteries will be acquired at different SOH levels and degrade further throughout second-life service, it is important to consider how degradation may impact the established electrical and thermal performance metrics. While degradation was not explicitly studied in this research project due to the significantly greater experimental resources required for pack-level degradation studies, enough experimental data was collected that results for similar packs at different SOH levels can be compared.

The 2019 Tesla Model3 SR+ battery pack used in this research project was first acquired and subjected to a baseline capacity test in March of 2020, at which time the pack was found to be at 100 % SOH. This battery pack was the subject of numerous experiments under various research projects over the next two and a half years. The first complete round of SCP tests was conducted in February of 2021, at which time the pack was found to be at 95 % SOH. The temperature monitoring technique applied to this pack was later upgraded to better capture interior module temperatures while operating with passive cooling. This upgrade was applied in a new round of SCP tests in August of 2022, at which time the pack was found to be 87 % SOH. The official SCP test results presented in Sections 5.3 and 5.4 for Model3-19 include only the August 2022 tests since the previously collected temperature data is considered inadequate. However, the electrical performance results collected in 2021 for both AL and PA tests can be compared to the 2022 results to assess how degradation from 95 % to 87 % SOH impacts the results. The temperature data collected in 2021 for the liquid-cooled Model3-19 can also be considered since Section 5.4.4 demonstrated that the Model3-19 module temperatures are fairly uniform when operating with liquid cooling.

The 2012 Nissan Leaf battery pack used in this research project was acquired and tested in August of 2020, at which time the pack was found to be at 76 % SOH. Prior to this, a 2014 Nissan Leaf battery pack (hereafter referred to as Leaf-14) was acquired and tested with the same SCP test protocol in February of 2020, at which time the pack was found to be at 83 % SOH. Both these Nissan Leaf packs were partially disassembled shortly after testing for the purposes of other research projects. Similar to the case of Model3-19, the temperature monitoring technique applied to Leaf-14 was later upgraded and applied to

Leaf-12. The official SCP test results presented in Sections 5.3 and 5.4 therefore include Leaf-12 but not Leaf-14, since the Leaf-12 thermal performance results are considered more reliable. However, the electrical performance results collected for Leaf-14 can be compared to Leaf-12 to assess how degradation from 83 % to 76 % SOH impacts the results.

5.6.1. Impact on Voltage Profile

Section 5.2 presented a series of voltage vs SOC charts to illustrate how the voltage profiles of different EV battery packs are impacted by power rate and thermal management. Figure 5.28 now adds a third dimension to this analysis. The left charts show the same voltage vs SOC charts for the liquid-cooled and passive-cooled Model3-19 (87 % SOH) and Leaf-12 (76 % SOH) that were shown in Section 5.2. These are contrasted with the right charts, which show the liquid-cooled and passive-cooled Model3-19 at 95 % SOH and Leaf-14 at 83 % SOH.

The Model3-19 results in Figure 5.28 clearly show that lower SOH is associated with larger voltage gaps (implying lower energy efficiency η) and narrower operational SOC ranges in symmetrical CP cycling (implying lower energy utilization ratio ζ), especially at higher power rates. While the minimum SOC values at each power rate appear fairly consistent for different SOH levels, the maximum SOC values exhibit clear SOH sensitivity. At 95 % SOH, the liquid-cooled Model3-19 reaches 93 % SOC at a 4 h rate and 80 % SOC at a 1 h rate, but at 87 % SOH the pack reaches 86 % SOC at a 4 h rate and 74 % SOC at a 1 h rate. At both 87 % SOH and 95 % SOH, the higher temperatures associated with passive cooling result in higher maximum SOC values and lower minimum SOC values than the liquid-cooled results. Each of these observations can be explained by the fact that both degradation and liquid-cooling result in greater internal resistance and thus greater overpotentials. As explained in Section 5.2.2, the shape of the NCA voltage profile makes the maximum SOC sensitive to overpotentials. Examination of the 4 h voltage profiles for Model3-19 also shows that the bumpy voltage profile typical of nickel-rich cells (described in Section 2.2.5) is more distinct at 95 % SOH than at 87 % SOH. Section 2.5.3 explained that some peaks in $\frac{\mathrm{dV}}{\mathrm{dQ}}$ and $\frac{\mathrm{dQ}}{\mathrm{dV}}$ profiles tend to shrink with degradation, so the fact that the 87 % SOH voltage profile is less bumpy is further evidence of degradation.

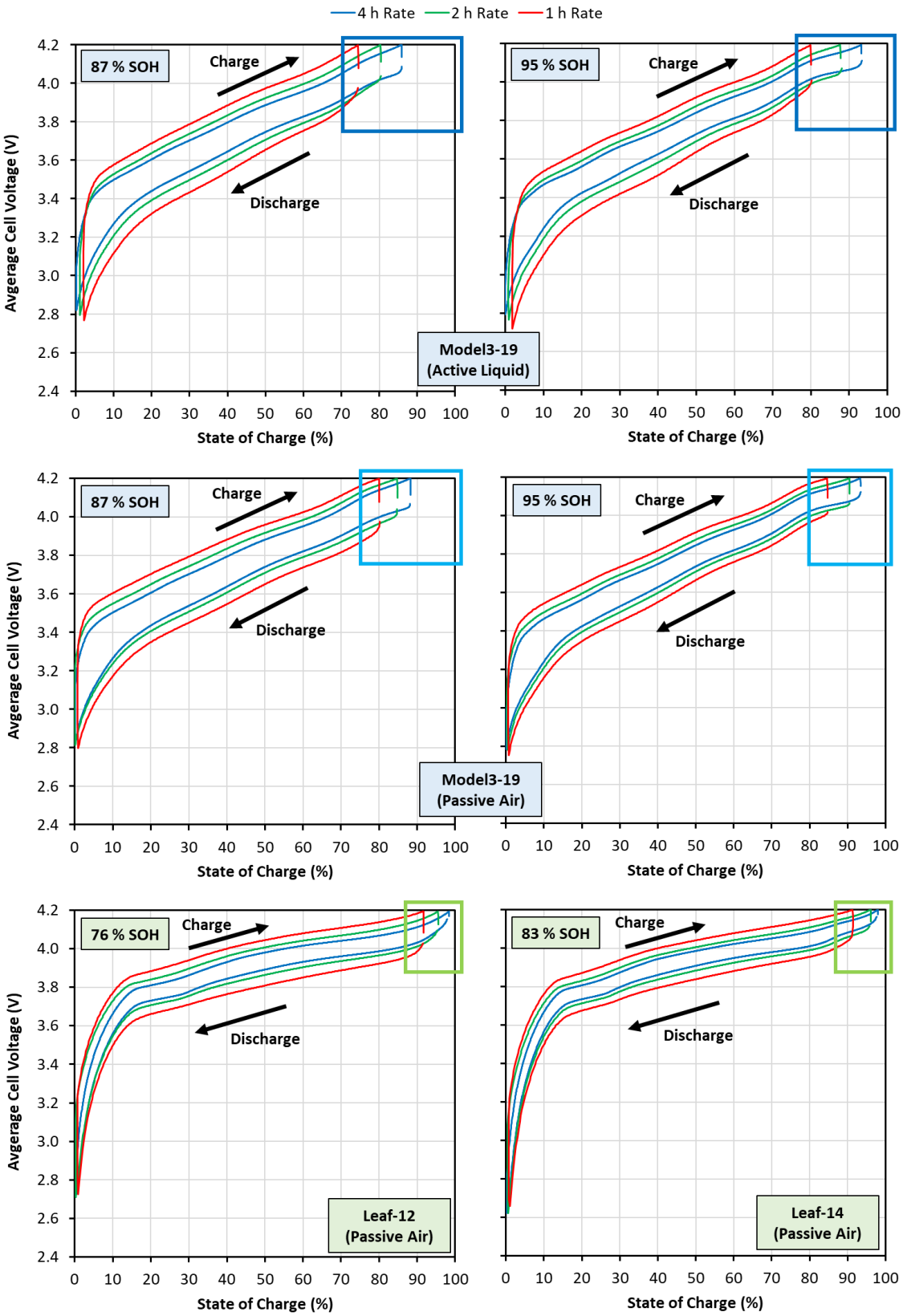


Figure 5.28 Superimposed average cell voltage profiles for 4 h, 2 h, and 1 h SCP cycles conducted at different SOH levels.

The Leaf-12 and Leaf-14 results in Figure 5.28 show noticeably larger voltage gaps for the pack at lower SOH, but the differences are less pronounced than those exhibited by Model3-19. Furthermore, the SOC window and voltage profile shape of the Leaf packs do not appear to be significantly impacted by degradation. This indicates that different EV battery cell designs may respond differently to similar changes in SOH (7 % for Leaf and 8 % for Model3-19).

It was established in Section 2.5 that NCA cells (used in Model3-19) tend to undergo greater rates of SEI growth than LMO cells (used in Leaf-12 and Leaf-14). Since SEI growth is a primary source of internal resistance growth in lithium-ion cells, this difference in cell chemistry may explain why Model3-19 seems to exhibit greater internal resistance growth than the Leaf packs in Figure 5.28. However, it is also important to recognize that these packs may have undergone different modes of degradation due to differences in operational history. It is possible that the degradation of Model3-19 produced greater internal resistance growth than the degradation of the Leaf packs due to differences in usage rather than differences in cell design. A conclusive comparison of degradation characteristics for different EV battery packs would require all packs to be subjected to a common degradation test duty cycle for many months, which was not feasible within this research project. This type of pack-level degradation study is recommended for future research in second-life battery performance characterization.

Figure 5.28 also provides an opportunity to assess how the proposed SCP test method performs when evaluating similar packs at different SOH levels. As explained in Section 4.4, the CP setpoint for each test is chosen such that the discharge duration t_{dis} is close to 4.0 h, 2.0 h, or 1.0 h regardless of SOH. This means that the power magnitude P (in kW) applied to a given pack design will be smaller for a lower SOH. Figure 5.28 shows that lower SOH levels still produce larger overpotentials despite the smaller currents being applied. This demonstrates that a fixed set of t_{dis} values is an effective test method for comparing similar packs at different SOH levels. Applying a fixed set of P values regardless of SOH would cause packs at lower SOH to exhibit inflated overpotentials, shortened discharge durations, underestimated energy capacities, and inflated temperatures. The test method described in Section 4.4 is therefore recommended.

5.6.2. Impact on Discharge Energy

As described in Section 2.5, battery degradation can give rise to both capacity loss and internal resistance growth, both of which contribute to decreased energy capacity. While the energy-based SOH metric quantifies the decrease in energy measured with a baseline capacity test (featuring a CCCV charge to 100 % SOC), Figure 5.29 quantifies the decrease in energy based on SCP tests conducted at 4 h, 2 h, and 1 h rates. The left and right chart respectively plot the measured module energy density $\bar{E}_v$ and the estimated BOL energy density $\bar{E}_v^{\mathrm{BOL}}$ against the power-to-energy ratio.

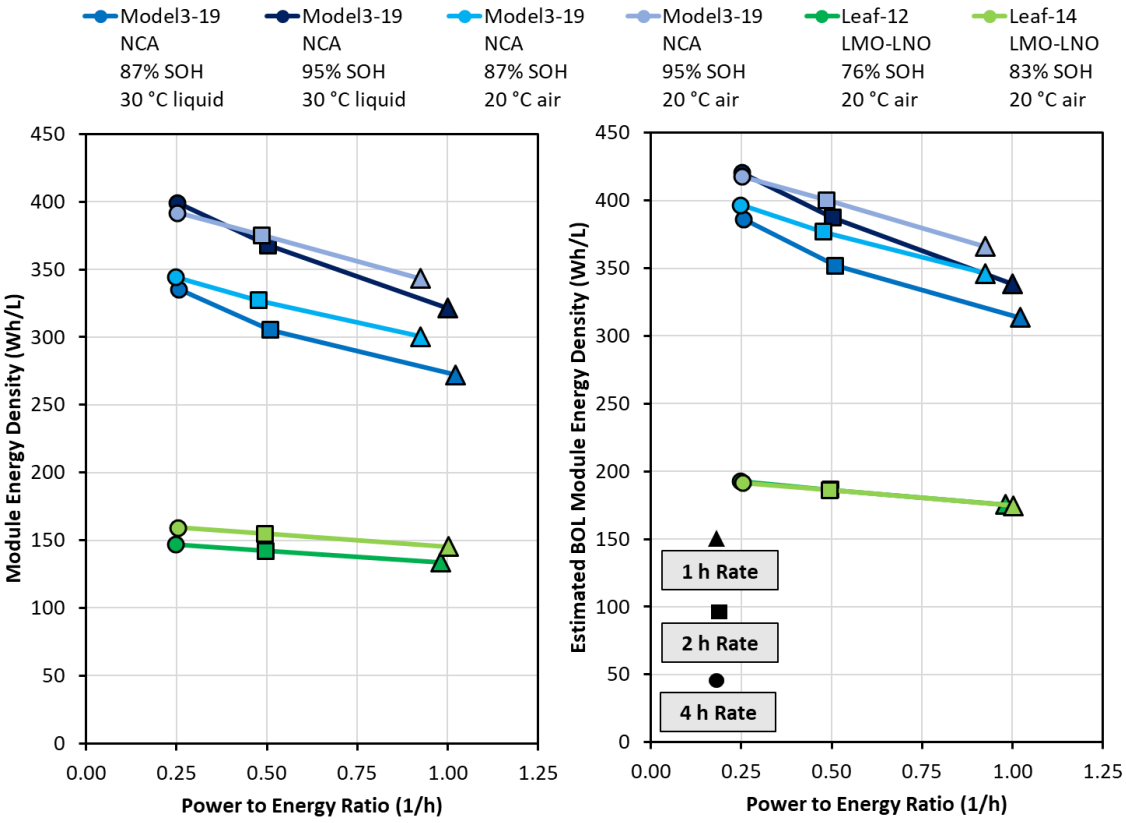


Figure 5.29 Measured (left) and estimated BOL (right) module energy densities taken at different SOH levels.

Though the pairs of Model3-19 and Leaf datasets share similar changes in SOH, the left chart of Figure 5.29 shows their corresponding changes in $\bar{E}_v$ are quite different. Leaf-12 is about 7 % lower than Leaf-14 in terms of both SOH and $\bar{E}_v$ results, but the $\bar{E}_v$ results for the liquid-cooled and passive-cooled Model3-19 respectively decrease by about 15 % and 12 % when SOH decreases by 8 %. As explained in Section 5.6.1, the operational SOC

range of Model3-19 is relatively sensitive to changes in SOH due to the combined effects of internal resistance growth and the shape of the NCA voltage profile. The SOH sensitivity of the Model3-19 SOC window manifests in the $\bar{E}_v$ results.

The left chart of Figure 5.29 scales the $\bar{E}_v$ results according to the SOH of each pack to produce the estimated BOL module energy density $\bar{E}_v^{\mathrm{BOL}}$. This eliminates the difference between the Leaf-12 and Leaf-14 $\bar{E}_v$ results, and halves the difference between the 87 % SOH and 95 % SOH $\bar{E}_v$ results for Model3-19. The Model3-19 $\bar{E}_v^{\mathrm{BOL}}$ results do not align perfectly because SOH is based on utilizing the entire SOC window while $\bar{E}_v$ is based on a reduced SOC window for SCP cycles. The SOH sensitivity of the Model3-19 SOC window therefore impacts the $\bar{E}_v^{\mathrm{BOL}}$ results. Even so, Figure 5.29 shows that $\bar{E}_v^{\mathrm{BOL}}$ is much less sensitive to SOH changes than $\bar{E}_v$. This suggests that $\bar{E}_v^{\mathrm{BOL}}$ is a more suitable metric for comparing the performance of different second-life battery pack designs independently of SOH.

The SOH sensitivity of the Model3-19 SOC window also manifests in the energy utilization ratio ζ, as shown in the left chart of Figure 5.30. The ζ results for the liquid-cooled and passive-cooled Model-19 respectively decrease by about 7 % and 5 % for an 8 % decrease in SOH, while Leaf-12 and Leaf-14 exhibit nearly identical ζ results at all three power rates despite their different SOH levels. The right chart of Figure 5.30 shows that when the ζ results are normalized to the 4 h value to produce the normalized energy utilization ratio ζ^*, the SOH sensitivity of Model3-19 is essentially eliminated. This suggests that ζ^* could be another suitable metric for comparing the performance of different second-life battery pack designs independently of SOH.

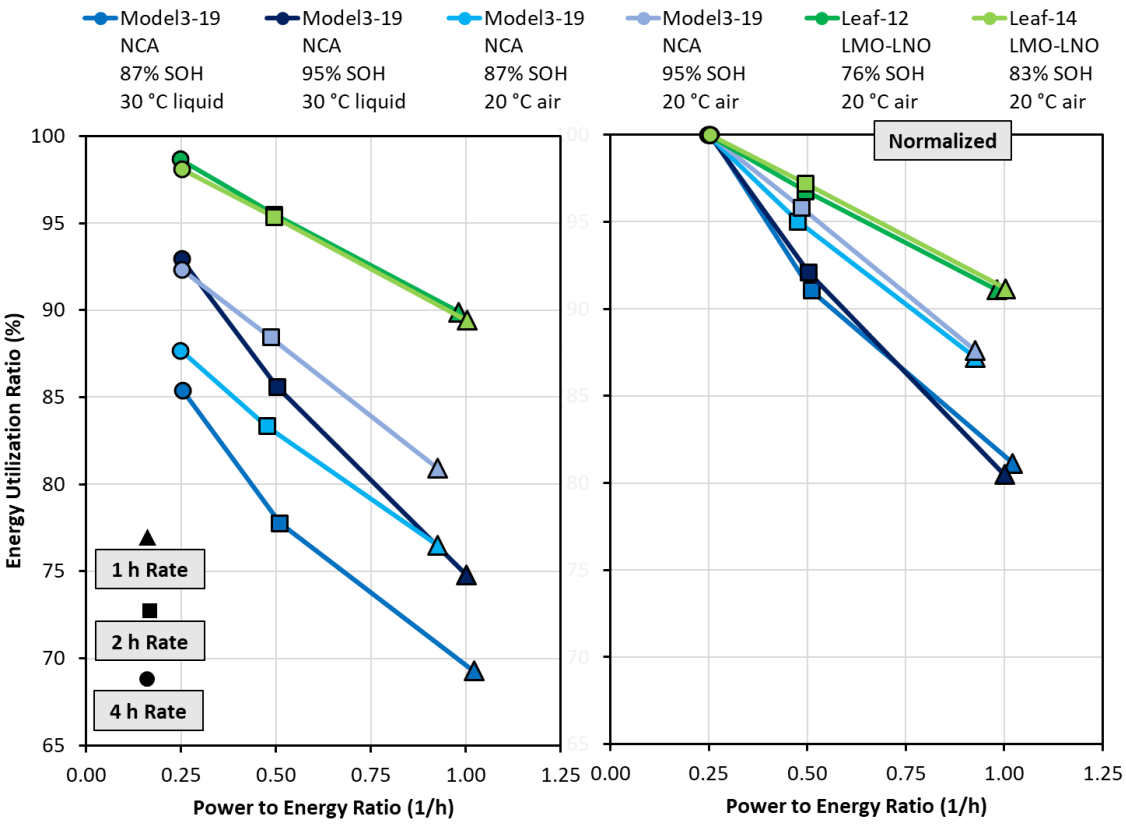


Figure 5.30 Calculated (left) and normalized (right) energy utilization ratios taken at different SOH levels.

5.6.3. Impact on Energy Efficiency

Since cycle energy efficiency η is an indicator of battery internal resistance, η should decrease when battery degradation causes internal resistance growth. The left chart of Figure 5.31 shows that η decreases with SOH in all three cases, though the decrease is visibly larger for Model3-19 than for Leaf. The η difference between Leaf-12 and Leaf-14 is about 0.3 % to 0.6 % , while the η decrease for Model3-19 is about 0.8 % to 1.2 % for the liquid-cooled case and about 1.1 % to 1.6 % for the passive-cooled case. This supports the suggestion from Section 5.6.1 that internal resistance growth is more pronounced for Model3-19 than the Leaf packs.

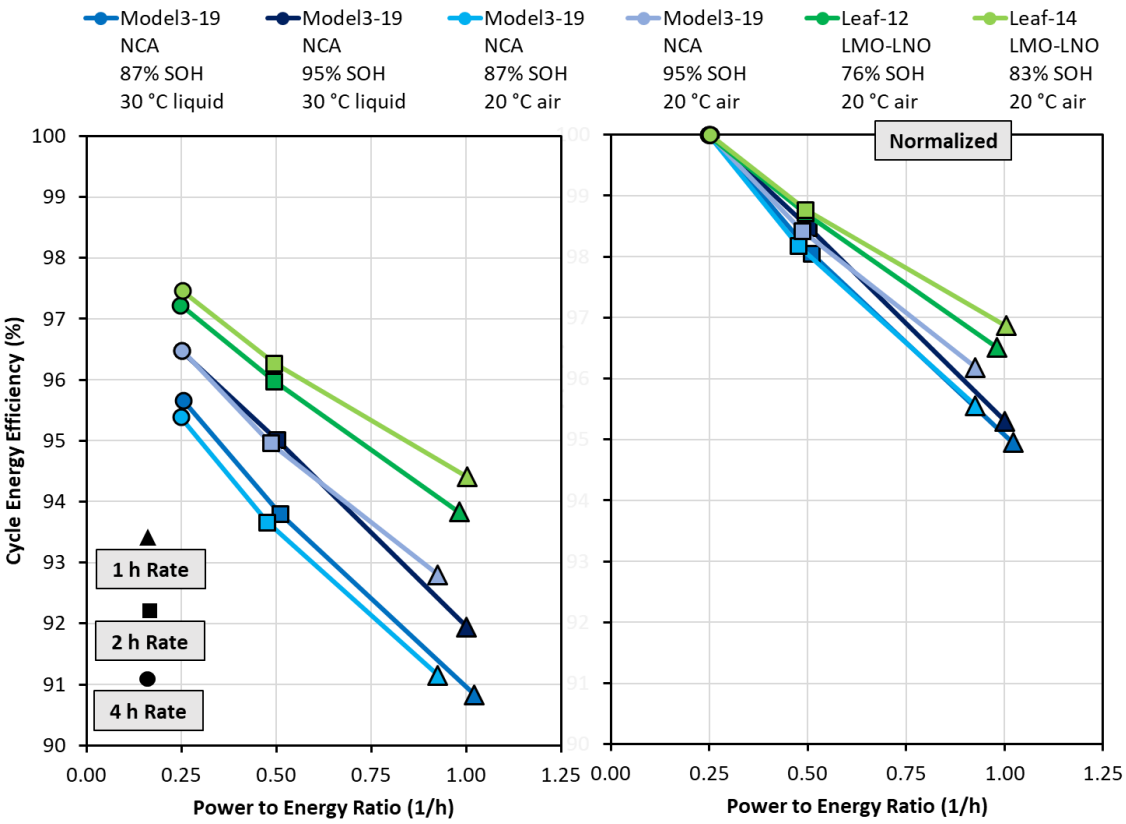


Figure 5.31 Calculated (left) and normalized (right) cycle energy efficiencies taken at different SOH levels.

The passive-cooled Model3-19 exhibits a slightly greater η decrease than the liquid-cooled Model3-19, but this is likely related to the upgraded temperature monitoring technique applied for the tests conducted at 87 % SOH. For the 95 % SOH tests, the higher temperatures of the module interior were not captured and were therefore not subject to the temperature control setpoint. While the Model3-19 module temperature is relatively uniform when liquid-cooling is applied (see Section 5.4.4), the 95 % SOH passive-cooled pack was likely at a significantly higher temperature throughout the SCP cycle than the measurements indicate, especially for higher power rates. The corresponding thermal influence on battery internal resistance may have slightly inflated the η results for the 95 % SOH passive-cooled Model3-19. The liquid-cooled Model3-19 tests provide more consistent conditions for assessing the impact of degradation on η, so the 0.8 % to 1.2 % decrease is the more reliable figure for Model3-19.

While a 1 % decrease in η over an 8 % decrease in SOH is much less sensitive than the SOH sensitivity of $\bar{E}_v$ and $\bar{E}_v^{\mathrm{BOL}}$ shown in Section 5.6.2, a 1 % change in η is significant compared to the 90 % to 98 % range of η results presented previously in Figure 5.9. This means that a comparison of η among different second-life battery packs will be somewhat sensitive to SOH. The right chart of Figure 5.31 normalizes the η results to the 4 h value, which largely mitigates the SOH sensitivity. This suggests that η^* could be a suitable metric for comparing different second-life battery pack designs independently of SOH. However, assigning $\eta^* = 100$ % at a 4 h rate fails to quantify the real charging costs associated with low-power cycling, so η has more practical value as a performance metric.

5.6.4. Impact on Heat Generation

Both energy density $\bar{E}_v$ and cycle energy efficiency η contribute to volumetric heat generation during an SCP cycle. Since Sections 5.6.2 and 5.6.3 respectively showed that both $\bar{E}_v$ and η tend to decrease with degradation, heat generation should be expected to be impacted by degradation as well. However, the definitions for cycle volumetric heat generation $\bar{q}_v = \bar{E}_v\left(\frac{1}{\eta} - 1\right)$ and average volumetric heat generation rate $\dot{\bar{q}}_v = \frac{\bar{E}_v}{t_{\mathrm{dis}}}\left(\frac{1-\eta}{1+\eta}\right)$ show that $\bar{E}_v$ and η have opposing influences on $\bar{q}_v$ and $\dot{\bar{q}}_v$. A lower discharge energy per unit volume translates to less heat generated per unit volume, but a lower energy efficiency translates to more waste heat generated. This means that degradation impacts on $\bar{E}_v$ and η will tend to offset in $\bar{q}_v$ and $\dot{\bar{q}}_v$, making $\bar{q}_v$ and $\dot{\bar{q}}_v$ inherently more stable than $\bar{E}_v$ and η as a battery degrades.

The left and right charts of Figure 5.32 respectively plot $\bar{q}_v$ and $\dot{\bar{q}}_v$ for Model3-19 and the two Leaf packs at different SOH levels. It was shown in Figure 5.29 and Figure 5.31 that both $\bar{E}_v$ and η are lower for Leaf-12 than for Leaf-14. Figure 5.32 now shows that these differences offset such that $\bar{q}_v$ and $\dot{\bar{q}}_v$ is quite consistent for Leaf-12 and Leaf-14 despite their different SOH levels. The $\bar{E}_v$ and η results for the Model 3 pack exhibited even greater SOH sensitivity than the Leaf packs, yet $\bar{q}_v$ and $\dot{\bar{q}}_v$ are also quite consistent for the liquid-cooled Model3-19 at 95 % SOH and 87 % SOH. The passive-cooled Model3-19 exhibits a slight increase in $\bar{q}_v$ and $\dot{\bar{q}}_v$ at 87 % SOH compared to 95 % SOH. This can be attributed to the slightly inflated η results for this dataset, which Section 5.6.3 explained as

being a result of the different temperature monitoring technique applied to the 95 % SOH tests. The results for the two Leaf packs and the liquid-cooled Model3-19 indicate that for a given temperature regime, $\bar{q}_v$ and $\dot{\bar{q}}_v$ are fairly insensitive to the moderate SOH changes that can be explored with the available experimental data. This suggests that $\bar{q}_v$ and $\dot{\bar{q}}_v$ could be suitable metrics for comparing the performance of different second-life battery pack designs independently of SOH.

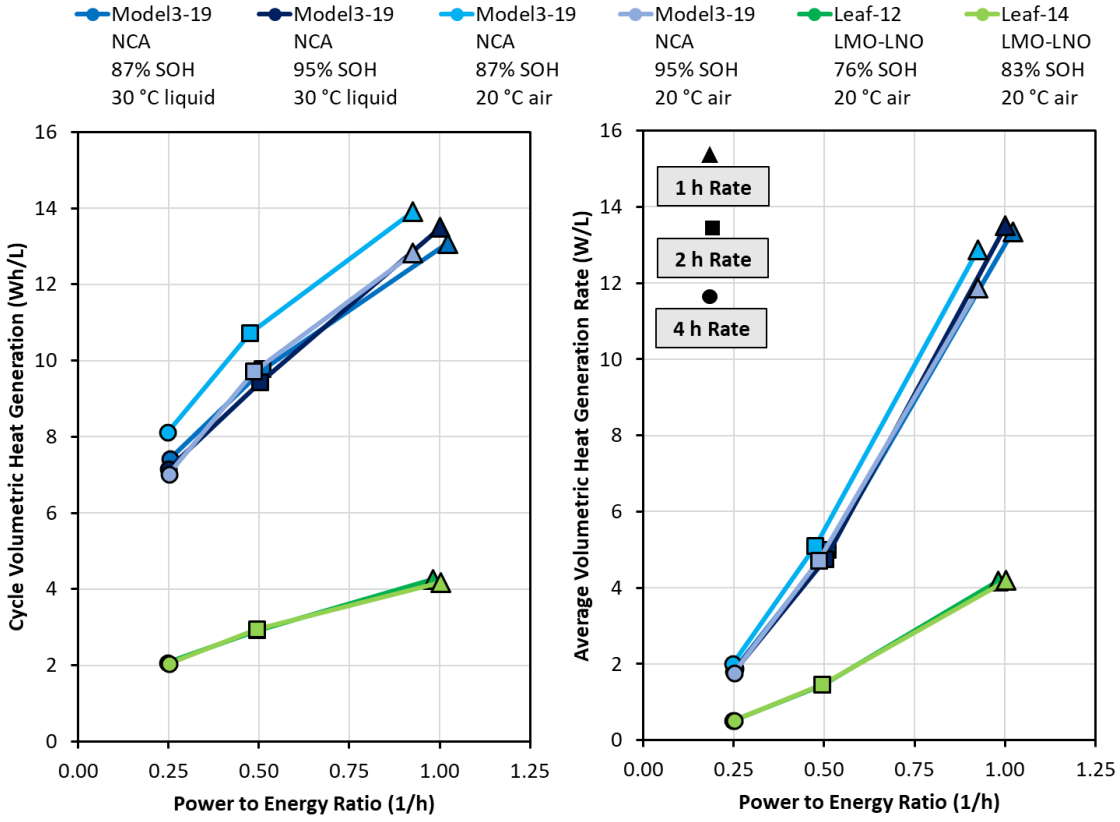


Figure 5.32 Calculated cycle volumetric heat generation (left) and average volumetric heat generation rate (right) taken at different SOH levels.

It should be recognized that whether $\bar{q}_v$ and $\dot{\bar{q}}_v$ increase, decrease, or remain constant as a battery degrades will depend on the mode of degradation. If internal resistance growth is significant enough in comparison to capacity loss, then the increase in $1-\eta$ will exceed the decrease in E_{dis} to produce an overall increase $\bar{q}_v$ and $\dot{\bar{q}}_v$, and vice versa. More research is needed to explore how different battery designs and operational conditions influence $\bar{q}_v$ and $\dot{\bar{q}}_v$ over greater SOH changes.

5.6.5. Impact on Temperature Rise

Section 5.4.5 demonstrated that the maximum temperature rise $\Delta T_{\max}$ and average temperature rise ΔT_{avg} for all five passive-cooled battery packs share a common correlation with the average volumetric heat generation rate $\dot{\bar{q}}_v$. The $\Delta T_{\max}$ and ΔT_{avg} results for the two liquid-cooled packs also correlate strongly with $\dot{\bar{q}}_v$, but the correlations are unique to a given liquid-cooled pack design. The only factors that should influence these correlations for a given battery pack and TMS are the mass density and specific heat capacity of the pack, which do not change significantly with SOH [184]. Since Section 5.6.4 demonstrated that $\dot{\bar{q}}_v$ is fairly insensitive to degradation, $\Delta T_{\max}$ and ΔT_{avg} should therefore also be fairly insensitive to degradation.

Due to improvements in the temperature monitoring technique applied to the more degraded packs, the only case that can be reliably explored with the collected experimental data is the liquid-cooled Model3-19. While the measured $\Delta T_{\max}$ and ΔT_{avg} are expected to be slightly smaller for the 95 % SOH case, the difference should be small due to the relatively uniform temperature distribution in the liquid-cooled Model3-19 modules. The left and right charts of Figure 5.33 respectively plot $\Delta T_{\max}$ and ΔT_{avg} for both SOH levels, showing that the results at 95 % and 87 % SOH are consistent to within about 0.5 °C. This confirms that $\Delta T_{\max}$ and ΔT_{avg} are insensitive to moderate SOH changes for the liquid-cooled Model3-19, which suggests that these metrics are suitable for comparing the performance of different second-life battery pack designs independently of SOH. However, more research is needed to assess the impacts of greater SOH changes on both liquid-cooled and passive-cooled packs.

The impacts of degradation on the average pack temperature differential $\Delta T_{\text{diff}}^{\text{avg}}$ and cycle cooldown duration t_{cool} are also important to consider. Since the liquid-cooled Model3-19 produces very small values for $\Delta T_{\text{diff}}^{\text{avg}}$ and t_{cool}, no experimental conclusions can be drawn for these metrics. However, since both $\Delta T_{\text{diff}}^{\text{avg}}$ and t_{cool} are dependent on temperature and physical properties (e.g. module thermal conductivity, exposed surface areas, etc.) it is expected that $\Delta T_{\text{diff}}^{\text{avg}}$ and t_{cool} will be relatively insensitive to changes in SOH, insofar as $\dot{\bar{q}}_v$ is insensitive to changes in SOH.

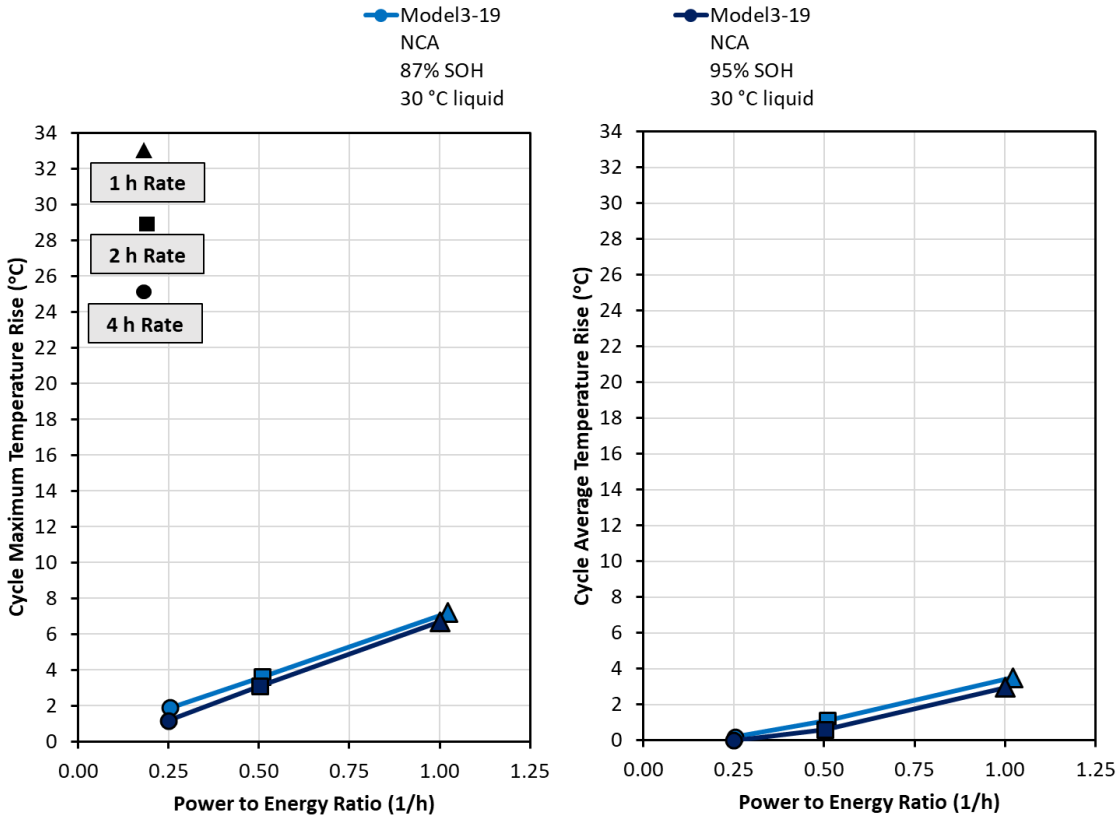


Figure 5.33 Measured maximum (left) and average (right) temperature rise taken at different SOH levels.

5.7. Ranking Battery Performance

Sections 5.3 and 5.4 presented experimental results for module energy density $\bar{E}_v$, energy utilization ratio ζ, energy efficiency η, maximum temperature rise $\Delta T_{\text{high}}^{\text{max}}$, average temperature rise $\Delta T_{\text{high}}^{\text{avg}}$, average pack temperature differential $\Delta T_{\text{diff}}^{\text{avg}}$, and cycle cooldown duration t_{cool}. Since the relative performance of the tested EV battery packs varied widely across these seven performance metrics, it is challenging to conclude which EV battery pack design is 'best' for second-life applications. It is also important to recognize that second-life energy storage project developers may assign greater importance to one or more performance metrics depending on the requirements of a specific project. To facilitate evaluation and selection of second-life battery packs for commercial applications, this section will present a series of novel analytical techniques for converting experimental test results into dimensionless 'performance scores' which can be used to rank different EV battery pack designs for specific second-life energy storage project requirements.

5.7.1. Volume Score

One important consideration for second-life energy storage is the physical space available to house batteries. While rural project locations generally have ample space to work with (e.g. wind farm), some projects will be constrained by volume (e.g. urban shipping container). In such cases, EV battery packs with higher energy density will provide greater energy storage capacity for the fixed volume and thus provide greater revenue generating capacity for the project. However, as explained in Section 5.3.5, batteries with higher energy density also tend to have lower energy efficiency, which translates to greater costs for recharging batteries from the electricity grid. The economic trade-off between energy density and energy efficiency will depend on the electricity market in question, but it can generally be expected that it is better to sell more (high energy density) and buy more (low energy efficiency) than to sell less (low energy density) and buy less (high energy efficiency). In cases where volume is not a constraint, energy efficiency may be the more important performance metric. Battery mass is generally not a constraint for stationary energy storage projects.

With these considerations in mind, a 'volume score' θ_v is proposed for ranking second-life battery performance, as defined in Equation 5.1. The volume score is determined by comparing the measured module energy density $\bar{E}_v$ at a given power rate to a fixed reference value $\bar{E}_v^{\text{best}}$ representing the best energy density among commercial EV battery modules. This produces θ_v values on a scale from 0 % to 100 %. Section 5.6.2 demonstrated that $\bar{E}_v$ is much less sensitive to SOH changes when adjusted for SOH, so Equation 5.1 includes an adjustment for SOH as well. This definition of θ_v allows different EV battery pack designs to be compared independently of SOH. When a project developer is selecting second-life battery packs for a given project, the SOH of available packs can be considered separately from the θ_v scores assigned to each battery pack design.

$$\theta_v = \frac{1}{\text{SOH}} \frac{\bar{E}_v}{\bar{E}_v^{\text{best}}} \times 100\ \% \tag{5.1}$$

Since the Tesla Model 3 battery module is one of the most energy-dense among commercial EVs, the maximum $\bar{E}_v^{\text{BOL}}$ value measured for Model3-19 can serve as a

reference point. A value of $\bar{E}_v^{\text{best}} = 400$ Wh/L is therefore recommended based on the $\bar{E}_v^{\text{BOL}} = 397$ Wh/L result obtained for the passive-cooled Model3-19 at a 4 h rate. If Equation 5.1 were to be applied to a different set of EV battery packs with higher $\bar{E}_v^{\text{BOL}}$ values, then $\bar{E}_v^{\text{best}}$ would be set to the highest value so that no battery exceeds $\theta_v = 100$ %.

Figure 5.34 shows the θ_v scores determined for the five EV battery packs, two TMS variants, and three power rates, with bars arranged left-to-right from highest score to lowest score. The passive-cooled Model3-19 has the highest scores at all three power rates, exceeding the liquid-cooled Model3-19 due to differences in temperature and the resulting impacts on charge termination (see Section 5.2.3). The lowest θ_v belongs to i3-15, which scores as low as 30 % at a 1 h rate.

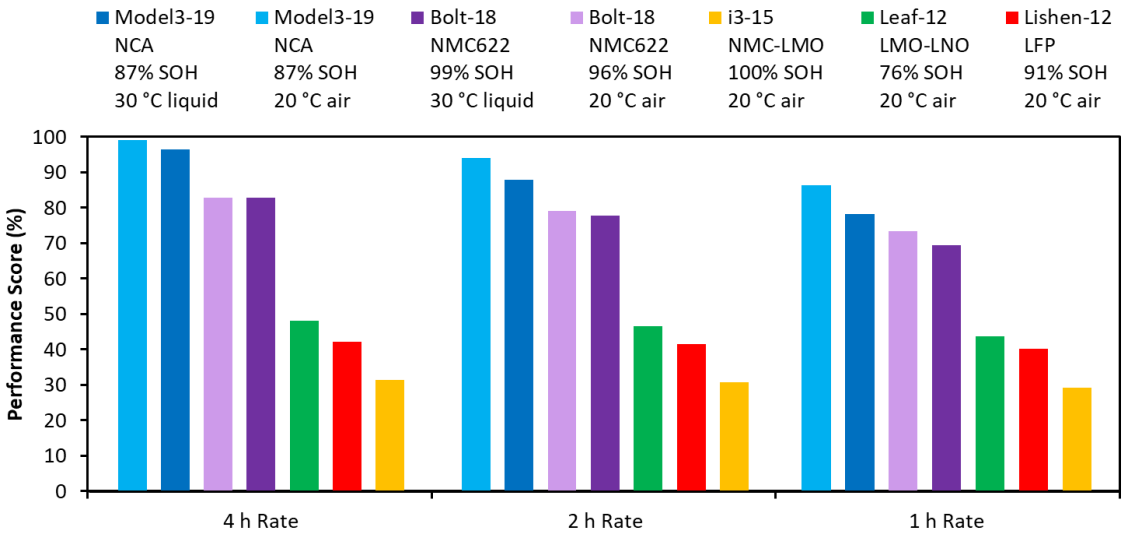


Figure 5.34 Battery rankings according to volume score.

Recall that $\bar{E}_v$ is determined for the module level in this research project. In practice, it is pack energy density that determines the energy capacity of a volume-constrained energy storage project. However, pack energy density must take into account the irregular shape of some EV battery pack designs, as well as how 'stackable' different pack designs are for commercial applications with multiple battery packs housed together. These considerations are outside the scope of this research project. Module energy density is simpler to quantify and is therefore sufficient for the purposes of performance ranking. Generally speaking, packs with higher module energy density will also have higher pack energy density.

5.7.2. Energy Score

Second-life batteries must of course be able to store and deliver energy in an economical way. While the volume score proposed in Section 5.7.1 assesses how battery energy density influences the economics of energy storage for a constrained volume, an 'energy score' θ_E is also proposed to evaluate second-life battery energy performance independently from volume. Energy utilization ratio ζ and cycle energy efficiency η both align with this purpose. A low ζ means that battery revenue-generating capacity will fall short of expectations, while a low η means greater expenses for recharging the battery. Both these metrics should therefore be considered in development of an energy score.

Section 5.6.2 demonstrated that ζ decreases with degradation, and that ζ is especially sensitive to SOH for the case of Model3-19 due to internal resistance growth and the shape of the nickel-rich NCA voltage profile. An energy score based on ζ for a relatively new Model 3 pack would therefore significantly overestimate the performance of a degraded Model 3 pack. However, Figure 5.30 revealed that this SOH sensitivity is significantly mitigated when ζ is normalized such that $\zeta^* = 100$ % at a 4 h rate. The normalized ζ^* is therefore a more suitable metric to use in developing an energy score that can be evaluated independently of battery SOH. The disadvantage of ζ^* is that it fails to quantify the unutilized energy when a battery cannot be charged to 100 % SOC with a long CV charge, but this information is not essential for applications such as energy arbitrage. It is sufficient to compare battery packs based on how much energy they deliver relative to a low-power SCP cycle.

To rank EV battery packs based on ζ^*, the measured ζ^* results should be evaluated relative to the range of ζ^* values that can be expected in practice. Equation 5.2 is proposed as a means of achieving this, where θ_ζ is the 'capacity score' and ζ^*_{limit} is the lowest value of ζ^* expected for second-life battery packs. The lowest ζ^* value measured in this research project was 81.1 % at a 1 h rate for the liquid-cooled Model3-19 at 87 % SOH. A value of 50 % would be considered extremely low, so $\zeta^*_{\text{limit}} = 50$ % is recommended. Note that since $\zeta^* = 100$ % at a 4 h rate for all battery packs, Equation 5.2 dictates that $\theta_\zeta = 100$ % at a 4 h rate for all battery packs as well.

$$\theta_\zeta = \left(1 - \frac{1-\zeta^*}{1-\zeta^*_{\text{limit}}}\right) \times 100\ \% \tag{5.2}$$

The energy score should also account for battery energy efficiency. Section 5.6.3 showed that while η decreases with degradation, the SOH sensitivity of η is much less pronounced than the SOH sensitivity of ζ. While the normalized η^* further mitigates SOH sensitivity, it does not reflect the real charging costs associated with operating a battery and therefore has less practical value than η. The relatively low SOH sensitivity of η is considered to be acceptable for the purposes of ranking second-life battery performance. For example, an energy score based on η for a relatively new Model 3 pack would only slightly overestimate the performance of a degraded Model 3 pack.

To rank EV battery packs based on η, the same technique from Equation 5.2 is applied to η in Equation 5.3, where θ_η is the 'efficiency score' and η_{limit} is the lowest acceptable value of η that would be expected for second-life battery packs. The lowest η value measured in this research project was 90.8 % at a 1 h rate for the liquid-cooled Model3-19 at 85 % SOH. A value of 75 % would be considered extremely low (comparable to a 3 V discharge and a 4 V charge), so $\eta_{\text{limit}} = 75\ \%$ is recommended.

$$\theta_\eta = \left(1 - \frac{1-\eta}{1-\eta_{\text{limit}}}\right) \times 100\ \% \tag{5.3}$$

To arrive at a single overall energy performance score, θ_ζ and θ_η must be combined. Equation 5.4 proposes a simple means of calculating a single overall energy score θ_E by taking a weighted average of θ_ζ and θ_η using weighting ratios $r_\zeta + r_\eta = 1$. This produces a θ_E score that is tailored to the relative importance of θ_ζ and θ_η for a given energy storage project based on the assigned weighting ratio set $[r_\zeta : r_\eta]$.

$$\theta_E = r_\zeta \theta_\zeta + r_\eta \theta_\eta \tag{5.4}$$

While the relative importance of θ_ζ and θ_η may vary depending on the requirements of a specific energy storage project, Section 5.3.5 demonstrated that batteries with higher η also

tend to have higher ζ^* due to the effects of internal resistance underpinning both these metrics (the main exception being Lishen-12, which exhibits high ζ^* despite relatively low η due to the advantageous shape of the LFP voltage profile). This means that ranking batteries by θ_ζ and θ_η will generally produce similar results, and thus θ_E should not have a strong sensitivity to the weighting ratio set $[r_\zeta : r_\eta]$. For the illustrative purposes of this chapter, it will be assumed that $r_\zeta = r_\eta = 0.5$ (i.e. equal weighting).

The θ_ζ, θ_η, and θ_E scores calculated for the five EV battery packs, two TMS variants, and three power rates are plotted in Figure 5.35, with bars arranged left-to-right from highest score to lowest score. One observation is that the differences in energy performance among the seven datasets are small at a 4 h rate, with all scores above 90 %. This suggests that all EV battery packs would deliver good energy performance at low power rates in second-life applications. However, the differences become increasingly significant for 2 h and 1 h rates, with scores falling as low as 63 % for the liquid-cooled Model3-19 at a 1 h rate. This indicates that the selection of EV batteries should be done carefully when high-power deep cycles are expected.

Figure 5.35 shows that i3-15 scores the highest θ_E at all three power rates, with Leaf-12 also ranking consistently high. Lishen-12 climbs significantly in the rankings as the power rate increases due to its high θ_ζ scores. Model3-19 and Bolt-18 tend to rank lowest, with the liquid-cooled variants struggling more at high power rates due to the higher internal resistance that results from active heat rejection. While liquid-cooled packs are slightly disadvantaged in terms of energy performance, they are of course advantaged in terms of thermal performance. Thermal considerations will be explored in Section 5.7.3.

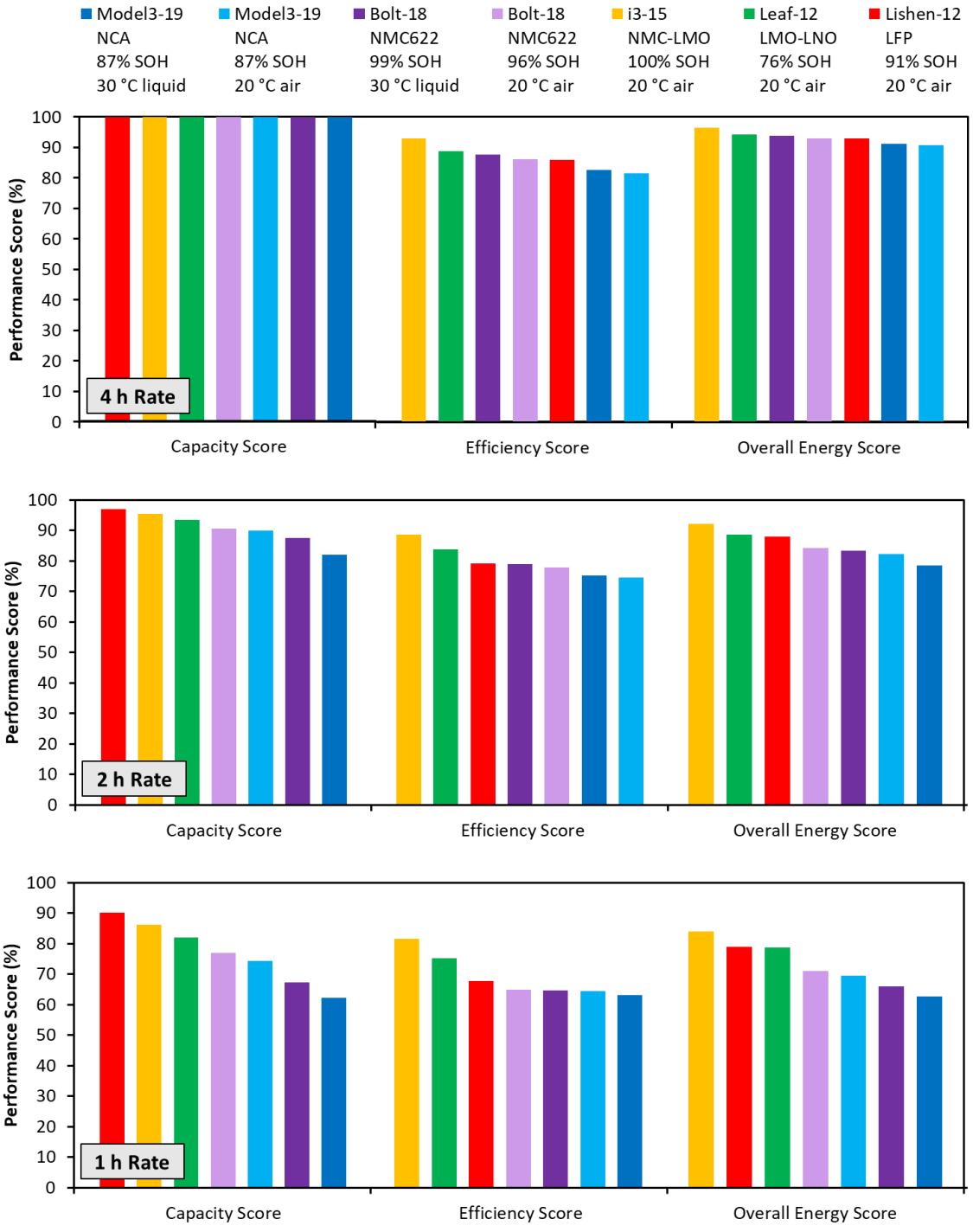


Figure 5.35 Battery rankings according to two unique energy scores and overall energy performance score.

5.7.3. Thermal Score

Thermal performance is another critical consideration for evaluating and selecting EV battery packs for a given second-life energy storage project. The operational temperatures of a second-life battery have important implications for safety, degradation rate, and the control of battery power. A 'thermal score' θ_T is therefore proposed to facilitate ranking of second-life battery performance. Section 5.4 presented the results of four thermal performance metrics which each provide unique information pertaining to practical thermal considerations, including maximum temperature rise $\Delta T_{\text{high}}^{\text{max}}$, average temperature rise $\Delta T_{\text{high}}^{\text{avg}}$, average pack temperature differential $\Delta T_{\text{diff}}^{\text{avg}}$, and cycle cooldown duration t_{cool}. Section 5.6 demonstrated that the average volumetric heat generation rate $\dot{\bar{q}}_v$ is relatively insensitive to SOH changes, and explained that $\Delta T_{\text{high}}^{\text{max}}$, $\Delta T_{\text{high}}^{\text{avg}}$, $\Delta T_{\text{diff}}^{\text{avg}}$, and t_{cool} should therefore be relatively insensitive to SOH changes as well (with some supporting evidence shown in Figure 5.33). This means that $\Delta T_{\text{high}}^{\text{max}}$, $\Delta T_{\text{high}}^{\text{avg}}$, $\Delta T_{\text{diff}}^{\text{avg}}$, and t_{cool} are suitable for developing a thermal score that can be evaluated separately from battery SOH.

To rank EV battery packs based on $\Delta T_{\text{high}}^{\text{max}}$, the measured $\Delta T_{\text{high}}^{\text{max}}$ results should be evaluated relative to a maximum allowable value that ensures battery safety. Equation 5.5 is proposed as a means of achieving this, where $\theta_{T_{\text{max}}}$ is the 'safety score' and $\Delta T_{\text{limit}}^{\text{max}}$ is an upper limit for $\Delta T_{\text{high}}^{\text{max}}$ that avoids safety issues. The high-temperature safety limit applied in this research project was 55 °C (see Section 4.4.3), so $\Delta T_{\text{high}}^{\text{max}} = 35$ °C is recommended based on a nominal ambient temperature of 20 °C. This $\Delta T_{\text{high}}^{\text{max}}$ value would technically correspond to a high-temperature safety limit of 65 °C for the case of liquid-cooled packs operating with a 30 °C liquid supply temperature, but liquid-cooled packs are unlikely to exceed $\Delta T_{\text{high}}^{\text{max}} = 25$ °C at practical power rates (Bolt-18 reached $\Delta T_{\text{high}}^{\text{max}} = 19$ °C at a 1 h rate). It is important to apply the same $\Delta T_{\text{limit}}^{\text{max}}$ to all battery packs so that the $\theta_{T_{\text{max}}}$ results of liquid-cooled and passive-cooled packs can be directly compared.

$$\theta_{T_{\text{max}}} = \left(1 - \frac{\Delta T_{\text{high}}^{\text{max}}}{\Delta T_{\text{limit}}^{\text{max}}}\right) \times 100\ \% \tag{5.5}$$

A similar approach can be used to evaluate $\Delta T_{\text{high}}^{\text{avg}}$ relative to a maximum allowable value. This is done in Equation 5.6, where $\theta_{T_{\text{avg}}}$ is a 'durability score' and $\Delta T_{\text{limit}}^{\text{avg}}$ is an upper limit for $\Delta T_{\text{high}}^{\text{avg}}$ that avoids significantly accelerated degradation. As explained in Section 2.5.2, most researchers agree that average battery temperatures should be kept below 45 °C to avoid this condition, so $\Delta T_{\text{limit}}^{\text{avg}} = 25$ °C is recommended for the purpose of ranking batteries according to $\theta_{T_{\text{avg}}}$.

$$\theta_{T_{\text{avg}}} = \left(1 - \frac{\Delta T_{\text{high}}^{\text{avg}}}{\Delta T_{\text{limit}}^{\text{avg}}}\right) \times 100\ \% \tag{5.6}$$

Equation 5.7 applies a similar approach to evaluate $\Delta T_{\text{diff}}^{\text{avg}}$ relative to a maximum allowable value, where $\theta_{T_{\text{diff}}}$ is a 'consistency score' and $\Delta T_{\text{limit}}^{\text{diff}}$ is an upper limit for $\Delta T_{\text{diff}}^{\text{avg}}$ that avoids significant divergence in cell degradation rates within a given pack. As explained in Section 3.1.3, it is generally recommended that $\Delta T_{\text{diff}}^{\text{avg}}$ be maintained below 5 °C. A doubling of this value would therefore be considered extreme. A limit of $\Delta T_{\text{limit}}^{\text{diff}} = 10$ °C is therefore recommended for the purpose of ranking batteries according to $\theta_{T_{\text{diff}}}$.

$$\theta_{T_{\text{diff}}} = \left(1 - \frac{\Delta T_{\text{diff}}^{\text{avg}}}{\Delta T_{\text{limit}}^{\text{diff}}}\right) \times 100\ \% \tag{5.7}$$

Commercial second-life battery systems will typically feature a means of controlling the battery power based on measured battery temperatures. As described in Section 4.4.1, the SCP test protocol is designed with a temperature control setpoint which forces cooldown periods following termination of discharge and charge. While commercial systems will not necessarily employ this particular control mechanism, it nonetheless provides a means of quantifying the lost revenue-generating capacity that may result from high battery temperatures. Batteries that yield a longer cycle cooldown duration t_{cool} will have less availability for providing energy storage services in a given application.

To rank EV battery packs based on t_{cool}, the measured t_{cool} results should be evaluated relative to a maximum allowable value. The theoretical limit for t_{cool} is of course the total

cycle time t_{cyc}, which would indicate that the battery required either an infinitely long cooldown period or zero discharge and charge time. While this condition is physically impossible, it provides a functional limit against which to compare the measured t_{cool}. This approach is shown in Equation 5.8, where $\theta_{t_{\mathrm{cool}}}$ is the 'availability score'. A value of $\theta_{t_{\mathrm{cool}}} = 100$ % indicates that no cooldown periods are required during the cycle, while very long cooldown periods will asymptotically approach $\theta_{t_{\mathrm{cool}}} = 0$ %.

$$\theta_{t_{\mathrm{cool}}} = \left(1 - \frac{t_{\mathrm{cool}}}{t_{\mathrm{cyc}}}\right) \times 100\ \% \tag{5.8}$$

Four thermal scores have now been established. To arrive at a single overall thermal performance score, these four scores must be combined. Equation 5.9 proposes a simple means of calculating a single overall thermal score θ_T by taking a weighted average of $\theta_{T_{\mathrm{max}}}$, $\theta_{T_{\mathrm{avg}}}$, $\theta_{T_{\mathrm{diff}}}$, and $\theta_{t_{\mathrm{cool}}}$ using weighting ratios $r_{T_{\mathrm{max}}} + r_{T_{\mathrm{avg}}} + r_{T_{\mathrm{diff}}} + r_{t_{\mathrm{cool}}} = 1$. This produces a θ_T score tailored to the relative importance of $\theta_{T_{\mathrm{max}}}$, $\theta_{T_{\mathrm{avg}}}$, $\theta_{T_{\mathrm{diff}}}$, and $\theta_{t_{\mathrm{cool}}}$ for a given energy storage project based on the assigned weighting ratio set $[r_{T_{\mathrm{max}}} : r_{T_{\mathrm{avg}}} : r_{T_{\mathrm{diff}}} : r_{t_{\mathrm{cool}}}]$.

$$\theta_T = r_{T_{\mathrm{max}}}\theta_{T_{\mathrm{max}}} + r_{T_{\mathrm{avg}}}\theta_{T_{\mathrm{avg}}} + r_{T_{\mathrm{diff}}}\theta_{T_{\mathrm{diff}}} + r_{t_{\mathrm{cool}}}\theta_{t_{\mathrm{cool}}} \tag{5.9}$$

While the relative importance of $\theta_{T_{\mathrm{max}}}$, $\theta_{T_{\mathrm{avg}}}$, $\theta_{T_{\mathrm{diff}}}$, and $\theta_{t_{\mathrm{cool}}}$ may vary depending on the requirements of a specific energy storage project, Section 5.4 demonstrated that batteries with higher $\Delta T_{\mathrm{high}}^{\mathrm{max}}$ also tend to have higher $\Delta T_{\mathrm{high}}^{\mathrm{avg}}$ and higher t_{cool}. Ranking batteries by $\theta_{T_{\mathrm{max}}}$, $\theta_{T_{\mathrm{avg}}}$, and $\theta_{t_{\mathrm{cool}}}$ will therefore generally produce similar results. There is no such correlation for $\Delta T_{\mathrm{diff}}^{\mathrm{avg}}$, since temperature gradients depend strongly on the pack design. This means that θ_T could be somewhat sensitive to the value of $r_{T_{\mathrm{diff}}}$. For the illustrative purposes of this chapter, it will be assumed that $r_{T_{\mathrm{max}}} = r_{T_{\mathrm{avg}}} = r_{T_{\mathrm{diff}}} = r_{t_{\mathrm{cool}}} = 0.25$ (i.e. equal weighting).

The $\theta_{T_{\max}}$, $\theta_{T_{\text{avg}}}$, $\theta_{T_{\text{diff}}}$, $\theta_{t_{\text{cool}}}$, and θ_T scores calculated for the five EV battery packs, two TMS variants, and three power rates are plotted in Figure 5.36, with bars arranged left-to-right from highest score to lowest score. The liquid-cooled Model3-19 consistently ranks the highest in all categories other than the consistency score, but scores high in this category as well. The liquid-cooled Bolt-18 consistently ranks second in nearly all categories, but is overtaken by i3-15 in the safety and consistency categories at a 1 h rate. Conversely, the passive cooled Model3-19 and Bolt-18 consistently rank as the bottom two in all categories other than consistency, as Leaf-12 also scores poorly in consistency due to its nonuniform module arrangements. In between these two extremes, i3-15, Leaf-12, and Lishen-12 consistently rank in the middle and achieve similar scores in most categories, with the main exception being the poor consistency scores of Leaf-12.

Figure 5.36 demonstrates that all tested battery packs achieve adequate thermal scores at a 4 h rate, but the passive-cooled packs struggle at higher power rates. The passive-cooled Model3-19 and Bolt-18 score very low at a 1 h rate ($\theta_T = 12$ % and $\theta_T = 22$ %, respectively) and should therefore be considered with caution as high-power options.

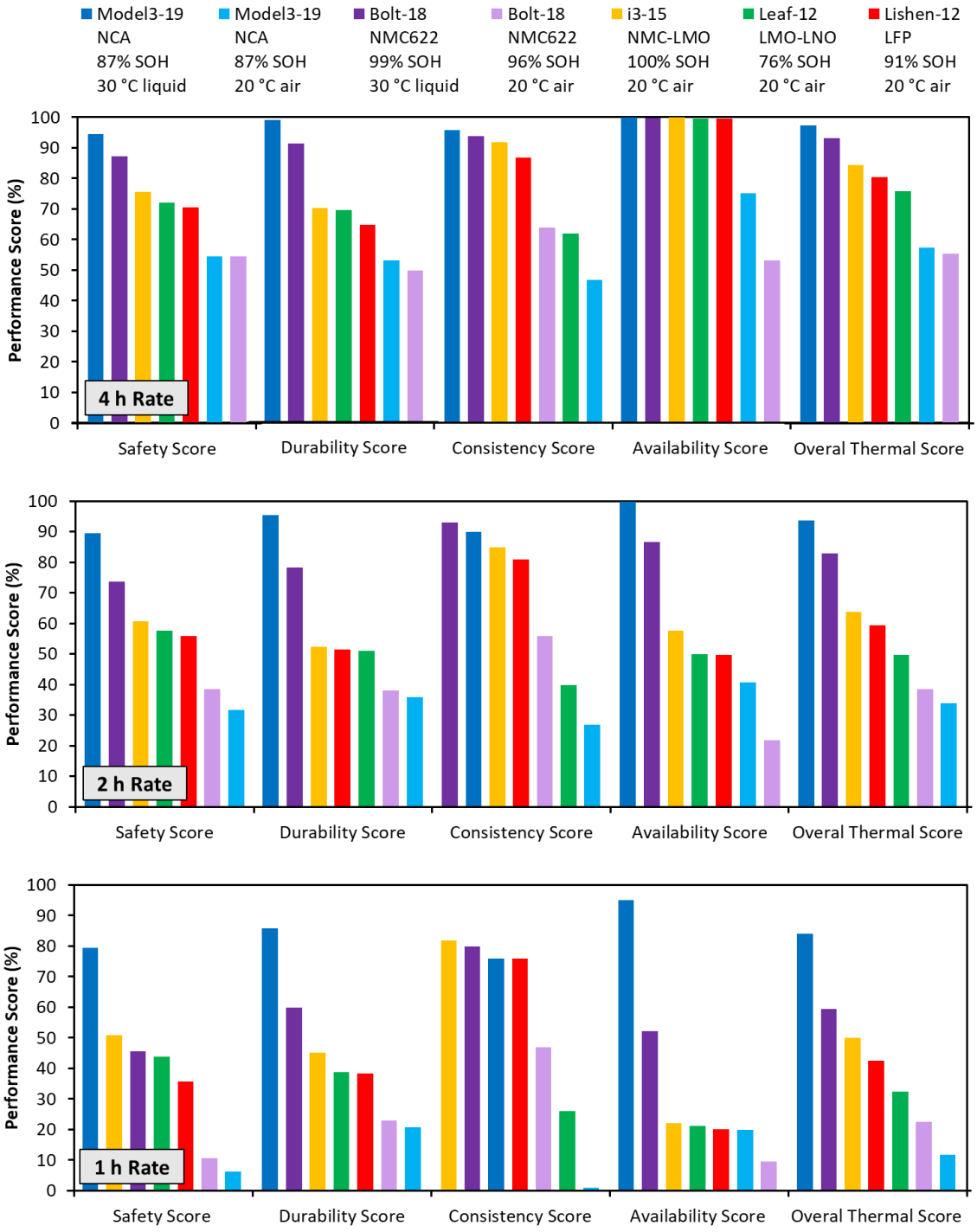


Figure 5.36 Battery rankings according to four unique thermal scores and overall thermal performance score.

5.7.4. Overall Performance Rankings

Seven performance metrics ($\bar{E}_v$, ζ, η, $\Delta T_{\text{high}}^{\text{max}}$, $\Delta T_{\text{high}}^{\text{avg}}$, $\Delta T_{\text{diff}}^{\text{avg}}$, and t_{cool}) have now been reduced to three dimensionless performance scores which describe the volume θ_v, energy θ_E, and thermal θ_T performance of second-life battery packs. It should be recognized that there is a degree of interdependence between these three categories: temperature is partially influenced by η and $\bar{E}_v$ (i.e. volumetric heat generation); $\bar{E}_v$ is partially influenced by ζ (less energy available at faster cycling rates); and $\bar{E}_v$, ζ, and η are all partially influenced by temperature (lower internal resistance at higher temperature). Nonetheless, θ_v, θ_E, and θ_T each provide unique information relevant to second-life energy storage applications.

The relative importance of θ_v, θ_E, and θ_T will depend on project-specific constraints such as physical space, electricity market dynamics, and local climate. To apply the performance scores to a specific project, θ_v, θ_E, and θ_T can be combined using a weighted average to achieve a single overall performance score θ. This technique is shown in Equation 5.10, where θ_v, θ_E, and θ_T are respectively scaled by weighting ratios $r_v + r_E + r_T = 1$. The resulting overall θ score represents the relative performance expectation of different second-life battery pack designs being considered for a given project described by the weighting ratio set $[r_v : r_E : r_T]$.

$$\theta = r_v\theta_v + r_E\theta_E + r_T\theta_T \tag{5.10}$$

To illustrate how the overall ranking of EV battery packs will change for different types of second-life energy storage projects, Figure 5.37 ranks the tested battery packs by θ for 4 h (low power) and 1 h (high power) rates in seven unique hypothetical energy storage scenarios described by the $[r_v : r_E : r_T]$ sets stated at the bottom of each bar chart. The unlabeled y-axes all range from 0 % to 100 %, and the bars within each chart are arranged left-to-right in order from highest to lowest score.

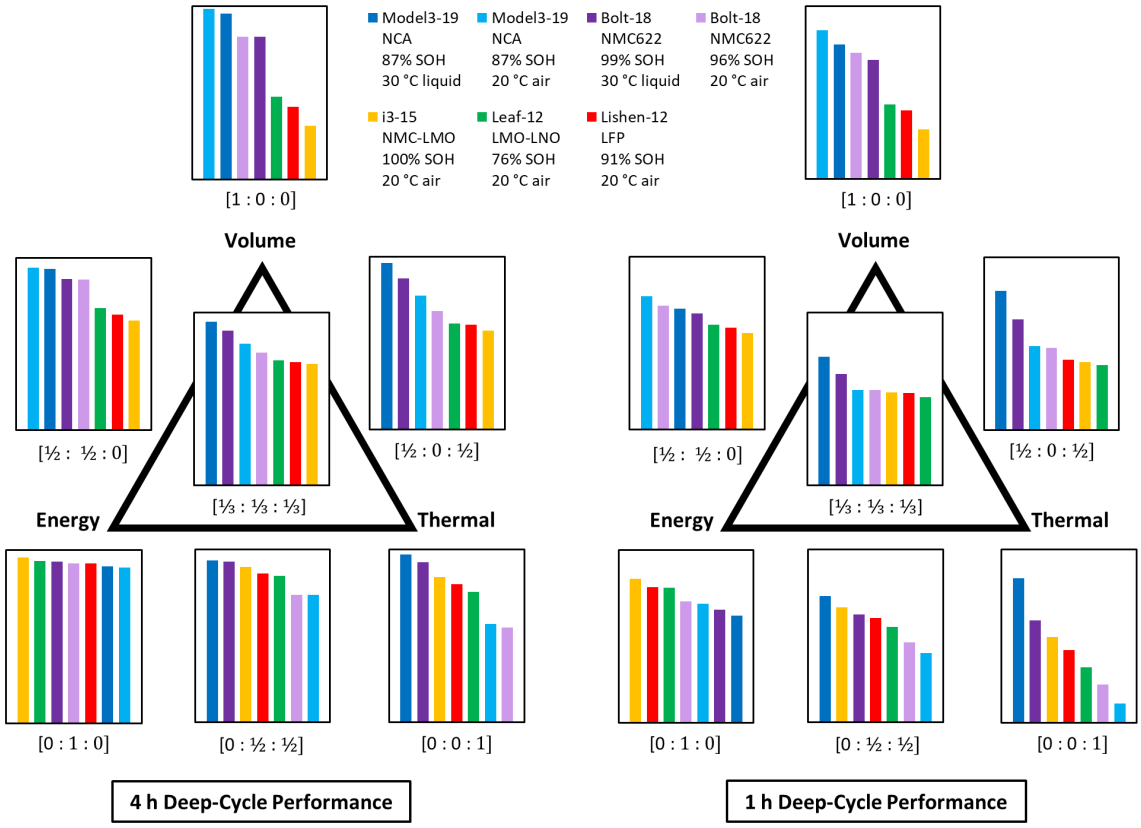


Figure 5.37 Overall performance ranking of EV battery samples for 4 h (left) and 1 h (right) rates according to weighted combinations of volume, energy, and thermal performance scores.

The seven $[r_v : r_E : r_T]$ sets in Figure 5.37 are used to illustrate the bounding scenarios between which all real-life scenarios will fall. The three corner scenarios [1:0:0], [0:1:0], and [0:0:1] respectively show the θ_v, θ_E, and θ_T scores presented in the previous three subsections. The four intermediate $[r_v : r_E : r_T]$ sets represent midway transitions between the three corner scenarios. The [0:½:½] scenario neglects the volume score, which could apply to energy storage projects where physical space is not a constraint (e.g. wind farm). The [½:0:½] scenario neglects the energy score, which could apply to energy storage projects in electricity markets with large price fluctuations, providing ample opportunity for low-cost charging and high-revenue discharging. The [½:½:0] scenario neglects the thermal score, which could apply to energy storage projects located at sites where ambient temperature can be used effectively for thermal management (e.g. cold northern environment). The [⅓:⅓:⅓] scenario is an even balance of all three scores, which could apply to space-constrained projects in a warm climate with a competitive electricity market.

One conclusion that can be drawn from Figure 5.37 is that the battery ranking order is not strongly dependent on power rate for most energy storage projects scenarios. The main exception is the [0:1:0] scenario where energy performance is supremely important. In this scenario, Lishen-12 excels more in high-power operation due to the high energy utilization of LFP batteries, while liquid-cooled Model3-19 and Bolt-18 struggle more in high-power operation due to the higher internal resistance that results from active heat rejection. In all other scenarios, the power rate has little impact on the ranking order. In practice, a project developer may design a second-life energy storage system for low power, high power, or a mix of both. Figure 5.37 suggests that the selection of EV battery packs for a given project can be primarily based on the relative importance of volume, energy, and thermal performance rather than the intended power rate. However, Figure 5.37 also shows that the power rate does have a clear impact on the range of performance scores in a given scenario. Considering the three corner scenarios, the range of volume scores narrows as the power rate increases while the range of energy and thermal scores widens significantly as the power rate increase. Each of these trends is due to internal resistance: batteries with higher energy density tend to underutilize energy density at higher power; greater overpotentials accentuate differences in energy performance; and greater heat generation accentuates differences in thermal performance. This means that battery selection is especially consequential for high-power applications where space is not a constraint.

The three corner scenarios in Figure 5.37 reveal two additional insights for second-life battery selection. First, the order of volume rankings in the [1:0:0] scenario is approximately opposite to the order of energy rankings in the [0:1:0] scenario at a given power rate (due to the trade-off between energy density and internal resistance), but the range of volume scores is much wider than the range of energy scores. This means that the trade-off between energy density and internal resistance favors high energy density in the context of volumetric revenue-generating capacity, which explains the ranking order in the [½:½:0] scenario. Second, more recent EV battery designs tend to have both higher energy density and the option for liquid cooling. This is why liquid-cooled Model3-19 and Bolt-18 rank highest in scenarios where both volume and thermal performance are important.

Figure 5.38 shows a graphical summary of the proposed performance ranking system. This system can be used to generate charts like Figure 5.37 for any given set of second-life battery designs that have been evaluated using a common test protocol. This provides a useful tool to help second-life project developers select the most appropriate batteries for their specific project requirements. A technique for assigning specific $[r_v : r_E : r_T]$ values for a given project is outside the scope of this thesis, and may be unnecessary. Instead, the layout of Figure 5.37 can serve as a performance map to help project developers understand the pros and cons of different second-life battery options before making selections.

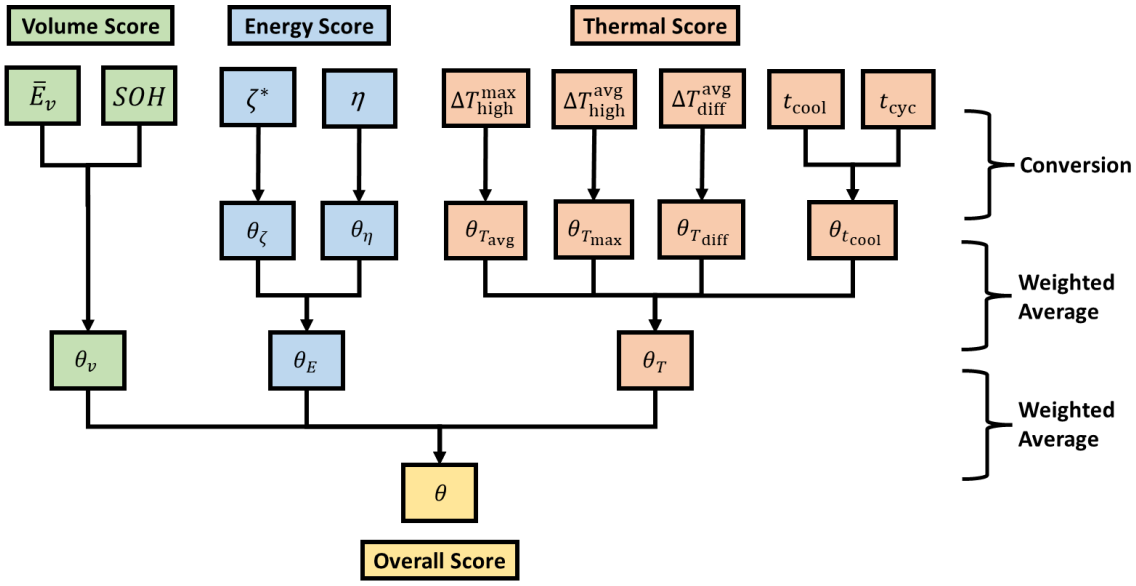


Figure 5.38 Graphical summary of the proposed performance ranking system.

Since the performance scores are designed to be relatively insensitive to changes in SOH, the SOH of available second-life batteries can be considered independently from the performance rankings. The proposed ranking system does not provide a means of characterizing how different EV battery designs degrade in second-life service, so future research should built on this system by developing a degradation score through a designated pack-level degradation study. It is also recommended that the thermal score in the [0:0:1] scenario always be given direct consideration as a precautionary measure. Any battery with an especially low thermal score at a given power rate (such as the passive-cooled Model3-19 and Bolt-18 at a 1 h rate) should be regarded as a potential safety risk regardless of how it ranks in other scenarios.

5.8. Chapter Summary

Chapter 5 has presented a detailed comparative analysis of second-life battery performance based on test results acquired using the experimental methods described in Chapter 4. The proposed SCP test protocol and associated performance metrics have proven to be effective for characterizing the electrical and thermal performance of different EV battery pack designs under a common test regime (though asymmetrical CP testing is worth exploring in future research). With seven primary performance metrics and 14 additional secondary performance metrics, many unique analyses can be carried out. The power-to-energy ratio (inverse of t_{dis}) has been shown to be a good choice as a standard independent variable for graphical analyses, and a total of 18 additional graphical techniques have helped to reveal valuable insights into the measured results. These novel graphical contributions include:

- Superimposed voltage profiles vs SOC
- ω_{DT}, ω_{CT}, and ω_{VD} as stacked bar charts
- Superimposed temperature profiles vs time relative to end of discharge or charge
- t_{dis}, $t_{\mathrm{cool}}^{\mathrm{dis}}$, t_{chg}, and $t_{\mathrm{cool}}^{\mathrm{chg}}$ as stacked bar charts
- $\bar{E}_v$ vs $\bar{E}_m$
- ζ vs $T_{\mathrm{high}}^{\mathrm{endChg}}$
- η vs $T_{\mathrm{high}}^{\mathrm{avg}}$
- η vs $\bar{E}_v^{\mathrm{BOL}}$
- η^* vs ζ^*
- $\bar{q}_v$ vs η
- $\bar{q}_v$ vs $\bar{E}_v$
- $\Delta T_{\mathrm{high}}^{\mathrm{max}}$ vs $\Delta T_{\mathrm{high}}^{\mathrm{avg}}$
- f_{cyc} vs $\Delta T_{\mathrm{high}}^{\mathrm{max}}$
- t_{cool} vs ΔT_{cool}
- τ vs ΔT_{cool}
- $\Delta T_{\mathrm{low}}^{\mathrm{avg}}$ vs $\Delta T_{\mathrm{high}}^{\mathrm{avg}}$
- $\Delta T_{\mathrm{high}}^{\mathrm{max}}$ or $\Delta T_{\mathrm{high}}^{\mathrm{avg}}$ vs $\bar{q}_v$
- $\Delta T_{\mathrm{high}}^{\mathrm{max}}$ or $\Delta T_{\mathrm{high}}^{\mathrm{avg}}$ vs $\dot{\bar{q}}_v$

The comparative analyses have shown that the electrical and thermal performance of repurposed EV battery packs varies widely cross different pack designs due to differences in chemistry, cell design, module design and layout, and thermal management design. Older pack designs (e.g. 2012 Nissan Leaf) tend to have lower energy density, higher energy utilization, higher energy efficiency, lower volumetric heat generation, and passive-air thermal management, while newer pack designs (e.g. 2019 Tesla Model 3) tend to have higher energy density, lower energy utilization, lower energy efficiency, higher volumetric heat generation, and active-liquid thermal management. The physical aspects of pack engineering can strongly influence temperature gradients and cooldown rates. These findings indicate that advancements in EV driving range are detrimental to second-life battery electrical performance (especially at high power rates and when space is not a constraint), and that liquid-cooled EV battery packs ought to be operated with liquid cooling in second-life applications to maintain satisfactory thermal performance.

Sensitivity analyses have shown that the measured results are highly repeatable at the present SOH of a given battery pack (indicating that two consecutive SCP cycles at each power rate may be sufficient for testing), and that most of the established performance metrics are not strongly influenced by moderate SOH changes. However, designated pack-level degradation studies will be necessary to properly characterize and compare the long-term performance of different EV battery packs in second-life applications. For now, a simple short-term performance ranking system has been developed to reduce the seven primary performance metrics into dimensionless performance scores that can be used to rank and select EV battery pack designs according to a specified mix of volume, energy, and thermal performance requirements for a given second-life energy storage project.

Some of the comparative analyses have revealed common trends that seem to govern how certain performance metrics vary with power rate. A number of interesting correlations between different performance metrics have also been identified. Given the significant diversity in pack design and performance that has been observed, the emergence of commonalities among the different packs suggests that mathematical relationships can be established to model the performance of EV battery packs under an SCP test protocol. This opportunity will be explored in Chapter 6.

Chapter 6 PERFORMANCE EXTRAPOLATION MODEL FOR SECOND-LIFE BATTERY PACKS

Chapter 5 demonstrated that different EV battery packs exhibit significant differences in electrical and thermal performance. However, the results also revealed a number of performance patterns which seem to govern the various packs. For example, packs with higher energy density tend to have higher internal resistance, which impacts both energy efficiency and energy utilization as the power rate increases. Passive-cooled packs also exhibit similar temperature rise results for a given average volumetric heat generation rate. Chapter 6 will conduct a more detailed investigation of the consistent patterns that all tested EV battery packs seem to follow, and propose novel empirical equations to quantify these relationships. The empirical equations will then be used to construct a second-life performance extrapolation model to enable accurate prediction of SCP test results at a desired power rate based on results obtained at a different power rate. Novel experimental methods will also be proposed as a means of acquiring the necessary empirical data for the extrapolation model with minimal testing time. Altogether, the proposed techniques provide a new tool to facilitate second-life battery research and development.

6.1. Empirical Relationships to Describe Battery Performance

The performance analysis in Chapter 5 presented results for various electrical and thermal performance metrics, including discharge energy E_{dis}, cycle energy efficiency η, average volumetric heat generation rate $\dot{\bar{q}}_v$, maximum pack temperature rise ΔT_{max}, and average pack temperature rise ΔT_{avg}. This section will demonstrate that simple empirical relationships can be used to describe how each of these performance metrics change as the discharge duration t_{dis} changes for SCP cycling. Such relationships are important since second-life researchers and developers may have access to battery specifications or test data at a rate that differs from the rate at which they wish to operate

6.1.1. Discharge Energy

Peukert's law was proposed in 1897 as an empirical relationship that approximates how the discharge coulombic capacity Q_{dis} of a fully charged lead-acid battery decreases when discharged at greater magnitudes of constant current rate I. The Peukert equation has

several equivalent expressions, including those shown in Equations 6.1 through 6.3, where σ is the Peukert number, t_{dis} is the discharge duration, and $Q_{\text{dis}} = It_{\text{dis}}$ for a CC discharge.

$$Q_{\text{dis}} t_{\text{dis}}^{\frac{1}{\sigma}-1} = constant \tag{6.1}$$

$$It_{\text{dis}}^{\frac{1}{\sigma}} = constant \tag{6.2}$$

$$Q_{\text{dis}}^{\frac{1}{\sigma}} I^{1-\frac{1}{\sigma}} = constant \tag{6.3}$$

The Peukert number σ is often treated as a constant parameter for a given battery design, though the electrical performance that it approximates has some dependence on temperature and SOH due to the influence of internal resistance on discharge capacity. A value of $\sigma = 1$ would indicate that Q_{dis} is independent of I, while larger values of σ indicate lower capacity utilization at greater currents. While lead-acid batteries typically have Peukert numbers in the range of 1.1 to 1.3, lithium-ion batteries have been shown to have lower Peukert numbers in the range of 1.0 to 1.1 [355], demonstrating the superior performance of lithium-ion technology.

Equations 6.1 through 6.3 can be modified to provide empirical relationships that approximates the discharge energy results presented in Section 5.3. This is done in Equations 6.4 through 6.6, where Q_{dis} is replaced with discharge energy E_{dis}, I is replaced with CP setpoint P, and $E_{\text{dis}} = Pt_{\text{dis}}$ for a CP discharge.

$$E_{\text{dis}} t_{\text{dis}}^{\frac{1}{\sigma}-1} = constant \tag{6.4}$$

$$Pt_{\text{dis}}^{\frac{1}{\sigma}} = constant \tag{6.5}$$

$$E_{\text{dis}}^{\frac{1}{\sigma}} P^{1-\frac{1}{\sigma}} = constant \tag{6.6}$$

The other notable difference between these equations and the original work by Peukert is that the results presented in Section 5.3 are based on SCP cycles (i.e. the same P setpoint for both discharge and charge without a CV charge). This means that the initial SOC at the beginning of discharge is dependent on P, instead of always beginning discharge at 100 %

SOC. While the coulomb-based Peukert number in Equations 6.1 through 6.3 is generally close to $\sigma = 1$ for lithium-ion batteries, the additional influence of overpotentials on E_{dis} and E_{chg} at higher power rates (see Section 5.2.2) should yield higher values for the energy-based Peukert number in Equations 6.4 through 6.6. In the remainder of this chapter, σ will refer to the energy-based Peukert number.

The left chart of Figure 6.1 fits Equation 6.4 to the measured E_{dis} results from Section 5.3. This shows that if a curve defined by Equation 6.4 is drawn between the 4 h and 1 h datapoints, the 2 h datapoint tends to sit slightly above the curve for all seven datasets. The unadjusted form of the Peukert equation therefore has limited applicability for this experimental dataset. However, the consistency of the limitation presents an opportunity to introduce a mathematical adjustment for enhanced accuracy.

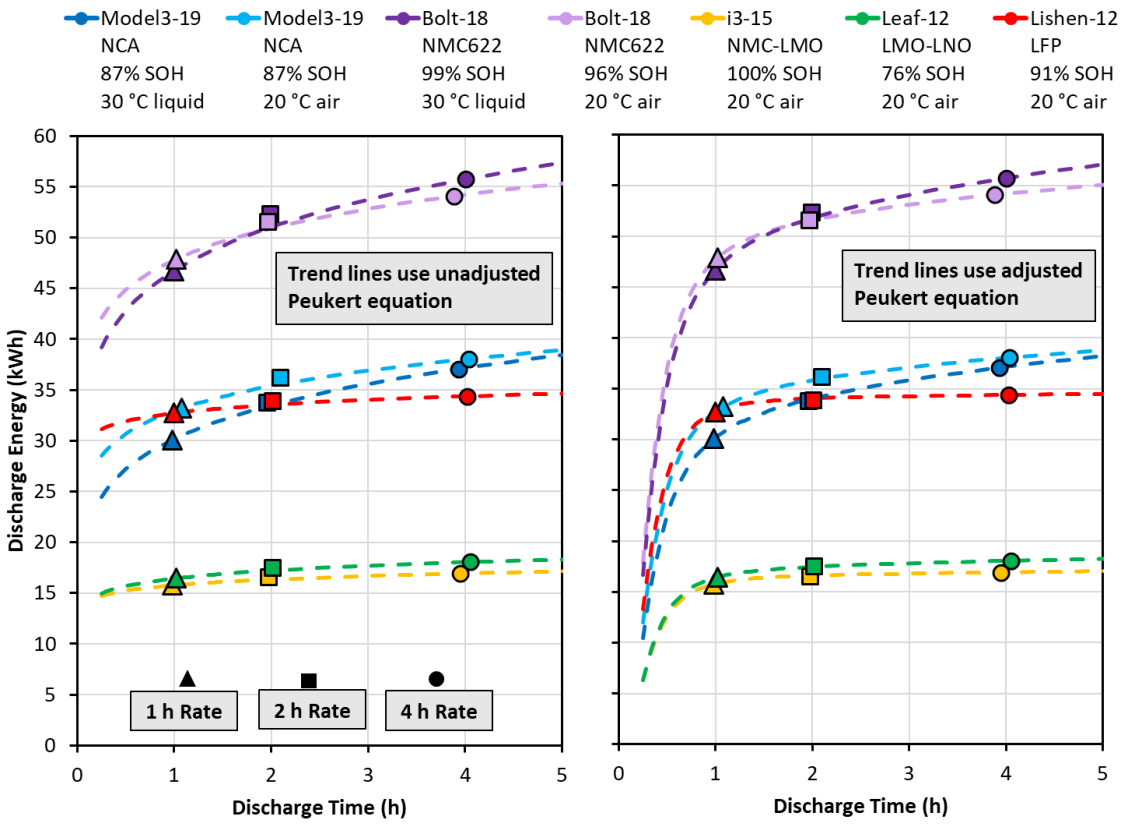


Figure 6.1 Unadjusted Peukert equation (left) and adjusted Peukert equation (right) fitted to measured data as a function of discharge duration.

A proposed adjustment to the Peukert equation is stated in Equations 6.7 through 6.9, which will be henceforth referred to as the 'adjusted Peukert equations'. The 'Peukert adjustment

factor' γ is dependent on t_{dis} as defined in Equation 6.10. Note that discharge energy E_{dis} and energy density $\bar{E}_v$ are interchangeable in these equations since battery volume is a constant (see Equations 4.2).

$$\gamma E_{\text{dis}} {t_{\text{dis}}}^{\frac{1}{\sigma}-1} = constant \tag{6.7}$$

$$\gamma P {t_{\text{dis}}}^{\frac{1}{\sigma}} = constant \tag{6.8}$$

$$\gamma {E_{\text{dis}}}^{\frac{1}{\sigma}} P^{1-\frac{1}{\sigma}} = constant \tag{6.9}$$

$$\gamma = 0.12 {t_{\text{dis}}}^{-2} - 0.15 {t_{\text{dis}}}^{-1} + 1.03 \tag{6.10}$$

The chosen expression for γ is designed to reshape the Peukert curve with a slight 'bulge' in the range of 1 h $< t_{\text{dis}} <$ 4 h, with $\gamma = 0.985$ for $t_{\text{dis}} = 2.0$ h and $\gamma = 1$ for both $t_{\text{dis}} = 1.0$ h and $t_{\text{dis}} = 4.0$ h. The result of this adjustment is illustrated in the right chart of Figure 6.1, which shows an improved fit to the measured data. Note that γ also causes the Peukert curve to be supressed for $t_{\text{dis}} <$ 1 h and $t_{\text{dis}} \gg$ 4 h. Since Equation 6.10 can only be verified for 1 h $\leq t_{\text{dis}} \leq$ 4 h, it cannot currently be recommended for application outside this range. For the given experimental data, Equation 6.10 provides an improved empirical relationship for E_{dis} vs t_{dis} for all seven datasets.

If results are obtained for E_{dis} at two or more different values of t_{dis} for a given battery, Equation 6.7 can be adapted to calculate σ for the battery. This is done in Equation 6.11.

$$\sigma = \frac{1}{1 - \log_{\left(\frac{t_{\text{dis2}}}{t_{\text{dis1}}}\right)} \left[\frac{\gamma_2 E_{\text{dis2}}}{\gamma_1 E_{\text{dis1}}}\right]} \tag{6.11}$$

Using Equation 6.11, a σ value is calculated for each of the seven measured datasets from Section 5.3. Since three E_{dis} vs t_{dis} datapoints are available within each dataset, σ is calculated based on the 4 h and 1 h datapoints to capture the lowest and highest values of E_{dis} and t_{dis}. Note that $\gamma_1 \approx \gamma_2 \approx 1$ when using 4 h and 1 h values due to the design of Equation 6.10. The left chart of Figure 6.2 highlights the 4 h and 1 h values used in the calculation, while the right chart plots the resulting σ calculations. The right chart shows

that σ values range from 1.04 to 1.08, with Lishen-12 giving the smallest values and the liquid-cooled Model3-19 giving the largest. The differences in σ represent the differences in E_{dis} rate dependence among the different battery packs and thermal management systems, similar to the normalized energy utilization ratio ζ^* results from Section 5.3.2.

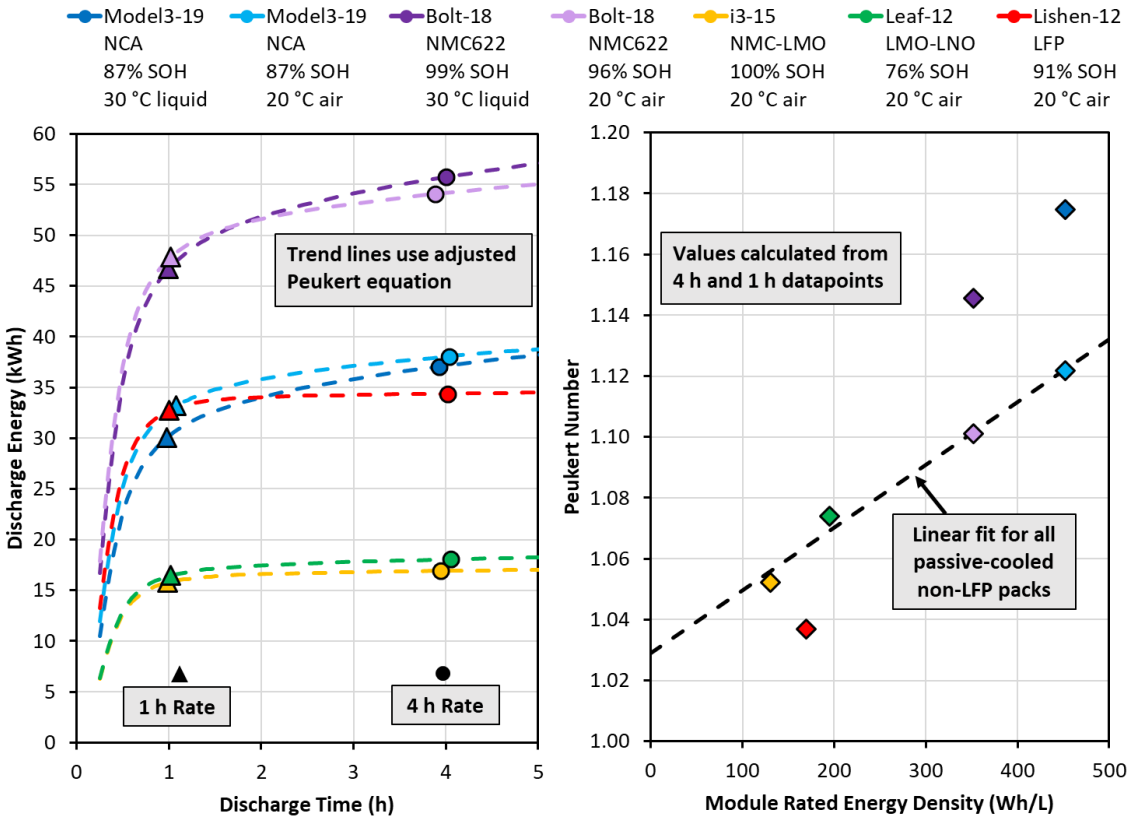


Figure 6.2 Measured 4 h and 1 h data (left) used to calculate Peukert numbers (right).

For the x-axis in the right chart of Figure 6.2, the rated discharge energy $E_{\text{dis}}^{\text{spec}}$ of each pack is scaled by its measured module volume v_{mod} to give the 'module rated energy density' $\bar{E}_v^{\text{spec}}$. This graphical technique reveals three insights which can be explained by principles discussed previously in Sections 5.2 and 5.3. The first insight is that the passive-cooled σ values calculated for Model3-19, Bolt-18, i3-15, and Leaf-12 exhibit a fairly linear dependence on $\bar{E}_v^{\text{spec}}$, as highlighted by the black dashed line. This can be explained by the tendency for batteries with higher energy density to feature higher internal resistance, which leads to earlier termination of discharge and charge and thus lower energy utilization (i.e. higher σ). Furthermore, the nickel-rich NCA positive electrode of Model3-19 provides both an enhancement in energy density and a voltage profile shape that promotes earlier

termination of charge for a given power rate. The second insight is that liquid cooling results in increased σ values compared to passive cooling for Model3-19 and Bolt-18. This can be explained by the effectiveness of liquid cooling in mitigating temperature rise at the end of discharge and charge, which increases internal resistance compared to passive cooling at a given power rate and thus promotes earlier termination of discharge and charge. The third insight is that Lishen-12 exhibits an anomalously low σ value compared to the other passive-cooled packs. This can be explained by the relatively flat voltage profile of LFP batteries, which enhances energy utilization at higher power rates compared to other lithium-ion chemistries.

The σ vs $\bar{E}_v^{\text{spec}}$ results in Figure 6.2 suggest that the Peukert number of a given EV battery pack can be estimated with reasonable accuracy if the manufacturer energy rating and total module volume are known. To this end, Equation 6.12 is proposed as a novel empirical relationship for electrical performance of EV battery packs, where $E_{\text{dis}}^{\text{spec}}$ is in kWh, v_{mod} is in L, and α_σ is a dimensionless correction factor to account for the effects of thermal management and the special case of LFP chemistry.

$$\sigma = \alpha_\sigma \left(1.03 + 0.20 \frac{E_{\text{dis}}^{\text{spec}}}{v_{\text{mod}}}\right) \tag{6.12}$$

Based on Figure 6.2, Equation 6.12 can be applied with $\alpha_\sigma = 1.04$ for liquid-cooled packs, $\alpha_\sigma = 0.97$ for LFP packs, and $\alpha_\sigma = 1$ otherwise. While these particular α_σ values cannot be recommended with confidence based on just two liquid-cooled datapoints and just one LFP datapoint, they will serve for the demonstrative purposes of this thesis, recognizing that a larger sample size is required for verification in future research. For the seven σ values shown in Figure 6.2, the corresponding estimates produced by Equation 6.12 are all within 0.4 % of the values calculated from experimental results.

With further empirical refinement and verification, Equation 6.12 could be used to predict Peukert numbers for second-life battery packs before any performance testing is carried out, as long as $E_{\text{dis}}^{\text{spec}}$ and v_{mod} can be ascertained from manufacturer specifications. Both

these specifications are set by the battery manufacturer and do not change with battery degradation. The impacts of degradation on σ will be considered in Section 6.5.1.

6.1.2. Energy Efficiency

Since the cycle energy efficiency η is the ratio of discharge energy E_{dis} to charge energy E_{chg}, an empirical relationship for η could be conceived simply by applying the adjusted Peukert equation for both E_{dis} and E_{chg}. While the adjusted Peukert equation can model the measured E_{dis} and E_{chg} values to within a 1 % tolerance of the measured values for all seven datasets, these errors become significant when carried through the η calculation. Section 5.3.4 showed that the tested EV batteries all exhibit $\eta > 90$ % for $t_{\mathrm{dis}} \geq 1$ h, which means that a 1 % error in η is effectively a > 10 % error in $1 - \eta$, the latter of which is a practical figure describing the relative amount of energy lost as heat that must be recouped as charge energy (e.g. $\eta = 95$ % corresponds to 5 % energy lost as heat). A different empirical relationship is therefore required to achieve a more accurate approximation of energy efficiency.

Based on the experimental results for η shown in Section 5.3.6, a new empirical relationship is now proposed in Equations 6.13, which will be referred to as the 'empirical energy efficiency equation'. This equation is similar in structure to the Peukert equation, but it instead relates $1 - \eta$ to the discharge duration t_{dis} for SCP cycling using an 'energy efficiency exponent' b_η. As with the Peukert number, b_η is considered to be a constant parameter for a given battery design at a given temperature and SOH. Since internal resistance varies with temperature and SOH, b_η may be influenced by these factors as well.

$$(1 - \eta){t_{\mathrm{dis}}}^{b_\eta} = constant \tag{6.13}$$

Figure 6.3 demonstrates how Equation 6.13 can be accurately fitted to the measured η results for all seven datasets, respectively using the power-to-energy ratio and discharge duration t_{dis} as the x-axes in the left and right charts. Unlike the Peukert equation, no adjustments are necessary to enhance the accuracy of the empirical energy efficiency equation.

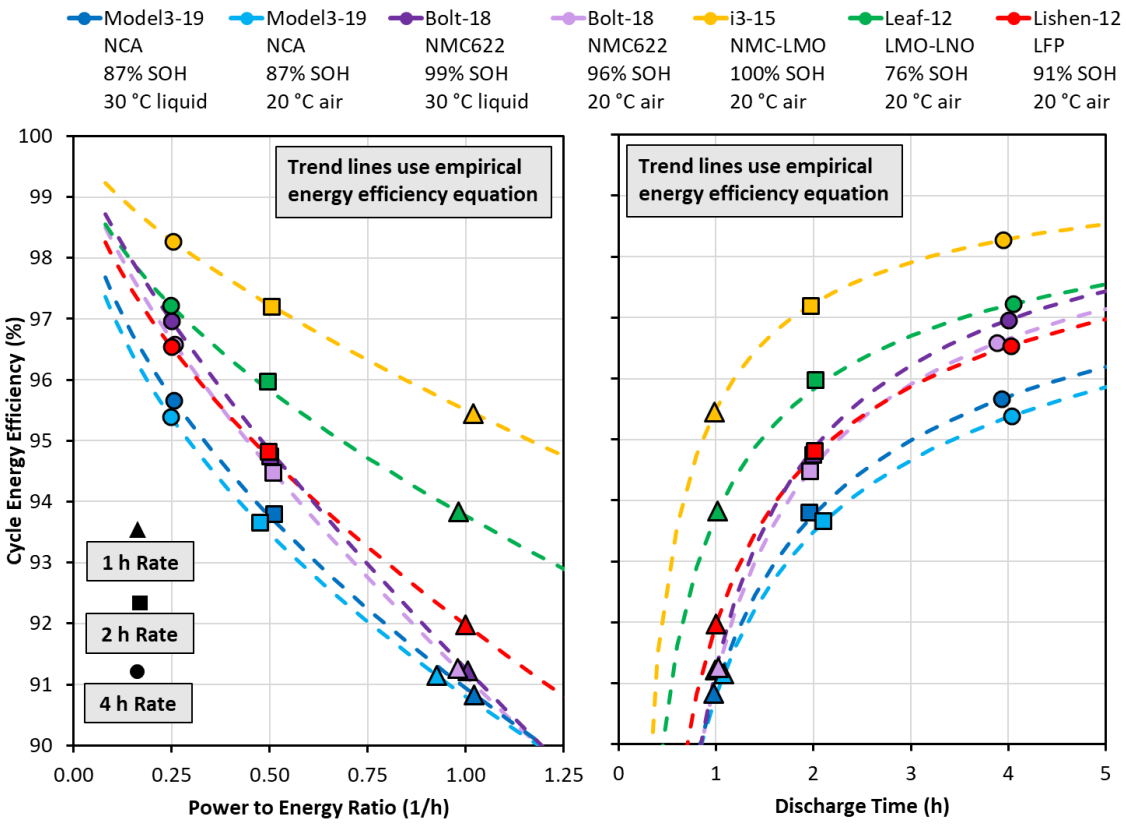


Figure 6.3 Empirical energy efficiency equation fitted to measured data as a function of power-to-energy ratio (left) and discharge duration (right).

Section 6.1.1 showed that σ can be determined for a given EV battery pack either by conducting two or more SCP tests (Equation 6.11) or by calculating an estimate based on the rated module energy density (Equation 6.12). To utilize Equation 6.13, b_η must be determined as well. As was done with the adjusted Peukert equation, Equation 6.13 can be adapted to calculate b_η from experimental η results obtained at two or more different values of t_{dis}. This is done in Equation 6.14.

$$b_\eta = -\log_{\left(\frac{t_{\text{dis2}}}{t_{\text{dis1}}}\right)}\left[\frac{1-\eta_2}{1-\eta_1}\right] \tag{6.14}$$

Using Equation 6.14, a b_η value is calculated for each of the seven measured datasets from Section 5.3, using the 4 h and 1 h datapoints to capture the lowest and highest values of η and t_{dis}. The left chart of Figure 6.4 highlights the 4 h and 1 h values used in the calculation, while the right chart plots the resulting b_η calculations against the rated module energy

density $\bar{E}_v^{\text{spec}}$. This shows that b_η values range from 0.50 to 0.76, with Model3-19 giving the smallest values and Bolt-18 giving the largest. The meaning of this variance can be understood by comparing Model3-19 and Bolt-18 in Figure 6.3. While Model3-19 has a notably lower η at a 4 h rate, the η of Bolt-18 decreases faster as the power rate increases to a 1 h rate. The magnitude of b_η can therefore be taken as an indicator of η rate dependence, similar to how the Peukert number σ is an indicator of E_{dis} rate dependence.

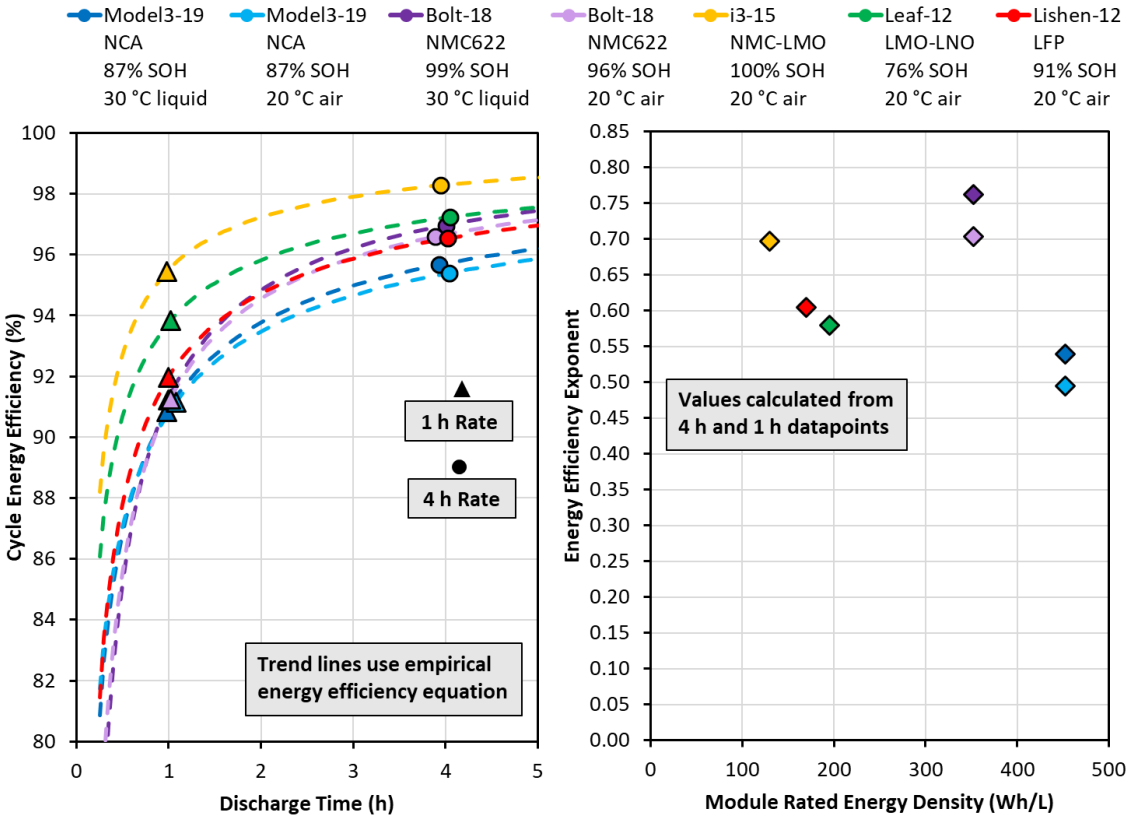


Figure 6.4 Measured 4 h and 1 h data (left) used to calculate energy efficiency exponents (right).

As explained in Section 6.1.1, the differences in E_{dis} rate dependence among the seven datasets can be explained by differences in internal resistance, voltage profile shape, and TMS. The difference in η rate dependence among the tested EV battery packs could stem from a variety of cell design factors, such as electrode porosity, active material blending, and electrolyte additives. The fact that Model3-19 exhibits the strongest E_{dis} rate dependence but the weakest η rate dependence among the five tested packs suggests that the factors which determine η rate dependence are not the same as the factors which

determine E_{dis} rate dependence. For both Model3-19 and Bolt-18, b_η is slightly higher when liquid-cooling is applied, which indicates that b_η is influenced somewhat by temperature in addition to cell design factors.

Figure 6.4 also shows that b_η does not exhibit any explainable dependence on $\bar{E}_v^{\text{spec}}$, which means it is unlikely that b_η can be conveniently predicted based on manufacturer specifications. Future research could investigate electrochemical influences on η rate dependence in hopes of establishing correlations between b_η and manufacturer-specified cell chemistry, but it is unlikely that the cell design factors contributing to b_η will be listed on EV battery spec sheets. It is therefore expected that experimental tests will be necessary to determine b_η for a given second-life battery pack.

6.1.3. Heat Generation

A novel performance metric called the average volumetric heat generation rate $\dot{\bar{q}}_v$ was defined for an SCP cycle in Section 4.5.1. Since $\dot{\bar{q}}_v$ depends on both discharge energy E_{dis} and cycle energy efficiency η, the adjusted Peukert equation and empirical energy efficiency equation can be substituted into the $\dot{\bar{q}}_v$ definition, as shown in Equation 6.15.

$$\begin{aligned}\dot{\bar{q}}_v &= \frac{E_{\text{dis}}}{v_{\text{mod}} t_{\text{dis}}}\left(\frac{1-\eta}{1+\eta}\right) \\ &= \frac{\left(\gamma^{-1} {t_{\text{dis}}}^{1-\frac{1}{\sigma}} constant\right)\left({t_{\text{dis}}}^{-b_\eta} constant\right)}{v_{\text{mod}} t_{\text{dis}}(1+\eta)} \\ &= \gamma^{-1}(1+\eta)^{-1} {t_{\text{dis}}}^{-\left(\frac{1}{\sigma}+b_\eta\right)} constant \end{aligned} \tag{6.15}$$

Based on the measured η results, the quantity $1+\eta$ should lie between 1.90 and 1.99 over a practical range of t_{dis}. It is therefore reasonable to treat $1+\eta$ as being approximately constant so that Equation 6.15 can be simplified with $\dot{\bar{q}}_v$ and t_{dis} as the only variables. This yields a new empirical relationship as stated in Equation 6.16, which will be referred to as the 'empirical heat generation equation'. The 'heat generation exponent' b_q is a combination of the Peukert number σ and the energy efficiency exponent b_η as defined in

Equation 6.17, and therefore represents the combined effects of E_{dis} rate dependence and η rate dependence on $\dot{\bar{q}}_v$.

$$\gamma \dot{\bar{q}}_v {t_{\text{dis}}}^{b_q} = constant \tag{6.16}$$

$$b_q \approx \frac{1}{\sigma} + b_\eta \tag{6.17}$$

Figure 6.5 demonstrates how Equations 6.16 and 6.17 can be fitted accurately to the measured $\dot{\bar{q}}_v$ results for all seven datasets, where the left chart and right charts respectively use the power-to-energy ratio and discharge duration t_{dis} for the x-axis. Each b_q value is calculated using the σ and b_η values shown in Figure 6.2 and Figure 6.4.

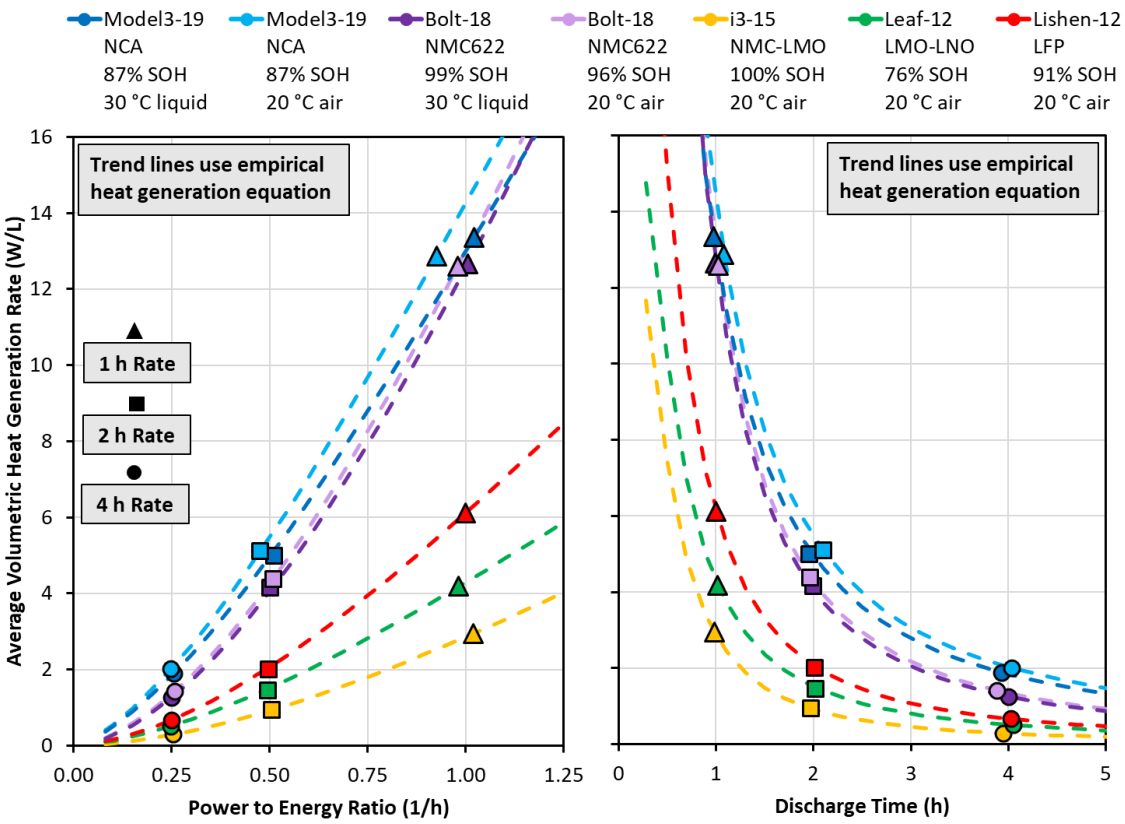


Figure 6.5 Empirical heat generation equation fitted to measured data as a function of power-to-energy ratio (left) and discharge duration (right).

A more complete definition of b_q can be derived by adapting Equation 6.16 to compare two $\dot{\bar{q}}_v$ datapoints measured at two different values of t_{dis}. This is done in Equation 6.18, which is expanded with the definition $\dot{\bar{q}}_v = \frac{P}{v_{\text{mod}}}\left(\frac{1-\eta}{1+\eta}\right)$.

$$\begin{aligned} b_q &= -\log_{\left(\frac{t_{\text{dis2}}}{t_{\text{dis1}}}\right)}\left[\frac{\gamma_2 \dot{\bar{q}}_{v2}}{\gamma_1 \dot{\bar{q}}_{v1}}\right] \\ &= -\log_{\left(\frac{t_{\text{dis2}}}{t_{\text{dis1}}}\right)}\left[\frac{\gamma_2 P_2}{\gamma_1 P_1}\left(\frac{1-\eta_2}{1+\eta_2}\right)\left(\frac{1+\eta_1}{1-\eta_1}\right)\right] \end{aligned} \tag{6.18}$$

By applying the expressions for σ and b_η respectively given in Equations 6.11 and 6.14, Equation 6.18 can be restated in the equivalent form shown in Equation 6.19. Since the quantity $1+\eta$ is approximately constant over a practical range of t_{dis}, the logarithmic term in Equation 6.19 is small and only accounts for about 1 % of b_q. This means that Equations 6.17 and 6.19 are approximately equivalent, but Equation 6.19 is the more complete expression for b_q.

$$b_q = \frac{1}{\sigma} + b_\eta + \log_{\left(\frac{t_{\text{dis2}}}{t_{\text{dis1}}}\right)}\left[\frac{1+\eta_2}{1+\eta_1}\right] \tag{6.19}$$

The right chart of Figure 6.6 plots the b_q values calculated from Equation 6.19 using the 4 h and 1 h datapoints, while the left chart plots the corresponding σ and b_η values shown previously in Figure 6.2 and Figure 6.6, respectively. This shows that b_q values range from 1.39 to 1.65, with Model3-19 giving the smallest values and Bolt-18 and i3-15 giving the largest. The distribution of b_q values is similar to the distribution of b_η values, but the b_q values of Model3-19 and Bolt-18 are shifted down compared to the b_η distribution due to the relatively large σ values for Model3-19 and Bolt-18. This shows how the rate dependence of both E_{dis} and η contribute to the rate dependence of $\dot{\bar{q}}_v$.

The rated module energy density $\bar{E}_v^{\text{spec}}$ is used as the x-axis in Figure 6.6 to explore any correlation between b_q and $\bar{E}_v^{\text{spec}}$. Since b_η does not exhibit a clear dependence on $\bar{E}_v^{\text{spec}}$, neither does b_q. For Model3-19 and Bolt-18, both σ and b_η clearly increase when

liquid-cooling is applied, but this dependence on thermal management is evidently dampened for b_q. This is due to the nature of Equation 6.17, which reflects the opposing influence of E_{dis} and η on $\dot{\bar{q}}_v$

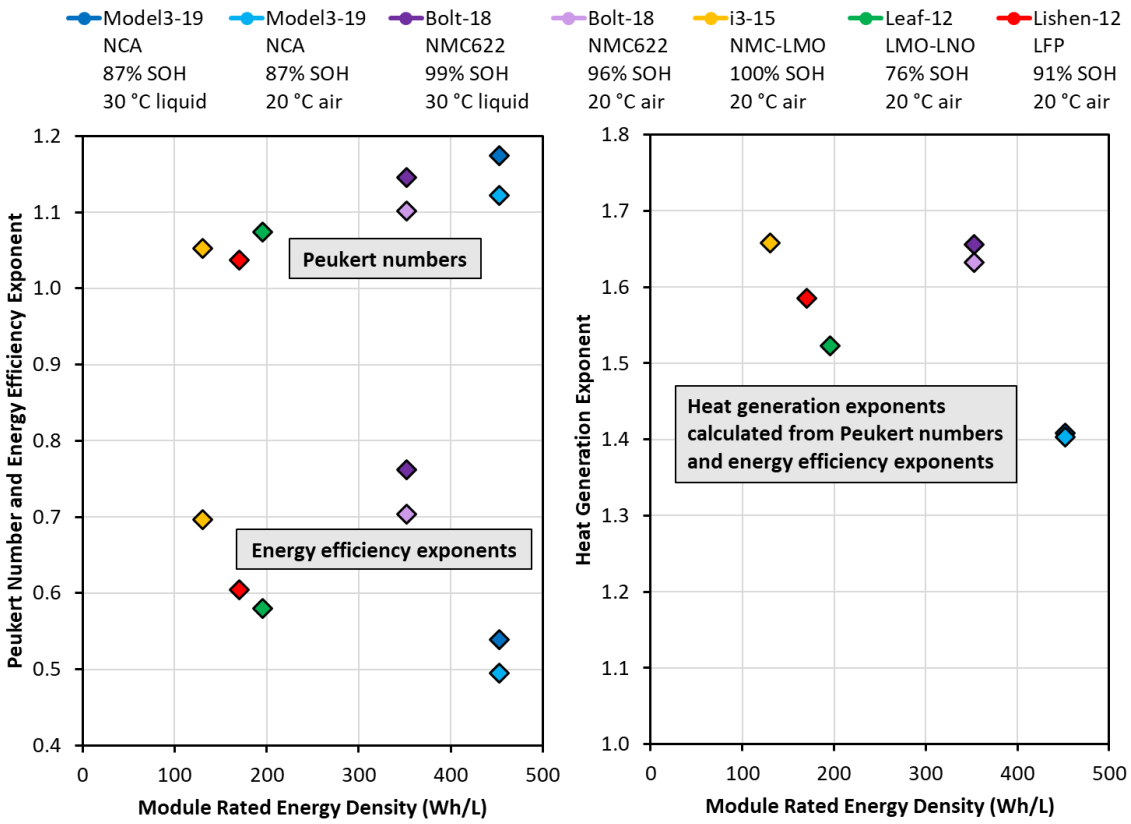


Figure 6.6 Peukert numbers and energy efficiency exponents (left) used to calculate heat generation exponents (right).

6.1.4. Temperature Rise

For a given thermal management system, Section 5.4.5 demonstrated that the maximum and average temperature rise $\Delta T_{\text{high}}^{\text{max}}$ and $\Delta T_{\text{high}}^{\text{avg}}$ both exhibit a clear correlation with the average volumetric heat generation rate $\dot{\bar{q}}_v$ for all tested battery packs. In contrast, no consistent correlations could be identified for the average pack temperature differential $\Delta T_{\text{diff}}^{\text{avg}}$ due to its strong dependence on the design and layout of cells and modules within each pack. Based on these observations, two more novel empirical relationships are proposed in Equations 6.20 and 6.21, where $b_{T_{\text{max}}}$ and $b_{T_{\text{avg}}}$ are respectively the maximum and average 'temperature rise exponents' used to relate $\Delta T_{\text{high}}^{\text{max}}$ and $\Delta T_{\text{high}}^{\text{avg}}$ to $\dot{\bar{q}}_v$ for SCP

cycling. From these two equations, a third equation can be derived which relates $\Delta T_{\text{high}}^{\max}$ and $\Delta T_{\text{high}}^{\text{avg}}$ to each other, as shown in Equation 6.22. Finally, Equations 6.20 and 6.21 can be combined with the empirical heat generation equation in Equation 6.16 to relate $\Delta T_{\text{high}}^{\max}$ and $\Delta T_{\text{high}}^{\text{avg}}$ to the discharge duration t_{dis}, as shown in Equations 6.23 and 6.24. Note that since there is no consistent empirical relationship describing the spatial temperature differentials between different points in a given battery pack, $\Delta T_{\text{high}}^{\max}$ and $\Delta T_{\text{high}}^{\text{avg}}$ are denoted as simply $\Delta T_{\max}$ and ΔT_{avg} for brevity, recognizing that both refer to the hottest measured point in a given battery pack and that "average" refers to a temporal average rather than a spatial average.

$$\Delta T_{\max} \dot{\bar{q}}_v^{\,-b_{T_{\max}}} = constant \tag{6.20}$$

$$(\Delta T_{\text{avg}} + offset) \dot{\bar{q}}_v^{\,-b_{T_{\text{avg}}}} = constant \tag{6.21}$$

$$(\Delta T_{\text{avg}} + offset) \Delta T_{\max}^{\,-\frac{b_{T_{\text{avg}}}}{b_{T_{\max}}}} = constant \tag{6.22}$$

$$\Delta T_{\max} t_{\text{dis}}^{\,b_q b_{T_{\max}}} = constant \tag{6.23}$$

$$(\Delta T_{\text{avg}} + offset) t_{\text{dis}}^{\,b_q b_{avg}} = constant \tag{6.24}$$

Equations 6.20 through 6.24 will be referred to as the 'empirical temperature rise equations', and are similar in structure to the Peukert equation, energy efficiency equation, and empirical heat generation equation described in the three preceding subsections. The main difference is the 'offset' featured in Equations 6.21 and 6.22, which accounts for the fact that a battery can experience a brief $\Delta T_{\max} > 0$ at the end of discharge (indicating $\dot{\bar{q}}_v > 0$) even if ΔT_{avg} (taken over the entire SCP cycle) is essentially zero. The parameters $b_{T_{\max}}$ and $b_{T_{\text{avg}}}$ should be solely dependent on physical and thermal properties and are therefore considered to be constants for a given battery design and thermal management system, with little dependence on SOH.

The left and right charts of Figure 6.7 respectively demonstrate how Equations 6.20 and 6.21 can be fitted fairly accurately to the measured $\Delta T_{\max}$ and ΔT_{avg} results as a function

of $\dot{\bar{q}}_v$ for all seven datasets. As discussed in Section 5.4.5, all passive-cooled datapoints follow a similar dependence on $\dot{\bar{q}}_v$ due to the asymptotic nature of passive cooling, the relatively slow passive cooling rates of the five battery packs, as well as their comparable size, shape, and material composition. Therefore, instead of applying the empirical temperature rise equations to each individual passive-cooled dataset, a single curve can be fitted to the five passive-cooled datasets for both $\Delta T_{\max}$ and ΔT_{avg} (the black dashed lines in Figure 6.7). All passive-cooled datapoints fall within 1.5 °C of these two curves. Considering that these datapoints (measured at exposed outer surfaces of modules or cells) only approximate the true core temperatures of each battery, and that the $\Delta T_{\max}$ and ΔT_{avg} results can vary slightly with ambient temperature T_∞ anyway (discussed in Section 5.5), a tolerance of 1.5 °C is acceptable. Since the liquid-cooled datapoints depend strongly on the liquid channel design of the given battery pack, Equations 6.20 and 6.21 must be fitted to each individual liquid-cooled dataset.

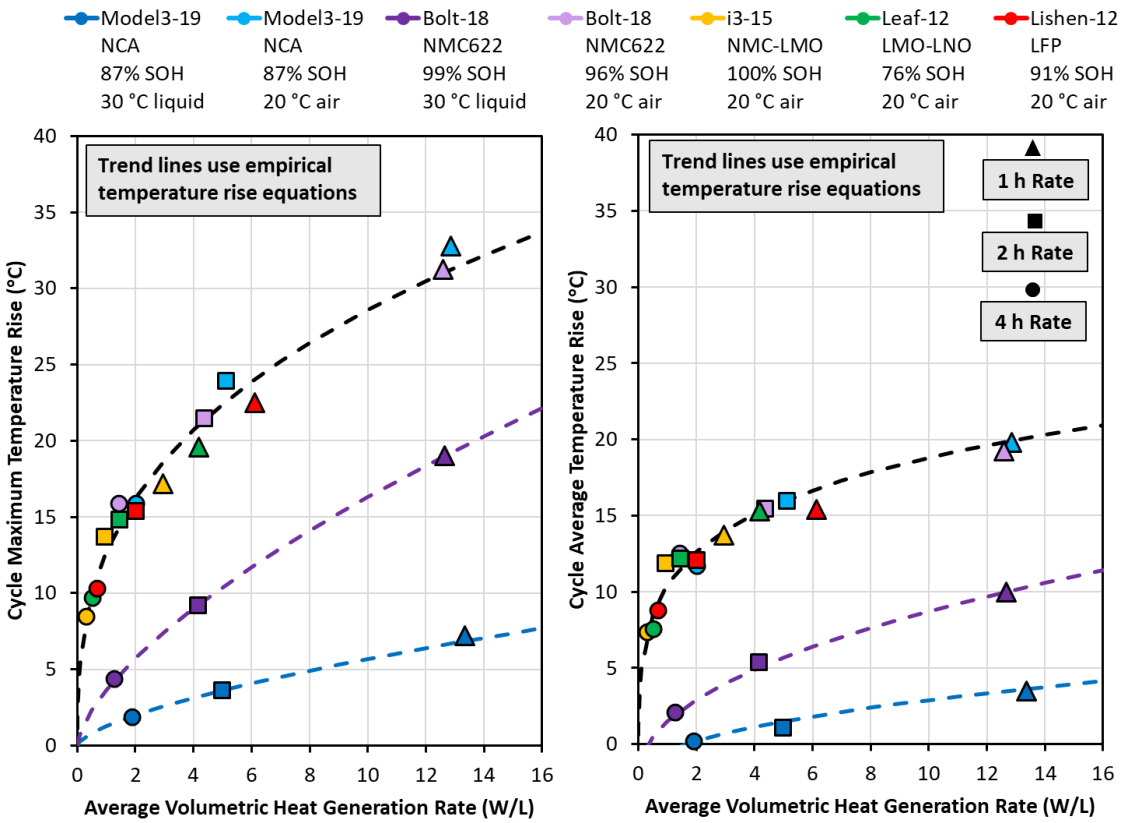


Figure 6.7 Empirical temperature rise equations fitted to experimental data for maximum (left) and average (right) temperature rise as a function of average volumetric heat generation rate.

Based on Figure 6.7, Equations 6.20 and 6.21 can be universally defined for the case of passive-cooled second-life battery packs, as shown in Equations 6.25 and 6.26. For the case of liquid-cooled packs, Equations 6.20 and 6.21 can be fitted accurately to both Model3-19 and Bolt-18 using a single value of $b_{T_{\max}}$ and $b_{T_{\text{avg}}}$, as shown in Equations 6.27 and 6.28. The trendlines plotted in Figure 6.7 are based on these four definitions.

$$\Delta T_{\max}^{\text{PA}} \dot{\bar{q}}_v^{\,-0.35} = 12.7 \tag{6.25}$$

$$\left(\Delta T_{\text{avg}}^{\text{PA}} + 6\right) \dot{\bar{q}}_v^{\,-0.18} = 16.5 \tag{6.26}$$

$$\Delta T_{\max}^{\text{AL}} \dot{\bar{q}}_v^{\,-0.65} = constant \tag{6.27}$$

$$\left(\Delta T_{\text{avg}}^{\text{AL}} + 2\right) \dot{\bar{q}}_v^{\,-0.48} = constant \tag{6.28}$$

Equations 6.25 through 6.28 can be used to universally define Equation 6.22 as shown in Equations 6.29 and 6.30. The resulting trends are shown in the left chart of Figure 6.8, which demonstrates that a single equation can accurately model the ΔT_{avg} vs $\Delta T_{\max}$ correlation for all passive-cooled packs and for both liquid-cooled packs (as suggested previously in Section 5.4.2). Note that the trendlines do not intersect the origin due to the offset. The liquid-cooled Model3-19 dataset in particular demonstrates the necessity of the offset. The right chart of Figure 6.8 shows the ΔT_{avg} vs $\dot{\bar{q}}_v$ trends for reference.

$$\left(\Delta T_{\text{avg}}^{\text{PA}} + 6\right) \Delta T_{\max}^{\text{PA}\,-0.50} = 4.6 \tag{6.29}$$

$$\left(\Delta T_{\text{avg}}^{\text{AL}} + 2\right) \Delta T_{\max}^{\text{AL}\,-0.73} = 1.4 \tag{6.30}$$

Using Equations 6.25 through 6.30, $\Delta T_{\max}$ and ΔT_{avg} can be predicted with reasonable accuracy for passive-cooled second-life battery packs undergoing SCP cycling without requiring any battery temperature measurements as long as $\dot{\bar{q}}_v$ is known. For liquid-cooled packs, temperature measurements from at least one experimental test are required to finish populating Equations 6.26 and 6.28 for the given battery pack.

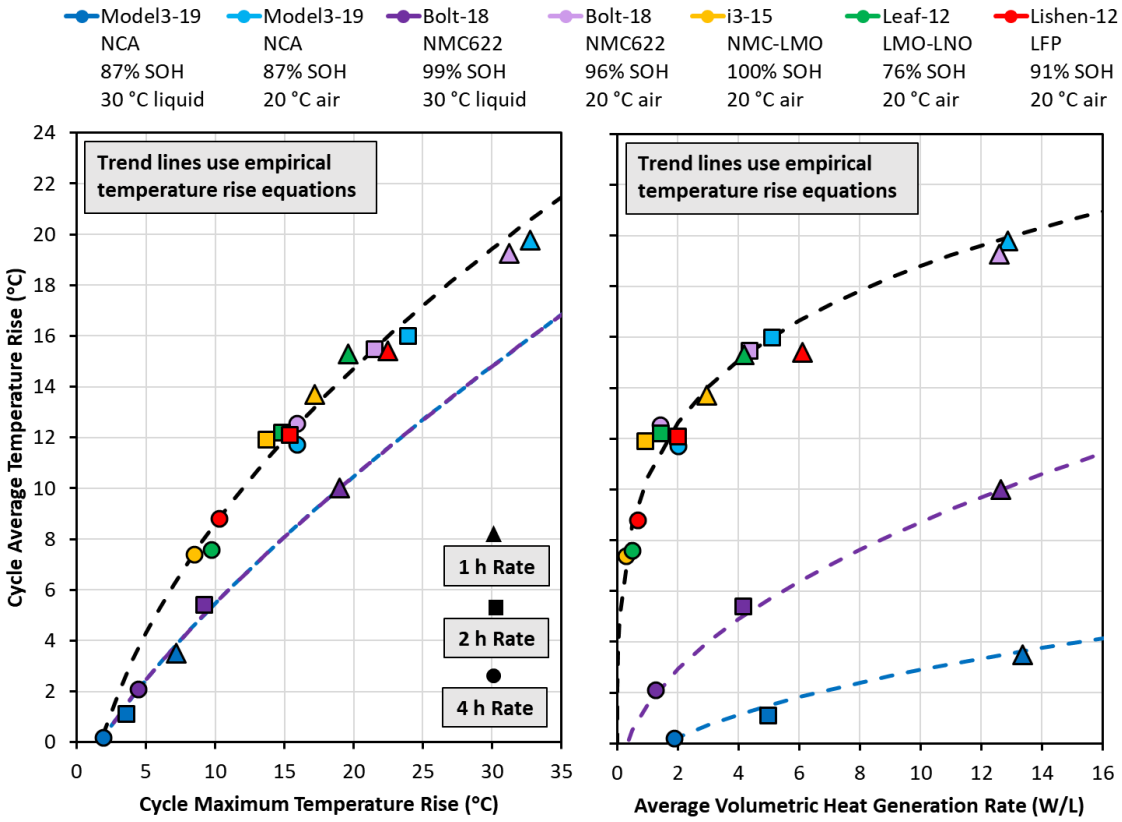


Figure 6.8 Comparison of measured average temperature rise data and fitted model as a function of maximum temperature rise (left) and average volumetric heat generation rate (right).

6.2. Performance Extrapolation Methods

The series of empirical relationships introduced in Section 6.1 can be used to predict the results of SCP battery performance tests if the necessary equation inputs are available. This section will first restate the empirical equations in a form that enables prediction or extrapolation of key battery performance metrics. Two different solutions for obtaining the necessary equation inputs will then be described: one requiring two experimental datasets and one requiring a single experimental dataset.

6.2.1. Extrapolative Empirical Equations for Battery Performance

If the Peukert number σ is known for a given battery, then SCP test results for discharge energy E_{dis} obtained at a particular value of discharge duration t_{dis} or applied power P can be used to extrapolate the E_{dis} results to another desired t_{dis} or P. To this end, Equations

6.7 through 6.9 are restated in their extrapolative forms in Equations 6.31 through 6.33, where the 'ref' superscript demarks values obtained from a single experimental reference test. In these equations, the adjustment factor γ must be calculated at both the measured $t_{\text{dis}}^{\text{ref}}$ and the desired t_{dis}. Note that Equation 6.32 can be used to predict the applied power P that would produce a desired value of t_{dis}. The energy density $\bar{E}_v$ and energy utilization ratio ζ can also be calculated for a given extrapolated E_{dis} value if v_{mod} and $E_{\text{dis}}^{\text{CCCV}}$ are known, as described in Section 4.5.1.

$$E_{\text{dis}} = \frac{\gamma^{\text{ref}}}{\gamma} E_{\text{dis}}^{\text{ref}} \left(\frac{t_{\text{dis}}^{\text{ref}}}{t_{\text{dis}}} \right)^{\frac{1}{\sigma}-1} \tag{6.31}$$

$$P = \frac{\gamma^{\text{ref}}}{\gamma} P^{\text{ref}} \left(\frac{t_{\text{dis}}^{\text{ref}}}{t_{\text{dis}}} \right)^{\frac{1}{\sigma}} \tag{6.32}$$

$$E_{\text{dis}} = \frac{\gamma^{\text{ref}}}{\gamma} E_{\text{dis}}^{\text{ref}} \left(\frac{P^{\text{ref}}}{P} \right)^{\sigma-1} \tag{6.33}$$

Similarly, if the energy efficiency exponent b_η is known for a given battery, then SCP test results for cycle energy efficiency η obtained at a particular value of t_{dis} can be used to extrapolate the η results to a desired t_{dis}. Equation 6.13 is restated in its extrapolative form in Equation 6.34, where the 'ref' superscript again demarks values obtained from a single experimental reference test. Alternatively, η results can be extrapolated from one applied power magnitude P to another by combining Equations 6.32 and 6.34.

$$\eta = 1 - \left(1 - \eta^{\text{ref}}\right) \left(\frac{t_{\text{dis}}^{\text{ref}}}{t_{\text{dis}}} \right)^{b_\eta} \tag{6.34}$$

Once E_{dis} and η are calculated for a desired t_{dis} or P, the definitions $\dot{\bar{q}}_v = \frac{E_{\text{dis}}}{v_{\text{mod}} t_{\text{dis}}} \left(\frac{1-\eta}{1+\eta} \right)$ or $\dot{\bar{q}}_v = \frac{P}{v_{\text{mod}}} \left(\frac{1-\eta}{1+\eta} \right)$ can be used to calculate the corresponding average volumetric heat generation rate $\dot{\bar{q}}_v$ at both the measured operating point and the desired operating point. Alternatively, $\dot{\bar{q}}_v$ can be directly extrapolated using Equation 6.35, which restates

Equation 6.16 in its extrapolative form. This approach has the advantage of being isolated from any errors in the extrapolations of E_{dis} and η.

$$\dot{\bar{q}}_v = \frac{\gamma^{\mathrm{ref}}}{\gamma} \dot{\bar{q}}_v^{\mathrm{ref}} \left(\frac{t_{\mathrm{dis}}^{\mathrm{ref}}}{t_{\mathrm{dis}}} \right)^{b_q} \tag{6.35}$$

With $\dot{\bar{q}}_v$ determined for a desired t_{dis} or P, the associated maximum ΔT_{max} and average ΔT_{avg} temperature rise can also be estimated. For passive-cooled packs, Equations 6.25, 6.26, and 6.29 are restated in their extrapolative forms in Equations 6.36 through 6.38. Note that these three equations are not a direct extrapolation from one operating point to another, since they depend only on $\dot{\bar{q}}_v$ at the desired operating point. However, Equations 6.36 through 6.38 are still considered to be 'extrapolative' within the context of the proposed performance extrapolation model since $\dot{\bar{q}}_v$ is extrapolated from an experimental reference test.

$$\Delta T_{\mathrm{max}}^{\mathrm{PA}} = 12.7 \dot{\bar{q}}_v^{\ 0.35} \tag{6.36}$$

$$\Delta T_{\mathrm{avg}}^{\mathrm{PA}} = 16.5 \dot{\bar{q}}_v^{\ 0.18} - 6 \tag{6.37}$$

$$\Delta T_{\mathrm{avg}}^{\mathrm{PA}} = 4.6 \Delta T_{\mathrm{max}}^{\mathrm{PA}\ 0.50} - 6 \tag{6.38}$$

While Equations 6.36 through 6.38 do not require temperature rise results from the reference test, battery temperatures must still be monitored during testing to ensure the safety of the test and to control the cooldown periods as described in Section 4.4. Additionally, the $\Delta T_{\mathrm{max}}^{\mathrm{PA}}$ and $\Delta T_{\mathrm{avg}}^{\mathrm{PA}}$ results from the reference test should be compared to the values predicted by Equations 6.36 through 6.38. If the predictions fall within about 1.5 °C of the measured values, then the researcher can feel confident that extrapolated values of $T_{\mathrm{max}}^{\mathrm{PA}}$ and $\Delta T_{\mathrm{avg}}^{\mathrm{PA}}$ will be reasonably accurate. If this condition is not met, then it is likely that the thermal characteristics (e.g. pack shape, cell material properties, module material properties, TMS design) of the battery pack in question differ significantly from the five battery packs tested in this research project, in which case Equations 6.36 through 6.38 cannot be reliably applied as stated.

For liquid-cooled packs, Equations 6.27, 6.28, and 6.30 are restated in their extrapolative forms in Equations 6.39 through 6.41. Unlike their passive-cooled counterparts, these equations do require direct extrapolation from measured values of $\Delta T_{\text{max}}^{\text{AL}}$ and $\Delta T_{\text{avg}}^{\text{AL}}$ acquired from the reference test.

$$\Delta T_{\text{max}}^{\text{AL}} = \Delta T_{\text{avg}}^{\text{ALref}} \left(\frac{\dot{\bar{q}}_v^{\text{ref}}}{\dot{\bar{q}}_v} \right)^{-0.65} \tag{6.39}$$

$$\Delta T_{\text{avg}}^{\text{AL}} = \left(\Delta T_{\text{avg}}^{\text{ALref}} + 2 \right) \left(\frac{\dot{\bar{q}}_v^{\text{ref}}}{\dot{\bar{q}}_v} \right)^{-0.48} - 2 \tag{6.40}$$

$$\Delta T_{\text{avg}}^{\text{AL}} = 1.4 \Delta T_{\text{max}}^{\text{AL}\ 0.73} - 2 \tag{6.41}$$

The temperature rise values for ΔT_{max} and ΔT_{avg} calculated by Equations 6.36 through 6.41 can also be converted to temperatures T_{max} and T_{avg} by adding the ambient temperature T_{∞}^{PA} or liquid supply temperature T_{∞}^{AL} as shown in Equations 6.42 through 6.45. When it comes to assessing the safety risk or degradation rate associated with the thermal performance of a given battery pack, T_{max} and T_{avg} are ultimately the metrics that must be considered. In this research project, T_{∞}^{PA} and T_{∞}^{AL} were respectively held near 20 °C and 30 °C during testing as explained in Section 4.4.3

$$T_{\text{max}}^{\text{PA}} = \Delta T_{\text{max}}^{\text{PA}} + T_{\infty}^{\text{PA}} \tag{6.42}$$

$$T_{\text{avg}}^{\text{PA}} = \Delta T_{\text{avg}}^{\text{PA}} + T_{\infty}^{\text{PA}} \tag{6.43}$$

$$T_{\text{max}}^{\text{AL}} = \Delta T_{\text{max}}^{\text{AL}} + T_{\infty}^{\text{AL}} \tag{6.44}$$

$$T_{\text{avg}}^{\text{AL}} = \Delta T_{\text{avg}}^{\text{AL}} + T_{\infty}^{\text{AL}} \tag{6.45}$$

The experimental reference test can also be used to calculate the average cooling time constant τ for a given battery pack, as described in Section 4.5.2. The calculated τ value can then be used to predict the cooldown time t_{cool} required for the battery to cool from the predicted value of T_{max} to a defined temperature control setpoint T_{ctrl}. This calculation is shown for passive-cooled and liquid-cooled packs in Equations 6.46 and 6.47,

respectively. Note that the logarithm is doubled in these equations such that the result estimates the total cooldown duration required for the full SCP cycle, including both the discharged cooldown and charged cooldown. In this research project, $T_{\text{ctrl}}^{\text{PA}}$ and $T_{\text{ctrl}}^{\text{AL}}$ were respectively set to 30.0 °C and 35.0 °C as explained in Section 4.4.3.

$$t_{\text{cool}}^{\text{PA}} = 2\tau \ln\left[\frac{\Delta T_{\text{max}}^{\text{PA}}}{T_{\text{ctrl}}^{\text{PA}} - T_{\infty}^{\text{PA}}}\right] \tag{6.46}$$

$$t_{\text{cool}}^{\text{AL}} = 2\tau \ln\left[\frac{\Delta T_{\text{max}}^{\text{AL}}}{T_{\text{ctrl}}^{\text{AL}} - T_{\infty}^{\text{AL}}}\right] \tag{6.47}$$

Using Equations 6.31 through 6.47, a complete set of SCP test results can be predicted at any desired power rate based on the results of a single experimental reference test, including E_{dis}, $\bar{E}_v$, ζ, η, T_{max}, T_{avg}, and t_{cool}. However, these equations are only useful if the Peukert number σ, energy efficiency exponent b_η, and heat generation exponent b_q are known for a given battery pack. Two different experimental solutions for determining these two essential parameters will be proposed in Sections 6.2.2 and 6.2.3.

6.2.2. Extrapolation from Two Experimental Datasets

If experimental tests are carried out at two different power rates for a given battery, Equations 6.11, and 6.14, and 6.19 can be respectively used to calculate σ, b_η, and b_q for the battery in question based on the measured values of t_{dis}, E_{dis}, and η. These three equations thus enable the prediction of SCP test results at any power rate based on measured results obtained at two different power rates (noting that only power rates in the range of 4 h to 1 h rates have been verified in this research project). This approach will be referred to as the 'two-dataset solution' for the performance extrapolation model.

The two-dataset solution has two practical benefits for second-life battery performance characterization. First, testing at a given power rate will not require iterative test repetitions to achieve a precise value of t_{dis}. In this research project, SCP testing of a given battery pack began with an initial guess for the applied power that would result in $t_{\text{dis}} = 4.0$ h. As an illustrative example, if the test results in $t_{\text{dis}} = 4.4$ h, then the applied power is increased to decrease the discharge duration. This iteration is repeated until t_{dis} is within about 2 %

of 4.0 h to ensure that the results could be directly compared with the other tested battery packs. The same iterative process must be carried out for the 2 h and 1 h SCP tests, resulting in each battery pack requiring a week or more to acquire three experimental datasets. With the proposed methods, two tests resulting in $t_{\text{dis}} = 4.4$ h and $t_{\text{dis}} = 1.8$ h (for example) could be used to predict the results that would be obtained for $t_{\text{dis}} = 4.0$ h, $t_{\text{dis}} = 2.0$ h, and $t_{\text{dis}} = 1.0$ h. By eliminating the need for iteration and reducing the number of required experimental datasets from three to two, the time required to obtain reliable results at standardized discharge durations would be significantly shortened. The time required to execute the two-dataset solution will be assessed in Section 6.4.

The second benefit is related to safety. As demonstrated in Section 5.4, cycling EV battery packs at a 1 h rate can produce high temperatures exceeding 50 °C, especially for packs with high energy density and passive cooling. Though battery test equipment includes appropriate safety features to interrupt testing if temperatures exceed set limits, there is still a risk that hotspots will arise at points which the applied temperature sensors will not detect. In this research project, the first 1 h SCP test applied to a given battery pack was conducted under direct visual and olfactory supervision to ensure that any thermal issues would be quickly detected. Furthermore, if the test is interrupted by a safety feature, the test is wasted and no datapoint is obtained. With the proposed methods, the 4 h and 2 h test results can be used to predict the 1 h test results without having to conduct this relatively high-risk test. At the very least, this technique can be applied to assess whether a 1 h SCP test would be safe to conduct on a given battery pack before the test is carried out.

6.2.3. Extrapolation from a Single Experimental Dataset

The extrapolation of E_{dis}, η, $\dot{\tilde{q}}_v$, $\Delta T_{\max}$, and ΔT_{avg} all rely on determination of the Peukert number σ and energy efficiency exponent b_η. Section 6.1.1 demonstrated that the Peukert number σ correlates strongly with the rated module energy density $\bar{E}_v^{\text{spec}}$, which allows for σ to be estimated for a given battery pack using Equation 6.12 before any testing is carried out. It follows then that if b_η and b_q could be determined from a single test, all experimental results could be extrapolated from this single experimental dataset. This would minimize

the required time to characterize the performance of second-life battery packs at standardized discharge durations.

A solution for determining b_η from a single SCP test can be derived by examining the b_η expression in Equation 6.14 and recalling from Section 2.4.2 that η is related to the ratio of discharge voltage V_{dis} to charge voltage V_{chg} taken at common SOC values. This 'voltage ratio' is plotted for all five battery packs and all three power rates in Figure 6.9, where the dashed lines indicate the measured η associated with each test. The yellow boxes highlight the SOC ranges where $\frac{V_{\mathrm{dis}}}{V_{\mathrm{chg}}}$ is within about 0.3 % of η at all three power rates. This shows that while some batteries have wider ranges of $\frac{V_{\mathrm{dis}}}{V_{\mathrm{chg}}} \approx \eta$ than others, all five ranges encompass the 30 % SOC mark, with the tightest tolerance always occurring between 20 % and 40 % SOC for each battery. Note that while Figure 6.9 only shows the liquid-cooled datasets for Model3-19 and Bolt-18, the respective passive-cooled datasets exhibit the same behaviour.

Figure 6.9 demonstrates that the voltage ratio can serve as a proxy for energy efficiency if V_{dis} and V_{chg} are taken at an appropriate SOC value. This means that simply pulsing to a different power magnitude P_{pulse} during both discharge and charge of an SCP test could produce the necessary voltage data to estimate the η value that would result from an SCP test carried out at P_{pulse}. Since all five acceptable ranges in Figure 6.9 encompass 30 % SOC despite significant diversity in electrode chemistry, one potential pulsing technique is to always carry out a single pulse at the 30 % SOC mark of an SCP test for any EV battery design. However, the 30 % mark is at the extreme of some of the acceptable ranges in Figure 6.9, and the acceptable ranges may change as a battery degrades (to be discussed in Section 6.5). A more robust pulsing technique is therefore required.

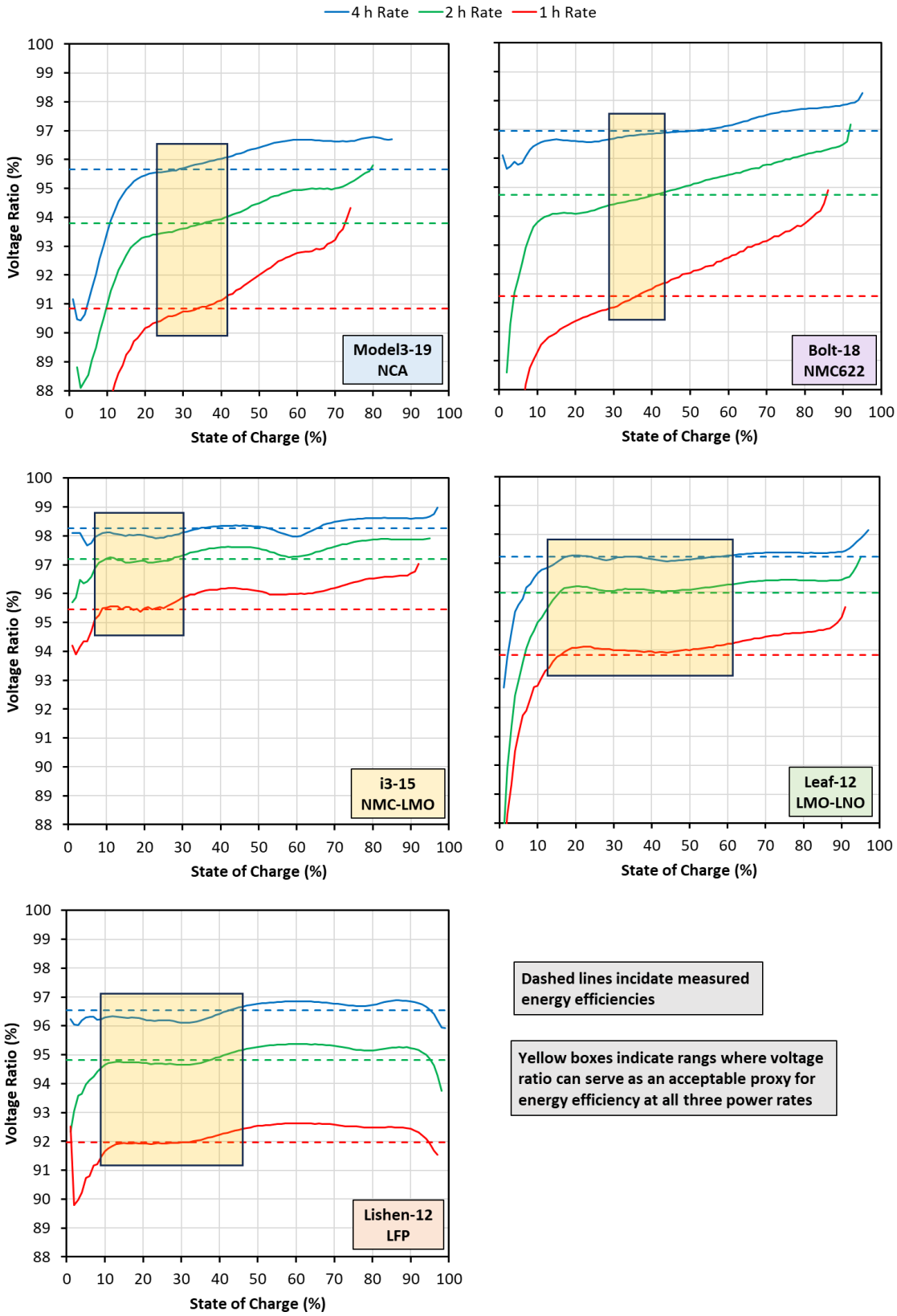


Figure 6.9 Ratio of discharge voltage to charge voltage at common SOC values for 4 h, 2 h, and 1 h power rates.

To explore the potential for using pulses to estimate energy efficiency, a symmetrical constant-power pulse (SCPP) test was carried out on the liquid-cooled Model3-19. The test protocol is based on the 2 h SCP cycle described in Section 4.4, but the power is pulsed to the 1 h rate every 20 minutes throughout discharge and charge. Section 2.3 explained how the electrochemical double layer between electrode and electrolyte behaves like a non-ideal capacitor, which produces a transient response to step changes in current or power. This transient response means that it will take time for the additional overpotential associated with P_{pulse} to be fully realized. A pulse duration of 120 s was therefore chosen for the SCPP test to ensure that each pulse has sufficient time to dissipate transients. The measured SCPP voltage profile is plotted as the solid black line in the left chart of Figure 6.10.

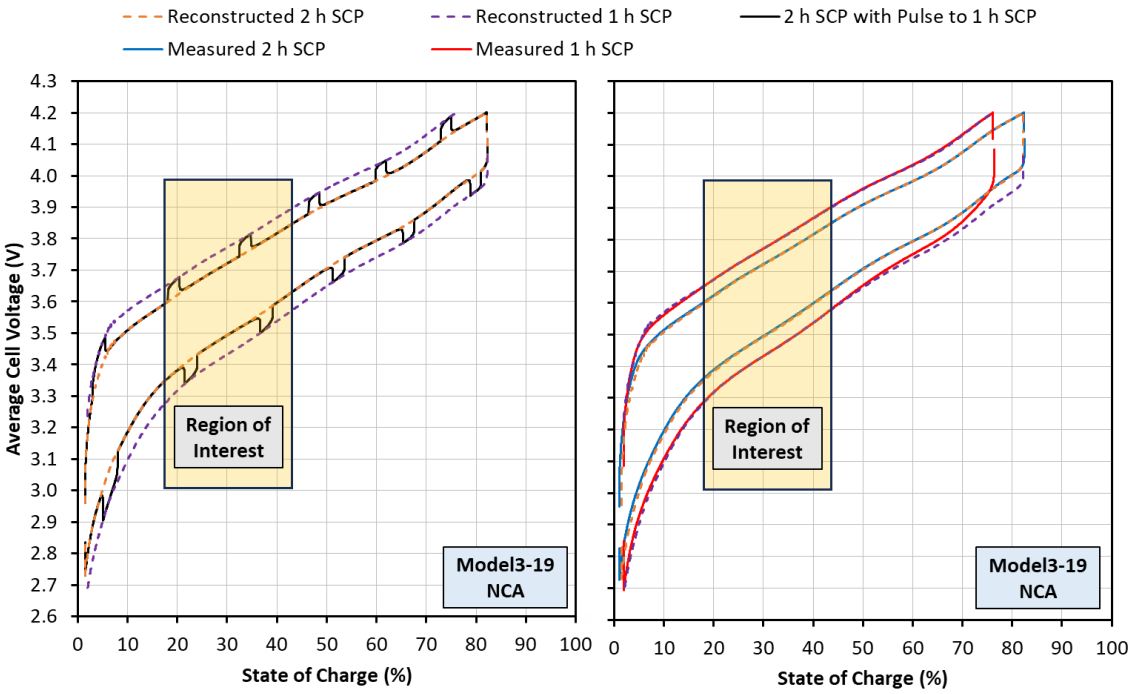


Figure 6.10 Results of an SCPP test showing SCP voltage profiles mathematically reconstructed from the SCPP voltage profile (left) and a comparison of the reconstructed SCP voltage profiles to measured SCP voltage profiles (right).

A simple program was coded in Visual Basic to process the raw test data and reconstruct the 2 h and 1 h SCP voltage profiles from the SCPP voltage profile. To accomplish this, the program first separates the pulses from the 2 h SCP baseline, leaving gaps in the 2 h baseline voltage profile. The 2 h SCP voltage profile is then reconstructed by taking the

derivative of the baseline profile as a function of SOC, interpolating linearly across the gaps in the derivative, and then integrating the interpolated derivative to fill the gaps in the baseline profile. The 1 h SCP voltage profile is then reconstructed by calculating the overpotential associated with each 120 s pulse, interpolating linearly between the pulses to build a continuous pulse overpotential profile as a function of SOC, and then adding this profile to the reconstructed 2 h SCP voltage profile. The reconstructed 2 h and 1 h SCP voltage profiles are respectively shown as dashed orange and purple lines in the left chart of Figure 6.10. The right chart of Figure 6.10 compares these reconstructions to 2 h and 1 h voltage profiles measured during regular SCP testing of the liquid-cooled Model3-19. While the reconstructed 1 h profile does not accurately model the beginning of discharge as a result of the different starting SOC, the reconstructions are otherwise a near-perfect match to the measurements.

The yellow boxes in Figure 6.10 highlight the SOC range which Figure 6.9 revealed as the range in which the voltage ratio $\frac{V_{\mathrm{dis}}}{V_{\mathrm{chg}}}$ can serve as a proxy for energy efficiency η. This shows that as few as two 120 s pulses carried out during both discharge and charge of a single SCPP test can provide the necessary information to obtain a continuous range of $\frac{V_{\mathrm{dis}}}{V_{\mathrm{chg}}}$ vs SOC at two different power rates. The SOC value that produces the closest match between the 2 h voltage ratio and the measured η result of the complete 2 h SCP cycle can then be chosen as the SOC at which to take the 1 h voltage ratio as a proxy for the η result of a complete 1 h SCP cycle without actually conducting a 1 h SCP test. In the generalized case where an SCPP test is carried out with a baseline power P_{CP} and a pulse power P_{pulse}, the voltage ratios are taken at the SOC value that best satisfies Equation 6.48. The same SOC value is applied for Equation 6.49.

$$\eta_{\mathrm{CP}} \approx \frac{V_{\mathrm{dis}}^{\mathrm{CP}}}{V_{\mathrm{chg}}^{\mathrm{CP}}} \tag{6.48}$$

$$\eta_{\mathrm{pulse}} \approx \frac{V_{\mathrm{dis}}^{\mathrm{pulse}}}{V_{\mathrm{chg}}^{\mathrm{pulse}}} \tag{6.49}$$

It is important to recognize that the reconstructed 1 h SCP voltage profile in Figure 6.10 is based on a lower temperature than a regular 1 h SCP cycle would experience. As shown in Section 5.4, the liquid-cooled Model3-19 experiences small temperature changes thanks to its effective AL-TMS, so this thermal discrepancy is not apparent in the right chart of Figure 6.10. For passive-cooled battery packs, the thermal discrepancy would be particularly apparent at the end of discharge and charge, where temperature rise is especially significant when cycling at a 1 h rate. In these regions, the reconstructed 1 h voltage profile would slightly overestimate the overpotential due to the higher internal resistance associated with the significantly smaller temperature peaks of a 2 h SCP test (about 9 °C lower in the most extreme case of the passive-cooled Model3-19). However, the thermal discrepancy between 2 h and 1 h tests is much smaller near 30 % SOC (just 4 °C in the most extreme case of the passive-cooled Model3-19), so the thermal impact on voltage profile reconstruction in the region of interest should not be significant. There was no opportunity within this research project to recreate Figure 6.10 for passive-cooled battery packs and assess the associated thermal impacts, but this is recommended for future research.

It is also important to consider how the act of pulsing might impact t_{dis}, E_{dis}, and η for an SCPP test compared to a regular 2 h SCP test. Since pulsing to a larger power magnitude temporarily decreases the discharge voltage and increases the charge voltage, E_{dis} and η will both be slightly lower for the SCPP test than a regular 2 h SCP test. For example, a 120 s pulse carried out during a 2 h discharge occupies about 1/60 of the total discharge duration. If the pulse entails a doubling of the applied power (approximately a doubling of the applied current), then the pulse occupies about 1/30 of the utilized SOC window. The 120 s pulses in the left chart of Figure 6.10 resulted in a voltage delta of about 60 mV per cell in the range of interest, which is about 1/60 of the 3.6 V average cell discharge voltage. This means that a single pulse only represents about 1/1800 or 0.056 % of E_{dis}. If two 120 s pulses are carried out during both discharge and charge, then E_{dis} will decrease by about 0.1 %, E_{chg} will increase by about 0.1 %, and η will decrease by about 0.2 %. These differences are already small, but they can be eliminated entirely by calculating E_{dis} and E_{chg} based on the reconstructed baseline voltage profile instead of the measured pulsed

voltage profile. As for t_{dis}, it can be shown that two 120 s pulses with doubled power during a 2 h discharge will reduce t_{dis} by about 3 %. While this is not a large enough difference to have a significant impact on battery temperature compared to a regular 2 h SCP test, the difference must be accounted for when using t_{dis} in the performance extrapolation calculations. Instead of using the measured t_{dis}, the effective CP discharge duration $t_{\mathrm{dis}}^{\mathrm{CP}}$ associated with the baseline power P_{CP} should be calculated according to Equation 6.50.

$$t_{\mathrm{dis}}^{\mathrm{CP}} = \frac{E_{\mathrm{dis}}}{P_{\mathrm{CP}}} \tag{6.50}$$

If η can be estimated from an SCPP test as demonstrated in Figure 6.9 and Figure 6.10, then this could displace the need to calculate b_η for η extrapolation. However, the SCPP test will only estimate the singular η value associated with P_{pulse}, whereas b_η can be used to estimate η at any desired power rate. Substituting Equations 6.48 and 6.49 into Equation 6.14 yields a new voltage-based expression which can be used to calculated b_η from a single SCPP test, as shown in Equation 6.51.

$$b_\eta \approx -\log_{\left(\frac{t_{\mathrm{dis}}^{\mathrm{pulse}}}{t_{\mathrm{dis}}^{\mathrm{CP}}}\right)}\left[\frac{1-\frac{V_{\mathrm{dis}}^{\mathrm{pulse}}}{V_{\mathrm{chg}}^{\mathrm{pulse}}}}{1-\frac{V_{\mathrm{dis}}^{\mathrm{CP}}}{V_{\mathrm{chg}}^{\mathrm{CP}}}}\right] \tag{6.51}$$

Equations 6.48 and 6.49 can also be substituted into the logarithmic term in Equation 6.19 to calculate b_q for the single-dataset solution. However, since there is already some uncertainty introduced by the SCPP method, the 1 % difference made by the logarithmic term can be neglected. It is therefore sufficient to calculate b_q using the simplified sum in Equation 6.17 for the single-dataset solution.

Equation 6.51 requires $t_{\mathrm{dis}}^{\mathrm{CP}}$ and $t_{\mathrm{dis}}^{\mathrm{pulse}}$, which respectively represent the t_{dis} values associated with a regular SCP test carried out at P_{CP} and P_{pulse}. The value of $t_{\mathrm{dis}}^{\mathrm{CP}}$ is

calculated using Equation 6.50, while $t_{\text{dis}}^{\text{pulse}}$ can be calculated using the adjusted Peukert equation as shown in Equation 6.52.

$$\gamma_{\text{pulse}} P_{\text{pulse}} {t_{\text{dis}}^{\text{pulse}}}^{\frac{1}{\sigma}} = \gamma_{\text{CP}} P_{\text{CP}} {t_{\text{dis}}^{\text{CP}}}^{\frac{1}{\sigma}} \tag{6.52}$$

Since the adjustment factor γ is a parabolic function of t_{dis}, the expanded form in Equation 6.53 shows that there is no analytical solution for $t_{\text{dis}}^{\text{pulse}}$. Instead, numerical root-finding methods must be used to solve for $t_{\text{dis}}^{\text{pulse}}$. Once this is carried out, b_η can be calculated for the battery in question using Equation 6.51.

$$\begin{aligned} &0.12 {t_{\text{dis}}^{\text{pulse}}}^{-\frac{2}{\sigma}} - 0.15 {t_{\text{dis}}^{\text{pulse}}}^{-\frac{1}{\sigma}} + 1.03 {t_{\text{dis}}^{\text{pulse}}}^{\frac{1}{\sigma}} \\ &\quad - \frac{P_{\text{CP}}}{P_{\text{pulse}}} \left(0.12 {t_{\text{dis}}^{\text{CP}}}^{-\frac{2}{\sigma}} - 0.15 {t_{\text{dis}}^{\text{CP}}}^{-\frac{1}{\sigma}} + 1.03 {t_{\text{dis}}^{\text{CP}}}^{\frac{1}{\sigma}} \right) = 0 \end{aligned} \tag{6.53}$$

Compared to the two-dataset solution, the proposed single-dataset solution for a battery performance extrapolation model is more complex in terms of both experimental procedure and data processing. Older and simpler battery test equipment may not be capable of executing pre-programmed power pulses, and the necessity of pulse analysis, voltage profile reconstruction, and numerical root-finding methods indicates that the single-dataset solution would require software to facilitate execution. For researchers and developers who can execute it, the single-dataset solution would provide the shortest possible time requirement for full characterization of second-life battery pack performance under an SCP test regime. The accuracy and experimental time requirement of the two-dataset and single-dataset solutions will be compared in Sections 6.3 and 6.4.

6.3. Accuracy of Performance Extrapolation Model

To demonstrate the accuracy that can be expected from the proposed performance extrapolation model, both the two-dataset and single-dataset versions of the model were constructed in Microsoft Excel. The experimental phase of this research project was already completed when this model was conceived, so the proposed SCPP test method could not be directly evaluated for all battery packs. However, Section 6.2.3 verified that

two or more 120 s pulses carried out during both discharge and charge are sufficient for obtaining the necessary voltage data to estimate the energy efficiency exponent b_η. For the demonstrative purposes of this chapter, it can therefore be assumed that the measured 2 h and 1 h SCP voltage profiles of each battery pack were obtained from an SCPP test so that the single-dataset solution can be executed and evaluated. The measured results from the 4 h and 2 h SCP tests are used to execute and evaluate the two-dataset solution. This section will assess and compare the accuracy of the two-dataset and single dataset solutions in terms of estimating model parameters σ, b_η, and b_q as well as extrapolating electrical performance metrics $\bar{E}_v$, ζ, and η and thermal performance metrics $\Delta T_{\max}$, ΔT_{avg}, and t_{cool}.

6.3.1. Estimation of Model Parameters

Figure 6.11 replots the values of Peukert number σ, energy efficiency exponent b_η, and heat generation exponent b_q calculated from the 4 h and 1 h datasets (the same values shown previously in Figure 6.2, Figure 6.4, and Figure 6.6, respectively), and treats these as 'true' values which the performance extrapolation methods seek to estimate. The bar charts compare these true values to the estimated values produced by the two-dataset solution and single-dataset solution. For the two-dataset solution, estimates are calculated from the 4 h and 2 h datasets, as it is assumed that the 1 h results would be extrapolated rather than measured due to the heightened risk of cycling second-life battery packs at high power. For the single-dataset solution, σ is estimated based on Equation 6.12, which uses a linear correlation between σ and rated module energy density as well as a correction factor α_σ to accommodate the special cases of LFP chemistry and active-liquid thermal management. The voltage ratio method described in Section 6.2.3 is used to estimate b_η for the single-dataset solution, while Equation 6.17 is used to calculate b_q from σ and b_η.

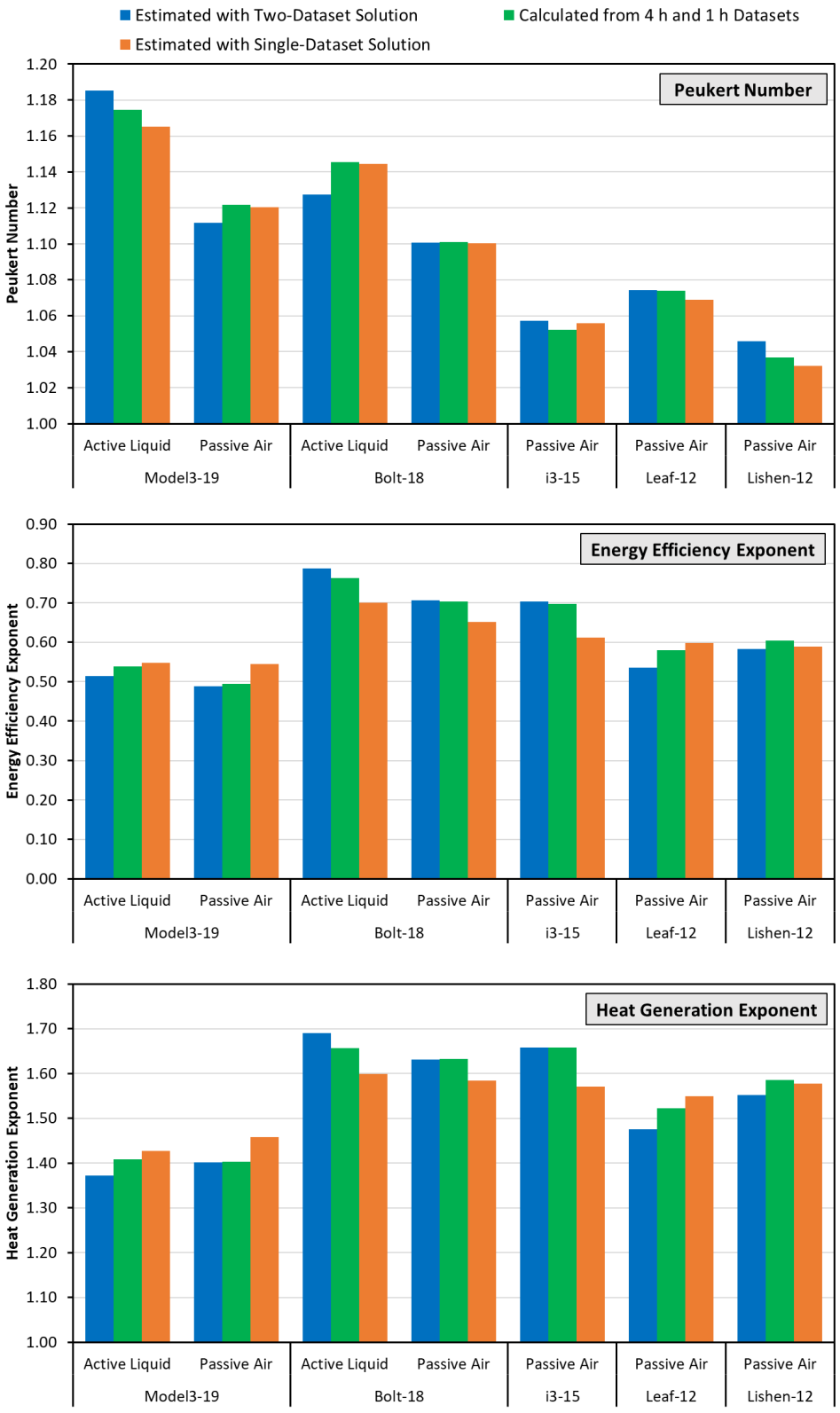


Figure 6.11 Comparison of performance extrapolation model parameters determined from the 4 h and 1 h datasets, the two-dataset estimation technique, and the single-dataset estimation technique.

The top chart of Figure 6.11 shows that both σ estimation methods produce fairly accurate results, though the single-dataset solution is slightly more accurate on average. This is because the two-dataset solution assumes that all E_{dis} values lie precisely on the adjusted Peukert curves. While the adjusted Peukert equation does give a good fit to all seven experimental datasets, it is not a perfect fit, so the calculated σ will vary slightly depending on which datapoints are used in the calculation. The liquid-cooled Bolt-18 did not fit the adjusted Peukert equation quite as well as the other six datasets (see Figure 6.1), and this produces the largest σ error in Figure 6.11. For the single-dataset solution, it is important to recognize that Equation 6.12 was formulated to give the best fit for these seven specific experimental datasets. Even if future research confirms that Equation 6.12 or some other empirical formula can estimate σ with reasonable accuracy for all EV battery packs, there will likely be some error in the σ estimation. It is therefore possible that the two-dataset solution will produce superior σ accuracy for the average second-life battery pack.

The middle chart of Figure 6.11 shows that both b_η estimation methods produce fairly accurate results, though the two-dataset solution is slightly more accurate on average. This is because all measured η values lie very close to the curves produced by the empirical energy efficiency equation, which means that b_η is relatively insensitive to the choice of datapoints used in the calculation. For the single dataset solution, the accuracy of the b_η estimation depends on how accurately the chosen voltage ratio for the 1 h rate reflects the 1 h cycle energy efficiency η, and Figure 6.11 shows that this technique produces reasonable estimations.

Both σ and b_η contribute to b_q, so the accuracy of the b_η estimations should be expected to be lower than the σ and b_η estimations. The bottom chart of Figure 6.11 shows that the accuracy of the b_q estimations largely reflect the accuracy of the b_η estimations, but with slightly lower accuracy due to the additional error introduced by σ. Overall, both the two-dataset and single-dataset solutions produce reasonable b_q estimates, but the two-dataset solution is slightly more accurate on average.

6.3.2. Extrapolation of Performance Metrics

Since the single-dataset solution extrapolates battery performance metrics for both 4 h and 1 h rates, these results will first be compared to the measured 4 h and 1 h metrics before the accuracy of the two-dataset and single-dataset solutions are compared. Figure 6.12 and Figure 6.13 respectively illustrate the effectiveness of the single-dataset solution in predicting electrical and thermal performance test results for second-life battery packs. The green bars show the 4 h and 1 h SCP test results as presented in Chapter 5, while the orange bars show the corresponding values extrapolated from the emulated SCPP test results using the mathematical methods described in Section 6.2. For energy density $\bar{E}_v$ and energy utilization ratio ζ, the extrapolated values give average and maximum relative errors of 0.46 % and 1.0 %. For cycle energy efficiency η, the extrapolated values give average and maximum absolute errors of 0.16 % and 0.28 %. For maximum $\Delta T_{\max}$ and average $\Delta T_{\max}$ temperature rise, all extrapolated values are within 1.4 °C of the measured values, with an average error of 0.6 °C. For the cycle cooldown duration t_{cool}, all extrapolated values are within 2.3 h of the measured values, with an average error of 0.5 h.

Note that in some cases, the modelled t_{cool} will inherently overestimate the measured value. One reason for this applies to packs that exhibit a significantly different temperature peak at the end of discharge compared to the end of charge, since the model assumes both the discharged cooldown and charged cooldown begin at the $T_{\max}$ of the entire SCP cycle. Another reason applies to tests that experience significant noise in the temperature measurement signal, since the cooldown period will be terminated somewhat prematurely when the measurement noise triggers the $T_{\max} < T_{\text{ctrl}}$ condition. This is why many of the t_{cool} extrapolations in Figure 6.13 exceed the corresponding measured values.

The most important takeaway from Figure 6.12 and Figure 6.13 is that for each of the six performance metrics shown, the extrapolation errors are small compared to the differences among the seven measured datasets. This means that a comparative performance analysis of the different battery packs and thermal management systems would yield essentially the same outcomes whether the measured datasets or extrapolated datasets are used. The proposed extrapolation model is therefore a viable tool for facilitating experimental performance characterization of second-life battery packs.

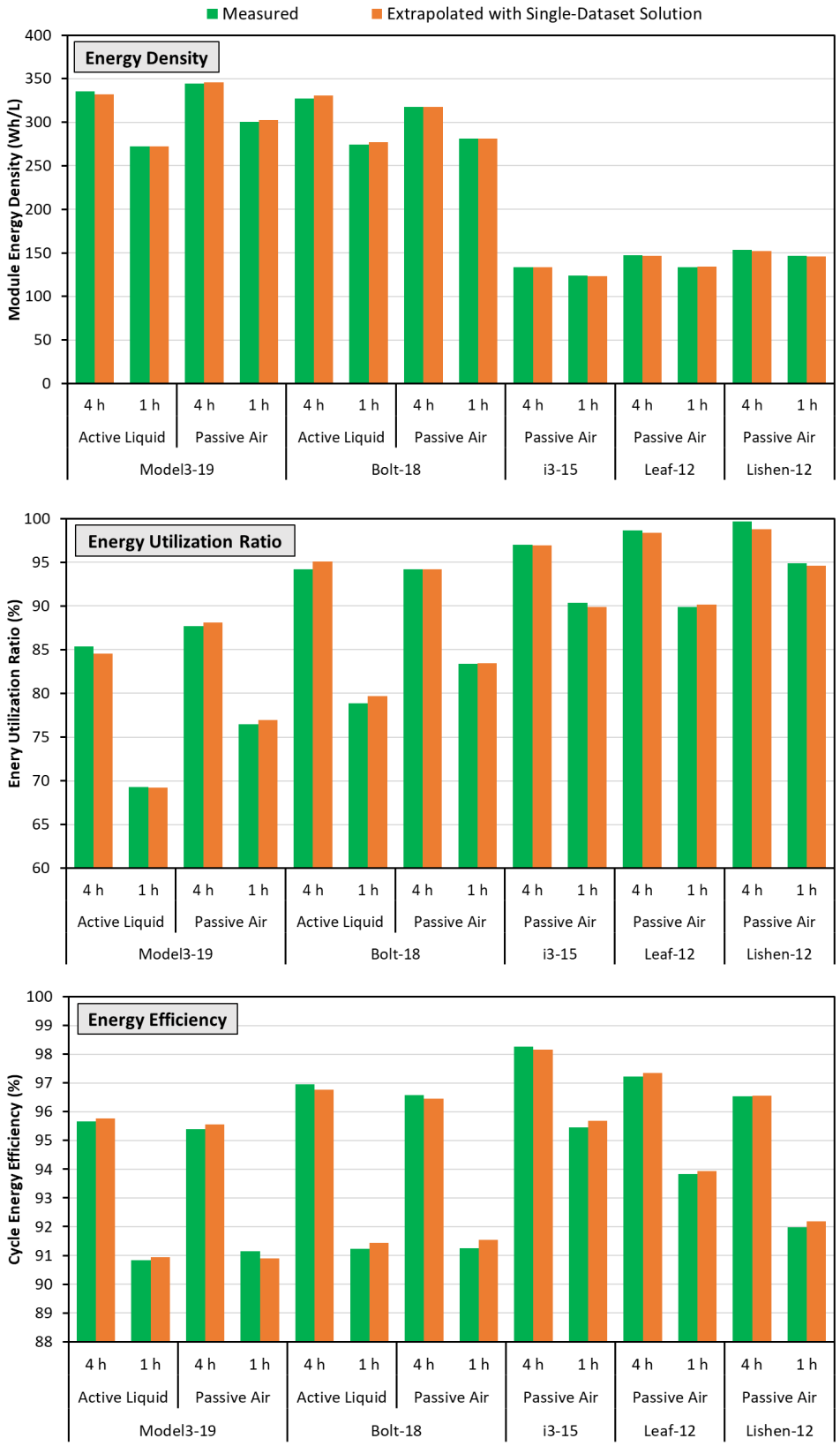


Figure 6.12 Measured electrical performance test results compared to values extrapolated from 2 h test results using the single-dataset solution.

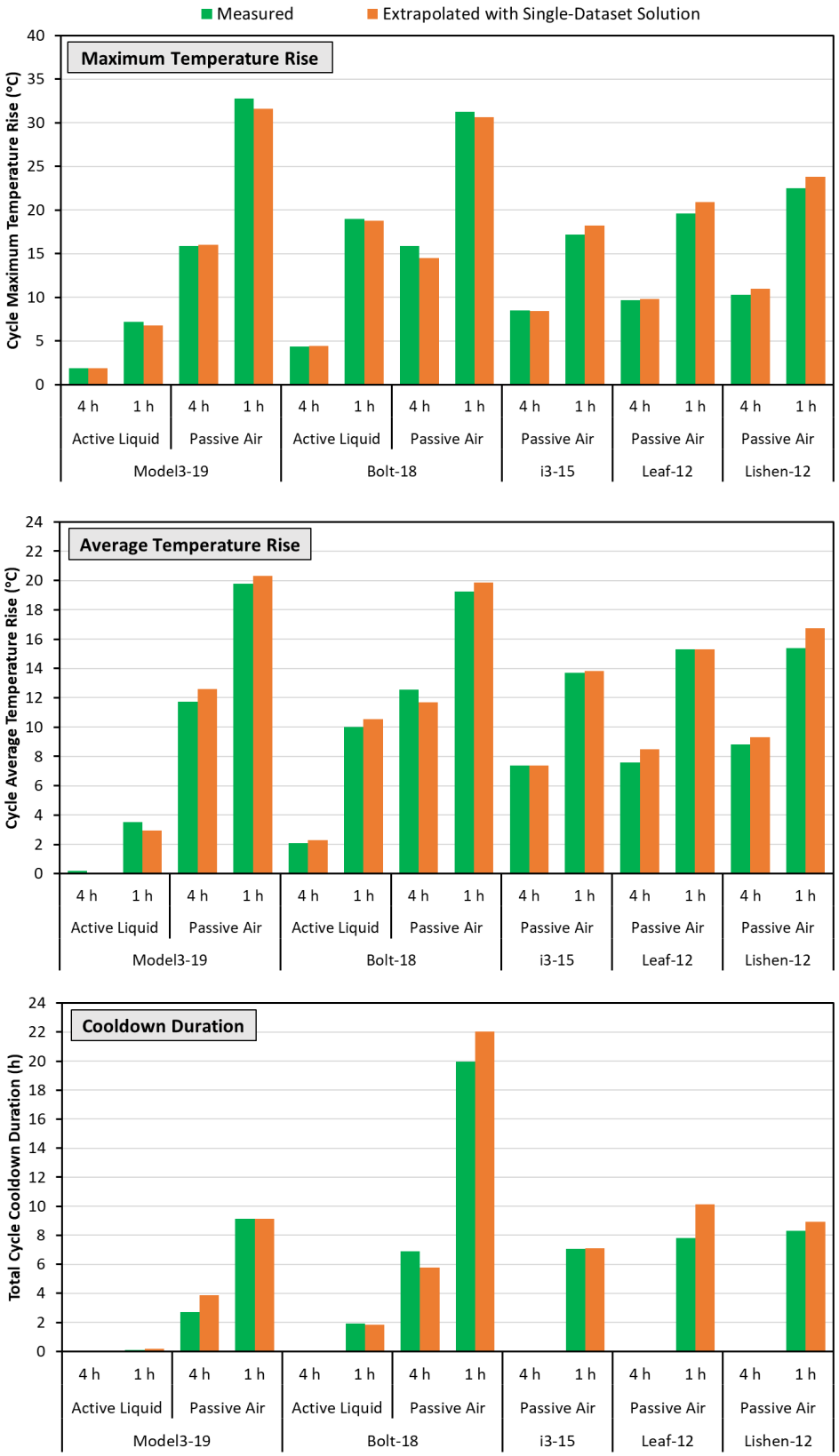


Figure 6.13 Measured thermal performance test results compared to values extrapolated from 2 h test results using the single-dataset solution.

The accuracy of the two-dataset and single-dataset solutions are compared for electrical and thermal performance metrics in Figure 6.14 and Figure 6.15, respectively. The blue bars show the extrapolation errors produced by the two-dataset solution, while the orange bars show the extrapolation errors produced by the single-dataset solution. Since the two-dataset solution uses 4 h and 2 h SCP test results in the extrapolation, errors are only shown for the extrapolated 1 h test results. For the single-dataset solution, errors are shown for both 4 h and 1 h extrapolated results.

Figure 6.14 shows that the two-dataset solution yields relatively large $\bar{E}_v$ and ζ errors for the liquid-cooled Bolt-18. As mentioned in Section 6.3.1, the liquid-cooled Bolt-18 did not fit the adjusted Peukert curve quite as well as the other six datasets (see Figure 6.1), and as a result, calculating the Peukert number σ from the 4 h and 2 h E_{dis} results yields a relatively large error in extrapolating the 1 h $\bar{E}_v$ and ζ results. Even so, the extrapolated values for these two metrics are still within 2 % of the measured value. With the exception of these liquid-cooled Bolt-18 results, Figure 6.14 and Figure 6.15 show that the errors produced by the two-dataset solution generally fall within the same bounds as those produced by the single dataset solution. This means that the main trade-off between the two-dataset and single-dataset solutions is simplicity vs experimental time requirement.

It is worth noting that the single-dataset solution can be significantly simplified if a fixed value of b_η is applied universally to all battery packs, as this eliminates the need for pulsing and numerical root-finding methods. However, the best results achieved with $b_\eta = 0.62$ resulted in η errors as high as 0.7 %, which is a significant error for energy efficiency. As mentioned in Section 6.1.2, any error in η should be multiplied by a factor of 10 to better reflect the implications of the corresponding error in energy inefficiency $1 - \eta$. With this in mind, an error of 0.7 % is a significant increase over the < 0.3 % error produced by the emulated SCPP test. Given the diversity in EV battery design, it is possible that a fixed value of $b_\eta = 0.62$ would produce even larger errors for some battery packs not tested in this research project. Unless future research can gain insight into how to estimate b_η based on the specified properties of EV battery packs, the SCPP test is the only reliable way to execute a single-dataset solution for performance extrapolation.

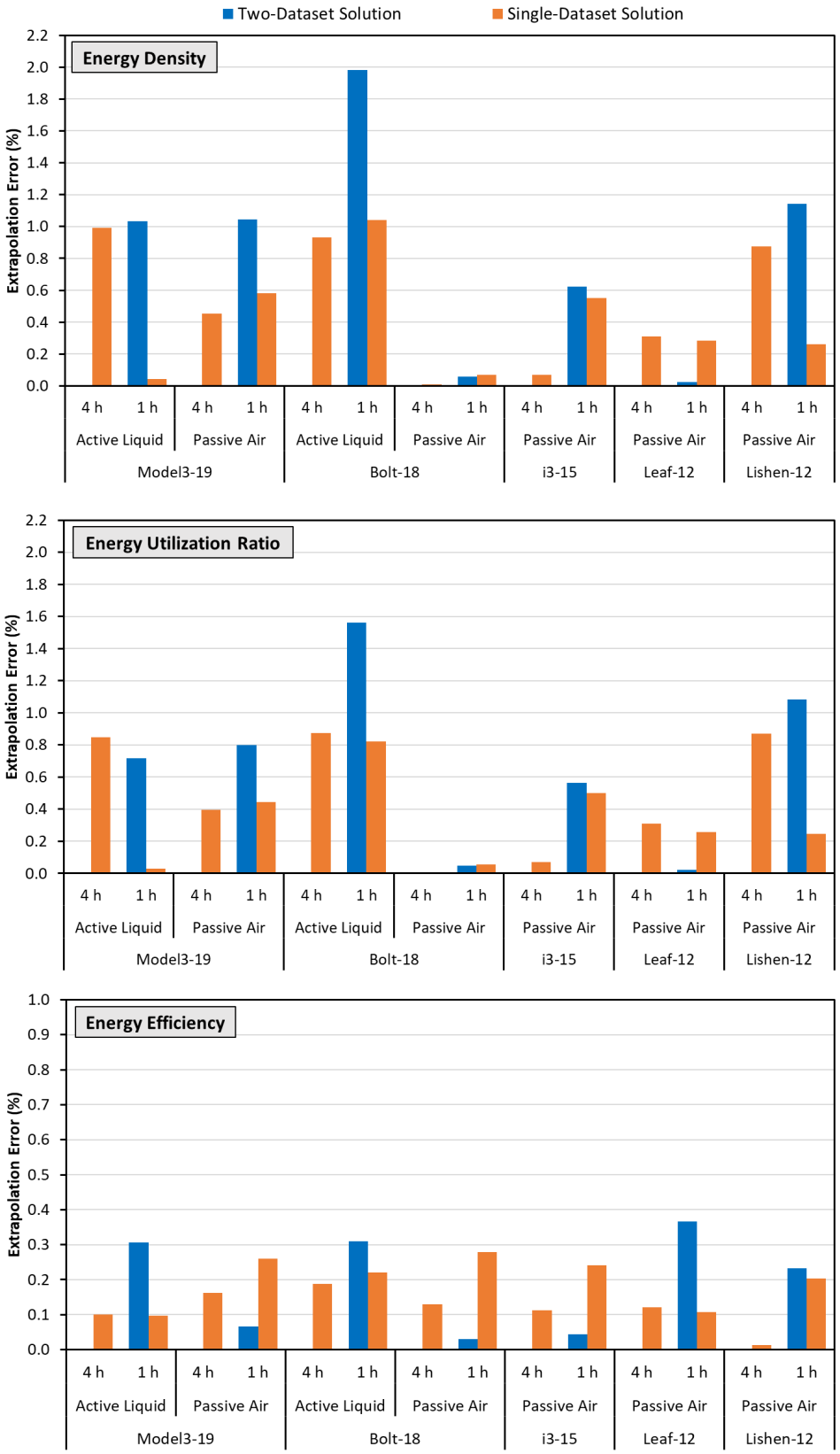


Figure 6.14 Errors produced by two-dataset and single-dataset solutions in extrapolation of electrical performance test results.

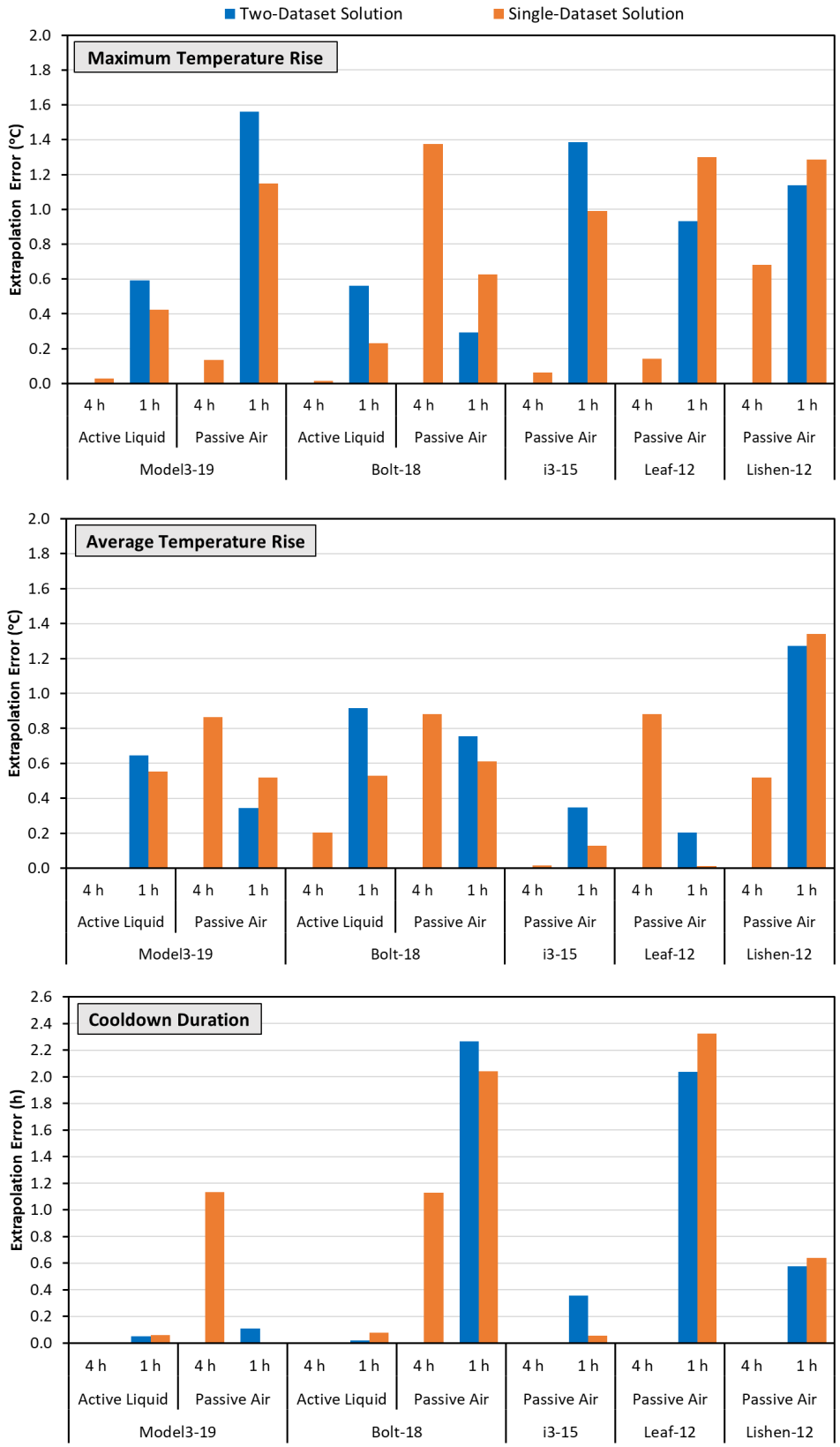


Figure 6.15 Errors produced by two-dataset and single-dataset solutions in extrapolation of thermal performance test results.

6.4. Condensed Performance Characterization Test Methods

Chapter 4 described a second-life battery performance test protocol consisting of a baseline capacity test and three SCP tests at different power rates, each of which includes three consecutive discharge-charge cycles with cooldown periods separating each discharge and charge. To ensure that the results obtained for different EV battery packs could be directly compared, the three SCP tests were repeated iteratively until the discharge durations were consistently close to 4.0 h, 2.0 h, and 1.0 h for all battery packs. While this test protocol proved effective for characterizing and comparing the electrical and thermal performance of different EV battery packs, the testing period is fairly lengthy and can require a week or more to characterize a single battery pack. Section 6.3 demonstrated that the proposed performance extrapolation model can accurately predict the test results that would be obtained at a desired power rate if results are obtained at just one or two other power rates, which presents an opportunity to condense the second-life battery performance test protocol described in Chapter 4. This section will propose two novel test protocols which significantly reduce the time and resources required to characterize the performance of second-life battery packs at standardized discharge durations.

6.4.1. Test Protocols

In assessing the experimental results obtained using the test protocol described in Chapter 4, it was observed that the measured energies and temperatures remain consistent through consecutive cycles as long as the temperature and SOC at the beginning of discharge and charge remain consistent. Section 5.5 confirmed that there are no significant differences between the measured results of the second and third cycle of a given test. This consistency is aided by the use of the temperature control setpoint, which ensures that each discharge and charge begins at or below T_{ctrl}, as described in Section 4.4.

It was also observed in Section 5.2 that the SOC reached at the end of CP discharge is relatively consistent for all three power rates, while the SOC reached at the end of CP charge can change significantly for different power rates. Since each SCP test begins with discharge, the first cycle serves to establish the SOC window for the given power rate based on the end of the first charge. The second and third discharges then operate within this established SOC window. Since the second and third cycles of the test give consistent

results, it can be concluded that a CP charge followed by a CP discharge could constitute a reliable SCP test cycle provided that the battery has already reached a consistent temperature (through cycling or pre-conditioning) before the beginning of charge.

When a second-life battery pack is newly acquired, whether for research or a commercial installation, a baseline capacity test such as the one described in Section 4.3 should be conducted to determine the total energy capacity and SOH of the battery. This test should include a complete charge to 100 % SOC using the CV charging technique, followed by a relatively low-rate discharge (typically around a 4 h rate). While the results of this test do not directly feed into the proposed performance extrapolation model, the test is nonetheless necessary to assess the extent of battery degradation that occurred prior to acquisition, which has implications for safety and energy storage economics. The exponential decay in electrical current associated with a CV charge also provides an opportunity for the BMS to mitigate any cell imbalance that may exist in the pack upon acquisition. Any second-life battery test protocol should therefore begin with a baseline capacity test.

Based on the points above, two condensed second-life battery performance test protocols are proposed in Figure 6.16. The top and bottom charts respectively illustrate the shortest possible test protocols that can be used to execute the two-dataset and single-dataset performance extrapolation techniques as described in Section 6.2. Both test protocols begin with a capacity test featuring a single cycle of constant-power-constant-voltage (CPCV) charge followed by CP discharge. The CP rate should be approximately a 4 h rate, and the CV charge should last long enough that the power decays to a set limit (e.g. a 20 h rate based on rated capacity) and the cell voltages converge to within a set limit (e.g. 5 mV). These limits will ensure that the battery has been charged to approximately 100 % SOC and that the cells have been balanced by the BMS. A CV time limit (e.g. 2 h) is also advisable to truncate elongated power decay in aged batteries [356]. A single CPCV cycle is sufficient even if the battery is at ambient temperature when the cycle begins. This is because battery temperature decreases significantly during a long CV charge, which means that the temperature at the beginning of the subsequent CP discharge will be relatively low regardless of how many cycles are carried out. The measured energy capacity of the first CP discharge is therefore a reliable representation of the full energy capacity of the battery.

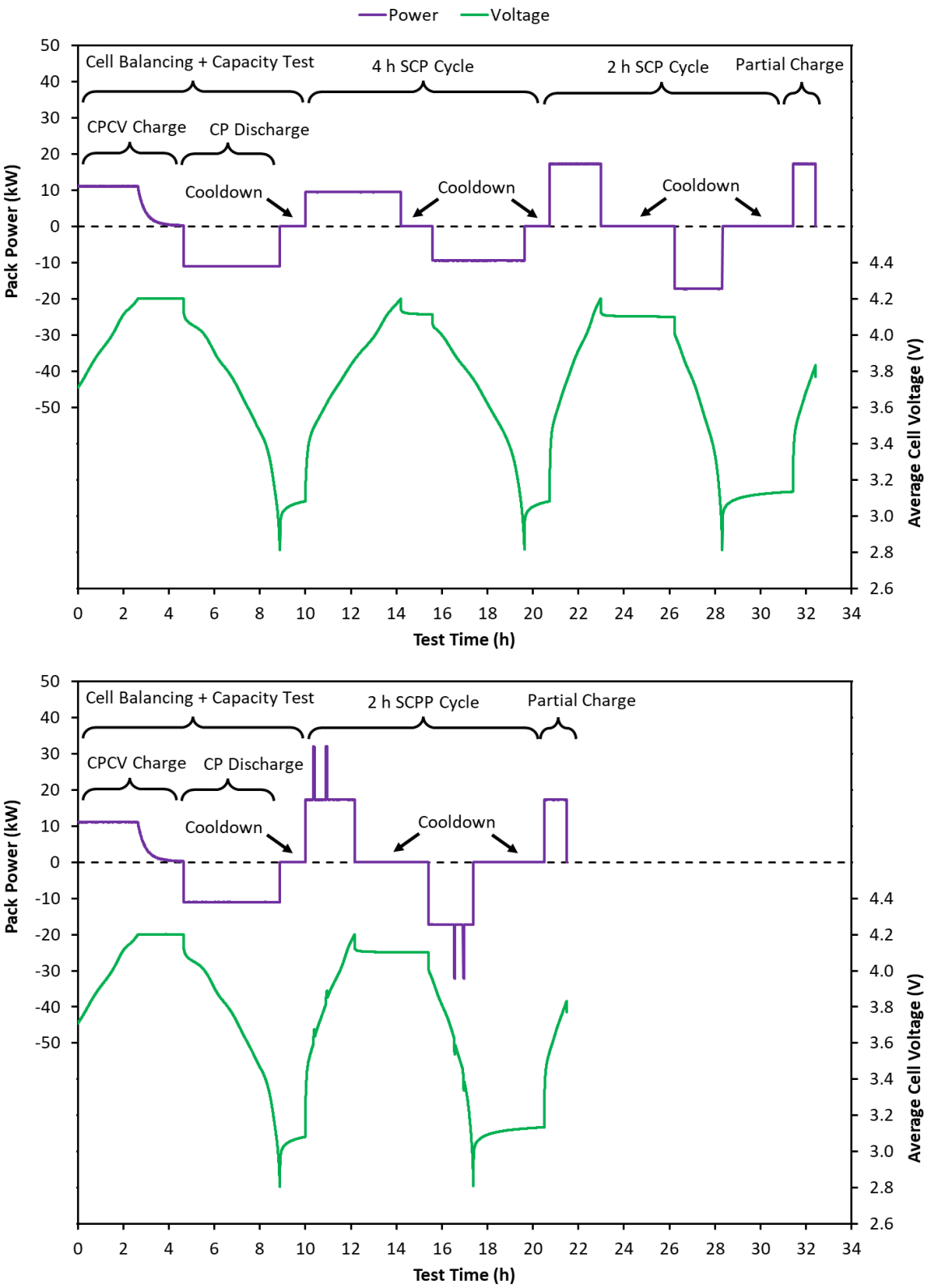


Figure 6.16 Proposed condensed test methods for performance characterization of second-life battery packs utilizing the two-dataset (top) and single-dataset (bottom) extrapolation techniques.

The capacity test ends with a cooldown period to ensure that the next step in each test protocol begins at or below the temperature control setpoint. For the two-dataset test protocol, this is followed by two SCP cycles consisting of CP charge, cooldown, CP discharge, and cooldown. The first SCP cycle is conducted at approximately a 4 h rate, while the second SCP cycle is conducted at approximately a 2 h rate. In the case of the single-dataset test protocol, the capacity test is followed by a single SCPP cycle consisting of CP charge with pulses, cooldown, CP discharge with pulses, and cooldown. The base power is approximately a 2 h rate, while the pulse power is approximately a 1 h rate. Both test protocols end with a partial charge to return the battery to a mid-level SOC of approximately 30 %, which is an appropriate state in which to leave a lithium-ion battery after testing (Section 2.5 explained that calendar aging is mitigated below 50 % SOC, and Section 3.4.1 explained that lithium-ion batteries are typically shipped at or below 30 % SOC). The partial charge has no impact on the test results, so any preferred charging rate can be used. A 2 h CP rate is recommended as it provides reasonable speed without excessive heat generation.

Comparing the top and bottom charts of Figure 6.16 shows that the two-dataset test protocol can be expected to require about 32 h, while the single-dataset test protocol can be expected to require about 22 h. These test durations are of course dependent on the standby cooldown rate of the battery under test. Figure 6.16 is based on the passive-cooled Model3-19, which exhibited relatively long cooldown durations due to large temperature rises. The slow passive cooling of Bolt-18 would result in longer testing times, while the relatively low temperature rise of i3-15 would require shorter testing times. In the case of the liquid-cooled Model3-19, cooldown durations would be essentially zero, resulting in total test times of 22 h and 14 h for the two-dataset and single-dataset test protocols, respectively. The test duration will also depend on the power rates used, since the prescribed 4 h and 2 h power rates will be estimated (to be discussed in Section 6.4.2) and may yield longer or shorter discharge durations than intended. Longer CV times may also be required if it is observed that a given battery pack needs additional cell balancing. Acknowledging these uncertainties, the single-dataset test protocol can generally be expected to save 8 to 12 hours compared to the two-dataset test protocol (20 to 40 % time savings).

6.4.2. Test Parameters

In general, the test parameters used to control the condensed test protocols described in Section 6.4.1 would be the same as those prescribed in Section 4.4.3. These include a lower cell voltage limit of 2.50 V, an upper cell voltage limit of 4.20 V (except for LFP batteries which typically use 3.55 V to 3.65 V), an ambient temperature setpoint near 20 °C, a liquid supply setpoint near 30 °C, and temperature control setpoints of 30 °C for passive-cooled batteries and 35 °C for liquid-cooled batteries. Since the condensed test protocols do not feature a 1 h test, the 55 °C high-temperature safety limit prescribed in Section 4.4.3 should be lowered to 50 °C.

The only new consideration for the defining of test parameters is regarding power setpoints. Whereas the test protocol described in Chapter 4 includes iteration of power setpoints until the right setpoint to achieve a desired discharge duration is found, the newly proposed condensed test protocols feature no iteration. While this is a beneficial feature for reducing the required test time, it means that the power setpoints must be chosen strategically so that the effectiveness of the extrapolation model is not compromised. For example, if the power setpoints are selected based on the rated energy capacity of a second-life battery pack that is actually at 70 % SOH, then the effective power rates will be significantly higher than intended. In addition to safety concerns, overestimated power setpoints could potentially impact the reliability of the performance extrapolation model, especially if the SCPP method is used with pulses significantly greater than a 1 h rate (the proposed methods have presently only been verified for 0.98 h $< t_{\mathrm{dis}} <$ 4.05 h). This presents a challenge since the capacity and SOH of a given battery pack will typically be unknown when the test begins. Simple guidelines will now be proposed to overcome this challenge.

The first power setpoint required for the condensed test protocols is the power magnitude P_{CPCV} used for the CP portion of the CPCV charge and the subsequent CP discharge (i.e. the capacity test). Ideally, this value should be close to a 4 h rate. A significant overestimation of P_{CPCV} will potentially produce an underrepresentation of the total energy capacity $E_{\mathrm{dis}}^{\mathrm{CPCV}}$ and corresponding SOH. A significant underestimation of P_{CPCV} should not have a major impact on $E_{\mathrm{dis}}^{\mathrm{CPCV}}$ since a 4 h rate is already a relatively low rate, but it will needlessly extend the duration of the capacity test. Based on these considerations,

Equation 6.54 is proposed as a guideline for estimating P_{CPCV} (in kW) based on the rated discharge energy $E_{\mathrm{dis}}^{\mathrm{spec}}$ specified by the manufacturer (in kWh).

$$P_{\mathrm{CPCV}} = \frac{E_{\mathrm{dis}}^{\mathrm{spec}}}{6} \tag{6.54}$$

Equation 6.54 is designed for the general case of a second-life battery pack with an unknown SOH and manufacturing year. The calculation will produce a 4 h rate if the pack is at 83 % SOH (near the commonly cited 80 % SOH expected for the average second-life battery pack). If the pack turns out to be near 100 % SOH (e.g. salvaged from a wrecked EV near BOL), the calculation will produce a 6 h rate, which should still yield comparable results to a 4 h rate when discharging after a full CPCV charge. If the pack turns out to be near 60 % SOH (an approximate lower limit expected for second-life battery packs), the calculation will produce a 3.6 h rate, which is sill close to the ideal 4 h rate. Equation 6.54 could be modified with a denominator of 5 if the pack is known to be less than about five years old (likely above 80 % SOH), while a denominator of 4 may be more appropriate if the pack is known to be near BOL.

For the two-dataset test protocol, power setpoints for the 4 h SCP cycle $P_{\mathrm{CP}}^{4\mathrm{h}}$ and 2 h SCP cycle $P_{\mathrm{CP}}^{2\mathrm{h}}$ are also required. As shown in Section 5.3.2, the discharge energy E_{dis} obtained from an SCP test can be much lower than the full energy capacity $E_{\mathrm{dis}}^{\mathrm{CCCV}}$ of a given battery (as described by the energy utilization ratio ζ), and this difference is highly inconsistent across different EV battery designs. A guideline as simple as Equation 6.54 will therefore be unable to provide satisfactory estimates of $P_{\mathrm{CP}}^{4\mathrm{h}}$ and $P_{\mathrm{CP}}^{2\mathrm{h}}$ for any given EV battery design. A more appropriate guideline would take into account the known characteristics of the battery under test.

Section 6.1.1 demonstrated that the Peukert number σ of EV battery packs can be estimated by a linear function of the rated module energy density $\bar{E}_v^{\mathrm{spec}}$ (with noted correction factors for LFP chemistry and liquid-cooled packs). Figure 6.17 takes the same approach for developing guidelines for estimating $P_{\mathrm{CP}}^{4\mathrm{h}}$ and $P_{\mathrm{CP}}^{2\mathrm{h}}$. The left and right charts respectively plot the measured 4 h and 2 h results for ζ as a function of $\bar{E}_v^{\mathrm{spec}}$ for each tested battery

pack, revealing rough linear correlations in both cases. This shows that batteries with higher energy density (and therefore higher internal resistance, as demonstrated in Section 5.3.5) tend to give a lower E_{dis} for a given $E_{\text{dis}}^{\text{CCCV}}$, and therefore require a lower $P_{\text{CP}}^{\text{4h}}$ and $P_{\text{CP}}^{\text{2h}}$ for a given P_{CPCV}. However, it is important to recall from Section 5.6.2 that ζ can be sensitive to SOH for some EV battery designs. The impact of this sensitivity on the correlations in Figure 6.17 will be considered in Section 6.5.3.

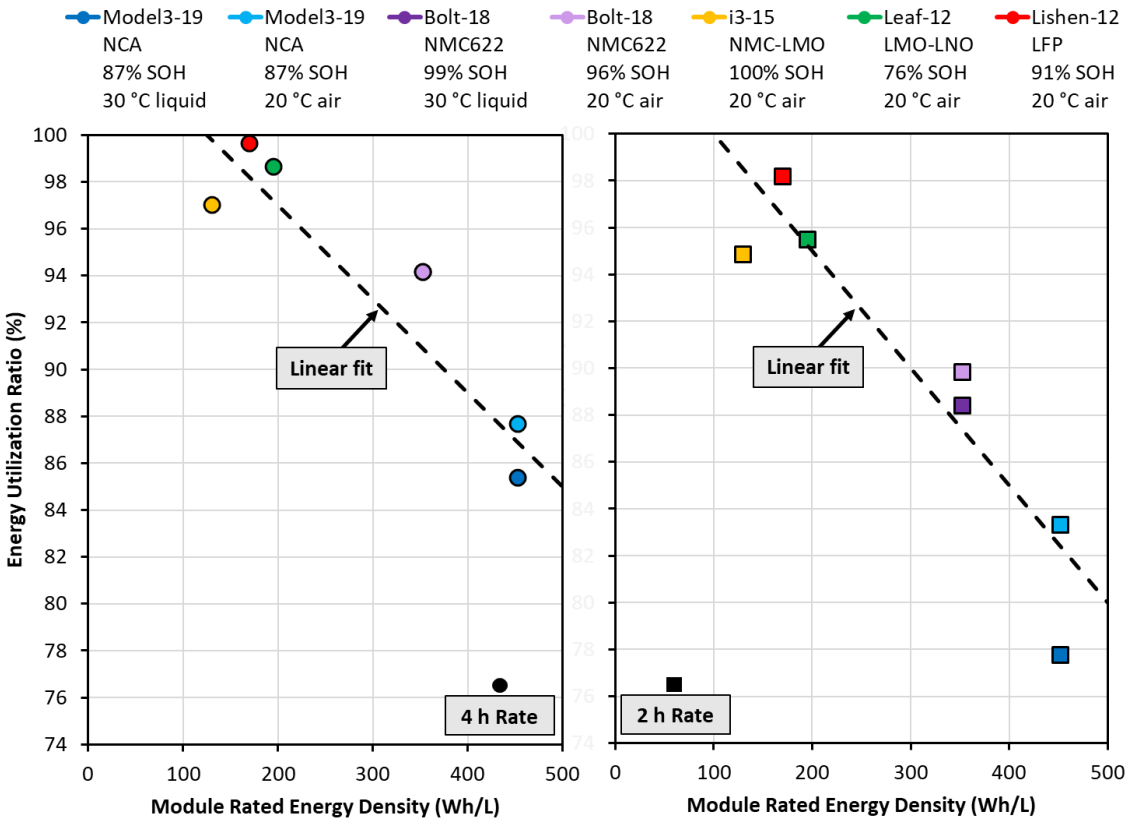


Figure 6.17 Energy utilization ratios from 4 h (left) and 2 h (right) SCP tests as a function of module rated energy density.

Based on the correlations in Figure 6.17, Equations 6.55 and 6.56 are proposed as guidelines for estimating $P_{\text{CP}}^{\text{4h}}$ and $P_{\text{CP}}^{\text{2h}}$ based on the rated discharge energy $E_{\text{dis}}^{\text{spec}}$, total module volume v_{mod}, and the result of the capacity test $E_{\text{dis}}^{\text{CPCV}}$. These equations are plotted as black dashed lines in Figure 6.17. The 'minimum' function is used to account for the fact that the ζ values plotted in Figure 6.17 can never exceed 100 % in practice. Note that $E_{\text{dis}}^{\text{CPCV}}$ should be essentially equivalent to the $E_{\text{dis}}^{\text{CCCV}}$ metric used in Figure 6.17 if measured at a comparable rate.

$$P_{\mathrm{CP}}^{4\mathrm{h}} = \frac{E_{\mathrm{dis}}^{\mathrm{CPCV}} \times \min\left(1.05 - 0.4\frac{E_{\mathrm{dis}}^{\mathrm{spec}}}{v_{\mathrm{mod}}}, 1\right)}{4} \tag{6.55}$$

$$P_{\mathrm{CP}}^{2\mathrm{h}} = \frac{E_{\mathrm{dis}}^{\mathrm{CPCV}} \times \min\left(1.05 - 0.5\frac{E_{\mathrm{dis}}^{\mathrm{spec}}}{v_{\mathrm{mod}}}, 1\right)}{2} \tag{6.56}$$

Since Equations 6.55 and 6.56 depend on the result of the capacity test, values for $P_{\mathrm{CP}}^{4\mathrm{h}}$ and $P_{\mathrm{CP}}^{2\mathrm{h}}$ must be calculated and assigned between the end of the capacity test and the beginning of the SCP cycles. Modern battery test software is capable of executing calculations such as these mid-test. Alternatively, the test operator could carry out the calculation manually and prescribe the calculated power setpoints during a brief pause in the test.

The rough linear correlations in Figure 6.17 show that Equations 6.55 and 6.56 will not provide precise estimates for $P_{\mathrm{CP}}^{4\mathrm{h}}$ and $P_{\mathrm{CP}}^{2\mathrm{h}}$, but precise estimates are not required. These equations merely ensure that the prescribed values of $P_{\mathrm{CP}}^{4\mathrm{h}}$ and $P_{\mathrm{CP}}^{2\mathrm{h}}$ will not be so inaccurate that the reliability of the extrapolation model may become compromised.

For the single-dataset test protocol, power setpoints for the baseline power P_{CP} and pulse power P_{pulse} are required. Since the SCPP cycle ideally pulses from a 2 h rate to a 1 h rate, Equation 6.56 can be used to estimate P_{CP}. For P_{pulse}, it is especially important to ensure that the prescribed value does not significantly exceed the true 1 h rate, since the SCPP test method has presently only been verified for $t_{\mathrm{dis}}^{\mathrm{pulse}} > 0.98$ h. The ideal ratio of P_{pulse} to P_{CP} will depend on the Peukert number σ as shown in Equation 6.57. Note that the Peukert adjustment factor γ is dropped here as it does not make a significant difference for the purpose of estimating power setpoints.

$$P_{\mathrm{pulse}} = P_{\mathrm{CP}}(2)^{\frac{1}{\sigma}} \tag{6.57}$$

Since the single-dataset extrapolation technique relies on σ being estimated from manufacturer specifications (see Equation 6.12), σ can be calculated before the condensed test protocol is initiated so that Equations 6.56 and 6.57 can be used to calculate and

prescribe both P_{CP} and P_{pulse} based on the results of the capacity test. Based on the seven Peukert numbers calculated and plotted in Figure 6.2, the ideal ratio of P_{pulse} to P_{CP} would range from 1.80 to 1.95 depending on the battery under test. It is better to underestimate P_{pulse} than overestimate, so a ratio of 1.8 could serve as a generalized guideline.

6.4.3. Test Evaluation

Once a condensed performance test is completed, an analysis of the results will provide complete performance characterization in the SCP test regime. First, the results of the capacity test are used to determine the SOH of the battery by comparing the measured discharge energy $E_{\mathrm{dis}}^{\mathrm{CPCV}}$ to the rated discharge energy $E_{\mathrm{dis}}^{\mathrm{spec}}$ as per Equation 6.58.

$$\mathrm{SOH} = \frac{E_{\mathrm{dis}}^{\mathrm{CPCV}}}{E_{\mathrm{dis}}^{\mathrm{spec}}} \tag{6.58}$$

Next, the performance extrapolation methods described in Section 6.2 are executed using the test results and manufacturer specifications as inputs. Figure 6.18 illustrates the process flow for testing and analysis in the case of the single-dataset test protocol and extrapolation model. Purple represents battery specifications, red represents test inputs, green represents measured test results, yellow represents user-specified model inputs, pale blue represents intermediate model calculations, and bright blue represents desired outcomes. The top half of the diagram depicts the extrapolation of electrical performance metrics, while the bottom half depicts the extrapolation of thermal performance metrics.

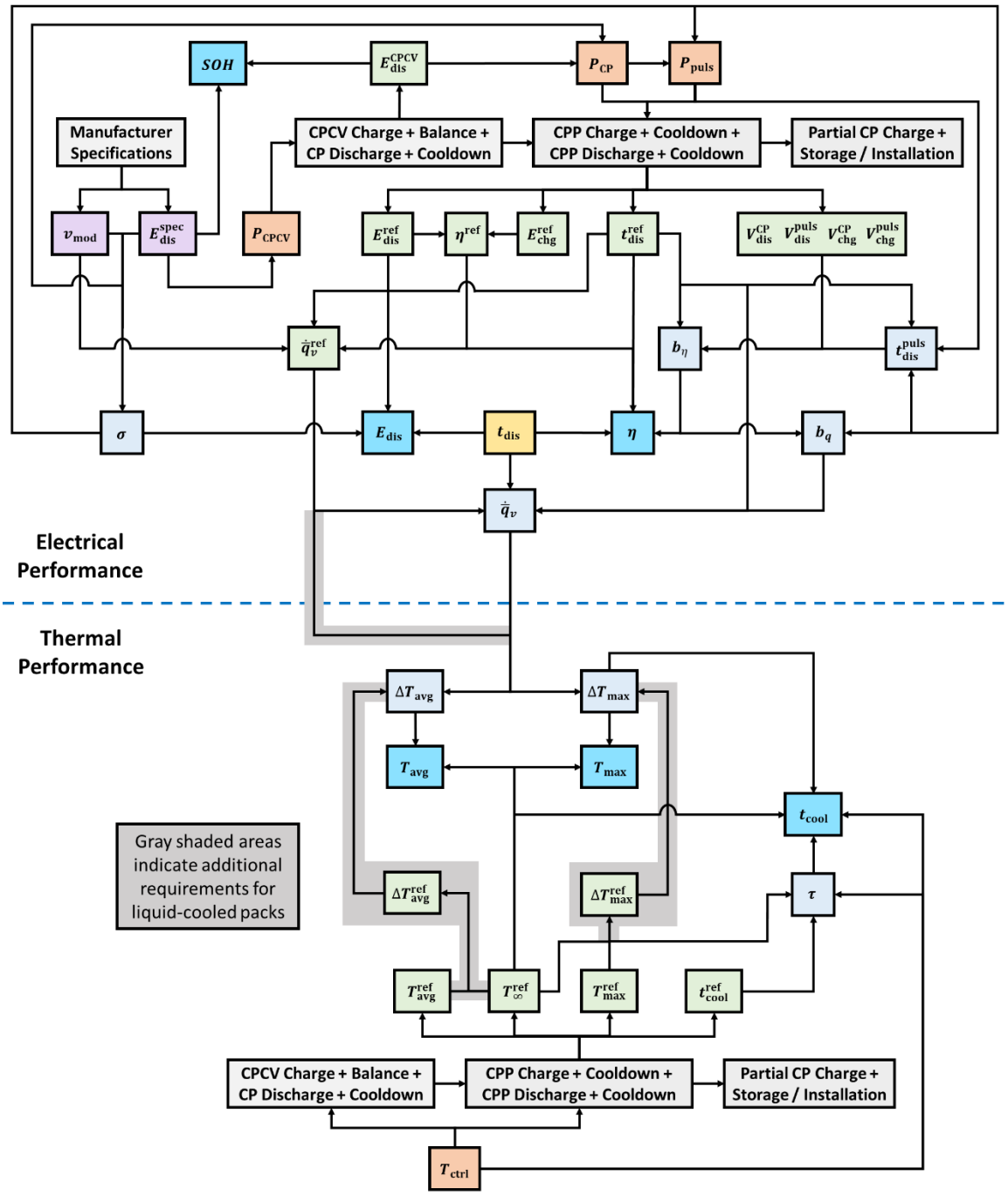


Figure 6.18 Visualization of the proposed condensed test procedure and performance extrapolation model utilizing the single-dataset extrapolation technique. Purple represents battery specifications, red represents test inputs, green represents measured test results, yellow represents user-specified model inputs, pale blue represents intermediate model calculations, and bright blue represents desired outcomes.

For electrical performance, the SCPP test provides measured reference values $t_{\mathrm{dis}}^{\mathrm{ref}}$, $E_{\mathrm{dis}}^{\mathrm{ref}}$, η^{ref}, and $\dot{\bar{q}}_v^{\mathrm{ref}}$, as well as voltage results from the pulses. Manufacturer specifications are used to estimate the Peukert number σ, which feeds into the estimation of $t_{\mathrm{dis}}^{\mathrm{pulse}}$ based on the prescribed power setpoints P_{CP} and P_{pulse}. This enables calculation of the energy efficiency exponent b_η based on the SCPP results, which then combines with σ to determine the heat generation exponent b_q. The parameters σ, b_η, and b_q are then used to extrapolate new values of E_{dis}, η, and $\dot{\bar{q}}_v$ for any user-specified value of t_{dis}. The measured $\dot{\bar{q}}_v^{\mathrm{ref}}$ and the extrapolated $\dot{\bar{q}}_v$ feed into the extrapolation of thermal performance metrics.

For passive-cooled packs, the temperature rise extrapolation for ΔT_{max} and ΔT_{avg} requires only the extrapolated value of $\dot{\bar{q}}_v$ for the specified t_{dis}. The extrapolated ΔT_{max} and ΔT_{avg} values then combine with the reference ambient temperature T_∞^{ref} to determine the temperature values T_{max} and T_{avg}. For liquid-cooled packs, the measured reference values $\dot{\bar{q}}_v^*$, $\Delta T_{\mathrm{max}}^{\mathrm{ref}}$, and $\Delta T_{\mathrm{avg}}^{\mathrm{ref}}$ are also required for the extrapolation of ΔT_{max} and ΔT_{avg}. These additional requirements are indicated by the gray shaded areas in Figure 6.18. Both passive-cooled and liquid-cooled packs use the same calculation for cycle cooldown duration t_{cool}. This requires the extrapolated ΔT_{max} as well as the cooling time constant τ, which is determined from the measured thermal reference values $T_{\mathrm{max}}^{\mathrm{ref}}$, T_∞^{ref}, and $t_{\mathrm{cool}}^{\mathrm{ref}}$. The temperature control setpoint T_{ctrl} must be prescribed within the condensed test protocol and also feeds into the calculations of τ and t_{cool}.

The case of the two-dataset test protocol and extrapolation model is similar to Figure 6.18, but two sets of measured reference values are acquired (one for the 4 h SCP cycle and one for the 2 h SCP cycle) and used to calculate σ and b_η without relying on manufacturer specifications or pulsing techniques. Either set of reference values can be used to extrapolate the electrical performance metrics, since both datasets will lie on the same curves defined by σ and b_η. However, only the 2 h dataset should be used as reference values for extrapolation of thermal performance metrics, since the measured 4 h values of $\Delta T_{\mathrm{max}}^{\mathrm{ref}}$, $\Delta T_{\mathrm{avg}}^{\mathrm{ref}}$, and $t_{\mathrm{cool}}^{\mathrm{ref}}$ will likely be too small to produce accurate extrapolations.

Whether the two-dataset or single-dataset variant is applied, the performance extrapolation model can be used to calculate electrical and thermal performance metrics corresponding to any desired value of t_{dis}, noting that presently the methods have only been verified for 0.98 h $< t_{\text{dis}} <$ 4.05 h. Standardized t_{dis} values would facilitate performance comparisons across different second-life battery packs, so it is recommended that the extrapolation model be used to obtain standardized results at precisely $t_{\text{dis}} = 4.0$ h, $t_{\text{dis}} = 2.0$ h, and $t_{\text{dis}} = 1.0$ h. Extrapolation to $t_{\text{dis}} = 8.0$ h may also be useful for second-life energy storage applications with longer discharge durations. Future research should confirm whether the proposed Peukert adjustment factor γ should be modified to accommodate $t_{\text{dis}} = 8.0$ h.

6.5. Impact of Degradation on Performance Extrapolation Model

Since the proposed performance extrapolation model is intended for use with second-life battery packs, it is important to consider how degradation may impact the parameters and methods associated with the condensed test protocols and extrapolation techniques. To explore this, the same six datasets described in Section 5.6 will be reconsidered within the context of the performance extrapolation model, including Model3-19 at 95 % SOH and 87 % SOH (both passive-cooled and liquid-cooled), Leaf-12 at 76 % SOH, and Leaf-14 at 83 % SOH. These six datasets will be used to assess how SOH influences the constant parameters used in the extrapolation equations, the proposed SCPP test method, and the proposed guidelines for prescribing power setpoints in the condensed test protocols.

6.5.1. Impact on Model Parameters

Since battery degradation can result in decreased capacity and increased internal resistance, the constant parameters used in the performance extrapolation model may not truly be constant when considering long term degradation of second-life batteries. It is therefore important to determine whether battery SOH has a significant impact on the adjusted Peukert equation and the newly proposed empirical equations from Section 6.1.

The left and right charts of Figure 6.19 respectively plot the measured discharge energy E_{dis} and calculated Peukert number σ for the six datasets. The black dashed line in the right chart is the same linear trend from Figure 6.2. The left chart shows that the adjusted Peukert equation still provides an accurate fit for all datasets, and the right chart shows that σ

remains consistent for each battery and TMS despite clear decreases in E_{dis} at lower SOH. The latter observation is an especially encouraging result for the single-dataset solution, which relies on the ability to predict σ for a given EV battery based on its rated module energy density. However, it is important to recognize that Figure 6.19 only shows moderate changes in SOH. Future research should explore how σ changes when a battery degrades from 100 % to 60 % SOH. If significant changes are observed, then the single-dataset solution would require a universal means of quantifying this SOH dependence so that SOH can be used as an additional input for estimating σ. In contrast, the two-dataset solution is inherently robust to any dependence of σ on SOH since σ is calculated based on E_{dis} results measured at the present SOH of the given battery.

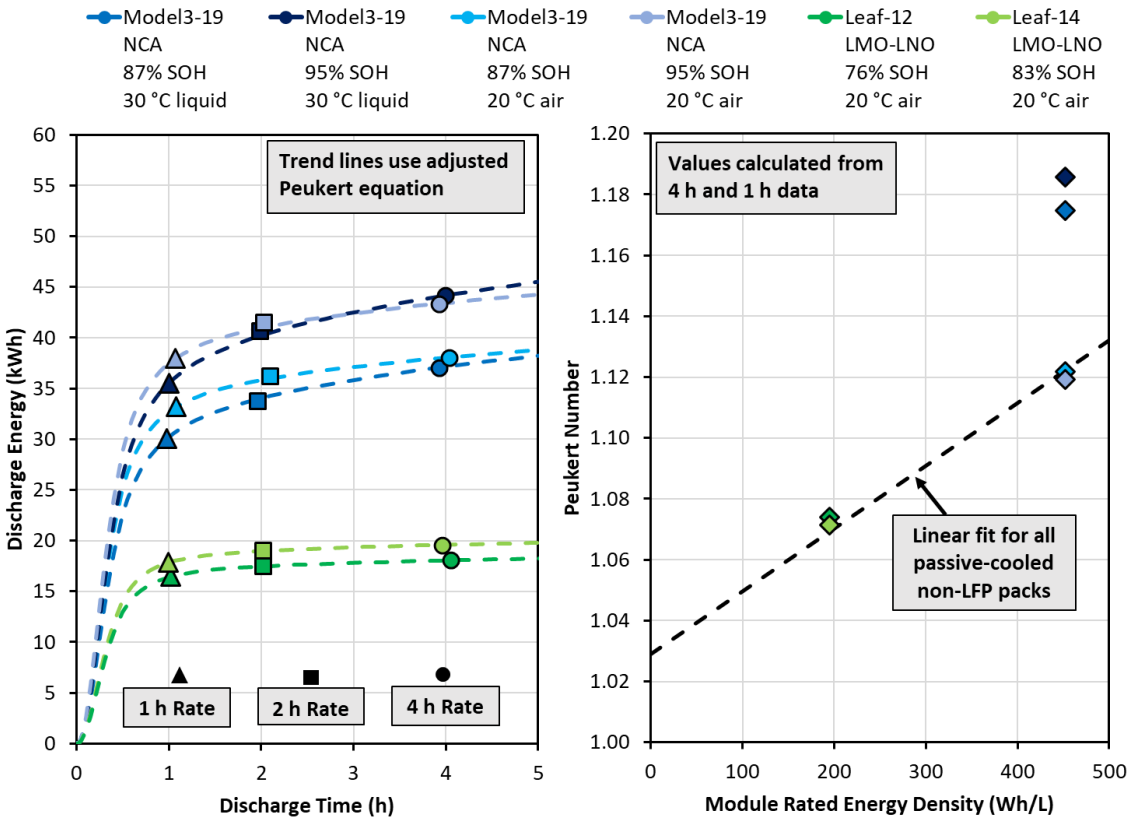


Figure 6.19 Adjusted Peukert equation fitted to results measured at different SOH levels (left) and associated Peukert numbers (right).

Figure 6.20 applies the same analysis to energy efficiency, where the left and right charts respectively plot the measured cycle energy efficiency η and calculated energy efficiency exponent b_η. The left chart shows that the empirical energy efficiency equation still

provides an accurate fit for all datasets. As described in Section 5.6.3, η can decrease notably at lower SOH for some battery designs such as Model3-19. The right chart of Figure 6.20 shows that b_η is somewhat dependent on SOH for Model3-19, exhibiting a decrease of about 10 % for degradation from 95 % SOH to 87 % SOH. This indicates that η rate dependence decreases with degradation, though Leaf-12 and Leaf-14 give essentially the same b_η despite their differences in SOH. Future research could explore whether b_η changes more significantly over greater changes in SOH, but any such SOH dependence would not be an issue for the performance extrapolation model. Both the two-dataset and single-dataset solutions determine b_η from measured results at the present SOH of the battery under test.

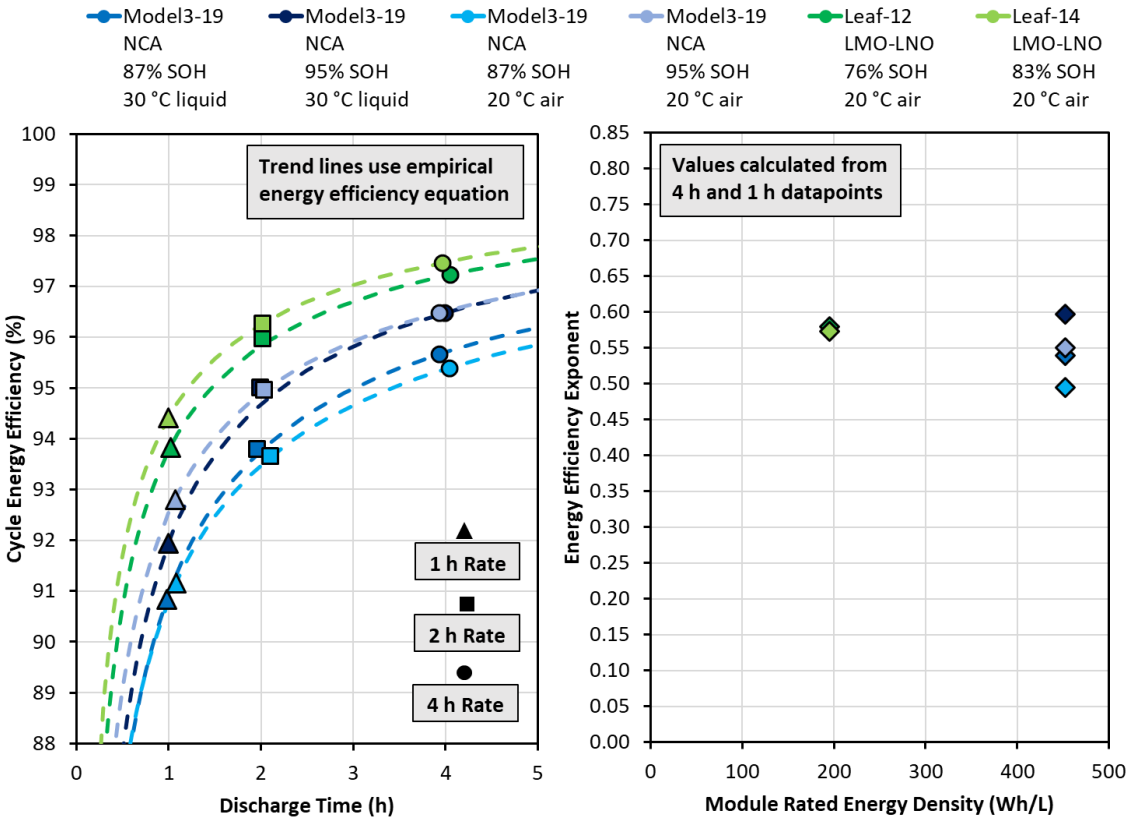


Figure 6.20 Empirical energy efficiency equation fitted to results measured at different SOH levels (left) and associated energy efficiency exponents (right).

Figure 6.21 applies the same analysis to heat generation, where the left and right charts respectively plot the measured average volumetric heat generation rate $\dot{\bar{q}}_v$ and calculated heat generation exponent b_q. The left chart shows that the empirical heat generation

equation still provides an accurate fit for all datasets. As described in Section 5.6.4, $\dot{\bar{q}}_v$ does not change significantly with changes in SOH due to offsetting influences from E_{dis} and η. The right chart of Figure 6.21 shows that b_q is somewhat dependent on SOH for Model3-19, due to the contribution of b_η to b_q. However the more SOH-independent contribution of the Peukert number σ to b_q means that the relative b_q decrease exhibited by Model3-19 for degradation from 95 % SOH to 87 % SOH is dampened compared to b_η (about a 5 % decrease in b_q compared to about a 10 % decrease in b_η). For the two-dataset solution, both σ and b_η are determined for the present SOH, so any SOH dependence in b_q will be accounted for. For the single-dataset solution, any SOH sensitivity in the σ estimation will propagate into b_q.

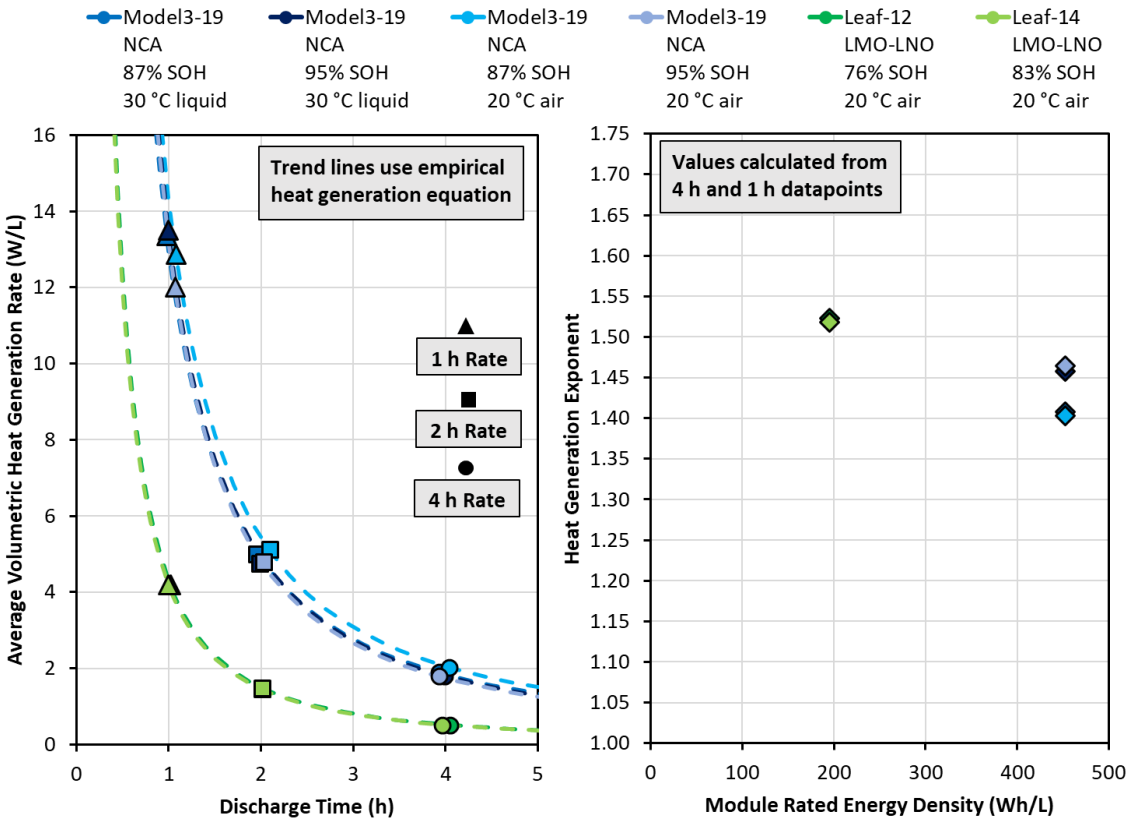


Figure 6.21 Empirical heat generation equation fitted to results measured at different SOH levels (left) and associated heat generation exponents (right).

As explained in Section 5.6.5, the maximum ΔT_{max} and average ΔT_{avg} temperature rise are fairly insensitive to changes in SOH due to their dependence on $\dot{\bar{q}}_v$ and constant physical

properties. The empirical temperature rise equations should therefore be robust to change in SOH, such that $\Delta T_{\max}$ and ΔT_{avg} increase or decrease when $\dot{\bar{q}}_v$ increases or decreases. The left and right charts of Figure 6.23 respectively plot $\Delta T_{\max}$ and ΔT_{avg} as a function of $\dot{\bar{q}}_v$ for the liquid-cooled Model3-19 at 95 % SOH and 87 % SOH. The previously presented trends for passive-cooled packs are also shown for reference. As described in Section 5.6.5, the temperature rise results are very similar at both SOH levels. The chosen parameters of $b_{T_{\max}} = 0.65$ and $b_{T_{\text{avg}}} = 0.48$ used in Equations 6.27 and 6.28 provide an accurate fit to the measured data at both 95 % SOH and 87 % SOH. Future research should confirm that passive-cooled packs exhibit the same consistency.

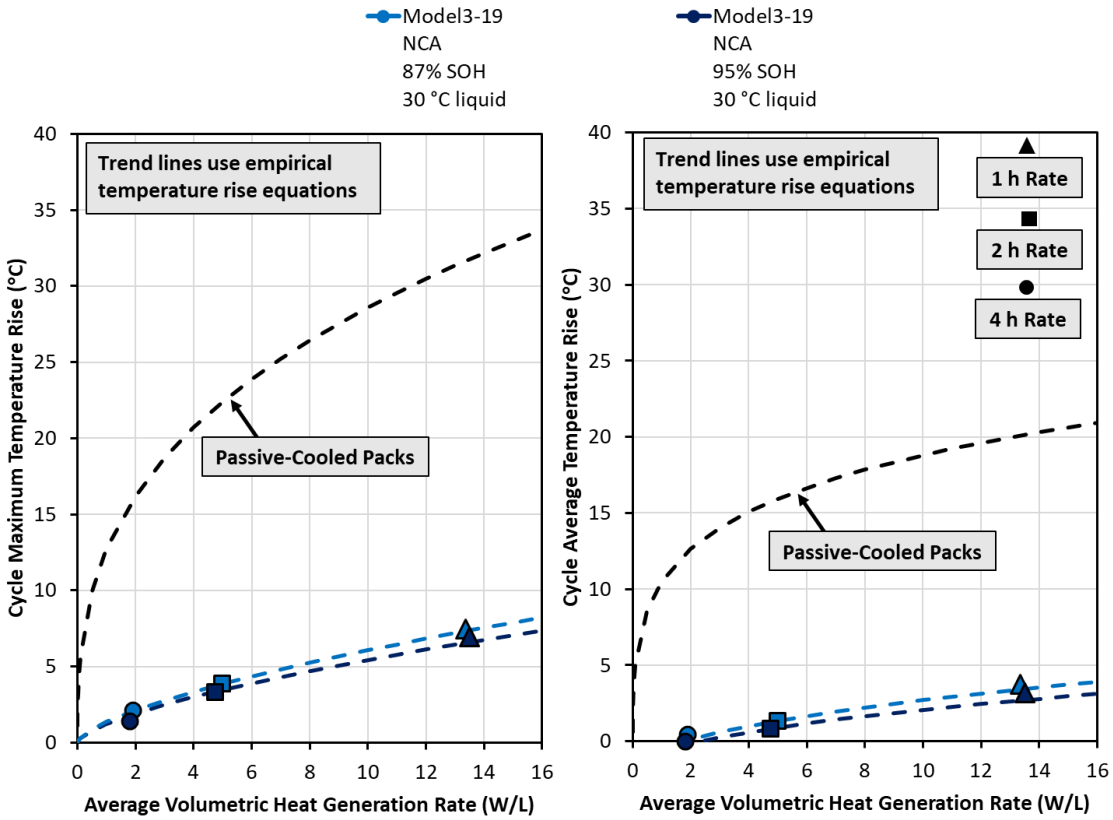


Figure 6.22 Empirical temperature rise equation fitted to experimental results measured at different SOH levels for maximum (left) and average (right) temperature rise as a function of average volumetric heat generation rate.

Overall, the empirical equations and constant parameters used in the performance extrapolation model are not significantly impacted by the moderate SOH changes that can be explored using the acquired experimental data. The condensed test protocols described

in Section 6.4 are designed in such a way that any dependence on greater SOH changes will be accounted for in the empirical determinations of σ, b_η, and b_q, making the two-dataset solution especially robust to changes in SOH. A strong dependence of σ on SOH could present a challenge for the single-dataset solution, but the results presented in Figure 6.19 offer cautious optimism.

6.5.2. Impact on Pulse Method

Section 6.2.3 demonstrated that each tested EV battery pack features an SOC range in which the voltage ratio $\frac{V_{\text{dis}}}{V_{\text{chg}}}$ can serve as an acceptable proxy for the energy efficiency η of an SCP cycle, which is the basis of the proposed SCPP method for the single-dataset extrapolation model. Figure 6.23 considers how battery degradation might impact the SCP voltage profile and the corresponding correlation between $\frac{V_{\text{dis}}}{V_{\text{chg}}}$ and η. The top charts plot the 4 h, 2 h, and 1 h CP voltage profiles for the liquid-cooled Model3-19, while the bottom charts plot the corresponding voltage ratios, with the 95 % SOH results on the left and the 87 % SOH charts on the right.

As discussed in Section 5.6.1, the internal resistance growth that results from battery degradation causes operational SOC window shrinks and also causes the voltage profile characteristics typical of graphite-based negative electrodes and nickel-rich positive electrodes to become less distinct. The effects of the narrowed SOC window and the changing voltage profile shape manifest in the voltage ratio profiles in the bottom charts of Figure 6.23. The dashed horizontal lines represent the cycle energy efficiencies η at each power rate, which are noticeably lower at lower SOH. The yellow boxes show the acceptable SOC range where all three voltage ratios are close to η, and this range clearly shifts towards lower SOC at lower SOH. It can therefore be concluded that there is no single SOC value at which $\frac{V_{\text{dis}}}{V_{\text{chg}}}$ can serve as a proxy for η across all battery designs and SOH levels. This finding supports the SCPP method proposed in Section 6.2.3, which features two pulses during both discharge and charge to enable partial reconstruction of the voltage profiles such that $\frac{V_{\text{dis}}}{V_{\text{chg}}}$ can be selected at the most appropriate SOC for the battery under test at its present SOH.

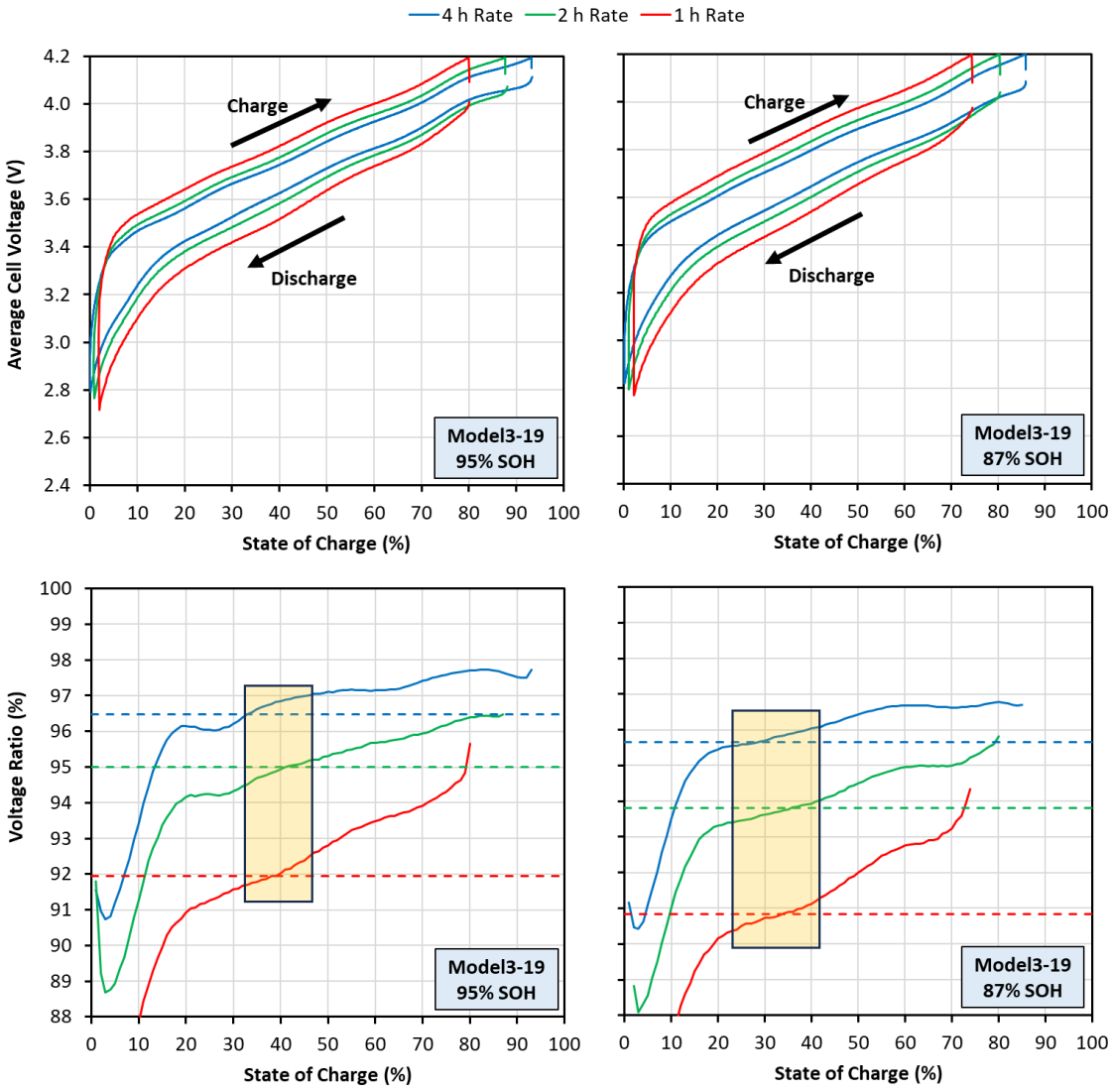


Figure 6.23 Voltage profiles (top) and voltage ratios (bottom) compared for the same battery pack at 95 % SOH (left) and 87 % SOH (right).

6.5.3. Impact on Test Parameters

Section 6.4.2 proposed that once the present energy capacity of a second-life battery pack is measured through a CCCV or CPCV capacity test, the rated module energy density $\bar{E}_v^{\text{spec}}$ of the pack can be used to estimate the power setpoints that will produce a 4 h or 2 h discharge in SCP cycling. Figure 6.24 applies the same analysis from Figure 6.17 for the passive-cooled and active-cooled Model3-19 (both at 95 % SOH and 87 % SOH), Leaf-12 (76 % SOH), and Leaf-14 (83 % SOH). The left and right charts respectively show the measured 4 h and 2 h energy utilization ratio ζ results for each battery pack. The black dashed lines are the same as those fitted to the seven original datasets in Figure 6.17. While

there is an insignificant difference between Leaf-12 and Leaf-14 in Figure 6.24, both the liquid-cooled and passive-cooled Model3-19 exhibit a strong dependence on SOH. The reasons for this were already discussed in Section 5.6.2. This means that the previously proposed estimation techniques for $P_{\mathrm{CP}}^{4\mathrm{h}}$ and $P_{\mathrm{CP}}^{2\mathrm{h}}$ in Equations 6.55 and 6.56 may yield significant inaccuracies depending on the SOH of a given battery, and Figure 6.24 suggests that this is especially likely for EV battery packs with high energy density.

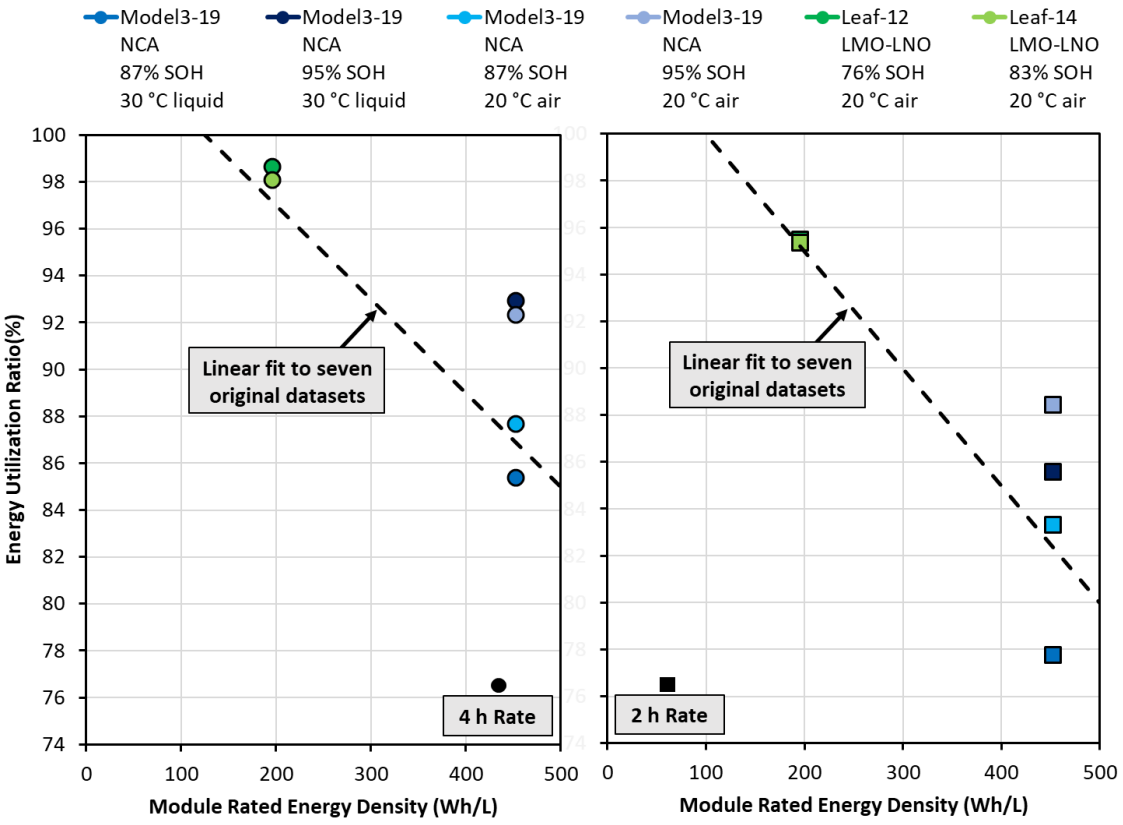


Figure 6.24 Energy utilization ratios from 4 h (left) and 2 h (right) SCP tests at different SOH levels.

While the accuracy of these estimations are not critical to the proposed condensed test methods, Equations 6.55 and 6.56 can be modified to account for changes in SOH as a means of enhancing accuracy. More experimental data is required to develop this, but a relatively simple option is provided in Equations 6.59 and 6.60 as an illustrative example. These two equations are respectively plotted in the left and right charts of Figure 6.25 at three different SOH levels, providing reasonable accuracy for all six datapoints in each chart. Note that $E_{\mathrm{dis}}^{\mathrm{CPCV}}$ is assumed to be equivalent to $E_{\mathrm{dis}}^{\mathrm{CCCV}}$ for illustrative purposes.

$$P_{\mathrm{CP}}^{4\mathrm{h}} = \frac{E_{\mathrm{dis}}^{\mathrm{CPCV}} \times \min\left(1.05 - \frac{0.25}{\mathrm{SOH}^3}\frac{E_{\mathrm{dis}}^{\mathrm{spec}}}{v_{\mathrm{mod}}}, 1\right)}{4} \tag{6.59}$$

$$P_{\mathrm{CP}}^{2\mathrm{h}} = \frac{E_{\mathrm{dis}}^{\mathrm{CPCV}} \times \min\left(1.05 - \frac{0.35}{\mathrm{SOH}^3}\frac{E_{\mathrm{dis}}^{\mathrm{spec}}}{v_{\mathrm{mod}}}, 1\right)}{2} \tag{6.60}$$

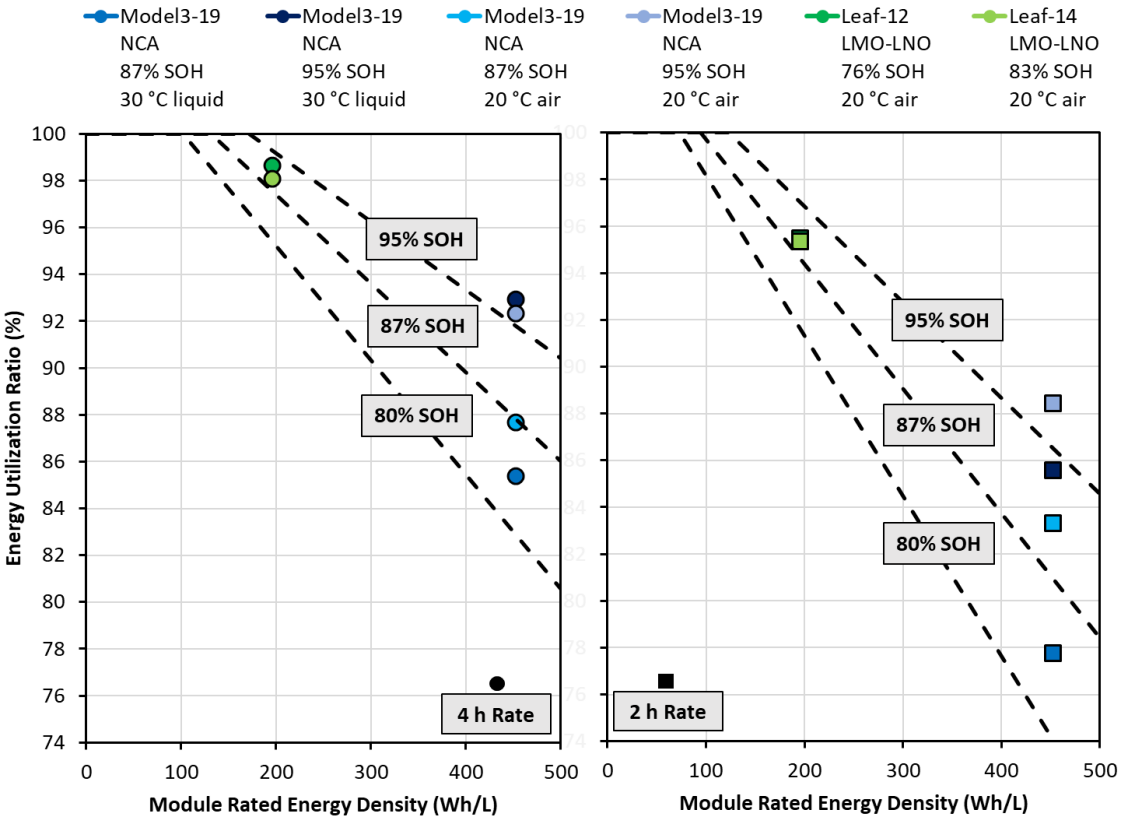


Figure 6.25 Proposed SOH-dependent technique for estimating 4 h (left) and 2 h (right) energy utilization ratios.

The best way to mitigate uncertainty regarding the $P_{\mathrm{CP}}^{4\mathrm{h}}$ and $P_{\mathrm{CP}}^{2\mathrm{h}}$ setpoints is to add a second cycle at each power rate to the condensed test protocols, such that the initial guess applied in the first cycle can be adjusted to a more appropriate value in the second cycle. The disadvantage of this approach is that the test duration will be nearly doubled. If a shorter test is preferred, then the proposed performance extrapolation methods should be sufficiently robust that simple estimation techniques such as Equations 6.59 and 6.60 can be used to select appropriate power setpoints for a given battery pack at a given SOH.

6.6. Limitations and Recommendations

Two variants of the proposed second-life battery performance extrapolation model have now been fully theorized, demonstrated, and analyzed. This section will comment on the limitations of the completed research and identify opportunities for continued development. Recommendations on how best to apply the proposed methods in practice will also be provided.

6.6.1. Limitations of Experimental Data

The reliability of both the two-dataset and single-dataset solutions depends on the accuracy of the adjusted Peukert equation, the empirical energy efficiency equation, the empirical heat generation equation, and the empirical temperature rise equations. While these equations have been verified to be accurate based on the acquired experimental data, there are a number of limitations to this data which should be acknowledged. These limitations present opportunities for future research.

The adjusted Peukert equation was designed to provide the best fit to the acquired datasets, which were limited to 4 h, 2 h, and 1 h SCP rates. While faster rates are likely impractical due to thermal safety limits, slower rates such as an 8 h rate are common in the energy storage industry. Future research should verify whether the proposed Peukert adjustment factor γ can be extended to an 8 h rate with reasonable accuracy and explore alternative γ expressions if necessary.

It is important to recognize that battery performance is influenced by the upper and lower voltage limits applied in the test protocol. This research project focused on the widest recommended cell voltage limits of 4.20 V at the upper limit (3.55 V for LFP) and 2.50 V at the lower limit, but narrower limits are commonly employed in industry. To facilitate comparison of different EV battery packs, a standardized set of voltage limits should be chosen for the performance extrapolation model. However, second-life battery project developers may prefer to characterize battery performance using the same voltage limits intended for a given commercial project. Future research should explore how the selection of voltage limits impacts the various aspects of the performance extrapolation model.

Battery performance is also influenced by temperature. The ambient temperature, liquid supply temperature, and temperature control setpoint all impact the measured electrical and thermal performance metrics. To facilitate comparison of different EV battery packs, a standardized set of temperature settings should be chosen for the performance extrapolation model. The thermal aspect of the proposed extrapolation model is highly simplified, so the present design of the model is not suited for extrapolating battery performance to any temperature settings other than those used in the reference test. Future research could aim to design a more sophisticated thermal extrapolation model so that performance measured with one set of temperature settings can be extrapolated to a different set of temperature settings. For passive-cooled packs, the characteristics of the ambient environment will also influence the empirical temperature rise equations. For example, Equations 6.36 through 6.38 are based on a packs tested in a relatively open space in a controlled laboratory environment, so these equations may underestimate temperatures for packs operating within a crowded battery array inside a shipping container. Different packs should still adhere to common trends, but new equations may be needed to describe these trends. Future research should explore how to modify Equations 6.36 through 6.38 based on the surroundings of the battery.

Battery performance is also influenced by SOH. As discussed in Section 6.5, the present design of the performance extrapolation model appears to be robust to the moderate changes in SOH that can be explored with the available experimental data. Long-term pack-level performance studies should be conducted to assess how larger SOH changes impact the extrapolation model and whether the proposed equations should be modified to include SOH as an input.

The fact that the proposed extrapolation model works well for five different positive electrode materials (NCA, NMC111, NMC622, LMO, LFP) is encouraging. However, the five tested battery packs all feature a graphite negative electrode (silicon-blended or unblended). It is therefore unclear as to whether the proposed methods can be reliably extended to other negative electrode materials such as hard carbon. While such cases are rare in the EV industry, future research should consider these cases. The applicability of the proposed methods to lithium-ion alternatives (e.g. sodium-ion) should also be explored.

6.6.2. Limitations of Single-Dataset Solution

In addition to the points raised in Section 6.6.1, the proposed single-dataset solution for the performance extrapolation model has several limitations which should be addressed with additional research before the method can be reliably implemented with any EV battery pack. The most significant of these limitations is the requirement that the Peukert number σ be predetermined for the battery pack under test. Figure 6.2 suggested that the Peukert number of passive-cooled EV battery packs increases linearly with the rated module energy density $\bar{E}_v^{\text{spec}}$, and that a simple constant correction factor α_σ can account for the unique electrochemical characteristics of LFP chemistry and the thermal impacts of liquid cooling. However, the available sample size is insufficient to state this conclusively. Future research should aim to verify this correlation with a larger sample size and modify Equation 6.12 as necessary so that it can be applied with confidence to any EV battery pack with reasonable accuracy. While Figure 6.19 suggested that the Peukert number is not strongly influenced by SOH, the available sample size is again insufficient to state this conclusively. Future research should confirm whether Equation 6.12 should include a dependence on SOH and quantify this dependence in a way that applies to all EV battery packs.

The proposed SCPP test method for executing the single-dataset solution must also be researched in greater depth to determine the optimal frequency, magnitude, and duration of pulses to estimate the energy efficiency exponent b_η. The SCPP method also requires that current measurements are sufficiently accurate that battery SOC can be reliably tracked during discharge and charge for the purpose of calculating the voltage ratio $\frac{V_{\text{dis}}}{V_{\text{chg}}}$. Future research should quantify this sensitivity so that minimum equipment requirements can be recommended for the SCPP method.

6.6.3. Extension to Other Cycle Types

The proposed performance extrapolation model has been developed based on experimental data acquired from SCP cycling, which is just one type of battery cycle. It is worth considering whether the extrapolation model can be easily extended to other cycle types, such as CC cycles (commonly used in battery research) and asymmetrical CP cycles where $P_{\text{dis}} \neq P_{\text{chg}}$ (relevant to some energy storage applications such as peak shaving).

One important consideration for other cycle types is the definition of the average volumetric heat generation rate $\dot{\bar{q}}_v$, which is essential for extrapolation of $\Delta T_{\max}$ and ΔT_{avg}. To explore this, Equation 6.61 states the general definition of $\dot{\bar{q}}_v$.

$$\begin{aligned}\dot{\bar{q}}_v &= \frac{1}{v_{\text{mod}}}\left(\frac{E_{\text{chg}} - E_{\text{dis}}}{t_{\text{chg}} + t_{\text{dis}}}\right) \\ &= \frac{E_{\text{dis}}}{v_{\text{mod}} t_{\text{dis}}}\left(\frac{\frac{1}{\eta} - 1}{\frac{t_{\text{chg}}}{t_{\text{dis}}} + 1}\right)\end{aligned} \tag{6.61}$$

For the general case of an asymmetrical CP cycle, the cycle energy efficiency η is defined by Equation 6.62. Using this definition, a new definition of $\dot{\bar{q}}_v$ for asymmetrical CP cycles can be derived, as shown in Equation 6.63. Note that when $P_{\text{dis}} = P_{\text{chg}}$ is applied, the expression simplifies to the symmetrical form of $\dot{\bar{q}}_v$ originally presented in Equation 4.22.

$$\eta = \frac{P_{\text{dis}} t_{\text{dis}}}{P_{\text{chg}} t_{\text{chg}}} \tag{6.62}$$

$$\dot{\bar{q}}_v = \frac{E_{\text{dis}}}{v_{\text{mod}} t_{\text{dis}}}\left(\frac{1 - \eta}{\frac{P_{\text{dis}}}{P_{\text{chg}}} + \eta}\right) \tag{6.63}$$

For the general case of an asymmetrical CC cycle, η is defined by Equation 6.64. This definition provides no opportunity to substitute η into the $\frac{t_{\text{chg}}}{t_{\text{dis}}}$ term in Equation 6.61. One option for a CC performance extrapolation model would be to make the assumptions stated in Equations 6.65 through 6.67. By taking the average discharge voltage $V_{\text{dis}}^{\text{avg}}$ and the average charge voltage $V_{\text{chg}}^{\text{avg}}$ and assuming that the ratio between them is close to η (similar to the voltage ratio described in Section 6.2.3), Equation 6.64 reduces to $\frac{t_{\text{chg}}}{t_{\text{dis}}} \approx \frac{I_{\text{chg}}}{I_{\text{dis}}}$. With these assumptions, $\dot{\bar{q}}_v$ can be defined by Equation 6.68 for an asymmetrical CC cycle. Since the $\frac{t_{\text{chg}}}{t_{\text{dis}}} + 1$ term in the denominator of Equation 6.61 has a relatively small impact on $\dot{\bar{q}}_v$ compared to the $\frac{1}{\eta} - 1$ term in the numerator, these assumptions may prove acceptable.

$$\eta = \frac{I_{\text{dis}} \int V_{\text{dis}} \mathrm{d}t_{\text{dis}}}{I_{\text{chg}} \int V_{\text{chg}} \mathrm{d}t_{\text{chg}}} \tag{6.64}$$

$$\int V_{\text{dis}} \mathrm{d}t_{\text{dis}} = V_{\text{dis}}^{\text{avg}} t_{\text{dis}} \tag{6.65}$$

$$\int V_{\text{chg}} \mathrm{d}t_{\text{chg}} = V_{\text{chg}}^{\text{avg}} t_{\text{chg}} \tag{6.66}$$

$$\frac{V_{\text{dis}}^{\text{avg}}}{V_{\text{chg}}^{\text{avg}}} \approx \eta \tag{6.67}$$

$$\dot{\bar{q}}_v \approx \frac{E_{\text{dis}}}{v_{\text{mod}} t_{\text{dis}}} \left(\frac{\frac{1}{\eta} - 1}{\frac{I_{\text{dis}}}{I_{\text{chg}}} + 1} \right) \tag{6.68}$$

Other elements of the performance extrapolation model will also be impacted by the choice of cycle type. Any given ratio of $\frac{P_{\text{dis}}}{P_{\text{chg}}}$ or $\frac{I_{\text{dis}}}{I_{\text{chg}}}$ will produce unique Peukert numbers and may require a unique definition of the Peukert adjustment factor γ. The relationship between $\dot{\bar{q}}_v$ and temperature rise will also be affected. For example, an asymmetrical CP cycle with $P_{\text{dis}} = 20$ kW and $P_{\text{chg}} = 10$ kW will yield the same ΔT_{max} as a cycle with $P_{\text{dis}} = 20$ kW and $P_{\text{chg}} = 5$ kW, but $\dot{\bar{q}}_v$ will be smaller for the latter. Any given ratio of $\frac{I_{\text{dis}}}{I_{\text{chg}}}$ or $\frac{P_{\text{dis}}}{P_{\text{chg}}}$ may therefore require its own temperature rise exponents $b_{T_{\text{max}}}$ and $b_{T_{\text{avg}}}$ for both passive-cooled and liquid-cooled packs, if there is indeed a consistent correlation at all when $\frac{P_{\text{dis}}}{P_{\text{chg}}} \neq 1$. It must also be confirmed whether the voltage ratio $\frac{V_{\text{dis}}}{V_{\text{chg}}}$ can serve as a proxy for η when $\frac{P_{\text{dis}}}{P_{\text{chg}}} \neq 1$, as this is essential for the single-dataset solution. The proposed empirical energy efficiency equation and empirical heat generation equation may also require modification for these other cycle types.

Future research should explore these questions to confirm whether the proposed performance extrapolation methods can be reliably extended to CC cycles and/or

asymmetrical CP cycles. To facilitate comparison of different EV battery packs, a standardized $\frac{P_{\mathrm{dis}}}{P_{\mathrm{chg}}}$ or $\frac{I_{\mathrm{dis}}}{I_{\mathrm{chg}}}$ ratio should be chosen for performance extrapolation. This chapter has demonstrated that an accurate model can be created for $\frac{P_{\mathrm{dis}}}{P_{\mathrm{chg}}} = 1$. Until thorough research verifies an accurate model for other cycle types, SCP cycling is the recommended test method for performance extrapolation.

6.6.4. Specification of Module Volume

Some of the equations and methods presented in this chapter rely on the total module volume v_{mod} being a known parameter for a given second-life battery pack. The single-dataset solution relies on a linear correlation with the rated module energy density $\bar{E}_v^{\mathrm{spec}}$ to determine the Peukert number σ, which in turn impacts the extrapolation of E_{dis}. The two-dataset extrapolations of E_{dis} is independent of v_{mod}, but both the two-dataset and single-dataset solutions predict temperature rise in passive-cooled packs based on a fixed dependence on the average volumetric heat generation rate $\dot{\bar{q}}_v$, which in turn impacts the prediction of t_{cool} (for active-cooled packs, v_{mod} cancels out of the temperature rise extrapolations). The condensed test protocols also rely on correlations with $\bar{E}_v^{\mathrm{spec}}$ to estimate appropriate power setpoints. The ease with which v_{mod} can be determined for second-life battery packs is therefore important to consider.

In some cases, v_{mod} can be determined based on module dimensions listed in the spec sheet or user manual for a given EV battery pack design, but this information is not always made available by manufacturers. Alternatively, v_{mod} can be determined by opening a battery pack and directly measuring the module dimensions. While direct measurement conveniently does not require removal of the module from the pack (as is required for measuring module mass), removing the housing cover of an EV battery pack can be an intrusive and time-consuming process, depending on the pack design. A more easily attainable parameter is the pack mass m_{pack}, which is often specified by manufacturers and can also be easily determined by placing the entire pack on an appropriately sized mass scale upon acquisition. The disadvantage of using m_{pack} instead of v_{mod} is that m_{pack} includes the inactive mass of the battery pack housing, circuitry, and power electronics.

The relative contribution of active and inactive mass to overall pack mass can vary significantly for different pack designs, and this variance may skew the correlations that were found to be fairly consistent across different pack designs when using v_{mod}.

To explore how replacing v_{mod} with m_{pack} might impact the performance extrapolation model, Figure 6.26 revisits previous plots using the rated pack specific energy $\bar{E}_m^{\mathrm{spec}}$ instead of the rated module energy density $\bar{E}_v^{\mathrm{spec}}$. The left chart shows that the Peukert number σ can still be estimated by a linear correlation (with correction factors for LFP and liquid-cooled packs), but the correlation is weaker than the one shown previously in Figure 6.2 with $\bar{E}_v^{\mathrm{spec}}$ as the independent variable. This turns out to have only a minor impact on the accuracy of the single-dataset extrapolation model, as the maximum extrapolation error for E_{dis} increase from 1.0 % to 1.3 %, the η extrapolation is independent of σ anyway. This suggests that single-dataset extrapolation of electrical performance metrics is no more likely to work well with v_{mod} than it is with m_{pack}. In both cases, additional research is required to verify the reliability of estimating Peukert numbers based on manufacturer specifications.

The right chart of Figure 6.26 shows that it is still possible to produce rough estimates for the 2 h CP setpoints $P_{\mathrm{CP}}^{2\mathrm{h}}$ used in the condensed test protocol based on a rough correlation between energy utilization ratio ζ and $\bar{E}_m^{\mathrm{spec}}$. Though not shown in Figure 6.26, the same is true for $P_{\mathrm{CP}}^{4\mathrm{h}}$. This suggests that power setpoint estimation is no more likely to be effective using v_{mod} than it is with m_{pack}. In both cases, additional research is needed to explore how these correlations can be optimized in a way that accounts for SOH dependence in different battery designs, as described in Section 6.5.3.

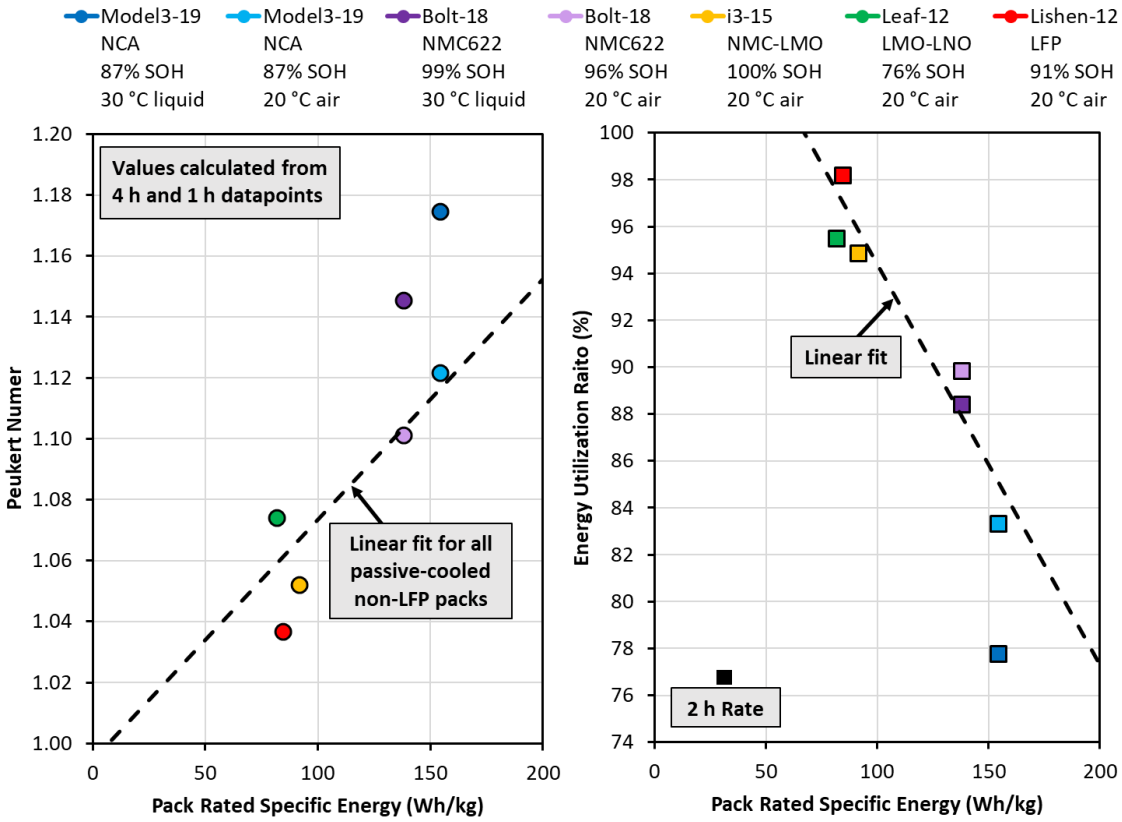


Figure 6.26 Peukert number (left) and energy utilization ratio (right) as a function of pack rated specific energy.

Figure 6.27 illustrates how replacing v_{mod} with m_{pack} impacts the extrapolation of thermal performance metrics. The left and right charts respectively plot the maximum ΔT_{max} and average ΔT_{avg} temperature rise of each experimental dataset against the pack average specific heat generation rate $\dot{\bar{q}}_m$, which is calculated the same way as $\dot{\bar{q}}_v$ but using m_{pack} instead of v_{mod}. New trendlines are fitted according to the empirical temperature rise equations for passive-cooled and liquid-cooled packs.

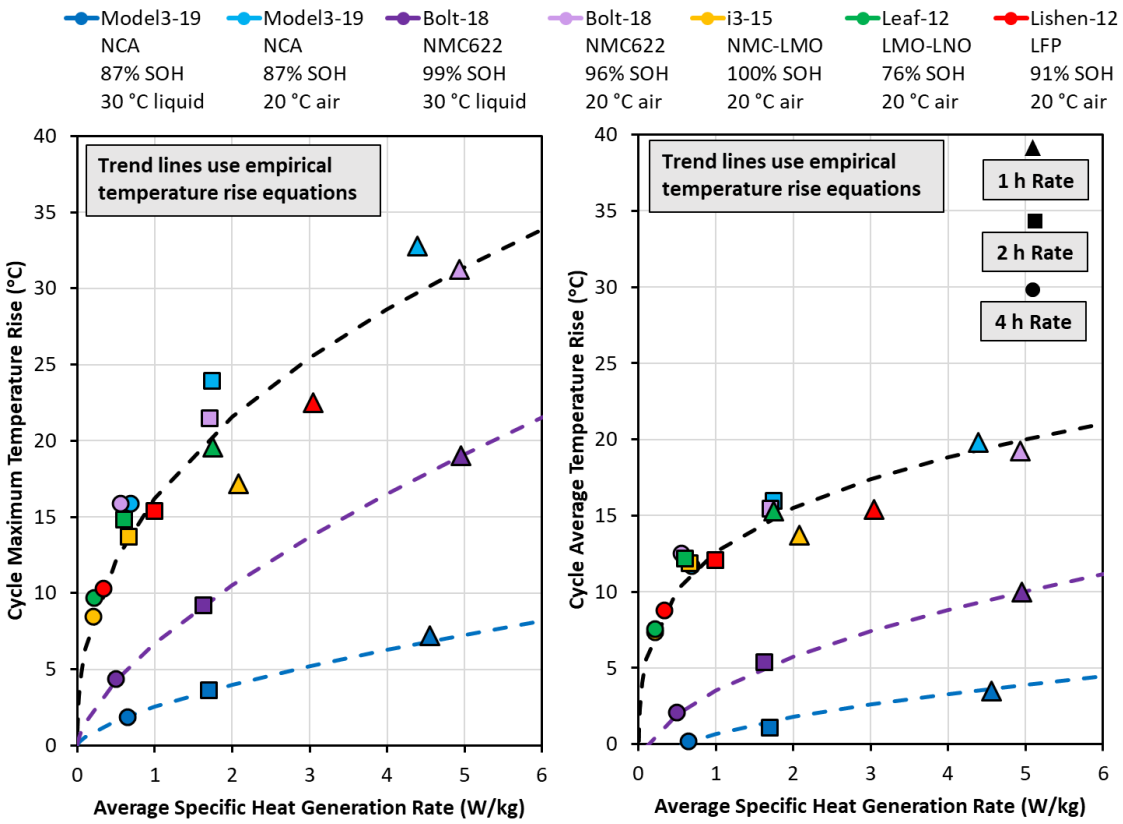


Figure 6.27 Empirical temperature rise equations fitted to experimental data for maximum (left) and average (right) temperature rise as a function of pack average specific heat generation rate.

Since the liquid-cooled versions of the empirical temperature rise equations are tailored to individual packs, the choice of $\dot{\bar{q}}_v$ or $\dot{\bar{q}}_m$ has no consequence for extrapolating $\Delta T_{\max}$ or ΔT_{avg} from a measured datapoint. However, prediction of $\Delta T_{\max}$ and ΔT_{avg} for passive-cooled packs relies on all battery packs adhering to a common trend. Figure 6.7 previously showed that the trends are very similar when $\dot{\bar{q}}_v$ is used as the independent variable. This is because temperatures were measured directly on module or cell surfaces, and these temperatures will be similar for a given $\dot{\bar{q}}_v$ since different packs are similar in terms of cell material composition as well as external size and shape. Figure 6.27 shows that when $\dot{\bar{q}}_m$ is used as the independent variable, the relatively significant variance in the inactive materials used in different pack designs causes the passive-cooled $\Delta T_{\max}$ and ΔT_{avg} to diverge. For ΔT_{avg}, all passive-cooled datapoints fall within about 2.0 °C of the trend shown in the right chart of Figure 6.27, which is not a major change from the 1.5 °C variance shown in Figure 6.7 when using $\dot{\bar{q}}_v$. However, some $\Delta T_{\max}$ datapoints lie as far

as 4.7 °C away from the trend shown in the left chart of Figure 6.27, which is a major change from the 1.5 °C variance shown in Figure 6.7. This indicates that prediction of $\Delta T_{\max}$ will be unreliable if m_{pack} is used instead of v_{mod}.

Based on Figure 6.26 and Figure 6.27, it can be concluded that m_{pack} is an acceptable substitute when v_{mod} cannot be determined for a given second-life battery pack, with the exception of estimating $\Delta T_{\max}$ for passive-cooled packs. A ± 5 °C uncertainty may be acceptable for $\Delta T_{\max}$ extrapolation if the extrapolation is strictly serving to confirm the safety of a high-power test in advance of running the test, but it is not acceptable for reliable performance characterization. Updated equations based on m_{pack} (in kg) are suggested in Equations 6.69 through 6.73. Based on the limited data available in Figure 6.26, correction factors of $\alpha_\sigma = 0.98$ and $\alpha_\sigma = 1.04$ provide the best Peukert number predictions for LFP and liquid-cooled packs, respectively.

$$\sigma = \alpha_\sigma \left(0.99 + 0.79 \frac{E_{\text{dis}}^{\text{spec}}}{m_{\text{pack}}} \right) \tag{6.69}$$

$$\Delta T_{\max}^{\text{PA}} = 16.0 \dot{\bar{q}}_m{}^{0.41} \tag{6.70}$$

$$\Delta T_{\text{avg}}^{\text{PA}} = 18.7 \dot{\bar{q}}_m{}^{0.20} - 6 \tag{6.71}$$

$$P_{\text{CP}}^{4\text{h}} = E_{\text{dis}}^{\text{CPCV}} \times \min \left(1.14 - 1.6 \frac{E_{\text{dis}}^{\text{spec}}}{m_{\text{pack}}}, 1 \right) \tag{6.72}$$

$$P_{\text{CP}}^{2\text{h}} = E_{\text{dis}}^{\text{CPCV}} \times \min \left(1.11 - 1.7 \frac{E_{\text{dis}}^{\text{spec}}}{m_{\text{pack}}}, 1 \right) \tag{6.73}$$

Given the potential for the proposed performance extrapolation model to enable rapid standardized performance characterization of second-life battery packs, the benefits of v_{mod} over m_{pack} suggest that v_{mod} should be a standard specification for the second-life battery supply chain. As explained in Section 3.4.4, the European Union will be requiring battery passports for new EV batteries starting in 2027, and other governments will likely follow suit. Total module volume could be included in battery passports to facilitate performance characterization.

6.6.5. Recommended Use Cases

Due to the uncertainties and advanced technical requirements associated with the single-dataset solution, the two dataset solution is presently recommended as the preferred option for the performance extrapolation model. While the two-dataset solution requires approximately 8 to 12 more hours of testing time compared to the single-dataset solution, the test duration is still significantly shorter than the test methods used to characterize second-life battery performance in this research project, requiring about 1.5 days for complete performance characterization instead of a week or more. The two-dataset solution is sufficiently simple, accurate, and robust that other researchers and project developers can adopt the method as described in this chapter without the need for additional experimental verification. One opportunity for verification would be confirmation that other passive-cooled and liquid-cooled packs adhere to the proposed empirical temperature rise equations.

While the two-dataset solution is likely the more reliable option for testing a second-life battery pack upon initial acquisition, the single-dataset solution could still prove valuable during second-life operation. The two-dataset solution will determine σ, b_η, and b_q for a given battery pack prior to commercial deployment in a second-life energy storage system, which will enable the prediction of E_{dis}, $\bar{E}_v$, ζ, η, $T_{\max}$, T_{avg}, and t_{cool} at any power rate at the present SOH of the battery. Throughout second-life operation, the performance of the battery should be recharacterized periodically to ensure that appropriate control settings are applied and that the economic expectations of the battery reflect its present capabilities. In this operational scenario, the time required for performance characterization must be minimized since this will interrupt the normal functioning of the battery. Since σ will have already been experimentally determined for the battery in question, the SCPP test cycle and single-dataset extrapolation technique can be applied reliably, enabling recharacterization of E_{dis}, $\bar{E}_v$, ζ, η, $T_{\max}$, T_{avg}, and t_{cool} in just 4 to 8 hours. This approach will assume that σ has not changed significantly with degradation, but it provides an opportunity to update b_η and b_q at the present SOH of the battery. The dependence of σ on SOH must be explored and quantified for different EV battery designs before this approach can be recommended.

6.7. Chapter Summary

Chapter 4 and Chapter 5 respectively demonstrated that the five tested EV battery packs exhibit significant diversity in terms of both design and performance. Chapter 6 has demonstrated that, in spite of this diversity, all tested battery packs seem to follow consistent patterns which can be used to map their performance over a continuous range of power rates for SCP testing. The practical implication of this apparent universality is the possibility of extrapolating performance results from a few experimental datapoints. Chapter 6 has therefore proposed and demonstrated a performance extrapolation model based on a series of novel empirical equations that describe how electrical and thermal performance metrics change with the applied power rate. This model has the potential to drastically reduce the time and resources required to fully characterize the electrical and thermal performance of second-life battery packs in a way that facilitates direct comparison of different EV battery designs. The proposed model offers a new tool to aid in the research and development of second-life battery energy storage systems, and presents an opportunity to establish a standardized system of performance evaluation. It should be reiterated here that the proposed methods have been developed for the scenario where a full EV battery pack can be repurposed without significant modifications (e.g. removing failed cell groups).

Four key developments have enabled the construction of the performance extrapolation model. The first development is the defining of a novel electrical performance metric, which has been named the average volumetric heat generation rate $\dot{\bar{q}}_v$. The second development is the modification of the Peukert equation, which allows for accurate modelling of discharge energy E_{dis} as a function of discharge duration t_{dis} for all tested battery packs in the range of 1 h $\leq t_{\mathrm{dis}} \leq$ 4 h. The third development is the discovery that the cycle energy efficiency η can be modelled accurately as a function of t_{dis} for all tested battery packs using a power curve, and the subsequent derivation of a novel equation that accurately models $\dot{\bar{q}}_v$ as a function of t_{dis}. The fourth development is the discovery that the cycle maximum ΔT_{max} and cycle average ΔT_{avg} temperature rise can be modelled accurately as a function of $\dot{\bar{q}}_v$ for all tested battery packs using a power curve, and that all

passive-cooled packs share a common dependence on $\dot{\bar{q}}_v$ in this regard. These novel mathematical contributions are summarized in Table 6.1.

Table 6.1 Summary of novel mathematical contributions.

Name	**Formula**
Definition of average volumetric heat generation rate	$\dot{\bar{q}}_v = \frac{E_{\text{dis}}}{v_{\text{mod}} t_{\text{dis}}} \left(\frac{1-\eta}{1+\eta}\right)$
Adjusted Peukert equation	$\gamma E_{\text{dis}} {t_{\text{dis}}}^{\frac{1}{\sigma}-1} = constant$
Definition of Peukert adjustment factor	$\gamma = 0.12 {t_{\text{dis}}}^{-2} - 0.15 {t_{\text{dis}}}^{-1} + 1.03$
Empirical energy efficiency equation	$(1-\eta) {t_{\text{dis}}}^{b_\eta} = constant$
Empirical heat generation equation	$\gamma \dot{\bar{q}}_v {t_{\text{dis}}}^{b_q} = constant$
Approximation of heat generation exponent	$b_q \approx \frac{1}{\sigma} + b_\eta$
Empirical maximum temperature rise equation	$\Delta T_{\max} {\dot{\bar{q}}_v}^{-b_{T_{\max}}} = constant$
Empirical average temperature rise equation	$(\Delta T_{\text{avg}} + offset) {\dot{\bar{q}}_v}^{-b_{T_{\text{avg}}}} = constant$

Two viable solutions to the performance extrapolation model have been described in detail. The proposed 'two-dataset solution' requires test data acquired at two different CP rates, while the proposed 'single-dataset solution' requires test data acquired at just one CP rate with the addition of power pulses during discharge and charge. The single dataset solution requires less time to acquire the necessary experimental data, but will require further experimental refinement and verification before it can be applied with confidence to all second-life battery packs. The two-dataset solution requires more test time, but its present design is already robust and can be applied with confidence to any second-life battery pack. Since the two-dataset solution still provides a significant reduction in the testing requirements and safety risks associated with second-life battery performance characterization, this method is recommended for adoption by second-life battery researchers and developers.

Potential alternative versions of the model have also been presented, including variants applicable to asymmetrical CP cycles or CC cycles, as well a variant based on pack mass as a more readily accessible battery parameter compared to total module volume. Based on the available data, the recommended model is based on SCP cycles and total module volume.

As described in Section, 3.4.1, second-life battery researchers are already working toward developing the best methods for rapid estimation of SOH and RUL. However, these methods do not fully characterize the electrical and thermal performance of a given EV battery. While it could be the case that the methods proposed in this chapter are not fast enough for second-life battery companies to be able to economically apply the methods to every single EV battery they process, the proposed methods are at the very least a viable solution for establishing *baseline* electrical and thermal performance characteristics for each unique EV battery pack design. Rapid SOH and RUL test results for a given EV battery sample in the production line could then be integrated with the established baseline performance of the battery design in question. It is recommended that this opportunity be explored through collaborations between researchers and the second-life battery industry.

The one battery performance metric from Chapter 5 that could not be modelled in a way that applies to all tested battery packs and TMS types is the average pack temperature differential $\Delta T_{\mathrm{diff}}^{\mathrm{avg}}$, due to the unique temperature distribution characteristics of individual EV battery designs. Chapter 7 will propose a novel thermal modelling tool which accounts for heat diffusion across second-life battery packs, focusing on one specific EV battery to demonstrate a proof of concept.

Chapter 7 SPATIAL EXTRAPOLATION MODEL FOR SECOND-LIFE BATTERY PACK TEMPERATURES

Chapter 5 demonstrated that significant temperature distributions can arise in EV battery packs, especially when operated with passive thermal management. Chapter 6 further demonstrated that these temperature distributions are strongly dependent on module and pack design and thus cannot be universally modelled with simple empirical relationships. Chapter 7 will propose and demonstrate a novel thermal modelling methodology to address a temperature distribution challenge specific to second-life battery packs.

This chapter has been published in the following journal article:

> C. White, L. G. Swan, Spatial extrapolation of temperature measurements in second-life battery packs using simplified thermal network modelling, Journal of Energy Storage 112 (2025) 115476. [357]

Chris White is the principal researcher and author for the article, which was completed over the course of this research project. The work is reprinted here under the terms of the license agreement with Elsevier, which is provided in Appendix D.

7.1. Motivation and Concept

Section 3.4.1 described the advantages and disadvantages of pack-level and module-level repurposing. Significant savings in time, labour, and material costs can be realized if pack-level repurposing can be done without making any modifications to the pack, but this offers little opportunity to customize the battery for a second-life system. One potential disadvantage of this is in regard to temperature monitoring. If the pack is repurposed without modification, the second-life operator will only be able to monitor the built-in temperature sensors installed at specific locations within the pack by the original manufacturer. In some cases, the original temperature sensor locations may not adequately capture the thermal performance metrics which the second-life operator wishes to monitor. This is especially likely if the EV battery pack will be operated with a different TMS in second life compared to EV service. For example, many modern EV battery packs are designed with liquid-cooling capability in EV service, but the built-in temperature monitoring system may not be adequate if a second-life project developer elects to operate

the battery pack with passive cooling. As an alternative to costly retrofitting measures, a numerical model could be used to accurately predict temperatures at desired locations in the pack without adding physical sensors. This would help to overcome one of the challenges of repurposing unmodified EV battery packs and thereby facilitate more cost-effective second-life battery project development.

Section 3.5.4 reviewed a variety of thermal modelling techniques applied to lithium-ion batteries, and concluded that theoretical models are not suited for second-life applications due to their reliance on proprietary battery design specifications. However, if a second-life operator has access to real-time temperature measurements from the built-in temperature sensors of a repurposed EV battery pack, these measurements could serve as inputs to an empirical thermal model. It was concluded further that while many empirical models require computationally expensive numerical simulations to account for three-dimensional heat diffusion at the pack level, thermal network models offer a simplified approach to empirical modelling of EV battery pack temperature distributions. A novel battery thermal network model called 'spatially extrapolated temperature sensors' (SETS) will be developed throughout this chapter with the goal of predicting EV battery pack temperature distributions based on real-time temperature measurements from within the pack.

The proposed SETS methodology includes the design of a thermal network featuring 'known' temperature nodes (i.e. temperatures measured by sensors installed by the original battery manufacturer) and 'unknown' temperature nodes (i.e. additional temperatures a second-life operator would like to monitor without retrofitting new sensors inside the pack). The numerical solution of the thermal network provides estimates for the 'unknown' temperatures based on real-time measurements of the 'known' temperatures. Since many of the physical and thermal properties of EV battery packs are not known to second-life battery operators, the parameters of the SETS model must be determined empirically. This is done by opening a 'pilot pack' for a given EV battery design, retrofitting additional temperature sensors at desired locations within the pack, and recording experimental test data representing commercial second-life battery operation. Parameter optimization is then used to fit the predicted 'unknown' temperatures of the SETS model to the measurements of the retrofitted sensors. Once the model parameters are optimized for the pilot pack, the

SETS model can be applied to an unlimited number of packs for the given EV battery design without needing to open or modify these packs with retrofitted temperature sensors. Note that the proposed methodology is related to inverse heat conduction problems, which use temperature measurements as inputs to estimate thermal properties and/or heat flux values [358].

This chapter presents a proof of concept for SETS technology by demonstrating the design and implementation of a SETS model for the 2019 Tesla Model 3 SR+ battery pack described in Section 4.1, which uses an active-liquid TMS in EV service. A simplified thermal network is developed to establish a robust mathematical relationship between a 'known' temperature node and an 'unknown' temperature node within the pack while operating with a passive-air TMS (i.e. natural convection) in second-life service. The established model does not require specification of any thermal or electrochemical properties for the battery. Instead, the model is governed by a set of seven constant parameters which must be determined empirically using experimental test data. The nuances of three-dimensional heat diffusion, temperature-dependent natural convection coefficients, and radiation are embedded within the SETS model using novel mathematical techniques. Novel methods for constraining the parameter optimization process are also presented. The target for model accuracy is defined as achieving a root-mean-square error within 0.5 °C, since this is a common thermistor measurement resolution.

It will ultimately be demonstrated that a simplified thermal network is sufficient to create a reliable SETS model that can accurately predict a single 'unknown' battery temperature node over a practical range of operating conditions based on real-time measurements of the ambient temperature and a single 'known' battery temperature node once the model parameters are optimized. This opens the door for future development of more advanced SETS models that can map real-time pack temperature distributions based on a small number of built-in temperature sensors during second-life operation.

7.2. Thermal Model

This section will first review the design characteristics of the Tesla Model 3 SR+ battery pack with a focus on heat transfer, temperature distribution, and temperature monitoring.

A simplified thermal network will then be proposed to model key heat flows between specific temperature nodes. A system of heat transfer equations will then be devised based the proposed thermal network. Novel mathematical techniques will be used to convert the heat transfer equations into a functional SETS model.

7.2.1. Battery Characteristics

Figure 7.1 shows the built-in temperature monitoring system a 2019 Tesla Model 3 SR+ battery pack. A BMS circuit board is adhered to the upper face of each of the four battery modules towards the rear of the pack, which is where the liquid coolant flows out of the modules. Each BMS circuit board features a pair of thermistors that make direct contact with exposed cell housing surfaces via small cutouts in the top of the plastic module housing. This thermistor placement allows for cell temperature monitoring near the liquid outlet, where cell temperatures would expected to be highest in liquid-cooled operation.

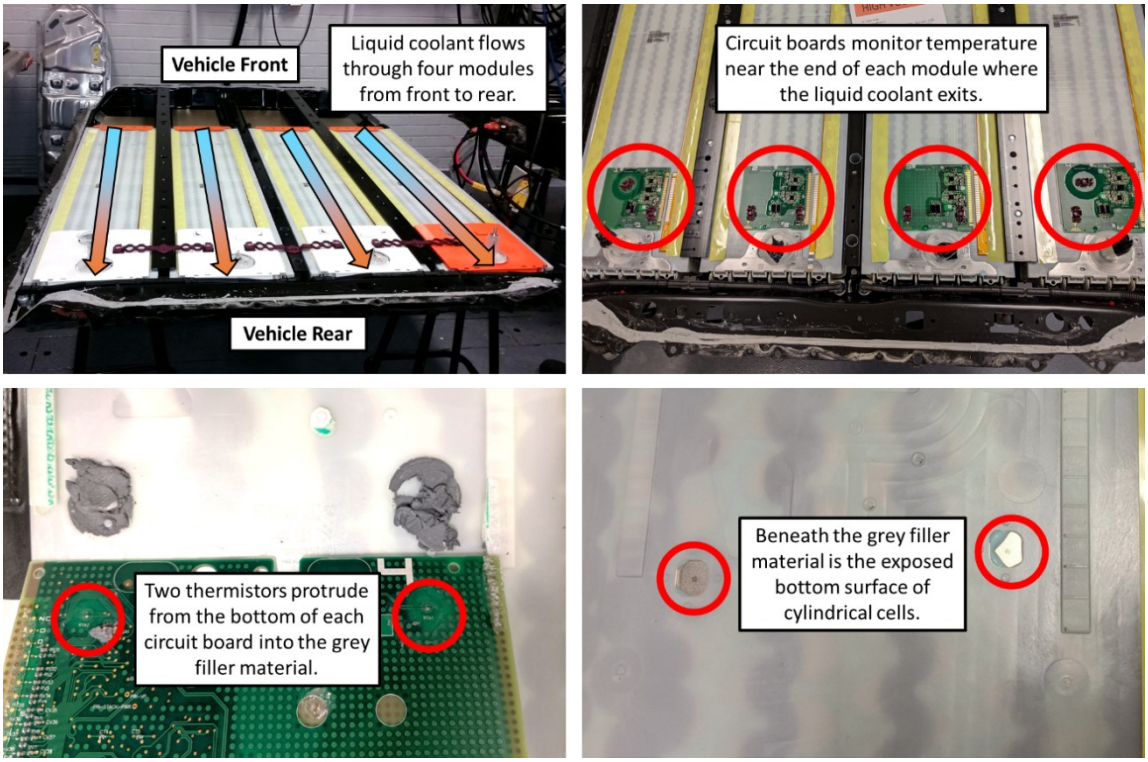


Figure 7.1 The built-in thermistors of a 2019 Tesla Model 3 SR+ battery pack.

The temperature sensor locations in Figure 7.1 are appropriate for capturing maximum pack temperatures when the battery is liquid-cooled. However, if a second-life project developer elects to operate the battery pack with passive cooling for the sake of simplicity

and cost, then Tesla's built-in temperature monitoring system would not be able to capture the highest pack temperature T_{high} (likely occurring near the middle of the inner modules), nor the increased pack temperature differential between T_{high} and the lowest pack temperature T_{low} (likely occurring near the outer module corners). This additional information would help ensure safe and economical operation for a passive-cooled second-life system. Specific examples might include more appropriate control of power envelopes or more accurate projection of capacity degradation.

The Tesla Model 3 SR+ battery is a good example of the complexity of heat transfer in EV battery packs. This is illustrated in Figure 7.2, where the red arrows represent conduction pathways and the blue arrows represent natural convection and radiation pathways. As described in Section 4.1, each of the four modules consists of 744 cylindrical cells and seven aluminum liquid channels running along the module length, with a foam filler material surrounding each cell except where it contacts the adjacent liquid channel. When the battery is operated with liquid cooling, forced convection in the liquid channels dominates the thermal system (as demonstrated in Section 5.4), but when the battery is operated with passive cooling, numerous other heat transfer pathways must be accounted for in the thermal model. These include three-dimensional heat diffusion through the modules and pack housing, as well as natural convection and radiation at both the inner and outer surfaces of the pack housing. The modules will share this anisotropic thermal conductivity of the cylindrical cells (discussed in Section 2.6.5), and the module design further complicates the heat diffusion pattern. For instance, the presence of the liquid channels means that the module thermal conductivity is anisotropic in three dimensions, since there are essentially 17 series thermal resistances through the width of each module (alternating between seven liquid channels and eight layers of cells/foam, as well as the outer module walls), and two parallel thermal resistances along the length of each module (the liquid channels and the cells/foam). The liquid channels themselves are also anisotropic since there will either be liquid coolant or air occupying the space within the channels. The composite thermal conductivity of the cells/foam is also dependent on the properties and geometry of each. The many influential factors of geometry and material properties will be difficult to quantify without manufacturer specifications.

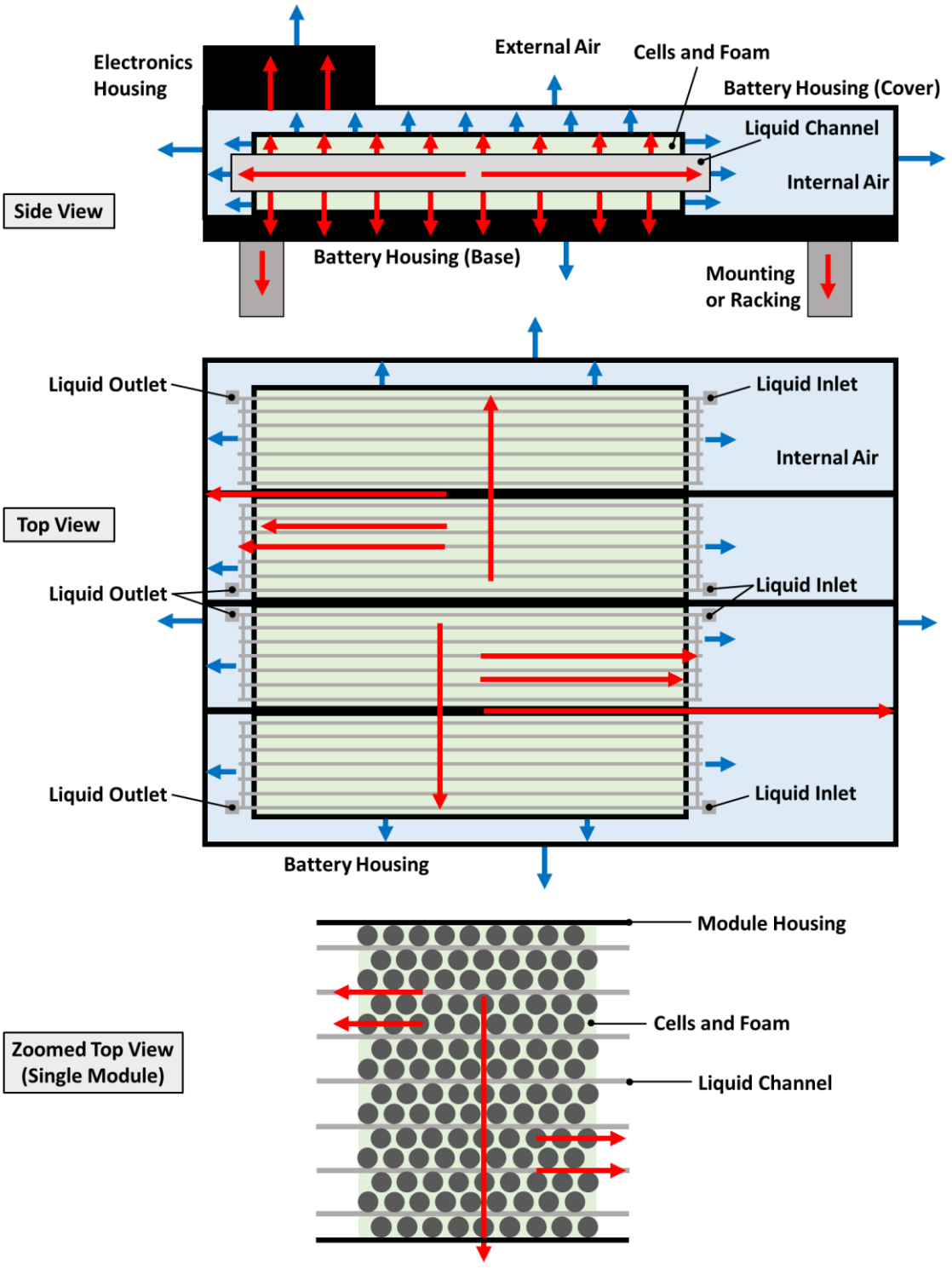


Figure 7.2 Illustration of heat transfer in an operational Tesla Model 3 SR+ battery pack. Red arrows represent heat conduction pathways. Blue arrows represent convection and radiation pathways. Not drawn to scale.

In commercial second-life battery applications, a series of SETS models would need to be developed for a given EV battery pack in order to estimate any specific temperature nodes the battery operator is interested in, including those representing T_{high} and T_{low}. This research project focuses on providing a proof-of-concept SETS model for a single 'unknown' temperature node rather than achieving a comprehensive characterization of the battery pack temperature distribution. For the Tesla Model 3 SR+ battery pack, a SETS model is most easily demonstrated for the cells at the outer corners of the pack, since the exposed surfaces of these particular cells facilitates the retrofitting of temperature sensors (see Figure 4.5) for acquisition of empirical training data (discussed in Section 7.4). The other cells in the pack cannot be directly accessed without cutting away portions of the plastic module housing, and while this should be possible if done carefully, this research project focuses on the more accessible option for the purpose of a proof of concept. A single SETS model will therefore be designed for one of the corner cells, which should be representative of T_{low} when the battery pack is operated with passive cooling.

7.2.2. Simplified Thermal Network

Given the numerous complexities and sources of uncertainty in building a complete three-dimensional thermal model, a simplified thermal network is described here for the purpose of developing a practical SETS model. Figure 7.3 illustrates the chosen thermal network design, which features only two cells: cell Z representing a cell located in the interior of an outer module, and cell X representing a cell located at the corner of the same outer module (and thus near the corner of the pack). Cell Z is chosen as one of the cells that is measured by Tesla's built-in thermistors as shown in Figure 7.1. The temperature of cell X is not monitored by Tesla's built-in thermistors,, but it is expected be near T_{low} based on its location at the corner of the pack. In this study, T_{z} refers to the 'known' temperature at the top of cell Z, while T_{x} refers to the 'unknown' temperature at the exposed cylindrical wall of cell X.

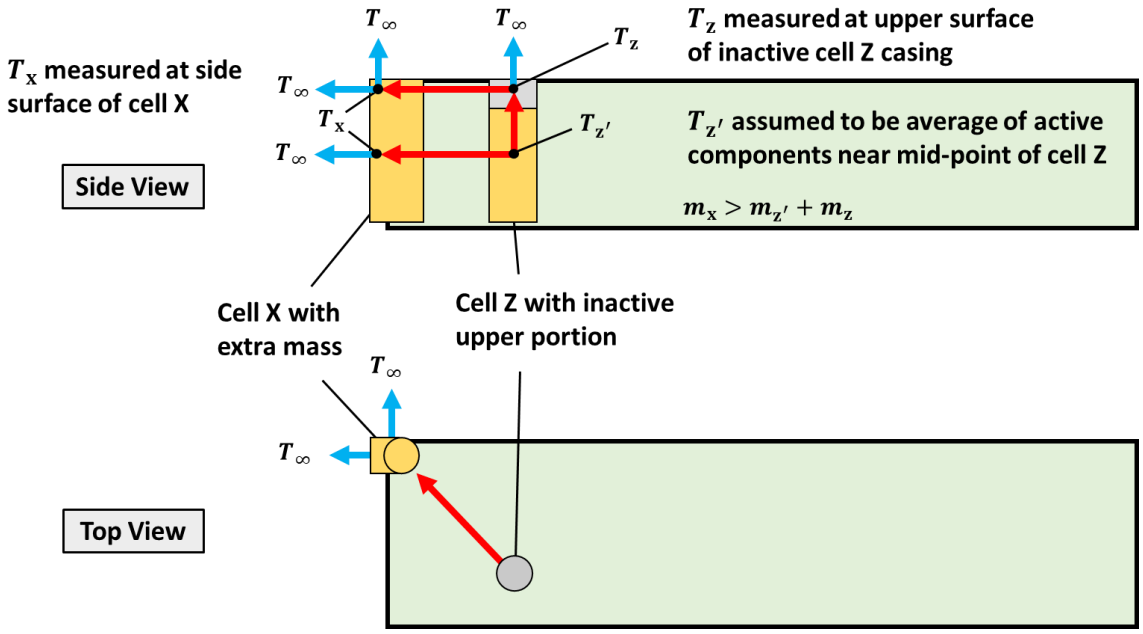


Figure 7.3 Illustration of the proposed simplified thermal model. Red arrows represent heat conduction pathways. Blue arrows represent convection and radiation pathways. Yellow masses generate heat, while grey masses do not. Not drawn to scale.

As shown in Figure 7.3, the module is treated as though cell X and cell Z are the only heat generation sources, while the remainder of the module volume is thermally insulating except for discrete thermally conductive pathways. The heat capacity of the internal air and battery housing cover are neglected, allowing for simplified heat dissipation from the exposed cell surfaces directly to the external air. Cell Z is divided into two discrete masses as a simple means of modelling axial heat diffusion within cell Z, the effects of which were observed experimentally (discussed later in Section 7.5.1). The lower mass $m_{z'}$ is modelled as an active cell stack which generates heat and has an average temperature $T_{z'}$ that cannot be measured directly. The upper mass m_z is modelled as an inactive cell housing material which does not generate heat and has a surface temperature of T_z that is measured by a temperature sensor. Note that in the case of the Tesla Model 3 battery, the steel cell housing serves as part of the negative electrode and therefore carries current, but the generated heat will be small compared to the heat generated by the cell stack and is therefore neglected. A heat conduction pathway is placed between $T_{z'}$ and T_z, while a convection/radiation pathway is placed between T_z and the ambient temperature T_∞.

Unlike cell Z, the effects of heat diffusion within cell X were not observed experimentally, possibly due to a masking effect caused by greater heat dissipation from cell X compared to cell Z. Cell X is therefore treated as a single mass m_{x} with an average surface temperature T_{x} that is measured by a retrofitted temperature sensor. A heat conduction pathway is placed between $T_{\mathrm{z}'}$ and T_{x} as well as between T_{z} and T_{x}, while a convection/radiation pathway is placed between T_{x} and T_{∞}. In the real system, there is likely lateral heat conduction into cell Z from warmer regions of the pack, and this is not shown explicitly in Figure 7.3. However, the net lateral heat conduction should be away from cell Z, and the simplified model in Figure 7.3 aims to approximate this net effect.

It is important to observe in Figure 7.3 that cell X is located next to the extended end of the liquid channel and the affixed liquid outlet, which provides additional inactive heat capacity at the corner of the module compared to the interior. Since heat diffusion from cell X to this extra mass is not included in the thermal network, this effectively means that the model assumes $m_{\mathrm{x}} > m_{\mathrm{z}'} + m_{\mathrm{z}}$.

Figure 7.3 is a significant simplification of a complex thermal system, but it provides an approximation of four key features that govern the real system: heat conducts axially from the core of cell Z to the upper surface; heat conducts laterally away from cell Z to cooler regions near the module edges; heat conducts laterally into cell X from warmer regions in the module interior; and heat dissipates from the exposed cell surfaces to the external environment.

7.2.3. System Equations

The thermal network design in Figure 7.3 includes three masses subject to heat transfer. The first step in deriving a mathematical equations for the SETS model is to apply an energy balance to all three masses based on Equation 7.1, where $\dot{q}_{\mathrm{gen}}$ is the heat generation rate, $\dot{q}_{\mathrm{in}}$ is the heat inflow rate, and $\dot{q}_{\mathrm{out}}$ is the heat outflow rate. The specific heat capacity c_p is assumed to be uniform throughout the battery module.

$$mc_p \frac{\mathrm{d}T}{\mathrm{d}t} = \dot{q}_{\mathrm{gen}} + \dot{q}_{\mathrm{in}} - \dot{q}_{\mathrm{out}} \tag{7.1}$$

This general energy balance is used to derive three system equations for m_{x}, $m_{z'}$, and m_z as stated in Equations 7.2, 7.3, and 7.4, respectively. Definitions of the various terms are provided in the paragraphs below.

$$\frac{\mathrm{d}T_{\mathrm{x}}}{\mathrm{d}t} = \Theta_{\mathrm{x}} + \frac{T_{\mathrm{z}} - T_{\mathrm{x}}}{\lambda_{\mathrm{x}}\lambda_{\mathrm{z}}\tau_{\mathrm{z'x}}} + \frac{T_{\mathrm{z'}} - T_{\mathrm{x}}}{\lambda_{\mathrm{x}}\tau_{\mathrm{z'x}}} - \frac{T_{\mathrm{x}} - T_{\infty}}{\tau_{\mathrm{x}\infty}} \tag{7.2}$$

$$\frac{\mathrm{d}T_{\mathrm{z'}}}{\mathrm{d}t} = \Theta_{\mathrm{z'}} - \frac{T_{\mathrm{z'}} - T_{\mathrm{x}}}{\tau_{\mathrm{z'x}}} - \frac{T_{\mathrm{z'}} - T_{\mathrm{z}}}{\tau_{\mathrm{z'z}}} \tag{7.3}$$

$$\frac{\mathrm{d}T_{\mathrm{z}}}{\mathrm{d}t} = \lambda_{\mathrm{z}}\frac{T_{\mathrm{z'}} - T_{\mathrm{x}}}{\tau_{\mathrm{z'z}}} - \frac{T_{\mathrm{z}} - T_{\mathrm{x}}}{\tau_{\mathrm{z'x}}} - \frac{T_{\mathrm{z}} - T_{\infty}}{\tau_{\mathrm{z}\infty}} \tag{7.4}$$

The system equations feature two heat diffusion time constants $\tau_{\mathrm{z'x}}$ and $\tau_{\mathrm{z'z}}$ as defined in Equations 7.5 and 7.6, as well as two heat dissipation time constants $\tau_{\mathrm{x}\infty}$ and $\tau_{\mathrm{z}\infty}$ as defined in Equations 7.7 and 7.8. These terms respectively quantify the rate of heat transfer from $m_{\mathrm{z'}}$ to m_{x}, from $m_{\mathrm{z'}}$ to m_{z}, from m_{x} to the ambient environment, and from m_{z} to the ambient environment. In these equations, h, k, A, and L respectively represent heat dissipation coefficients (i.e. convection and radiation combined), thermal conductivities, heat transfer areas, and heat transfer lengths. Since the thermal properties of the battery pack are unknown, the four time constants are employed in the system equations to reduce the number of parameters in the SETS model. Note that the thermal network design in Figure 7.3 implies $L_{\mathrm{zx}} = L_{\mathrm{z'x}}$ and $\frac{A_{\mathrm{zx}}}{A_{\mathrm{z'x}}} = \frac{m_{\mathrm{z}}}{m_{\mathrm{z'}}}$.

$$\tau_{\mathrm{z'x}} = \frac{m_{\mathrm{z'}}c_p L_{\mathrm{z'x}}}{k_{\mathrm{z'x}}A_{\mathrm{z'x}}} \tag{7.5}$$

$$\tau_{\mathrm{z'z}} = \frac{m_{\mathrm{z'}}c_p L_{\mathrm{z'z}}}{k_{\mathrm{z'z}}A_{\mathrm{z'z}}} \tag{7.6}$$

$$\tau_{\mathrm{x}\infty} = \frac{m_{\mathrm{x}}c_p}{h_{\mathrm{x}}A_{\mathrm{x}\infty}} \tag{7.7}$$

$$\tau_{\mathrm{z}\infty} = \frac{m_{\mathrm{z}}c_p}{h_{\mathrm{z}}A_{z\infty}} \tag{7.8}$$

The parameters λ_x and λ_z are used to denote 'mass ratios' that quantify the relative magnitudes of m_x, $m_{z'}$, and m_z, as defined by Equations 7.9 and 7.10. These parameters are employed in Equations. 7.2 and 7.4 instead of using six unique heat diffusion time constants, thereby reducing the number of parameters in the SETS model. Note that the values of λ_x and λ_z are not predefined in the model since they are tools used to approximate the effects of heat diffusion and do not necessarily represent true physical properties of the battery pack.

$$\lambda_x = \frac{m_x}{m_{z'}} \tag{7.9}$$

$$\lambda_z = \frac{m_{z'}}{m_z} \tag{7.10}$$

Finally, the variables Θ_x and $\Theta_{z'}$ are used to denote the heat generation rates of cell X and cell Z per unit heat capacity, as defined by Equations 7.11 and 7.12. These quantities will hereafter be referred to as 'adiabatic temperature rates' since they represent the temperature rate of change that would result from cell heat generation in a hypothetical adiabatic condition. Recall that $m_{z'}$ refers to the heat generating portion of cell Z.

$$\Theta_x = \frac{\dot{q}_{gen,x}}{m_x c_p} \tag{7.11}$$

$$\Theta_{z'} = \frac{\dot{q}_{gen,z'}}{m_{z'} c_p} \tag{7.12}$$

Overall, the thermal network is now described by six constant parameters $\tau_{z'x}$, $\tau_{z'z}$, $\tau_{x\infty}$, $\tau_{z\infty}$, λ_x, and λ_z as well as two adiabatic temperature rate variables Θ_x and Θ_z. Section 7.3 will modify $\tau_{x\infty}$ and $\tau_{z\infty}$ to account for the temperature dependence of natural convection coefficients. A seventh constant parameter will also be introduced in Section 7.3 to separate radiation from natural convection.

7.2.4. Numerical Solutions

To achieve the simplest solution to the three system equations, it is preferable to express the equations in the simplified forms shown in Equations 7.13 through 7.15.

$$\frac{\mathrm{d}T_{\mathrm{x}}}{\mathrm{d}t} = \Theta_{\mathrm{x}} - \frac{T_{\mathrm{x}} - T_{\infty}}{\tau_{\mathrm{x}}} \tag{7.13}$$

$$\frac{\mathrm{d}T_{\mathrm{z}'}}{\mathrm{d}t} = \Theta_{z'} - \frac{T_{\mathrm{z}'} - T_{\infty}}{\tau_{\mathrm{z}'}} \tag{7.14}$$

$$\frac{\mathrm{d}T_{\mathrm{z}}}{\mathrm{d}t} = -\frac{T_{\mathrm{z}} - T_{\infty}}{\tau_{\mathrm{z}}} \tag{7.15}$$

These simplified equations require τ_{x}, $\tau_{\mathrm{z}'}$, and τ_z to have the definitions given in Equations 7.16, 7.17, and 7.18, respectively. These quantities will be referred to as 'time variables' to distinguish them from time constants. The time variables are a function of temperature as well as the time constants and mass ratios defined in Section 7.2.3.

$$\frac{1}{\tau_{\mathrm{x}}} = \frac{1}{\tau_{\mathrm{x}\infty}} - \frac{1}{\lambda_{\mathrm{x}}\tau_{\mathrm{z}'\mathrm{x}}}\left(\frac{T_{\mathrm{z}'} - T_{\mathrm{x}}}{T_{\mathrm{x}} - T_{\infty}}\right) - \frac{1}{\lambda_{\mathrm{x}}\lambda_{\mathrm{z}}\tau_{\mathrm{z}'\mathrm{x}}}\left(\frac{T_{\mathrm{z}} - T_{\mathrm{x}}}{T_{\mathrm{x}} - T_{\infty}}\right) \tag{7.16}$$

$$\frac{1}{\tau_{\mathrm{z}'}} = \frac{1}{\tau_{\mathrm{z}'\mathrm{x}}}\left(\frac{T_{\mathrm{z}'} - T_{\mathrm{x}}}{T_{\mathrm{z}'} - T_{\infty}}\right) + \frac{1}{\tau_{\mathrm{z}'\mathrm{z}}}\left(\frac{T_{\mathrm{z}'} - T_{\mathrm{z}}}{T_{\mathrm{z}'} - T_{\infty}}\right) \tag{7.17}$$

$$\frac{1}{\tau_{\mathrm{z}}} = \frac{1}{\tau_{\mathrm{z}\infty}} + \frac{1}{\tau_{\mathrm{z}'\mathrm{x}}}\left(\frac{T_{\mathrm{z}} - T_{\mathrm{x}}}{T_{\mathrm{z}} - T_{\infty}}\right) - \frac{\lambda_{\mathrm{z}}}{\tau_{\mathrm{z}'\mathrm{z}}}\left(\frac{T_{\mathrm{z}'} - T_{\mathrm{z}}}{T_{\mathrm{z}} - T_{\infty}}\right) \tag{7.18}$$

Analytical solutions can be derived for the three simplified system equations in Equations 7.13 through 7.15. The analytical steps are detailed in Appendix A. The final results are shown in Equations 7.19 through 7.21, where T_{∞} is assumed to be non-constant and the zero subscript indicates an initial condition at time $t = 0$.

$$T_{\mathrm{x}} = \mathrm{e}^{-\frac{t}{\tau_{\mathrm{x}}}}\left(T_{\mathrm{x},0} + \int_0^t \mathrm{e}^{\frac{t}{\tau_{\mathrm{x}}}}\left(\frac{1}{\tau_{\mathrm{x}}}T_{\infty} + \Theta_{\mathrm{x}}\right)\mathrm{d}t\right) \tag{7.19}$$

$$T_{\mathrm{z}'} = \mathrm{e}^{-\frac{t}{\tau_{\mathrm{z}'}}}\left(T_{\mathrm{z}',0} + \int_0^t \mathrm{e}^{\frac{t}{\tau_{\mathrm{z}'}}}\left(\frac{1}{\tau_{\mathrm{z}'}}T_{\infty} + \Theta_{\mathrm{z}'}\right)\mathrm{d}t\right) \tag{7.20}$$

$$T_{\mathrm{z}} = \mathrm{e}^{-\frac{t}{\tau_{\mathrm{z}}}}\left(T_{\mathrm{z},0} + \int_0^t \frac{1}{\tau_{\mathrm{z}}}T_{\infty}\mathrm{e}^{\frac{t}{\tau_{\mathrm{z}}}}\mathrm{d}t\right) \tag{7.21}$$

Note that these solutions can only be derived analytically if τ_{x}, $\tau_{\mathrm{z}'}$, and τ_{z} are treated as constants. Since these 'time variables' are not constant, Equations 7.19 through 7.21 are

not true analytical solutions. However, these solutions provide a starting point from which functional numerical solutions can be developed. The next step is to convert the solutions from continuous form to discretized form, as shown in Equations 7.22 through 7.24.

$$T_{\mathrm{x},j} = \mathrm{e}^{-\frac{t_j}{\tau_{\mathrm{x},j}}}\left(T_{\mathrm{x},0} + \sum_{i=1}^{j} \mathrm{e}^{\frac{t_i}{\tau_{\mathrm{x},i}}}\left(\frac{1}{\tau_{\mathrm{x},i}}T_{\infty,i} + \Theta_{\mathrm{x},i}\right)\Delta t_i\right) \tag{7.22}$$

$$T_{\mathrm{z}',j} = \mathrm{e}^{-\frac{t_j}{\tau_{\mathrm{z}',j}}}\left(T_{\mathrm{z}',0} + \sum_{i=1}^{j} \mathrm{e}^{\frac{t_i}{\tau_{\mathrm{z}',i}}}\left(\frac{1}{\tau_{\mathrm{z}',i}}T_{\infty,i} + \Theta_{z',i}\right)\Delta t_i\right) \tag{7.23}$$

$$T_{\mathrm{x},j} = \mathrm{e}^{-\frac{t_j}{\tau_{\mathrm{z},j}}}\left(T_{\mathrm{z},0} + \sum_{i=1}^{j} \mathrm{e}^{\frac{t_i}{\tau_{\mathrm{z},i}}}\left(\frac{1}{\tau_{\mathrm{z},i}}T_{\infty,i}\right)\Delta t_i\right) \tag{7.24}$$

These discretized equations require a summation of calculated values from time interval $i = 1$ to time interval $i = j$ in order to calculate the temperature for interval j. This method is computationally expensive to repeat over an indefinite series of real-time datapoints, as would be the case in a commercial second-life battery project. To reduce the computational requirements, the discretized equations can be converted to a functional recursive form. The derived recursive system equations are shown in Equations 7.25 through 7.27. The complete conversion steps are detailed in Appendix B.

$$T_{\mathrm{x},i} = T_{\mathrm{x},i-1}\mathrm{e}^{-\frac{\Delta t_i}{\tau_{\mathrm{x},i}}} + \frac{\Delta t_i}{\tau_{\mathrm{x},i}}T_{\infty,i} + \Theta_{\mathrm{x},i}\Delta t_i \tag{7.25}$$

$$T_{\mathrm{z}',i} = T_{\mathrm{z}',i-1}\mathrm{e}^{-\frac{\Delta t_i}{\tau_{\mathrm{z}',i}}} + \frac{\Delta t_i}{\tau_{\mathrm{z}',i}}T_{\infty,i} + \Theta_{\mathrm{z}',i}\Delta t_i \tag{7.26}$$

$$T_{\mathrm{z},i} = T_{\mathrm{z},i-1}\mathrm{e}^{-\frac{\Delta t_i}{\tau_{\mathrm{z},i}}} + \frac{\Delta t_i}{\tau_{\mathrm{z},i}}T_{\infty,i} \tag{7.27}$$

7.2.5. Heat Generation Approximation

The proposed SETS model seeks to describe T_{x} as a function of T_{z} and T_{∞} measurements, but Equations 7.25 through 7.27 show that T_{x} also depends on $\Theta_{\mathrm{z}'}$ (since τ_{x} is a function of $T_{\mathrm{z}'}$) and Θ_{x}. The model therefore requires that $\Theta_{\mathrm{z}'}$ and Θ_{x} be describable in terms of the

measured T_{z} and T_{∞}. Such a definition for $\Theta_{\mathrm{z}'}$ can be approximated by rearranging the differential form previously stated in Equation 7.14 and converting to discrete form using the finite difference method. These steps are carried out in Equations 7.28 and 7.29.

$$\Theta_{\mathrm{z}'} = \frac{\mathrm{d}T_{\mathrm{z}'}}{\mathrm{d}t} + \frac{T_{\mathrm{z}'} - T_{\infty}}{\tau_{\mathrm{z}'}} \tag{7.28}$$

$$\Theta_{\mathrm{z}',i} \approx \frac{T_{\mathrm{z}',i} - T_{\mathrm{z}',i-1}}{\Delta t_i} + \frac{T_{\mathrm{z}',i} - T_{\infty,i}}{\tau_{\mathrm{z}',i}} \tag{7.29}$$

Equation 7.29 is not useful since $T_{\mathrm{z}'}$ is unknown. However, the measured value $T_{\mathrm{z}}^{\mathrm{meas}}$ can be used to apply the numerical approximation shown in Equation 7.30. Note that $T_{\mathrm{z}}^{\mathrm{meas}}$ will henceforth be used to denote the 'known' temperature measured at the top of cell Z by the original temperature monitoring system of the battery pack, to distinguish from the value of T_{z} produced by the SETS model. Similarly, T_{∞} will henceforth be written as $T_{\infty}^{\mathrm{meas}}$ so that all measured temperatures are denoted as such. The variable α_{Θ} is a correction factor which will be defined in Section 7.2.6.

$$\Theta_{\mathrm{z}',i} \approx \alpha_{\Theta}\left(\frac{T_{\mathrm{z},i}^{\mathrm{meas}} - T_{\mathrm{z},i-1}^{\mathrm{meas}}}{\Delta t_i} + \frac{T_{\mathrm{z},i}^{\mathrm{meas}} - T_{\infty,i}^{\mathrm{meas}}}{\tau_{\mathrm{z}',i}}\right) \tag{7.30}$$

The validity of Equation 7.30 relies on the assumption that T_z and $T_{z'}$ exhibit similar rates of change. This is a reasonable assumption since T_z and $T_{z'}$ belong to the same cell and are only separated by axial heat diffusion, which is relatively fast in cylindrical lithium-ion cells (explained in Section 2.6.5). However, it should be recognized that the validity of this assumption may deteriorate at very high heat generation rates (e.g. high-power discharge at low SOC) or large step changes in heat generation (e.g. switching on or off at high power). This will be considered with the results of the SETS model in Section 7.5.

With $\Theta_{\mathrm{z}'}$ now adequately described in terms of known values, the SETS model requires an additional equation to relate Θ_{x} and $\Theta_{\mathrm{z}'}$. Based on the equation for the total reversible and irreversible heat generation rate of a cell (see Section 2.6.3), Θ can be redefined as

Equation 7.31, where I is the cell current ($I < 0$ for discharge), V is the cell voltage, V_{rev} is the cell reversible voltage, and $\frac{\partial V_{\text{rev}}}{\partial T}$ is the cell entropic heat coefficient.

$$\begin{aligned} \Theta &= \frac{\dot{q}_{\text{gen}}}{mc_p} \\ &= \frac{I(V - V_{\text{rev}}) + IT\frac{\partial V_{\text{rev}}}{\partial T}}{mc_p} \end{aligned} \tag{7.31}$$

The relationship between Θ_{x} and $\Theta_{\text{z}'}$ is therefore given by Equation 7.32.

$$\begin{aligned} \frac{\Theta_{\text{x}}}{\Theta_{\text{z}'}} &= \frac{m_{\text{z}'}\dot{q}_{\text{gen,x}}}{m_{\text{x}}\dot{q}_{\text{gen,z}'}} \\ &= \frac{m_{\text{z}'}I_{\text{x}}\left(V_{\text{x}} - V_{\text{rev}} + T_{\text{x}}\frac{\partial V_{\text{rev}}}{\partial T}\right)}{m_{\text{x}}I_{\text{z}'}\left(V_{\text{z}'} - V_{\text{rev}} + T_{\text{z}'}\frac{\partial V_{\text{rev}}}{\partial T}\right)} \end{aligned} \tag{7.32}$$

The quantity $V - V_{\text{rev}}$ depends on the cell internal resistance, which varies with temperature, SOC, and SOH. For aged second-life batteries, it is especially likely that any two series-connected cell groups in the battery pack will exhibit different voltages, but the BMS provides this voltage information. Current is equivalent in series-connected cells, but since each cell group in the Tesla Model 3 SR+ battery pack consists of 31 parallel-connected cells, it is not necessarily true that $I_{\text{x}} = I_{\text{z}'}$, and the BMS does not provide this current distribution information. Equation 7.32 also requires that V_{rev} and $\frac{\partial V_{\text{rev}}}{\partial T}$ are known as a function of SOC and SOH, and this information is rarely available for a given EV battery pack unless lengthy testing is carried out over a range of controlled temperatures in a specialized test chamber.

For this proof-of-concept SETS model, it is assumed that $\dot{q}_{\text{gen,x}} \approx \dot{q}_{\text{gen,z}'}$, which reduces Equation 7.32 to Equation 7.33. This assumption will prove adequate for this particular SETS model, but it may not always be an appropriate assumption for large and/or aged battery packs. This is discussed further in Section 7.6.1.

$$\Theta_{\mathrm{x}} \approx \frac{m_{\mathrm{z}'}}{m_{\mathrm{x}}}\Theta_{\mathrm{z}'}$$
$$\approx \frac{1}{\lambda_{\mathrm{x}}}\Theta_{\mathrm{z}'} \tag{7.33}$$

7.2.6. Functionality

A few final steps are required to make the three system equations functional for the SETS model. One unresolved issue is that the time variables τ_{x}, τ_{z}, and $\tau_{\mathrm{z}'}$ must be calculated from T_{x}, T_{z}, and $T_{\mathrm{z}'}$. This issue can be overcome by employing the finite difference method, whereby the values of τ_{x}, τ_{z}, and $\tau_{\mathrm{z}'}$ in time interval i are calculated using the temperatures in the previous time interval $i-1$. This method is expressed in Equations 7.34 through 7.36. Note that these equations use the modelled T_{z} instead of the measured $T_{\mathrm{z}}^{\mathrm{meas}}$ in order to maintain energy conservation within the model.

$$\tau_{\mathrm{x},i} = \frac{1}{\frac{1}{\tau_{\mathrm{x}\infty,i}} - \frac{1}{\lambda_{\mathrm{x}}\tau_{\mathrm{z}'\mathrm{x}}}\left(\frac{T_{\mathrm{z}',i-1} - T_{\mathrm{x},i-1}}{T_{\mathrm{x},i-1} - T_{\infty,i-1}^{\mathrm{meas}}}\right) - \frac{1}{\lambda_{\mathrm{x}}\lambda_{\mathrm{z}}\tau_{\mathrm{z}'\mathrm{x}}}\left(\frac{T_{\mathrm{z},i-1} - T_{\mathrm{x},i-1}}{T_{\mathrm{x},i-1} - T_{\infty,i-1}^{\mathrm{meas}}}\right)} \tag{7.34}$$

$$\tau_{\mathrm{z}',i} = \frac{1}{\frac{1}{\tau_{\mathrm{z}'\mathrm{x}}}\left(\frac{T_{\mathrm{z}',i-1} - T_{\mathrm{x},i-1}}{T_{\mathrm{z}',i-1} - T_{\infty,i-1}^{\mathrm{meas}}}\right) + \frac{1}{\tau_{\mathrm{z}'\mathrm{z}}}\left(\frac{T_{\mathrm{z}',i-1} - T_{\mathrm{z},i-1}}{T_{\mathrm{z}',i-1} - T_{\infty,i-1}^{\mathrm{meas}}}\right)} \tag{7.35}$$

$$\tau_{\mathrm{z},i} = \frac{1}{\frac{1}{\tau_{\mathrm{z}\infty,i}} + \frac{1}{\tau_{\mathrm{z}'\mathrm{x}}}\left(\frac{T_{\mathrm{z},i-1} - T_{\mathrm{x},i-1}}{T_{\mathrm{z},i-1} - T_{\infty,i-1}^{\mathrm{meas}}}\right) - \frac{\lambda_{\mathrm{z}}}{\tau_{\mathrm{z}'\mathrm{z}}}\left(\frac{T_{\mathrm{z}',i-1} - T_{\mathrm{z},i-1}}{T_{\mathrm{z},i-1} - T_{\infty,i-1}^{\mathrm{meas}}}\right)} \tag{7.36}$$

The correction factor α_{Θ} in Equation 7.30 is also required to make the model functional. This variable must be defined in a way that compensates for the errors that arise in the model due to $\Theta_{\mathrm{z}'}$ being approximated from $T_{\mathrm{z}}^{\mathrm{meas}}$. When the battery is in standby mode ($I = 0$), there is no heat generation ($\Theta = 0$), so this condition requires $\alpha_{\Theta} = 0$. When the battery is operating ($|I| > 0$), both cell X and cell Z will generate heat ($\Theta > 0$), so this condition requires $\alpha_{\Theta} \geq 1$. The simplest scheme for α_{Θ} is to compare the calculated value $T_{\mathrm{z},i-1}$ to the measured value $T_{\mathrm{z},i-1}^{\mathrm{meas}}$ for each time interval i, and use this comparison to determine the value of $\alpha_{\Theta,i}$ for that time interval. While proportional, integral, or derivative-based controls could be applied to adjust α_{Θ} during battery operation, for this

proof-of-concept SETS model it is sufficient to use a fixed $\alpha_{\Theta,i} \geq 1$ value whenever $T_{\mathrm{z},i-1} < T_{\mathrm{z},i-1}^{\mathrm{meas}}$, and otherwise set $\alpha_{\Theta,i} = 1$. This allows for a simple SETS model which requires no iteration whatsoever. By trial and error, the accuracy of the SETS model was found to be fairly insensitive to α_Θ values between 1.1 and 1.5, with $\alpha_\Theta = 1.2$ giving optimal results. The full definition of α_Θ is given in Equation 7.37.

$$\alpha_{\Theta,i} = \begin{cases} 0 \ , & I_i = 0 \\ 1 \ , & |I_i| > 0, \quad T_{\mathrm{z},i-1} \geq T_{\mathrm{z},i-1}^{\mathrm{meas}} \\ 1.2 \ , & |I_i| > 0, \quad T_{\mathrm{z},i-1} < T_{\mathrm{z},i-1}^{\mathrm{meas}} \end{cases} \tag{7.37}$$

The overall functionality of this SETS model is visualized in Figure 7.4, showing how the present value of T_{x} is determined using measured data, a set of constant parameters, and the calculated results of the previous time interval.

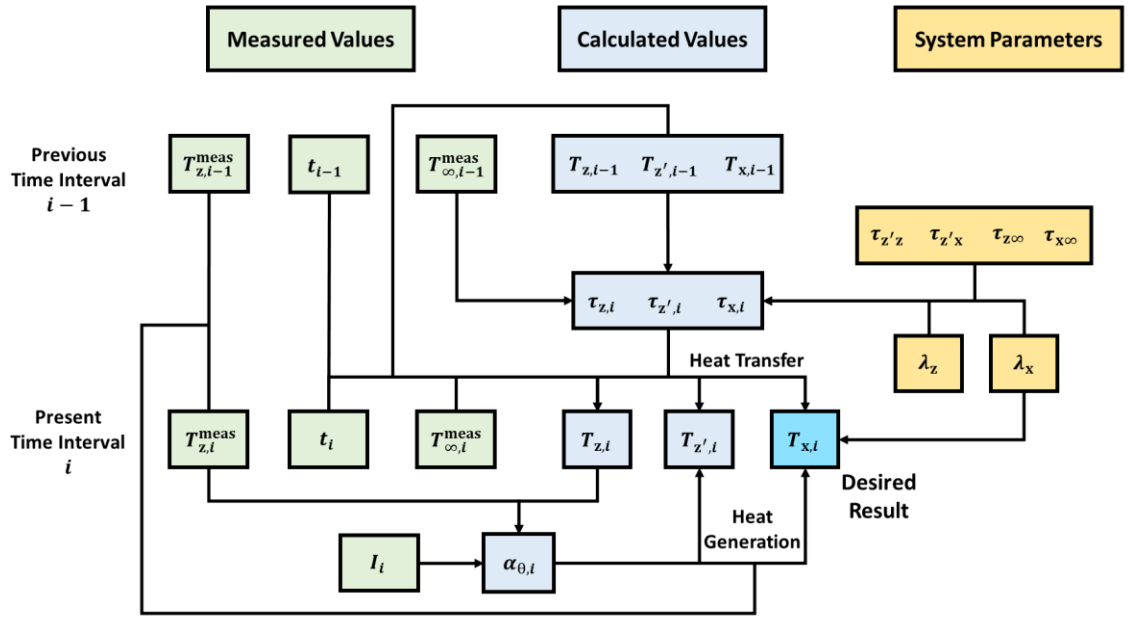


Figure 7.4 Visualization of the proposed SETS model.

The final requirement of the SETS model is a set of initial conditions for the first interval at $i = 0$, specifically $T_{\mathrm{z},0}$, $T_{\mathrm{z}',0}$, and $T_{\mathrm{x},0}$. While it is straightforward to equate $T_{\mathrm{z},0}$ to its measured value $T_{\mathrm{z},0}^{\mathrm{meas}}$, initial guesses must be made for the unknown $T_{\mathrm{z}',0}$ and $T_{\mathrm{x},0}$. If the battery has been idle in a consistent ambient environment for a sufficient period of time (e.g. one day or more) then the battery temperature should be close to a uniformity

condition at $T_{\infty,0}^{\text{meas}}$. However, a more general definition of initial conditions should be established to account for cases where the uniformity condition is not met. In this particular SETS model, Figure 7.3 implies $T_{\text{z}'} \geq T_{\text{z}} \geq T_{\text{x}} \geq T_{\infty}$, and it is expected that $T_{\text{z}'}$ should remain fairly close to T_{z} under most circumstances. Equations 7.38 through 7.40 therefore provide a reasonable set of generalized initial conditions for this SETS model:

$$T_{\text{z},0} = T_{\text{z},0}^{\text{meas}} \tag{7.38}$$

$$T_{\text{z}',0} = T_{\text{z},0}^{\text{meas}} \tag{7.39}$$

$$T_{\text{x},0} = \frac{T_{\text{z},0}^{\text{meas}} + T_{\infty,0}^{\text{meas}}}{2} \tag{7.40}$$

Even if there is a significant error in the initial guesses, the exponential terms in Equations 7.25 through 7.27 will cause the error to dissipate from the model in a relatively short amount of time (e.g. a few hours). This practical feature of the SETS model will be discussed further in Section 7.5.2.

7.3. Heat Dissipation Parameters

The system equations presented in Section 7.2.3 include four time constants: $\tau_{\text{z}'\text{x}}$ to model lateral heat diffusion from cell Z to cell X, $\tau_{\text{z}'\text{z}}$ to model axial heat diffusion within cell Z, $\tau_{\text{z}\infty}$ to model heat dissipation from cell Z, and $\tau_{\text{x}\infty}$ to model heat dissipation from cell X. For heat diffusion (i.e. conduction), $\tau_{\text{z}'\text{x}}$ and $\tau_{\text{z}'\text{z}}$ depend on geometry, heat capacity, and thermal conductivity. Though thermal conductivity and specific heat capacity vary with temperature, studies indicate the dependence relatively weak [183], so it is reasonable to treat these as constant values over a typical operational battery temperature range. This means that $\tau_{\text{z}'\text{x}}$ and $\tau_{\text{z}'\text{z}}$ can be modelled as constant parameters without detriment to the SETS model. For heat dissipation (i.e. convection and radiation), $\tau_{\text{z}\infty}$ and $\tau_{\text{x}\infty}$ depend on geometry, heat capacity, emissivity ε_{rad}, and convection coefficient h_{conv}. Section 2.6.4 described how h_{conv} can have a strong dependence on temperature in the case of natural convection. Since this SETS model deals with a battery cooled passively by natural convection, the corresponding temperature dependence of $\tau_{\text{z}\infty}$ and $\tau_{\text{x}\infty}$ must be accounted for in the model.

7.3.1. Pack Geometry

The temperature dependence of h_{conv} is described by empirical expressions developed for specific surface geometries and orientations. The geometry of a typical passenger car EV battery pack can be approximated by a rectangular prism, with a wide, flat, horizonal top surface and short, flat, vertical sides. Empirical expressions for h_{conv} have been established for both these surface types. This SETS model will therefore employ two unique convection coefficients for the top $h_{\text{conv,top}}$ and sides $h_{\text{conv,side}}$ of the battery pack. Radiation is typically described by the same expression regardless of geometry, so a single radiation coefficient h_{rad} will be used. This allows for the application of a single heat dissipation coefficient for the top h_{top} and sides h_{side} of the battery pack, as shown in Equations 7.41 and 7.42.

$$h_{\text{top}} = h_{\text{conv,top}} + h_{\text{rad}} \tag{7.41}$$

$$h_{\text{side}} = h_{\text{conv,side}} + h_{\text{rad}} \tag{7.42}$$

Since the heat-generating modules are encased in a pack housing, convection and radiation are occurring both at the module surfaces within the pack housing and at the outer surface of the pack housing. As described in Section 7.2.1, the simplified thermal model neglects the effect of the housing cover and assumes that the modules dissipate heat directly to the ambient environment. Figure 7.5 illustrates the layout of the pack with the housing cover removed. Both cell X and cell Z have exposed surface at the top of the module, and cell X also has a portion of its cylindrical wall exposed at the corner of the module. The relative contributions of h_{top} and h_{side} to the total heat dissipation from cell X depend on the relative magnitude of the corresponding surface areas. Rather than calculate these surface areas for the cylindrical dimensions of a single cell, it is more appropriate to use the dimensions of the heat-generating modules and divide the rectangular surface areas of the top, side, and front side by the number of cells adjacent to each surface. Figure 7.5 shows these dimensions.

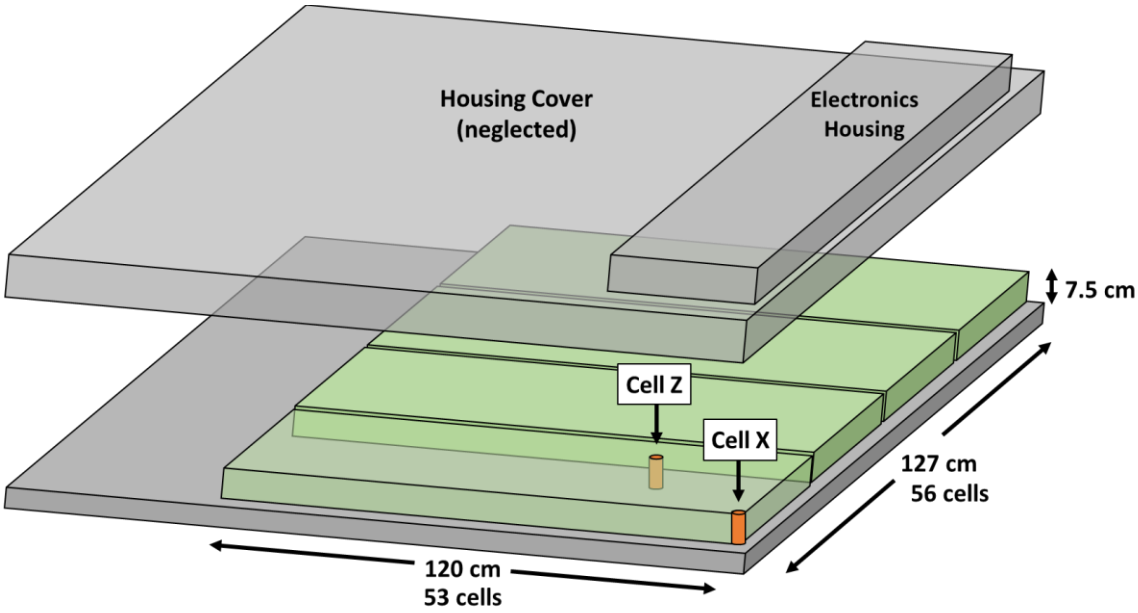


Figure 7.5 Dimensions of the Tesla Model 3 SR+ battery modules and the number of cells adjacent to the front and side surfaces. Not drawn to scale.

There are a total of 2976 cells in the battery (96 series groups with 31 parallel cells each), and each cell lies adjacent to the top surface of the modules. Therefore, cell X and cell Z are each assumed to dissipate heat through $\frac{1}{2976}$ of the total surface area of the top of the modules. Each of the four modules features seven liquid channels running through their length, and each liquid channel makes contact with one row of cells on each side, for a total of 14 cell rows per module. This gives 56 cells along the front of the modules. The modules should therefore feature $\frac{2796}{56} \approx 53$ cells along their sides. Since cell X is at the corner of the modules where the side and front meet, cell X is assumed to dissipate heat through $\frac{1}{56}$ of the total surface area of the front of the modules and $\frac{1}{53}$ of the total surface area of the side of the modules.

Based on Figure 7.5, the relative contributions of h_{top} and h_{side} to cell X are calculated in Equation 7.43. This shows that approximately 87 % of total convection and radiation from cell X is contributed by h_{side}. It is therefore assumed that h_{side} is sufficient to characterize convection from cell X for the purposes of this simplified thermal model. Note that this does not neglect heat dissipation from the top of cell X, but rather assumes that this component is small enough that it can be adequately captured by the h_{side} formulation.

$$h_x = \frac{h_{top}\frac{A_{top}}{2976} + h_{side}\frac{A_{side}}{53} + h_{side}\frac{A_{front}}{56}}{\frac{A_{top}}{2176} + \frac{A_{side}}{53} + \frac{A_{front}}{56}}$$
$$= 0.131h_{top} + 0.869h_{side}$$
$$\approx h_{side} \quad (7.43)$$

Since convection and radiation from cell Z can only occur through the top of the module, h_{top} is used to characterize convection from cell Z as shown in Equation 7.44. The fact that A_{side} and A_{front} dominate A_{top} in Equation 7.43 suggests that convective and radiative heat dissipation rates are significantly lower for cell Z compared to cell X.

$$h_z = h_{top} \quad (7.44)$$

Since $\tau_{z\infty}$ and $\tau_{x\infty}$ are temperature-dependent variables, they can be defined in terms of constant reference values $\tau^*_{z\infty}$ and $\tau^*_{x\infty}$ corresponding to a specific temperature, as shown in Equations 7.45 and 7.46.

$$\tau_{z\infty} = \tau^*_{z\infty}\frac{h^*_{top}}{h_{top}} \quad (7.45)$$

$$\tau_{x\infty} = \tau^*_{x\infty}\frac{h^*_{side}}{h_{side}} \quad (7.46)$$

The $\tau^*_{z\infty}$ and $\tau^*_{x\infty}$ reference values can be employed as constant system parameters within the SETS model. However, mathematical expressions are still required for h_{top} and h_{side} as well as their corresponding reference values h^*_{top} and h^*_{side}. These expressions will be developed in the remainder of Section 7.3.

7.3.2. Natural Convection

Section 2.6.4 reviewed the principles of forced and natural convection as they apply to a general fluid. Equations 7.47 through 7.49 restate the expressions for the convection coefficient h_{conv}, Rayleigh number Ra, and Prandtl number Pr for natural convection in air. Recall that Nu is the Nusselt number, L_{conv} is the 'characteristic length' of the exposed

surface, $g = 9.81$ m/s^2 is acceleration due to gravity, T_s is the surface temperature, and k_{air}, β_{air}, ν_{air}, ρ_{air}, and $c_{p,air}$ are respectively the thermal conductivity, expansion coefficient, kinematic viscosity, mass density, and specific heat capacity of air.

$$h_{conv} = Nu \frac{k_{air}}{L_{conv}} \tag{7.47}$$

$$Ra = \frac{g\beta_{air}\rho_{air}c_{p,air}(T_s - T_\infty)L_{conv}^3}{\nu_{air}k_{air}} \tag{7.48}$$

$$Pr = \frac{\nu_{air}\rho_{air}c_{p,air}}{k_{air}} \tag{7.49}$$

While the various fluid properties have some dependence on temperature, they can be assumed to be approximately constant over a typical operational battery temperature range of 20 to 50 °C. For ideal gases, β_{air} can be approximated as the inverse of the average boundary layer temperature T_{BL} (an absolute temperature), which in turn can be approximated as the average of T_s and T_∞ [189]. Assuming an average battery temperature of 35 °C and an average ambient temperature of 19 °C (typical for the experimental results presented in Chapter 5), this gives an average T_{BL} of 300 K. The value of each air property at this temperature is listed in Table 7.1 based on [189].

Table 7.1 Properties of air evaluated at a 300 K average boundary layer temperature.

Property	**Value**
β_{air} (K^{-1})	0.00333
ρ_{air} (kg/m^3)	1.16
$c_{p,air}$ (J/kg·K)	1007
k_{air} (W/m·K)	0.0263
ν_{air} (m^2/s)	1.59×10^{-5}
Pr	0.707

Note that while the temperature is non-uniform across the battery surface and fluctuates during battery operation, this variance should not have a significant effect on the air properties. A constant value of $T_{BL} = 300$ K is therefore applied for the purposes of the simplified thermal model.

Since the dynamics of convection are occurring over the rectangular surfaces of the modules, it is more appropriate to determine L_{conv} and Rayleigh number based on the module dimensions rather than the cell dimensions. For a flat, horizontal surface, L_{conv} is defined as the area-to-perimeter ratio of the surface, while for a vertical surface, L_{conv} is defined as the height of the surface [189]. Figure 7.5 previously showed the dimensions of the Tesla Model 3 SR+ battery modules, which were measured at 120 cm length, 127 cm width (all four modules side-by-side in the pack), and 7.5 cm height. Based on these dimensions, the characteristic lengths for the top and side of the battery modules are respectively calculated as $L_{\mathrm{top}} = 0.31$ m and $L_{\mathrm{side}} = 0.075$ m.

Using the air properties listed in Table 7.1 and the calculated values for L_{top} and L_{side}, Equation 2.53 reduces to give temperature-dependent Rayleigh numbers for the top Ra_{top} and side Ra_{side} of the battery modules, as shown in Equations 7.50 and 7.51.

$$Ra_{\mathrm{top}} = 2.72 \times 10^{6}(T_{\mathrm{z}} - T_{\infty}) \tag{7.50}$$

$$Ra_{\mathrm{side}} = 3.86 \times 10^{4}(T_{\mathrm{x}} - T_{\infty}) \tag{7.51}$$

For natural convection at the top of a flat, horizontal surface, Equation 7.52 gives two empirical formulations for the Nusselt number for different Rayleigh number ranges [189].

$$Nu_{\mathrm{top}} = \begin{cases} 0.54\left(Ra_{\mathrm{top}}\right)^{1/4}, & 10^{4} < Ra_{\mathrm{top}} < 10^{7} \\ 0.15\left(Ra_{\mathrm{top}}\right)^{1/3}, & 10^{7} < Ra_{\mathrm{top}} < 10^{11} \end{cases} \tag{7.52}$$

Based on Equation 7.50, the range of $10^{7} < Ra_{\mathrm{top}} < 10^{11}$ will apply for all operational temperature conditions except $T_{\mathrm{z}} - T_{\infty} < 3.7$ °C. Since $T_{\mathrm{z}} > T_{\mathrm{x}} > T_{\infty}$, the SETS model error will be inherently small when $T_{\mathrm{z}} - T_{\infty} < 3.7$ °C. Furthermore, $T_{\mathrm{z}} - T_{\infty} < 3.7$ °C would indicate that the battery has been idle for an extended period of time, in which case the accuracy of the SETS model is not critical anyway. It can therefore be assumed that the Nu_{top} formulation for $10^{7} < Ra_{\mathrm{top}} < 10^{11}$ is adequate for the entire temperature range of the battery. Applying this Nu_{top} formulation with Ra_{top}, L_{top} and k_{air} gives Equation 7.53

for the convection coefficient $h_{\text{conv,top}}$ at the top surface of the battery modules. Due to the 1/3 exponent in this equation, $h_{\text{conv,top}}$ is independent of L_{top} for $10^7 < Ra_{\text{top}} < 10^{11}$.

$$h_{\text{conv,top}} = 1.78(T_s - T_\infty)^{1/3} \tag{7.53}$$

For natural convection at a vertical surface, Equation 7.54 gives an empirical formulation for the Nusselt number below an upper Rayleigh number threshold [189].

$$Nu_{\text{side}} = 0.68 + \frac{0.67(Ra_{\text{side}})^{1/4}}{\left(1 + \left(\frac{0.492}{Pr}\right)^{9/16}\right)^{4/9}}, \qquad Ra_{\text{side}} < 10^9 \tag{7.54}$$

Based on Equation 7.51, the range $Ra_{\text{side}} < 10^9$ will apply for all operational temperature conditions. This Rayleigh number formulation therefore covers all practical operational scenarios for battery energy storage. Applying this equation with Ra_{side}, Pr, L_{side} and k_{air} gives Equation 7.55 for the convection coefficient $h_{\text{conv,side}}$ at the sides of the battery modules. Note that the 0.24 is small enough that it can be dropped without detriment. Due to the 1/4 exponent, $h_{\text{conv,side}}$ remains dependent on L_{side}.

$$h_{\text{conv,side}} = 0.24 + 2.53(T_s - T_\infty)^{1/4} \tag{7.55}$$

7.3.3. Radiation

Section 2.6.4 showed that the general expression for radiative heat transfer $\dot{q}_{\text{rad}}$ depends on the fourth power of absolute temperature, and that this expression can be linearized through Taylor expansion so that convection and radiation can be combined into a single heat dissipation coefficient h. The true and linearized expressions for $\dot{q}_{\text{rad}}$ are respectively restated in Equations 7.56 and 7.57. Recall that $\sigma_{\text{SB}} = 5.67 \times 10^{-8}$ W/m^2·K, A_{rad} is the exposed surface area, and $0 < \varepsilon_{\text{rad}} < 1$ is the surface emissivity. Figure 7.6 compares the linearized expression to the true expression over the expected operational battery temperature range for this SETS model, with $T_\infty = 19$ °C.

$$\dot{q}_{\text{rad}} = \sigma_{\text{SB}} \varepsilon_{\text{rad}} A_{\text{rad}} ((T_s + 273\text{ K})^4 - (T_\infty + 273\text{ K})^4) \tag{7.56}$$

$$\dot{q}_{\text{rad}} \approx 4\sigma_{\text{SB}}\varepsilon_{\text{rad}}A_{\text{rad}}(T_\infty + 273)^3(T_\text{s} - T_\infty) \tag{7.57}$$

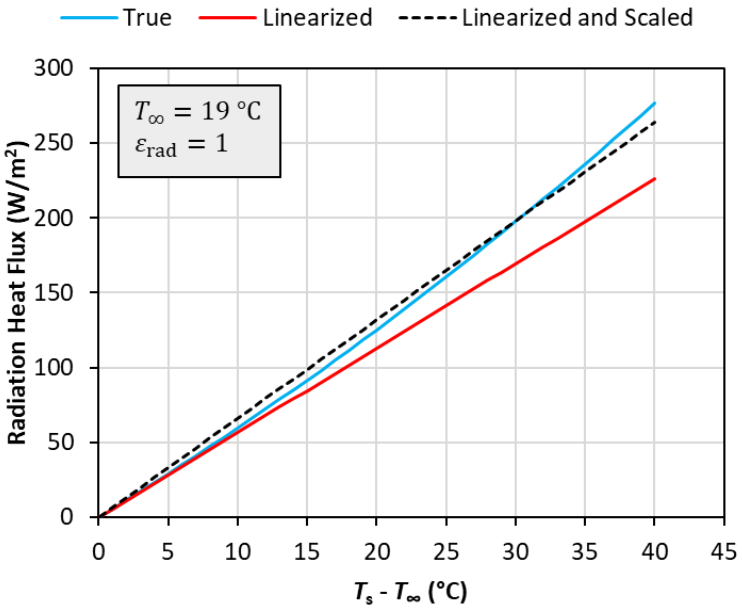


Figure 7.6 Approximation of the radiation equation over a typical operational battery temperature range using linearization and scaling.

Figure 7.6 shows that the linearized form is a poor approximation for $T_\text{s} - T_\infty > 10$ °C. However, a scaling factor can be applied to improve the approximation. Through trial and error, a scaling factor of 1.17 was found to minimize the error over this temperature range. This gives Equation 7.58 as an expression for radiation.

$$\dot{q}_{\text{rad}} \approx 4.67\sigma_{\text{SB}}\varepsilon_{\text{rad}}A_{\text{rad}}(T_\infty + 273)^3(T_\text{s} - T_\infty) \tag{7.58}$$

This linearization allows for a simple definition of h_{rad}, as shown in Equation 7.59. If the ambient temperature can be assumed to be relatively consistent, then h_{rad} can be stated as a temperature-independent constant parameter. In this case, $T_\infty \approx 19$ °C is assumed.

$$\begin{aligned} h_{\text{rad}} &\approx 4.67\sigma_{\text{SB}}\varepsilon_{\text{rad}}(T_\infty + 273)^3 \\ &\approx 6.59\varepsilon_{\text{rad}} \end{aligned} \tag{7.59}$$

With this definition of h_{rad}, complete expressions for h_{top} and h_{side} can now be defined as shown in Equations 7.60 and 7.61, respectively. Both expressions include a

temperature-dependent convection term and a temperature-independent radiation term which depends on ε_{rad}.

$$h_{\text{top}} = 1.78(T_s - T_\infty)^{1/3} + 6.59\varepsilon_{\text{rad}} \tag{7.60}$$

$$h_{\text{side}} = 2.41(T_s - T_\infty)^{1/4} + 6.59\varepsilon_{\text{rad}} \tag{7.61}$$

7.3.4. Practical Expression

The expected values for the convective and radiative components of the heat dissipation coefficients are plotted over the expected temperature range in Figure 7.7. This shows that radiation plays a significant role in total heat dissipation unless ε_{rad} is very small. The value of ε_{rad} therefore has a significant impact on both the magnitude and temperature dependence of h_{top} and h_{side}. This must be accounted for in the SETS model.

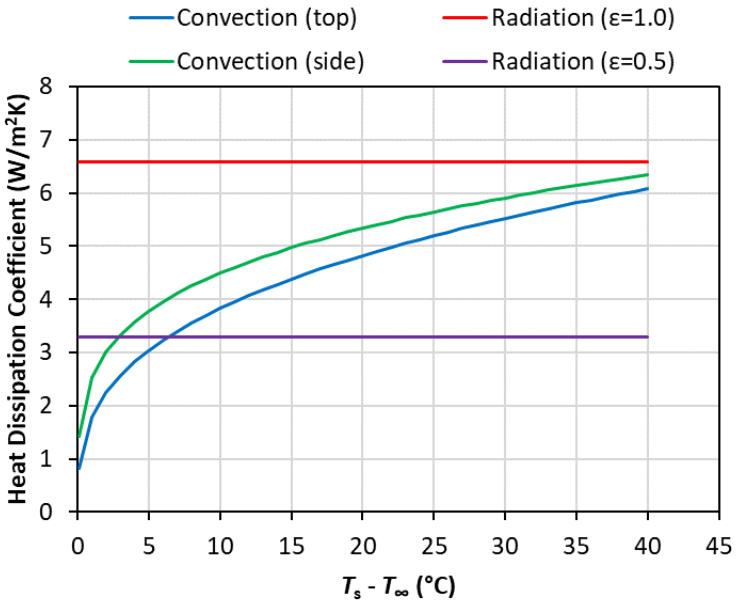


Figure 7.7 Expected values of convective and radiative components of the heat dissipation coefficients over a typical operational battery temperature range.

The value of ε_{rad} depends strongly on the specific type of material and any paint or coating applied to its surface [191]. Without specific information on the surface materials of the cells, modules, and pack housing, emissivity values cannot be assumed. Furthermore, since the system equations are based on a simplified thermal network model, the effective role of radiation in the SETS model may not correspond directly to the true value of ε_{rad}, even

if it were known. Due to these uncertainties, ε_{rad} must be used as an additional (seventh) system parameter to control the relative contribution of radiation to total heat dissipation in the SETS model.

Section 7.3.1 mentioned that h_{top} and h_{side} must be defined in terms of reference values h^*_{top} and h^*_{side} (corresponding to a specific temperature) in order to include $\tau^*_{\text{z}\infty}$ and $\tau^*_{\text{x}\infty}$ as constant parameters in the SETS model. As shown in Equations 7.62 and 7.63, h^*_{top} and h^*_{side} are arbitrarily defined as the values of h_{top} and h_{side} for a given ε_{rad} at the point where $T_{\text{s}} - T_{\infty} = 16$ °C (i.e. $T_{\text{s}} = 35$ °C and $T_{\infty} = 19$ °C).

$$h^*_{\text{top}} = 1.78(16)^{1/3} + 6.59\varepsilon_{\text{rad}} = 4.49 + 6.59\varepsilon_{\text{rad}} \tag{7.62}$$

$$h^*_{\text{side}} = 2.53(16)^{1/4} + 6.59\varepsilon_{\text{rad}} = 5.06 + 6.59\varepsilon_{\text{rad}} \tag{7.63}$$

The fact that these reference values are dependent on an unknown ε_{rad} makes it challenging to define a practical expression of h_{top} and h_{side} in terms of h^*_{top} and h^*_{side}. This issue is illustrated in Figure 7.8, which shows an attempt to define practical expressions using a multiplier and an exponent, as stated in Equations 7.64 and 7.65.

$$h_{\text{top}} = 0.61h^*_{\text{top}}(T_s - T_{\infty})^{0.182} \tag{7.64}$$

$$h_{\text{side}} = 0.67h^*_{\text{side}}(T_s - T_{\infty})^{0.144} \tag{7.65}$$

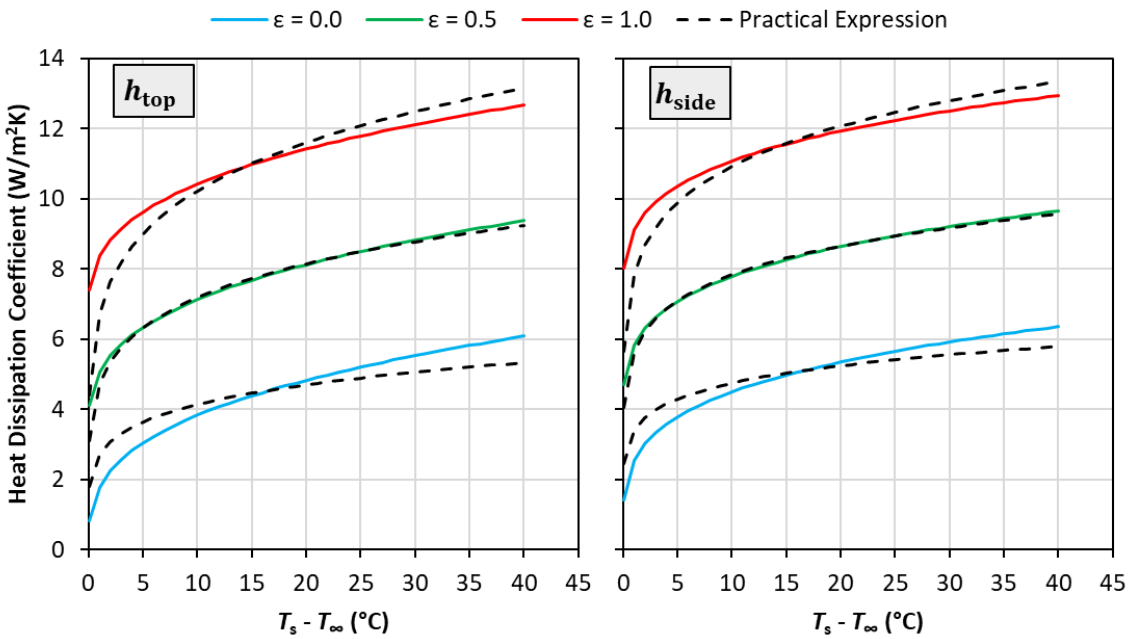


Figure 7.8 Practical expression of the heat dissipation coefficients with inconsistent accuracy.

While the equation structure employed in Figure 7.8 can work well for a specific value of ε_{rad}, it cannot maintain accuracy over the full range of $0 \leq \varepsilon_{\text{rad}} \leq 1$. Therefore, a more complex equation structure is required, in which both the multiplier and the exponent are a function of ε_{rad}. The equation structure in Equations 7.66 and 7.67 was found to work reasonably well, with the numerical values determined by Microsoft Excel Solver (a parameter optimization software described later in Section 7.4.2) such that the error is minimized. The results are plotted in Figure 7.9, showing significantly enhanced accuracy compared to Figure 7.8.

$$h_{\text{top}} = (0.43 + 0.31\varepsilon_{\text{rad}})h^*_{\text{top}}(T_s - T_\infty)^{(0.66-0.20\varepsilon_{\text{rad}})^{2.81}} \tag{7.66}$$

$$h_{\text{side}} = (0.54 + 0.25\varepsilon_{\text{rad}})h^*_{\text{side}}(T_s - T_\infty)^{(0.50-0.18\varepsilon_{\text{rad}})^{2.14}} \tag{7.67}$$

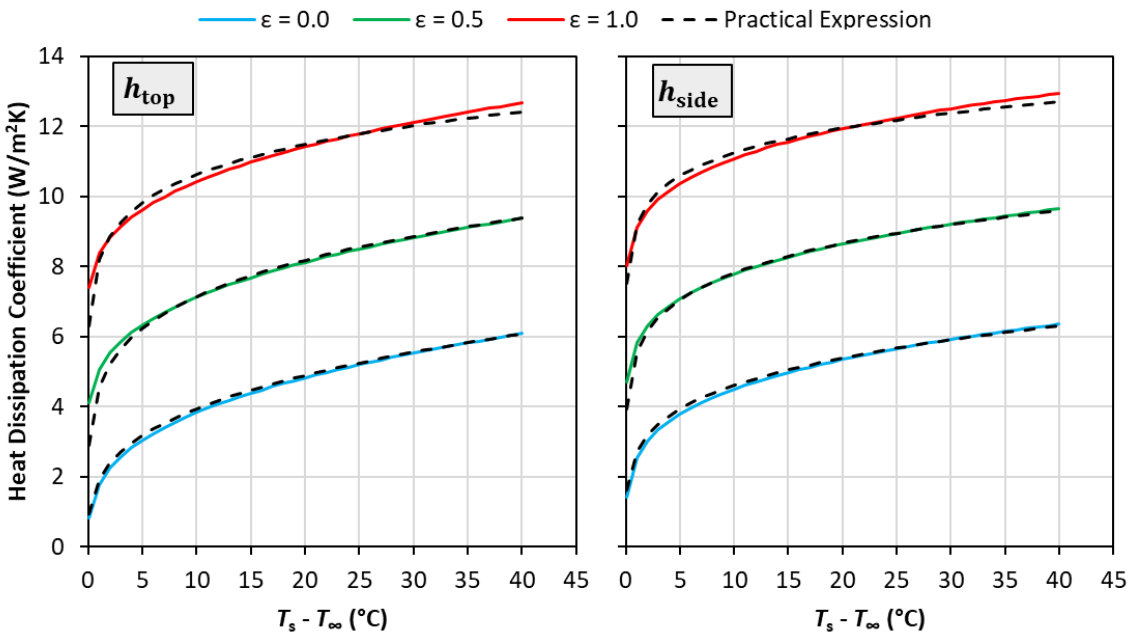


Figure 7.9 Practical expression of the heat dissipation coefficients with enhanced accuracy.

This enhanced equation structure allows for practical expressions of $\tau_{z\infty}$ and $\tau_{x\infty}$ in terms of constant reference values $\tau^*_{z\infty}$ and $\tau^*_{x\infty}$, as shown in Equations 7.68 and 7.69. The finite difference method is applied so that these expressions can be incorporated into the system equations described in Section 7.2.4, where the time variables in each time interval i are calculated based on the temperature values in the previous time interval $i-1$.

$$\tau_{z\infty,i} = \frac{\tau^*_{z\infty}}{(0.43 + 0.31\varepsilon_{rad})\left(T_{z,i-1} - T^{meas}_{\infty,i-1}\right)^{(0.66-0.20\varepsilon_{rad})^{2.81}}} \tag{7.68}$$

$$\tau_{x\infty,i} = \frac{\tau^*_{x\infty}}{(0.54 + 0.25\varepsilon_{rad})\left(T_{x,i-1} - T^{meas}_{\infty,i-1}\right)^{(0.50-0.18\varepsilon_{rad})^{2.14}}} \tag{7.69}$$

7.3.5. Finalized Model

With the defining of Equations 7.68 and 7.69, the SETS model now features $\tau^*_{z\infty}$, $\tau^*_{x\infty}$, and ε_{rad} as constant system parameters which enable simplified modelling of natural convection and radiation. The complete list of seven system parameters is now $\tau_{z'x}$, $\tau_{z'z}$, $\tau^*_{z\infty}$, $\tau^*_{x\infty}$, λ_z, λ_x, and ε_{rad}, all of which are constants to be determined empirically. The SETS model now features a total of 14 equations which are summarized in Table 7.2.

Table 7.2 Summary of equations used in the SETS model.

Equation	Purpose
$T_{\mathrm{z},0} = T_{\mathrm{z},0}^{\mathrm{meas}}$	Temperature initializations
$T_{\mathrm{z}',0} = T_{\mathrm{z},0}^{\mathrm{meas}}$	
$T_{\mathrm{x},0} = \frac{T_{\mathrm{z},0}^{\mathrm{meas}} + T_{\infty,0}^{\mathrm{meas}}}{2}$	
$\tau_{\mathrm{z}\infty,i} = \frac{\tau_{\mathrm{z}\infty}^{*}}{(0.43 + 0.31\varepsilon_{\mathrm{rad}})\left(T_{\mathrm{z},i-1} - T_{\infty,i-1}^{\mathrm{meas}}\right)^{(0.66-0.20\varepsilon_{\mathrm{rad}})^{2.81}}}$	Heat dissipation time constants
$\tau_{\mathrm{x}\infty,i} = \frac{\tau_{\mathrm{x}\infty}^{*}}{(0.54 + 0.25\varepsilon_{\mathrm{rad}})\left(T_{\mathrm{x},i-1} - T_{\infty,i-1}^{\mathrm{meas}}\right)^{(0.50-0.18\varepsilon_{\mathrm{rad}})^{2.14}}}$	
$\tau_{\mathrm{z},i} = \frac{1}{\frac{1}{\tau_{\mathrm{z}\infty,i}} + \frac{1}{\tau_{\mathrm{z}'\mathrm{x}}}\left(\frac{T_{\mathrm{z},i-1} - T_{\mathrm{x},i-1}}{T_{\mathrm{z},i-1} - T_{\infty,i-1}^{\mathrm{meas}}}\right) - \frac{\lambda_{\mathrm{z}}}{\tau_{\mathrm{z}'\mathrm{z}}}\left(\frac{T_{\mathrm{z}',i-1} - T_{\mathrm{z},i-1}}{T_{\mathrm{z},i-1} - T_{\infty,i-1}^{\mathrm{meas}}}\right)}$	Heat transfer time variables
$\tau_{\mathrm{z}',i} = \frac{1}{\frac{1}{\tau_{\mathrm{z}'\mathrm{x}}}\left(\frac{T_{\mathrm{z}',i-1} - T_{\mathrm{x},i-1}}{T_{\mathrm{z}',i-1} - T_{\infty,i-1}^{\mathrm{meas}}}\right) + \frac{1}{\tau_{\mathrm{z}'\mathrm{z}}}\left(\frac{T_{\mathrm{z}',i-1} - T_{\mathrm{z},i-1}}{T_{\mathrm{z}',i-1} - T_{\infty,i-1}^{\mathrm{meas}}}\right)}$	
$\tau_{\mathrm{x},i} = \frac{1}{\frac{1}{\tau_{\mathrm{x}\infty,i}} - \frac{1}{\lambda_{\mathrm{x}}\tau_{\mathrm{z}'\mathrm{x}}}\left(\frac{T_{\mathrm{z}',i-1} - T_{\mathrm{x},i-1}}{T_{\mathrm{x},i-1} - T_{\infty,i-1}^{\mathrm{meas}}}\right) - \frac{1}{\lambda_{\mathrm{x}}\lambda_{\mathrm{z}}\tau_{\mathrm{z}'\mathrm{x}}}\left(\frac{T_{\mathrm{z},i-1} - T_{\mathrm{x},i-1}}{T_{\mathrm{x},i-1} - T_{\infty,i-1}^{\mathrm{meas}}}\right)}$	
$\alpha_{\Theta,i} = \begin{cases} 0 \ , & I_i = 0 \\ 1 \ , & \lvert I_i \rvert > 0, \quad T_{\mathrm{z},i-1} \geq T_{\mathrm{z},i-1}^{\mathrm{meas}} \\ 1.2 \ , & \lvert I_i \rvert > 0, \quad T_{\mathrm{z},i-1} < T_{\mathrm{z},i-1}^{\mathrm{meas}} \end{cases}$	Heat generation approximations
$\Theta_{\mathrm{z}',i} = \alpha_{\Theta}\left(\frac{T_{\mathrm{z},i}^{\mathrm{meas}} - T_{\mathrm{z},i-1}^{\mathrm{meas}}}{\Delta t_i} + \frac{T_{\mathrm{z},i}^{\mathrm{meas}} - T_{\infty,i}^{\mathrm{meas}}}{\tau_{\mathrm{z}',i}}\right)$	
$\Theta_{\mathrm{x}} = \frac{1}{\lambda_{\mathrm{x}}}\Theta_{\mathrm{z}'}$	
$T_{\mathrm{x},i} = T_{\mathrm{x},i-1}\mathrm{e}^{-\frac{\Delta t_i}{\tau_{\mathrm{x},i}}} + \frac{\Delta t_i}{\tau_{\mathrm{x},i}} T_{\infty,i} + \Theta_{\mathrm{x},i}\Delta t_i$	Temperature predictions
$T_{\mathrm{z}',i} = T_{\mathrm{z}',i-1}\mathrm{e}^{-\frac{\Delta t_i}{\tau_{\mathrm{z}',i}}} + \frac{\Delta t_i}{\tau_{\mathrm{z}',i}} T_{\infty,i} + \Theta_{\mathrm{z}',i}\Delta t_i$	
$T_{\mathrm{z},i} = T_{\mathrm{z},i-1}\mathrm{e}^{-\frac{\Delta t_i}{\tau_{\mathrm{z},i}}} + \frac{\Delta t_i}{\tau_{\mathrm{z},i}} T_{\infty,i}$	

Altogether, the computational methods listed in Table 7.2 can be executed in a standard Microsoft Excel spreadsheet without any need for iterative modelling software. The simplicity of the execution is an attractive feature of the SETS model. Figure 7.10 visualizes the finalized SETS model with temperature-dependent heat dissipation coefficients.

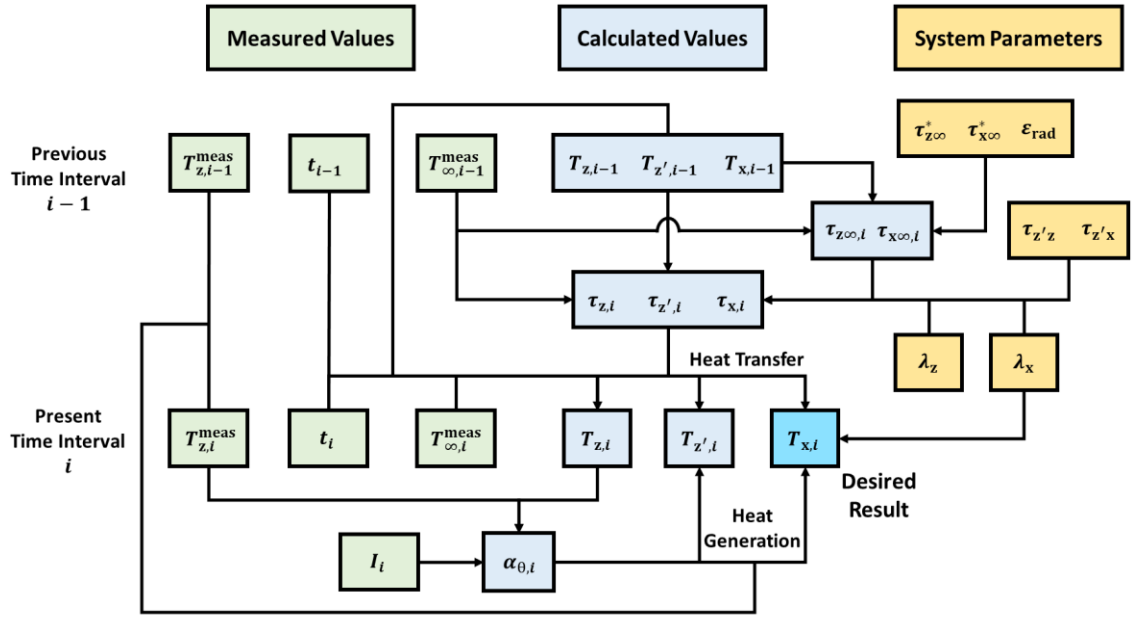


Figure 7.10 Visualization of the finalized SETS model with temperature-dependent heat dissipation coefficients.

7.4. Parameter Optimization

The proposed SETS model requires numerical values for the seven constant parameters that feed into the system equations. These constant values must be determined empirically using experimental training data featuring measurements of T_z^{meas} and T_∞^{meas} as well as the desired 'unknown' temperature T_x^{meas}. Numerical parameter optimization techniques can be employed to determine a set of parameter values that optimizes the fit between the predicted temperatures of the SETS model and the measured temperatures of the empirical dataset. This section will describe the methods used to carry out parameter optimization for this particular SETS model.

7.4.1. Empirical Training Data

Acquiring an experimental dataset for the 'unknown' $T_{\mathrm{x}}^{\mathrm{meas}}$ necessitates the partial disassembly of the 'pilot pack' and the retrofitting of a temperature sensor on cell X. If a SETS model can be established for a single EV battery pack of a given design, the model should be applicable to any battery pack of the same design without the need for pack disassembly. Section 4.1.2 already described how retrofitted T-type thermocouples were applied to a 2019 Tesla Model 3 SR+ battery pack (see Figure 4.5) and the laboratory ambient environment, and these thermocouple placements provide the necessary measurements of $T_{\mathrm{x}}^{\mathrm{meas}}$, $T_{\mathrm{z}}^{\mathrm{meas}}$, and $T_{\infty}^{\mathrm{meas}}$ for the proposed SETS model.

Since second-life batteries will operate under a range of power signals and ambient conditions, a SETS model must be robust to ensure accuracy is maintained in any operational scenario. The empirical data used to determine the system parameters should therefore encompass the complete range of operational scenarios that are expected in second-life energy storage applications. This would entail testing the battery at low, medium, and high power, at constant and variable power, and in cold, temperate, and warm test environments. Section 5.4.1 already presented experimental temperature data for a passive-cooled 2019 Tesla Model 3 SR+ battery pack, including 4 h , 2 h, and 1 h CP rates in a relatively consistent ambient temperature near $T_{\infty} = 19$ °C. These three datasets are therefore used for empirical 'training' of the SETS model to determine optimal values for the seven constant parameters. While the robustness of the SETS model in different ambient conditions cannot be explored using these particular datasets, robustness in different power ranges can be demonstrated.

The three empirical datasets are shown in Figure 7.11, showing a significant difference between T_{x} and T_{z} at all three power rates and a more pronounced difference at higher power rates. Without a SETS model to predict T_{x}, this significant difference would go undetected if a Tesla Model 3 battery pack were directly repurposed in a passive-cooled second-life energy storage application, which could lead to thermal mismanagement resulting in degradation divergence and decreased pack lifetime.

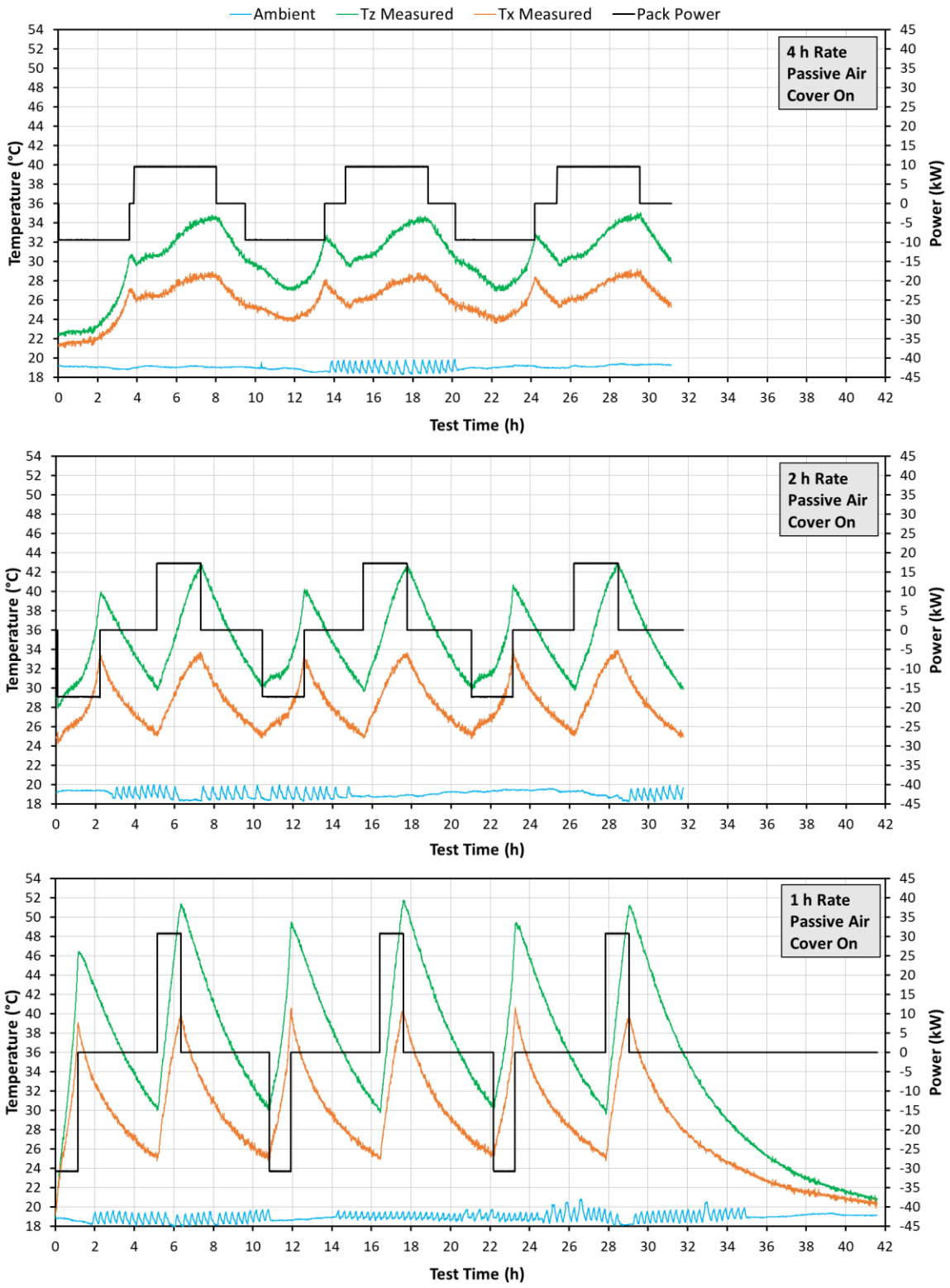


Figure 7.11 Experimental datasets used for empirical determination of SETS model parameters, including 4 h (top), 2 h (middle), and 1 h (bottom) constant power tests conducted on a 2019 Tesla Model 3 SR+ battery pack.

Note that since the system equations employ the finite difference method, the effectiveness of the model depends on the data sampling rate. By filtering the raw 1 s test data to adjust the data interval Δt, it was found that the SETS model works best when 100 or more datapoints are available for a complete discharge or charge. This corresponds to maximum data intervals of 36 s, 72 s, and 144 s for a 1 h rate, 2 h rate, and 4 h rate, respectively. For this SETS model, $\Delta t = 10$ s was selected since this gives high-quality results without unnecessary computational requirements.

7.4.2. Curve Fitting

A variety of parameter optimization algorithms are available in different software languages. For this SETS model, parameter optimization was carried out using the generalized reduced gradient nonlinear solving method within Microsoft Excel Solver, developed by Frontline Systems Inc. [359]. This is a free optimization tool which operates within a standard Excel spreadsheet. The Solver algorithm determines optimal values (within defined constraints) for a set of 'decision variables' in order to minimize or maximize an 'objective value'. For the proposed SETS model, the seven constant parameters are specified as the decision variables, and the error of the SETS model is specified as the objective value to be minimized. This approach is illustrated in Figure 7.12

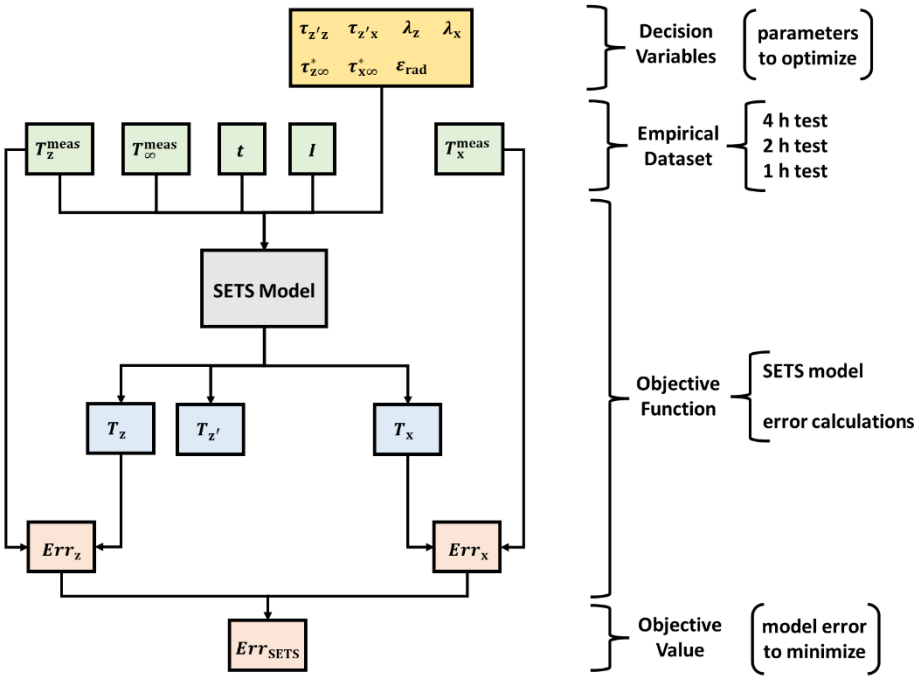


Figure 7.12 Visualization of parameter optimization scheme applied to the SETS model.

Since the SETS model calculates values for both T_z and T_x, both these values can be compared to their measured values T_z^{meas} and T_x^{meas} to calculate the total model error. First, the root-mean-square errors Err_z and Err_x are respectively calculated for T_z and T_x over the three empirical datasets from Figure 7.11, as shown in Equations 7.70 and 7.71. The total error for the SETS model Err_{SETS} is then taken as the sum of Err_z and Err_x, as shown in Equation 7.72.

$$(Err_z)^2 = \frac{1}{i_{end}+1}\sum_{i=0}^{i_{end}}\left(T_{z,i} - T_{z,i}^{meas}\right)^2 \tag{7.70}$$

$$(Err_x)^2 = \frac{1}{i_{end}+1}\sum_{i=0}^{i_{end}}(T_{x,i} - T_{x,i}^{meas})^2 \tag{7.71}$$

$$Err_{SETS} = Err_z + Err_x \tag{7.72}$$

For parameter optimization, the initial guess for T_x is set at $T_{x,0} = T_{x,0}^{meas}$ so that the optimization is not influenced by any initial error. The impact of error in the initial guess on the SETS model results will be explored in Section 7.5.2.

7.4.3. Heat Generation Constraints

When carrying out parameter optimization for the SETS model, it is important to constrain the results within expected physical realities. One such reality is the actual amount of heat generated during the empirical tests. While it can be challenging to compute the total reversible and irreversible heat generation rate at a given point in time, it is relatively simple to compute the total cycle heat generation q_{gen}^{cyc} during a complete cycle of discharge and charge between fixed SOC limits. The net reversible heat is zero for this condition, while the total irreversible heat is the difference between the total charge energy and the total discharge energy, which can each be defined as time integrals of electrical power. The resulting definition of q_{gen}^{cyc} is stated in Equation 7.73, where I is the cell current ($I < 0$ during discharge) and V is the cell voltage. Note that I is taken as the average cell current (measured pack current divided by 31 parallel cells) since the cell-to-cell current distribution within a given cell group is unknown and therefore assumed to be uniform.

$$
\begin{aligned}
q_{\text{gen}}^{\text{cyc}} &= q_{\text{irr}}^{\text{dis}} + q_{\text{irr}}^{\text{chg}} \\
&= E_{\text{chg}} - E_{\text{dis}} \\
&= \int_{t_{\text{startChg}}}^{t_{\text{endChg}}} IV\mathrm{d}t + \int_{t_{\text{startDis}}}^{t_{\text{endDis}}} IV\mathrm{d}t
\end{aligned}
\tag{7.73}
$$

To compute $q_{\text{gen}}^{\text{cyc}}$ using empirical data, Equation 7.73 must be converted to discretized form. The resulting expressions for cell X and cell Z are given in Equations 7.74 and 7.75.

$$
q_{\text{gen,x}}^{\text{cyc}} = \sum_{i=i_{\text{startDis}}}^{i_{\text{endDis}}} I_i V_{\text{x},i} \Delta t_i + \sum_{i=i_{\text{startChg}}}^{i_{\text{endChg}}} I_i V_{\text{x},i} \Delta t_i \tag{7.74}
$$

$$
q_{\text{gen,z}'}^{\text{cyc}} = \sum_{i=i_{\text{startDis}}}^{i_{\text{endDis}}} I_i V_{\text{z},i} \Delta t_i + \sum_{i=i_{\text{startChg}}}^{i_{\text{endChg}}} I_i V_{\text{z},i} \Delta t_i \tag{7.75}
$$

By visual inspection of the cell voltage sensor layout of the Tesla Model 3 SR+ battery pack, it is evident that V_{x} corresponds to cell group 1 while V_{z} corresponds to cell group 4 (out of 96 cell groups). The BMS cell voltage data can therefore be used to compute $q_{\text{gen,x}}^{\text{cyc}}$ and $q_{\text{gen,z}'}^{\text{cyc}}$ for a given dataset. For this SETS model, these quantities are computed for the third cycle of the 1 h, 2 h, and 4 h empirical datasets from Figure 7.11. An example of a conversion from time-series data to a cycle heat summation is illustrated in Figure 7.13 for the case of cell X during the 2 h test, where the area of the shaded region on the right chart is equivalent to $q_{\text{gen,x}}^{\text{cyc}}$ for this particular test, as described in Section 2.4.2.

The calculated values of $q_{\text{gen,x}}^{\text{cyc}}$ and $q_{\text{gen,z}'}^{\text{cyc}}$ for each test are shown in Figure 7.14. These results indicate that cell X generates slightly more heat than cell Z, and that this difference is more pronounced at higher power rates (though the difference is no more than 2 %). Since this battery pack is at approximately 87 % SOH, the internal resistances of the two cells should be similar for a given temperature. However, the measured temperature datasets in Figure 7.11 show that cell X is at a lower temperature than cell Z during testing, and this difference is more pronounced at higher power rates. Section 2.3 described how

battery internal resistance decreases at higher temperatures, so the results in Figure 7.14 likely reflect the correlation between the lower temperature and higher internal resistance of cell X compared to cell Z. The fact that the measured cell voltages can quantify this difference in cell heat generation presents a potential opportunity to strengthen the SETS model, which presently assumes $\dot{q}_{\mathrm{gen,x}} \approx \dot{q}_{\mathrm{gen,z'}}$. This will be discussed in Section 7.6.1.

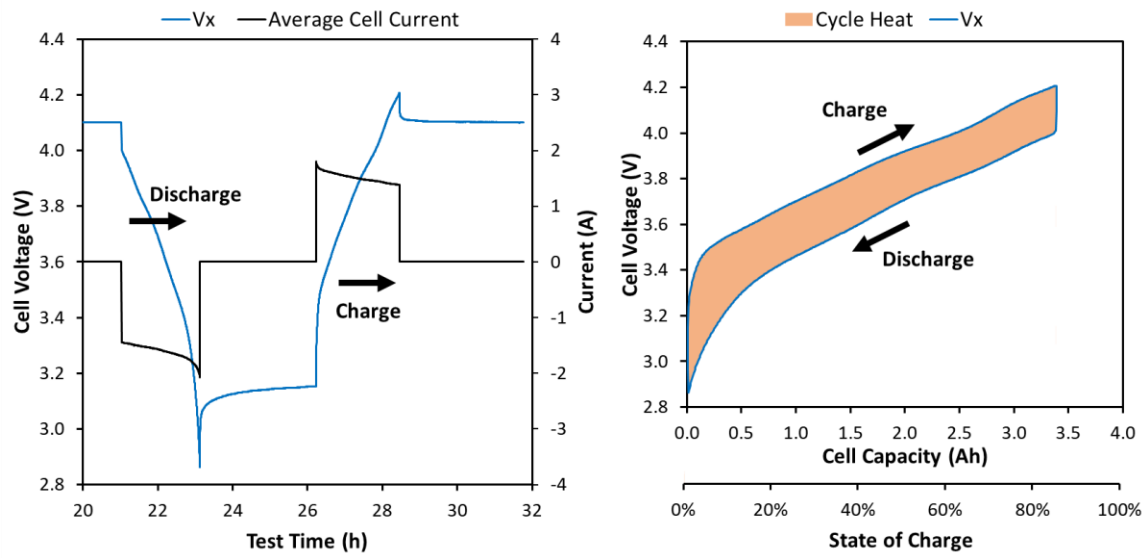


Figure 7.13 Example of time-series data (left) converted to a summation of total cycle heat generation for the third cycle of a 2 h constant-power test conducted on a 2019 Tesla Model 3 SR+ battery pack (cell X data shown).

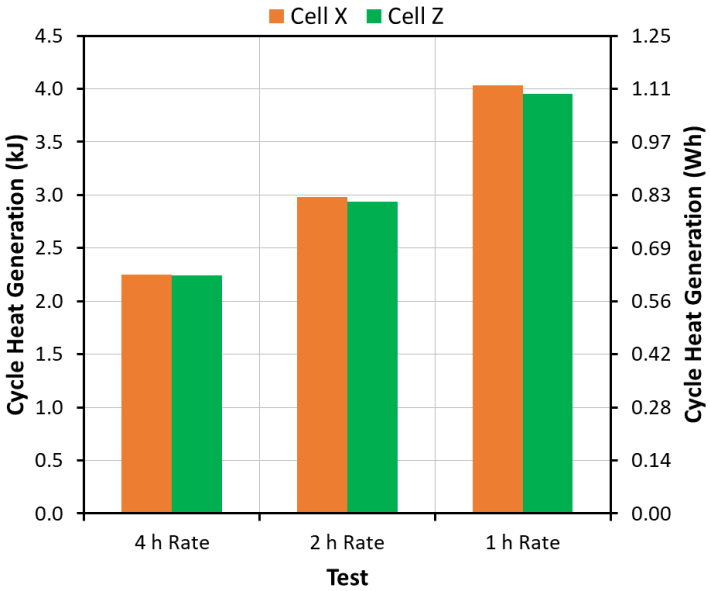


Figure 7.14 Calculated heat generation for cell X and cell Z during the third cycle of each test.

The cycle heat generation $q_{\text{gen}}^{\text{cyc}}$ can also be expressed as the product of the heat capacity mc_p and the 'adiabatic temperature change' of the cycle $\Delta T_{\text{ad}}^{\text{cyc}}$, as shown in Equation 7.76. The $\Delta T_{\text{ad}}^{\text{cyc}}$ term is effectively the temperature change that would occur during the complete discharge-charge cycle in a theoretical adiabatic condition where heat cannot be exchanged with the surroundings (neglecting the influence of temperature on the heat generation rate). Since there is no heat generation when the current is zero, the $\Delta T_{\text{ad}}^{\text{cyc}}$ term can be treated as the sum of a discharge component $\Delta T_{\text{ad}}^{\text{dis}}$ and a charge component $\Delta T_{\text{ad}}^{\text{chg}}$.

$$\begin{aligned} q_{\text{gen}}^{\text{cyc}} &= mc_p \Delta T_{\text{ad}}^{\text{cyc}} \\ &= mc_p \left(\Delta T_{\text{ad}}^{\text{dis}} + \Delta T_{\text{ad}}^{\text{chg}} \right) \end{aligned} \tag{7.76}$$

Definitions for $\Delta T_{\text{ad}}^{\text{dis}}$ and $\Delta T_{\text{ad}}^{\text{chg}}$ can be derived by rearranging the differential form of the system equations (see Equations 7.13 and 7.14) to give Equation 7.77.

$$\frac{\dot{q}_{\text{gen}}}{mc_p} = \frac{\mathrm{d}T}{\mathrm{d}t} + \frac{T - T_\infty}{\tau} \tag{7.77}$$

Integrating both sides of Equation 7.77 over the discharge period and charge period gives expressions for $\Delta T_{\text{ad}}^{\text{dis}}$ and $\Delta T_{\text{ad}}^{\text{chg}}$ as shown in Equations 7.78 and 7.79, where ΔT^{dis} and ΔT^{chg} represent the net change in the actual cell temperature during discharge and charge.

$$\begin{aligned} \Delta T_{\text{ad}}^{\text{dis}} &= \frac{q_{\text{gen}}^{\text{dis}}}{mc_p} \\ &= \Delta T^{\text{dis}} + \int_{t_{\text{startDis}}}^{t_{\text{endDis}}} \left(\frac{T - T_\infty}{\tau} \right) \mathrm{d}t \end{aligned} \tag{7.78}$$

$$\begin{aligned} \Delta T_{\text{ad}}^{\text{chg}} &= \frac{q_{\text{gen}}^{\text{chg}}}{mc_p} \\ &= \Delta T^{\text{chg}} + \int_{t_{\text{startChg}}}^{t_{\text{endChg}}} \left(\frac{T - T_\infty}{\tau} \right) \mathrm{d}t \end{aligned} \tag{7.79}$$

To compute $\Delta T_{\text{ad}}^{\text{dis}}$ and $\Delta T_{\text{ad}}^{\text{chg}}$ using empirical data, Equations 7.78 and 7.79 must be converted to discretized form. The resulting expressions for cell X and cell Z are given in Equations 7.80 through 7.83. Recall from Section 7.2.6 that values of τ_{x} and $\tau_{\text{z}'}$ are calculated for each interval i using the seven constant parameters and the calculated temperatures from the previous interval $i-1$.

$$\Delta T_{\text{ad,x}}^{\text{dis}} = T_{\text{x},i_{\text{endDis}}} - T_{\text{x},i_{\text{startDis}}} + \sum_{i=i_{\text{startDis}}}^{i_{\text{endDis}}} \left(\frac{T_{\text{x},i} - T_{\infty,i}}{\tau_{\text{x},i}} \right) \Delta t_i \tag{7.80}$$

$$\Delta T_{\text{ad,x}}^{\text{chg}} = T_{\text{x},i_{\text{endChg}}} - T_{\text{x},i_{\text{startChg}}} + \sum_{i=i_{\text{startChg}}}^{i_{\text{endChg}}} \left(\frac{T_{\text{x},i} - T_{\infty,i}^{\text{meas}}}{\tau_{\text{x},i}} \right) \Delta t_i \tag{7.81}$$

$$\Delta T_{\text{ad,z}'}^{\text{dis}} = T_{\text{z}',i_{\text{endDis}}} - T_{\text{z}',i_{\text{startDis}}} + \sum_{i=i_{\text{startDis}}}^{i_{\text{endDis}}} \left(\frac{T_{\text{z}',i} - T_{\infty,i}^{\text{meas}}}{\tau_{\text{z}',i}} \right) \Delta t_i \tag{7.82}$$

$$\Delta T_{\text{ad,z}'}^{\text{chg}} = T_{\text{z}',i_{\text{endChg}}} - T_{\text{z}',i_{\text{startChg}}} + \sum_{i=i_{\text{startChg}}}^{i_{\text{endChg}}} \left(\frac{T_{\text{z}',i} - T_{\infty,i}^{\text{meas}}}{\tau_{\text{z}',i}} \right) \Delta t_i \tag{7.83}$$

Since $q_{\text{gen}}^{\text{cyc}}$, $\Delta T_{\text{ad}}^{\text{chg}}$, and $\Delta T_{\text{ad}}^{\text{chg}}$ can each be calculated for any discharge-charge cycle of a given cell, there should be a single constant value of mc_p which balances Equation 7.76 for any discharge-charge cycle at any power rate for the given cell. While mc_p is not a known quantity in the SETS model, values can be computed for cell X and cell Z using Equations 7.84 and 7.85, respectively. These equations can be used to constrain the SETS model such that the seven constant parameters produce consistent mc_p values that fall within the physical expectations adapted from the review by Steinhardt et al. [183].

$$m_{\text{x}} c_p = \frac{q_{\text{gen,x}}^{\text{cyc}}}{\Delta T_{\text{ad,x}}^{\text{dis}} + \Delta T_{\text{ad,x}}^{\text{chg}}} \tag{7.84}$$

$$m_{\text{z}'} c_p = \frac{q_{\text{gen,z}'}^{\text{cyc}}}{\Delta T_{\text{ad,z}'}^{\text{dis}} + \Delta T_{\text{ad,z}'}^{\text{chg}}} \tag{7.85}$$

Since the empirical training data includes complete discharge-charge cycles at three different power rates Equations 7.84 and 7.85 will produce three values each for $m_{\mathrm{x}}c_p$ and $m_{\mathrm{z}'}c_p$. The heat capacity of a given cell should be consistent for all power rates, so the relative standard deviation of the calculated mc_p values will be used as a SETS model verification metric.

The magnitude of the calculated mc_p values can also be compared to physical expectations. To establish expectations, a single cell from a Tesla Model 3 battery pack was acquired and weighed at $m_{\mathrm{cell}} = 70$ g. This can be related to the SETS model using Equation 7.86.

$$\begin{aligned} m_{\mathrm{cell}} &= m_{\mathrm{z}'} + m_{\mathrm{z}} \\ &= \left(1 + \frac{1}{\lambda_{\mathrm{z}}}\right) m_{\mathrm{z}'} \end{aligned} \tag{7.86}$$

The review by Steinhardt et al. [183] reported c_p values for five cylindrical NCA/graphite cells in the range of 830 to 1133 J/kg·K. This gives the inequality in Equation 7.87 as a constraint for the SETS model.

$$58\ \frac{\mathrm{J}}{\mathrm{K}} < m_{\mathrm{cell}}c_p < 79\ \frac{\mathrm{J}}{\mathrm{K}} \tag{7.87}$$

7.4.4. Parameter Estimates and Constraints

Parameter optimization typically requires an initial estimate as well as constraints (e.g. lower and upper bounds) for each parameter in a given model. For this SETS model, the simplified nature of the thermal network in Figure 7.3 means that the optimized values of the seven parameters will not necessarily represent true physical/thermal properties. The seven parameters should therefore be thought of as *effective* properties of the battery pack which enable the simplified thermal network to accurately reproduce empirical measurements. Even so, a well-designed SETS model should give parameter values that are within a reasonable range of the expected true values. This section provides estimates for all seven SETS model parameters based on the measured dimensions of the 2019 Tesla Model 3 SR+ battery pack and the typical ranges of lithium-ion cell thermal properties reported in recent literature (see Section 2.6). These estimates are used to initiate and

constrain the parameter optimization process and to validate the optimized parameter values.

The definitions of the seven SETS model parameters are convenient for mathematical representation in the system equations, but most of these definitions do not carry an intuitive physical meaning that facilitates estimation and validation. Mathematical relationships will therefore be used to convert between the SETS model parameters and their equivalent 'physical parameters'. For example, the two mass ratios λ_z and λ_x can be redefined in reference to the total cell mass m_{cell} as shown in Equations 7.88 and 7.89. These physical parameters respectively describe the active portion of cell Z and the excess mass of cell X.

$$\frac{m_{z'}}{m_{cell}} = \frac{\lambda_z}{1+\lambda_z} \tag{7.88}$$

$$\frac{m_x}{m_{cell}} = \frac{\lambda_x \lambda_z}{1+\lambda_z} \tag{7.89}$$

Based on four mass compositions of cylindrical lithium-ion cells reported by Steinhardt et al. [183], values between 0.73 and 0.86 should be expected for $\frac{m_{z'}}{m_{cell}}$. To give ample flexibility for the simplified model of cell Z, a range of 0.6 to 0.97 was selected for $\frac{m_{z'}}{m_{cell}}$, which corresponds to λ_z values of 1.5 and 32, respectively. An initial value of $\frac{m_{z'}}{m_{cell}} = 0.8$ was selected to reflect the midpoint of the range reported by Steinhardt et al., which corresponds to $\lambda_z = 4$. Lower values of $\frac{m_{z'}}{m_{cell}}$ are likely unrealistic since inactive mass must be minimized in EV battery applications.

Based on a visual assessment of the liquid channel and liquid outlet extending from cell X, it is judged that their combined mass is likely less than the mass of the cell itself. This means that $\frac{m_x}{m_{cell}}$ should be between 1 and 2. An initial estimate of 1.5 is therefore selected to reflect the mid-range. The corresponding value of λ_x depends on λ_z. For example, an initial estimate of $\lambda_z = 4$ will give an initial estimate of $\lambda_x = 1.9$.

The emissivity $\varepsilon_{\mathrm{rad}}$ is already a physical parameter and thus requires no modification. A range of 0 to 1 was selected for $\varepsilon_{\mathrm{rad}}$ (the entire possible range for emissivity), with an initial mid-range estimate of 0.5. However, the heat dissipation time constants $\tau^*_{\mathrm{z}\infty}$ and $\tau^*_{\mathrm{x}\infty}$ are not physically intuitive and depend on both convection and radiation parameters. For the purpose of parameter estimation and validation, pure convection parameters $h^*_{\mathrm{conv,z}}$ and $h^*_{\mathrm{conv,x}}$ are more suitable. Initial estimates for these values are calculated in Equations 7.90 and 7.91. These equations are respectively based on Equations 7.53 and 7.55 using an arbitrary reference condition where $T - T_\infty = 16$ °C.

$$h^*_{\mathrm{conv,z}} = 1.78(16)^{\frac{1}{3}} = 4.49\,\frac{\mathrm{W}}{\mathrm{m^2K}} \tag{7.90}$$

$$h^*_{\mathrm{conv,x}} = 2.53(16)^{\frac{1}{4}} = 5.06\,\frac{\mathrm{W}}{\mathrm{m^2K}} \tag{7.91}$$

Since the thermally resistive effects of the pack housing cover are neglected in the simplified thermal network model, it is expected that the parameter optimization will produce values of $\tau^*_{\mathrm{z}\infty}$ and $\tau^*_{\mathrm{x}\infty}$ which correspond to smaller heat dissipation coefficients $h^*_{\mathrm{z}\infty}$ and $h^*_{\mathrm{x}\infty}$ than the thermal model predicts. In order to validate the optimized values, convection and radiation must be separable. It is therefore assumed that convection and radiation scale proportionally. For example, if the optimized $h^*_{\mathrm{z}\infty}$ is 50 % of the initial estimate, it is assumed that both the convection and radiation components of the optimized $h^*_{\mathrm{z}\infty}$ are 50 % of their respective initial estimates. This assumption is expressed mathematically in Equations 7.92 and 7.93, giving new formulations for $h^*_{\mathrm{z}\infty}$ and $h^*_{\mathrm{x}\infty}$.

$$h^*_{\mathrm{z}\infty} = h^*_{\mathrm{conv,z}} + \frac{h^*_{\mathrm{conv,z}}}{4.49}6.59\varepsilon_{\mathrm{rad}} = h^*_{\mathrm{conv,z}}(1 + 1.47\varepsilon_{\mathrm{rad}}) \tag{7.92}$$

$$h^*_{\mathrm{x}\infty} = h^*_{\mathrm{conv,x}} + \frac{h^*_{\mathrm{conv,x}}}{5.06}6.59\varepsilon_{\mathrm{rad}} = h^*_{\mathrm{conv,x}}(1 + 1.30\varepsilon_{\mathrm{rad}}) \tag{7.93}$$

With an initial estimate of $\varepsilon_{\text{rad}} = 0.5$, the initial estimates for the heat dissipation coefficients are calculated to be $h^*_{\text{z}\infty} = 7.78$ W/m^2·K and $h^*_{\text{x}\infty} = 8.36$ W/m^2·K. To convert these coefficients to their corresponding time constants $\tau^*_{\text{z}\infty}$ and $\tau^*_{\text{x}\infty}$ requires estimates for heat capacity and exposed cell surface area. An initial estimate of $m_{\text{cell}}c_p = 67$ J/K is selected based on the measured cell mass of 70 g and the mean c_p value of 963 J/kg·K reported for cylindrical NCA/graphite cells in the review by Steinhardt et al. [183]. With an initial estimate of $\lambda_{\text{z}} = 4$, this corresponds to $m_{\text{z}'}c_p = 54$ J/K. The exposed surface areas are determined using the same methods described in Section 7.3.1, where the module surface dimensions are scaled down to a single cell. The initial estimates for $\tau^*_{\text{z}\infty}$ and $\tau^*_{\text{x}\infty}$ are calculated in Equations 7.94 and 7.95.

$$\begin{aligned}\tau^*_{\text{z}\infty} &= \frac{m_{\text{z}}c_p}{h^*_{\text{z}\infty}A_{\text{z}\infty}} \\ &= \frac{\left(\frac{m_{\text{z}'}c_p}{\lambda_{\text{z}}}\right)}{h^*_{\text{z}\infty}A_{\text{z}\infty}} \\ &= \frac{\frac{54}{4}\,\frac{\text{J}}{\text{K}}}{\left(7.78\frac{\text{W}}{\text{m}^2\text{K}}\right)(0.00051\ \text{m}^2)}\left(\frac{1\ \text{h}}{3600\ \text{s}}\right) \\ &= 0.94\ \text{h}\end{aligned} \tag{7.94}$$

$$\begin{aligned}\tau^*_{\text{x}\infty} &= \frac{m_{\text{x}}c_p}{h^*_{\text{x}\infty}A_{\text{x}\infty}} \\ &= \frac{\lambda_{\text{x}}m_{\text{z}'}c_p}{h^*_{\text{x}\infty}A_{\text{x}\infty}} \\ &= \frac{(1.9)54\ \frac{\text{J}}{\text{K}}}{\left(8.36\frac{\text{W}}{\text{m}^2\text{K}}\right)(0.0039\ \text{m}^2)}\left(\frac{1\ \text{h}}{3600\ \text{s}}\right) \\ &= 0.87\ \text{h}\end{aligned} \tag{7.95}$$

Similarly, the heat diffusion time constants $\tau_{\text{z}'\text{z}}$ and $\tau_{\text{z}'\text{x}}$ are more intuitive if they are represented as thermal conductivity values. For the axial thermal conductivity $k_{\text{z}'\text{z}}$ within cell Z, an initial estimate of 30 W/m·K is selected based on the $k_{\parallel}$ range of 20 to 40 W/m·K reported for lithium-ion cells in the review by Steinhardt et al. To convert this value to $\tau_{\text{z}'\text{z}}$, the area is taken as the axial cross-sectional area of the cell (a circle with 21 mm diameter),

while the length is taken as half of the 70 mm cell height based on the assumption that $T_{z'}$ is located in the centre of cell Z. The initial estimate for $\tau_{z'z}$ is calculated in Equation 7.96.

$$\tau_{z'z} = \frac{m_{z'} c_p L_{z'z}}{k_{z'z} A_{z'z}}$$

$$= \frac{\left(54 \ \frac{\text{J}}{\text{K}}\right)(0.035 \text{ m})}{\left(30 \frac{\text{W}}{\text{m} \cdot \text{K}}\right)(0.00035 \text{ m}^2)} \left(\frac{1 \text{ h}}{3600 \text{ s}}\right)$$

$$= 0.050 \text{ h} \tag{7.96}$$

The lateral thermal conductivity $k_{z'x}$ through the module is a composite of all module components that lie between cell Z and cell X, including other cells, the foam filler material, and the liquid channels. The design of the module makes the heat conduction path from cell Z to cell X two-dimensional, as illustrated in Figure 7.15.

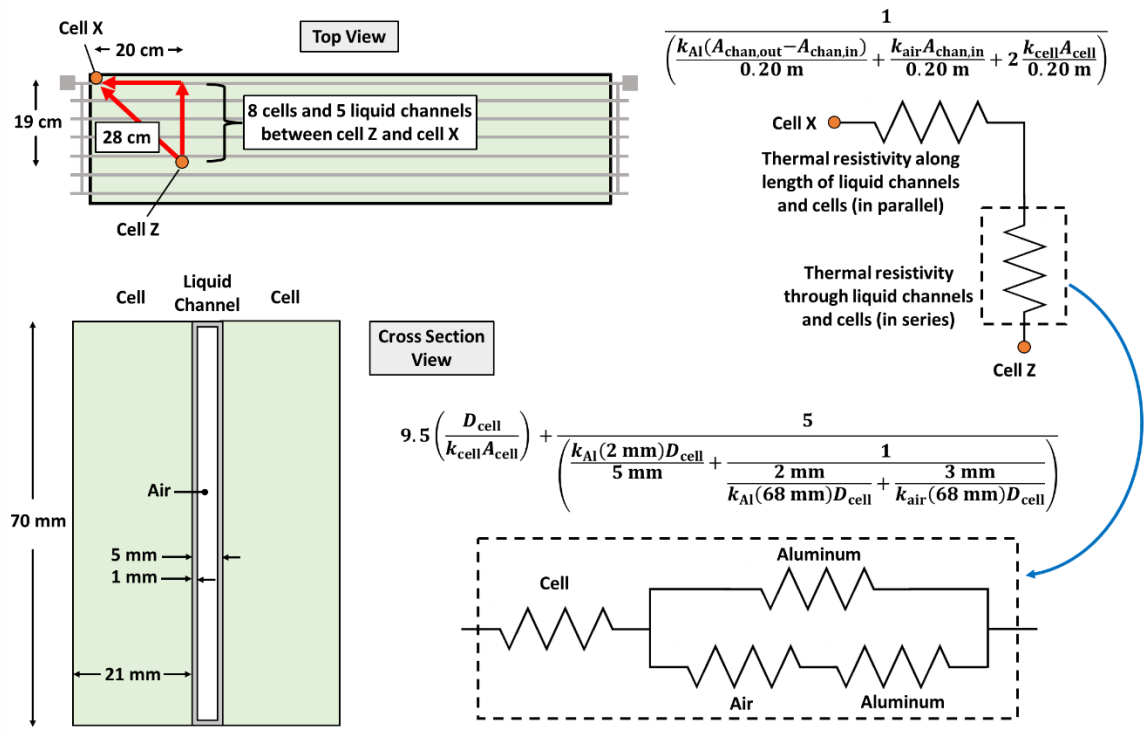


Figure 7.15 Model used to estimate thermal conductivity between cell Z and cell X.

Through the width of the module, a total of five liquid channels and eight cells lie between cell Z and cell X, which act as thermal resistors placed in series. Since the distance between $T_{z'}$ and T_x also includes half the width of cell Z and the full width of cell X, the radial cell

thermal resistivity is multiplied by 9.5. The radial thermal conductivity of the cells is taken as 0.76 W/m·K, which is the median $k_{\perp}$ value reported for NCA/graphite cylindrical cells in the review by Steinhardt et al. [183]. The properties of the foam filler material are unknown and are therefore assumed to be the same as the cell properties for this calculation. Modelling heat conduction through the thickness of the liquid channels requires three thermal resistors, as shown in Figure 7.15. Heat can either conduct around the solid shell or through the fluid-filled interior. The liquid channels are composed of aluminum with $k_{\mathrm{Al}} = 238$ W/m·K [189]. The channel thickness was measured to be 5 mm using a caliper, and while the channels are slightly shorter than the cells, they are assumed to have the same 70 mm height as the cells for the purposes of this calculation. The internal dimensions of the liquid channels are unknown, so a 1 mm wall thickness is used as a reasonable assumption. The liquid channels are assumed to contain static air with $k_{\mathrm{air}} = 0.027$ W/m·K [189] since this SETS model applies to passive-cooled operation. Heat conduction along the length of the module has three parallel pathways: cells, aluminum, and static air.

The calculations shown in Figure 7.15 give composite thermal resistivities of 181 K/W through the width the module and 5.4 K/W along the length of the module (or 0.71 W/m·K and 10.6 W/m·K when converted to thermal conductivity using appropriate lengths and areas). While the true values will depend on the properties of the foam filler material and the true wall thickness of the liquid channels, these results suggest that the presence of the liquid channels causes heat diffusion to be dominant along the module length compared to through its width. Combining these two values in series gives an effective thermal resistivity of 186 K/W between cell Z and cell X. Note that if k_{air} is replaced with the $k_{\mathrm{water}} = 0.61$ W/m·K [189], it has a negligible impact on the effective thermal resistivity calculation. This indicates that there would be no heat diffusion benefit if the liquid channels were filled with a water-based liquid coolant.

The length between cell X and cell Z was measured to be 28 cm, while the heat diffusion area is taken as the cell cross-sectional area with 70 mm height and 21 mm diameter. With these values, the effective thermal resistivity can be converted to a module lateral thermal conductivity of $k_{\mathrm{z'x}} = 1.0$ W/m·K. The corresponding initial estimate for $\tau_{\mathrm{z'z}}$ is calculated in Equation 7.97, where $A_{\mathrm{z'x}}$ is the cell cross-sectional area scaled by $\frac{m_{\mathrm{z'}}}{m_{\mathrm{cell}}} = 0.8$.

$$\tau_{z'x} = \frac{m_{z'} c_p L_{z'x}}{k_{z'x} A_{z'x}}$$

$$= \frac{\left(54\ \frac{\text{J}}{\text{K}}\right)(0.28\ \text{m})}{\left(1.0 \frac{\text{W}}{\text{mK}}\right)(0.00118\ \text{m}^2)} \left(\frac{1\ \text{h}}{3600\ \text{s}}\right)$$

$$= 3.6\ \text{h} \tag{7.97}$$

Table 7.3 summarizes the estimated value, lower bound, and upper bound for each physical parameter, with the equivalent estimate for each SETS model parameter listed on the far right. For $h^*_{\text{conv,z}}$ and $h^*_{\text{conv,x}}$, it is expected that the optimized values will be lower than the initial estimates since the estimates do not account for the thermally resistive effects of the pack housing cover. Lower bounds of 0.1 W/m^2·K are therefore selected for both $h^*_{\text{conv,z}}$ and $h^*_{\text{conv,x}}$, while the upper bounds are set slightly higher than the estimates at 6 W/m^2·K. For $k_{z'z}$, the lower and upper bounds are respectively set at 10 W/m·K and 50 W/m·K, which lie just outside the $k_{\parallel}$ range reported by Steinhardt et al. [183]. Given the uncertainties in the estimation of $k_{z'x}$, a relatively wide range is specified with lower and upper bounds respectively set at 0.1 W/m·K and 5 W/m·K. The lower and upper bounds of the other parameters in Table 7.3 have already been described in this section. The corresponding SETS model parameter estimates on the far right of Table 7.3 are used to initialize the decision variables in the Solver parameter optimization tool. Note that in the SETS model, $m_{\text{cell}} c_p$ is a result rather than a parameter (see Section 7.4.3).

Table 7.3 Estimated values and ranges for physical and SETS model parameters.

Parameter (physical)	Estimated Value	Lower Bound	Upper Bound		Parameter (SETS model)	Estimated Value
$m_{\text{cell}} c_p$ (J/K)	67	58	79		$m_{\text{cell}} c_p$ (J/K)	*result*
$\frac{m_{z'}}{m_{\text{cell}}}$	0.80	0.6	0.97		λ_z	4.0
$\frac{m_x}{m_{\text{cell}}}$	1.5	1.0	2.0		λ_x	1.9
ε_{rad}	0.50	0.0	1.0		ε_{rad}	0.50
$h^*_{\text{conv,z}}$ (W/m^2·K)	4.49	0.1	6		$\tau^*_{z\infty}$ (h)	0.94
$h^*_{\text{conv,x}}$ (W/m^2·K)	5.06	0.1	6		$\tau^*_{x\infty}$ (h)	0.87
$k_{z'z}$ (W/m·K)	30	10	50		$\tau_{z'z}$ (h)	0.050
$k_{z'x}$ (W/m·K)	1.0	0.1	5		$\tau_{z'x}$ (h)	3.6

Figure 7.16 illustrates the complete parameter optimization scheme including the role of the physical parameters and the mc_p outputs as optimization constraints. During parameter optimization, the present values of the seven SETS model parameters are converted to their corresponding physical parameters. These physical values are used to constrain the parameter optimization within the lower and upper bounds in Table 7.3. For example, Solver can only use values of $\tau_{z'z}$ that produce values of $k_{z'z}$ between 10 W/m·K and 50 W/m·K based on the specified $L_{z'z}$ and $A_{z'z}$ and the present result for $m_{z'}c_p$ (see Equation 7.6), where $m_{z'}c_p$ is determined from the calculated $\Delta T_{ad,z'}^{dis}$ and $\Delta T_{ad,z'}^{chg}$.

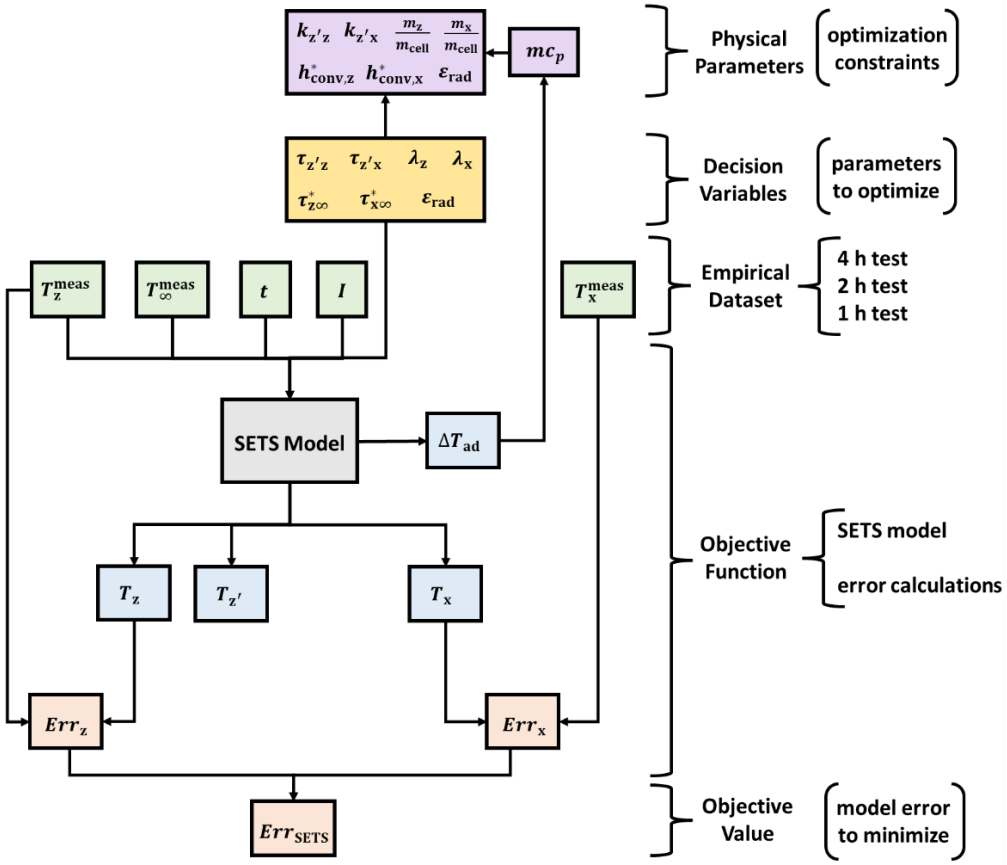


Figure 7.16 Updated parameter optimization scheme including physical constraints.

7.5. Results

Parameter optimization revealed that there are many possible combinations of parameter values that can produce accurate results for this SETS model. Essentially, each parameter has a range within which the accuracy of the model can be retained by adjusting one or more of the other six parameters. This section will first examine the effectiveness of the

SETS model for the set of parameter values that was ultimately selected as the most appropriate. Section 7.5.5 will present a detailed sensitivity analysis which explores the full range of parameter values that can be used without sacrificing model accuracy.

7.5.1. Model Accuracy

The best results achieved by the parameter optimization are shown in Figure 7.17. The modelled T_z and T_x are in very good agreement with the measured values throughout the entire test duration at all three power rates. This demonstrates that the simplified thermal network in Figure 7.3 is capable of accurately reproducing the empirical data when the right parameter values are assigned. The resulting Err_x value over the complete dataset (4 h, 2 h, and 1 h datasets combined) is 0.27 °C, which is about half of the 0.5 °C target that was specified in Section 7.1 based on typical thermistor resolution. The value of Err_z is slightly higher at 0.34 °C.

The T_x model shown in Figure 7.17 is highly accurate in nearly all conditions, but underestimates the measured values slightly (by < 1 °C) at the very end of each 1 h discharge. This demonstrates the shortcomings of the $\dot{q}_{gen,x} \approx \dot{q}_{gen,z'}$ assumption. As discussed in Section 7.4.3, cell X is expected to generate slightly more heat than cell Z at a given time since cell X is always cooler than cell Z during passive-cooled operation and cooler temperatures give higher internal resistance. The impacts of this relationship will be most obvious at the end of a high-power discharge, since heat generation rates are especially high in this condition (see Figure 2.32). In this particular case, the high temperatures associated with a 1 h discharge (exceeding 50 °C) indicate that a passive-cooled Tesla Model 3 SR+ battery pack should not be subjected to 1 h deep-discharge cycles in commercial applications (though it is feasible with liquid cooling, as demonstrated in Section 5.4), so this SETS model would be highly accurate in all practical use cases. The T_z model in Figure 7.17 is also highly accurate for the entire dataset.

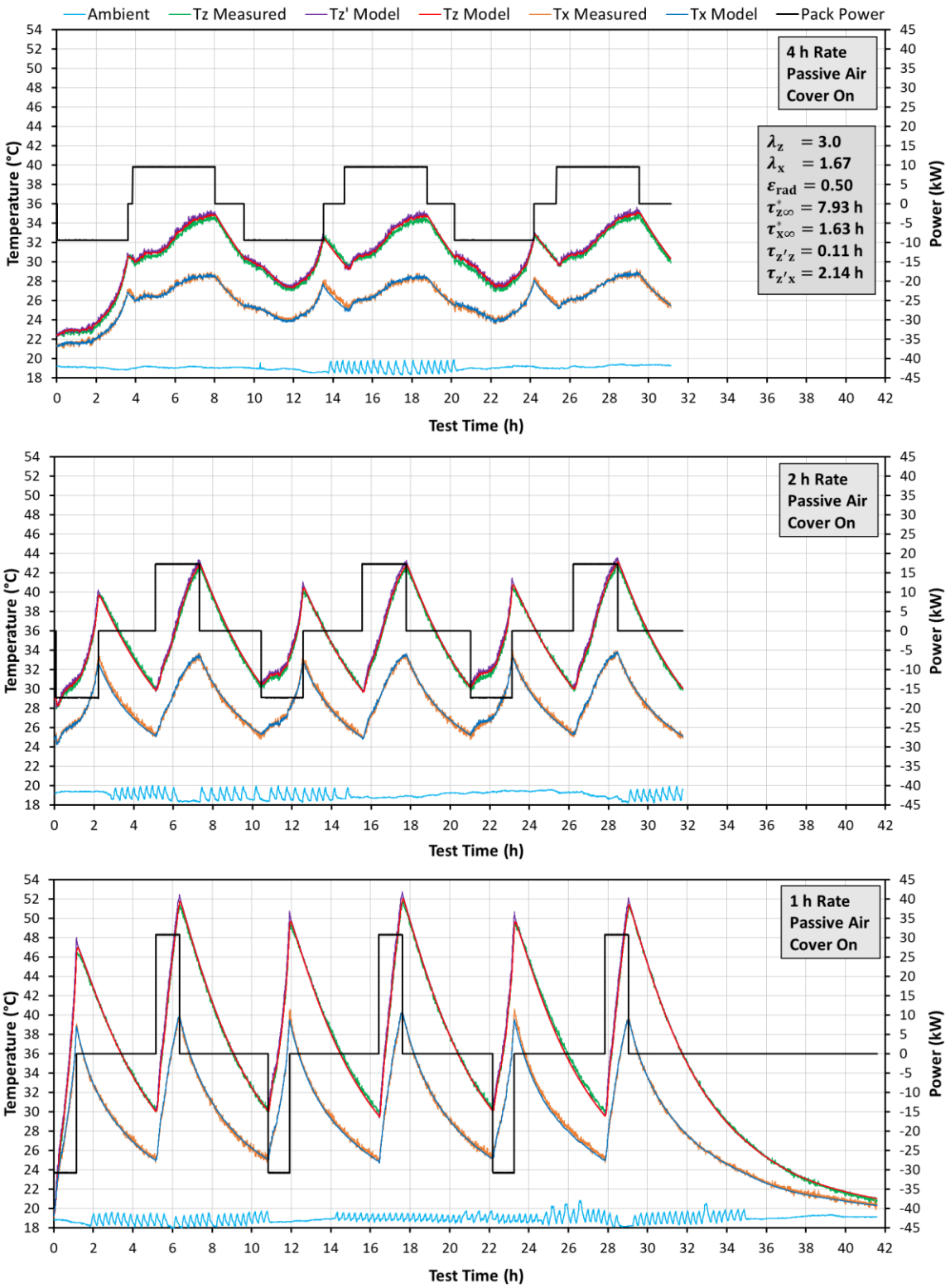


Figure 7.17 Optimized parameters applied to the SETS model with an empirical dataset featuring three tests at three different constant-power rates.

It is worth mentioning that the complete empirical dataset consisting of the 4 h test, 2 h test, and 1 h test is not necessary for optimizing the parameters in this SETS model. There is no significant difference in the model accuracy at any power rate when only the 1 h test data is used for parameter optimization. However, the model accuracy deteriorates noticeably for the 1 h and 2 h tests when only the 4 h test data is used for parameter optimization. This difference is likely due to the fact that the 1 h test data includes both high-power operation and zero-power operation (during lengthy standby cooling periods), thereby covering the complete operational range of the battery. In contrast, the 4 h test data does not feature high-power operation and is therefore inadequate for parameter optimization. While the 1 h test data is sufficient for parameter optimization, optimizing for three different power rates allows for a more rigorous application of the heat generation constraints described in Section 7.4.3. These constraints will be assessed in Section 7.5.3.

Figure 7.18 highlights a specific section of Figure 7.17 to demonstrate how the inclusion of $T_{z'}$ in the thermal network enables the SETS model to successfully reproduce the heat diffusion lag observed in T_z after the end of each 1 h discharge. After power is interrupted, T_z continues to rise slightly and then tapers off as heat diffusion from the cell interior to the cell surface briefly exceeds the rate of heat transfer away from the cell surface.

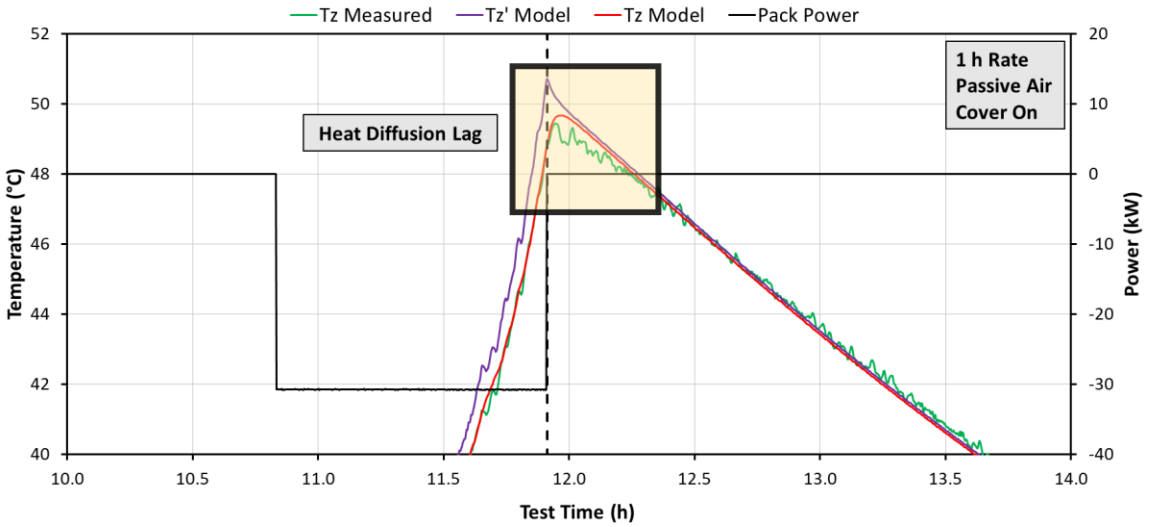


Figure 7.18 Effectiveness of modelling heat diffusion lag in T_z using a $T_{z'}$ 'pseudo-temperature'.

It should be emphasized here that $T_{z'}$ cannot be interpreted as a true representation of the interior cell temperature. The sensitivity analysis in Section 7.5.5 will demonstrate how a range of different parameter values can achieve an accurate SETS model with different magnitudes of $T_{z'}$. It is therefore more appropriate to consider $T_{z'}$ as a 'pseudo-temperature' that enables accurate modelling of T_z and T_x but cannot be verified in its own right without direct measurement of the cell interior. Even so, the effectiveness of including $T_{z'}$ in the thermal network supports the suggestion that the tapered shape of T_z after a 1 h discharge is due to axial heat diffusion from a hotter cell interior.

7.5.2. Inherent Error Decay

In practice, an initial guess for an unknown T_x may introduce as much as 10 °C of error into the SETS model. It is therefore important to consider how the SETS model handles errors. Figure 7.19 demonstrates an example of this, where the optimal parameters from Figure 7.17 are applied to the 2 h empirical dataset. The initial guess $T_{x,0}$ at the beginning of the first discharge is set to a value near $T_{\infty,0}^{meas}$, and the same guess is applied at the beginning of the first charge. This shows how T_x converges to T_x^{meas} within 2 to 3 hours in spite of the significant error introduced. This 'error decay' is plotted directly in the right chart of Figure 7.19.

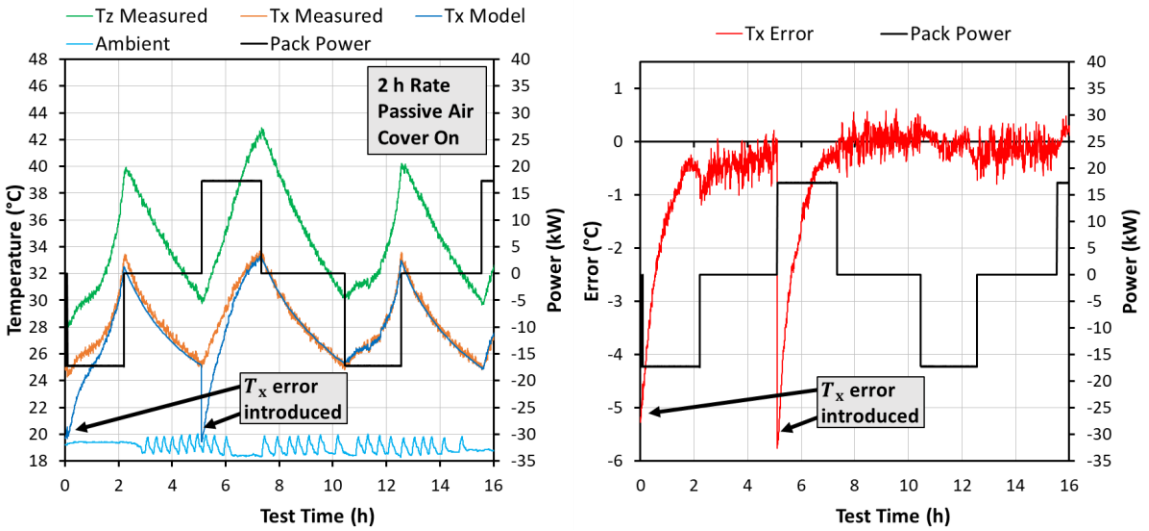


Figure 7.19 Illustrative example of inherent error decay in the SETS model.

The inherent error decay of the SETS model can be explained by examining the system equations from Section 7.2.4. For a given time interval j, the temperature of $T_{\mathrm{x},j}$ of cell X can be modelled from a given starting point $T_{\mathrm{x},0}$ using Equation 7.98.

$$T_{\mathrm{x},j} = T_{\mathrm{x},0}\mathrm{e}^{-\frac{t_j}{\tau_{\mathrm{x},j}}} + \sum_{i=1}^{j3} \mathrm{e}^{\frac{t_i - t_j}{\tau_{\mathrm{x},i}}} \left(\Theta_{\mathrm{x},i} + \frac{1}{\tau_{\mathrm{x},i}} T_{\infty,i}^{\mathrm{meas}} \right) \Delta t_i \tag{7.98}$$

The measured value $T_{\mathrm{x},j}^{\mathrm{meas}}$ can be considered to follow the same mathematical formula with an additional term for the measurement noise $T_{\mathrm{x},j}^{\mathrm{noise}}$, as shown in Equation 7.99. In this case, the expression depends on a hypothetical time variable $\tau_{\mathrm{x}}^{\mathrm{true}}$ and hypothetical adiabatic temperature rate $\Theta_{\mathrm{x}}^{\mathrm{true}}$. These are the 'true' values of these variables which the SETS model aims to approximate.

$$T_{\mathrm{x},j}^{\mathrm{meas}} = T_{\mathrm{x},0}^{\mathrm{meas}}\mathrm{e}^{-\frac{t_j}{\tau_{\mathrm{x},j}^{\mathrm{true}}}} + \sum_{i=1}^{j} \mathrm{e}^{\frac{t_i - t_j}{\tau_{\mathrm{x},i}^{\mathrm{true}}}} \left(\Theta_{\mathrm{x},i}^{\mathrm{true}} + \frac{1}{\tau_{\mathrm{x},i}^{\mathrm{true}}} T_{\infty,i}^{\mathrm{meas}} \right) \Delta t_i + T_{\mathrm{x},j}^{\mathrm{noise}} \tag{7.99}$$

If the SETS model is designed well, then $\tau_{\mathrm{x}} \approx \tau_{\mathrm{x}}^{\mathrm{true}}$ and $\Theta_{\mathrm{x}} \approx \Theta_{\mathrm{x}}^{\mathrm{true}}$. This gives Equation 7.100 as an expression for the error in T_{x}.

$$T_{\mathrm{x},j} - T_{\mathrm{x},j}^{\mathrm{meas}} = \left(T_{\mathrm{x},0} - T_{\mathrm{x},0}^{\mathrm{meas}}\right)\mathrm{e}^{-\frac{t_j}{\tau_{\mathrm{x},i}}} - T_{\mathrm{x},j}^{\mathrm{noise}} \tag{7.100}$$

This shows that an instantaneous error in T_{x} (such as an incorrect initial guess) will follow an exponential decay curve dependent on time t and the time variable τ_{x}. Smaller positive values of τ_{x} (indicating faster heat dissipation) will cause the error to decrease at a faster rate. For example, if there is a temporary error in the $\Theta_{\mathrm{x}} \approx \Theta_{\mathrm{x}}^{\mathrm{true}}$ assumption at the end of a high-power discharge (as appears to be the case in Figure 7.17), the resulting instantaneous error in T_{x} will decay over time as long as the assumption of $\Theta_{\mathrm{x}} \approx \Theta_{\mathrm{x}}^{\mathrm{true}}$ becomes valid again. Standby periods will therefore expedite error decay, since during that time $\Theta_{\mathrm{x}} = \Theta_{\mathrm{x}}^{\mathrm{true}} = 0$. As demonstrated in Figure 7.19, error decay occurs even if the battery is operational, which is a useful feature for commercial applications.

7.5.3. Heat Validation

Section 7.4.3 described a novel technique for estimating cell heat capacity values from the SETS model results using 'adiabatic temperature change' (see Equations 7.84 and 7.85), which provides a means of constraining and validating the model. The calculated adiabatic temperature changes for cell X and cell Z during each discharge and charge are plotted in Figure 7.20. The final values of each discharge and charge are sustained during the subsequent standby periods where $\theta = 0$, and these sustained values are annotated for the third cycle of each test to illustrate how the values of $\Delta T_{\mathrm{ad,x}}^{\mathrm{dis}}$, $\Delta T_{\mathrm{ad,x}}^{\mathrm{chg}}$, $T_{\mathrm{ad,z}}^{\mathrm{dis}}$, and $\Delta T_{\mathrm{ad,z}}^{\mathrm{chg}}$ are determined for each test dataset.

It is interesting to note in Figure 7.20 that $\Delta T_{\mathrm{ad}}^{\mathrm{chg}} > \Delta T_{\mathrm{ad}}^{\mathrm{dis}}$ for all three tests. This is due to the effects of reversible heating described in Section 2.6.3. During discharge, the deintercalation of graphite causes a net increase in cell entropy (endothermic) which subtracts from the irreversible heat generation. During charge, the intercalation of graphite causes a net decrease in cell entropy (exothermic) which adds to the irreversible heat generation. This means that the total heat generation will be greater for charge than discharge (assuming comparable current and SOC range). Since the tests in Figure 7.20 are constant-power tests, the discharge current will be slightly greater than the charge current, but this does not appear to make a significant difference in Figure 7.20. The $\Delta T_{\mathrm{ad}}^{\mathrm{chg}} > \Delta T_{\mathrm{ad}}^{\mathrm{dis}}$ difference is less pronounced at higher power rates in Figure 7.20 since the reversible component of total heat generation is smaller at larger currents. The fact that the heating characteristics shown in Figure 7.20 align with theoretical expectations gives merit to the SETS model.

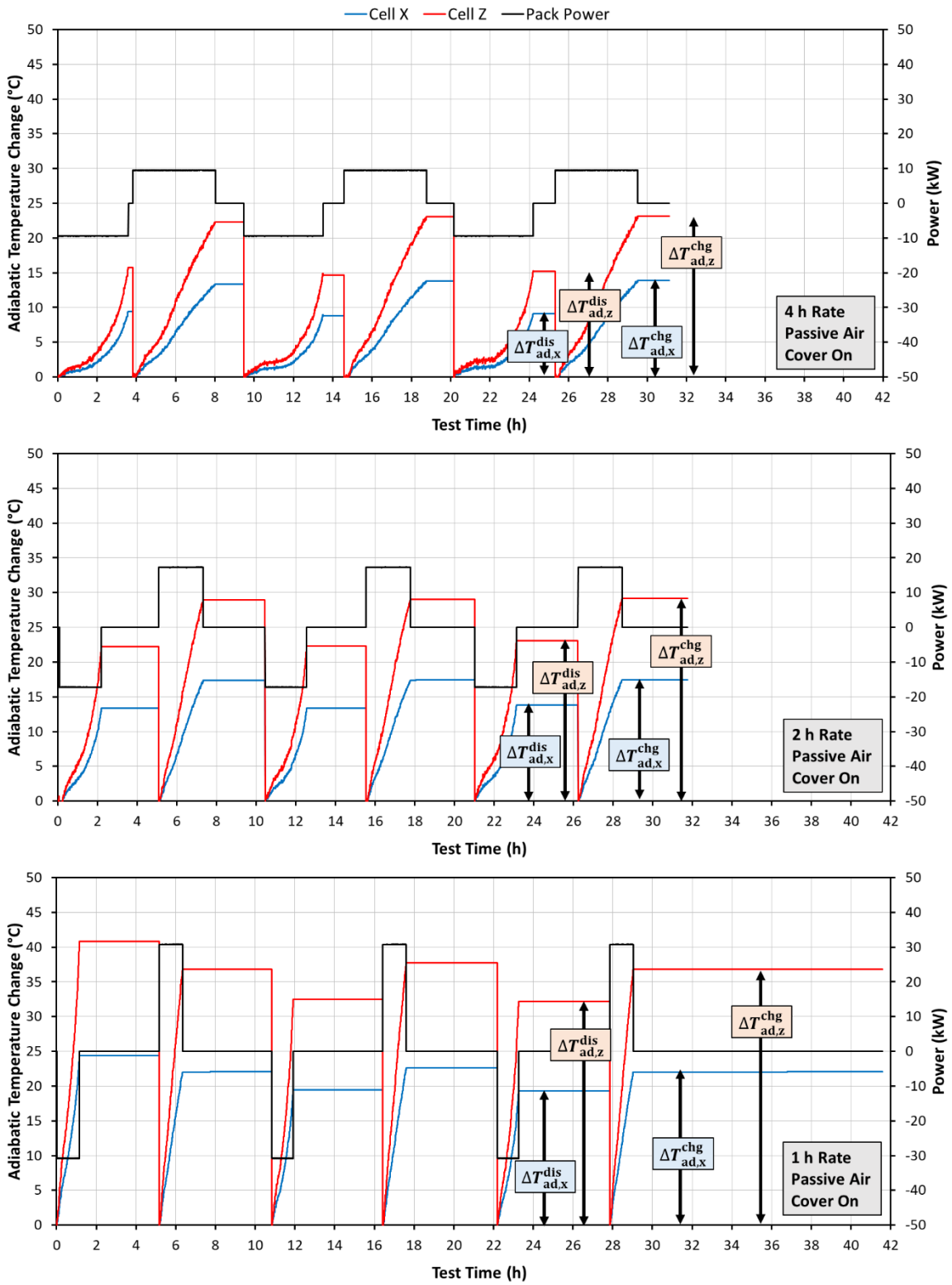


Figure 7.20 Adiabatic temperature change datapoints used to determine cell heat capacity.

The calculated adiabatic temperature change values are summarized in Table 7.4, along with the corresponding $q_{\text{gen}}^{\text{cyc}}$ values (derived in Section 7.4.3) and calculations of $m_{\text{x}}c_p$ and $m_{\text{z}'}c_p$. Note that the adiabatic temperature change values are larger for cell Z because of the mass ratio $\lambda_{\text{x}} = 1.67$, but the heat generation values are similar for both cells.

Table 7.4 Heat capacity calculations for each cell and power rate.

	Cell X			Cell Z (Z' only)		
Calculation	**4 h Rate**	**2 h Rate**	**1 h Rate**	**4 h Rate**	**2 h Rate**	**1 h Rate**
$q_{\text{gen}}^{\text{cyc}}$ (kJ)	2.25	2.98	4.03	2.24	2.93	3.95
$\Delta T_{\text{ad}}^{\text{dis}}$ (K)	9.1	13.8	19.3	15.2	23.1	32.2
$\Delta T_{\text{ad}}^{\text{chg}}$ (K)	13.9	17.5	22.0	23.3	29.2	36.8
mc_p (J/K)	98.0	95.2	97.6	58.2	56.1	57.3

The values in Table 7.4 are used to calculate mean cell heat capacities of $m_{\text{x}}c_p = 96.9$ J/K and $m_{\text{z}'}c_p = 57.2$ J/K with relative standard deviations of 1.6 % and 1.8 %, respectively. The fact that the standard deviations are within 2 % of the mean values demonstrates that the SETS model has achieved the high level of mc_p consistency that should be expected.

The calculated value of $m_{\text{z}'}c_p$ can be scaled to the full cell Z value using the value of $\lambda_{\text{z}} = 3.0$ obtained from parameter optimization. These results are stated in Equation 7.101.

$$m_{\text{cell}}c_p = m_{\text{z}'}c_p\left(\frac{\lambda_{\text{z}} + 1}{\lambda_{\text{z}}}\right) = 76.3\ \frac{\text{J}}{\text{K}} \pm 1.8\ \% \tag{7.101}$$

This value is within the 59 to 78 J/K range reported by Steinhardt et al. [183], which gives further merit to this SETS model and the optimized parameter values. The fact that the calculated value is towards the higher end of the reported range may suggest that $m_{\text{cell}}c_p$ includes a small amount of heat capacity from the adjacent liquid channels and foam filler material that surround the cells within the battery module.

7.5.4. Parameter Validation

Table 7.5 compares the optimized parameter values from Figure 7.17 to the initial estimates from Section 7.4.4. To facilitate comparison, the SETS model parameters are converted

back to physical parameters by reversing the conversion methods presented in Section 7.4.4, where the mc_p values are now based on the model results from Section 7.5.3. Note that Table 7.5 shows just one of many viable sets of parameter values. A sensitivity analysis will be presented in Section 7.5.5 to explore the optimal ranges of each parameter in more detail.

The optimized value of $\frac{m_{z'}}{m_{\text{cell}}} = 0.75$ is within the 0.73 to 0.86 range reported by Steinhardt et al. [183] and corresponds to 25 % of the cell mass being inactive. The optimized value of $\frac{m_{x}}{m_{\text{cell}}} = 1.25$ means that cell X is modelled with 25 % excess mass compared to cell Z to account for the liquid channel and liquid outlet extending from cell X at the corner of the module. This seems like a reasonable value based on a visual assessment of the battery. It should be emphasized that $\frac{m_{x}}{m_{\text{cell}}}$ does not necessarily represent the true extra heat capacity of the liquid channel and liquid outlet extending from cell X. Rather, $\frac{m_{x}}{m_{\text{cell}}}$ is a practical method of accounting for the heat diffusion from cell X to these inactive components without actually modelling this heat diffusion, which would require additional temperature sensors and SETS model parameters.

Table 7.5 Comparison of optimized physical parameters to initial estimates and constraints.

Parameter	Estimated Values	Lower Bound	Upper Bound	Optimized Values
$m_{\text{cell}}c_p$ (J/K)	67	59	78	76.3
$\frac{m_{z'}}{m_{\text{cell}}}$	0.80	0.6	0.97	0.75
$\frac{m_{x}}{m_{\text{cell}}}$	1.5	1.0	2.0	1.25
ε_{rad}	0.50	0.0	1.0	0.50
$h^*_{\text{conv,z}}$ (W/m^2·K)	4.49	0.1	6	0.75
$h^*_{\text{conv,x}}$ (W/m^2·K)	5.06	0.1	6	2.52
$k_{z'z}$ (W/m·K)	30	10	50	14.9
$k_{z'x}$ (W/m·K)	1.0	0.1	5	1.89

The optimized value of $\varepsilon_{\text{rad}} = 0.50$ is in the middle of the $0.0 \leq \varepsilon_{\text{rad}} \leq 1.0$ emissivity range, but the sensitivity analysis in Section 7.5.5 will show that the SETS model is fairly

insensitive to $\varepsilon_{\mathrm{rad}}$. The accuracy of the model is not significantly impacted when radiation is lumped together with natural convection by setting $\varepsilon_{\mathrm{rad}} = 0$ in Equations 7.68 and 7.69.

The optimized value of $h^*_{\mathrm{conv,z}} = 0.75$ W/m^2·K is about 17 % of the initial estimate of 4.49 W/m^2·K, while the optimized value of $h^*_{\mathrm{conv,x}} = 2.52$ W/m^2·K is about 50 % of the initial estimate of 5.06 W/m^2·K. Both convection coefficients are smaller than their initial estimates, which is expected since the estimates neglect the thermally resistive effects of the pack housing cover. It is interesting to note that $h^*_{\mathrm{conv,z}}$ is substantially smaller than $h^*_{\mathrm{conv,x}}$ despite their similar initial estimates. This may reflect the fact that there is more air space between the module and housing cover at the module corner compared to its top surface. Furthermore, there is additional heat capacity above cell Z and cell X due to the electronics housing at the rear of the pack (see Figure 7.5), which further inhibits heat dissipation from cell Z.

The optimized value of $k_{\mathrm{z'x}} = 1.89$ W/m·K is 89 % higher than the initial estimate of 1.0 W/m·K. This may indicate that the foam filler material with unspecified properties is beneficial for heat conduction, though this would be unlikely if the foam intended to inhibit thermal propagation during a failure event. The difference between the estimated and optimized values is more likely due to the simplifications of the employed thermal network. The optimized value of $k_{\mathrm{z'z}} = 14.9$ W/m·K is just below the 20 to 40 W/m·K range reported by Steinhardt et al. [183]. It should be noted that Steinhardt et al. only found ten reported values for axial thermal conductivity $k_{\parallel}$ in their review, and none of these values were for NCA/graphite cells, so it is possible that the Tesla Model 3 cell has a lower $k_{\parallel}$ than the ten reported values. The result for $k_{\mathrm{z'z}}$ is likely also influenced by the simplifications of the employed thermal network, which separates cell Z into two discrete masses. Even so, both $k_{\mathrm{z'x}}$ and $k_{\mathrm{z'z}}$ give reasonable values, and $k_{\mathrm{z'z}}$ is about an order of magnitude larger than $k_{\mathrm{z'x}}$, which reflects the expected difference between $k_{\parallel}$ and $k_{\perp}$.

Overall, the optimized value of each parameter can be justified in comparison to physical expectations, and this validation gives merit to the SETS model. It should be emphasized again that the model parameters serve as *effective* values for a simplified thermal network and should not be interpreted as the true properties of the battery.

7.5.5. Sensitivity Analysis

Since the SETS model depends on seven unknown parameters, the relative impact of each parameter on the overall accuracy of the model should be examined. To explore the sensitivity of the model in relation to each parameter, the parameter optimization was re-run about 60 times, divided into seven series. Within each series, a single SETS model parameter is held fixed at a range of values while the other six parameters are re-optimized. This determines how accurate the SETS model can be when the given parameter is fixed at the specified value. To facilitate interpretation of the sensitivity analysis, all resulting SETS model parameter values are converted to physical parameters by reversing the equations presented in Section 7.4.4.

It is important to note that Solver can either produce a 'locally optimized' solution or a 'globally optimized' solution depending on user specification. A globally optimized solution should be the single set of parameter values that produces a lower model error than any other combination of parameter values. A locally optimized solution is dependent on how the parameters are initialized, and does not necessarily represent the global solution. For this SETS model, it was found that local optimization requires about 10 to 15 minutes, while global optimization can take 2 to 3 hours. Given the number of optimization runs required for this sensitivity analysis, local optimization was selected. The unfixed parameter values were initialized to values near the global solution to ensure that sensitivity is assessed around an appropriate 'operating point'.

The results of the sensitivity analysis are shown in Figure 7.21, where the top left chart assesses the convection coefficients $h^*_{\mathrm{conv,x}}$ and $h^*_{\mathrm{conv,z}}$, the top right chart assesses the emissivity $\varepsilon_{\mathrm{rad}}$, the bottom left chart assesses the thermal conductivities $k_{\mathrm{z'x}}$ and $k_{\mathrm{z'z}}$, and the bottom right chart assesses the mass ratios $\frac{m_{\mathrm{x}}}{m_{\mathrm{cell}}}$ and $\frac{m_{\mathrm{z'}}}{m_{\mathrm{cell}}}$. Each chart in Figure 7.21 shows the locally optimized error Err_{SETS} obtained at each parameter value. The horizontal dashed line at $Err_{\mathrm{SETS}} = 0.4$ °C in each chart represents the maximum allowable average error required for the modelled T_{x} and T_{z} to pass a visual assessment when plotted in charts like those shown previously in Figure 7.17.

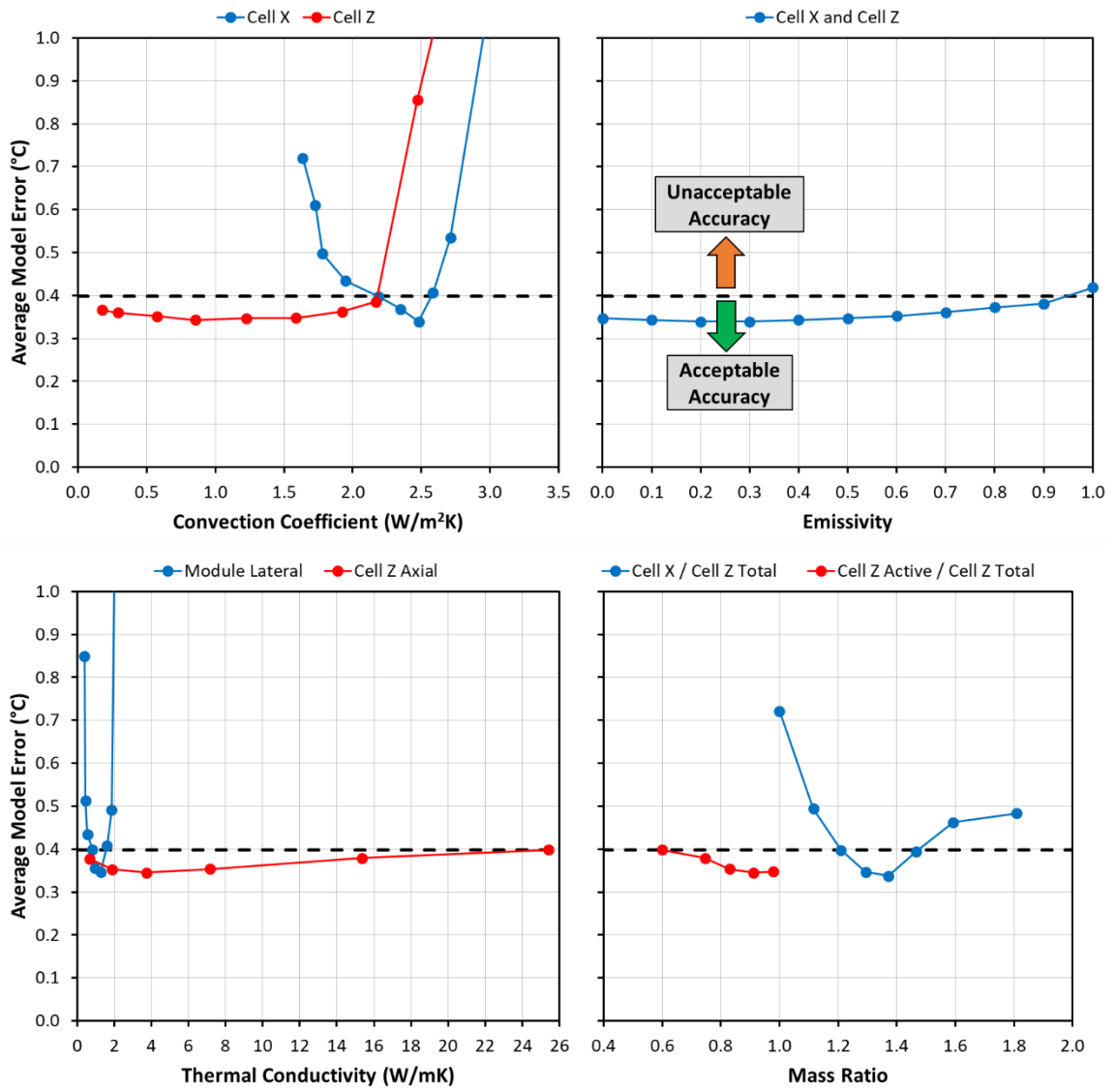


Figure 7.21 Sensitivity analysis results for all seven physical parameters.

Figure 7.21 shows that the SETS model is relatively sensitive to $h^*_{\mathrm{conv,x}}$, requiring values in the range of 2.2 to 2.6 W/m^2·K in order to achieve acceptable model accuracy. In contrast, the SETS model is relatively insensitive to $h^*_{\mathrm{conv,z}}$, with acceptable results in the range of 0.2 to 2.2 W/m^2·K. This difference in sensitivity likely arises because heat dissipation to the environment is dominated by cell X due to its position at the module corner. A change in $h^*_{\mathrm{conv,x}}$ therefore has a significant impact on the system, while a change in $h^*_{\mathrm{conv,z}}$ can be easily compensated by adjusting the other parameters. Figure 7.22 shows that as $h^*_{\mathrm{conv,z}}$ gets smaller, $k_{\mathrm{z'z}}$ gets smaller (i.e. less axial heat diffusion to the surface of cell Z) and $k_{\mathrm{z'x}}$ gets larger (i.e. more lateral heat diffusion from cell Z to cell X). This

demonstrates how heat transfer can be redirected within the model to compensate for changes in $h^*_{\text{conv,z}}$.

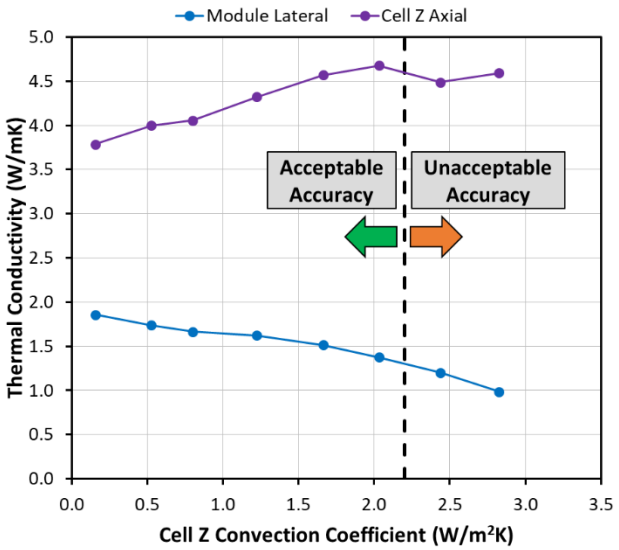


Figure 7.22 Changes in $h^*_{\text{conv,z}}$ compensated by changes in $k_{z'z}$ and $k_{z'x}$.

Figure 7.21 also shows that the SETS model is insensitive to ε_{rad}, with acceptable results achievable using any value between 0 and 0.95. This suggests that the convection equations are sufficient for modelling heat dissipation for the employed empirical dataset. The only detectable impact of ε_{rad} appears towards the end of the long standby period after the 1 h test in Figure 7.17, when $T - T_\infty$ is relatively small. In this range, the SETS model accuracy appears to improve slightly as ε_{rad} is increased above 0.2, but this improvement seems to be outweighed by other inaccuracies when $\varepsilon_{\text{rad}} > 0.6$. Since the accuracy of a SETS model is of little practical consequence when $T - T_\infty$ is small, ε_{rad} could be dropped from this SETS model without detriment. However, this may not be the case for other EV battery pack designs and/or variable ambient temperatures. Parameter optimization should therefore include an ε_{rad} term to determine whether or not ε_{rad} is necessary for a given SETS model.

Figure 7.21 also shows that the SETS model is relatively sensitive to $k_{z'x}$ (requiring values in the range of 0.8 to 1.6 W/m·K), but relatively insensitive to $k_{z'z}$ (allowing for any value in the range of 0.6 to 25 W/m·K). Similarly, the SETS model is relatively sensitive to $\frac{m_x}{m_{\text{cell}}}$

(requiring values between 1.20 and 1.45), but relatively insensitive to $\frac{m_{z'}}{m_{cell}}$ (allowing for any value between 0.60 and 0.98). The reason for these differences in sensitivity is likely the inclusion of the unknown 'pseudo-temperature' $T_{z'}$ in the thermal network model. If $T_{z'}$ were a measured quantity, the parameter optimization would converge on values of $k_{z'z}$ and $\frac{m_{z'}}{m_{cell}}$ that produce an accurate model of both T_z and $T_{z'}$. But since $T_{z'}$ is unknown, a relatively wide range of $k_{z'z}$, and $\frac{m_{z'}}{m_{cell}}$ values can produce an accurate model of the measured T_z data while $T_{z'}$ is left unconstrained. In contrast, relatively narrow ranges of $k_{z'x}$, and $\frac{m_x}{m_{cell}}$ are required for an accurate model of the measured T_x data.

Figure 7.23 shows the results of one series of local parameter optimizations to illustrate the relationship between axial heat diffusion and cell Z mass ratio within the SETS model. The optimized results feature values of $\tau_{z'z}$ that correlate linearly with λ_z, as shown in the left chart. This translates to a linear correlation between $\frac{m'_z}{m_{cell}}$ and $k_{z'z}$, as shown in the right chart. While all datapoints shown in Figure 7.23 produce acceptable accuracy in the SETS model, most of these datapoints lie outside the expected ranges of $\frac{m'_z}{m_{cell}}$ and $k_{z'z}$ drawn from Steinhardt et al. [183], and no datapoints lie in the overlapping region which meets expectations for both parameters. Using the same series of optimizations, Figure 7.24 demonstrates how the SETS model can produce different values of $m_{cell}c_p$ depending on the optimized parameter values, with larger $k_{z'z}$ values generally corresponding to larger $m_{cell}c_p$ values (though the correlation is not as linear as the one in Figure 7.23). Again, no single datapoint meets the physical expectations of both parameters.

Any datapoint in Figure 7.23 and Figure 7.24 could be arbitrarily selected for the SETS model based on accuracy alone, so the most appropriate choice should provide the best agreement with physical expectations. The datapoint with $k_{z'z} = 14.9$ W/m·K, $\frac{m_{z'}}{m_{cell}} = 0.75$, and $m_{cell}c_p = 76.3$ J/K is selected since this brings $k_{z'z}$ as close as possible to its expected range while maintaining both $\frac{m_{z'}}{m_{cell}}$ and $m_{cell}c_p$ within expected ranges. The SETS model results associated with this datapoint were already presented in Figure 7.17.

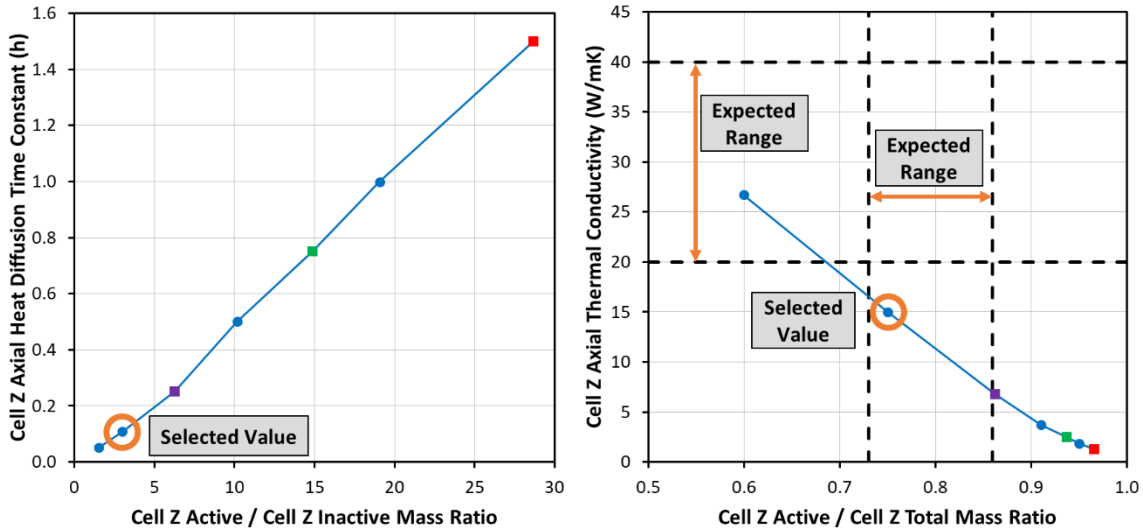


Figure 7.23 Correlation between λ_z and $\tau_{z'z}$ (left) and between $m_{z'}/m_{cell}$ and $k_{z'z}$ (right). All datapoints give acceptable accuracy for T_z and T_x in the SETS model.

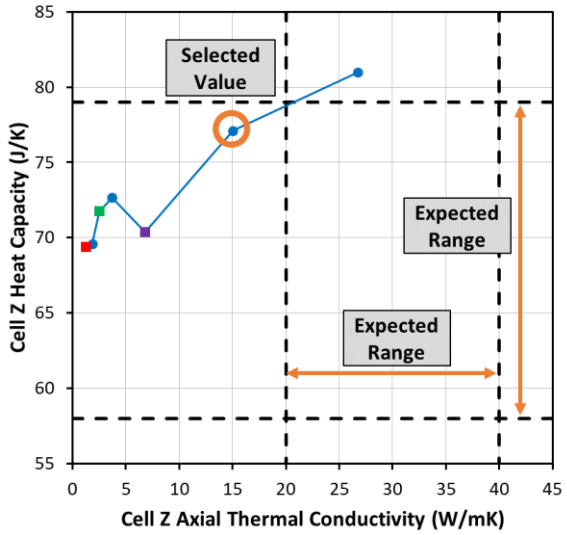


Figure 7.24 Correlation between $k_{z'z}$ and $m_{cell}c_p$. All datapoints give acceptable accuracy for T_z and T_x in the SETS model

The effect of the unconstrained $T_{z'}$ pseudo-temperature on the SETS model results is illustrated in Figure 7.25. The top, middle, and lower charts respectively show the model results associated with the red, green, and purple square data markers from Figure 7.23 and Figure 7.24 (the corresponding values of λ_z and $\tau_{z'z}$ are highlighted in Figure 7.25 using blue font). This demonstrates how slower axial heat diffusion within cell Z (i.e. larger $\tau_{z'z}$) gives a larger gap between $T_{z'}$ and T_z while maintaining accuracy in both T_z and T_x.

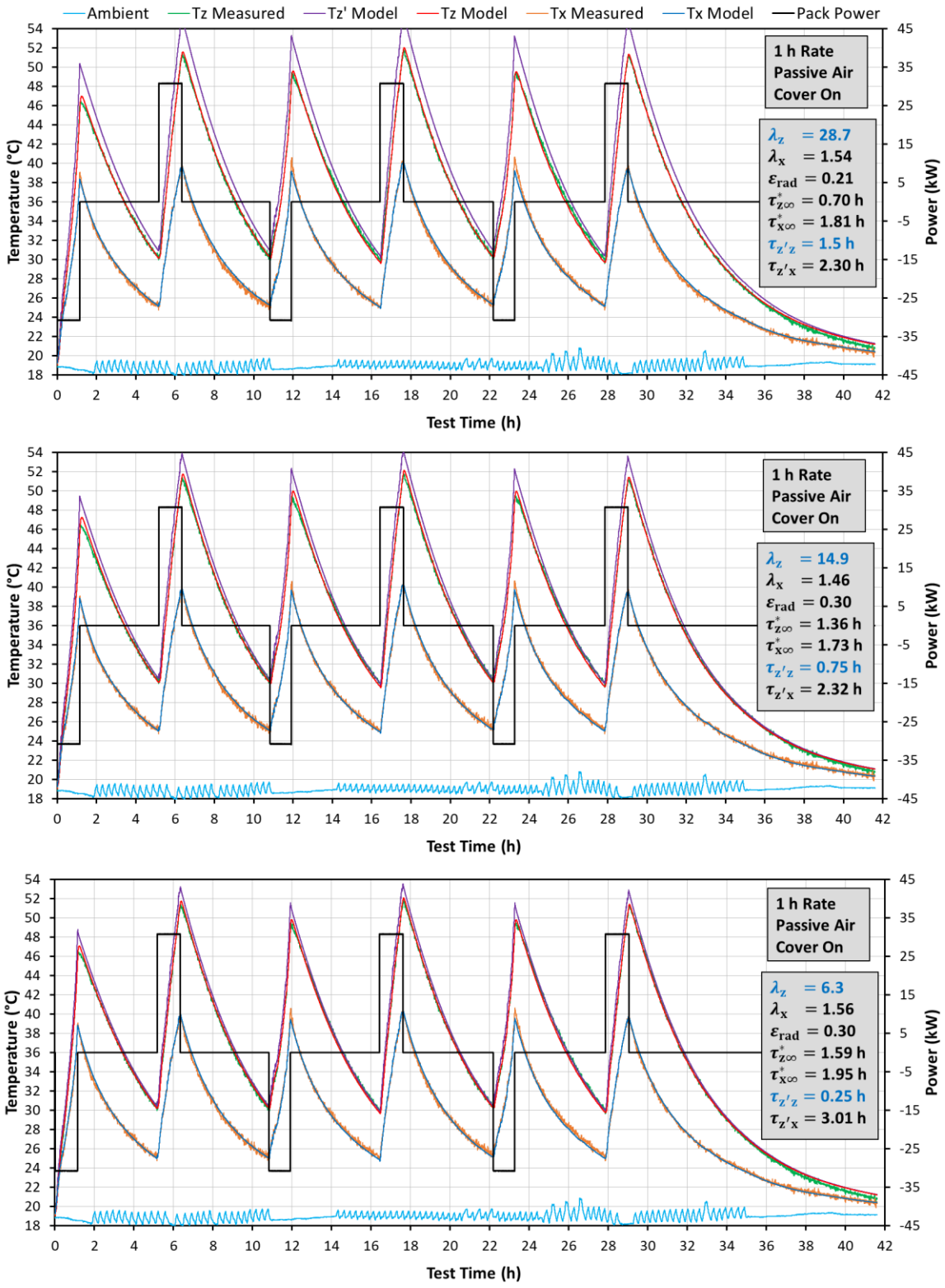


Figure 7.25 Three viable sets of parameter values illustrating the effect of λ_z and $\tau_{z'z}$ on the modelled $T_{z'}$ profile.

The three charts in in Figure 7.25 show that different sets of parameter values can produce essentially the same T_x and T_z results despite significant changes in the $T_{z'}$ results. Since $T_{z'}$ is unconstrained, parameter values should be chosen such that the corresponding $T_{z'}$ results agree with physical expectations. It is known that $k_{\parallel}$ allows for relatively fast axial heat diffusion in cylindrical lithium-ion cells (discussed in Section 2.6.5), so there should be little difference between T_z and $T_{z'}$ except when the heat generation rate is great enough to dominate heat diffusion. The top and middle charts in Figure 7.25 show that $T_{z'}$ remains notably higher than T_z even during standby periods, which seems unrealistic. This is improved in the bottom chart in Figure 7.25, but the most realistic results are produced by the selected parameters shown in Figure 7.17 and Figure 7.18, where $T_{z'}$ rises above T_z during high-power cycling but rapidly converges to T_z when power is interrupted.

The sensitivity analysis has demonstrated that the proposed SETS model has substantial flexibility due to the use of a pseudo-temperature for modelling two-dimensional heat diffusion. However, the availability of published experimental values for lithium-ion battery thermal properties makes it possible to better constrain the SETS model within physical expectations. This increases the likelihood that $T_{z'}$ reflects the true internal temperature trends of cell Z.

7.5.6. Model Versatility

In order to demonstrate the versatility of the SETS model, the seven SETS model parameters were re-optimized for a second empirical dataset. To obtain this second dataset, the 4 h, 2 h, and 1 h constant-power tests described in Section 7.4.1 were repeated with the battery housing cover removed, since this changes the rate of convection and radiation from the cells. The seven SETS model parameters were initialized to the values obtained from the original parameter optimization (see Figure 7.17), and only $\tau_{z\infty}$, $\tau_{x\infty}$ and ε_{rad} were permitted to change in the re-optimization. If the SETS model is designed well, then it should be able to fit this new set of empirical training data using the same values of λ_z, λ_x, $\tau_{z'z}$, and $\tau_{z'x}$, since these parameters are independent of the housing cover. It was found that the SETS model remained insensitive to ε_{rad} despite the change in environmental conditions, so this parameter was fixed at $\varepsilon_{rad} = 0.5$ so that only $\tau_{z\infty}$ and $\tau_{x\infty}$ could be re-optimized.

The results of the re-optimization are shown in Figure 7.26. Five of the seven parameters have the same values from the original optimization in Figure 7.17, but $\tau_{z\infty}$ decreased from 7.93 h to 1.65 h and $\tau_{x\infty}$ decreased from 1.63 h to 1.59 h. The decrease in $\tau_{z\infty}$ and $\tau_{x\infty}$ corresponds to an increased rate of heat dissipation from both cell Z and cell X, which should be expected in the absence of the housing cover. With only these two changes, the SETS model is able to give an accurate fit to the new empirical dataset at all three power rates, and the accuracy is comparable to the results in Figure 7.17. The notable difference between Figure 7.26 and Figure 7.17 is that Figure 7.26 features a larger difference between T_z and $T_{z'}$ during operation. This makes physical sense since cell Z is now able to dissipate more heat directly to the environment with the housing cover removed, which will result in a larger temperature gradient between the core and the surface. Even so, $T_{z'}$ still quickly converges to T_z once power is interrupted. This shows that the SETS model is robust and adaptable to different environmental conditions.

The initial estimates of $h^*_{conv,z}$ and $h^*_{conv,x}$ were based on a simplified thermal model which neglected the housing cover. Since the re-optimized values apply to a scenario where there is no housing cover, these values should agree more closely with the initial estimates compared to the optimized values for a covered battery pack. Based on the pack geometry described in Section 7.3.1, the parameter re-optimization resulted in an increase in $h^*_{conv,z}$ from 0.75 to 3.62 W/m^2·K and an increase in $h^*_{conv,x}$ from 2.52 to 2.59 W/m^2·K. These values are compared to the initial estimates in Table 7.6, showing that removing the housing cover causes $h^*_{conv,z}$ to increase from 17 % of its initial estimate to 81 %, while $h^*_{conv,z}$ increases from 50 % of its initial estimate to 51 %. The fact that $h^*_{conv,z}$ is now close to its estimated value gives merit to the SETS model, and suggests that the housing cover significantly inhibits heat dissipation from the top of cell Z. This suggestion is supported by the fact that the battery cover features an electronics housing which sits directly on top of cell Z (see Figure 7.5), potentially adding significant thermal resistance.

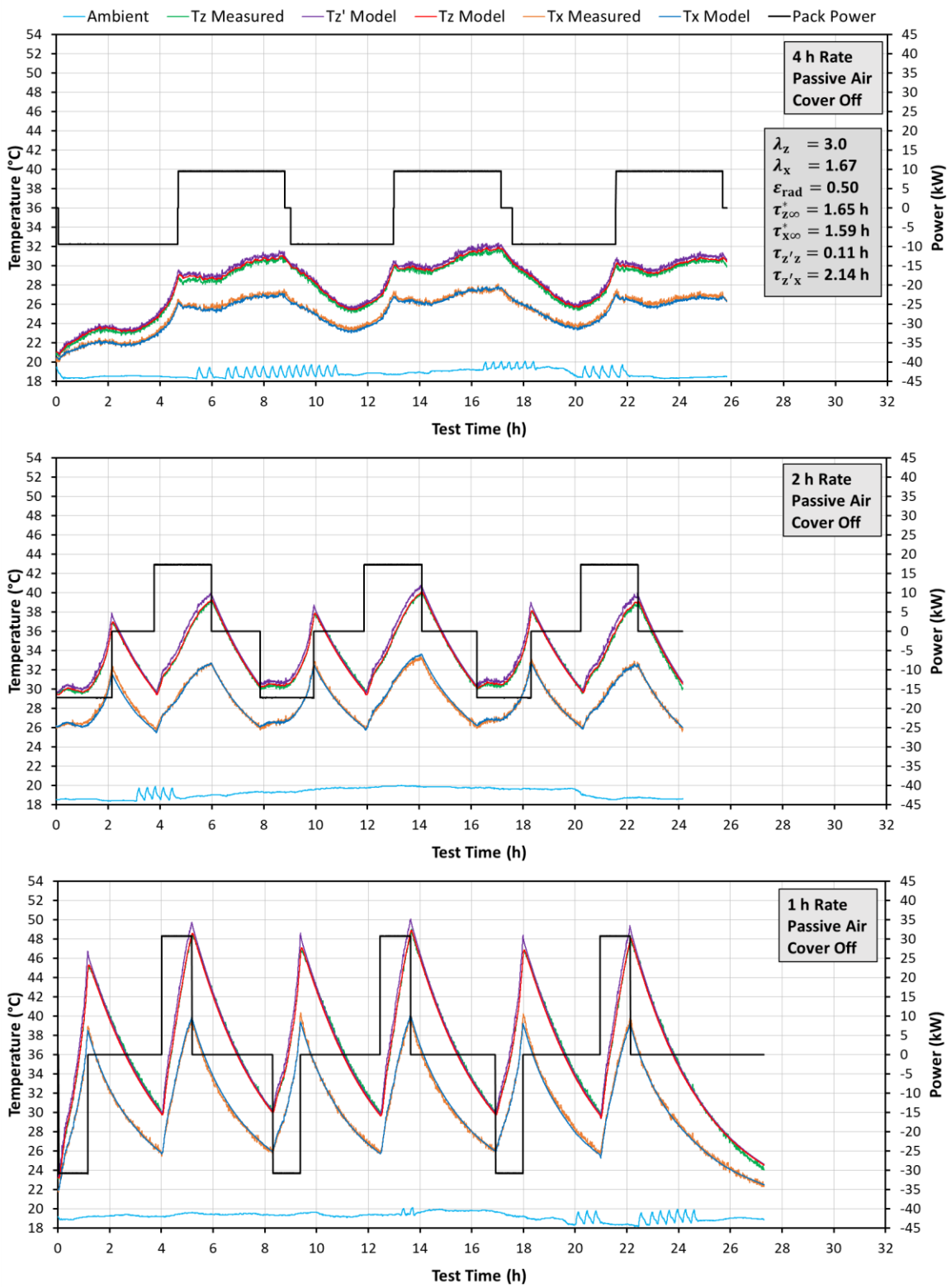


Figure 7.26 SETS model results with re-optimized values of heat dissipation parameters $\tau_{z\infty}$ and $\tau_{x\infty}$ based on a new empirical dataset with the battery housing cover removed.

Table 7.6 Comparison of optimized convection coefficients to initial estimates.

Parameter	Estimated Value	Optimized Value (Battery Cover On)	Optimized Value (Battery Cover Off)
$h^*_{\mathrm{conv,z}}$ (W/m^2·K)	4.49	0.75	3.62
$h^*_{\mathrm{conv,x}}$ (W/m^2·K)	5.06	2.52	2.59

In contrast, the parameter re-optimization suggests that $h^*_{\mathrm{conv,x}}$ is about half of the expected value regardless of the housing cover. This could be related to the simplifications of the cell X model. For example, the model neglects the effects of the plastic module housing, which covers about half of the 'exposed' surface area of cell X and thus adds thermal resistance. Furthermore, the liquid channels extending from the end of the module may partially shield cell X from convective air flow, which would decrease $h^*_{\mathrm{conv,x}}$ with or without a housing cover. While there is little air space between the housing cover and the top of the module, there is substantial space for airflow between the housing cover and the module corner, which may help explain why cell X is less affected by the housing cover compared to cell Z.

7.5.7. Practical Case Study

The empirical datasets presented in Section 7.5.1 and Section 7.5.6 are based on T-type thermocouples retrofitted to the inside of a Tesla Model 3 SR+ battery pack after removing the housing cover. In a commercial second-life application with unmodified EV battery packs, the SETS model would rely on real-time temperature data measured by Tesla's built-in thermistors and read by Tesla's built-in BMS. The SETS model must therefore be adaptable to this data input.

The orange and green data trends in the top chart of Figure 7.27 represent thermistor data from a Tesla Model 3 long range (LR) battery pack, read directly from Tesla's built-in BMS with a 5 s sampling interval during testing. This battery pack was tested as-received without any attempt to remove the housing cover. Passive cooling was employed for these particular tests. The Model 3 LR features longer battery modules than the Model 3 SR+, so the optimized parameter values determined for a Model 3 SR+ do not necessarily apply to a Model 3 LR. However, these two battery types are nearly identical at the rear of the

pack where T_z and T_x are located, so the Model 3 LR dataset provides an opportunity to illustrate how the SETS model can be applied in practice.

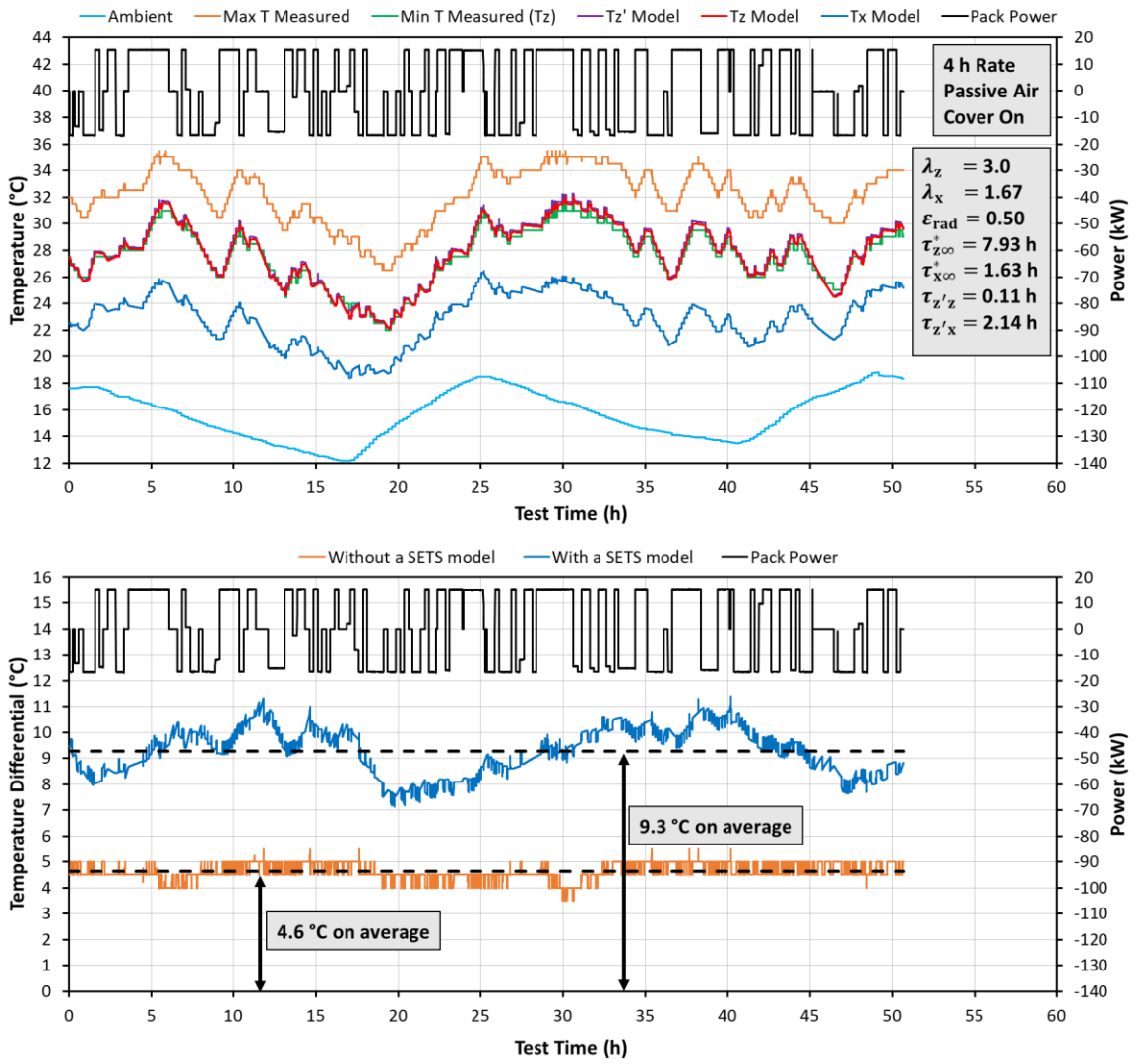


Figure 7.27 Example of how a SETS model can predict a more accurate battery pack temperature differential during second-life operation based on real-time BMS temperature data and pre-determined SETS model parameters.

The test protocol shown in Figure 7.27 features a duty cycle designed to simulate a realistic energy storage power profile for a battery deployed in day-ahead and real-time energy markets in the United States. The power is limited to a 4 h rate and the battery SOC is permitted to fluctuate within cell voltage bounds of 3.0 V and 4.15 V. Due to the thermally uninsulated enclosure used for this test, the ambient temperature also fluctuates between 12 °C and 18 °C on a 24 h cycle with the outdoor environment. While both the power

profile and ambient conditions differ from the empirical datasets used to optimize the SETS model parameters, Figure 7.27 can still be used as an illustrative case study.

The Tesla BMS data reported T_{high} corresponding to a thermistor located in one of the two interior modules of the pack, and $T_{\mathrm{low}} = T_{\mathrm{z}}$ corresponding to the thermistor attached to cell Z in the middle of the outer module. Using the seven optimized parameter values from Figure 7.17, the SETS model is applied to predict the temperature of cell X at the corner of the outer module based on the measured thermistor data from cell Z. The results in Figure 7.27 show that the SETS model is able to accurately reproduce the T_{z} trend and generate a T_{x} trend using the equations listed in Table 7.2. Since T_{x} is unknown in this case, the initial guess for $T_{\mathrm{x},0}$ is taken as the average of $T_{\mathrm{z},0}$ and $T_{\infty,0}$, with the understanding that any error in this guess will dissipate in a few hours due to the inherent error decay of the SETS model (as discussed in Section 7.5.2).

The bottom chart in Figure 7.27 plots the pack temperature differential calculated from the Tesla thermistor measurements alone (i.e. no SETS model) and the pack temperature differential calculated by the SETS model. Without a SETS model, the system operator would believe the pack temperature differential to be about 4.6 °C, but the SETS model shows that the true pack temperature differential is at least double this value (nearly 10 °C). As explained in Section 3.1.3, it is typically recommended that pack temperature differentials be maintained below 5 °C to mitigate degradation divergence, so this finding is significant. If a second SETS model were developed to predict the temperature near the centre of the battery pack, the true pack temperature differential would likely be revealed to be even higher (> 10 °C), and this difference would be even more pronounced at greater power rates. The proposed SETS model technology offers improved accuracy for these important thermal performance metrics, which can be used by system operators in the control of real-time battery operation and the prediction of remaining useful life.

7.6. Future SETS Research

This chapter has demonstrated a proof of concept for SETS technology, but more research is needed before SETS models can be reliably deployed in commercial second-life battery projects. This section will highlight specific recommendations for future work in this field.

7.6.1. Heat Generation Modelling

One important consideration for future SETS research is cell heat generation. As described in Section 7.2.5, the SETS model presented in this chapter assumes that $\dot{q}_{\mathrm{gen,x}} \approx \dot{q}_{\mathrm{gen,z}'}$. For this particular SETS model, this assumption proved adequate with only a slight limitation when discharging to a low voltage limit at a 1 h power rate. However, it may not always be possible to create an accurate SETS model using this assumption. This is illustrated in Figure 7.28, which plots the cell voltage and total heat generation during the third cycle of the 4 h, 2 h, and 1 h tests as was done in Section 7.4.3.

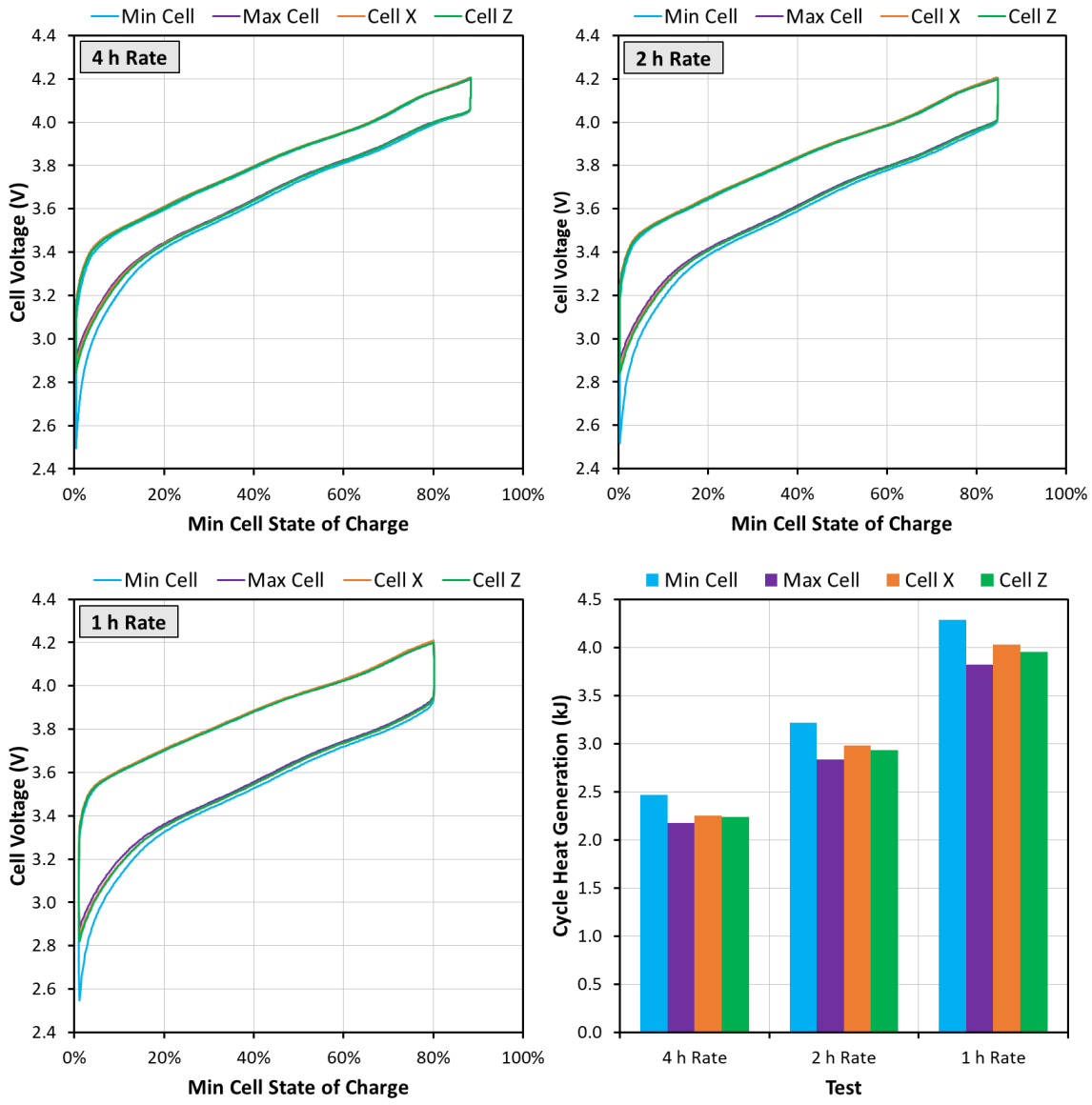


Figure 7.28 Voltage and heat generation for four different cells in the Tesla Model 3 SR+ battery pack during a single cycle at three different power rates.

Figure 7.28 compares the measurements for cell X and cell Z to the two cells which exhibited the lowest and highest voltage during discharge (respectively named 'min cell' and 'max cell'). This shows that while cell X and cell Z happen to have fairly similar cycle heat generation (within about 2 %), the min cell and max cell have a much greater difference (about 13 %). If cell X and cell Z had exhibited a 13 % difference in cycle heat generation, then the $\dot{q}_{\mathrm{gen,x}} \approx \dot{q}_{\mathrm{gen,z'}}$ assumption may not have proved adequate for this SETS model.

The 2019 Tesla Model 3 SR+ battery pack used in development of this SETS model was at approximately 87 % SOH at the time of testing. Since most second-life battery packs will be acquired at 60 to 80 % SOH, it is likely that commercial second-life batteries will exhibit an even greater cell-to-cell variance in heat generation than shown in Figure 7.28, and this variance will likely increase as batteries continue to degrade in second life. This means that a commercially viable SETS model should include a heat generation model which quantifies the relative real-time heat generation rate of one cell/module compared to another. The goal of such a heat generation model would be to estimate the ratio shown in Equation 7.102, where T_{x} and $T_{\mathrm{z'}}$ are absolute temperatures.

$$\frac{\dot{q}_{\mathrm{gen,x}}}{\dot{q}_{\mathrm{gen,z'}}} = \frac{I_{\mathrm{x}}\left(V_{\mathrm{x}} - V_{\mathrm{rev}} + T_{\mathrm{x}}\frac{\partial V_{\mathrm{rev}}}{\partial T}\right)}{I_{\mathrm{z'}}\left(V_{\mathrm{z'}} - V_{\mathrm{rev}} + T_{\mathrm{z'}}\frac{\partial V_{\mathrm{rev}}}{\partial T}\right)} \tag{7.102}$$

Since all that is needed is a ratio rather than the actual $\dot{q}_{\mathrm{gen}}$ values, precise estimates for V_{rev} and $\frac{\partial V_{\mathrm{rev}}}{\partial T}$ may not be necessary. If these quantities cannot be determined experimentally for a given EV battery pack, it may suffice to make estimates based on published data for similar cell chemistries. However, both V_{rev} and $\frac{\partial V_{\mathrm{rev}}}{\partial T}$ are functions of cell SOC, and since the BMS balances the cells in the charged state, cells with lower SOH values will reach lower SOC values when the battery is discharged. This means that an accurate result for Equation 7.102 may require the SOC and SOH of individual cell groups to be known or at least approximated, especially for aged batteries where cell-to-cell SOH variance is more likely. As explained in Section 3.1.2, modern EV batteries typically

feature an advanced BMS capable of estimating SOH and SOC for each cell group in the pack, so this information should be available for most second-life EV battery packs where BMS accessibility allows for pack-level repurposing. Alternatively, second-life battery companies could use BMS cell voltage readings as inputs for their own in-house SOH and SOC estimation algorithms. In either case, Figure 7.29 illustrates how SOH and SOC estimation algorithms could be integrated into a more advanced SETS model that compensates for non-uniform battery degradation. Development of this more advanced SETS model is beyond the scope of this thesis, but it is recommended as a worthwhile opportunity for future research.

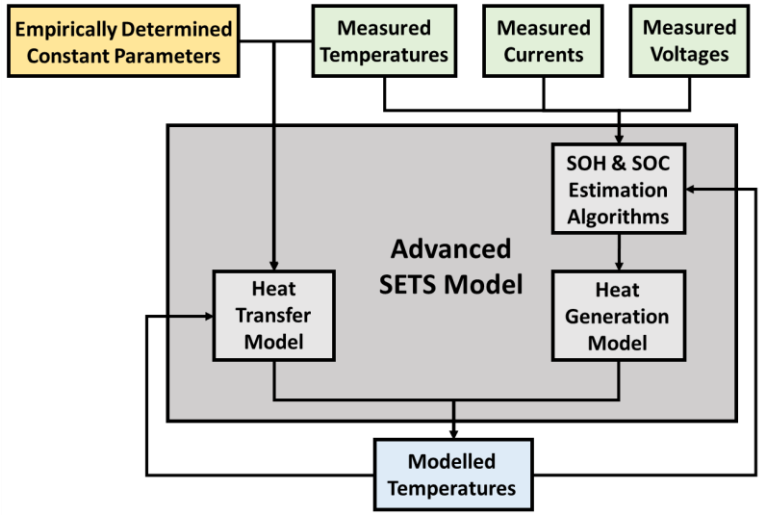


Figure 7.29 Graphical summary of advanced SETS model concept proposed for future research.

As discussed in Section 3.4.1, some second-life battery operators may elect to constrain batteries within a relatively narrow SOC range (e.g. 30 % to 70 %) as a means of slowing degradation rates and extending system lifetime. In such a scenario, the $\dot{q}_{\mathrm{gen,x}} \approx \dot{q}_{\mathrm{gen,z'}}$ assumption may be sufficient since the battery will avoid the low SOC region where cell-specific heat generation rates are most likely to diverge. Future SETS research could explore whether the $\dot{q}_{\mathrm{gen,x}} \approx \dot{q}_{\mathrm{gen,z'}}$ assumption is sufficient in specific SOC ranges for aged second-life battery packs.

7.6.2. Diverse Training Data

Future SETS research should also explore beyond the limited operational and environmental conditions employed in this research project. The SETS model presented in this chapter was trained using an empirical dataset consisting of constant-power tests at three different power rates in a relatively consistent ambient environment. While this training data was sufficient for a proof of concept, it may not adequately capture the full range of operational scenarios and ambient conditions that arise in commercial second-life energy storage projects.

Figure 7.27 already demonstrated how commercial second-life battery projects can feature a fluctuating power profile and a varying ambient temperature. To ensure model reliability in such conditions, the SETS model parameters should be optimized using training data that captures this variability. Future SETS research should explore a wider range of training data and verify SETS reliability in a wide range of conditions. Suggested conditions include cold and warm environments, fluctuating environments, frequency regulation duty cycles, and stacked-service duty cycles. The results presented in this Section 7.5.1 suggest that a single high-power deep-discharge test with lengthy standby cooling periods may be sufficient training data to optimize SETS model parameters for any operational scenario, but this must be explored in future research.

One notable consideration is the handling of radiation in the heat dissipation parameters. The methods described in Section 7.3.3 include a linearization of the radiation equation, and this linearization is only reliable for a given ambient temperature T_∞. If the SETS model is deployed in an environment where T_∞ varies significantly (e.g. 10 °C daily fluctuation), the linearization would introduce an inaccuracy into the SETS model. New methods could be developed to build T_∞ compensation into the heat dissipation parameters. However, the SETS model presented in this chapter proved to be fairly independent of $\varepsilon_{\mathrm{rad}}$, so such methods may not be necessary. Future research should explore whether $\varepsilon_{\mathrm{rad}}$ is more impactful when the SETS model is applied at different T_∞ values (e.g. 15 °C vs 30 °C).

7.6.3. Customized Parameter Optimization

Another worthy area of exploration is parameter optimization This chapter employed a common parameter optimization software in order to demonstrate a proof of concept for SETS models, but it may be beneficial to develop parameter optimization algorithms that are tailored to SETS models. This may be especially necessary for more complex SETS models with many unknown parameters. Parameter optimization algorithms are outside the scope of this thesis, but it is recommended as a consideration for future SETS research.

7.6.4. Different SETS Models

Future SETS research will need to grapple with the significant diversity among EV battery pack designs. This chapter has presented one SETS model to serve as a proof of concept for SETS technology, but each unique EV battery pack design will require a unique SETS model tailored to the architecture and geometry of the given pack. A range of SETS models may also be required for a single battery pack if temperature models are required at multiple locations with different geometries. For example, a SETS model could be developed to model the temperature in the centre of the Tesla Model 3 SR+ battery pack based on the measured T_{z}. This would require a different SETS model design compared to the one presented in this chapter, since a cell in the centre of the pack must be modelled differently than cell X at the outer module corner.

Different TMS designs will also require different SETS models. For example, the SETS model presented in this chapter would need to be modified if the Tesla Model 3 SR+ battery pack was to be operated with liquid cooling. In this case, the model would need to account for forced convection between the liquid coolant and the liquid channel. Heat conduction from the cells to the liquid channels would likely dominate the heat conduction within the modules and the natural convection from the modules to the ambient air, so parameters like $\tau^{*}_{\mathrm{x}\infty}$, $\tau^{*}_{\mathrm{z}\infty}$, and $\tau_{\mathrm{z}'\mathrm{x}}$ may not be necessary in a liquid-cooled SETS model. Future research should explore these possibilities.

Hybrid SETS models may be required for second-life battery projects featuring variable TMS designs, such that different sets of SETS parameters are activated under different conditions. For example, if a cooling fan is engaged intermittently, then different values of

$\tau^*_{x\infty}$ and $\tau^*_{z\infty}$ would need to be activated to account for the switching between natural convection and forced convection. If liquid cooling is engaged intermittently, then two completely different SETS models would need to be activated intermittently to account for the significant change in thermal management. In such cases as these, the SETS model parameters would have to be determined using training data that reflects the operational conditions as closely as possible. Thermal management setpoints such as liquid pressure and flow speed could be used as real-time inputs for the SETS model.

7.6.5. Recommended Approach

Since there are numerous unique EV battery pack designs, SETS models will need to be tailored specifically to the battery pack in question. While the SETS design process may vary considerably for different EV battery packs, a generalized approach is described below to guide future SETS research and development.

Pilot Pack

A 'pilot pack' for a given EV battery design must be opened and retrofitted with temperature sensors placed at the desired locations for temperature prediction. Care should be taken to ensure that any modifications or retrofits to the pack do not significantly impact its heat transfer properties.

Thermal Network

A thermal network model must be designed to establish relationships between relevant temperature nodes in the battery pack. This requires visual inspection of the opened pilot pack. Significant simplifications may be necessary in order to keep the number of unknown parameters to a minimum. This chapter has presented examples of such simplifications, such as employing the mass ratio λ_x to account for heat diffusion away from cell X. The thermal network may also need to account for heat diffusion from the cell interior to a temperature sensor location. This chapter has presented a simple means of accomplishing this using an unverifiable 'pseudo-temperature' to model the cell interior temperature.

System Equations

A set of system equations must be developed based on the established thermal network. These equations should derive from a fundamental energy balance for each temperature node in the thermal network, including any pseudo-temperatures. This chapter has

presented novel methods to simplify the system equations into a form which can be solved analytically and adapted numerically. This approach is recommended for future SETS research.

The system equations will require ratios to describe the heat generation rates at 'unknown' temperature nodes (e.g. cell X) compared to 'known' temperature nodes (e.g. cell Z). Depending on the age and intended application of the battery, it may suffice to assume a unity ratio. Otherwise, a heat generation model may need to be developed which receives real-time BMS cell voltage measurements as inputs. This may also require an algorithm to estimate cell-specific SOC and SOH values.

When natural convection is the dominant heat dissipation pathway, the heat dissipation parameters will be dependent on temperature. This chapter has presented a novel technique to account for this temperature dependence using constant parameters. The heat dissipation parameters may also need to separate radiation from convection. This chapter has presented a simple means of accomplishing this using a linearized radiation equation and a novel heat dissipation expression featuring separate terms for convection and radiation.

Parameter Optimization

A constant value must be determined empirically for each unknown parameter in the SETS model. This requires empirical training data acquired from retrofitted temperature sensors applied to the pilot pack during operational tests. The pilot pack should be restored to its as-received form as closely as possible for these tests (other than the retrofitted temperature sensors) to ensure that its heat transfer properties accurately reflect a commercially deployed battery pack of the same design. The tests should cover the complete range of power profiles, ambient temperatures, and thermal management conditions that are expected in commercial applications. Data sampling at 10 s intervals is recommended.

An appropriate parameter optimization software must be selected based on the number of SETS model parameters being optimized. Microsoft Excel Solver proved to be an adequate optimization software for the proof-of-concept SETS model presented in this chapter. For more complex models, it may be necessary to develop a customized parameter optimization algorithm. Physical parameters should be estimated for the pilot pack as a means of constraining the SETS model parameters during the optimization process. This chapter also

presented a novel technique for estimating cell heat capacity values from the SETS model results using ‘adiabatic temperature change’ calculations, which can provide an additional constraint for parameter optimization.

Implementation

Once the SETS model parameters are optimized for the pilot pack, the SETS model can be implemented with an unlimited number of second-life battery packs of the same design without requiring any modifications to the packs. To produce the desired temperature predictions, a commercially deployed SETS model must be provided with real-time measurements from original battery temperature sensors as well as ambient temperature sensors installed on-site. Data sampling intervals of 10 s to 60 s are recommended to ensure reliability in the model.

7.7. Chapter Summary

Chapter 7 has proposed the concept of ‘spatially extrapolated temperature sensors’ as a novel battery monitoring technology. While SETS technology could theoretically be used in any battery application to reduce the number of physical sensors required to monitor battery temperature distributions, this chapter has focused on practical applications for second-life battery packs. When the EV battery packs are directly repurposed without modification to save time and costs, it can introduce significant uncertainty regarding battery thermal performance, especially when deviating from the original TMS. The proposed SETS technology can mitigate this uncertainty by providing a non-invasive means of monitoring temperatures at any desired location in the battery pack based on real-time measurements from the original temperature monitoring system.

The primary contribution of this study is demonstrating a detailed SETS proof of concept for a Tesla Model 3 SR+ battery pack. This includes the development of a novel battery thermal network model and the derivation of the associated system equations in a numerically solvable form, as well as the use of seven constant parameters to capture the key physical and thermal characteristics of the battery and its surroundings. Numerous novel mathematical techniques have been presented to simplify the complexities of battery pack thermal behaviour, including heat generation, three-dimensional heat diffusion, natural convection, and radiation. The simplified modelling approach relies on the

retrofitting of temperature sensors to a ‘pilot pack’ so that the constant parameters can be quantified for a given EV battery pack design using parameter optimization with empirical training data. Novel methods for constraining the parameter optimization process within expected physical limits have also been presented.

The proposed methods for thermal modelling and parameter optimization have been validated for a SETS model designed for a 2019 Tesla Model 3 SR+ battery pack. The novel numerical methods are simple enough to be executed in a standard Microsoft Excel spreadsheet, yet yield highly accurate and versatile temperature predictions after parameter optimization. The root-mean-square error in the model was about 0.3 °C, which is smaller than a typical thermistor resolution. The SETS model has also been shown to exhibit inherent error decay, which enhances the reliability of the predicted temperatures. In a preliminary case study, the SETS model revealed that the battery pack temperature gradient was more than double the 4.6 °C value given by the original temperature sensors. This shows that SETS technology can be used to control battery thermal management systems and/or control battery power to improve the safety and cycle life of second-life battery energy storage systems.

This pilot study has also identified a number of opportunities for future SETS research and development. In particular, integrating SETS models with cell-specific SOC and SOH estimation algorithms will likely yield the most reliable results in commercial applications. A generalized approach to SETS modelling has also been provided to help guide other researchers in developing SETS models for EV battery packs.

Chapter 8 CONCLUSIONS AND RECOMMENDATIONS

Significant research and development efforts are being made in the field of second-life batteries, but the diversity and complexity of EV battery pack designs still pose a significant technical challenge for the nascent second-life battery industry. This thesis has advanced the field by demonstrating a set of novel experimental and numerical methods for evaluating and comparing the electrical and thermal performance of different EV battery designs in second-life applications. These methods provide new tools to aid in the modelling, design, and control of stationary energy storage systems composed of repurposed EV batteries. To fill knowledge gaps related to pack-level thermal performance, the research project has focused exclusively on full EV battery packs. Application of the proposed experimental methods has produced a first-of-its-kind experimental dataset where five unique EV battery packs are directly compared in terms of second-life performance capabilities. The experimental results have yielded a wealth of practical insights regarding the electrical and thermal performance of second-life battery packs. This final chapter will summarize the main conclusions of the research project and offer recommendations to other researchers and developers in the second-life battery industry.

8.1. Methods for Evaluating Second-life Battery Performance

The second-life battery performance evaluation methods proposed in this research project include experimental, analytical, and numerical methods. Based on the outcomes of the research project, the following conclusions can be drawn regarding second-life battery performance evaluation methods:

Experiment Design

1. The symmetrical constant power test protocol described in Section 4.4 has proven effective for experimentally characterizing the electrical and thermal performance of repurposed EV batteries. The application of 4 h, 2 h, and 1 h power rates produced sufficient results to describe the full range of battery performance in relation to second-life applications, and the use of prescribed cooldown periods based on a fixed temperature control setpoint also proved effective for producing consistent thermal test conditions and characterizing battery cooldown rates.
2. Discharge duration has proven to be an appropriate standard parameter on which to base the experimental test protocol. When all batteries use the same amount of time to discharge their stored energy, batteries with different capacities and SOH levels can be equitably compared both electrically and thermally. This is superior to

the C rate method which neglects the effects of degradation on second-life battery energy capacity.

3. Charging a given battery to 100 % SOC before initiating the test sequence facilitates the tracking of battery SOC throughout the test sequence, which is useful for evaluating how the operational SOC window is impacted by the power rate.
4. The thermal performance results have demonstrated the importance of evaluating the liquid cooling capabilities of second-life batteries designed with active-liquid thermal management. Experimental techniques have been described to enable these battery packs to be tested with and without active-liquid thermal management.
5. The thermal performance results have also demonstrated the importance of ensuring temperature sensors are placed appropriately when testing EV battery packs, so as to capture temperature maximums and temperature gradients.

Data Analysis

6. A total of seven primary performance metrics and 14 secondary performance metrics have proven useful for evaluating and comparing the experimental performance results obtained for different EV batteries using the SCP test protocol. Many of the proposed performance metrics appear to be fairly insensitive to changes in SOH, which is especially valuable for comparing second-life batteries at different SOH levels.
7. The power-to-energy ratio (inverse of discharge duration) has proven to be an appropriate standard independent variable against which to graphically evaluate the various performance metrics. A total of 18 additional graphical techniques have also proven useful for comparing the electrical and thermal performance characteristics of different EV battery packs, as summarized in Section 5.8.
8. The average volumetric heat generation rate $\dot{\bar{q}}_v$ has proven to be a particularly useful performance metric, as this novel metric bridges electrical and thermal performance and also provides an effective independent variable against which to compare measured battery temperatures.
9. Section 5.7 has demonstrated a novel analytical technique for converting the primary performance metrics into a scoring and ranking system for EV battery packs, according to volume, energy, and thermal performance categories. The ranking system provides a simple mechanism to help project developers understand which EV battery designs are best suited for a given second-life application, though this will need to be considered alongside degradation performance metrics in practice. The ranking system is useful whether a second-life project developer is working with multiple EV battery types or deciding on a single EV manufacturer to partner with for all second-life projects.

Standardized Performance Testing

10. Novel empirical equations have been used to construct a new numerical modelling tool that can extrapolate experimental test results to a desired discharge duration, as described in Chapter 6. This facilitates the characterization of second-life battery

electrical and thermal performance at standardized discharge durations (e.g. 4.0 h, 2.0 h, 1.0 h), which would otherwise require many test iterations over many days of testing.

11. The proposed performance extrapolation model allows for a condensed version of the original test protocol to achieve complete electrical and thermal performance characterization of a used EV battery pack in approximately 22 to 32 h of testing, while avoiding relatively risky high-power tests. A proposed alternative model could potentially achieve similar extrapolation accuracy with an even shorter test protocol requiring approximately 14 to 22 h of testing, but this model will require further experimental validation before it can be implemented.

Thermal Modelling

12. Due to the unique temperature distribution characteristics of different EV battery pack designs, no simple empirical relationship can consistently describe how pack temperature gradients of all EV batteries change with the applied power rate. To model the dynamic relationship between different temperature nodes in a given EV battery pack, a more advanced modelling approach is required.
13. A simplified thermal network modelling method has proven to be capable of spatially extrapolating the temperature at one node in an EV battery pack to another node during real-time battery operation. A proof of concept for this novel SETS model technology has been demonstrated for the case of the Tesla Model 3 SR+ battery back, producing highly accurate fits to experimental data.
14. The proposed SETS model technology would be especially valuable for a second-life battery company that wishes to monitor additional temperature nodes in repurposed EV battery packs during second-life service, since the model would negate the need to undertake costly modifications and retrofits to all battery packs other than a single pilot pack used to empirically optimize the model parameters for a given EV battery pack design.

8.2. Electrical Performance of Second-life Batteries

The comparative performance study in Chapter 5 revealed that electrical performance varies considerably among different EV batteries due to differences in cell chemistry and other cell design parameters that influence the trade-off between energy density and internal resistance. The following conclusions can be drawn regarding the electrical performance of second-life batteries:

Energy Density

1. Different EV batteries can have very different energy densities regardless of SOH. The five EV battery packs tested in this research project yielded module energy density values ranging from 130 to 390 Wh/L at a 4 h discharge rate when accounting for differences in SOH levels.

2. Newer EV batteries can generally be expected to have higher energy densities as EV manufacturers strive for longer driving ranges.

Energy Efficiency

3. Most EV batteries can generally be expected to yield high energy efficiencies when cycled at relatively low power rates (> 96 % at a 4 h rate in this research project).
4. At higher power rates, EV batteries with high energy density (such as Tesla Model 3 and Chevrolet Bolt) or LFP chemistry (such as Lishen) will likely experience notably lower energy efficiencies (< 92 % at a 1 h rate in this research project).

Internal Resistance

5. Advancements in EV battery designs toward higher energy density evidently come at the cost of increased internal resistance and therefore lower energy efficiency. In this research project, the relatively new 2019 Tesla Model 3 battery and 2018 Chevrolet Bolt battery gave higher energy densities and lower energy efficiencies (> 300 Wh/L and < 95 % at a 2 h rate), while the relatively old 2015 BMW i3 battery and 2012 Nissan Leaf battery gave lower energy densities and higher energy efficiencies (< 150 Wh/L and > 96 % at a 2 h rate).
6. The observed influence of internal resistance on electrical performance indicates that newer EV battery designs are at an electrical disadvantage for second-life applications where energy efficiency and power capability are important (such as energy arbitrage), which could have implications for second-life battery competitiveness compared to new stationary batteries that are purpose-built for a given application.

Charge Termination

7. The usable energy capacity of an EV battery can decrease significantly if the battery is charged at higher power rates without a CV charge, due to charge termination occurring below 100 % SOC. This was most evident for the liquid-cooled Tesla Model 3 battery in this research project, which only delivered 85 % of its total energy capacity when cycled at a 4 h rate and only 69 % when cycled at a 1 h rate. This limitation could be detrimental in some second-life battery applications such as energy arbitrage, where electricity price volatility may call for brief, high-power charging periods (see Figure 3.14).
8. The impact of charge termination on usable energy capacity at higher power rates is influenced by both internal resistance and the shape of the battery voltage profile. The effect of internal resistance on charge termination is not a novel observation, but it is especially important for second-life batteries since battery internal resistance tends to increase over time and use.
9. The effect of voltage profile shape on charge termination is not commonly discussed in the literature, but it is highly relevant for second-life batteries since the range of cell chemistries used in the EV battery industry results in many unique cell voltage profiles for different EV batteries entering the second-life market. In this

research project, the nickel-rich NCA voltage profile of the Tesla Model 3 battery produced the most detrimental effect on charge termination, resulting in only 69 % of total energy capacity being delivered when cycled at a 1 h rate. In contrast, the LFP voltage profile of the Lishen battery produced the most advantageous effect on charge termination, delivering 95 % of total energy capacity when cycled at a 1 h rate. Given that most stationary batteries use LFP chemistry, second-life batteries using other chemistries may be disadvantaged in terms of high-power charge termination.

8.3. Thermal Performance of Second-life Battery Packs

The comparative performance study in Chapter 5 also revealed that thermal performance varies widely among different EV battery packs due to differences in electrical performance and thermal management design. Testing EV batteries at the pack level has provided valuable thermal performance insights specific to pack-level repurposing, which cell-level and module-level studies cannot provide. The following conclusions can be drawn regarding the thermal performance of second-life battery packs:

Heat Generation

1. Since high energy density and low energy efficiency both contribute to volumetric heat generation, newer EV battery packs designed for high energy density at the expense of energy efficiency are doubly disadvantaged in terms of volumetric heat generation. In this research project, the relatively new 2019 Tesla Model 3 battery and 2018 Chevrolet Bolt battery yielded high volumetric heat generation rates (> 12 W/L at a 1 h rate) compared to the relatively old 2015 BMW i3 battery and 2012 Nissan Leaf battery (< 4 W/L at a 1 h rate). This is why newer EV battery pack designs are typically equipped with active cooling systems.

Heat Rejection

2. Active cooling capabilities can differ significantly across different EV battery pack designs. In this research project, the measured temperature rise was much lower for the liquid-cooled Tesla Model 3 SR+ battery pack (< 8 °C at a 1 h rate) compared to the liquid-cooled Chevrolet Bolt battery pack (up to 19 °C at a 1 h rate) despite both batteries exhibiting similar volumetric heat generation rates. This implies a superior liquid channel design for the Model 3 battery.
3. While active cooling systems provide greater heat rejection rates than passive cooling, this does not necessarily mean that active-cooled batteries will always exhibit lower temperature rise results than passive-cooled batteries at a given power rate. In this research project, the liquid-cooled Chevrolet Bolt battery exhibited a greater temperature rise (19 °C) than the passive-cooled BMW i3 battery (17 °C) at a 1 h rate due to differences in volumetric heat generation rates. At 4 h and 2 h

power rates (i.e. lower heat generation rates), all active-cooled batteries exhibited lower temperature rise than all passive-cooled batteries.

Temperature Limits

4. Most EV battery packs using original TMS capabilities should be able to undergo a 2 h deep discharge at room temperature without exceeding preferred upper temperature limits (e.g. > 40 °C), though continuous cycling at this rate would be unsustainable for most passive-cooled packs. A 1 h deep discharge may approach preferred upper temperature limits, but should remain below typical upper safety limits (e.g. > 55 °C). However, some passive-cooled EV battery packs with non-uniform module arrangements may exceed preferred pack temperature gradient limits (e.g. > 5 °C) even at a 2 h rate, as was the case for the 2012 Nissan Leaf battery pack in this research project.

Cooldown Rates

5. Active cooling systems provide significant advantages over passive cooling when the battery is in standby and therefore not generating heat. This has important practical implications for stationary energy storage applications that call for the battery to undergo frequent deep cycles (such as energy arbitrage as shown in Figure 3.14). If the battery heats up significantly during one cycle and needs substantial time to cool down, it may be unavailable for the next opportunity to produce economic value. In this research project, the cycle cooldown durations of the liquid-cooled Tesla Model 3 SR+ and Chevrolet Bolt battery packs (< 2 h at a 1 h rate) were drastically reduced compared to the three passive-cooled packs (up to 8 h at a 1 h rate), allowing for 2 to 4 times as many complete deep cycles per day.

Disabling Active Cooling Capabilities

6. Disabling the original active cooling capabilities of an EV battery pack can have dramatic consequences for thermal performance. Newer EV battery pack designs with high energy density feature active cooling capabilities for good reason, as they tend to exhibit high volumetric heat generation rates. When these active cooling capabilities are disabled, temperature maximums and temperature gradients can easily exceed preferred upper limits (e.g. > 40 °C) when the battery pack is cycled at a 2 h rate, and potentially reach unsafe levels (e.g. > 55 °C) at a 1 h rate. In the case of the Tesla Model SR+ battery pack, the measured temperature gradient slightly exceeded the recommended 5 °C limit even at a relatively mild 4 h power rate when liquid cooling was disabled, and reached 9 °C at a 1 h rate.
7. The especially significant passive-cooled temperature gradients observed in the Tesla Model 3 battery modules are believed to arise due to restricted passive heat transfer through the internal liquid channels and the foam material that fills the modules. This shows how EV battery module design can have significant impacts on thermal performance, especially when active cooling capabilities are disabled in second-life service.

8.4. Recommendations for Industry

Based on the findings of this research project, the following recommendations are offered to the second-life battery industry:

System Design

1. Be aware of the significant differences in both electrical and thermal performance that different EV battery packs can exhibit. Different EV battery pack designs will have different degrees of suitability and profitability for a given second-life application. Battery control strategies for second-life operations will need to be tailored to the performance characteristics of a given EV battery pack design.
2. Be aware of the negative correlation between energy density and energy efficiency, and how this negative correlation compounds volumetric heat generation. The energy density value specified by an EV battery manufacturer could be used to qualitatively judge the energy efficiency and cooling requirements that can be expected for an EV battery pack in second-life service.
3. Be aware of published EV battery performance measurements, metrics, and rankings, such as those presented in this thesis. Apply this data to aid in the modelling and design of second-life battery systems.

Battery Performance Characterization

4. Collaborate with researchers to refine existing electrical and thermal performance characterization methods, such as those presented in this thesis. Establish standard methods to be used industry-wide so that datasets can be directly compared.
5. Apply standard electrical and thermal performance characterization methods to representative samples of acquired EV batteries, as a supplement to existing rapid health screening techniques. Rapid health screening tests will be especially limited regarding battery thermal performance since this depends on both heat generation and heat rejection
6. Advocate for the inclusion of 'total module volume' as a standard parameter to be included in future 'battery passport' protocols for EV battery packs. This parameter proved powerful for the proposed performance extrapolation model described in Chapter 6, but it has less value for industry if EV battery packs must be partially disassembled in order to measure it directly.

Performance Limitations

7. Be aware that newer EV battery pack designs are increasingly energy-dense, which increases internal resistance, decreases energy efficiency, decreases power capability, and increases cooling requirements. This means that newer EV battery pack designs are at a performance disadvantage in stationary applications without space constraints, even when the battery is in perfect health. This disadvantage is worsened when the battery is partially degraded after years of EV service. Active

cooling and low production costs may be necessary to compete with purpose-built stationary batteries.

8. Be aware that a diminishing portion of battery energy capacity can be utilized as the power rate increases, especially if a CV charge cannot be applied. The severity of this relationship can be heavily influenced both by battery internal resistance and by the shape of the voltage profile. Nickel-rich chemistries will likely be disadvantaged in this respect, while LFP batteries will likely be advantaged.

Thermal Management

9. Be aware that the warmest and coolest points in the battery modules should be monitored during second-life service and that thermal management strategies should maintain temperatures and temperature gradients within preferred limits. This may limit passive-cooled EV battery packs to low-power operation and potentially require oversizing of the second-life battery system.
10. Be aware of the significant difference that active cooling can make for second-life batteries, both for mitigating operational temperature rise (i.e. improving battery safety and longevity) and for enhancing standby cooldown rates (i.e. mitigating opportunity costs). Economic analyses are outside the scope of this research project, but second-life battery companies should compare the long term benefits of increased power capability and temperature control to the costs of constructing and maintaining an active cooling system.
11. Be aware of the significant heat rejection rates of some EV battery active cooling systems, and proceed with caution when electing to disable the original active cooling capabilities of an EV battery pack. Test at low power first to observe the thermal response. Expect the pack to be limited to low power if active cooling is disabled.
12. Be aware that module designs that are beneficial for active cooling (e.g. internal liquid channels) may be detrimental for passive cooling. Ensure that module temperature distributions are monitored when operating an EV battery pack with the original active cooling system disabled.
13. Be aware that the original temperature sensor locations within an EV battery pack may not be suitable for capturing temperature distributions in second-life service, especially if the original cooling system is to be modified or disabled. Additional temperature sensors may need to be retrofitted to the pack.
14. As an alternative to costly retrofitting measures, considering building one or more SETS models for the EV battery pack design in question so that pack temperature distributions can be numerically modelled during real-time operation.

8.5. Recommendations for Research

To build upon the work presented in this thesis, the following recommendations are made for future research:

Standardized Performance Testing

1. Collaborate with the second-life battery industry to refine the proposed electrical and thermal performance characterization methods and work towards establishing new standardized methods and metrics.
2. Apply standardized electrical and thermal performance characterization methods to as many different EV battery pack designs as possible. Given that LFP batteries and new cell formats (e.g. 'blade' prismatic, 4680 cylindrical) are becoming more mainstream in the EV industry, it is especially important to characterize the performance of EV batteries using these technologies in comparison to other established technologies. This research project only evaluated one LFP battery.
3. Establish an open-source database where all stakeholders can upload, view, and download comparable performance characterizations for different EV battery designs. Incorporate degradation performance characterizations as well.

Advancement of Experimental Methods

4. Expand the proposed performance ranking system described in Section 5.7 by adding a fourth dimension based on appropriate degradation metrics. To inform this work, conduct pack-level degradation studies to gain insights that cell-level degradation studies cannot provide.
5. Investigate the viability of the proposed 'single-dataset solution' for battery performance extrapolation, as described in Chapter 6. If the Peukert number can be reliably predicted for any EV battery based on manufacturer specifications such as energy density, then the single-dataset solution would allow for complete experimental characterization of electrical and thermal performance with even shorter test durations than the proven two-dataset solution.

Advancement of Modelling Methods

6. Apply published electrical and thermal performance characterizations in conjunction with degradation performance characterizations to inform technoeconomic models for second-life battery systems.
7. Explore opportunities to enhance the proposed performance characterization methods with data-driven techniques so reduce testing requirements even further.
8. Develop more advanced SETS models by integrating the proposed methods described in Chapter 7 with state-of-the-art SOC and SOH estimation algorithms as a means of modelling cell-specific heat generation.

REFERENCES

[1] Accelerating to Zero Coalition, “Zero Emission Vehicles Declaration.” Accessed: Mar. 01, 2025. [Online]. Available: https://acceleratingtozero.org/the-declaration/

[2] IEA, “World Energy Outlook 2024,” IEA, Paris, 2024. [Online]. Available: https://www.iea.org/reports/world-energy-outlook-2024

[3] IEA, “Global EV Outlook 2024,” IEA, Paris, 2024. [Online]. Available: https://www.iea.org/reports/global-ev-outlook-2024

[4] BloombergNEF, “Headwinds in Largest Energy Storage Markets Won’t Deter Growth,” BloombergNEF. Accessed: Mar. 02, 2025. [Online]. Available: https://about.bnef.com/blog/headwinds-in-largest-energy-storage-markets-wont-deter-growth/

[5] L. C. Casals, M. Etxandi-Santolaya, P. A. Bibiloni-Mulet, C. Corchero, and L. Trilla, “Electric Vehicle Battery Health Expected at End of Life in the Upcoming Years Based on UK Data,” *Batteries*, vol. 8, no. 10, p. 164, Oct. 2022, doi: 10.3390/batteries8100164.

[6] L. Ahmadi, S. B. Young, M. Fowler, R. A. Fraser, and M. A. Achachlouei, “A cascaded life cycle: reuse of electric vehicle lithium-ion battery packs in energy storage systems,” *Int. J. Life Cycle Assess.*, vol. 22, no. 1, pp. 111–124, Jan. 2017, doi: 10.1007/s11367-015-0959-7.

[7] L. C. Casals, B. Amante García, and C. Canal, “Second life batteries lifespan: Rest of useful life and environmental analysis,” *J. Environ. Manage.*, vol. 232, pp. 354–363, Feb. 2019, doi: 10.1016/j.jenvman.2018.11.046.

[8] Nissan Motor Co., “Europe’s largest energy storage system now live at the Johan Cruijff Arena,” Nissan News. Accessed: Mar. 02, 2025. [Online]. Available: https://global.nissannews.com/ja-JP/releases/europes-largest-energy-storage-system-now-live-at-the-johan-cruijff-arena

[9] S. Hanley, “Old Nissan LEAF Batteries Being Used For Grid-Scale Storage In California,” CleanTechnica. Accessed: Mar. 02, 2025. [Online]. Available: https://cleantechnica.com/2021/10/25/old-nissan-leaf-batteries-being-used-for-grid-scale-storage-in-california/

[10] C. Murray, “25MW BESS in Germany using second use battery cells completed by JT Energy Systems,” Energy-Storage.News. Accessed: Mar. 02, 2025. [Online]. Available: https://www.energy-storage.news/25mw-bess-in-germany-using-second-use-battery-cells-completed-by-jt-energy-systems/

[11] Connected Energy, “Two Second Life Battery Energy Storage Systems Installed At AMRC.” Accessed: Mar. 02, 2025. [Online]. Available: https://connected-energy.co.uk/news/two-second-life-battery-energy-storage-systems-installed-at-amrc-northwest/

[12] European Parliament, “Regulation (EU) 2023/1542 of the European Parliament and of the Council of 12 July 2023 concerning batteries and waste batteries, amending Directive 2008/98/EC and Regulation (EU) 2019/1020 and repealing Directive 2006/66/EC,” 2023. Accessed: Mar. 01, 2025. [Online]. Available: https://eur-lex.europa.eu/eli/reg/2023/1542/oj

[13] Smartville, “DOE Awards Smartville $10M for Long Duration, Second-Life Energy Storage Projects, Providing Energy Reliability to HBCUs Among Others,” Smartville. Accessed: Mar. 02, 2025. [Online]. Available: https://smartville.io/doe-awarded-ten-million/

[14] Moment Energy, “Moment Energy Secures $20.3M for EV Battery Repurposing Facility in US.” Accessed: Mar. 02, 2025. [Online]. Available: https://www.momentenergy.com/news-articles/moment-energy-awarded-us-20-3-million-by-us-dept-of-energy-to-establish-first-certified-ev-battery-repurposing-facility-in-the-us

[15] V. S *et al.*, “State of Health (SoH) estimation methods for second life lithium-ion battery—Review and challenges,” *Appl. Energy*, vol. 369, p. 123542, Sep. 2024, doi: 10.1016/j.apenergy.2024.123542.

[16] H. Rallo, G. Benveniste, I. Gestoso, and B. Amante, “Economic analysis of the disassembling activities to the reuse of electric vehicles Li-ion batteries,” *Resour. Conserv. Recycl.*, vol. 159, p. 104785, Aug. 2020, doi: 10.1016/j.resconrec.2020.104785.

[17] X. Hu *et al.*, “A Review of Second-Life Lithium-Ion Batteries for Stationary Energy Storage Applications,” *Proc. IEEE*, vol. 110, no. 6, pp. 735–753, Jun. 2022, doi: 10.1109/JPROC.2022.3175614.

[18] E. Fonseca, R. A. Franco, B. Simons, and M. D. Paiss, “Challenges in Deploying a Second-Life Battery System: Engineering, Fire Safety, UL Certifications, and NFPA Requirements,” in *2024 IEEE Electrical Energy Storage Application and Technologies Conference (EESAT)*, San Diego, CA, USA: IEEE, Jan. 2024, pp. 1–5. doi: 10.1109/EESAT59125.2024.10471221.

[19] A. Kampker, H. H. Heimes, C. Offermanns, J. Vienenkötter, M. Frank, and D. Holz, “Identification of Challenges for Second-Life Battery Systems—A Literature Review,” *World Electr. Veh. J.*, vol. 14, no. 4, p. 80, Mar. 2023, doi: 10.3390/wevj14040080.

[20] E. Braco, I. San Martín, P. Sanchis, and A. Ursúa, “Fast capacity and internal resistance estimation method for second-life batteries from electric vehicles,” *Appl. Energy*, vol. 329, p. 120235, Jan. 2023, doi: 10.1016/j.apenergy.2022.120235.

[21] D. Linden and T. B. Reddy, Eds., *Handbook of Batteries*, 3. ed. in McGraw-Hill handbooks. New York, NY: McGraw-Hill, 2002.

[22] L. Ma, J. Xia, and J. R. Dahn, “Improving the High Voltage Cycling of Li[$Ni_{0.42}$ $Mn_{0.42}$ $Co_{0.16}$]O_2 (NMC442)/Graphite Pouch Cells Using Electrolyte Additives,” *J. Electrochem. Soc.*, vol. 161, no. 14, pp. A2250–A2254, 2014, doi: 10.1149/2.1041414jes.

[23] K. Momma and F. Izumi, “VESTA : a three-dimensional visualization system for electronic and structural analysis,” *J. Appl. Crystallogr.*, vol. 41, no. 3, pp. 653–658, Jun. 2008, doi: 10.1107/S0021889808012016.

[24] A. Jain *et al.*, “Commentary: The Materials Project: A materials genome approach to accelerating materials innovation,” *APL Mater.*, vol. 1, no. 1, p. 011002, Jul. 2013, doi: 10.1063/1.4812323.

[25] J.-H. Kim, M.-J. Jung, M.-J. Kim, and Y.-S. Lee, “Electrochemical performances of lithium and sodium ion batteries based on carbon materials,” *J. Ind. Eng. Chem.*, vol. 61, pp. 368–380, May 2018, doi: 10.1016/j.jiec.2017.12.036.

[26] M. S. Whittingham and F. R. Gamble, “The lithium intercalates of the transition metal dichalcogenides,” *Mater. Res. Bull.*, vol. 10, no. 5, pp. 363–371, 1975, doi: 10.1016/0025-5408(75)90006-9.

[27] A. Yoshino, “The Birth of the Lithium-Ion Battery,” *Angew Chem Int Ed*, no. 51, pp. 5798–5800, 2012, doi: https://doi.org/10.1002/anie.201105006.

[28] H. D. Yoo, E. Markevich, G. Salitra, D. Sharon, and D. Aurbach, “On the challenge of developing advanced technologies for electrochemical energy storage and conversion,” *Mater. Today*, vol. 17, no. 3, pp. 110–121, Apr. 2014, doi: 10.1016/j.mattod.2014.02.014.

[29] H. Walvekar, H. Beltran, S. Sripad, and M. Pecht, “Implications of the Electric Vehicle Manufacturers’ Decision to Mass Adopt Lithium-Iron Phosphate Batteries,” *IEEE Access*, vol. 10, pp. 63834–63843, 2022, doi: 10.1109/ACCESS.2022.3182726.

[30] S.-J. Kwon, S.-E. Lee, J.-H. Lim, J. Choi, and J. Kim, “Performance and Life Degradation Characteristics Analysis of NCM LIB for BESS,” *Electronics*, vol. 7, no. 12, p. 406, Dec. 2018, doi: 10.3390/electronics7120406.

[31] W. Li and J. C. Currie, “Morphology Effects on the Electrochemical Performance of LiNi1-xCoxO2,” *J. Electrochem. Soc.*, vol. 144, no. 8, pp. 2773–2779, Aug. 1997, doi: 10.1149/1.1837894.

[32] H. Arai, S. Okada, Y. Sakurai, and J. Yamaki, “Electrochemical and Thermal Behavior of LiNi1-zMzO2 (M = Co, Mn, Ti),” *J. Electrochem. Soc.*, vol. 144, no. 9, pp. 3117–3125, Sep. 1997, doi: 10.1149/1.1837968.

[33] T. Ohzuku, A. Ueda, and M. Kouguchi, “Synthesis and Characterization of LiAl1/4Ni3/4O2 (R $\bar{3}$m) for Lithium-Ion (Shuttlecock) Batteries,” *J. Electrochem. Soc.*, vol. 142, no. 12, pp. 4033–4039, Dec. 1995, doi: 10.1149/1.2048458.

[34] M. Yoshio, H. Noguchi, J. Itoh, M. Okada, and T. Mouri, “Preparation and properties of LiCoyMnxNi1-x-yO2 as a cathode for lithium ion batteries,” 2000.

[35] T. Ohzuku and Y. Makimura, “Layered Lithium Insertion Material of LiCo1/3Ni1/3Mn1/3O2 for Lithium-Ion Batteries,” *Chem. Lett.*, vol. 30, no. 7, pp. 642–643, Jul. 2001, doi: 10.1246/cl.2001.642.

[36] Z. Lu, D. D. MacNeil, and J. R. Dahn, “Layered Li+NixCo1-2xMnxO2 Cathode Materials for Lithium-Ion Batteries,” *Electrochem. Solid-State Lett.*, vol. 4, no. 12, pp. A200–A203, 2001.

[37] S. Madhavi, G. V. Subba Rao, B. V. R. Chowdari, and S. F. Y. Li, “Effect of aluminium doping on cathodic behaviour of LiNi0.7Co0.3O2,” *J. Power Sources*, vol. 93, no. 1–2, pp. 156–162, Feb. 2001, doi: 10.1016/S0378-7753(00)00559-0.

[38] K. K. Lee, W. S. Yoon, K. B. Kim, K. Y. Lee, and S. T. Hong, “Characterization of LiNi0.85Co0.10M0.05O2 (M = Al, Fe) as a cathode material for lithium secondary batteries,” *J. Power Sources*, vol. 97–98, pp. 308–312, Jul. 2001, doi: 10.1016/S0378-7753(01)00516-X.

[39] M. D. Radin *et al.*, “Narrowing the Gap between Theoretical and Practical Capacities in Li-Ion Layered Oxide Cathode Materials,” *Adv. Energy Mater.*, vol. 7, no. 20, p. 1602888, Oct. 2017, doi: 10.1002/aenm.201602888.

[40] K. Min *et al.*, “A comparative study of structural changes in lithium nickel cobalt manganese oxide as a function of Ni content during delithiation process,” *J. Power Sources*, vol. 315, pp. 111–119, May 2016, doi: 10.1016/j.jpowsour.2016.03.017.

[41] Y. Ding, D. Mu, B. Wu, R. Wang, Z. Zhao, and F. Wu, “Recent progresses on nickel-rich layered oxide positive electrode materials used in lithium-ion batteries for electric vehicles,” *Appl. Energy*, vol. 195, pp. 586–599, Jun. 2017, doi: 10.1016/j.apenergy.2017.03.074.

[42] D. J. Xiong *et al.*, “Measuring Oxygen Release from Delithiated LiNix Mny Co1-x-yO2 and Its Effects on the Performance of High Voltage Li-Ion Cells,” *J. Electrochem. Soc.*, vol. 164, no. 13, pp. A3025–A3037, 2017, doi: 10.1149/2.0291713jes.

[43] U.-H. Kim, L.-Y. Kuo, P. Kaghazchi, C. S. Yoon, and Y.-K. Sun, “Quaternary Layered Ni-Rich NCMA Cathode for Lithium-Ion Batteries,” *ACS Energy Lett.*, vol. 4, no. 2, pp. 576–582, Feb. 2019, doi: 10.1021/acsenergylett.8b02499.

[44] N. Nitta, F. Wu, J. T. Lee, and G. Yushin, “Li-ion battery materials: present and future,” *Mater. Today*, vol. 18, no. 5, pp. 252–264, Jun. 2015, doi: 10.1016/j.mattod.2014.10.040.

[45] M. Armand *et al.*, “Lithium-ion batteries – Current state of the art and anticipated developments,” *J. Power Sources*, vol. 479, p. 228708, Dec. 2020, doi: 10.1016/j.jpowsour.2020.228708.

[46] H. Beltran, S. Harrison, A. Egea-Àlvarez, and L. Xu, “Techno-Economic Assessment of Energy Storage Technologies for Inertia Response and Frequency Support from Wind Farms,” *Energies*, vol. 13, no. 13, p. 3421, Jul. 2020, doi: 10.3390/en13133421.

[47] A. Manthiram, B. Song, and W. Li, “A perspective on nickel-rich layered oxide cathodes for lithium-ion batteries,” *Energy Storage Mater.*, vol. 6, pp. 125–139, Jan. 2017, doi: 10.1016/j.ensm.2016.10.007.

[48] A. Yamada, S. C. Chung, and K. Hinokuma, “Optimized $LiFePO_4$ for Lithium Battery Cathodes.,” *ChemInform*, vol. 32, no. 29, pp. 17–17, Jul. 2001, doi: 10.1002/chin.200129017.

[49] A. Manthiram, “A reflection on lithium-ion battery cathode chemistry,” *Nat. Commun.*, vol. 11, no. 1, p. 1550, Mar. 2020, doi: 10.1038/s41467-020-15355-0.

[50] J. Quan, S. Zhao, D. Song, T. Wang, W. He, and G. Li, “Comparative life cycle assessment of LFP and NCM batteries including the secondary use and different recycling technologies,” *Sci. Total Environ.*, vol. 819, p. 153105, May 2022, doi: 10.1016/j.scitotenv.2022.153105.

[51] J. F. Peters, M. Baumann, B. Zimmermann, J. Braun, and M. Weil, “The environmental impact of Li-Ion batteries and the role of key parameters – A review,” *Renew. Sustain. Energy Rev.*, vol. 67, pp. 491–506, Jan. 2017, doi: 10.1016/j.rser.2016.08.039.

[52] P. Li, X. Xia, and J. Guo, “A review of the life cycle carbon footprint of electric vehicle batteries,” *Sep. Purif. Technol.*, vol. 296, p. 121389, Sep. 2022, doi: 10.1016/j.seppur.2022.121389.

[53] A. J. Smith, S. R. Smith, T. Byrne, J. C. Burns, and J. R. Dahn, “Synergies in Blended $LiMn_2O_4$ and $Li[Ni_{1/3}Mn_{1/3}Co_{1/3}]O_2$ Positive Electrodes,” *J. Electrochem. Soc.*, vol. 159, no. 10, pp. A1696–A1701, 2012, doi: 10.1149/2.056210jes.

[54] C. Heubner, T. Liebmann, C. Lämmel, M. Schneider, and A. Michaelis, “Insights into the buffer effect observed in blended lithium insertion electrodes,” *J. Power Sources*, vol. 363, pp. 311–316, Sep. 2017, doi: 10.1016/j.jpowsour.2017.07.108.

[55] S. B. Chikkannanavar, D. M. Bernardi, and L. Liu, “A review of blended cathode materials for use in Li-ion batteries,” *J. Power Sources*, vol. 248, pp. 91–100, Feb. 2014, doi: 10.1016/j.jpowsour.2013.09.052.

[56] W.-J. Huang *et al.*, “Boosting rate performance of LiNi0.8Co0.15Al0.05O2 cathode by simply mixing lithium iron phosphate,” *J. Alloys Compd.*, vol. 827, p. 154296, Jun. 2020, doi: 10.1016/j.jallcom.2020.154296.

[57] H. Y. Tran, C. Täubert, M. Fleischhammer, P. Axmann, L. Küppers, and M. Wohlfahrt-Mehrens, “LiMn2O4 Spinel/LiNi0.8Co0.15Al0.05O2 Blends as Cathode Materials for Lithium-Ion Batteries,” *J. Electrochem. Soc.*, vol. 158, no. 5, p. A556, 2011, doi: 10.1149/1.3560582.

[58] D. Andre *et al.*, “Future generations of cathode materials: an automotive industry perspective,” *J. Mater. Chem. A*, vol. 3, no. 13, pp. 6709–6732, 2015, doi: 10.1039/C5TA00361J.

[59] Y. Nishi, “Lithium ion secondary batteries; past 10 years and the future,” *J. Power Sources*, vol. 100, no. 1–2, pp. 101–106, Nov. 2001, doi: 10.1016/S0378-7753(01)00887-4.

[60] J. Asenbauer, T. Eisenmann, M. Kuenzel, A. Kazzazi, Z. Chen, and D. Bresser, “The success story of graphite as a lithium-ion anode material – fundamentals, remaining challenges, and recent developments including silicon (oxide) composites,” *Sustain. Energy Fuels*, vol. 4, no. 11, pp. 5387–5416, 2020, doi: 10.1039/D0SE00175A.

[61] T. Zheng, J. S. Xue, and J. R. Dahn, “Lithium Insertion in Hydrogen-Containing Carbonaceous Materials,” *Chem. Mater.*, vol. 8, no. 2, pp. 389–393, Jan. 1996, doi: 10.1021/cm950304y.

[62] A. Shellikeri *et al.*, “Investigation of Pre-lithiation in Graphite and Hard-Carbon Anodes Using Different Lithium Source Structures,” *J. Electrochem. Soc.*, vol. 164, no. 14, pp. A3914–A3924, 2017, doi: 10.1149/2.1511714jes.

[63] A. Ghosh and F. Ghamouss, “Role of Electrolytes in the Stability and Safety of Lithium Titanate-Based Batteries,” *Front. Mater.*, vol. 7, p. 186, Jul. 2020, doi: 10.3389/fmats.2020.00186.

[64] S. Chae, S.-H. Choi, N. Kim, J. Sung, and J. Cho, “Integration of graphite and silicon anodes for the commercialization of high-energy lithium-ion batteries,” *Angew Chem Int Ed*, no. 59, pp. 110–135, 2020.

[65] S. Chae, N. Kim, J. Ma, J. Cho, and M. Ko, “One-to-one comparison of graphite-blended negative electrodes using silicon nanolayer-embedded graphite versus commercial benchmarking materials for high-energy lithium-ion batteries,” *Adv Energy Mater*, no. 7, p. 1700071, 2017.

[66] C. Heubner, T. Liebmann, O. Lohrberg, S. Cangaz, S. Maletti, and A. Michaelis, “Understanding Component-Specific Contributions and Internal Dynamics in Silicon/Graphite Blended Electrodes for High-Energy Lithium-Ion Batteries,” *Batter. Supercaps*, vol. 5, no. 1, p. e202100182, Jan. 2022, doi: 10.1002/batt.202100182.

[67] R. Schmuch, R. Wagner, G. Hörpel, T. Placke, and M. Winter, “Performance and cost of materials for lithium-based rechargeable automotive batteries,” *Nat. Energy*, vol. 3, no. 4, pp. 267–278, Apr. 2018, doi: 10.1038/s41560-018-0107-2.

[68] T. Waldmann *et al.*, “A Direct Comparison of Pilot-Scale Li-Ion Cells in the Formats PHEV1, Pouch, and 21700,” *J. Electrochem. Soc.*, vol. 168, no. 9, p. 090519, Sep. 2021, doi: 10.1149/1945-7111/ac208c.

[69] F. Wu and G. Yushin, “Conversion cathodes for rechargeable lithium and lithium-ion batteries,” *Energy Environ. Sci.*, vol. 10, no. 2, pp. 435–459, 2017, doi: 10.1039/C6EE02326F.

[70] S. A. Arote, *Lithium-ion and Lithium–Sulfur Batteries: Fundamentals to performance*. IOP Publishing, 2022. doi: 10.1088/978-0-7503-4881-2.

[71] H.-K. Kim, J. H. Choi, and K.-J. Lee, “A Numerical Study of the Effects of Cell Formats on the Cycle Life of Lithium Ion Batteries,” *J. Electrochem. Soc.*, vol. 166, no. 10, pp. A1769–A1778, 2019, doi: 10.1149/2.0261910jes.

[72] S. Golmon, K. Maute, and M. L. Dunn, “A design optimization methodology for Li+ batteries,” *J. Power Sources*, vol. 253, pp. 239–250, May 2014, doi: 10.1016/j.jpowsour.2013.12.025.

[73] C. Heubner *et al.*, “Understanding thickness and porosity effects on the electrochemical performance of LiNi0.6Co0.2Mn0.2O2-based cathodes for high energy Li-ion batteries,” *J. Power Sources*, vol. 419, pp. 119–126, Apr. 2019, doi: 10.1016/j.jpowsour.2019.02.060.

[74] A. Manthiram, A. Vadivel Murugan, A. Sarkar, and T. Muraliganth, “Nanostructured electrode materials for electrochemical energy storage and conversion,” *Energy Environ. Sci.*, vol. 1, no. 6, p. 621, 2008, doi: 10.1039/b811802g.

[75] M. Xu, B. Reichman, and X. Wang, “Modeling the effect of electrode thickness on the performance of lithium-ion batteries with experimental validation,” *Energy*, vol. 186, p. 115864, Nov. 2019, doi: 10.1016/j.energy.2019.115864.

[76] M. J. Lain, J. Brandon, and E. Kendrick, “Design Strategies for High Power vs. High Energy Lithium Ion Cells,” *Batteries*, vol. 5, no. 4, p. 64, Oct. 2019, doi: 10.3390/batteries5040064.

[77] Y. Gao, K. Myrtle, M. Zhang, J. N. Reimers, and J. R. Dahn, “Valence band of LiNixMn2-xO4 and its effects on the voltage profiles of LiNixMn2-xO4/Li electrochemical cells,” *Phys. Rev. B*, vol. 54, no. 23, pp. 16670–16675, Dec. 1996, doi: 10.1103/PhysRevB.54.16670.

[78] W. Li, J. N. Reimers, and J. R. Dahn, “Lattice-gas-model approach to understanding the structures of lithium transition-metal oxides Li *M* O 2,” *Phys. Rev. B*, vol. 49, no. 2, pp. 826–831, Jan. 1994, doi: 10.1103/PhysRevB.49.826.

[79] W. R. McKinnon, “Physical Mechanisms of Inercalation Batteries,” PhD, University of British Columbia, 1980.

[80] W. R. McKinnon and R. R. Haering, “Strain effects in Intercalation Systems,” *Solid State Ion.*, vol. 1, pp. 111–120, 1980.

[81] J. R. Dahn, W. R. McKinnon, J. J. Murray, R. R. Haering, R. S. McMillan, and A. H. Rivers-Bowerman, “Entropy of the intercalation compound LixMo6Se8 from calorimetry of electrochemical cells,” *Phys. Rev. B*, vol. 32, no. 5, pp. 3316–3318, Sep. 1985, doi: 10.1103/PhysRevB.32.3316.

[82] F. Zhou, T. Maxisch, and G. Ceder, “Configurational Electronic Entropy and the Phase Diagram of Mixed-Valence Oxides: The Case of Li x FePO 4,” *Phys. Rev. Lett.*, vol. 97, no. 15, p. 155704, Oct. 2006, doi: 10.1103/PhysRevLett.97.155704.

[83] S. T. Coleman, W. R. McKinnon, and J. R. Dahn, “Lithium intercalation in LixMo6Se8: A model mean-field lattice gas,” *Phys. Rev. B*, vol. 29, no. 7, pp. 4147–4149, Apr. 1984, doi: 10.1103/PhysRevB.29.4147.

[84] O. K. Andersen, W. Klose, and H. Nohl, “Electronic structure of Chevrel-phase high-critical-field superconductors,” *Phys. Rev. B*, vol. 17, no. 3, pp. 1209–1237, Feb. 1978, doi: 10.1103/PhysRevB.17.1209.

[85] J. R. Dahn, “Phase diagram of LixC6,” *Phys. Rev. B*, vol. 44, no. 17, pp. 9170–9177, Nov. 1991, doi: 10.1103/PhysRevB.44.9170.

[86] H. Daumas and A. Hérold, “Notes des Membres et Correspon- tants et Notes Présentéesou Transmises par Leurs Soins,” *C R Acad Sci Ser C*, no. 268, pp. 373–375, 1969.

[87] C. Didier, W. K. Pang, Z. Guo, S. Schmid, and V. K. Peterson, “Phase Evolution and Intermittent Disorder in Electrochemically Lithiated Graphite Determined Using in Operando Neutron Diffraction,” *Chem. Mater.*, vol. 32, no. 6, pp. 2518–2531, Mar. 2020, doi: 10.1021/acs.chemmater.9b05145.

[88] C. Liu, Z. G. Neale, and G. Cao, “Understanding electrochemical potentials of cathode materials in rechargeable batteries,” *Mater. Today*, vol. 19, no. 2, pp. 109–123, Mar. 2016, doi: 10.1016/j.mattod.2015.10.009.

[89] J. R. Dahn, D. C. Dahn, and R. R. Haering, “Elastic energy and staging in intercalation compounds,” *Solid State Commun.*, vol. 42, no. 3, pp. 179–183, Apr. 1982, doi: 10.1016/0038-1098(82)90999-1.

[90] S. Schweidler, L. De Biasi, A. Schiele, P. Hartmann, T. Brezesinski, and J. Janek, “Volume Changes of Graphite Anodes Revisited: A Combined *Operando* X-ray Diffraction and *In Situ* Pressure Analysis Study,” *J. Phys. Chem. C*, vol. 122, no. 16, pp. 8829–8835, Apr. 2018, doi: 10.1021/acs.jpcc.8b01873.

[91] J. R. Dahn, R. Fong, and M. J. Spoon, “Suppression of staging in lithium-intercalated carbon by disorder in the host,” *Phys. Rev. B*, vol. 42, no. 10, pp. 6424–6432, Oct. 1990, doi: 10.1103/PhysRevB.42.6424.

[92] V. Srinivasan and J. Newman, “Discharge Model for the Lithium Iron-Phosphate Electrode,” *J. Electrochem. Soc.*, vol. 151, no. 10, p. A1517, 2004, doi: 10.1149/1.1785012.

[93] T. Zheng, J. N. Reimers, and J. R. Dahn, “Effect of turbostratic disorder in graphitic carbon hosts on the intercalation of lithium,” *Phys. Rev. B*, vol. 51, no. 2, pp. 734–741, 1995.

[94] M. Saubanère, M. B. Yahia, S. Lebègue, and M.-L. Doublet, “An intuitive and efficient method for cell voltage prediction of lithium and sodium-ion batteries,” *Nat. Commun.*, vol. 5, no. 1, p. 5559, Nov. 2014, doi: 10.1038/ncomms6559.

[95] D. D. L. Chung, “Review Graphite,” *J. Mater. Sci.*, no. 37, pp. 1475–1489, 2002.

[96] P. A. Derosa and P. B. Balbuena, “A Lattice-Gas Model Study of Lithium Intercalation in Graphite,” *J. Electrochem. Soc.*, vol. 146, no. 10, pp. 3630–3638, Oct. 1999, doi: 10.1149/1.1392525.

[97] J. R. Dahn *et al.*, “Correlation between x-ray absorption and chemical potential measurements in lithium intercalated carbons,” *Phys. Rev. Lett.*, vol. 68, no. 6, pp. 835–838, Feb. 1992, doi: 10.1103/PhysRevLett.68.835.

[98] J. M. Tarascon *et al.*, “In Situ Structural and Electrochemical Study of Ni1−xCoxO2 Metastable Oxides Prepared by Soft Chemistry,” *J. Solid State Chem.*, vol. 147, no. 1, pp. 410–420, Oct. 1999, doi: 10.1006/jssc.1999.8465.

[99] A. O. Kondrakov *et al.*, “Charge-Transfer-Induced Lattice Collapse in Ni-Rich NCM Cathode Materials during Delithiation,” *J. Phys. Chem. C*, vol. 121, no. 44, pp. 24381–24388, Nov. 2017, doi: 10.1021/acs.jpcc.7b06598.

[100] B. C. Melot and J.-M. Tarascon, “Design and Preparation of Materials for Advanced Electrochemical Storage,” *Acc. Chem. Res.*, vol. 46, no. 5, pp. 1226–1238, May 2013, doi: 10.1021/ar300088q.

[101] G. Hautier *et al.*, “Phosphates as Lithium-Ion Battery Cathodes: An Evaluation Based on High-Throughput *ab Initio* Calculations,” *Chem. Mater.*, vol. 23, no. 15, pp. 3495–3508, Aug. 2011, doi: 10.1021/cm200949v.

[102] T. Ohzuku, M. Kitagawa, and T. Hirai, “Electrochemistry of Manganese Dioxide in Lithium Nonaqueous Cell: II . X-Ray Diffractional and Electrochemical Characterization on Deep Discharge Products of Electrolytic Manganese Dioxide,” *J. Electrochem. Soc.*, vol. 137, no. 1, pp. 40–46, Jan. 1990, doi: 10.1149/1.2086435.

[103] A. K. Padhi, K. S. Nanjundaswamy, and J. B. Goodenough, “Phospho-olivines as Positive-Electrode Materials for Rechargeable Lithium Batteries,” *J. Electrochem. Soc.*, vol. 144, no. 4, pp. 1188–1194, Apr. 1997, doi: 10.1149/1.1837571.

[104] T. Muraliganth and A. Manthiram, “Understanding the Shifts in the Redox Potentials of Olivine $LiM_{1-y}M_yPO_4$ (M = Fe, Mn, Co, and Mg) Solid Solution Cathodes,” *J. Phys. Chem. C*, vol. 114, no. 36, pp. 15530–15540, Sep. 2010, doi: 10.1021/jp1055107.

[105] K. Ariyoshi, H. Yamamoto, and Y. Yamada, “Relationship between changes in ionic radius and lattice dimension of lithium manganese oxide spinels during lithium insertion/extraction,” *Solid State Ion.*, vol. 343, p. 115077, Dec. 2019, doi: 10.1016/j.ssi.2019.115077.

[106] J. M. Paulsen, C. L. Thomas, and J. R. Dahn, “Layered Li-Mn-Oxide with the O2 Structure: A Cathode Material for Li-Ion Cells Which Does Not Convert to Spinel,” *J. Electrochem. Soc.*, vol. 146, no. 10, pp. 3560–3565, Oct. 1999, doi: 10.1149/1.1392514.

[107] J. B. Goodenough and K.-S. Park, “The Li-Ion Rechargeable Battery: A Perspective,” *J. Am. Chem. Soc.*, vol. 135, no. 4, pp. 1167–1176, Jan. 2013, doi: 10.1021/ja3091438.

[108] A. Yamada *et al.*, “Room-temperature miscibility gap in LixFePO4,” *Nat. Mater.*, vol. 5, no. 5, pp. 357–360, May 2006, doi: 10.1038/nmat1634.

[109] J. N. Reimers and J. R. Dahn, “Electrochemical and In Situ X-Ray Diffraction Studies of Lithium Intercalation in Li x CoO2,” *J. Electrochem. Soc.*, vol. 139, no. 8, pp. 2091–2097, Aug. 1992, doi: 10.1149/1.2221184.

[110] A. Van Der Ven, M. K. Aydinol, G. Ceder, G. Kresse, and J. Hafner, “First-principles investigation of phase stability in Li x CoO 2,” *Phys. Rev. B*, vol. 58, no. 6, pp. 2975–2987, Aug. 1998, doi: 10.1103/PhysRevB.58.2975.

[111] K. Amine, R. Kanno, and Y. Tzeng, “Rechargeable lithium batteries and beyond: Progress, challenges, and future directions,” *MRS Bull.*, vol. 39, no. 5, pp. 395–401, May 2014, doi: 10.1557/mrs.2014.62.

[112] M. Okubo *et al.*, “Nanosize Effect on High-Rate Li-Ion Intercalation in $LiCoO_2$ Electrode,” *J. Am. Chem. Soc.*, vol. 129, no. 23, pp. 7444–7452, Jun. 2007, doi: 10.1021/ja0681927.

[113] V. J. Ovejas and A. Cuadras, “Effects of cycling on lithium-ion battery hysteresis and overvoltage,” *Sci. Rep.*, vol. 9, no. 1, p. 14875, Oct. 2019, doi: 10.1038/s41598-019-51474-5.

[114] C. Julien, A. Mauger, K. Zaghib, and H. Groult, “Comparative Issues of Cathode Materials for Li-Ion Batteries,” *Inorganics*, vol. 2, no. 1, pp. 132–154, Mar. 2014, doi: 10.3390/inorganics2010132.

[115] H. Li, N. Zhang, J. Li, and J. R. Dahn, "Updating the Structure and Electrochemistry of $Li_x NiO_2$ for $0 \leq x \leq 1$," *J. Electrochem. Soc.*, vol. 165, no. 13, pp. A2985–A2993, 2018, doi: 10.1149/2.0381813jes.

[116] A. Manthiram, K. Chemelewski, and E.-S. Lee, "A perspective on the high-voltage LiMn1.5Ni0.5O4 spinel cathode for lithium-ion batteries," *Energy Environ. Sci.*, vol. 7, no. 4, p. 1339, 2014, doi: 10.1039/c3ee42981d.

[117] Y. Koyama, N. Yabuuchi, I. Tanaka, H. Adachi, and T. Ohzuku, "Solid-state chemistry and electrochemistry of LiCo1/3Ni1/3Mn1/3O2 for advanced lithium-ion batteries," *J. Electrochem. Soc.*, vol. 151, no. 10, pp. A1545-1551, 2004.

[118] B. J. Hwang, Y. W. Tsai, D. Carlier, and G. Ceder, "A Combined Computational/Experimental Study on $LiNi_{1/3} Co_{1/3} Mn_{1/3} O_2$," *Chem. Mater.*, vol. 15, no. 19, pp. 3676–3682, Sep. 2003, doi: 10.1021/cm030299v.

[119] J. Graetz, C. C. Ahn, R. Yazami, and B. Fultz, "An Electron Energy-Loss Spectrometry Study of Charge Compensation in $LiNi_{0.8} Co_{0.2} O_2$," *J. Phys. Chem. B*, vol. 107, no. 13, pp. 2887–2891, Apr. 2003, doi: 10.1021/jp026484y.

[120] C. J. Han, J. H. Yoon, W. I. Cho, and H. Jang, "Electrochemical properties of LiNi0.8Co0.2−xAlxO2 prepared by a sol–gel method," *J. Power Sources*, vol. 136, no. 1, pp. 132–138, Sep. 2004, doi: 10.1016/j.jpowsour.2004.05.006.

[121] K. He, Z. Ruan, X. Teng, and Y. Zhu, "Facile synthesis and electrochemical properties of spherical LiNi 0.85−x Co 0.15 Al x O 2 with sodium aluminate via co-precipitation," *Mater. Res. Bull.*, vol. 90, pp. 131–137, Jun. 2017, doi: 10.1016/j.materresbull.2017.01.039.

[122] E. Rossen, C. D. W. Jones, and J. R. Dahn, "Structure and electrochemistry of LixMnyNi1-yO2," *Solid State Ion.*, vol. 57, pp. 311–318, 1992.

[123] W. Li, J. N. Reimers, and J. R. Dahn, "In situ X-ray diffraction and electrochemical studies of Lil1-xNiO2," *Solid State Ion.*, vol. 67, pp. 123–130, 1993.

[124] H.-J. Noh, S. Youn, C. S. Yoon, and Y.-K. Sun, "Comparison of the structural and electrochemical properties of layered Li[NixCoyMnz]O2 (x = 1/3, 0.5, 0.6, 0.7, 0.8 and 0.85) cathode material for lithium-ion batteries," *J. Power Sources*, vol. 233, pp. 121–130, Jul. 2013, doi: 10.1016/j.jpowsour.2013.01.063.

[125] H. Arai, S. Okada, H. Ohtsuka, M. Ichimura, and J. Yamaki, "Characterization and cathode performance of Li1-xNi1+xO2 prepared with the excess lithium method," *Solid State Ion.*, vol. 80, pp. 261–269, 1995.

[126] N. Yabuuchi, Y. Makimura, and T. Ohzuku, "Solid-State Chemistry and Electrochemistry of LiCo1/3Ni1/3Mn1/3O2 for Advanced Lithium-Ion Batteries," *J. Electrochem. Soc.*, vol. 154, no. 4, pp. A314–A321, 2007.

[127] T. Kobayashi, N. Kawasaki, Y. Kobayashi, K. Shono, Y. Mita, and H. Miyashiro, "A method of separating the capacities of layer and spinel compounds in blended cathode," *J. Power Sources*, vol. 245, pp. 1–6, Jan. 2014, doi: 10.1016/j.jpowsour.2013.06.039.

[128] S. Jung, "Mathematical model of lithium-ion batteries with blended-electrode system," *J. Power Sources*, vol. 264, pp. 184–194, Oct. 2014, doi: 10.1016/j.jpowsour.2014.04.072.

[129] K. P. C. Yao, J. S. Okasinski, K. Kalaga, J. D. Almer, and D. P. Abraham, "Operando Quantification of (De)Lithiation Behavior of Silicon–Graphite Blended Electrodes for Lithium-Ion Batteries," *Adv. Energy Mater.*, vol. 9, no. 8, p. 1803380, Feb. 2019, doi: 10.1002/aenm.201803380.

[130] V. Pop, H. J. Bergveld, P. P. L. Regtien, J. H. G. Op Het Veld, D. Danilov, and P. H. L. Notten, "Battery Aging and Its Influence on the Electromotive Force," *J. Electrochem. Soc.*, vol. 154, no. 8, p. A744, 2007, doi: 10.1149/1.2742296.

[131] P. Yu, S. Wang, C. Yu, W. Shi, and B. Li, "Study of hysteresis voltage state dependence in lithium-ion battery and a novel asymmetric hysteresis modeling," *J. Energy Storage*, vol. 51, p. 104492, Jul. 2022, doi: 10.1016/j.est.2022.104492.

[132] D. Theuerkauf and L. Swan, "Characteristics of Open Circuit Voltage Relaxation in Lithium-Ion Batteries for the Purpose of State of Charge and State of Health Analysis," *Batteries*, vol. 8, no. 8, p. 77, Jul. 2022, doi: 10.3390/batteries8080077.

[133] U. Krewer, F. Röder, E. Harinath, R. D. Braatz, B. Bedürftig, and R. Findeisen, "Review—Dynamic Models of Li-Ion Batteries for Diagnosis and Operation: A Review and Perspective," *J. Electrochem. Soc.*, vol. 165, no. 16, pp. A3656–A3673, 2018, doi: 10.1149/2.1061814jes.

[134] C. Zhang *et al.*, "Real-time estimation of negative electrode potential and state of charge of lithium-ion battery based on a half-cell-level equivalent circuit model," *J. Energy Storage*, vol. 51, p. 104362, Jul. 2022, doi: 10.1016/j.est.2022.104362.

[135] L. O. Valøen and J. N. Reimers, "Transport Properties of LiPF6-Based Li-Ion Battery Electrolytes," *J. Electrochem. Soc.*, vol. 152, no. 5, pp. A882–A891, 2005.

[136] M. S. Ding, K. Xu, S. S. Zhang, K. Amine, G. L. Henriksen, and T. R. Jow, "Change of Conductivity with Salt Content, Solvent Composition, and Temperature for Electrolytes of LiPF6 in Ethylene Carbonate-Ethyl Methyl Carbonate," *J. Electrochem. Soc.*, vol. 48, no. 10, pp. A1196–A1204, 2001.

[137] E. Barsoukov and J. R. Macdonald, Eds., *Impedance Spectroscopy*, 1st ed. Wiley, 2005. doi: 10.1002/0471716243.fmatter.

[138] X. Wang, X. Wei, and H. Dai, "Estimation of state of health of lithium-ion batteries based on charge transfer resistance considering different temperature and

state of charge," *J. Energy Storage*, vol. 21, pp. 618–631, Feb. 2019, doi: 10.1016/j.est.2018.11.020.

[139] F. Hao *et al.*, "Highly catalytic cross-stacked superaligned carbon nanotube sheets for iodine-free dye-sensitized solar cells," *J. Mater. Chem.*, vol. 22, no. 42, p. 22756, 2012, doi: 10.1039/c2jm35095e.

[140] Y. Bensaad *et al.*, "Embedded real-time fractional-order equivalent circuit model for internal resistance estimation of lithium-ion cells," *J. Energy Storage*, vol. 67, p. 107516, Sep. 2023, doi: 10.1016/j.est.2023.107516.

[141] S. Atlung, K. West, and T. Jacobsen, "Dynamic Aspects of Solid Solution Cathodes for Electrochemical Power Sources," *J. Electrochem. Soc.*, vol. 126, no. 8, pp. 1311–1321, Aug. 1979, doi: 10.1149/1.2129269.

[142] S. Skoog and S. David, "Parameterization of linear equivalent circuit models over wide temperature and SOC spans for automotive lithium-ion cells using electrochemical impedance spectroscopy," *J. Energy Storage*, vol. 14, pp. 39–48, Dec. 2017, doi: 10.1016/j.est.2017.08.004.

[143] P. Shafiei Sabet, G. Stahl, and D. U. Sauer, "Non-invasive investigation of predominant processes in the impedance spectra of high energy lithium-ion batteries with nickel–cobalt–aluminum cathodes," *J. Power Sources*, vol. 472, p. 228189, Oct. 2020, doi: 10.1016/j.jpowsour.2020.228189.

[144] J. Illig, M. Ender, T. Chrobak, J. P. Schmidt, D. Klotz, and E. Ivers-Tiffée, "Separation of Charge Transfer and Contact Resistance in $LiFePO_4$ -Cathodes by Impedance Modeling," *J. Electrochem. Soc.*, vol. 159, no. 7, pp. A952–A960, 2012, doi: 10.1149/2.030207jes.

[145] *GT-AutoLion*. Gamma Technologies. [Online]. Available: https://www.gtisoft.com/gt-autolion/

[146] J. C. Burns, D. A. Stevens, and J. R. Dahn, "In-Situ Detection of Lithium Plating Using High Precision Coulometry," *J. Electrochem. Soc.*, vol. 162, no. 6, pp. A959–A964, 2015, doi: 10.1149/2.0621506jes.

[147] J. Deveau, C. White, and L. G. Swan, "Lead-acid battery response to various formation levels – Part A: Recommended formation levels for off-grid solar and conventional applications," *Sustain. Energy Technol. Assess.*, vol. 11, pp. 1–10, Sep. 2015, doi: 10.1016/j.seta.2015.04.001.

[148] H. Chen, T. N. Cong, W. Yang, C. Tan, Y. Li, and Y. Ding, "Progress in electrical energy storage system: A critical review," *Prog. Nat. Sci.*, vol. 19, no. 3, pp. 291–312, Mar. 2009, doi: 10.1016/j.pnsc.2008.07.014.

[149] M. S. Guney and Y. Tepe, "Classification and assessment of energy storage systems," *Renew. Sustain. Energy Rev.*, vol. 75, pp. 1187–1197, Aug. 2017, doi: 10.1016/j.rser.2016.11.102.

[150] J. Schmitt, A. Maheshwari, M. Heck, S. Lux, and M. Vetter, “Impedance change and capacity fade of lithium nickel manganese cobalt oxide-based batteries during calendar aging,” *J. Power Sources*, vol. 353, pp. 183–194, Jun. 2017, doi: 10.1016/j.jpowsour.2017.03.090.

[151] M. Dubarry, C. Truchot, and B. Y. Liaw, “Synthesize battery degradation modes via a diagnostic and prognostic model,” *J. Power Sources*, vol. 219, pp. 204–216, Dec. 2012, doi: 10.1016/j.jpowsour.2012.07.016.

[152] T. Waldmann, B.-I. Hogg, and M. Wohlfahrt-Mehrens, “Li plating as unwanted side reaction in commercial Li-ion cells – A review,” *J. Power Sources*, vol. 384, pp. 107–124, Apr. 2018, doi: 10.1016/j.jpowsour.2018.02.063.

[153] B. Epding, B. Rumberg, H. Jahnke, I. Stradtmann, and A. Kwade, “Investigation of significant capacity recovery effects due to long rest periods during high current cyclic aging tests in automotive lithium ion cells and their influence on lifetime,” *J. Energy Storage*, vol. 22, pp. 249–256, Apr. 2019, doi: 10.1016/j.est.2019.02.015.

[154] R. Fong, U. Von Sacken, and J. R. Dahn, “Studies of Lithium Intercalation into Carbons Using Nonaqueous Electrochemical Cells,” *J. Electrochem. Soc.*, vol. 137, no. 7, pp. 2009–2013, Jul. 1990, doi: 10.1149/1.2086855.

[155] S. J. An, J. Li, C. Daniel, D. Mohanty, S. Nagpure, and D. L. Wood, “The state of understanding of the lithium-ion-battery graphite solid electrolyte interphase (SEI) and its relationship to formation cycling,” *Carbon*, vol. 105, pp. 52–76, Aug. 2016, doi: 10.1016/j.carbon.2016.04.008.

[156] R. Pan, E. Jo, Z. Cui, and A. Manthiram, “Degradation Pathways of Cobalt-Free $LiNiO_2$ Cathode in Lithium Batteries,” *Adv. Funct. Mater.*, vol. 33, no. 10, p. 2211461, Mar. 2023, doi: 10.1002/adfm.202211461.

[157] Z. Mao, M. Farkhondeh, M. Pritzker, M. Fowler, and Z. Chen, “Calendar Aging and Gas Generation in Commercial Graphite/NMC-LMO Lithium-Ion Pouch Cell,” *J. Electrochem. Soc.*, vol. 164, no. 14, pp. A3469–A3483, 2017, doi: 10.1149/2.0241714jes.

[158] B. Gulsoy, T. A. Vincent, C. Briggs, J. E. H. Sansom, and J. Marco, “In-situ measurement of internal gas pressure within cylindrical lithium-ion cells,” *J. Power Sources*, vol. 570, p. 233064, Jun. 2023, doi: 10.1016/j.jpowsour.2023.233064.

[159] B. Michalak, H. Sommer, D. Mannes, A. Kaestner, T. Brezesinski, and J. Janek, “Gas Evolution in Operating Lithium-Ion Batteries Studied In Situ by Neutron Imaging,” *Sci. Rep.*, vol. 5, no. 1, p. 15627, Oct. 2015, doi: 10.1038/srep15627.

[160] S. Müller *et al.*, “Quantification and modeling of mechanical degradation in lithium-ion batteries based on nanoscale imaging,” *Nat. Commun.*, vol. 9, no. 1, p. 2340, Jun. 2018, doi: 10.1038/s41467-018-04477-1.

[161] F. Schipper, E. M. Erickson, C. Erk, J.-Y. Shin, F. F. Chesneau, and D. Aurbach, "Review—Recent Advances and Remaining Challenges for Lithium Ion Battery Cathodes: I. Nickel-Rich, $LiNi_x\ Co_y\ Mn_z\ O_2$," *J. Electrochem. Soc.*, vol. 164, no. 1, pp. A6220–A6228, 2017, doi: 10.1149/2.0351701jes.

[162] M. Wohlfahrt-Mehrens, C. Vogler, and J. Garche, "Aging mechanisms of lithium cathode materials," *J. Power Sources*, vol. 127, no. 1–2, pp. 58–64, Mar. 2004, doi: 10.1016/j.jpowsour.2003.09.034.

[163] E. R. Logan, H. Hebecker, A. Eldesoky, A. Luscombe, M. B. Johnson, and J. R. Dahn, "Performance and Degradation of $LiFePO_4$ /Graphite Cells: The Impact of Water Contamination and an Evaluation of Common Electrolyte Additives," *J. Electrochem. Soc.*, vol. 167, no. 13, p. 130543, Oct. 2020, doi: 10.1149/1945-7111/abbbbe.

[164] H. Kim *et al.*, "Positive electrode–Li metal crosstalk behavior-induced morphology change of Li deposits," *J. Mater. Chem. A*, vol. 10, no. 34, pp. 17659–17667, 2022, doi: 10.1039/D2TA03666E.

[165] A. Rougier, I. Saadoune, P. Gravereau, P. Willmann, and C. Delmas, "Effect of cobalt subsitution on cationic distribution in LiNi1-yCoyO2 electrode materials," *Solid State Ion.*, vol. 90, pp. 83–90, 1996.

[166] N. Zhang *et al.*, "Structural, Electrochemical, and Thermal Properties of Nickel-Rich $LiNi_x\ Mn_y\ Co_z\ O_2$ Materials," *Chem. Mater.*, vol. 30, no. 24, pp. 8852–8860, Dec. 2018, doi: 10.1021/acs.chemmater.8b03827.

[167] Y. Wei, C. Zhou, D. Zhao, and G. Wang, "Enhanced electrochemical performance and safety of LiNi0.8Co0.15Al0.05O2 by LiFePO4 modification," *Chem. Phys. Lett.*, vol. 751, p. 137480, Jul. 2020, doi: 10.1016/j.cplett.2020.137480.

[168] T. R. Ashwin, A. Barai, K. Uddin, L. Somerville, A. McGordon, and J. Marco, "Prediction of battery storage ageing and solid electrolyte interphase property estimation using an electrochemical model," *J. Power Sources*, vol. 385, pp. 141–147, May 2018, doi: 10.1016/j.jpowsour.2018.03.010.

[169] P. Keil *et al.*, "Calendar Aging of Lithium-Ion Batteries: I. Impact of the Graphite Anode on Capacity Fade," *J. Electrochem. Soc.*, vol. 163, no. 9, pp. A1872–A1880, 2016, doi: 10.1149/2.0411609jes.

[170] D. Anseán *et al.*, "Operando lithium plating quantification and early detection of a commercial LiFePO4 cell cycled under dynamic driving schedule," *J. Power Sources*, vol. 356, pp. 36–46, Jul. 2017, doi: 10.1016/j.jpowsour.2017.04.072.

[171] A. J. Smith, J. C. Burns, and J. R. Dahn, "A High Precision Study of the Coulombic Efficiency of Li-Ion Batteries," *Electrochem. Solid-State Lett.*, vol. 13, no. 12, p. A177, 2010, doi: 10.1149/1.3487637.

[172] J. Li, J. Harlow, N. Stakheiko, N. Zhang, J. Paulsen, and J. Dahn, "Dependence of Cell Failure on Cut-Off Voltage Ranges and Observation of Kinetic Hindrance in $LiNi_{0.8}\ Co_{0.15}\ Al_{0.05}\ O_2$," *J. Electrochem. Soc.*, vol. 165, no. 11, pp. A2682–A2695, 2018, doi: 10.1149/2.0491811jes.

[173] S. Nowak and M. Winter, "The Role of Cations on the Performance of Lithium Ion Batteries: A Quantitative Analytical Approach," *Acc. Chem. Res.*, vol. 51, no. 2, pp. 265–272, Feb. 2018, doi: 10.1021/acs.accounts.7b00523.

[174] A. A. Pesaran, "Battery thermal models for hybrid vehicle simulations," *J. Power Sources*, vol. 110, no. 2, pp. 377–382, Aug. 2002, doi: 10.1016/S0378-7753(02)00200-8.

[175] N. Yang, X. Zhang, B. Shang, and G. Li, "Unbalanced discharging and aging due to temperature differences among the cells in a lithium-ion battery pack with parallel combination," *J. Power Sources*, vol. 306, pp. 733–741, Feb. 2016, doi: 10.1016/j.jpowsour.2015.12.079.

[176] Q. Wang, B. Jiang, B. Li, and Y. Yan, "A critical review of thermal management models and solutions of lithium-ion batteries for the development of pure electric vehicles," *Renew. Sustain. Energy Rev.*, vol. 64, pp. 106–128, Oct. 2016, doi: 10.1016/j.rser.2016.05.033.

[177] D. Chen, J. Jiang, G.-H. Kim, C. Yang, and A. Pesaran, "Comparison of different cooling methods for lithium ion battery cells," *Appl. Therm. Eng.*, vol. 94, pp. 846–854, Feb. 2016, doi: 10.1016/j.applthermaleng.2015.10.015.

[178] S. Yang, C. Zhang, J. Jiang, W. Zhang, L. Zhang, and Y. Wang, "Review on state-of-health of lithium-ion batteries: Characterizations, estimations and applications," *J. Clean. Prod.*, vol. 314, p. 128015, Sep. 2021, doi: 10.1016/j.jclepro.2021.128015.

[179] B. Ma *et al.*, "Remaining useful life and state of health prediction for lithium batteries based on differential thermal voltammetry and a deep-learning model," *J. Power Sources*, vol. 548, p. 232030, Nov. 2022, doi: 10.1016/j.jpowsour.2022.232030.

[180] W. Diao, J. Jiang, C. Zhang, H. Liang, and M. Pecht, "Energy state of health estimation for battery packs based on the degradation and inconsistency," *Energy Procedia*, vol. 142, pp. 3578–3583, Dec. 2017, doi: 10.1016/j.egypro.2017.12.248.

[181] M. Elliott, L. G. Swan, M. Dubarry, and G. Baure, "Degradation of electric vehicle lithium-ion batteries in electricity grid services," *J. Energy Storage*, vol. 32, p. 101873, Dec. 2020, doi: 10.1016/j.est.2020.101873.

[182] T. M. Bandhauer, S. Garimella, and T. F. Fuller, "A Critical Review of Thermal Issues in Lithium-Ion Batteries," *J. Electrochem. Soc.*, vol. 158, no. 3, p. R1, 2011, doi: 10.1149/1.3515880.

[183] M. Steinhardt, J. V. Barreras, H. Ruan, B. Wu, G. J. Offer, and A. Jossen, "Meta-analysis of experimental results for heat capacity and thermal conductivity in lithium-ion batteries: A critical review," *J. Power Sources*, vol. 522, p. 230829, Feb. 2022, doi: 10.1016/j.jpowsour.2021.230829.

[184] J. Geder, R. Arunachala, S. Jairam, and A. Jossen, "Thermal behavior of aged lithium-ion batteries: calorimetric observations," in *2015 IEEE Green Energy and Systems Conference (IGESC)*, Long Beach, CA, USA: IEEE, Nov. 2015, pp. 24–29. doi: 10.1109/IGESC.2015.7359386.

[185] Y. Kobayashi, H. Miyashiro, K. Kumai, K. Takei, T. Iwahori, and I. Uchida, "Precise Electrochemical Calorimetry of LiCoO2ÕGraphite Lithium-Ion Cell," *J. Electrochem. Soc.*, vol. 149, no. 8, pp. A978–A982, 2002.

[186] H. Yang and J. Prakash, "Determination of the Reversible and Irreversible Heats of a LiNi0.8Co0.15Al0.05O2ÕNatural Graphite Cell Using Electrochemical-Calorimetric Technique," *J. Electrochem. Soc.*, vol. 151, no. 8, pp. A1222–A1229, 2004.

[187] D. Bernardi, E. Pawlikowski, and J. Newman, "A General Energy Balance for Battery Systems," *J. Electrochem. Soc.*, vol. 132, no. 1, pp. 5–12, Jan. 1985, doi: 10.1149/1.2113792.

[188] M. Song, Y. Hu, S.-Y. Choe, and T. R. Garrick, "Analysis of the Heat Generation Rate of Lithium-Ion Battery Using an Electrochemical Thermal Model," *J. Electrochem. Soc.*, vol. 167, no. 12, p. 120503, Aug. 2020, doi: 10.1149/1945-7111/aba96b.

[189] T. L. Bergman, *Fundamentals of Heat and Mass Transfer*. John Wiley & Sons, 2011.

[190] R. W. Cook, L. G. Swan, and K. P. Plucknett, "Failure mode analysis of lithium ion batteries operated for low Earth orbit CubeSat applications," *J. Energy Storage*, vol. 31, p. 101561, Oct. 2020, doi: 10.1016/j.est.2020.101561.

[191] T. D. Hatchard, D. D. MacNeil, D. A. Stevens, L. Christensen, and J. R. Dahn, "Importance of heat transfer by radiation in Li-ion batteries during thermal abuse," *Electrochem. Solid-State Lett.*, vol. 3, no. 7, pp. 305–308, 2000, doi: 10.1149/1.1391131.

[192] X. Feng *et al.*, "Thermal runaway features of large format prismatic lithium ion battery using extended volume accelerating rate calorimetry," *J. Power Sources*, vol. 255, pp. 294–301, Jun. 2014, doi: 10.1016/j.jpowsour.2014.01.005.

[193] H. Yang, S. Amiruddin, H. J. Bang, Y.-K. Sun, and J. Prakash, "A review of Li-ion cell chemistries and their potential use in hybrid electric vehicles," *J Ind Eng Chem*, vol. 12, no. 1, pp. 12–38, 2006.

[194] S. Ma *et al.*, “Temperature effect and thermal impact in lithium-ion batteries: A review,” *Prog. Nat. Sci. Mater. Int.*, vol. 28, no. 6, pp. 653–666, Dec. 2018, doi: 10.1016/j.pnsc.2018.11.002.

[195] Y.-S. Duh, C.-Y. Lee, Y.-L. Chen, and C.-S. Kao, “Characterization on the exothermic behaviors of cathode materials reacted with ethylene carbonate in lithium-ion battery studied by differential scanning calorimeter (DSC),” *Thermochim. Acta*, vol. 642, pp. 88–94, Oct. 2016, doi: 10.1016/j.tca.2016.09.007.

[196] M. Fleischhammer, T. Waldmann, G. Bisle, B.-I. Hogg, and M. Wohlfahrt-Mehrens, “Interaction of cyclic ageing at high-rate and low temperatures and safety in lithium-ion batteries,” *J. Power Sources*, vol. 274, pp. 432–439, Jan. 2015, doi: 10.1016/j.jpowsour.2014.08.135.

[197] I. Belharouak, Y.-K. Sun, J. Liu, and K. Amine, “Li(Ni1/3Co1/3Mn1/3)O2 as a suitable cathode for high power applications,” *J. Power Sources*, vol. 123, no. 2, pp. 247–252, Sep. 2003, doi: 10.1016/S0378-7753(03)00529-9.

[198] D. Doughty and E. P. Roth, “A General Discussion of Li Ion Battery Safety,” *Electrochem. Soc. Interface*, 2012.

[199] F. Pampel, S. Pischinger, and M. Teuber, “A systematic comparison of the packing density of battery cell-to-pack concepts at different degrees of implementation,” *Results Eng.*, vol. 13, p. 100310, Mar. 2022, doi: 10.1016/j.rineng.2021.100310.

[200] G. Silva, T. Assis Dutra, J. Nunes-Pereira, and A. P. Silva, “Coupled and decoupled structural batteries: A comparative analysis,” *J. Power Sources*, vol. 604, p. 234392, Jun. 2024, doi: 10.1016/j.jpowsour.2024.234392.

[201] C. Yang, N. Sunderlin, W. Wang, C. Churchill, and M. Keyser, “Compressible battery foams to prevent cascading thermal runaway in Li-ion pouch batteries,” *J. Power Sources*, vol. 541, p. 231666, Sep. 2022, doi: 10.1016/j.jpowsour.2022.231666.

[202] P. Weicker, *A systems approach to lithium-ion battery management*. in Artech house power engineering series. Boston: Artech house, 2014.

[203] M. R. M. Kassim, W. A. W. Jamil, and R. M. Sabri, “State-of-Charge (SOC) and State-of-Health (SOH) Estimation Methods in Battery Management Systems for Electric Vehicles,” in *2021 IEEE International Conference on Computing (ICOCO)*, Kuala Lumpur, Malaysia: IEEE, Nov. 2021, pp. 91–96. doi: 10.1109/ICOCO53166.2021.9673580.

[204] S. B and P. Pradeepa, “Review on Battery Management System in EV,” in *2022 International Conference on Intelligent Controller and Computing for Smart Power (ICICCSP)*, Hyderabad, India: IEEE, Jul. 2022, pp. 1–4. doi: 10.1109/ICICCSP53532.2022.9862367.

[205] S. Mishra, S. C. Swain, and R. K. Samantaray, “A Review on Battery Management system and its Application in Electric vehicle,” in *2021 International Conference on Advances in Computing and Communications (ICACC)*, Kochi, Kakkanad, India: IEEE, Oct. 2021, pp. 1–6. doi: 10.1109/ICACC-202152719.2021.9708114.

[206] P. R. Tete, M. M. Gupta, and S. S. Joshi, “Developments in battery thermal management systems for electric vehicles: A technical review,” *J. Energy Storage*, vol. 35, p. 102255, Mar. 2021, doi: 10.1016/j.est.2021.102255.

[207] W. Wu, S. Wang, W. Wu, K. Chen, S. Hong, and Y. Lai, “A critical review of battery thermal performance and liquid based battery thermal management,” *Energy Convers. Manag.*, vol. 182, pp. 262–281, Feb. 2019, doi: 10.1016/j.enconman.2018.12.051.

[208] C. Roe *et al.*, “Immersion cooling for lithium-ion batteries – A review,” *J. Power Sources*, vol. 525, p. 231094, Mar. 2022, doi: 10.1016/j.jpowsour.2022.231094.

[209] M. Bernagozzi, A. Georgoulas, N. Miché, and M. Marengo, “Heat pipes in battery thermal management systems for electric vehicles: A critical review,” *Appl. Therm. Eng.*, vol. 219, p. 119495, Jan. 2023, doi: 10.1016/j.applthermaleng.2022.119495.

[210] X. Zhang, Z. Li, L. Luo, Y. Fan, and Z. Du, “A review on thermal management of lithium-ion batteries for electric vehicles,” *Energy*, vol. 238, p. 121652, Jan. 2022, doi: 10.1016/j.energy.2021.121652.

[211] V. Mali, R. Saxena, K. Kumar, A. Kalam, and B. Tripathi, “Review on battery thermal management systems for energy-efficient electric vehicles,” *Renew. Sustain. Energy Rev.*, vol. 151, p. 111611, Nov. 2021, doi: 10.1016/j.rser.2021.111611.

[212] G. Zhao, X. Wang, M. Negnevitsky, and H. Zhang, “A review of air-cooling battery thermal management systems for electric and hybrid electric vehicles,” *J. Power Sources*, vol. 501, p. 230001, Jul. 2021, doi: 10.1016/j.jpowsour.2021.230001.

[213] L. He, H. Jing, Y. Zhang, P. Li, and Z. Gu, “Review of thermal management system for battery electric vehicle,” *J. Energy Storage*, vol. 59, p. 106443, Mar. 2023, doi: 10.1016/j.est.2022.106443.

[214] B. Gohla-Neudecker, V. S. Maiyappan, S. Juraschek, and S. Mohr, “Battery 2nd life: Presenting a benchmark stationary storage system as enabler for the global energy transition,” in *2017 6th International Conference on Clean Electrical Power (ICCEP)*, Santa Margherita Ligure, Italy: IEEE, Jun. 2017, pp. 103–109. doi: 10.1109/ICCEP.2017.8004799.

[215] S. Arora, “Selection of thermal management system for modular battery packs of electric vehicles: A review of existing and emerging technologies,” *J. Power Sources*, vol. 400, pp. 621–640, Oct. 2018, doi: 10.1016/j.jpowsour.2018.08.020.

[216] J. R. Patel and M. K. Rathod, “Recent developments in the passive and hybrid thermal management techniques of lithium-ion batteries,” *J. Power Sources*, vol. 480, p. 228820, Dec. 2020, doi: 10.1016/j.jpowsour.2020.228820.

[217] Y. Ma, H. Mou, and H. Zhao, “Cooling optimization strategy for lithium-ion batteries based on triple-step nonlinear method,” *Energy*, vol. 201, p. 117678, Jun. 2020, doi: 10.1016/j.energy.2020.117678.

[218] Y. Zhao *et al.*, “A Review on Battery Market Trends, Second-Life Reuse, and Recycling,” *Sustain. Chem.*, vol. 2, no. 1, pp. 167–205, Mar. 2021, doi: 10.3390/suschem2010011.

[219] Circular Energy Storage, “The lithium-ion battery life cycle report,” Dec. 2020.

[220] A. Devie and M. Dubarry, “Durability and Reliability of Electric Vehicle Batteries under Electric Utility Grid Operations. Part 1: Cell-to-Cell Variations and Preliminary Testing,” *Batteries*, vol. 2, no. 3, p. 28, Sep. 2016, doi: 10.3390/batteries2030028.

[221] G. Harper *et al.*, “Recycling lithium-ion batteries from electric vehicles,” *Nature*, vol. 575, no. 7781, pp. 75–86, Nov. 2019, doi: 10.1038/s41586-019-1682-5.

[222] A. Zanoletti, E. Carena, C. Ferrara, and E. Bontempi, “A Review of Lithium-Ion Battery Recycling: Technologies, Sustainability, and Open Issues,” *Batteries*, vol. 10, no. 1, p. 38, Jan. 2024, doi: 10.3390/batteries10010038.

[223] P. Li *et al.*, “Progress, challenges, and prospects of spent lithium-ion batteries recycling: A review,” *J. Energy Chem.*, vol. 89, pp. 144–171, Feb. 2024, doi: 10.1016/j.jechem.2023.10.012.

[224] Y. E. Milian, N. Jamett, C. Cruz, S. Herrera-León, and J. Chacana-Olivares, “A comprehensive review of emerging technologies for recycling spent lithium-ion batteries,” *Sci. Total Environ.*, vol. 910, p. 168543, Feb. 2024, doi: 10.1016/j.scitotenv.2023.168543.

[225] A. A. Pesaran, “Lithium-Ion Battery Technologies for Electric Vehicles: Progress and challenges,” *IEEE Electrification Mag.*, vol. 11, no. 2, pp. 35–43, Jun. 2023, doi: 10.1109/MELE.2023.3264919.

[226] L. Olsson, S. Fallahi, M. Schnurr, D. Diener, and P. Van Loon, “Circular Business Models for Extended EV Battery Life,” *Batteries*, vol. 4, no. 4, p. 57, Nov. 2018, doi: 10.3390/batteries4040057.

[227] L. Ahmadi, A. Yip, M. Fowler, S. B. Young, and R. A. Fraser, “Environmental feasibility of re-use of electric vehicle batteries,” *Sustain. Energy Technol. Assess.*, vol. 6, pp. 64–74, Jun. 2014, doi: 10.1016/j.seta.2014.01.006.

[228] P. Eleftheriadis *et al.*, “Second Life Batteries: Current Regulatory Framework, Evaluation Methods, and Economic Assessment: Reuse, refurbish, or recycle,” *IEEE Ind. Appl. Mag.*, vol. 30, no. 1, pp. 46–58, Jan. 2024, doi: 10.1109/MIAS.2023.3325091.

[229] Nova Scotia Power, “Hourly Total Net Nova Scotia Load.” Accessed: Mar. 01, 2025. [Online]. Available: https://www.nspower.ca/oasis/monthly-reports/hourly-total-net-nova-scotia-load

[230] M. Diesendorf, “The Concept of Base-Load Power,” in *Alternative Energy and Shale Gas Encyclopedia*, Hoboken, NJ: John Wiley & Sons, Inc., 2016.

[231] J. F. Manwell, J. G. McGowan, and A. L. Rogers, *Wind energy explained: theory, design and application*, 2nd ed. Chichester: Wiley, 2009.

[232] European Commission. Joint Research Centre. Institute for Energy and Transport., *Study on the state of play of energy efficiency of heat and electricity production technologies.* LU: Publications Office, 2012. Accessed: Mar. 03, 2025. [Online]. Available: https://data.europa.eu/doi/10.2790/57624

[233] B. Lian, D. Yu, C. Wang, S. Le Blond, and R. W. Dunn, “Investigation of energy storage and open cycle gas turbine for load frequency regulation,” in *2014 49th International Universities Power Engineering Conference (UPEC)*, Cluj-Napoca, Romania: IEEE, Sep. 2014, pp. 1–6. doi: 10.1109/UPEC.2014.6934664.

[234] A. Palamar, E. Pettai, and V. Beldjajev, “Control System for a Diesel Generator and UPS Based Microgrid,” *Sci. J. Riga Tech. Univ. Power Electr. Eng.*, vol. 26, no. 1, pp. 48–53, Jan. 2010, doi: 10.2478/v10144-010-0019-x.

[235] “Environmental Issues,” in *Wind Energy - The Facts*, European Wind Energy Association, 2009, pp. 372–373. Accessed: Mar. 01, 2025. [Online]. Available: https://www.wind-energy-the-facts.org/downloads.html

[236] P. Denholm, Y. Sun, and T. Mai, “An Introduction to Grid Services: Concepts, Technical Requirements, and Provision from Wind,” *Renew. Energy*, 2019, Accessed: Mar. 01, 2025. [Online]. Available: https://www.nrel.gov/docs/fy19osti/73590.pdf

[237] D. B. Harrington, “Turbine Generators,” in *Encyclopedia of Physical Science and Technology*, Elsevier, 2003, pp. 193–215. doi: 10.1016/B0-12-227410-5/00794-8.

[238] P. W. Carlin, A. S. Laxson, and E. B. Muljadi, “The History and State of the Art of Variable-Speed Wind Turbine Technology,” 2001. Accessed: Mar. 01, 2025. [Online]. Available: https://www.nrel.gov/docs/fy01osti/28607.pdf

[239] P. Denholm, T. Mai, R. Kenyon, B. Kroposki, and M. O’Malley, “Inertia and the Power Grid: A Guide Without the Spin,” National Renewable Energy Laboratory, NREL/TP-6A20-73856, 1659820, MainId:6231, May 2020. doi: 10.2172/1659820.

[240] E. Hirst and B. Kirby, “Separating and measuring the regulation and load-following ancillary services,” *Util. Policy*, vol. 8, no. 2, pp. 75–81, Jun. 1999, doi: 10.1016/S0957-1787(99)00011-9.

[241] NERC Resources Subcommittee, “Balancing And Frequency Control,” North American Electric Reliability Corporation, 2021. Accessed: Mar. 01, 2025. [Online]. Available: https://www.nerc.com/comm/RSTC_Reliability_Guidelines/Reference_Document_NERC_Balancing_and_Frequency_Control.pdf

[242] B. J. Kirby, “Frequency Regulation Basics and Trends,” Oak Ridge National Laboratory, 2004. Accessed: Mar. 01, 2025. [Online]. Available: https://info.ornl.gov/sites/publications/Files/Pub57475.pdf

[243] R. Eriksson, N. Modig, and K. Elkington, “Synthetic inertia versus fast frequency response: a definition,” *IET Renew. Power Gener.*, vol. 12, no. 5, pp. 507–514, Apr. 2018, doi: 10.1049/iet-rpg.2017.0370.

[244] A. Scott and J. MacIsaac, “Modernizing Energy: From Transition to Transformation,” Nova Scotia Clean Electricity Solutions Task Force, 2024. Accessed: Mar. 01, 2025. [Online]. Available: https://cetaskforce.ca/wp-content/uploads/2024/02/FInal-Report-February-23.pdf

[245] RMI, “The Economics of Battery Energy Storage,” Rocky Mountain Institute, Oct. 2015. Accessed: Mar. 01, 2025. [Online]. Available: https://rmi.org/wp-content/uploads/2017/03/RMI-TheEconomicsOfBatteryEnergyStorage-FullReport-FINAL.pdf

[246] AESO, “Capacity Market 101.” Accessed: Mar. 03, 2025. [Online]. Available: https://www.aeso.ca/third-party/capacity-market-101/index.html

[247] R. Madrigal, “California ISO: Overview of Market Processes,” CAISO, 2022. Accessed: Mar. 01, 2025. [Online]. Available: https://www.westerneim.com/Documents/Presentation-MarketOverview-CAISO.pdf

[248] “Overview of New England’s Wholesale Electricity Markets and Market Oversight,” ISO-NE, May 2014. Accessed: Mar. 01, 2025. [Online]. Available: https://www.iso-ne.com/pubs/spcl_rpts/2014/2014_market_overview_050614.pdf

[249] C. Hinman, “Day-Ahead Market Overview,” CAISO, 2019. Accessed: Mar. 01, 2025. [Online]. Available: https://www.caiso.com/Documents/Presentation-Existing-Day-Ahead-Market-Overview.pdf

[250] R. H. Byrne, T. A. Nguyen, D. A. Copp, R. J. Concepcion, B. R. Chalamala, and I. Gyuk, “Opportunities for Energy Storage in CAISO: Day-Ahead and Real-Time Market Arbitrage,” in *2018 International Symposium on Power Electronics, Electrical Drives, Automation and Motion (SPEEDAM)*, Amalfi: IEEE, Jun. 2018, pp. 63–68. doi: 10.1109/SPEEDAM.2018.8445408.

[251] H. Wang and B. Zhang, “Energy Storage Arbitrage in Real-Time Markets via Reinforcement Learning,” in *2018 IEEE Power & Energy Society General Meeting (PESGM)*, Portland, OR: IEEE, Aug. 2018, pp. 1–5. doi: 10.1109/PESGM.2018.8586321.

[252] S. U. Agamah and L. Ekonomou, “Peak demand shaving and load-levelling using a combination of bin packing and subset sum algorithms for electrical energy storage system scheduling,” *IET Sci. Meas. Technol.*, vol. 10, no. 5, pp. 477–484, Aug. 2016, doi: 10.1049/iet-smt.2015.0218.

[253] T. Bowen, I. Chernyakhovskiy, and P. Denholm, “Grid-Scale Battery Storage: Frequently Asked Questions,” National Renewable Energy Laboratory, 2019. Accessed: Mar. 01, 2025. [Online]. Available: https://www.nrel.gov/docs/fy19osti/74426.pdf

[254] S. Tewari and N. Mohan, “Value of NAS Energy Storage Toward Integrating Wind: Results From the Wind to Battery Project,” *IEEE Trans. Power Syst.*, vol. 28, no. 1, pp. 532–541, Feb. 2013, doi: 10.1109/TPWRS.2012.2205278.

[255] M. Uddin, M. F. Romlie, M. F. Abdullah, S. Abd Halim, A. H. Abu Bakar, and T. Chia Kwang, “A review on peak load shaving strategies,” *Renew. Sustain. Energy Rev.*, vol. 82, pp. 3323–3332, Feb. 2018, doi: 10.1016/j.rser.2017.10.056.

[256] E. Reihani, M. Motalleb, R. Ghorbani, and L. Saad Saoud, “Load peak shaving and power smoothing of a distribution grid with high renewable energy penetration,” *Renew. Energy*, vol. 86, pp. 1372–1379, Feb. 2016, doi: 10.1016/j.renene.2015.09.050.

[257] M. F. AL-Sunni, T. Bin-Mohaya, K. Alshehri, H. Saleh, and A.-W. Saif, “On Smoothing the Duck Curve: A Control Perspective,” in *2022 19th International Multi-Conference on Systems, Signals & Devices (SSD)*, Sétif, Algeria: IEEE, May 2022, pp. 1518–1522. doi: 10.1109/SSD54932.2022.9955984.

[258] M. S. Ziegler *et al.*, “Storage Requirements and Costs of Shaping Renewable Energy Toward Grid Decarbonization,” *Joule*, vol. 3, no. 9, pp. 2134–2153, Sep. 2019, doi: 10.1016/j.joule.2019.06.012.

[259] X. Li, D. Hui, and X. Lai, “Battery Energy Storage Station (BESS)-Based Smoothing Control of Photovoltaic (PV) and Wind Power Generation Fluctuations,” *IEEE Trans. Sustain. Energy*, vol. 4, no. 2, pp. 464–473, Apr. 2013, doi: 10.1109/TSTE.2013.2247428.

[260] O. Palizban and K. Kauhaniemi, “Energy storage systems in modern grids—Matrix of technologies and applications,” *J. Energy Storage*, vol. 6, pp. 248–259, May 2016, doi: 10.1016/j.est.2016.02.001.

[261] X. Luo, J. Wang, M. Dooner, and J. Clarke, “Overview of current development in electrical energy storage technologies and the application potential in power

system operation," *Appl. Energy*, vol. 137, pp. 511–536, Jan. 2015, doi: 10.1016/j.apenergy.2014.09.081.

[262] L. Meng *et al.*, "Fast Frequency Response From Energy Storage Systems—A Review of Grid Standards, Projects and Technical Issues," *IEEE Trans. Smart Grid*, vol. 11, no. 2, pp. 1566–1581, Mar. 2020, doi: 10.1109/TSG.2019.2940173.

[263] D. M. Greenwood, K. Y. Lim, C. Patsios, P. F. Lyons, Y. S. Lim, and P. C. Taylor, "Frequency response services designed for energy storage," *Appl. Energy*, vol. 203, pp. 115–127, Oct. 2017, doi: 10.1016/j.apenergy.2017.06.046.

[264] FERC, "Frequency Regulation Compensation in the Organized Wholesale Power Markets," FERC Order No. 755, Oct. 2011. Accessed: Mar. 01, 2025. [Online]. Available: https://www.ferc.gov/sites/default/files/2020-06/OrderNo.755.pdf

[265] Z. Zhao, C. Wang, and M. H. Nazari, "Revenue Analysis of Stationary and Transportable Battery Storage for Power Systems with High Penetration of Renewable Sources: A Market Participant Perspective," Oct. 15, 2021, *arXiv*: arXiv:2001.01771. doi: 10.48550/arXiv.2001.01771.

[266] M. Rezaeimozafar, R. F. D. Monaghan, E. Barrett, and M. Duffy, "A review of behind-the-meter energy storage systems in smart grids," *Renew. Sustain. Energy Rev.*, vol. 164, p. 112573, Aug. 2022, doi: 10.1016/j.rser.2022.112573.

[267] D. De Simone and L. Piegari, "Integration of Stationary Batteries for Fast Charge EV Charging Stations," *Energies*, vol. 12, no. 24, p. 4638, Dec. 2019, doi: 10.3390/en12244638.

[268] FERC, "Electric Storage Participation in Markets Operated by Regional Transmission Organizations and Independent System Operators," FERC Order No. 841, Feb. 2018. Accessed: Mar. 01, 2025. [Online]. Available: https://ferc.gov/sites/default/files/2020-06/Order-841.pdf

[269] B. P. Heard, B. W. Brook, T. M. L. Wigley, and C. J. A. Bradshaw, "Burden of proof: A comprehensive review of the feasibility of 100% renewable-electricity systems," *Renew. Sustain. Energy Rev.*, vol. 76, pp. 1122–1133, Sep. 2017, doi: 10.1016/j.rser.2017.03.114.

[270] AEMO, "Initial operation of the Hornsdale Power Reserve Battery Energy Storage System," Australian Energy Market Operator, Apr. 2018. Accessed: Mar. 01, 2025. [Online]. Available: https:// www.aemo.com.au/-/media/Files/Media_Centre/2018/Initial-operation-of-the- Hornsdale-Power-Reserve.pdf

[271] Aurecon, "Hornsdale Power Reserve: Year 2 Impact Case Study," 2020. Accessed: Mar. 01, 2025. [Online]. Available: https://www.aurecongroup.com/-/media/files/downloads-library/thought-leadership/aurecon-hornsdale-power-reserve-impact-study-2020.pdf

[272] Canadian Vehicle Manufacturers' Association and Call2Recycle, "Electric Vehicle Battery Management at End-of-Vehicle Life: A Primer for Canada," 2022. Accessed: Mar. 01, 2025. [Online]. Available: https://www.cvma.ca/wp-content/uploads/2022/11/EV-Battery-Primer-%E2%80%93-CVMA-Call2Recycle-%E2%80%93-November-25-2022.pdf

[273] Cox Automotive, "Cox Automotive Charges Forward With New EV Battery Solutions Facility in Georgia," EV Battery Solutions. Accessed: Mar. 01, 2025. [Online]. Available: https://www.coxautoinc.com/ev-battery-solutions/insights/new-ev-battery-solutions-facility-in-georgia/

[274] H. Huo, Y. Xing, M. Pecht, B. J. Züger, N. Khare, and A. Vezzini, "Safety Requirements for Transportation of Lithium Batteries," *Energies*, vol. 10, no. 6, p. 793, Jun. 2017, doi: 10.3390/en10060793.

[275] Transport Canada, "Transportation of Dangerous Goods Bulletin: Transporting Batteries," Jan. 2018. Accessed: Mar. 01, 2025. [Online]. Available: https://tc.canada.ca/sites/default/files/2024-09/tdg_bulletin_transportation_of_batteries.pdf

[276] Y. Kotak *et al.*, "End of Electric Vehicle Batteries: Reuse vs. Recycle," *Energies*, vol. 14, no. 8, p. 2217, Apr. 2021, doi: 10.3390/en14082217.

[277] M. Terkes, A. Demirci, E. Gokalp, and U. Cali, "Battery Passport for Second-Life Batteries: Potential Applications and Challenges," *IEEE Access*, vol. 12, pp. 128424–128467, 2024, doi: 10.1109/ACCESS.2024.3450790.

[278] J. C. Kelly and O. Winjobi, "Battery Second Life: A Review of Challenges and Opportunities," presented at the 33rd Electric Vehicle Symposium (EVS33) Portland, Oregon, June 14-17, 2020, 2020.

[279] F. Salek, S. Resalati, M. Babaie, P. Henshall, D. Morrey, and L. Yao, "A Review of the Technical Challenges and Solutions in Maximising the Potential Use of Second Life Batteries from Electric Vehicles," *Batteries*, vol. 10, no. 3, p. 79, Feb. 2024, doi: 10.3390/batteries10030079.

[280] M. F. Börner *et al.*, "Challenges of second-life concepts for retired electric vehicle batteries," *Cell Rep. Phys. Sci.*, vol. 3, no. 10, p. 101095, Oct. 2022, doi: 10.1016/j.xcrp.2022.101095.

[281] L. C. Casals and B. A. Garca, "Communications concerns for reused electric vehicle batteries in smart grids," *IEEE Commun. Mag.*, vol. 54, no. 9, pp. 120–125, Sep. 2016, doi: 10.1109/MCOM.2016.7565258.

[282] P. A. Christensen, W. Mrozik, and M. S. Wise, "A Study on the Safety of Second-life Batteries in Battery Energy Storage Systems," Office for Product Safety & Sandards, United Kingdom, Jan. 2023. Accessed: Mar. 01, 2025. [Online]. Available:

https://assets.publishing.service.gov.uk/media/63d91ff0e90e0773da7fdb92/safety-of-second-life-batteries-in-bess.pdf

[283] Underwriters Laboratories, “ANSI/CAN/UL 1974, Evaluation for Repurposing Batteries,” Standard for Safety, 2018.

[284] M. Resendiz, “Moment Energy First in North America to Achieve UL 1974 Certification,” Moment Energy. Accessed: Mar. 01, 2025. [Online]. Available: https://www.momentenergy.com/news-articles/moment-energy-ul-1974-certification

[285] Underwriters Laboratories, “UL Issues World’s First Certification for Repurposed EV Batteries to 4R Energy,” UL Solutions. Accessed: Mar. 01, 2025. [Online]. Available: https://www.ul.com/news/ul-issues-worlds-first-certification-repurposed-ev-batteries-4r-energy

[286] C. A. Rufino Júnior *et al.*, “Towards to Battery Digital Passport: Reviewing Regulations and Standards for Second-Life Batteries,” *Batteries*, vol. 10, no. 4, 2024, doi: 10.3390/batteries10040115.

[287] S. A. Hasib *et al.*, “A Comprehensive Review of Available Battery Datasets, RUL Prediction Approaches, and Advanced Battery Management,” *IEEE Access*, vol. 9, pp. 86166–86193, 2021, doi: 10.1109/ACCESS.2021.3089032.

[288] ReJoule, “Product Solution,” ReJoule Energy. Accessed: Mar. 01, 2025. [Online]. Available: https://rejouleenergy.com/solution

[289] N. Mukherjee and D. Strickland, “Analysis and Comparative Study of Different Converter Modes in Modular Second-Life Hybrid Battery Energy Storage Systems,” *IEEE J. Emerg. Sel. Top. Power Electron.*, vol. 4, no. 2, pp. 547–563, Jun. 2016, doi: 10.1109/JESTPE.2015.2460334.

[290] A. Hassan *et al.*, “Second-Life Batteries: A Review on Power Grid Applications, Degradation Mechanisms, and Power Electronics Interface Architectures,” *Batteries*, vol. 9, no. 12, p. 571, Nov. 2023, doi: 10.3390/batteries9120571.

[291] M. Bauer, J. Wiesmeier, and J. Lygeros, “A comparison of system architectures for high-voltage electric vehicle batteries in stationary applications,” *J. Energy Storage*, vol. 19, pp. 15–27, Oct. 2018, doi: 10.1016/j.est.2018.06.007.

[292] X. Ning, “Mixed Battery Array Energy Storage System,” M.A.Sc., Dalhousie University, Halifax, Canada, 2024.

[293] D.-I. Stroe, V. Knap, M. Swierczynski, A.-I. Stroe, and R. Teodorescu, “Operation of a Grid-Connected Lithium-Ion Battery Energy Storage System for Primary Frequency Regulation: A Battery Lifetime Perspective,” *IEEE Trans. Ind. Appl.*, vol. 53, no. 1, pp. 430–438, Jan. 2017, doi: 10.1109/TIA.2016.2616319.

[294] J. Lacap, J. W. Park, and L. Beslow, “Development and Demonstration of Microgrid System Utilizing Second-Life Electric Vehicle Batteries,” *J. Energy Storage*, vol. 41, p. 102837, Sep. 2021, doi: 10.1016/j.est.2021.102837.

[295] CSE, “Short-Term Duty Cycle Test Report: PV Firming Duty Cycle,” Report prepared for NREL by Center for Sustainable Energy, Mar. 2015. Accessed: Mar. 01, 2025. [Online]. Available: https://energycenter.org/sites/default/files/docs/nav/programs/second-life/PV-Firming-Report_04-07-2015.pdf

[296] CSE, “Final Long-Term Duty Cycle Report: Primary Frequency Response (PFR) Duty Cycle,” Report prepared for NREL by Center for Sustainable Energy, Jul. 2015. Accessed: Mar. 01, 2025. [Online]. Available: https://energycenter.org/sites/default/files/docs/nav/programs/second-life/Long-Term-Test-Report_PFR_CH1-CH4_Final_08-21-2015.pdf

[297] D. Kamath, R. Arsenault, H. C. Kim, and A. Anctil, “Economic and Environmental Feasibility of Second-Life Lithium-Ion Batteries as Fast-Charging Energy Storage,” *Environ. Sci. Technol.*, vol. 54, no. 11, pp. 6878–6887, Jun. 2020, doi: 10.1021/acs.est.9b05883.

[298] R. Li, A. Hassan, N. Gupte, W. Su, and X. Zhou, “Degradation Prediction and Cost Optimization of Second-Life Battery Used for Energy Arbitrage and Peak-Shaving in an Electric Grid,” *Energies*, vol. 16, no. 17, p. 6200, Aug. 2023, doi: 10.3390/en16176200.

[299] F. McLoughlin and M. Conlon, “Secondary Re-Use of Batteries From Electric Vehicles for Building Integrated Photo-Voltaic (BIPV) applications,” Technological University Dublin, PV CROPS Technical Report, Apr. 2015. Accessed: Mar. 01, 2025. [Online]. Available: https://arrow.tudublin.ie/context/dubenrep/article/1001/viewcontent/PV_Crops_Final_Report.pdf

[300] M. H. S. M. Haram, J. W. Lee, G. Ramasamy, E. E. Ngu, S. P. Thiagarajah, and Y. H. Lee, “Feasibility of utilising second life EV batteries: Applications, lifespan, economics, environmental impact, assessment, and challenges,” *Alex. Eng. J.*, vol. 60, no. 5, pp. 4517–4536, Oct. 2021, doi: 10.1016/j.aej.2021.03.021.

[301] J. Zhu *et al.*, “End-of-life or second-life options for retired electric vehicle batteries,” *Cell Rep. Phys. Sci.*, vol. 2, no. 8, p. 100537, Aug. 2021, doi: 10.1016/j.xcrp.2021.100537.

[302] A. Y. Ku, E. A. Kocs, Y. Fujita, A. Z. Haddad, and R. W. Gray, “Materials scarcity during the clean energy transition: Myths, challenges, and opportunities,” *MRS Energy Sustain.*, vol. 11, no. 1, pp. 173–180, Jan. 2024, doi: 10.1557/s43581-023-00077-9.

[303] J. Seika and M. Kubli, “Repurpose or recycle? Simulating end-of-life scenarios for electric vehicle batteries under the EU battery regulation,” *Sustain. Prod. Consum.*, vol. 51, pp. 644–656, Nov. 2024, doi: 10.1016/j.spc.2024.09.023.

[304] Global Battery Alliance, “A Vision for a Sustainable Battery Value Chain in 2030: Unlocking the Full Potential to Power Sustainable Development and Climate Change Mitigation,” World Economic Forum, Sep. 2019. Accessed: Mar. 01, 2025. [Online]. Available: https://www3.weforum.org/docs/WEF_A_Vision_for_a_Sustainable_Battery_Value_Chain_in_2030_Report.pdf

[305] Elsa Dominish, Sven Teske, and Nick Florin, “Responsible minerals sourcing for renewable energy,” Report prepared for Earthworks by the Institute for Sustainable Futures, University of Technology Sydney, 2019. Accessed: Mar. 01, 2025. [Online]. Available: https://earthworks.org/wp-content/uploads/2019/04/Responsible-minerals-sourcing-for-renewable-energy-MCEC_UTS_Earthworks-Report.pdf

[306] B. Faber, B. Krause, and R. Sánchez de la Sierra, “Artisanal Mining, Livelihoods, and Child Labor in the Cobalt Supply Chain of the Democratic Republic of Congo,” UC Berkeley, May 2017. Accessed: Mar. 01, 2025. [Online]. Available: https://escholarship.org/uc/item/17m9g4wm

[307] F. M. Dorn, H. Gundermann, and H. Gundermann, “Mining companies, indigenous communities, and the state: the political ecology of lithium in Chile (Salar de Atacama) and Argentina (Salar de Olaroz-Cauchari),” *J. Polit. Ecol.*, vol. 29, no. 1, May 2022, doi: 10.2458/jpe.5014.

[308] C. Church and A. Crawford, “Green Conflict Minerals: The fuels of conflict in the transition to a low-carbon economy,” International Institute for Sustainable Development, Aug. 2018. Accessed: Mar. 01, 2025. [Online]. Available: https://www.iisd.org/system/files/publications/green-conflict-minerals.pdf

[309] J.-M. Clairand, P. Guerra-Terán, X. Serrano-Guerrero, M. González-Rodríguez, and G. Escrivá-Escrivá, “Electric Vehicles for Public Transportation in Power Systems: A Review of Methodologies,” *Energies*, vol. 12, no. 16, p. 3114, Aug. 2019, doi: 10.3390/en12163114.

[310] M. Philippot *et al.*, “Environmental impact of the second life of an automotive battery: Reuse and repurpose based on ageing tests,” *J. Clean. Prod.*, vol. 366, p. 132872, Sep. 2022, doi: 10.1016/j.jclepro.2022.132872.

[311] K. Richa, C. W. Babbitt, N. G. Nenadic, and G. Gaustad, “Environmental trade-offs across cascading lithium-ion battery life cycles,” *Int. J. Life Cycle Assess.*, vol. 22, no. 1, pp. 66–81, Jan. 2017, doi: 10.1007/s11367-015-0942-3.

[312] Action Canada, “Positive Charge: Maximizing Canada’s Electric Vehicle Battery Repurposing and Recycling Ecoystem,” 2024. Accessed: Mar. 01, 2025. [Online].

Available: https://actioncanada.ca/publications/positive-charge-maximizing-canadas-electric-vehicle-battery-repurposing-and-recycling-ecosystem/

[313] G. Kostenko and A. Zaporozhets, “World experience of legislative regulation for Lithium-ion electric vehicle batteries considering their second-life application in power sector,” *Syst. Res. Energy*, vol. 2024, no. 2, pp. 97–114, May 2024, doi: 10.15407/srenergy2024.02.097.

[314] O. US EPA, “Extended Producer Responsibility Framework for Batteries.” Accessed: Mar. 01, 2025. [Online]. Available: https://www.epa.gov/infrastructure/extended-producer-responsibility-framework-batteries

[315] E. Martinez-Laserna *et al.*, “Battery second life: Hype, hope or reality? A critical review of the state of the art,” *Renew. Sustain. Energy Rev.*, vol. 93, pp. 701–718, Oct. 2018, doi: 10.1016/j.rser.2018.04.035.

[316] A. N. Patel *et al.*, “Lithium-ion battery second life: pathways, challenges and outlook,” *Front. Chem.*, vol. 12, p. 1358417, Apr. 2024, doi: 10.3389/fchem.2024.1358417.

[317] Sumitomo Corporation, “World’s First Large-Scale Power Storage System Made From Reused EV Batteries Completed in Japan.” Accessed: Mar. 01, 2025. [Online]. Available: http://www.sumitomocorp.com/en/jp//news/release/2014/group/20140207

[318] The Mobility House, “World’s largest 2nd-use battery storage goes online.” Accessed: Mar. 01, 2025. [Online]. Available: https://www.mobilityhouse.com/int_en/our-company/newsroom/article/worlds-largest-2nd-use-battery-storage-is-starting-up

[319] Connected Energy, “Battery Energy Storage Systems | Connected Energy.” Accessed: Mar. 01, 2025. [Online]. Available: https://connected-energy.co.uk/

[320] BeePlanet Factory, “BeePlanet Factory SL,” B Corporation. Accessed: Mar. 01, 2025. [Online]. Available: https://www.bcorporation.net/en-us/find-a-b-corp/company/bee-planet-factory-sl

[321] Allye Energy, “Allye Energy | Distributed energy storage.” Accessed: Mar. 01, 2025. [Online]. Available: https://www.allye.com

[322] ECO STOR, “ECO STOR | An Ecosystem For Battery Storage Systems.” Accessed: Mar. 01, 2025. [Online]. Available: https://www.eco-stor.com

[323] Zenobē, “Zenobe | Discover Zenobe.” Accessed: Mar. 01, 2025. [Online]. Available: https://www.zenobe.com/

[324] Reefilla, “Energy for tomorrow with yesterday’s batteries.” Accessed: Mar. 01, 2025. [Online]. Available: https://www.reefilla.com/en/

[325] B2U Storage Solutions, “B2U Storage Solutions.” Accessed: Mar. 01, 2025. [Online]. Available: https://www.b2uco.com

[326] RePurpose Energy, “RePurpose Energy.” Accessed: Mar. 01, 2025. [Online]. Available: https://www.repurpose.energy

[327] Smartville, “Smartville - High Value Battery Circularity.” Accessed: Mar. 01, 2025. [Online]. Available: https://smartville.io/

[328] Higher Wire Inc., “Higher Wire: ReNewed Lithium Ion Batteries Made in the USA.” Accessed: Mar. 01, 2025. [Online]. Available: https://higherwire.com/

[329] Moment Energy, “Moment Energy - Repurpose. Recharge. Reimagine.” Accessed: Mar. 01, 2025. [Online]. Available: https://www.momentenergy.com/

[330] Relectrify, “Relectrify - World leaders in battery cell-level control technology.” Accessed: Mar. 01, 2025. [Online]. Available: https://www.relectrify.com/

[331] BELECTRIC, “BELECTRIC: Solar Energy for a Green Future.” Accessed: Mar. 01, 2025. [Online]. Available: https://belectric.com/

[332] Enel X, “Technologies and Innovation for Smart Energy Solutions.” Accessed: Mar. 03, 2025. [Online]. Available: https://www.enelx.com/n-a/en

[333] TERREPOWER, “Battery Energy Storage Systems.” Accessed: Mar. 01, 2025. [Online]. Available: https://form.jotform.com/242985730039968

[334] M. Abdel-Monem, O. Hegazy, N. Omar, K. Trad, P. Van Den Bossche, and J. Van Mierlo, “Lithium-ion batteries: Comprehensive technical analysis of second-life batteries for smart grid applications,” in *2017 19th European Conference on Power Electronics and Applications (EPE’17 ECCE Europe)*, Warsaw: IEEE, Sep. 2017, p. P.1-P.16. doi: 10.23919/EPE17ECCEEurope.2017.8099385.

[335] E. Martinez-Laserna *et al.*, “Evaluation of lithium-ion battery second life performance and degradation,” in *2016 IEEE Energy Conversion Congress and Exposition (ECCE)*, Milwaukee, WI, USA: IEEE, Sep. 2016, pp. 1–7. doi: 10.1109/ECCE.2016.7855090.

[336] E. Braco, I. San Martin, A. Berrueta, P. Sanchis, and A. Ursua, “Experimental Assessment of First- and Second-Life Electric Vehicle Batteries: Performance, Capacity Dispersion, and Aging,” *IEEE Trans. Ind. Appl.*, vol. 57, no. 4, pp. 4107–4117, Jul. 2021, doi: 10.1109/TIA.2021.3075180.

[337] Y. Zhang *et al.*, “Performance assessment of retired EV battery modules for echelon use,” *Energy*, vol. 193, p. 116555, Feb. 2020, doi: 10.1016/j.energy.2019.116555.

[338] D. H. Castillo-Martínez *et al.*, “Design and On-Field Validation of an Embedded System for Monitoring Second-Life Electric Vehicle Lithium-Ion Batteries,” *Sensors*, vol. 22, no. 17, p. 6376, Aug. 2022, doi: 10.3390/s22176376.

[339] D. Conover *et al.*, “Protocol for Uniformly Measuring and Expressing the Performance of Energy Storage Systems,” Prepared by Pacific Northwest National Laboratory and Sandia National Laboratories, Apr. 2016.

[340] M. Rasheed *et al.*, “Active Reconditioning of Retired Lithium-Ion Battery Packs From Electric Vehicles for Second-Life Applications,” *IEEE J. Emerg. Sel. Top. Power Electron.*, vol. 12, no. 1, pp. 388–404, Feb. 2024, doi: 10.1109/JESTPE.2023.3325251.

[341] K. Smith and C.-Y. Wang, “Power and thermal characterization of a lithium-ion battery pack for hybrid-electric vehicles,” *J. Power Sources*, vol. 160, no. 1, pp. 662–673, Sep. 2006, doi: 10.1016/j.jpowsour.2006.01.038.

[342] C. Zhu, X. Li, L. Song, and L. Xiang, “Development of a theoretically based thermal model for lithium ion battery pack,” *J. Power Sources*, vol. 223, pp. 155–164, Feb. 2013, doi: 10.1016/j.jpowsour.2012.09.035.

[343] P. Amiribavandpour, W. Shen, D. Mu, and A. Kapoor, “An improved theoretical electrochemical-thermal modelling of lithium-ion battery packs in electric vehicles,” *J. Power Sources*, vol. 284, pp. 328–338, Jun. 2015, doi: 10.1016/j.jpowsour.2015.03.022.

[344] Y. Ye, Y. Shi, N. Cai, J. Lee, and X. He, “Electro-thermal modeling and experimental validation for lithium ion battery,” *J. Power Sources*, vol. 199, pp. 227–238, Feb. 2012, doi: 10.1016/j.jpowsour.2011.10.027.

[345] S. J. Bazinski and X. Wang, “Predicting heat generation in a lithium-ion pouch cell through thermography and the lumped capacitance model,” *J. Power Sources*, vol. 305, pp. 97–105, Feb. 2016, doi: 10.1016/j.jpowsour.2015.11.083.

[346] S. C. Chen, C. C. Wan, and Y. Y. Wang, “Thermal analysis of lithium-ion batteries,” *J. Power Sources*, vol. 140, no. 1, pp. 111–124, Jan. 2005, doi: 10.1016/j.jpowsour.2004.05.064.

[347] Z. Zhang, L. Jia, N. Zhao, and L. Yang, “Thermal modeling and cooling analysis of high-power lithium ion cells,” *J. Therm. Sci.*, vol. 20, no. 6, pp. 570–575, Dec. 2011, doi: 10.1007/s11630-011-0512-3.

[348] K. Yoo and J. Kim, “Thermal behavior of full-scale battery pack based on comprehensive heat-generation model,” *J. Power Sources*, vol. 433, p. 226715, Sep. 2019, doi: 10.1016/j.jpowsour.2019.226715.

[349] V. V. Ganesan and A. Jain, “Computationally-efficient thermal simulations of large Li-ion battery packs using submodeling technique,” *Int. J. Heat Mass Transf.*, vol. 165, p. 120616, Feb. 2021, doi: 10.1016/j.ijheatmasstransfer.2020.120616.

[350] L. Ramotar, G. L. Rohrauer, R. Filion, and K. MacDonald, “Experimental verification of a thermal equivalent circuit dynamic model on an extended range

electric vehicle battery pack," *J. Power Sources*, vol. 343, pp. 383–394, Mar. 2017, doi: 10.1016/j.jpowsour.2017.01.040.

[351] Ying Shi, K. Smith, E. Wood, and A. Pesaran, "A multi-node thermal system model for lithium-ion battery packs," in *2015 American Control Conference (ACC)*, Chicago, IL, USA: IEEE, Jul. 2015, pp. 723–727. doi: 10.1109/ACC.2015.7170819.

[352] C. White and L. G. Swan, "Pack-level performance of electric vehicle batteries in second-life electricity grid energy services," *J. Energy Storage*, vol. 57, p. 106265, Jan. 2023, doi: 10.1016/j.est.2022.106265.

[353] C. White, B. Thompson, and L. G. Swan, "Comparative performance study of electric vehicle batteries repurposed for electricity grid energy arbitrage," *Appl. Energy*, vol. 288, p. 116637, Apr. 2021, doi: 10.1016/j.apenergy.2021.116637.

[354] "Bolt EV Service Manual: Hybrid/EV System Heating and Cooling," Chevrolet, 2017.

[355] N. Omar, P. Bossche, T. Coosemans, and J. Mierlo, "Peukert Revisited—Critical Appraisal and Need for Modification for Lithium-Ion Batteries," *Energies*, vol. 6, no. 11, pp. 5625–5641, Oct. 2013, doi: 10.3390/en6115625.

[356] A. Eddahech, O. Briat, and J.-M. Vinassa, "Determination of lithium-ion battery state-of-health based on constant-voltage charge phase," *J. Power Sources*, vol. 258, pp. 218–227, Jul. 2014, doi: 10.1016/j.jpowsour.2014.02.020.

[357] C. White and L. G. Swan, "Spatial extrapolation of temperature measurements in second-life battery packs using simplified thermal network modelling," *J. Energy Storage*, vol. 112, p. 115476, Mar. 2025, doi: 10.1016/j.est.2025.115476.

[358] K. A. Woodbury, H. Najafi, F. de Monte, and J. V. Beck, "Inverse Heat Conduction Problems: An Overview," in *Inverse Heat Conduction: Ill-Posed Problems, Second Edition*, John Wiley & Sons, Inc., 2023.

[359] *Solver*. Frontline Systems, Inc, Incline Village, NV. Accessed: Mar. 01, 2025. [Online]. Available: https://www.solver.com/

[360] T. Beckwith, R. Marangoni, and J. Lienhard, "Mechanical Measurement," 6th ed., Upper Saddle River, NJ: Pearson/Prentice-Hall, 2007.

Appendix A ANALYTICAL SOLUTION FOR SETS MODEL SYSTEM EQUATIONS

Section 7.2.4 presented simplified differential heat transfer equations that can be solved analytically for the SETS model. The derivation of the analytical solution is demonstrated here for the case of T_x. The same procedure can be applied for the cases of $T_{z'}$ and T_z. The initial differential form is given in Equation A.1.

$$\frac{dT_x}{dt} = \Theta_x - \frac{T_x - T_\infty}{\tau_x} \tag{A.1}$$

The first step is to separate the variables such that all T_x terms are on the left side of the equation, as shown in Equation A.2.

$$\frac{dT_x}{dt} + \frac{1}{\tau_x} T_x = \frac{1}{\tau_x} T_\infty + \Theta_x \tag{A.2}$$

Multiplying both sides of Equation A.2 by $e^{\frac{t}{\tau_x}}$ yields Equation A.3.

$$e^{\frac{t}{\tau_x}} \frac{dT_x}{dt} + e^{\frac{t}{\tau_x}} \frac{1}{\tau_x} T_x = e^{\frac{t}{\tau_x}} \left(\frac{1}{\tau_x} T_\infty + \Theta_x \right) \tag{A.3}$$

Substituting $\frac{1}{\tau_x} e^t = \frac{d}{dt}\left(e^{\frac{t}{\tau_x}}\right)$ into Equation A.3 yields the Equation A.4.

$$e^{\frac{t}{\tau_x}} \frac{d}{dt}(T_x) + \frac{d}{dt}\left(e^{\frac{t}{\tau_x}}\right) T_x = e^{\frac{t}{\tau_x}} \left(\frac{1}{\tau_x} T_\infty + \Theta_x \right) \tag{A.4}$$

Applying the product rule to the left side of Equation A.4 yields Equation A.5.

$$\frac{d}{dt}\left(T_x e^{\frac{t}{\tau_x}} \right) = e^{\frac{t}{\tau_x}} \left(\frac{1}{\tau_x} T_\infty + \Theta_x \right) \tag{A.5}$$

Integrating both sides of Equation A.5 with respect to t yields Equation A.6.

$$T_x e^{\frac{t}{\tau_x}} - constant = \int e^{\frac{t}{\tau_x}} \left(\frac{1}{\tau_x} T_\infty + \Theta_x \right) dt \tag{A.6}$$

Isolating T_{x} on the left side of the equation yields Equation A.7.

$$T_{\mathrm{x}} = \mathrm{e}^{-\frac{t}{\tau_{\mathrm{x}}}}\left(constant + \int_0^t \mathrm{e}^{\frac{t}{\tau_{\mathrm{x}}}}\left(\frac{1}{\tau_{\mathrm{x}}}T_{\infty} + \Theta_{\mathrm{x}}\right)\mathrm{d}t\right) \tag{A.7}$$

Applying the initial condition of $T_{\mathrm{x},0}$ at $t = 0$ yields Equation A.8.

$$\begin{aligned} T_{\mathrm{x},0} &= \mathrm{e}^{0}\left(constant + \int_0^0 \mathrm{e}^{0}\left(\frac{1}{\tau_{\mathrm{x}}}T_{\infty} + \Theta_{\mathrm{x}}\right)\mathrm{d}t\right) \\ &= constant \end{aligned} \tag{A.8}$$

Substituting Equation A.8 into Equation A.7 yields Equation A.9, which is the final analytical solution.

$$T_{\mathrm{x}} = \mathrm{e}^{-\frac{t}{\tau_{\mathrm{x}}}}\left(T_{\mathrm{x},0} + \int_0^t \mathrm{e}^{\frac{t}{\tau_{\mathrm{x}}}}\left(\frac{1}{\tau_{\mathrm{x}}}T_{\infty} + \Theta_{\mathrm{x}}\right)\mathrm{d}t\right) \tag{A.9}$$

Appendix B RECURSIVE SOLUTION FOR SETS MODEL SYSTEM EQUATIONS

Section 7.2.4 presented the SETS model system equations in a discretized form which can be converted to a recursive form to reduce computational requirements. The derivation of the recursive form is demonstrated here for the case of T_{x}. The same procedure can be applied for the cases of $T_{\mathrm{z}'}$ and T_{z}. The initial discretized form is given in Equation B.1.

$$T_{\mathrm{x},j} = \mathrm{e}^{-\frac{t_j}{\tau_{\mathrm{x},j}}}\left(T_{\mathrm{x},0} + \sum_{i=1}^{j} \mathrm{e}^{\frac{t_i}{\tau_{\mathrm{x},i}}}\left(\frac{1}{\tau_{\mathrm{x},i}}T_{\infty,i} + \Theta_{\mathrm{x},i}\right)\Delta t_i\right) \tag{B.1}$$

Expressions of $T_{\mathrm{x},j}$ for the first three intervals at $j = 1$, $j = 2$, and $j = 3$ are given in Equations B.1 through B.4.

$$T_{\mathrm{x},1} = T_{\mathrm{x},0}\mathrm{e}^{\frac{-t_1}{\tau_{\mathrm{x},1}}} + \left(\frac{T_{\infty,1}}{\tau_{\mathrm{x},1}} + \Theta_{\mathrm{x},1}\right)\Delta t_1 \tag{B.2}$$

$$T_{\mathrm{x},2} = T_{\mathrm{x},0}\mathrm{e}^{\frac{-t_2}{\tau_{\mathrm{x},2}}} + \mathrm{e}^{\frac{-t_2}{\tau_{\mathrm{x},2}}}\mathrm{e}^{\frac{t_1}{\tau_{\mathrm{x},1}}}\left(\frac{T_{\infty,1}}{\tau_{\mathrm{x},1}} + \Theta_{\mathrm{x},1}\right)\Delta t_1 + \left(\frac{T_{\infty,2}}{\tau_{\mathrm{x},2}} + \Theta_{\mathrm{x},2}\right)\Delta t_2 \tag{B.3}$$

$$\begin{aligned} T_{\mathrm{x},3} = T_{\mathrm{x},0}\mathrm{e}^{\frac{-t_3}{\tau_{\mathrm{x},3}}} &+ \mathrm{e}^{\frac{-t_3}{\tau_{\mathrm{x},3}}}\mathrm{e}^{\frac{t_1}{\tau_{\mathrm{x},1}}}\left(\frac{T_{\infty,1}}{\tau_{\mathrm{x},1}} + \Theta_{\mathrm{x},1}\right)\Delta t_1 + \mathrm{e}^{\frac{-t_3}{\tau_{\mathrm{x},3}}}\mathrm{e}^{\frac{t_2}{\tau_{\mathrm{x},2}}}\left(\frac{T_{\infty,2}}{\tau_{\mathrm{x},2}} + \Theta_{\mathrm{x},2}\right)\Delta t_2 \\ &+ \left(\frac{T_{\infty,3}}{\tau_{\mathrm{x},3}} + \Theta_{\mathrm{x},3}\right)\Delta t_3 \end{aligned} \tag{B.4}$$

Multiplying both sides of Equation B.2 by $\mathrm{e}^{\frac{-t_2}{\tau_{\mathrm{x},2}}}\mathrm{e}^{\frac{t_1}{\tau_{\mathrm{x},1}}}$ yields Equation B.5.

$$T_{\mathrm{x},1}\mathrm{e}^{\frac{-t_2}{\tau_{\mathrm{x},2}}}\mathrm{e}^{\frac{t_1}{\tau_{\mathrm{x},1}}} = T_{\mathrm{x},0}\mathrm{e}^{\frac{-t_2}{\tau_{\mathrm{x},2}}} + \mathrm{e}^{\frac{-t_2}{\tau_{\mathrm{x},2}}}\mathrm{e}^{\frac{t_1}{\tau_{\mathrm{x},1}}}\left(\frac{T_{\infty,1}}{\tau_{\mathrm{x},1}} + \Theta_{\mathrm{x},1}\right)\Delta t_1 \tag{B.5}$$

Comparing Equation B.3 to Equation B.5 reveals that Equation B.3 can be restated as Equation B.6.

$$T_{\mathrm{x},2} = T_{\mathrm{x},1}\mathrm{e}^{\frac{-t_2}{\tau_{\mathrm{x},2}}}\mathrm{e}^{\frac{t_1}{\tau_{\mathrm{x},1}}} + \left(\frac{T_{\infty,2}}{\tau_{\mathrm{x},2}} + \Theta_{\mathrm{x},2}\right)\Delta t_2 \tag{B.6}$$

Multiplying both sides of Equation B.3 by $e^{\frac{-t_3}{\tau_{x,3}}}e^{\frac{t_2}{\tau_{x,2}}}$ yields Equation B.7.

$$T_{x,2}e^{\frac{-t_3}{\tau_{x,3}}}e^{\frac{t_2}{\tau_{x,2}}} = T_{x,0}e^{\frac{-t_3}{\tau_{x,3}}} + e^{\frac{-t_3}{\tau_{x,3}}}e^{\frac{t_1}{\tau_{x,1}}}\left(\frac{T_{\infty,1}}{\tau_{x,1}} + \Theta_{x,1}\right)\Delta t_1 + e^{\frac{-t_3}{\tau_{x,3}}}e^{\frac{t_2}{\tau_{x,2}}}\left(\frac{T_{\infty,2}}{\tau_{x,2}} + \Theta_{x,2}\right)\Delta t_2 \quad \text{(B.7)}$$

Comparing Equation B.4 to Equation B.7 reveals that Equation B.4 can be restated as Equation B.8.

$$T_{x,3} = T_{x,2}e^{\frac{-t_3}{\tau_{x,3}}}e^{\frac{t_2}{\tau_{x,2}}} + \left(\frac{T_{\infty,3}}{\tau_{x,3}} + \Theta_{x,3}\right)\Delta t_3 \quad \text{(B.8)}$$

Comparing Equation B.6 to Equation B.8 reveals the recursive nature of the equations. The generalized recursive form is stated in Equation B.9.

$$T_{x,i} = T_{x,i-1}e^{\frac{-t_i}{\tau_{x,i}}}e^{\frac{t_{i-1}}{\tau_{x,i-1}}} + \frac{\Delta t_i}{\tau_{x,i}}T_{\infty,i} + \Theta_{x,i}\Delta t_i \quad \text{(B.9)}$$

Due to the use of finite difference method in the computations, it must be assumed that Equation B.10 is approximately true for small Δt_i in order to make the SETS model functional.

$$e^{\frac{-t_i}{\tau_{x,i}}}e^{\frac{t_{i-1}}{\tau_{x,i-1}}} \approx e^{\frac{-t_i}{\tau_{x,i}}}e^{\frac{t_{i-1}}{\tau_{x,i}}} \approx e^{-\frac{\Delta t_i}{\tau_{x,i}}} \quad \text{(B.10)}$$

Substituting Equation B.10 into Equation B.9 yields Equation B.11, which is the final recursive form.

$$T_{x,i} = T_{x,i-1}e^{-\frac{\Delta t_i}{\tau_{x,i}}} + \frac{\Delta t_i}{\tau_{x,i}}T_{\infty,i} + \Theta_{x,i}\Delta t_i \quad \text{(B.11)}$$

Appendix C UNCERTAINTY ANALYSIS

Uncertainties in the measured currents, voltages, and temperatures depend only on the corresponding sensor accuracies described in Section 4.2.1. Uncertainties in the calculated battery energy capacities, energy efficiencies, and differential temperatures depend on multiple measurements and therefore require calculation.

For a variable $y = f(x_1, x_2, \dots, x_n)$, the uncertainty u_y in the calculated result is given by Equation C.1, based on [360].

$$u_y = \sqrt{\left(\frac{\partial y}{\partial x_1}u_1\right)^2 + \left(\frac{\partial y}{\partial x_2}u_2\right)^2 + \cdots + \left(\frac{\partial y}{\partial x_n}u_n\right)^2} \tag{C.1}$$

For battery power as a function of measured current and voltage $P = IV$, the uncertainty in the power measurement u_P can be calculated as a function of the uncertainties in the current and voltage measurements u_I and u_V as per Equation C.2

$$\begin{aligned} u_P &= \sqrt{\left(\frac{\partial P}{\partial I}u_I\right)^2 + \left(\frac{\partial P}{\partial V}u_V\right)^2} \\ &= \sqrt{(Vu_I)^2 + (Iu_V)^2} \end{aligned} \tag{C.2}$$

For constant power, the energy is given by $E = Pt$. If time measurements are assumed to be accurate, then the uncertainty in the energy calculation u_E is given by Equation C.3.

$$\begin{aligned} u_E &= \sqrt{\left(\frac{\partial E}{\partial t}u_P\right)^2 + \left(\frac{\partial E}{\partial P}u_t\right)^2} \\ &= tu_P \\ &= t\sqrt{(Vu_I)^2 + (Iu_V)^2} \end{aligned} \tag{C.3}$$

For energy efficiency as a function of discharge and charge energies $\eta = \frac{E_{\text{dis}}}{E_{\text{chg}}}$, the uncertainty in the energy efficiency calculation is given by Equation C.4.

$$
\begin{aligned}
u_\eta &= \sqrt{\left(\frac{\partial \eta}{\partial E_{\text{dis}}} u_{E_{\text{dis}}}\right)^2 + \left(\frac{\partial \eta}{\partial E_{\text{chg}}} u_{E_{\text{chg}}}\right)^2} \\
&= \sqrt{\left(\frac{1}{E_{\text{chg}}} u_{E_{\text{dis}}}\right)^2 + \left(-\frac{E_{\text{dis}}}{{E_{\text{chg}}}^2} u_{E_{\text{chg}}}\right)^2} \\
&= \sqrt{\left(\eta \frac{1}{E_{\text{dis}}} u_{E_{\text{dis}}}\right)^2 + \left(\eta \frac{1}{E_{\text{chg}}} u_{E_{\text{chg}}}\right)^2} \\
&= \eta \sqrt{\left(\frac{u_{E_{\text{dis}}}}{E_{\text{dis}}}\right)^2 + \left(\frac{u_{E_{\text{chg}}}}{E_{\text{chg}}}\right)^2}
\end{aligned}
\tag{C.4}
$$

If it can be assumed that the relative uncertainty in the energy calculation is approximately the same for both discharge and charge $\frac{u_{E_{\text{dis}}}}{E_{\text{dis}}} \approx \frac{u_{E_{\text{chg}}}}{E_{\text{chg}}}$, and that $\eta > 90$ %, then Equation C.4 can be approximated by Equation C.5.

$$
\begin{aligned}
u_\eta &\approx \eta\sqrt{2}\frac{u_{E_{\text{dis}}}}{E_{\text{dis}}} \\
&\approx 1.3\frac{u_E}{E} \\
&\approx 1.3\frac{t}{E}\sqrt{(Vu_I)^2 + (Iu_V)^2} \\
&\approx \frac{1.3}{P}\sqrt{(Vu_I)^2 + (Iu_V)^2}
\end{aligned}
\tag{C.5}
$$

The Gustav Klein power cycler used in this research project specifies the voltage and current measurement accuracies listed in Table C-1. These specifications give the absolute uncertainty in current u_I and voltage u_V.

Table C-1 Uncertainty associated with power cycler voltage and current measurements.

Parameter	Measurement Range	Measurement Accuracy	Absolute Uncertainty
Pack voltage	0 - 800 V	within 0.1 % of range	0.8 V
Pack current	± 200 A	within 0.1 % of range	0.2 A

To estimate u_E and u_η ranges for the experimental method described in Chapter 4, a nominal voltage of 360 V can be used for a typical EV battery pack. The highest uncertainty will result when the current is low compared to the rated current of the power cycler. Table C-2 shows the uncertainty results associated with 4.3 kW of battery power, which was the lowest battery power prescribed in Chapter 4. A nominal value of $\eta = 97$ % is chosen for illustrative purposes based on the high-power results in Chapter 5. The results show that the energy uncertainty is less than 2 % in relative terms, which is good. However, a 2 % uncertainty in energy efficiency is rather significant since the nominal value is 97 %.

Table C-2 Estimated uncertainty in energy and energy efficiency for a low-power test.

Parameter	Nominal Value	Absolute Uncertainty	Relative Uncertainty
Voltage (V)	360	0.80	0.22 %
Current (A)	12	0.20	1.67 %
Power (kW)	4.3	0.07	1.68 %
Time (h)	4	0.00	0.00 %
Energy (kWh)	17	0.29	1.68 %
Efficiency (%)	97	2.19	2.25 %

In contrast, Table C-3 shows the uncertainty results associated with 47 kW of battery power, which was the highest battery power prescribed in Chapter 4. A nominal value of $\eta = 92$ % is chosen for illustrative purposes based on the high-power results in Chapter 5. Both u_E and u_η are markedly lower compared to the low-power test, especially in relative terms. This shows the importance of sizing a power cycler appropriately for a given battery.

Table C-3 Estimated uncertainty in energy and energy efficiency for a high-power test.

Parameter	Nominal Value	Absolute Uncertainty	Relative Uncertainty
Voltage (V)	360	0.80	0.22 %
Current (A)	130	0.20	0.15 %
Power (kW)	47	0.13	0.27 %
Time (h)	1	0.0	0.00 %
Energy (kWh)	47	0.13	0.27 %
Efficiency (%)	92	0.35	0.38 %

For a differential temperature $\Delta T = T_1 - T_2$, the uncertainty can be calculated as a function of the uncertainties in the two temperature measurements being compared. This is shown in Equation C.6, where $u_{T_1} = u_{T_2} = u_T$ for a given temperature sensor type.

$$\begin{aligned} u_{\Delta T} &= \sqrt{\left(\frac{\partial \Delta T}{\partial T_1} u_{T_1}\right)^2 + \left(\frac{\partial \Delta T}{\partial T_2} u_{T_2}\right)^2} \\ &= \sqrt{\left(u_{T_1}\right)^2 + \left(u_{T_2}\right)^2} \\ &= u_T \sqrt{2} \end{aligned} \tag{C.6}$$

Since $u_T = 1.0$ °C for the calibrated T-type thermocouples used in this research project, Equation C.6 gives $u_{\Delta T} \approx 1.4$ °C for differential temperature calculations.

Appendix D COPYRIGHT LICENSE AGREEMENT

What follows are the rights retained by an author of an article published by Elsevier. A complete list of rights and other copyright details can be found on the Elsevier website at: https://www.elsevier.com/about/policies-and-standards/copyright

Authors' rights in the article

Re-use their article in their own new works, without permission from Elsevier or payment to Elsevier, including by:

- making copies of the article (or part of the article) to promote companies or products they own, whether or not such promotion is commercial
- including the article in a thesis or dissertation
- extending the article to a book, including the article in a subsequent compilation of their own work, or re-using portions, excerpts, and their own figures, tables and images from the article in their own new works (which in each case may be published with Elsevier or with a third party commercial or non-commercial publisher, at the author's discretion)